AN INVESTIGATION INTO THE INDUCED STATE OF STRESS AROUND INCLINED BOREHOLES UNDER NON-HYDROSTATIC STRESS CONDITIONS

BY

KENNETH WADDELL MACGREGOR, BSc (hons) Min/Pet Eng.

Thesis Presented to The University of Strathclyde

For the Degree of

Doctor of Philosophy in Engineering

DEPARTMENT OF MINERAL RESOURCES ENGINEERING

UNIVERSITY OF STRATHCLYDE

GLASGOW

SEPTEMBER 1987

"And he that will not apply

New Remedies, must expect New Evils,

For Time is the greatest Innovator"

Francis Bacon

1561 – 1626

CONTENTS

CONTENTS (Continued) Page

CHAPTER TWO
EXAMINATION OF THE INDUCED STATE OF STRESS AROUND INCLINED BOREHOLES USING THE PHOTOELASTIC TECHNIQUE OF STRESS FREEZING

CONTENTS (Continued) Page

CHAPTER THREE
THE DETERMINATION OF ROCK MECHANICAL PROPERTIES AND APPLICATION OF THE BRINELL HARDNESS TEST TO ROCK

CONTENTS (Continued) Page

CHAPTER 4
ANALYTICAL ANALYSIS OF THE STABILITY OF INCLINED BOREHOLES UNDER NON-HYDROSTATIC STRESS CONDTIONS

CHAPTER FIVE
THE DEVELOPMENT OF A LABORATORY TECHNIQUE FOR THE MEASUREMENT OF FRACTURE PERMEABILITY/CONDUCTIVITY

CONTENTS (Continued)

CONTENTS (Continued) Page

ACKNOWLEDGEMENTS

The author wishes to thank Professor G.M. Maxwell B.Sc., Ph.D., ARCST., C.Eng, FIME., for the opportunity to conduct this research and to gratefully acknowledge Mr W. Boyle, ARCST, B.Sc., C.Eng., for his supervision and guidance throughout the duration of this research. The author also wishes to express his sincere thanks to Dr. B.G.D. Smart B.Sc., Ph.D, C.Eng., MIME., for his continuous support and direction, and without whose efforts, much of this work would not have been possible. Thanks are also extended to Dr D.O.D. Davies B.Sc., Ph.D., Dip. Met. Min., FIME., FGS., for his advice on photoelasticity, to Dr J.M. Somerville B.Sc., Ph.D., for his many helpful discussions and assistance with the borehole stability work, and to Dr T.E. Vaughan M.Sc., Ph.D., FICE., MIMM., for the use of an oedometer.

The author wishes to express his gratitude to Dr P.T. Burtwistle B.Sc., Ph.D. and Mr W. McGraw B.Sc. for assistance with computing, and also Mr A. Morrison B.Sc., Mr L. Grant B.Sc. and Mr M. Craig B.Sc. for their assistance with laboratory work. The author wishes to acknowledge the SERC and Britoil plc for the research funding which made this work possible. Finally, the workshop team are gratefully acknowledged for their invaluable assistance, their humour and hospitality, and for making my stay both memorable and enjoyable. The author also wishes to recognise Mr C. McWilliams who fabricated the various specialised items of equipment detailed herein. This thesis represents only part of the useful knowledge gained and will be forgotten long before the friendship and understanding enjoyed there.

ABSTRACT

This thesis details research conducted towards investigating the state of stress around inclined boreholes with the ultimate aim of predicting borehole stability and providing realistic estimates of closure stress.

Chapter 1 discusses the factors affecting the stability of boreholes and reviews previous research conducted into borehole failure. The mechanics of hydraulic fracturing are reviewed as are methods of predicting fracture gradients. The manner in which closure stress is estimated is also critically reviewed.

Chapter 2 describes an initial investigation into the stresses around inclined boreholes using the photoelastic technique of Stress Freezing.

Chapter 3 details the laboratory determination of rock properties required for the borehole stability work detailed in Chapter 4. The applicability of the Brinell Hardness test to rock is also examined.

Chapter 4 presents a detailed analysis of borehole stability. Failure criteria are developed and applied to estimate the mud weight required to maintain the hole in an elastic condition. To investigate the post-failure stability, existing 'yield zone' equations are modified to allow the effect of rock strength, oil flow rate, in-situ stress and hole angle to be examined.

Chapter 5 describes the design and in-house manufacture of the specialised equipment required to measure fracture conductivity in the laboratory, the development of experimental procedures, the various test results and the conclusions drawn from them. Finally, the direct effect of a yield zone on the estimation of closure stress and on proppant selection is examined

Chapter 6 summarises the conclusions that may be drawn from the work detailed in this thesis. The chapter also describes possible fields of future research which have been stimulated by the work presented.

Two appendices are included, one providing a data-base of proppant properties, the other detailing the results of the application of the data-base to formation samples.

LIST OF FIGURES

Figure - CHAPTER TWO - Page

LIST OF TABLES

Table - CHAPTER FIVE - Page

CHAPTER ONE

ROCK MECHANICAL ASPECTS OF BOREHOLE INSTABILITY

1.1 INTRODUCTION

A knowledge of the stress distribution around a borehole is of great importance in several situations, such as when drilling, during production or injection, and when estimating fracturing pressures.

Problems of borehole instability cost the petroleum industry a considerable amount of lost drilling time and may contribute to the reduction in recovery from the reservoir. In particular, the problems associated with deviated boreholes will become more relevant with the future trends to develop marginal fields and also the possibility of enhanced oil recovery through horizontal penetration of the reservoir.

In hydraulic fracturing operations, a knowledge of the stress concentration or closure stress acting on the face of the fracture is essential for the determination of the optimum type of proppant for use in a specific formation.

The objective of this investigation was to examine and develop methods of predicting the stress distribution around vertical and inclined wells to enable the prediction of borehole instability, and provide realistic estimates of the closure stress acting in the immediate vicinity of the wellbore in order to optimise proppant selection.

The purpose of this chapter was to review previous work on the prediction of borehole instability, including borehole failure in

tension as well as in compression, with a view to establishing the state-of-the-art knowledge of the stress distribution around both vertical and inclined boreholes. Emphasis was given towards understanding the mechanical factors that influence rock failure and borehole stability in open holes, the prediction of borehole failure and the application of rock mechanical concepts to control borehole stability. Finally, the manner in which the closure stress is estimated was critically reviewed.

1.2 GENERAL CONSIDERATIONS OF STRESS ANALYSIS

1.2.1 Introduction

In the context of this chapter and over the course of this thesis, various references to the stress system will be made. This section was intended to clarify the terminology used in basic rock mechanical stress analysis.

Comparing the results of one reference using a 'tension positive' sign convention with another using a 'compression positive' sign convention can cause confusion. In structural work, tensile stresses are assumed to be positive, and hence the major principal stress is the maximum tensile or algebraically the minimum compressive stress. In rock mechanics, however, it is useful to assume that compressive stresses are positive as sub-surface in-situ stresses are generally compressive. Therefore, unless otherwise stated, a 'compression positive' sign convention has been used throughout the course of this investigation.

1.2.2 Specification of the Cartesian Stress Convention

In cartesian coordinates, the three mutually perpendicular axes x, y and z are used as axes of reference. A normal stress acting on a plane which is perpendicular to the x-axis and parallel to the y and z-axes is denoted by σ_x. Similarly, normal stresses σ_y and σ_z act on the xz and xy-planes respectively.

Two subscripts are required to identify a shearing stress. The first specifies the normal to the plane on which the shearing stress acts, while the second indicates the direction of the stress in the plane. Thus the symbol τ_{xy} represents a shearing stress acting in a plane normal to the x-axis and directed parallel to the y-axis.

The quantities σ_x, σ_y, σ_z, τ_{xy}, τ_{yx}, τ_{yz}, τ_{zy}, τ_{zx} and τ_{xz} are called the components of stress and their action on a small rectangular element with its edges parallel to the coordinate system are shown in Figure 1.1, with the shearing stresses shown in their positive directions. Taking moments of stress about the x-axis will yield the equilibrium condition $\tau_{zy} = \tau_{yz}$. Similarly, taking components about the y and z-axes respectively, we obtain $\tau_{zx} = \tau_{xz}$ and $\tau_{xy} = \tau_{yx}$. Therefore, only six of the nine stress components are independent quantities [1].

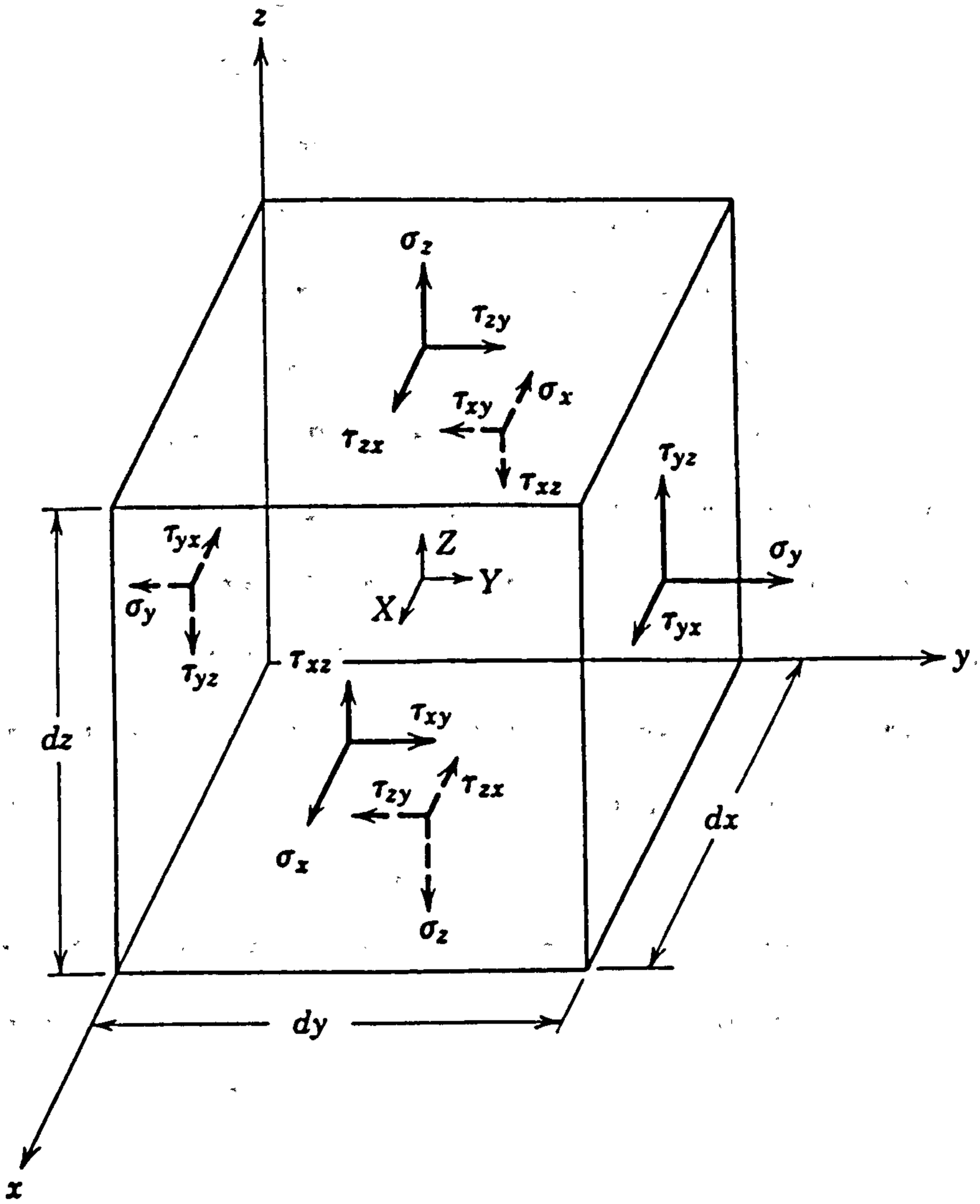

Figure 1.1 : Three-dimensional State of Stress (after Obert & Duvall [13])

1.2.3 Principal Stresses and Principal Planes of Stress.

In the three-dimensional stress system described above there are always three mutually perpendicular directions for which the normal stress components (σ_N) have stationary values. These three directions are termed the principal axes of stress and their normals are known as the principal planes of stress. As the resultant stress on a principal plane is normal, no shearing stresses act on such a plane. Hence, around any point 0, it is possible to construct a small cube, as shown in Figure 1.2(a), so orientated that the stresses on its six faces are normal. The three principal stresses are denoted by the symbols σ_1, σ_2 and σ_3, with magniudes in the order $\sigma_1 > \sigma_2 > \sigma_3$. If two of the principal stresses are equal, say $\sigma_2 = \sigma_3$, all planes perpendicular to the σ_1 plane are principal planes acted on by the stresses σ_2 and σ_3, as shown in Figure 1.2(b). In the case of where all the principal stresses are equal, as illustrated in Figure 1.2(c) every plane is a principal plane acted on by the principal stress σ_N. This state of stress, in which no shear stresses act on any plane, is termed hydrostatic.

1.2.4 Secondary Principal Planes

Rotation of the cube in Figure 1.2(a) about any of the axes, say the z axis, through an angle θ will produce changes in σ_x, σ_y and τ_{xy}. A pair of planes may be found orthogonal to each other and to the z-plane on which τ_{xy} vanishes and the normal stresses σ_x'' and σ_y'' (subscripts denote state of stress having different orientations) become one of the largest, and the other the smallest which acts on

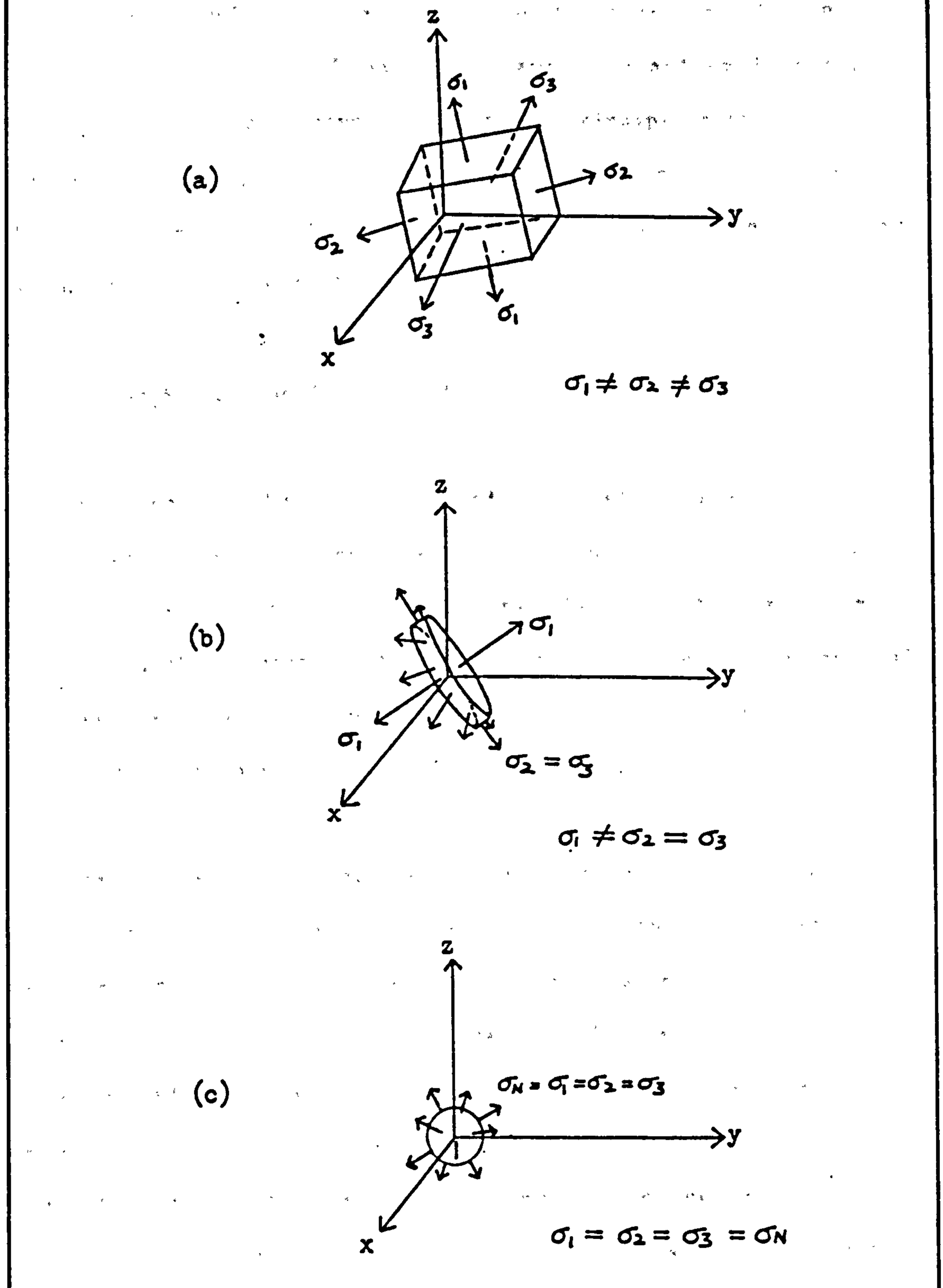

Figure 1.2 : Schematic Representation of Principal Planes Existing at a Point

the planes normal to the z-plane. These planes are not principal because shear stresses τ''_{yz} and τ''_{zx} remain to act on them and on the z-plane. They are known as 'secondary principal planes' and the stresses σ''_x and σ''_y are therefore 'secondary principal stresses'. They are of importance in the solution of three-dimensional problems by the photoelastic method.

1.2.5 Plane Stress and Plane Strain

A body is said to be in a state of plane stress when the applied forces act parallel to one plane. This condition is realised in plates uniformly loaded in their own plane. If the xy-plane is considered, the components of stress normal to the two surfaces of the plate must equal zero, i.e $\sigma_z = \tau_{xz} = \tau_{yz} = 0$ and that the stress field is characterised only by σ_x, σ_y and τ_{xy}.

A state of plane strain exists when all the particles originally in one plane in a body remain co-planer after the body is strained. While plane stress involves a two-dimensional state of stress and three-dimensional strain, plane strain involves a three-dimensional state of stress and two-dimensional strain. Plane strain is encountered in a prismatic body having one dimension much greater than the perpendicular dimensions and loaded by a uniform, transverse load along its length. Typical examples are long tunnels, dams and long cylinders loaded radially by fluid pressure. If the section under plane strain is normal to the z-axis, the stresses σ_x and σ_y in the plane of the section is related to the stress σ_z by the equation:

$$\sigma_z = \gamma\ (\sigma_x + \sigma_y) \qquad \text{.. .. .. (1.1)}$$

where γ is Poisson's ratio and has a value of 0.5 for an elastic material.

1.2.6 Polar and Cylindrical Coordinates

In many problems the geometry of the component is such that it is not practical to use cartesian coordinates. Such problems include stress analysis of curved beams, circular openings and hollow cylinders. For problems of this nature, polar coordinates r and θ are used for the case of two-dimensional analysis while cylindrical coordinates r, θ and z are used for three-dimensional analysis.

Using polar coordinates, as shown in Figure 1.3(a), the position of a point P is specified by its distance r from the origin 0 and by the angle θ, the direction OP makes with a reference direction OX. The stress components relative to this system are designated σ_r, σ_θ, and $\tau_{r\theta}$. The mathematical relationship between polar and cartesian coordinates is as indicated in the figure.

The cylindrical coordinate system involves polar coordinates in the OXY plane and a perpendicular Z coordinate, shown in Figure 1.3(b). The stress components for this system are then σ_r, σ_θ, σ_z, $\tau_{r\theta}$, $\tau_{\theta z}$ and τ_{zr}. The stress-strain relationships are similar to those in cartesian coordinates.

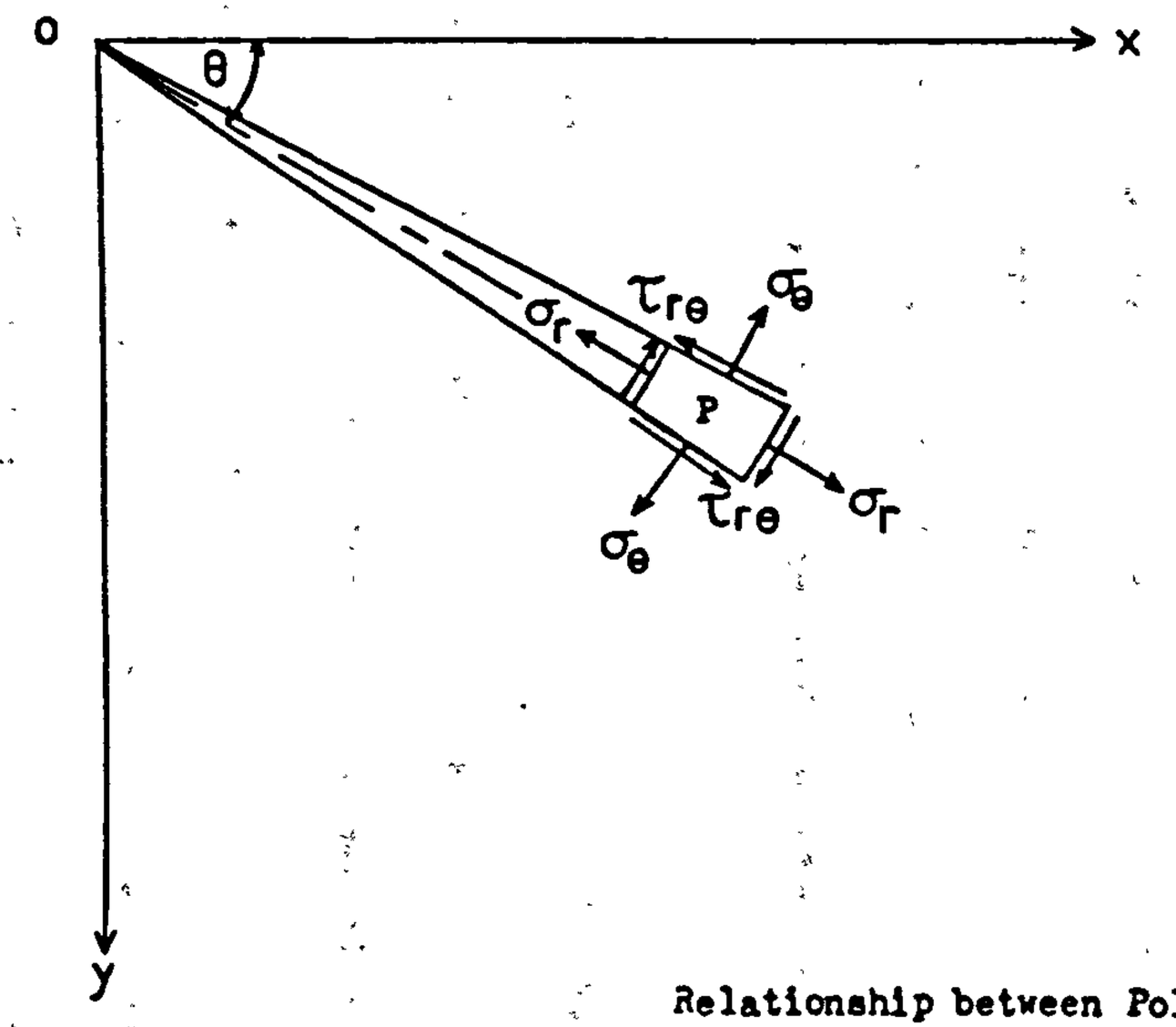

Relationship between Polar and Cartesian Coordinates

$r = OP,\ r^2 = x^2 + y^2$

$x = r \cos\theta,\ y = r \sin\theta$

$\tan\theta = y/x$

Figure 1.3(a) : Polar Coordinates

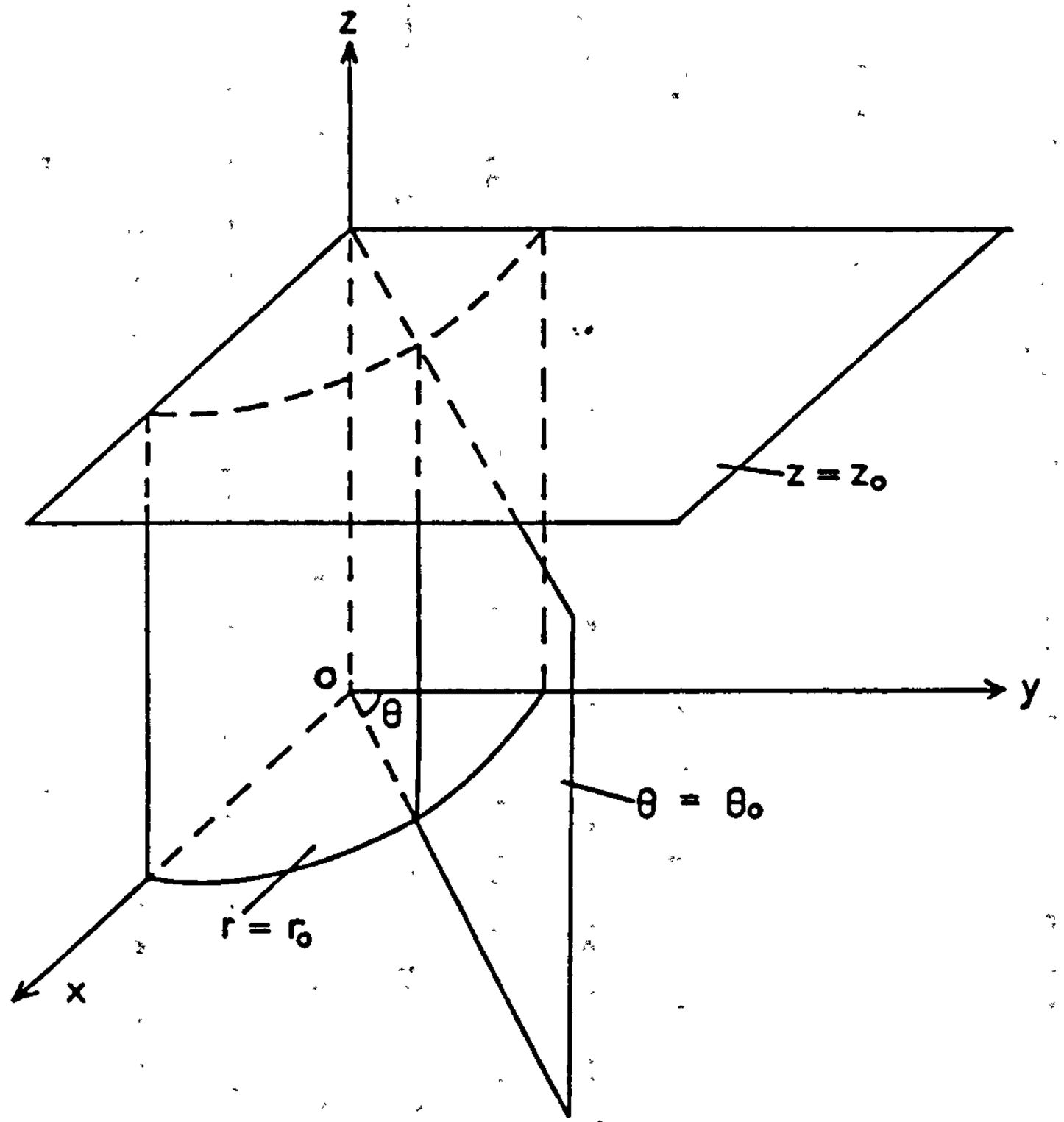

Figure 1.3(b) : Cylindrical Coordinate Planes

1.3 CONSIDERATIONS FOR THE PREDICTION OF BOREHOLE STABILITY

1.3.1 Introduction

Borehole stability can be said to be a balance between the uncontrollable factors such as earth stresses, rock strength and pore pressure, and the controllable factors such as wellbore fluid pressure and mud chemical composition. All underground rock is under a state of compressive stress due to the weight of the overlying strata and to possible stresses of tectonic origin. Any underground opening produces additional stresses in the rock surrounding the opening, and this rock will fail if the induced stresses exceed the in-situ rock strength. Thus the problem of designing a stable borehole is reduced to determining,

(1) the state of stress prior to drilling

(2) the maximum induced stress surrounding the borehole

(3) the strength of the in-situ rock.

(4) the effect of the mud on the rock strength

The magnitude and distribution of the stresses around a single underground opening in massive rock can be determined either analytically or from laboratory model studies, provided simplifying assumptions are made regarding the state of stress prior to drilling, the shape of the opening and the mechanical properties of the rock. The strength of the in-situ rock can be approximated from physical property tests of drill-core rock specimens or by applying

rock failure criteria. The purpose of this section was to review the uncontrollable factors and to introduce existing analytical solutions for the state of stress surrounding a circular opening at depth.

1.3.2 The State of Stress Prior to Drilling : In-situ Stress

1.3.2.1 Effective Stress

The concept of effective stress was introduced by Terzaghi in 1923 [2] and has subsequently been used extensively in mechanical applications. Basically, a hydrostatic stress (P_p) within a pore fluid has no influence on deformation, which is controlled by the effective stress. This 'pore' or 'reservoir' pressure is therefore a 'neutral' stress, one that acts equally in all directions. This stress is regarded to exist in both the solid and the liquid, therefore the effective stresses arise exclusively from the solid skeleton, i.e. the strata. Major studies on rock deformations by Handin et al [3], have shown that fracture is controlled by the effective stresses, provided the rocks have a connected pore system, viz.

$$\sigma_1' = \sigma_1 - P_p$$
$$\sigma_2' = \sigma_2 - P_p \qquad .. \quad .. \quad .. \quad .. \quad .. \quad (1.2)$$
$$\sigma_3' = \sigma_3 - P_p$$

To apply this concept to a subsurface environment, it must be assumed that the permeability is sufficient to allow movement of

fluid and that the pore fluid is inert, so that the effects are purely mechanical. It is therefore apparent that a reduction in fluid pressure will lead to a corresponding increase in effective pressure, and vice verse. Thus, the pressure drawdown is of major significance in the stability of a producing formation.

1.3.2.2 Theoretical Sub-surface Stress States

For estimating the actual petrophysical and mechanical properties of rock, and for many other rock mechanics problems encountered in the petroleum industry, an accurate estimate of the in-situ earth stress is desired.

It is usual to assume that the vertical stress at a given depth is equal to the overburden pressure. The overburden pressure is obtained by integrating bulk density with respect to depth [4]. viz,

$$S = \int_o^z (g\rho)\partial z \qquad .. \quad .. \quad .. \quad .. \quad .. \quad (1.3)$$

where S = Overburden pressure

g = Acceleration due to gravity

ρ = Bulk density of the overburden

z = Depth

There are two major schools of thought regarding the state of stress within the earths crust :

(a) The stress state is hydrostatic. i.e. the three principal stresses are equal.

(b) The horizontal principal stresses are a function of the effective vertical stress and Poisson's ratio.

The first hypothesis is generally termed Heim's rule [4]. It was stated in the form that the three principal stresses, in geological time, tend to become equal due to the ability of the rocks to creep. This hypothesis is generally applied to the relatively soft rocks of the coal measures [5], however, it is most often applied throughout the field of rock mechanics to simplify stress state calculations.

The second hypothesis describes the state of stress in an elastic, flat-lying stratum of semi-infinite extent that is laterally constrained and under a condition of plane strain. If the weight of the overlying strata is the only source of stress, then the following relationship is derived [4].

$$\sigma'_h = \sigma'_v \frac{\gamma}{1-\gamma} \qquad \ldots\ldots\ldots\ldots\ldots (1.4)$$

Where σ'_h and σ'_v represent the effective horizontal and vertical stress components respectively and γ is poissons ratio.

Common to both hypotheses is the assumption that one principal total stress is vertical and equal to the weight per unit area of the over- lying rocks, and that the horizontal principal stresses are equal and act only in the horizontal plane. Onshore, for well compacted sediments, the overburden gradient may be assumed to be in

the order of 1 psi/ft (22 kPa/m) [6], however, offshore the actual overburden gradient may be much less than this due to the effect of seawater and the air gap as overburden pressure is measured from the rig floor. Depending on the water depth, offshore overburden pressure gradients may be as low as 0.73 psi/ft at 5000 ft (16.5 kPa/m at 1520 m) [7].

However, the picture is never quite as simple as this. In sedimentary basins that are still undergoing compaction, the geopressure gradient varies with depth making prediction of the stress-state all the more difficult. In tectonic regions, the principal stresses are seldom orientated in the vertical and horizontal planes and take on varying quantitative values [8]. Faulting and folding of rock bears witness to the fact that the principal stresses must have at some time had different values.

1.3.2.3 Measuring In-situ Stresses

Three techniques for measuring the in-situ stress are in common use. These are :-

(1) Injection Tests

(2) Long spaced sonic logs

(3) Strain recovery methods on core samples.

Injection tests are often referred to as formation integrity or leak off tests. It comprises of perforating a short interval of the formation, isolating the zone with straddle packers and fracturing

the formation by the injection of a very small volume of fluid. The advantage of this test is that definite data is produced, however, the results may be difficult to interpret, especially in highly permeable formations [9].

Long spaced sonic logs are special logs used to measure the shear wave velocity of the rocks in conjunction with the more traditional compressional wave velocity measurement. These velocities are used to calculate a dynamic Poisson's ratio which in turn is used to calculate the horizontal stress by means of equation (1.4). There is little sound theoretical basis for the validity of the use of a dynamic elastic constant to represent geological behaviour over geological time. However, the log does offer a direct mechanical measurement of the formation and reasonable results have been found in several sand/shale reservoirs [10].

Strain recovery measurements consist of monitoring the time dependent relaxation of full diameter core immediately after its recovery at the surface. Laboratory tests are then used to measure the mechanical and thermo-mechanical properties of the core, correct the data for thermal strain, and back calculate the in-situ stresses. The method has the advantage of providing all three stresses and yields the stress orientations [11]; however, it requires full diameter core and extensive calibration and laboratory data correction.

1.3.2.4 Fluid Pressure Regimes - Reservoir Pressures

So far only hydrostatic fluid pressures have been considered. Hydrocarbon pressure regimes are different in that the densities of oil and gas are less than that of water and consequently, the pressure gradients are smaller, typical figures being :

$$\left[\frac{dp}{dD}\right]_{water} = 0.465 \text{ psi/ft } (10.5 \text{ kPa/m})$$

$$\left[\frac{dp}{dD}\right]_{oil} = 0.350 \text{ psi/ft } (7.9 \text{ kPa/m})$$

$$\left[\frac{dp}{dD}\right]_{gas} = 0.080 \text{ psi/ft } (1.8 \text{ kPa/m})$$

Abnormal reservoir pressures occur when fluids expelled by a compacting sediment cannot migrate freely to the surface [12]. This condition typically occurs in a black argillaceous series, because clays develop very low permeabilities when compacted. Such shales are said to be geopressured, or abnormally pressured. Any sand body, either embedded in, or contiguous with the shale will also be geopressured if it is isolated from the surface either by pinch-out or faulting.

Geopressures may have any value up to the total weight of the overburden, and the density of the mud must be increased accordingly to control formation fluids.

1.3.3 Stress Conditions Around Circular Underground Openings

1.3.3.1 Elastic Theory

The distribution and magnitudes of stresses around a single subsurface opening can be approximated by the mathematical theory of elasticity or from models made from elastic materials, as for example, photoelastic models. The two-dimensional 'Kirsh' solution is well known [13]. The exact solution for stresses around a horizontal circular opening in a biaxial field considering tension as positive, assuming plane strain conditions and that the horizontal stress is related to the vertical stress by the relationship $\sigma_h = m\sigma_v$, is given below :

$$\sigma_r = \left[\frac{\sigma_h + \sigma_v}{2}\right]\left[1 - \frac{a^2}{r^2}\right] + \left[\frac{\sigma_h - \sigma_v}{2}\right]\left[1 + \frac{3a^4}{r^4} - \frac{4a^2}{r^2}\right] \text{Cos } 2\theta \quad (1.5)$$

$$\sigma_\theta = \left[\frac{\sigma_h + \sigma_v}{2}\right]\left[1 - \frac{a^2}{r^2}\right] - \left[\frac{\sigma_h - \sigma_v}{2}\right]\left[1 + \frac{3a^4}{r^4}\right] \text{Cos } 2\theta \quad .. (1.6)$$

$$\tau_{r\theta} = \left[\frac{\sigma_h - \sigma_v}{2}\right]\left[1 - \frac{3a^4}{r^4} + \frac{2a^2}{r^2}\right] \text{Sin } 2\theta \quad .. \; .. \; .. (1.6)$$

where σ_h, σ_v = the horizontal and vertical stresses

σ_r, σ_θ = the radial and tangential stresses

$\tau_{r\theta}$ = the shear stress

r = the radial distance from the centre of the hole

a = radius of the borehole

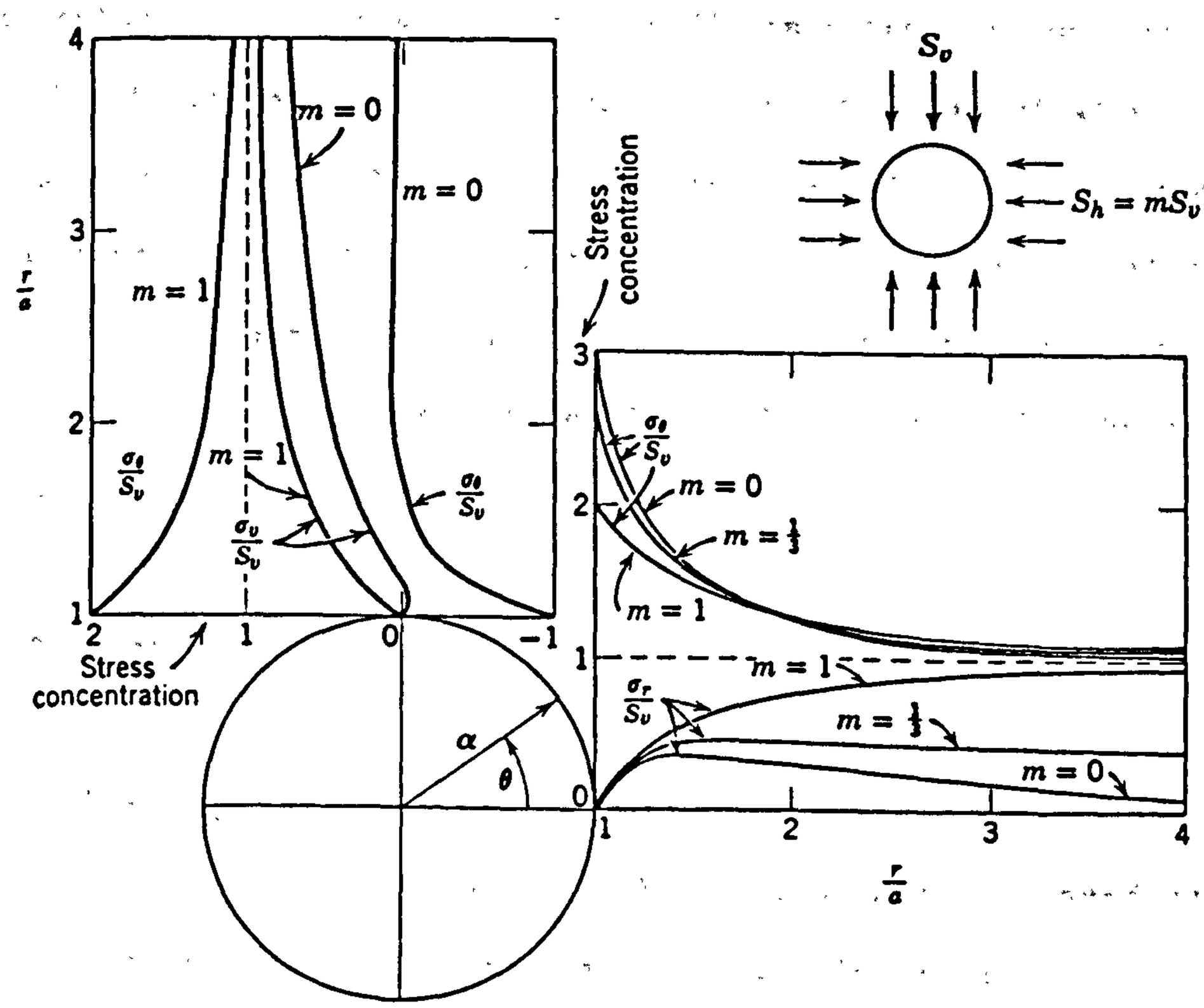

Figure 1.4 : Axial Stress Concentrations for a Circular Hole in a Biaxial Stress Field (after Obert & Duvall [13])

θ = the polar coordinate: x-axis represents $\theta = 0^{\circ}$.

These equations reveal that the stresses around the borehole are independent of the elastic constraints of the material and the radius of the hole which appears in the equations only in the dimensionless ratio a/r specifying the distance from the boundary of the hole. It can be seen from Figure 1.4 that the tangential stress σ_θ is at a maximum at the boundary of the hole and decreases rapidly with distance from the periphery. The radial stress σ_r at the borehole wall is equal to zero, but changes rapidly so that at a/r > 4, σ_r is approximately equal to the applied stress in the same direction.

1.3.3.2 Elastoplastic Theory

In the same way that the initial problem of stress redistribution around a circular opening was approached by considering a perfectly elastic host rock, the problem of a failed or yielded region around the opening can be studied by considering the host rock to be perfectly elastoplastic. Perfectly elastoplastic material, also called the St. Venant material, is perfectly elastic for stress less than σ, and perfectly plastic for stress greater than σ [Figure 1.5(a)], undergoing permanent irrecoverable strain at that stress. Therefore, elastoplastic material is an idealisation of the two forms of the behaviour of the rock mass surrounding circular openings at depth.

The elastoplastic solution is, however, more complex than the perfectly elastic solution and accordingly further simplifying assumptions are necessary, the foremost being the assumption of hydrostatic conditions. The following solution, although intended to represent a horizontal tunnel at depth, may be applied to examine the induced plastic stresses around a borehole in a hydrostatic stress field. The complete mathematical solution for the stresses around a cylindrical opening in an elastoplastic material is [13]:

(i) $r_o < r < \bar{r}$: Stress solution for the plastic zone

$$\bar{\sigma}_r = 2\ a\ q\ \ln\left[\frac{r}{r_o}\right] \qquad .. \quad .. \quad .. \quad .. \quad (1.7)$$

$$\bar{\sigma}_\theta = 2\ a\ q\ \ 1 + \ln\left[\frac{r}{r_o}\right] \qquad .. \quad .. \quad .. \quad .. \quad (1.8)$$

$$\bar{\sigma}_z = a\ q\ \ 1 + 2\ \ln\left[\frac{r}{r_o}\right] \qquad .. \quad .. \quad .. \quad .. \quad (1.9)$$

(ii) $\bar{r} < r$: Stress solution in the elastic zone

$$\sigma_r = q\ \ 1 - \left[\frac{a r_o^2}{r^2}\right] e^{(1-a)/a} \qquad .. \quad .. \quad .. \quad .. \quad (1.10)$$

$$\sigma_\theta = q\ \ 1 + \left[\frac{a r_o^2}{r^2}\right] e^{(1-a)/a} \qquad .. \quad .. \quad .. \quad .. \quad (1.11)$$

$$\sigma_z = 2\ \gamma q \qquad .. \quad .. \quad .. \quad .. \quad (1.12)$$

$$\bar{r} = r_o\ e^{(1-a)/2a} \qquad .. \quad .. \quad .. \quad .. \quad (1.13)$$

where $\bar{\sigma}_r$, σ_r = Radial stress in the plastic and elastic zone

$\bar{\sigma}_\theta$, σ_θ = Tangential stress in the plastic and elastic zone

$\bar{\sigma}_z$, σ_z = Axial stresses in the elastic and plastic zones

γ = Poisson's ratio of the material in its elastic state

q = The applied hydrostatic stress

r_0 = The radius of the opening

$\bar{r}$ = Radius of plastic zone

r = The radius at the point of interest

and $a = A/q$

where $\sigma_\theta - \sigma_r = 2A$ is the criterion for yield in the elastoplastic material

and $\bar{\sigma}_\theta - \bar{\sigma}_r = 2A$ in the plastic region

A graph illustrating the stress concentrations for the elastoplastic solution is shown in Figure 1.5(b) together with the elastic solution. It can be seen that the maximum tangential stress is closest to the boundary of the opening for elastic material and moves away from the opening as the strength of the elastoplastic material decreases.

1.3.4 Failure Criteria

1.3.4.1 Failure Criteria and the Failure Process

The set of principal stress values at which rock failure occurs can be represented by a point in the stress space and the totality of these points describes the failure surface. The form of the failure surface is empirical and may be defined by observing rock failure

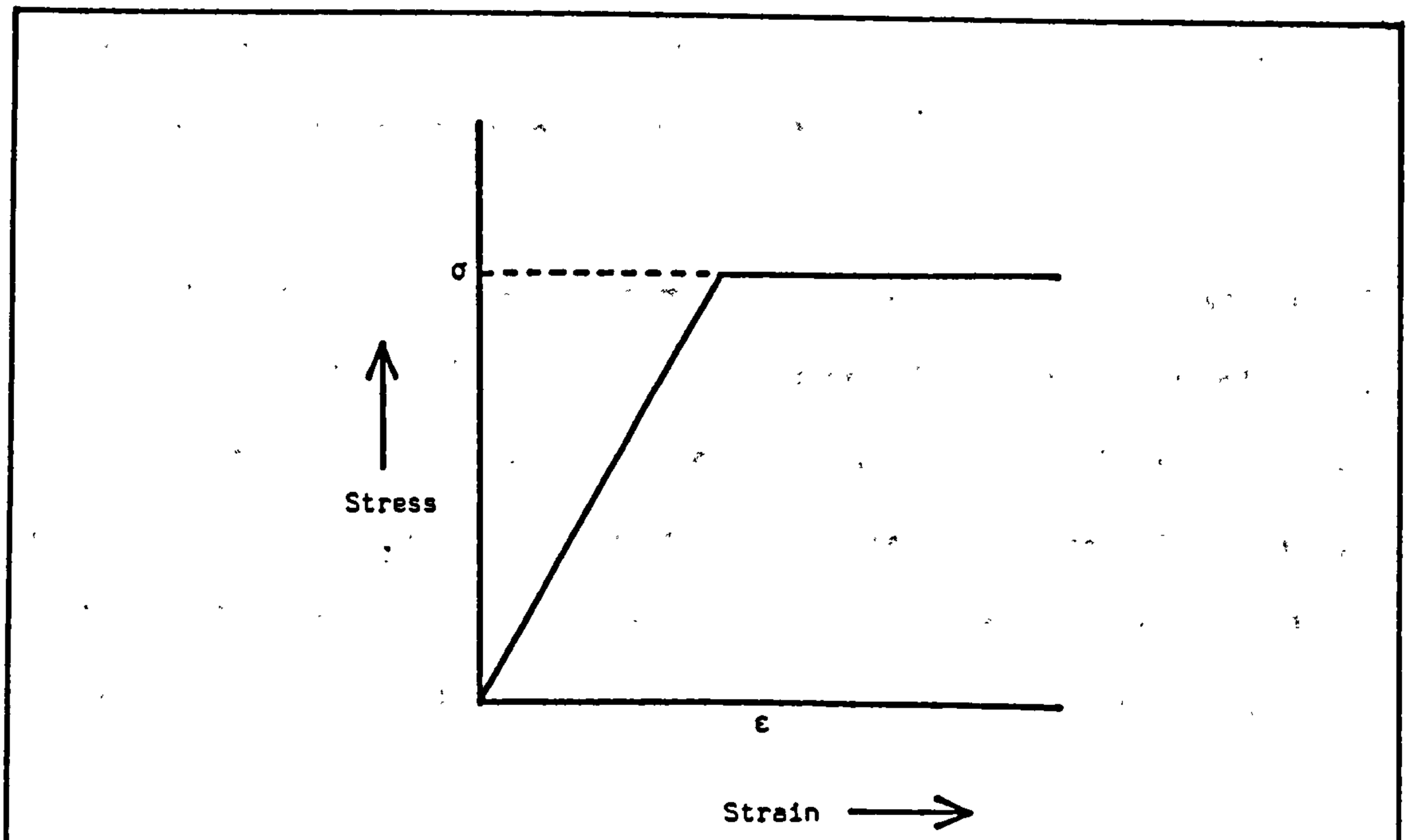

Figure 1.5(a) : Stress-Strain Behaviour of St Venant Material (after Obert & Duvall [13])

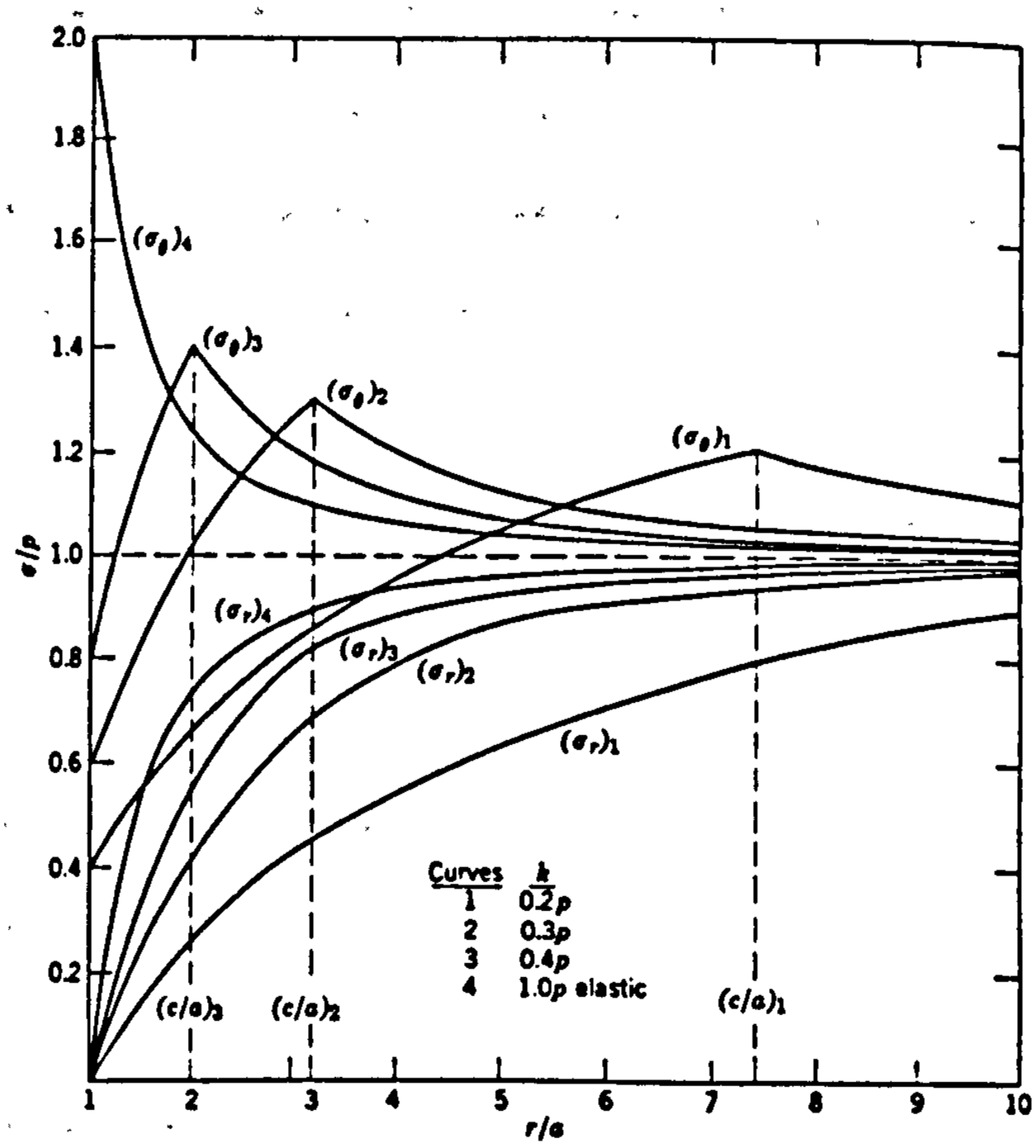

Figure 1.5(b) : Stress Distribution around a Cylindrical Tunnel in Elastoplastic Rock (after Obert & Duvall [13])

under various stress conditions. The attributes of the failure surface for rocks have been summarised by Franklin [14].

Failure is a process by which a material changes from one state of behaviour to another. The principal types of failure are elastic, yield or plastic failure, fracture and rupture. A failure criterion is an algegraic expression used to describe the form of a failure surface. The main functions of such a criterion are to allow strength prediction for structural design and rock classification according to strength.

A criterion describing a failure surface would necessarily be three-dimensional, a function of σ_1, σ_2 and σ_3. In practice, however, most criteria are restricted to defining a two-dimensional curve in the failure surface intersecting a rendulic plane, e.g. $\sigma_2 = \sigma_3$. A further attribute of the failure surface is commonly assumed, namely that strength is independent of the intermediate strength. This assumption enables the complete strength surface to be constructed, for an isotropic material, once the triaxial strength surface has been defined.

Distinction must be made between a failure criterion and a failure mechanism, which describes the processes leading to failure. Preferably, a failure criterion should be based on a knowledge of the failure mechanism, but this is not always the case. Various failure criteria have been proposed on both theoretical and empirical grounds. Those which have proved to be reasonably valid for rock are summarised below.

1.3.4.2 The Coulomb Criterion

The simplist and most important criterion was introduced in 1773 by Coulomb [15] and postulated that the shear stress tending to cause failure across a plane is resisted by the cohesion of the material and by a constant multiplied by the normal stress across the plane. Thus, the criterion for shear failure in a plane is,

$$\tau = S_0 + \mu\sigma \qquad .. \quad .. \quad .. \quad .. \quad .. \quad (1.15)$$

where σ and τ are the normal and shear stresses across the plane, S_0 is a constant which may be regarded as the cohesion or inherent shear strength of the material, and μ is the internal angle of friction.

1.3.4.3 Mohr's Hypothesis

According to Mohr's hypothesis [16], the basic elements of the shear strength of a rock were cohesion and internal friction. He proposed that at failure the relationship between the normal and shear stresses on the failure plane was as follows:

$$\tau = f(\sigma) \qquad .. \quad .. \quad .. \quad .. \quad .. \quad (1.16)$$

This functional relationship is determined experimentally as an envelope to Mohr's circles for various values of maximum and minimum principal stresses at failure. Mohr's hypothesis is therefore a

graphical method of determining the limits of failure. Rock subjected to the stress relationship represented by a circle tangent to the envelope will fail along the plane at an angle ϕ to the direction of maximum principal stress (Figure 1.6).

For the special case when the envelope is a straight line, the Coulomb and Mohr criteria are identical, viz.

$$\frac{(\sigma_1 - \sigma_3)}{2} = \frac{(\sigma_1 + \sigma_3)}{2} \text{Sin } \alpha + S_0 \text{ Cos } \alpha \quad .. \quad .. \quad .. \quad (1.17)$$

One disadvantage of the Mohr approach is that it does not predict failure of brittle material in tension. In addition, it recognises only the maximum and minimum principal stresses while neglecting the effect of the mean stress.

1.3.4.4 Griffith's Theory of Brittle Strength

Griffith's theory [17], postulates that in a two-dimensional stress field, rock fracture is initiated due stress concentrations induced at the boundaries of microscopic, randomly orientated elliptical cracks associated with grain boundaries. This theory has been substantiated by experimental work on glass and states that if $\sigma_1 + 3\sigma_3 < 0$, fracture will be initiated when the minor principal stress equals the uniaxial tensile strength (T_0) of the material, i.e $\sigma_3 = - T_0$ at an angle $\theta = 0$. If $\sigma_1 + 3\sigma_3 > 0$, fracture will be initiated when,

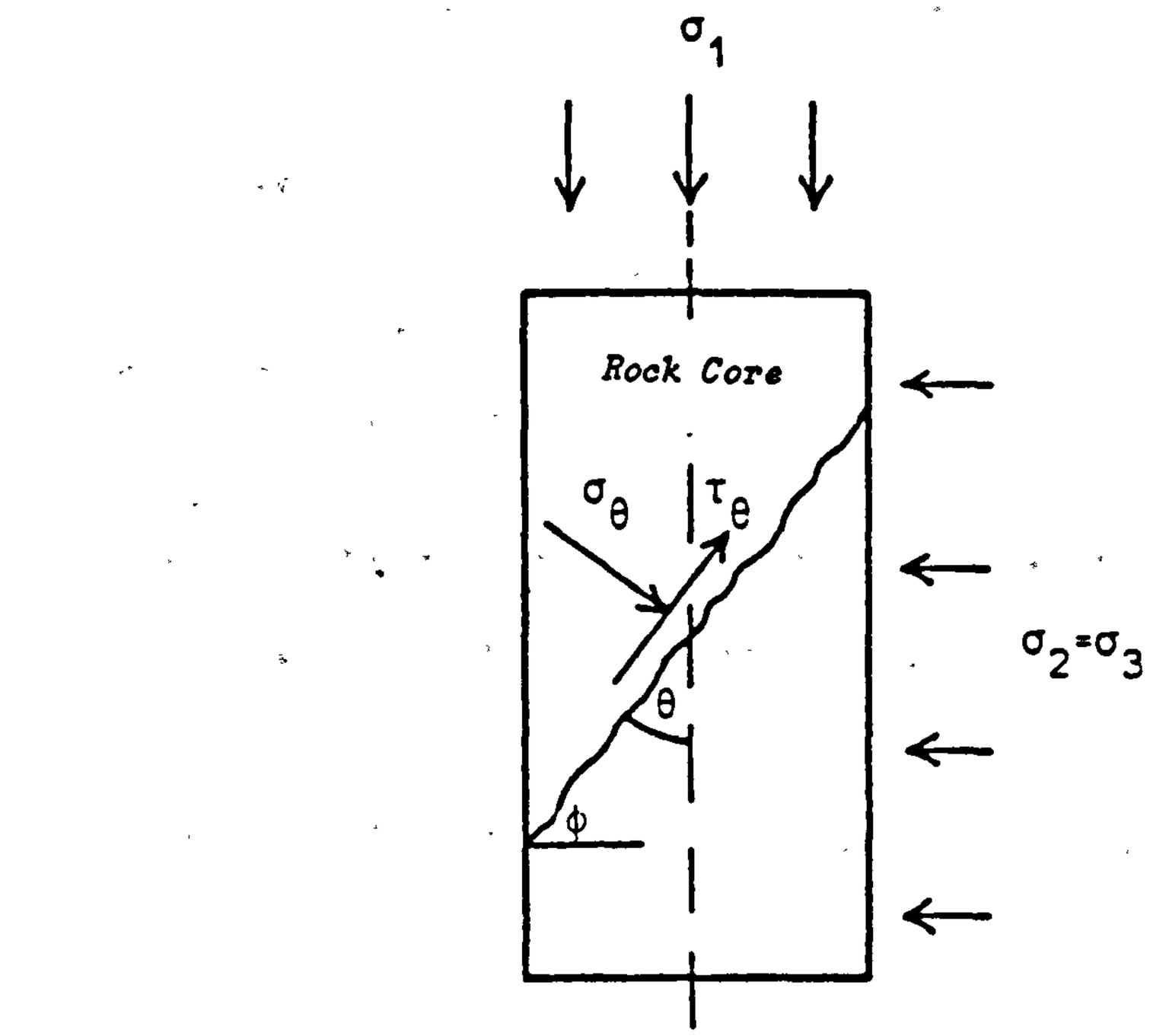

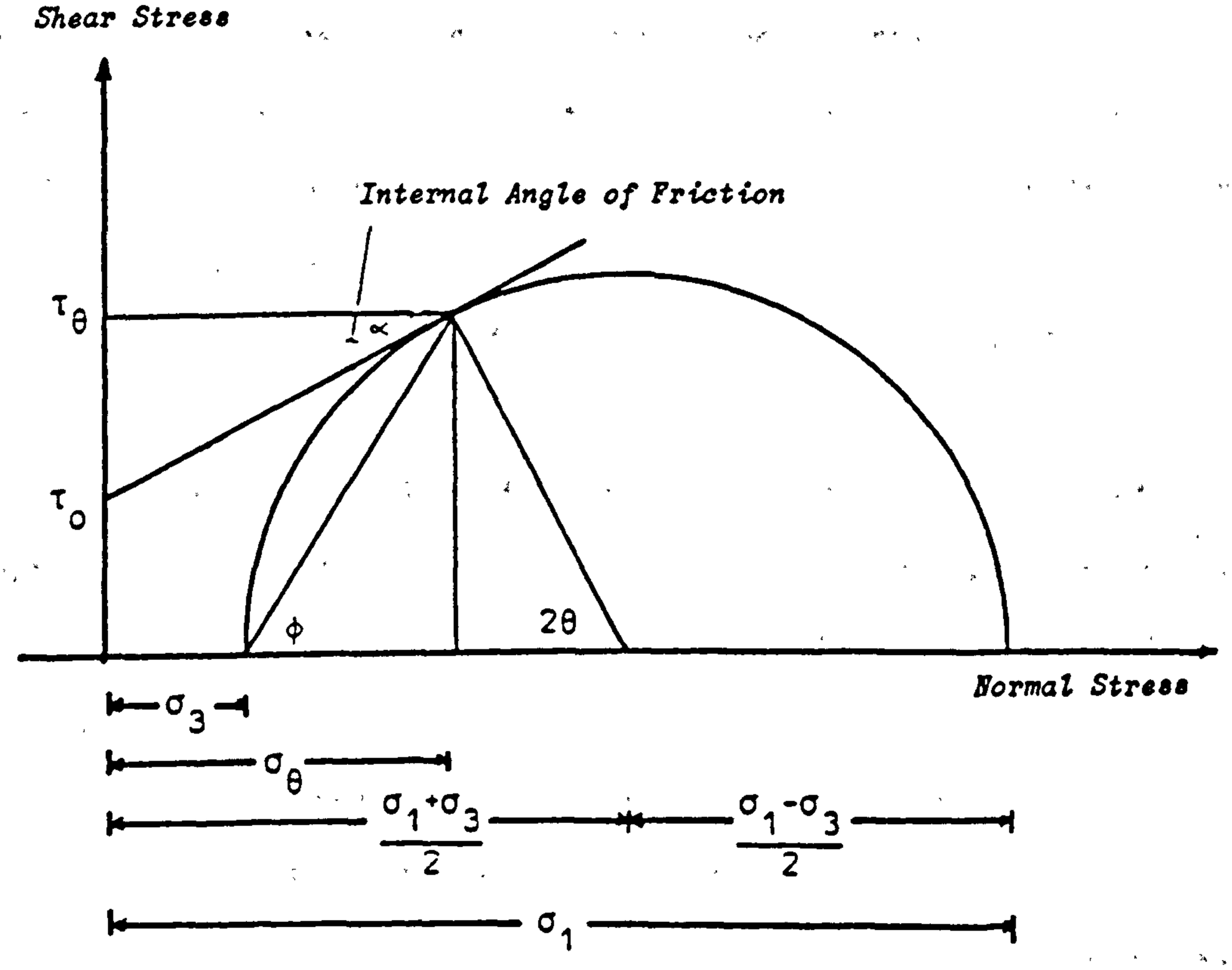

Figure 1.6 : Stress Relations at Failure - Mohr's Hypothesis

$$(\sigma_1 - \sigma_3)^2 = -8T_0(\sigma_1 + \sigma_3) \qquad .. \quad .. \quad .. \quad .. \quad .. \quad (1.18)$$

at an angle given by,

$$\text{Cos } 2\theta = \frac{1}{2}\left[\frac{\sigma_1 - \sigma_3}{\sigma_1 + \sigma_3}\right] \qquad .. \quad .. \quad .. \quad .. \quad .. \quad (1.19)$$

By combining the above equations, a failure equation can be obtained for comparison with the Mohr/Coulomb strength criterion:

$$\tau_f = 2\left[T_0\sigma + T_0^2\right] \qquad .. \quad .. \quad .. \quad .. \quad .. \quad (1.20)$$

The two-dimensional Griffith failure criterion is plotted in Figure 1.7(a). The envelope is curved and is seen to indicate a much lower tensile strength than would be deduced from a linear envelope; it is consequently more in accordance with experience. In addition, the envelope on the compressive side of the origin has a decreasing gradient, starting at 45° to the y-axis. This is also in general agreement with the results of triaxial testing of rocks [18].

The theory leading to the Griffith criterion neglects the fact that cracks may be expected to close under sufficiently high compressive stress. If they do close, it may be expected that frictional forces operate between the closed surfaces. A modification to take this into account has been proposed by Mclintock and Walsh [19] and is referred to as the Modified Griffith's Theory. In which, after allowing for a transition period and after all the cracks have closed, the theory becomes identical to the Coulomb theory, which gives a linear stress-strain curve and therefore a linear Mohr

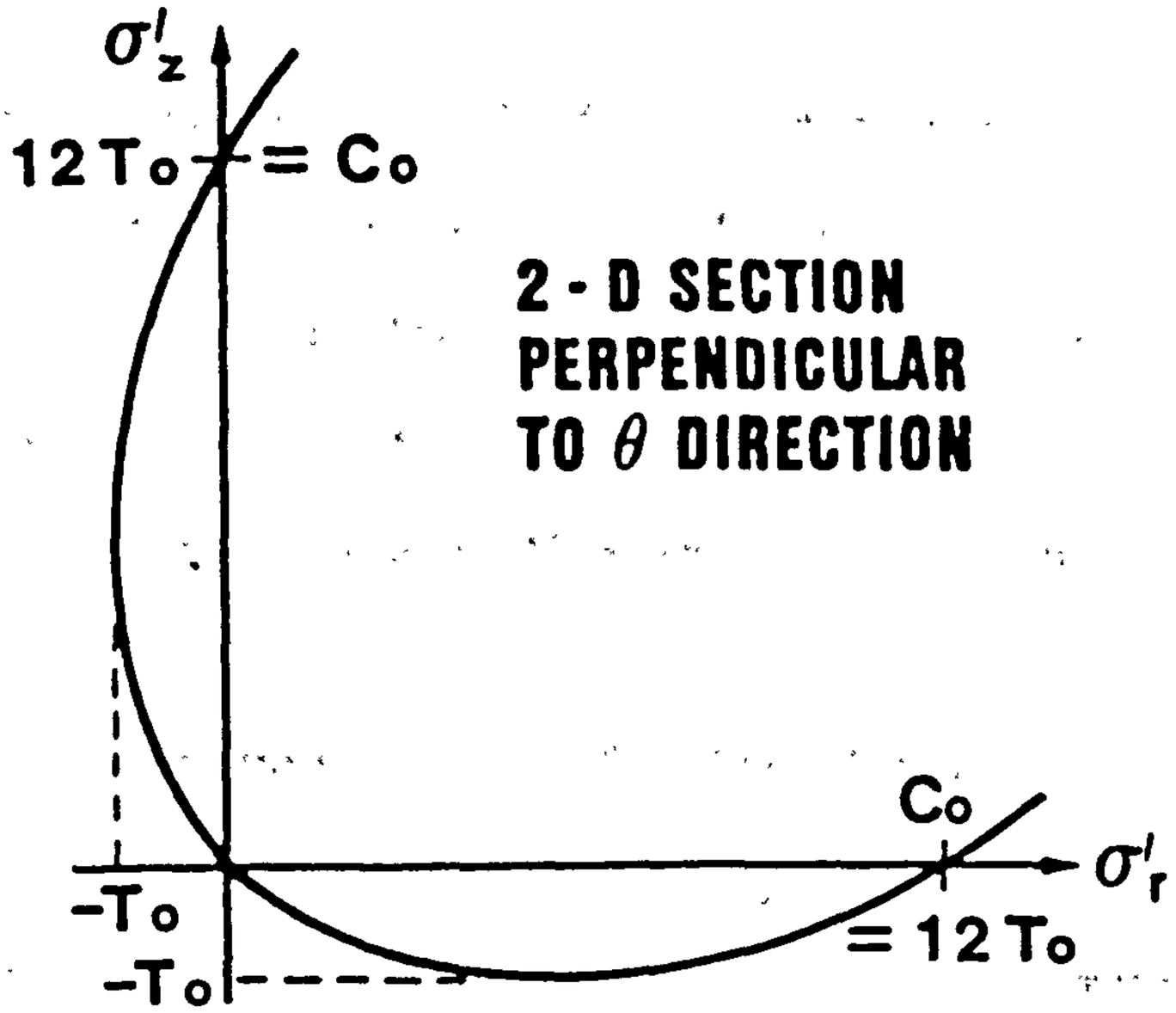

Figure 1.7(a) : Two-dimensional Griffith Envelope [41]

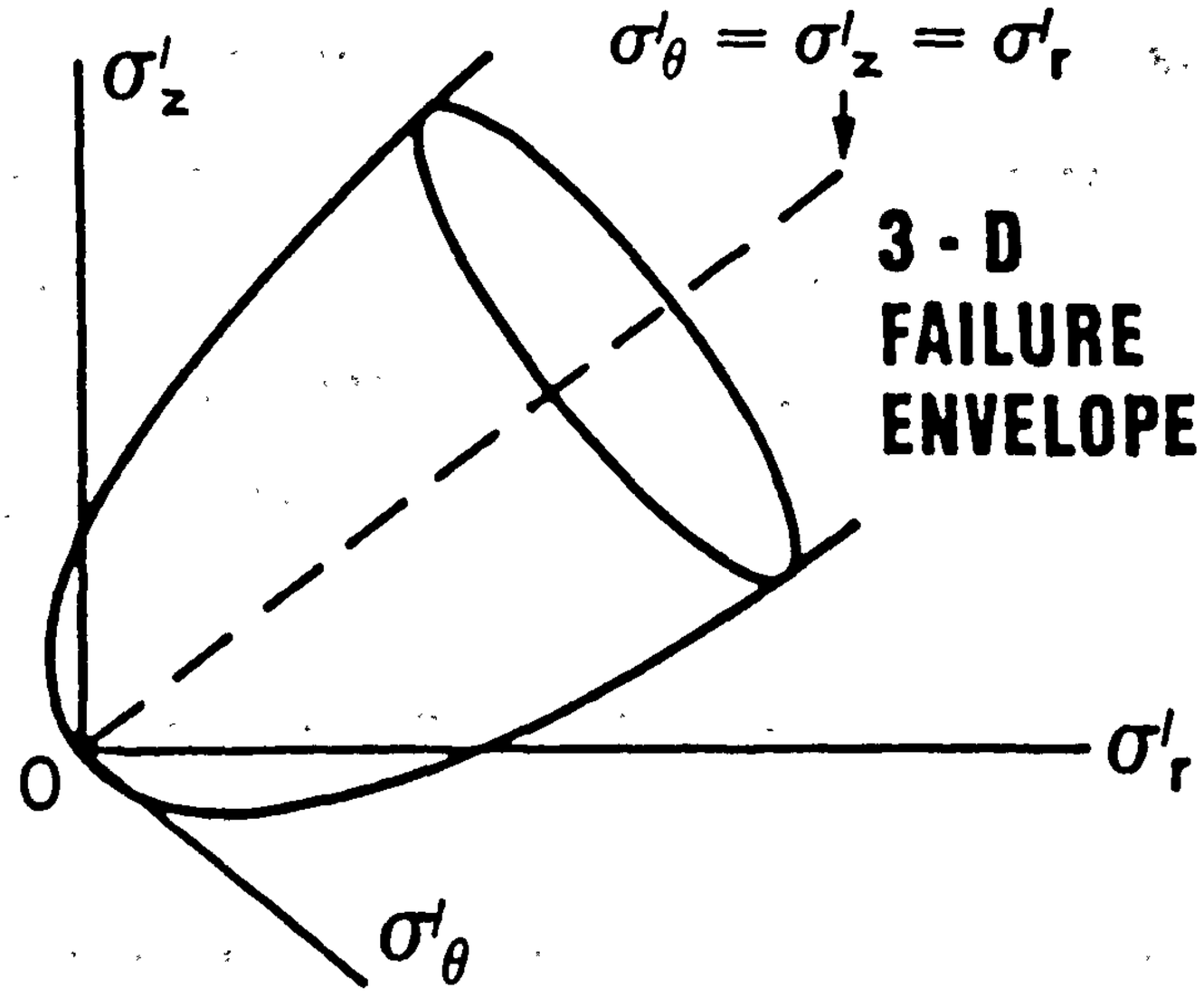

Figure 1.7(b) : Three-dimensional Griffith Envelope [41]

envelope.

Both the original and modified Griffith theories are two-dimensional as they are derived from the study of flat elliptical cracks. A true three-dimensional generalisation would require a complete study of ellipsoidal cracks, and as this has not yet been given, Murrel [20], proposed a logical extension of this theory into three-dimensions.

1.3.4.5 Murrell's Extension to the Griffith Theory

The Griffith failure envelope extended to three-dimensions may be defined as [20],

$$(\sigma_2-\sigma_3)^2 + (\sigma_3-\sigma_1)^2 + (\sigma_1-\sigma_2)^2 = 24T_0(\sigma_1+\sigma_2+\sigma_3) \quad .. \quad .. (1.21)$$

The mathematical properties of this criteria are such that if two of the three stresses are set to zero, the third stress, being at the crucial condition, must be equal to the uniaxial compressive strength C_0, thus $C_0 = 12T_0$. Knowing C_0, the three-dimensional failure envelope is fully defined (Figure 1.7(b)).

1.3.4.6 The Octahedral Shear Stress Theory

This theory, empirically derived by Nadai [21], is explained as a limiting state of mechanical strength. Given that the principal stresses acting on an element are σ_1, σ_2 and σ_3, it is possible to define two quantities, the mean and the octahedral shear stress, viz.

$$\sigma_{oct} = 1/3(\sigma_1 + \sigma_2 + \sigma_3) \quad .. \quad .. \quad .. \quad .. \quad (1.22)$$

$$\tau_{oct} = 1/3\ (\sigma_1 - \sigma_2)^2 + (\sigma_1 - \sigma_3)^2 + (\sigma_2 - \sigma_3)^2 \quad .. \quad (1.23)$$

The mean octahedral stress (σ_{oct}) is a measure of the tension or compression that the element is undergoing, while the octahedral shear stress (τ_{oct}) is a measure of the deformation stress to which the element is subjected. These two quantities have also a geometric significance - they represent the normal and shear stress acting on a surface whose normal makes the same angle with the direction of the three principal stresses.

The Octahedral Shear Stress theory therefore assumes that the octahedral shear stress at the limit of yielding is a function of the octahedral normal stress. Further, the octahedral normal stress is the mean of the three principal stresses, which implies that the intermediate principal stress has an influence on failure.

1.3.4.7 Discussion of Failure Criteria

The Coulomb and Mohr criteria provide empirical relationships between the applied stress at failure. Griffith's criterion provides an internal mechanism and a mathematical model which relates the stress relationship at fracture to the fundamental physical properties of the material. As these properties are difficult to determine, an empirical approach is adopted by evaluating the criterion in terms of compressive strength and the coefficient of

internal friction.

Simple strength criteria rarely provide a close fit over the complete failure surface. Of the above criteria, only Griffiths criterion can be validly extrapolated into the tensile quadrant. This is because the Coulomb and Mohr criteria assume failure occurs in shear whereas, in a tensile stress field, tensile failure occurs prior to shear failure. It has been suggested that different failure criteria should be applied at different stress levels [22]. This approach may be justified by the fact that different mechanisms operate depending on the region of the stress space in which failure occurs.

The foregoing criteria describe the upper limit of rock strength; however, once peak strength has been exceeded, the rock retains a load bearing ability. This residual strength is characterised by the fall in strength reaching asymtotic values. Rock strengths in situ will develop between these upper and lower limits depending on the stress field and the extent to which the rock has failed.

1.4 CAUSES AND TYPES OF BOREHOLE FAILURE

1.4.1 Criteria for Borehole Stability

From the above analysis, when a hole is drilled into a sub-surface rock the horizontal stresses are relieved, the load is transferred to the circumference of the hole as a hoop stress and the borehole contracts until the radial stress at its walls equals the pressure

acting within the borehole (Figure 1.8). If the strain so caused does not reach the elastic limit of the rock, the reduction in hole diameter will be negligible. If the strain exceeds the elastic limit, the resulting deformation will be plastic because of the high confining stresses prevailing at great depths. A ring of plastically deformed rock therefore forms around the borehole. The radius of the borehole decreases and the outer radius of the plastic zone increases until the radial stress at the borehole walls becomes equal to the borehole pressure. The extent of the plastic zone depends on the ductility and the cohesive strength of the rock, the stress distribution in both the plastic and elastic zones, production rate and borehole inclination.

If the ultimate strain is not exceeded, the hole is then stable. If, however, the ultimate strain is exceeded before the required width of the plastic zone is reached, the borehole will collapse.

In order to prevent the rock from failing, the pressure in the wellbore is raised by increasing the weight of the drilling fluid and adding filtrate control to enable the wellbore to carry a proportion of the stress concentration acting on the well. Increasing the mud weight too far, however, may result in formation fracturing in tension causing lost circulation. Therefore, a balance is required in the mud weight to prevent hole collapse without accidentally fracturing the formation.

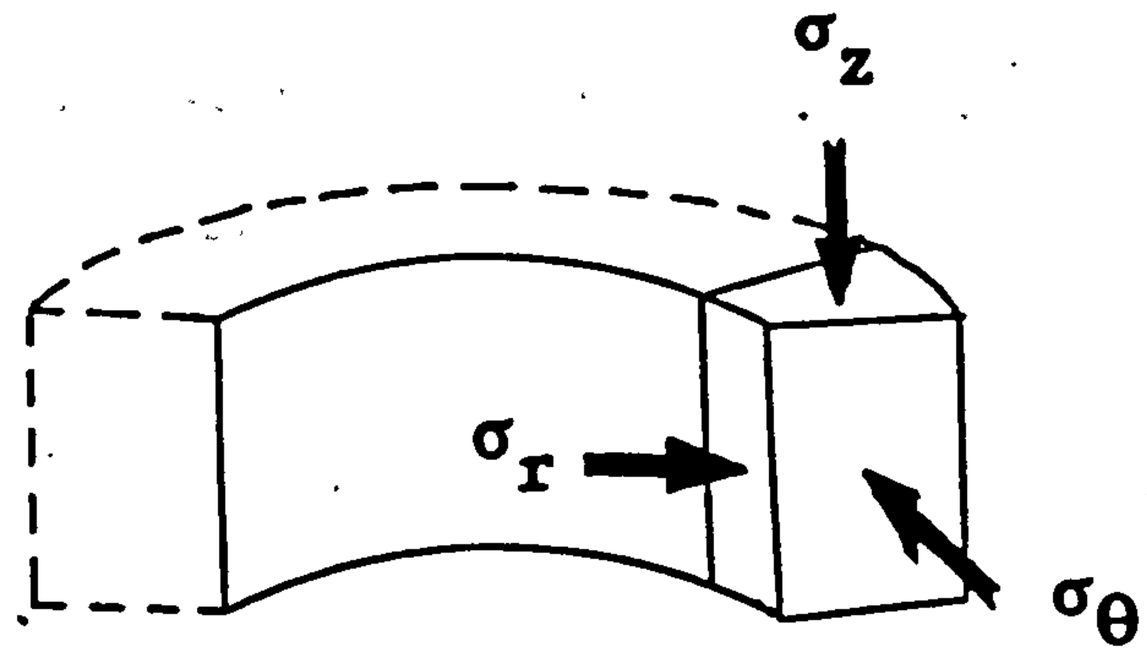

STATE OF STRESS ACTING ON A BOREHOLE WALL

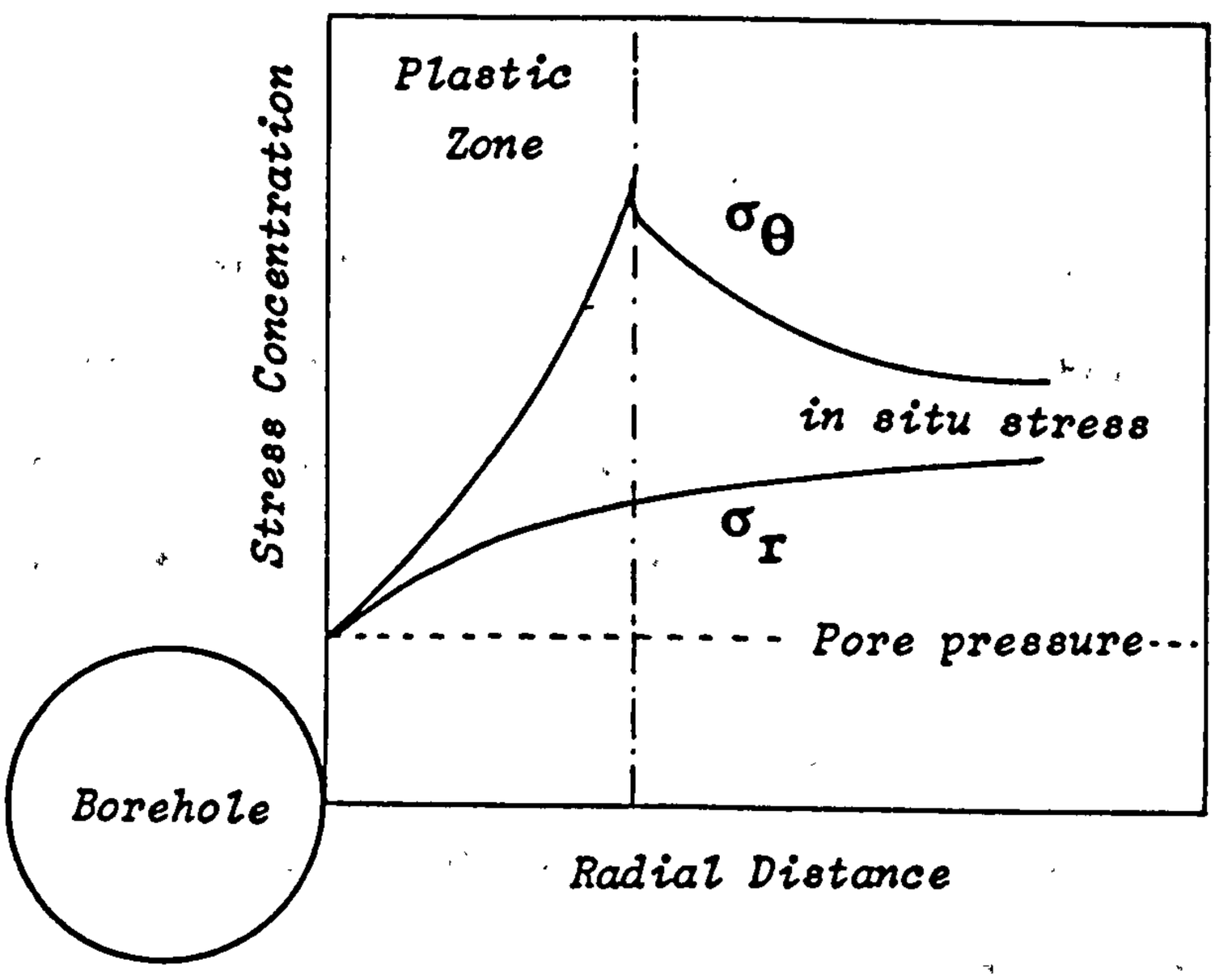

Figure 1.8 : Induced State of Stress around a Borehole

1.4.2 Types of Borehole Failure

Stress induced borehole failures may be grouped into the following three classes, as illustrated in Figure 1.9 :-

(1) Hole size reduction due to plastic flow of the rock into the borehole. Symptoms of this condition are repeated requirements of reaming the hole to bottom, stuck pipe and excessive torque while rotating the drill string or excessive drag when pulling the string. Such problems occur, although not exclusively, in formations with a high clay content and in salt zones.

(2) Hole enlargement due to compressive failure of the rock in a brittle manner and falling into the wellbore (sloughing shale). Problems resulting from hole enlargement include fill on trips, poor directional control and poor cementing.

(3) Fracturing due to tensile splitting of the rock resulting from excessive wellbore pressure. Severe loss of drilling fluid to the formation from fracturing, known as lost circulation, causes lost time as well as increased costs and often results in well control problems experienced as a 'kick' or 'blow out'.

Once the cause of borehole instability is recognised, remedial or preventative action may be taken. Although the rock mechanical principles related to borehole failure are presently not fully

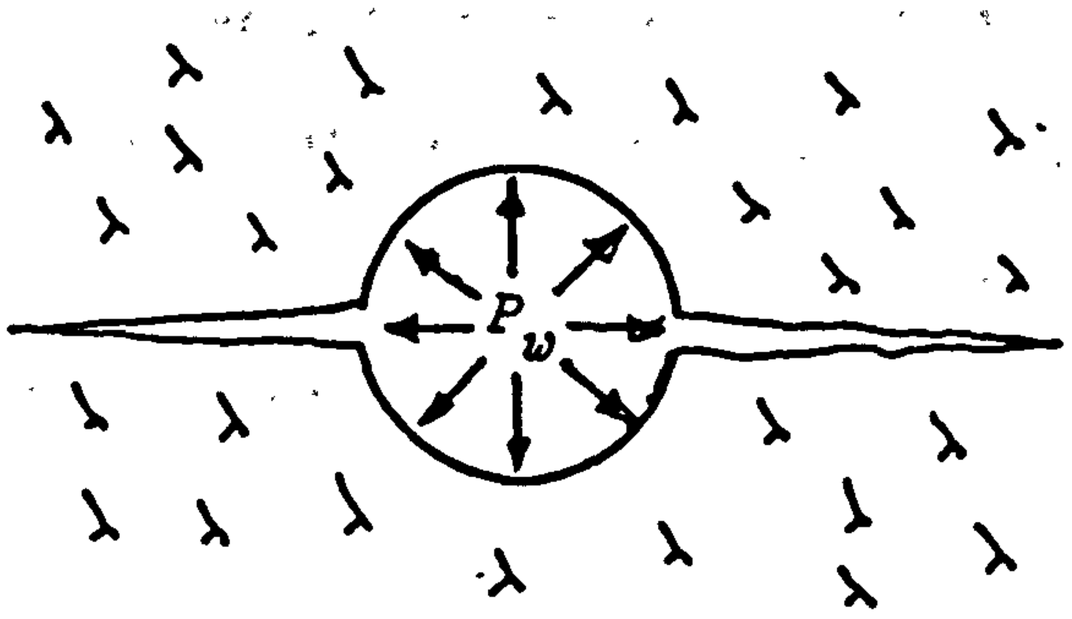

Tensile Failure

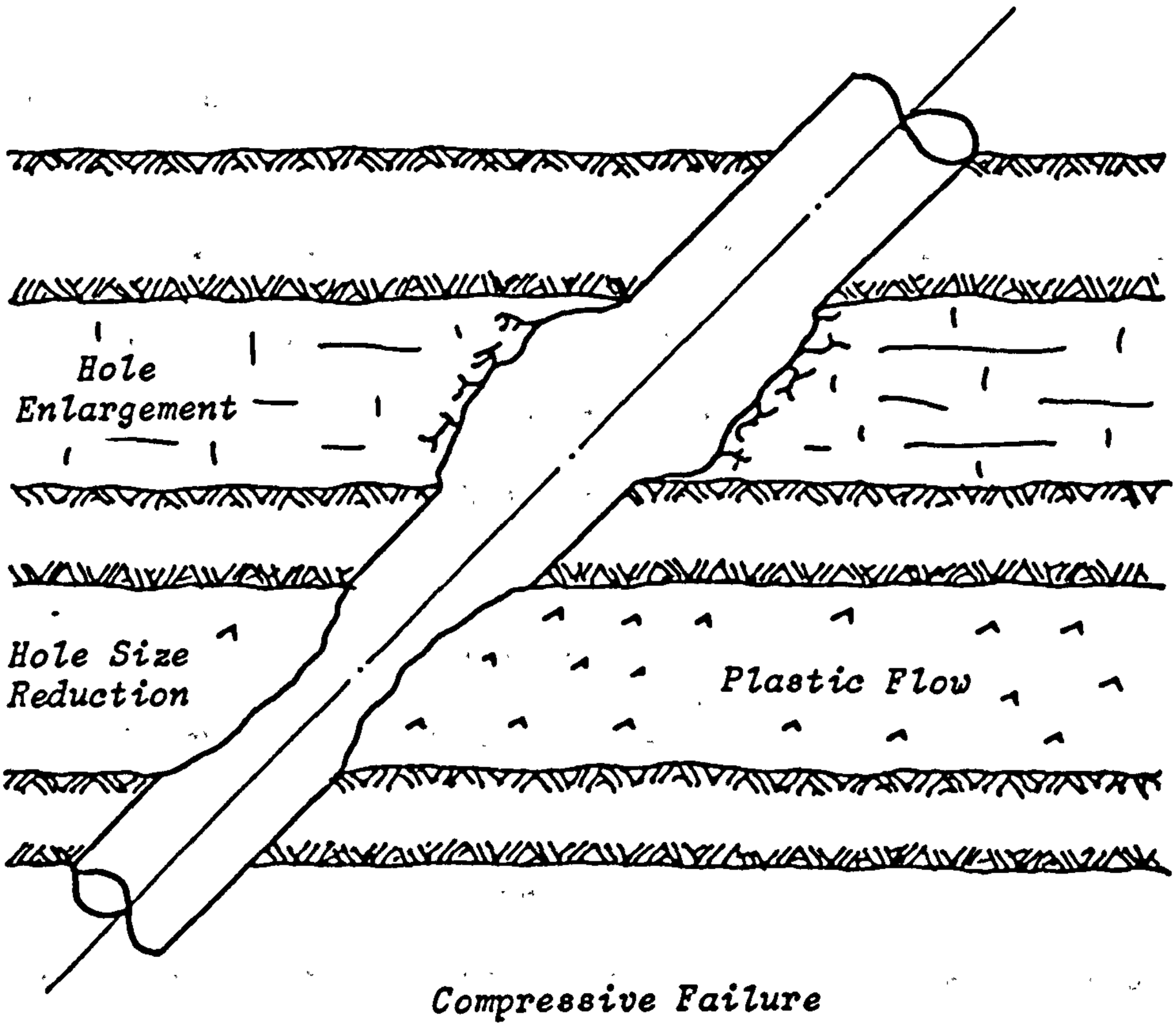

Compressive Failure

Figure 1.9 : Types of Borehole Failure (after Bradley [31])

understood, progress has been made in recent years. In the case of inclined boreholes, however, less information is known. With a view to gathering information on the state-of-the-art knowledge in the mechanics of borehole stability, an extensive literature review was conducted. This involved a detailed examination of borehole failure in tension as well as in compression, thus the mechanics of hydraulic fracturing were reviewed.

1.5 BOREHOLE FAILURE IN COMPRESSION

1.5.1 Introduction

All in-situ stresses in the unexcavated form are, in general, compressional stresses. On the introduction of the borehole, compressional failure may occur if the formation pressure is greater than the wellbore pressure. This may be due to either :

(a) Sudden formation pressure increase,

or (b) The mud weight being too low.

This gives rise to the problem known as 'sloughing shale' which encompasses both hole size reduction, with the the related problems of stuck pipe, and hole enlargement. From a rock mechanics approach, the problem remains as to the accurate prediction of the occurrence of borehole failure in compression.

It was not the intention to reproduce the various compressive stress-state solutions developed by the following workers as the

formulae are lengthy and may be found in the respective references. Emphesis was therefore given to reviewing the various assumptions and results obtained and to detail the conclusions which were drawn.

1.5.2 Review of Previous Work

The problem of the stability of an uncased deep well under plastic conditions was first studied by Westergaard [23], who considered that the plastic behaviour of the formation material was described by a simple Mohr's envelope. In his work, published in 1940, Westergaard used the concept of effective stress to determine the stress distribution around an empty borehole and concluded that at great depths a plastic state exists around the well which relieves the stresses and prevents the hole from collapse.

A more detailed discussion of the influence of the pore pressure resulting from a fluid contained in a porous rock was given by the following year by Biot [24]. Biot gave a general theory of three-dimensional consolidation, taking into account also the possibility of a flowing pore fluid. Many of the later works are based on this study.

One of these is the work of Paslay and Cheatham [25], which was published in 1963. They studied rock stresses caused by a fluid flowing into the borehole. In their study, they also considered the case where permeability was reduced in a region adjacent to the wellbore. Paslay and Cheatham assumed that the wellbore was situated

in a state of hydrostatic stress under a condition of plane strain and that the rock behaved elastically, thus their study ignored the effect of a plastic zone around the wellbore.

In 1968, Mahtab and Goodman [26], examined the state of stress around a vertical wellbore in a nonlinear, elastic material by means of finite element analysis. Their results, which were derived chiefly from the investigations of Miles and Topping [27] and the photoelastic work of Galle and Wilhoit [28], in conjunction with Word and Wilhoit [29], indicated that that the effect of nonlinearity was restricted to one well radius from the bottom periphery of the hole. Beyond a distance of one-quarter wellbore radius, the effect of nonlinearity of stresses was generally less than 5% for the cases examined. They concluded by stating that the consideration of a static pressure inside the well did not magnify the effect of nonlinearity on borehole stresses.

Gnirk [30], realised the existance of a plastic zone around the well and published his analysis in 1972. He assumed that the rock was situated in a hydrostatic stress field in a condition of plane strain, was incompressible and that it obeyed the Mohr-Coulomb criterion of plastic yield. Gnirk calculated the wellbore pressures required to prevent plastic yielding of an uncased wellbore, assuming no fluid flow would be involved. His results could be used in drawing up mud-weight programmes for a particular well. In his concluding remarks, Gnirk stated that for weak rocks wellbore collapse could occur at contractions of approximately 10%. For expansion, the limiting wellbore pressure could be when the radial

increase is in the order of 300%. This appeared to be unrealistic, however, Gnirk went on to state that fracture probably occurred at much smaller values of expansion in the plastic state. As with similar studies, his work suffered from unrealistic, ideal assumptions from the beginning and also from lack of testing of the theories in practical situations.

In 1978/9, Bradley [31], published a theoretical concept that could provide limits for borehole stability in deviated boreholes. He used the three-dimensional stress-state equations developed by Fairhurst [32] in combination with an extended Mises Failure Criterion along with the concept of the stress cloud to predict borehole failure. Due to the large amount of variables involved, a computer was used to calculate and plot, on the failure criterion axis, all the possible stress states for all hole angles and directions. The result was an area, or 'stress cloud'. Any change in variable would produce a change in shape of the stress cloud. From an examination of the location of the stress cloud with respect to the failure envelope defined by the Mises Criterion, the proximity of the borehole to failure could then be assessed. This method can also be used to predict pressure induced lost circulation due to tensile failure.

An example of Bradley's stress cloud analysis is given in Figure 1.10. From an examination of the figure, it is evident that the effect of decreasing wellbore pressure on the stress cloud is to move it upwards towards the failure envelope, thus indicating an increased possibility of borehole failure in compression.

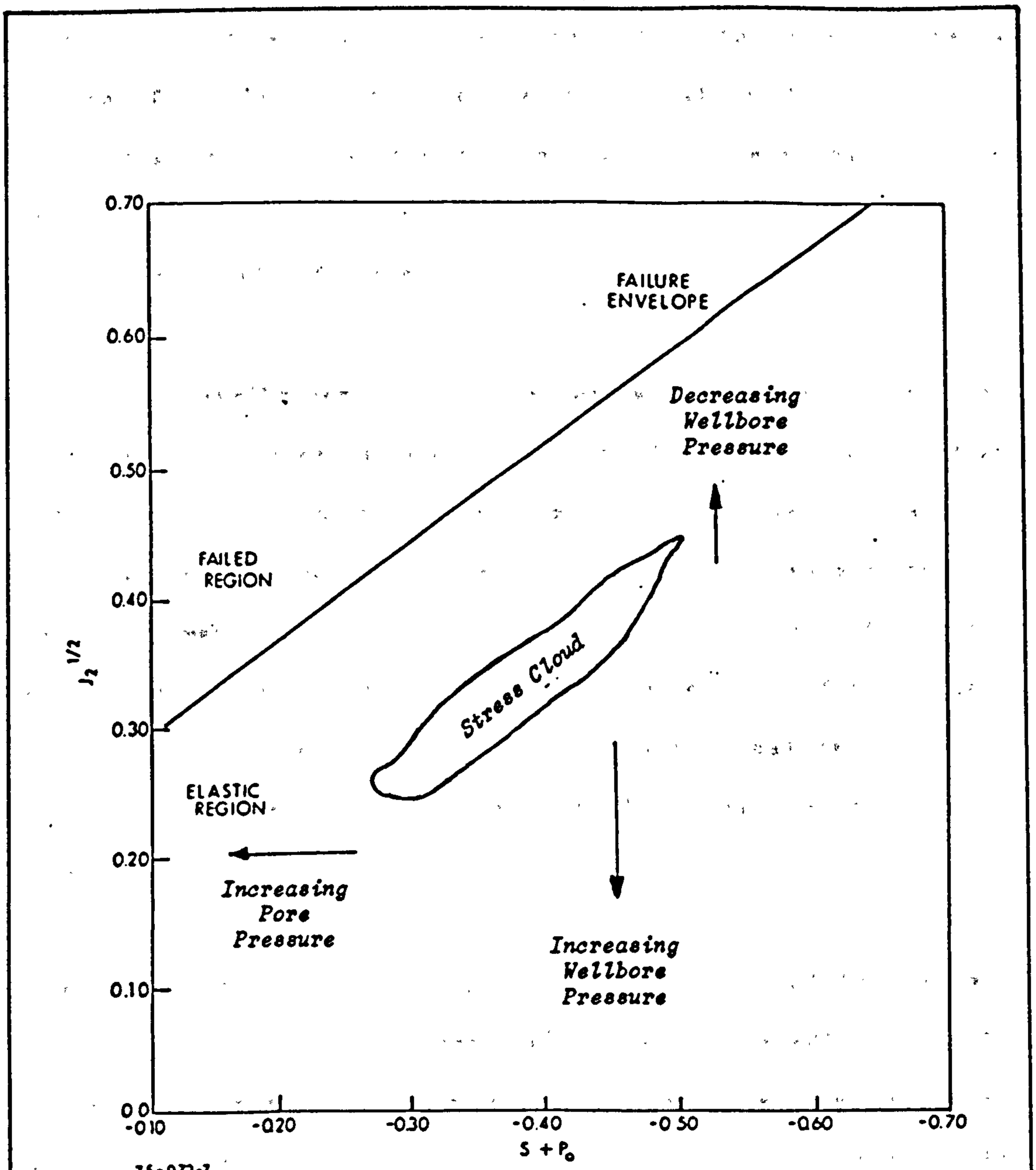

Figure 1.10 : Example of Stress Cloud Concept (after Bradley [31])

Conversely, increasing wellbore pressure moves the cloud downwards and away from the envelope and toward hole failure in tension. The effect of an increase in pore pressure causes the stress cloud to move to the left, indicating an increased susceptibility to borehole collapse and tensile failure.

The major contribution of Bradley's work was providing information about the stability of inclined boreholes. This work showed that an inclined borehole required a greater mud weight to prevent stability problems and hole collapse. He illustrated that in a normally stressed formation, increasing the borehole angle from 0° to 60° may require increasing the mud weight by 2.5 lb/gal. In a further paper [33], Bradley showed that in addition to inclination, borehole direction could also influence borehole stability in tectonic regions.

In a paper presented in 1978, Geertsma [34] stated that it was impractical to apply linear poro-elastic theory to predict borehole failure in compression. The reason he gave was that compressional failure is largely strain controlled unlike tensile failure. He stated that stress and strain solutions required modifications due to the effect of strain-softening of the rock in compression. The yield condition of the rock material decreases with increased plastic deformation due to loss in cohesion. This was a departure from perfect plasticity which appeared to be valid as few materials perform in such an ideal manner. Geertsma proposed that influx into the borehole would commence when failure occured at a point when there was little trace of the original cohesion.

A most useful approach made by Geertsma was the attempt to make such poro-plastic theory more applicable to field use by proposing that a simple hardness test may be used to assess particle-influx risk. He argued that hardness or indentation experimental results may be controlled by the same parameters that affect elastic-plastic behaviour. Correlation of experimental data appears to qualify this view. A plot of failure pressure of thick walled cylinders, as shown in Figure 1.11, gives a near straight line relationship when plotted against Brinell hardness.

Geertsma concluded by proposing further investigations into the mechanics of indention of more friable rock materials to establish more soundly a link with the mechanics of failure in compression and that more research was required into the application of elastic-plastic theory taking into account the effects of strain softening on weaker rock types. He went on to state that it would be most useful if samples of rock known to be of similar type to formations to be drilled through could be simply tested on-site to assess the suceptibility to compressional failure.

Geertsma's study suffered from being essentially two-dimensional in a hydrostatic stress field and accordingly did not consider the induced stresses around inclined wells. He did, however, reintroduce the concept of Brinell hardness, originally presented by Van Der Vlis [35], which appears to have an empirical relationship with the elastic modulus of the rock and therefore has potential in estimating the behaviour of the well.

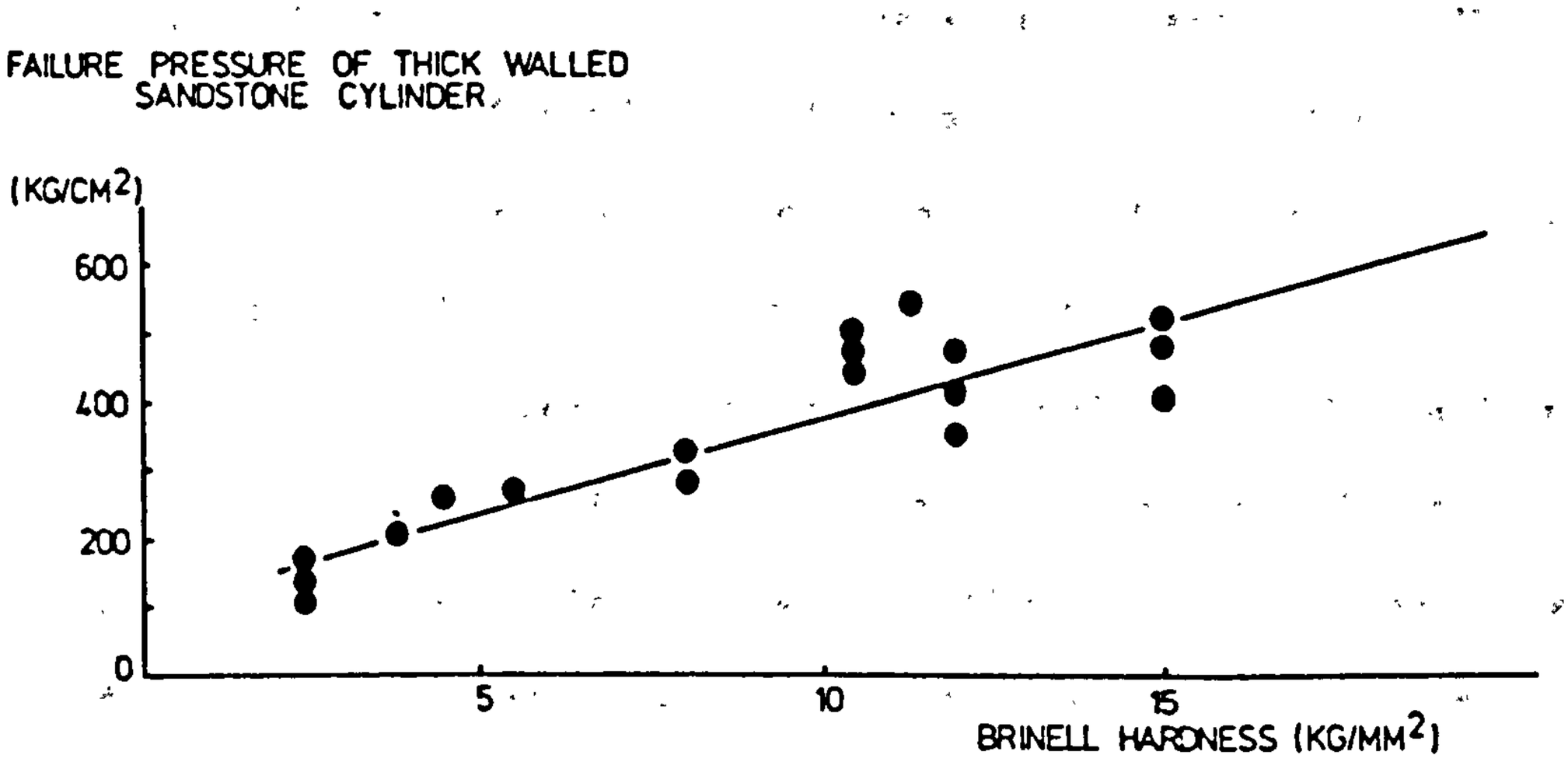

Figure 1.11 : Failure of Thick-Walled Sandstone Cylinders plotted against Brinell Hardness (after Geertsma [34])

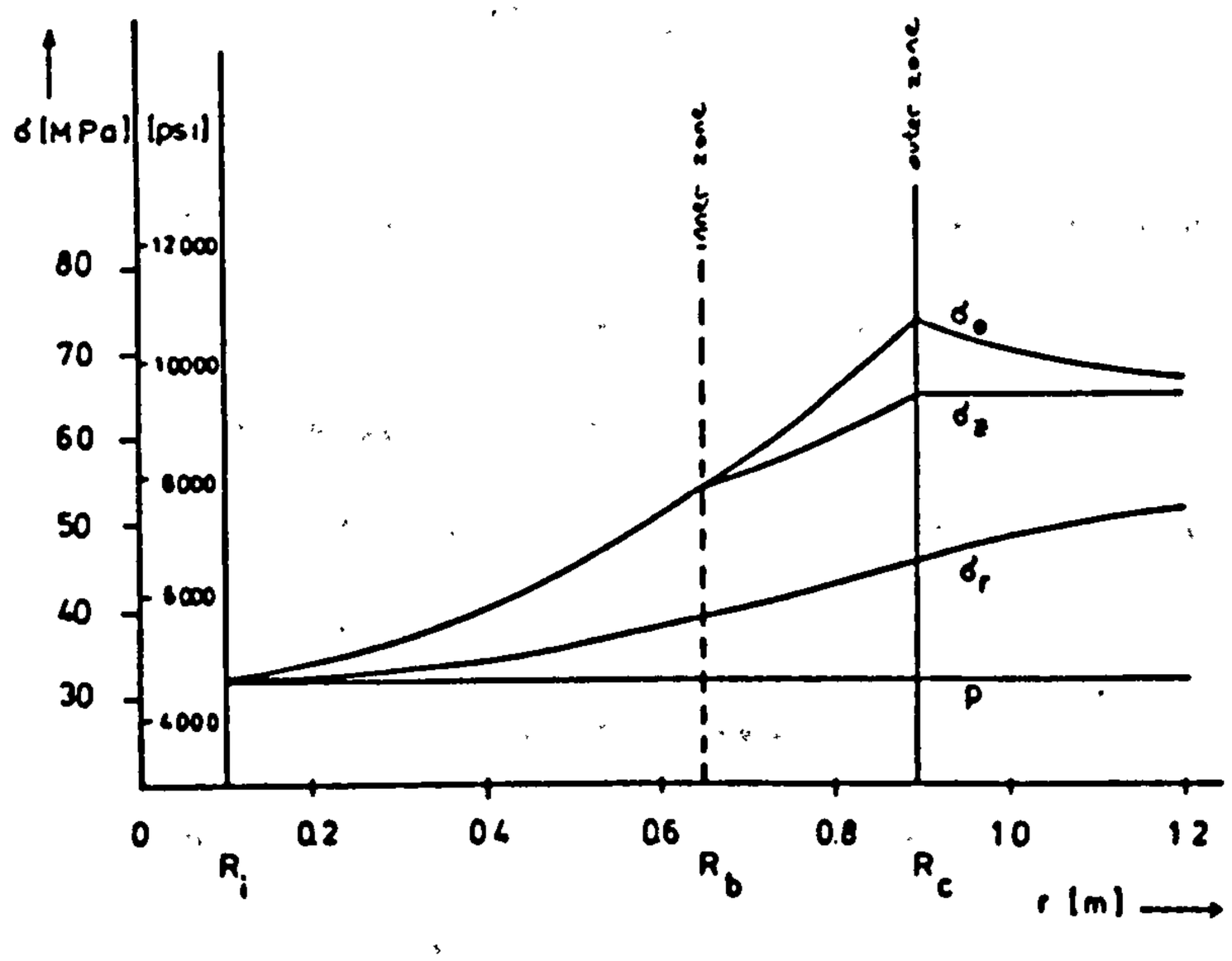

Figure 1.12 : Inner and Outer Plastic Zone Concept (after Rinses et al [37])

Rinses et al [36] studied in detail the stresses around a wellbore in poorly consolidated sand to determine the size of the plastic zone around a well. They have also developed a stability criterion relating the effect of fluid flow on the state of stress and hence the ultimate rock failure. This analysis, which was published in 1982, does not apply to inclined boreholes or boreholes in techtonically active regions; however, the solutions that they proposed were such that small changes in geometry and stresses would require only slight modifications to their solutions. As with poro-elastic theory, the rock was assumed to be isotropic, homogeneous and the pore space was assumed to be completely filled with fluid. The Coulomb Failure Criterion was taken to hold true for the material. The work was based on an earlier paper on solid particle influx by the same authors [37].

Assuming no fluid flow, Rinses et al derived two solutions for the state of stress around the wellbore. These solutions, for the case in which either the tangential stresses or the vertical stress was greater, showed that at some point the two stresses must become equal. The region in which this occured was named the Inner Plastic Zone. A graphical representation of these results is illustrated in Figure 1.12. The inner plastic zone is clearly seen as the point at which the intermediate stress, tangential or vertical, departs from the maximum stress. The elastic zone being the region where the vertical stress becomes constant.

Their analysis illustrated that if the rock had high cohesive strength, the extent of the plastic zone would be small and elastic behaviour will predominate around the hole. A cohesive strength of 15800 kPa (2300 psi) was quoted for theoretical, elastic behaviour. It was indicated however, that further practical investigation into limiting sizes of the plastic zone would be necessary in order to apply the theory to the practical use of predicting failure. Using numerical examples, Rinses et al went on to illustrate that the extent of the plastic zone increased if there was any fluid flow.

The results achieved by Rinses et al appear to be more soundly based theoretically than the models proposed by Bradley, Geertsma and Gnirk. However, the solutions are extemely complicated and it would be advisable, if applying these solutions to drawing up working limits for mud weights in inclined holes, to employ a factor of saftey proportional to the inclination of the borehole.

Brandis and Barton [38] conducted experimental investigations based on 3-D physical models to demonstrate the effect of the intermediate principal stress and published their preliminary results in 1986. Numerical analyses based on two-dimensional plane strain idealisation of the problem were obtained by solving the equation of equilibrium in the radial direction and satisfying the linear Coulomb criterion in the plastic zone; however, no account of the procedure was given.

Also in 1986, Infante and Chenevert [39] presented a mathematical and laboratory analysis which provided solutions to the problem of

plastic flow of salt formations into wellbores. In the mathematical analysis, it was assumed that the incipience of plasticity in the formation was regulated by the level of octahedral shear stress and that the formation was neither permeable nor porous but homogeneous and isotropic, and was under a state of hydrostatic stress. They derived equations which, in terms of constants of the formation material, yielded the limit of elasticity, the radius of the plastic zone, and the amount of borehole contraction as a function of the mud weight used. They went on to state that after salt zones are drilled and cemented, there was still the possibility that salt creep and subsequent casing collapse may occur and as such, casing design should take this into consideration. The study proceeded to offer recommendations for drilling obtained as a result of the mathematical analysis and field applications.

They concluded that salt zones were capable of creep and plastic behaviour at low levels of octahedral shear stress and when drilling in such a formation, plastic borehole contraction would occur if an appropriately high mud weight was not used. A figure of 19.2 lb/gal was quoted to ensure that a borehole, in a normally stressed salt formation, would remain in equilibrium and that neither creep nor plastic deformations would take place.

As regards wireline methods of predicting formation collapse, the Mechanical Properties Log (MPL) computation [40], has been available to the petroleum industry since 1973 for the purpose of detecting weak oil bearing formations. The logs required for the original MPL computation were the Formation Density and Sonic logs. Additional

data was required to determine clay content and Poisson's ratio of the sand under investigation. In 1981, Schlumberger proposed an alternative method of predicting sanding problems based on stress analysis. The Mechanical Properties Computer Analysis (MECHPRO) [41], was devised to compute the elastic moduli, radial and tangential stresses, the initial shear strength, the pressure drawdown limit for avoiding sand production and to determine the fracture gradient. Application of this data to specific problems is achieved by estimating the downhole stress. An overview of the MECHPRO chain is given in Figure 1.13. The accuracy and reliability of wireline mechanical property logs is questionable and as such have not gained universal acceptance in the petroleum industry.

In the foregoing review of compressive wellbore failure, the influence of the drilling fluid on the rock strength is a factor which was rarely considered. It is known that the nature of the mud affects both the stress at failure and the mode of failure. Also the effect of the drilling fluid on swelling shales and brittle shales was little mentioned. As only the mechanical or uncontrollable factors influencing borehole instability were of interest in this investigation, however, the effect of drilling fluids on the rock properties was considered to be outwith the scope of this project. Separate studies, including those done by Darley [42], Chenevert [43], and Simpson [44] cover the subject in detail while an excellent review on the subject has been presented by Dempster [45].

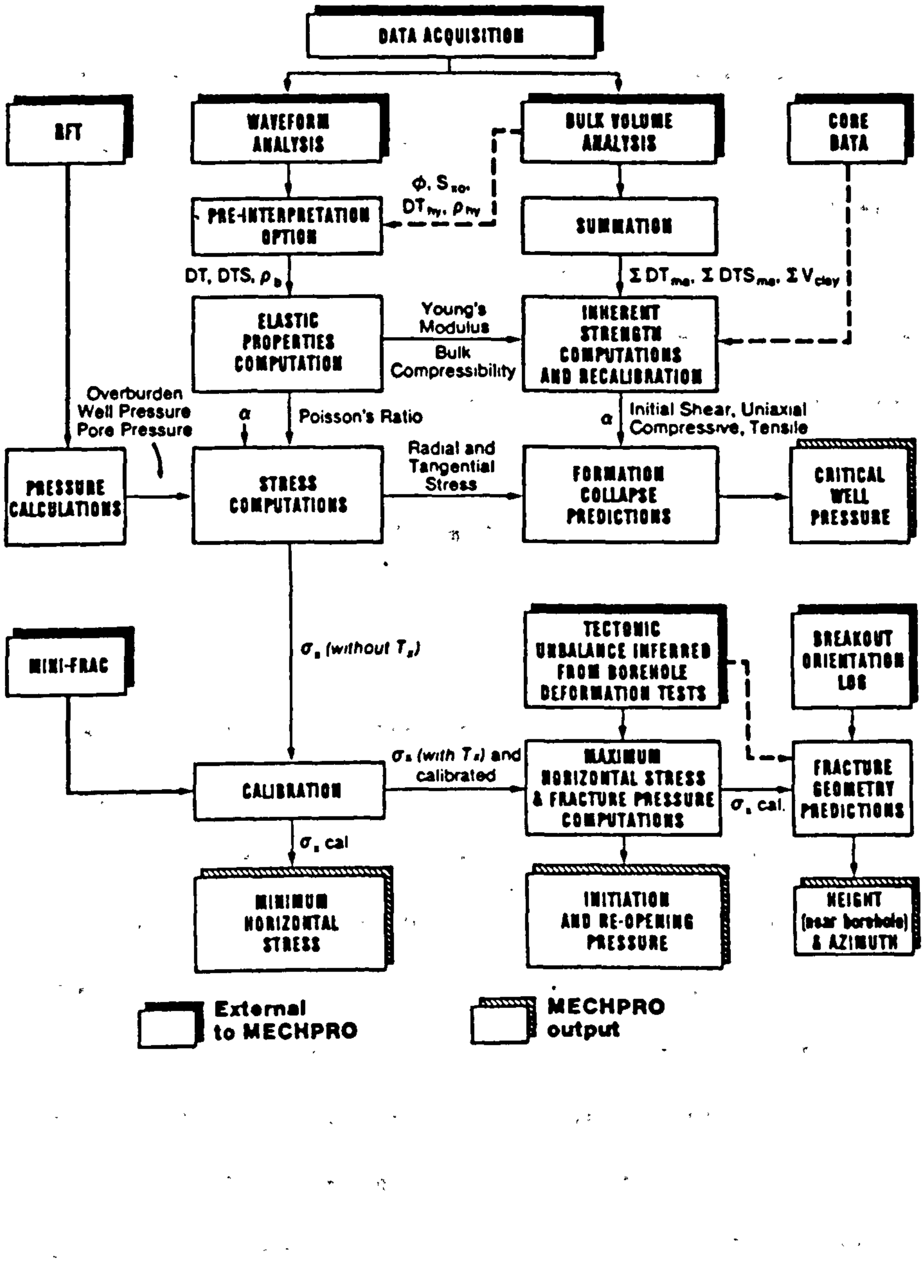

Figure 1.13 : Overview of MECHPRO Chain [41]

1.6 BOREHOLE FAILURE IN TENSION

1.6.1 Lost Circulation

Borehole failure in tension occurs when the difference between the wellbore pressure and the pore pressure exceeds the sum of the compressive stress around the wellbore plus the tensile strength of the rock. In a drilling well, the effect of mud infiltration to the fracture is known as lost circulation, which is how the problem is diagnosed at the surface. There are other possible causes for lost circulation, such as drilling into subnormal pressurised zones or penetrating a cavernous, vuggy formation, however, they are outside the scope of this review.

To avoid or at least minimise the danger of well kicks, stuck pipe and lost circulation, a basic understanding of formation pore pressure and fracture pressure is necessary. Pore pressure and fracture gradient are the two basic parameters in a well drilling and completion plan and are equally important in cementing, hydraulic fracturing, fluid injection and sand consolidation [46]. The concept of pore pressure has been previously reviewed in Section 1.3.3. In order to obtain an understanding of fracture gradient, it was necessary to review the mechanics of hydraulic fracturing. Induced fracturing in a drilling well is similar to hydraulic fracturing during well completion; the only difference is that the latter is deliberate and desirable while the former is unintentional and most unwelcome.

1.6.2 Hydraulic Fracturing

The technique of hydraulic fracturing for stimulating the production of oil and gas is one of the major developments in petroleum engineering. Before 1950, acidizing was the primary method used to stimulate well productivity. Stimulation of nonreactive formations such as sandstones, however, was generally ineffective until the hydraulic fracturing process was introduced to the industry in 1949 by Clark [47]. Hydraulic fracturing increases well productivity by creating a highly conductive path compared to the reservoir permeability. Normally, this technique is applied to sandstone reservoirs having relatively low permeabilities.

Events leading to the evolution of the fracturing process are documented in the SPE monograph of Howard and Fast [48]. Methods and procedures have changed significantly since fracturing began, however, the basic principles remain the same. Hydraulic fracturing is the process of injecting a viscous fluid into a formation at a faster rate that it can leak off into the rock, thereby producing a pressure within the borehole such that the formation fails in tension and fractures to accept the fluid. The fracture will continue to propagate or grow as more fluid is injected; however, when this pressure is released, the fracture will begin to close. To prevent the fracture from fully closing, a propping agent is mixed with the gelled fluid which acts to keep the fracture open.

The fluids used to create the fracture are chemically designed so that, after a predetermined time, they lose their viscosity. If the well is then allowed to produce, the fracturing fluids flow out, leaving the proppant, which is held in place by the closing action of the fracture. The proppant-filled hydraulic fracture, which may be as wide as 6 mm to 12 mm [49], provides a conductive flow path to the wellbore.

It is important to distinguish between the wellbore pressure required to initiate a fracture and that required to extend it. In order to initiate a fracture, the wellbore pressure must be greater than the minimum hoop or tangential stress σ_θ, and in order to extend the fracture beyond the hoop stress zone, it must be greater than the minimum horizontal stress σ_3. The minimum hoop stress may vary from a value of $2\sigma_3$ to zero, therefore the initiation pressure may be greater or smaller than the extension pressure (Figure 1.14), although for a vertical well in a normally stressed formation, the former is generally greater.

Therefore the ability to predict the fracture gradient is important in order to prevent lost circulation and to estimate hydraulic fracture initiation pressure at a specific depth. In general, formation fracture pressure gradients are related to formation pore pressure, lithology, age and depth of the formation, and to the in-situ rock stress environments [46].

In 1957, Hubbert and Willis [6] published a classical paper in which they critically reviewed previous reports that all hydraulic

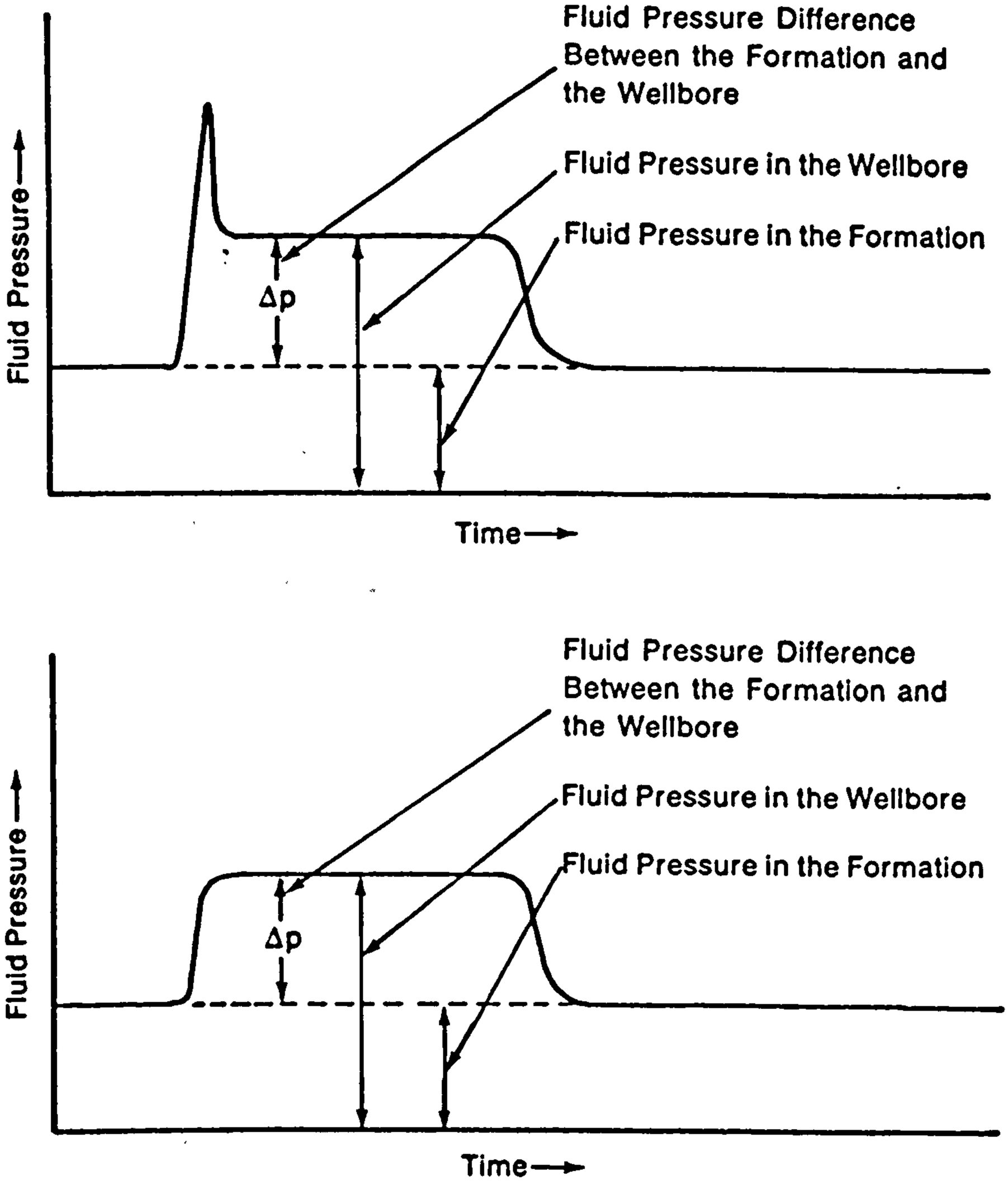

Figure 1.14 : Possible Types of Pressure Behaviour During Fracturing Treatments (after Hubbert & Willis [6])

fractures were horizontal or bedding-plane fractures. Through the use of accepted engineering theory, they showed that a hydraulically induced fracture should form in a manner which was perpendicular to the direction of the least principal stress, as shown in Figure 1.15(a). Therefore, in tectonically relaxed areas, as characterised by normal faulting, they illustrated that the least principal stress would be horizontal therefore a vertical fracture would form. In regions of tectonic compression however, they indicated that the least principal stress could be vertical and accordingly a fracture induced in such a formation would be horizontal. For the case of vertical fractures, the direction or azimuth of the minimum principal stress is also important as this controls the azimuth of the fracture [Figure 1.15(b)].

Hubbert and Willis showed that the minimum injection pressure in an area of incipient normal faulting was,

$$P_f = 1/3\ (\sigma_z - P_p) + P_p \qquad .. \quad .. \quad .. \quad .. \quad .. \quad (1.24)$$

where P_f = Minimum injection pressure

σ_z = Overburden pressure

P_p = Pore pressure

This expression provided an estimate of the minimum fracture pressures that were likely to occur in a relaxed basin which was on the point of normal faulting. Hubbert and Willis concluded that fracture pressures are affected by the magnitude of the in-situ stresses, by the hole geometry and by the penetrating quality of the

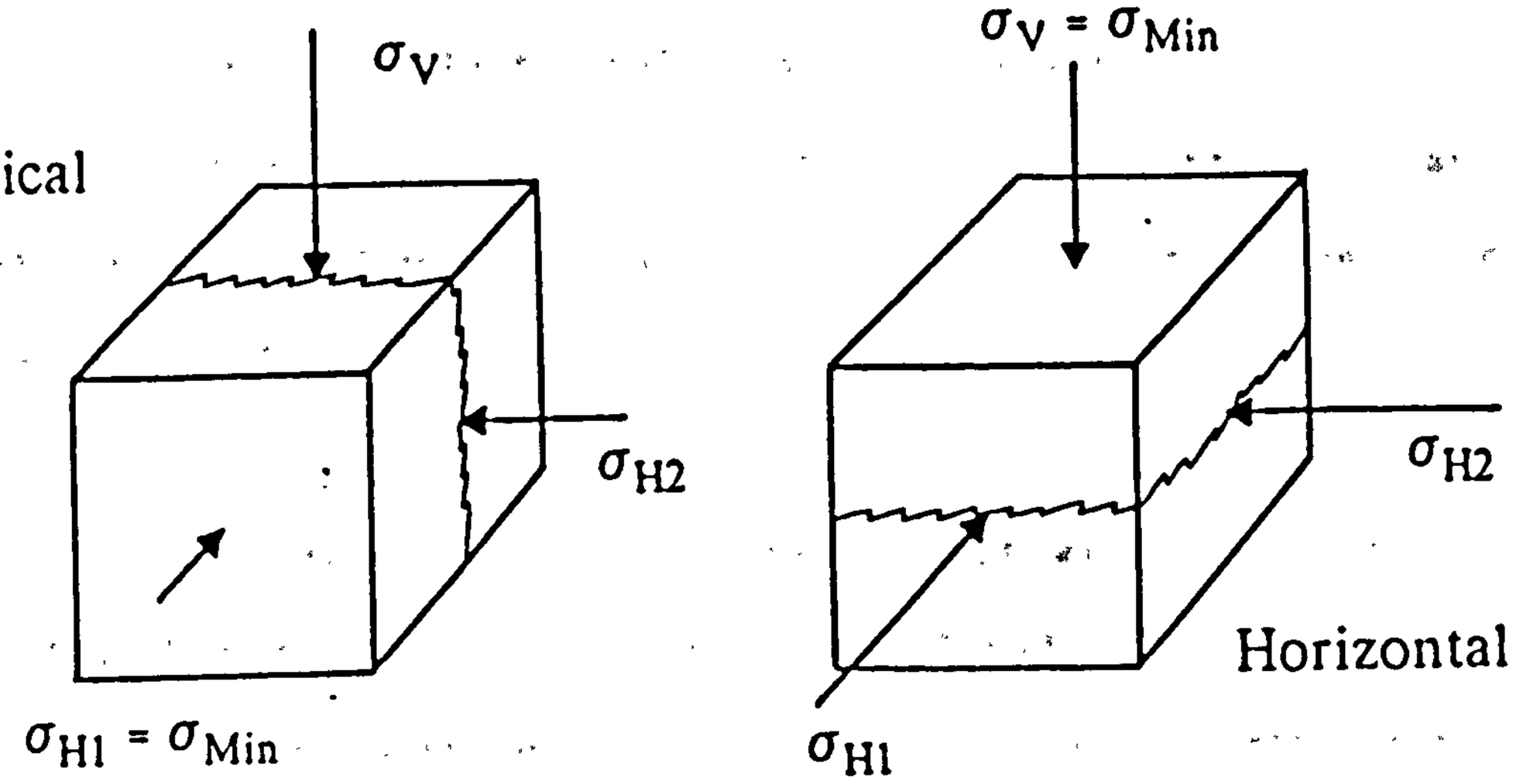

Figure 1.15(a) : Possible Fracture Orientations [10]

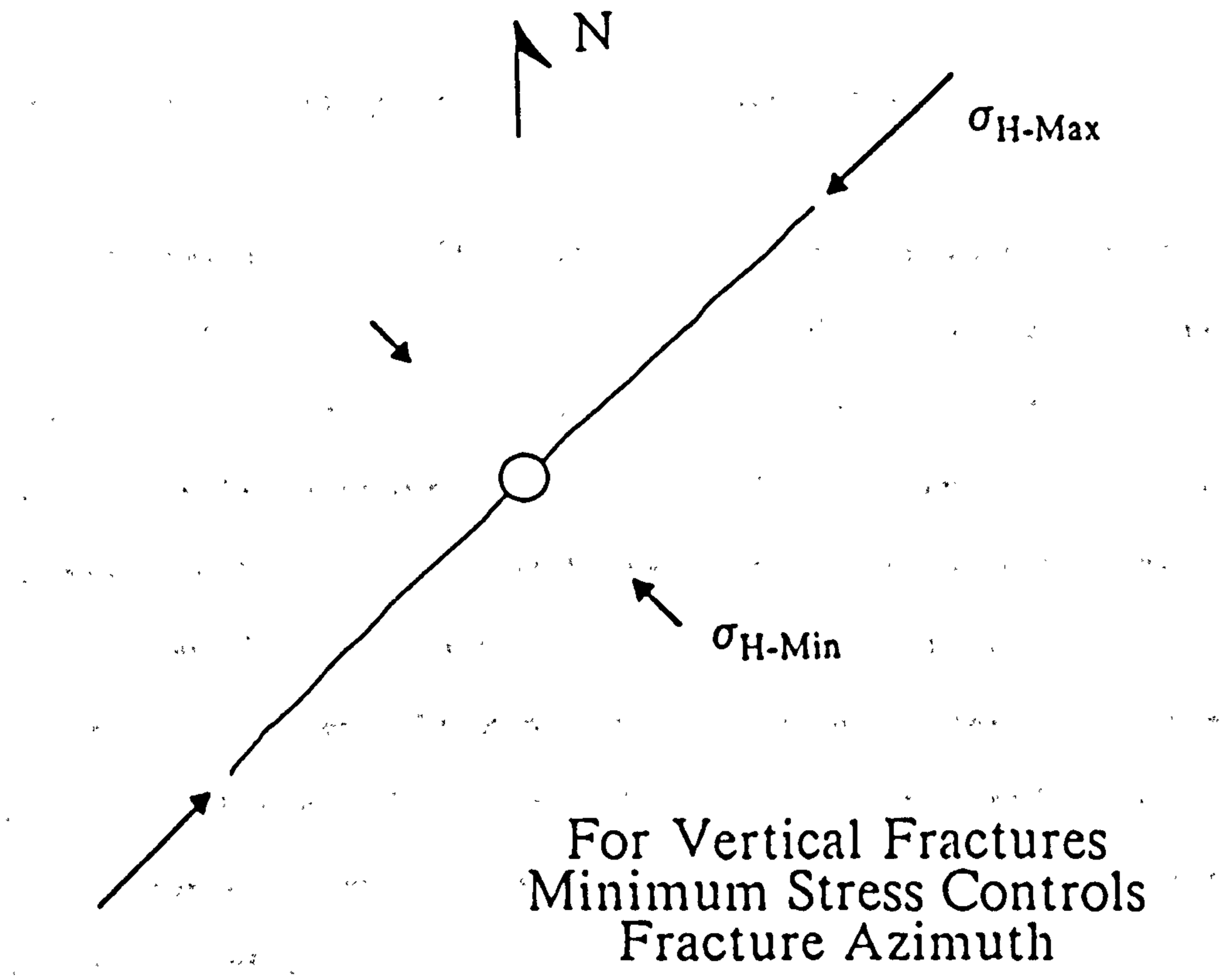

Figure 1.15(b) : Direction of a Vertical Fracture [10]

fluid. Their analysis provided the theoretical and technical basis for many future studies and presented evidence that hydraulic fractures were vertical in tectonically realaxed areas. However, the main disadvantage of this approach was that it was imprecise and generally predicted fracture gradients which were lower than field data suggested [46].

Numerous articles in the past years have dealt with the theory of hydraulic fracturing. The prediction of hydraulic fracture initiation pressures has been approached from two different points of view, one employing classical elasticity theory and the other using empirical formulae in conjunction with information obtained from well-logs.

1.6.3 Empirical Methods of Predicting Fracture Pressures

In 1967, Matthews and Kelly [50] published a study in which fracture pressures could be predicted in some U.S. Gulf Coast sand reservoirs by the use of empirical data. Unfortunately, they did not further the progress made by Hubbert and Willis. Matthews and Kelly chose the minimum fracture pressure as being equal to the pore pressure, and the maximum fracture initiation pressure as being equal to the weight of the overburden. Their prediction method differed from the Hubbert and Willis model in that it considered the effect of a variable horizontal to vertical stress ratio, termed a matrix stress coefficient, K_i, viz.

$$P_f = P_p + K_i \sigma_z \quad .. \quad .. \quad .. \quad .. \quad .. \quad (1.25)$$

Values for K_i may be obtained empirically by substituting field data for fracture initiation pressures into the above equation and solving for K_i. A graphical interpretation of the above relationship illustrating fracture initiation gradients for the U.S. Gulf Coast area is shown in Figure 1.16. These empirical values and relationships however, are limited solely to the area of study.

In 1969, Eaton [51] extended the concept of Matthews and Kelly by introducing Poisson's ratio into the mathematical expression for the fracture pressure gradient and therefore taking into account the effect of a variable overburden gradient:

$$P_{fg} = \left[\frac{\sigma_z}{D} - \frac{P_p}{D}\right]\left[\frac{\gamma}{1-\gamma}\right] + \frac{P_p}{D} \quad .. \quad .. \quad .. \quad .. \quad (1.26)$$

Eaton surmounted the problem of predicting or measuring the Poisson's ratio of every in-situ rock in a borehole by resorting to an empirical relationship. Furthermore, his 'Poisson's ratio' was not a function of the rock itself but of the regional stress field - the horizontal to vertical stress ratio. Accordingly, Eaton suggested that the minimum horizontal compressive stress should be taken as the fracture pressure. He claimed that in a permeable formation there is little difference between the fracture initiation and extension pressure and therefore did not distinguish between the two.

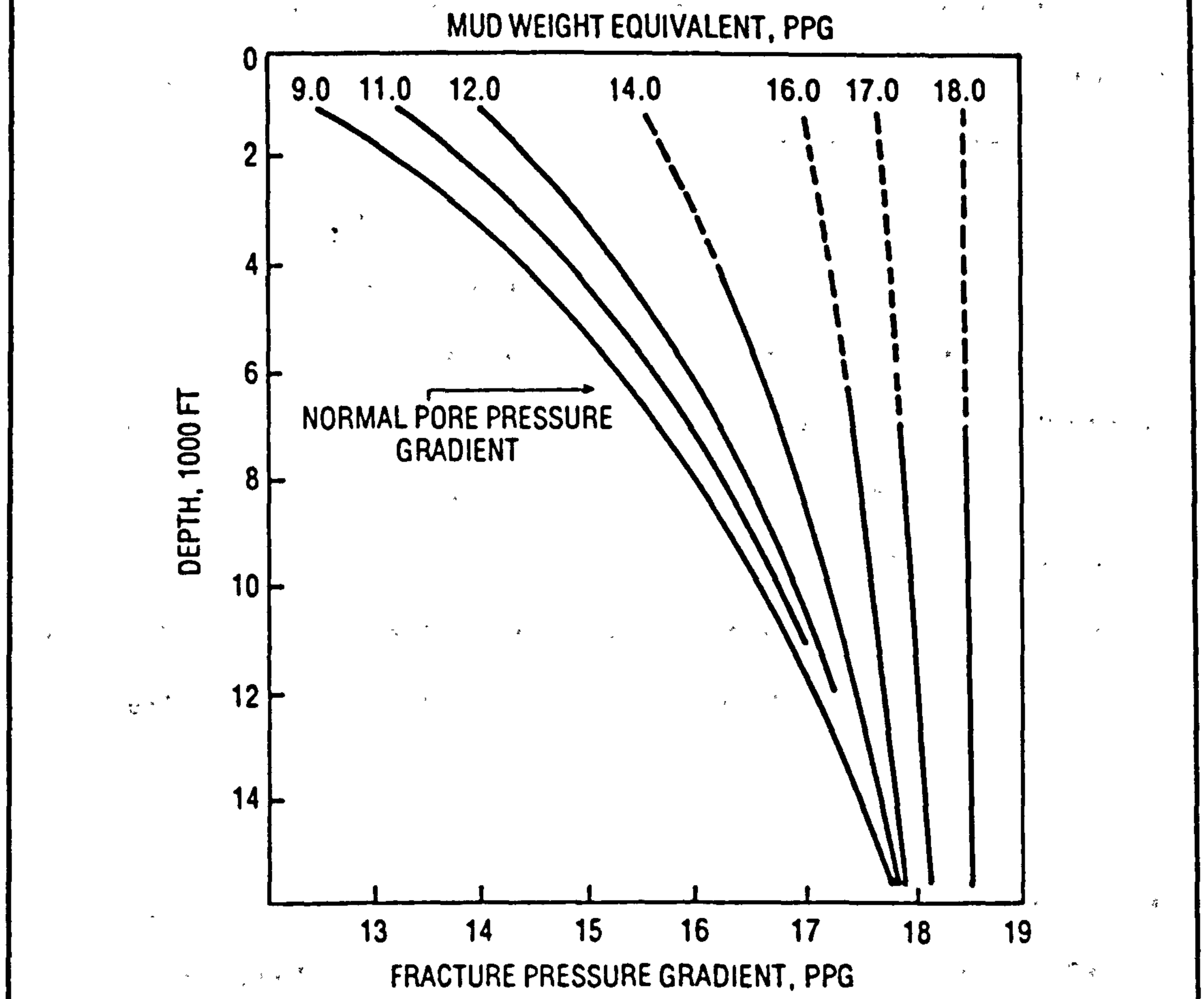

Figure 1.16 : Graphical Fracture Gradient Predictions for the U.S. Gulf Coast using the Matthews-Kelly Concept [50]

Eaton presented empirical curves for 'Poisson's ratio' versus depth calculated from U.S. Gulf Coast data. These curves, which are independent of rock type, are illustrated in Figure 1.17(a) and it can be seen that with depth they approach the Poisson's ratio upper limit of 0.5. Simplified local and/or regional fracture pressure gradient prediction charts may then be developed. Figure 1.17(b) shows a chart for the U.S. Gulf Coast area. The major contribution of Eatons's paper was the concept of variable overburden. Since overburden pressures play a major role in empirical fracture gradient estimations, the increase in accuracy of this variable allowed better fracture gradient predictions. Eaton's technique can only be applied in other areas if the 'Poisson's ratio' curve is known. Thus it is limited to areas of concentrated exploration in tectonically relaxed regions and cannot be used reliably on wildcat wells.

The concept of predicting fracture pressure gradients from well logs was investigated by Macpherson and Berry [52] in ten offshore Louisiana fields. A quantitive relationship was found to exist between the ratio of sand elastic modulus to overburden and the fracture pressure. The authors claimed that using this concept predictions should generally fall within 700 psi (4800 kPa) of true fracture initiation pressure. In their analysis, fracture pressure gradients vs depth were found to be different in all the ten offshore fields studied, but did correlate with the sand/shale ratio, geological age and overpressure. Fracture pressure gradients in shales were significantly higher than in sand, whereas breakdown in overpressured and normally pressured intervals were similar.

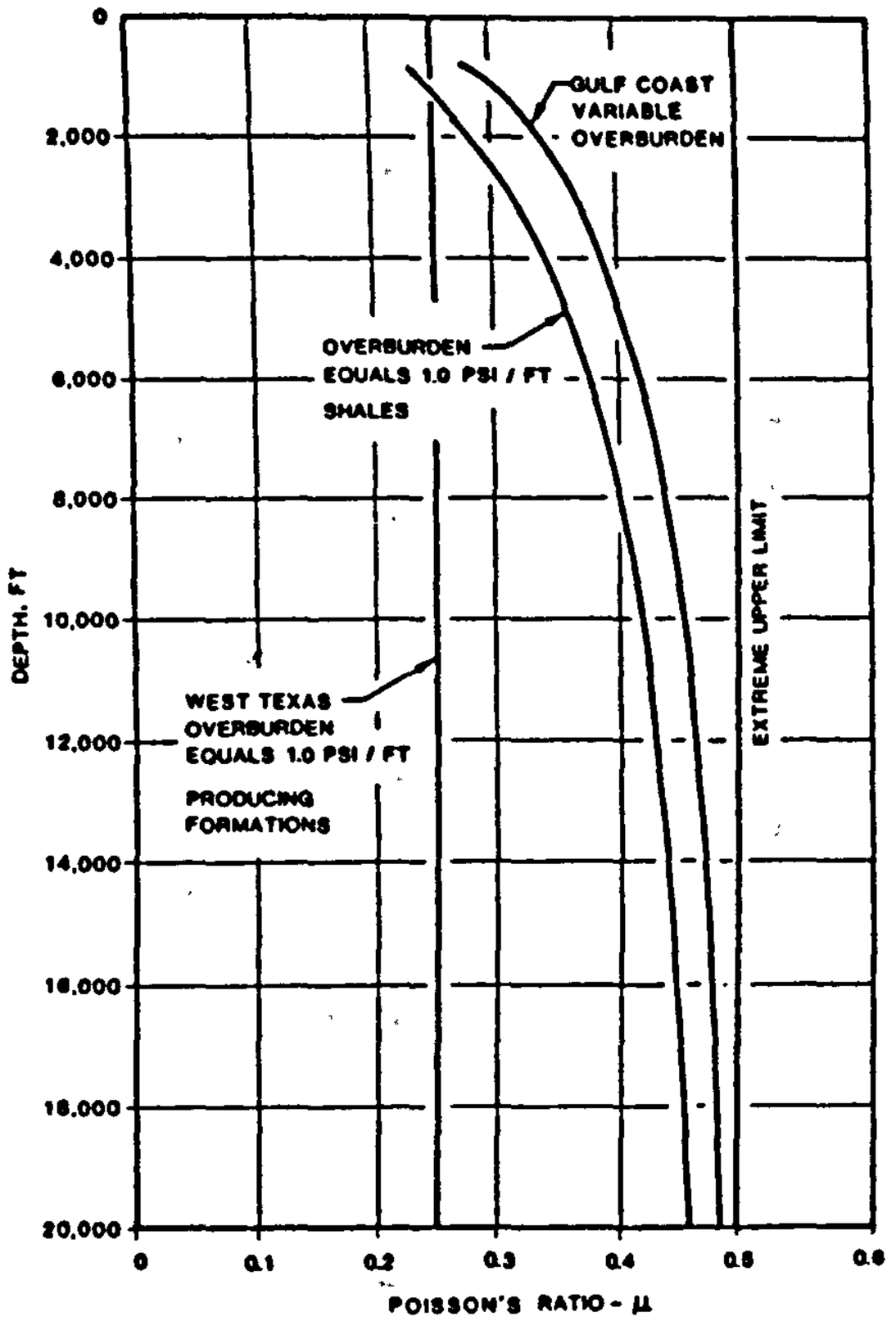

Figure 1.17(a) : Poissons's Ratio Curves (after Eaton [51]

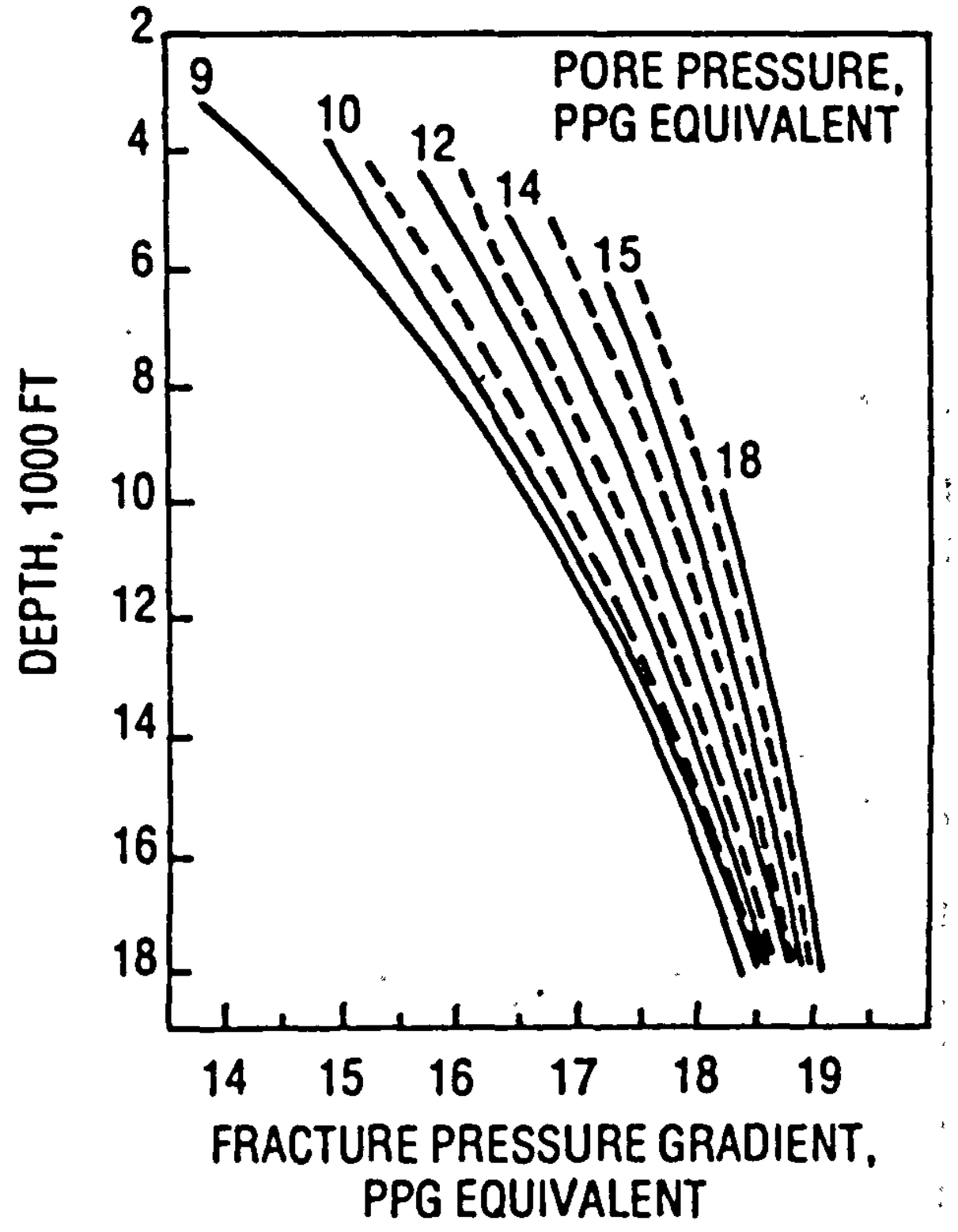

Figure 1.17(b) : U.S Gulf Coast Fracture Predictions (after Eaton [51])

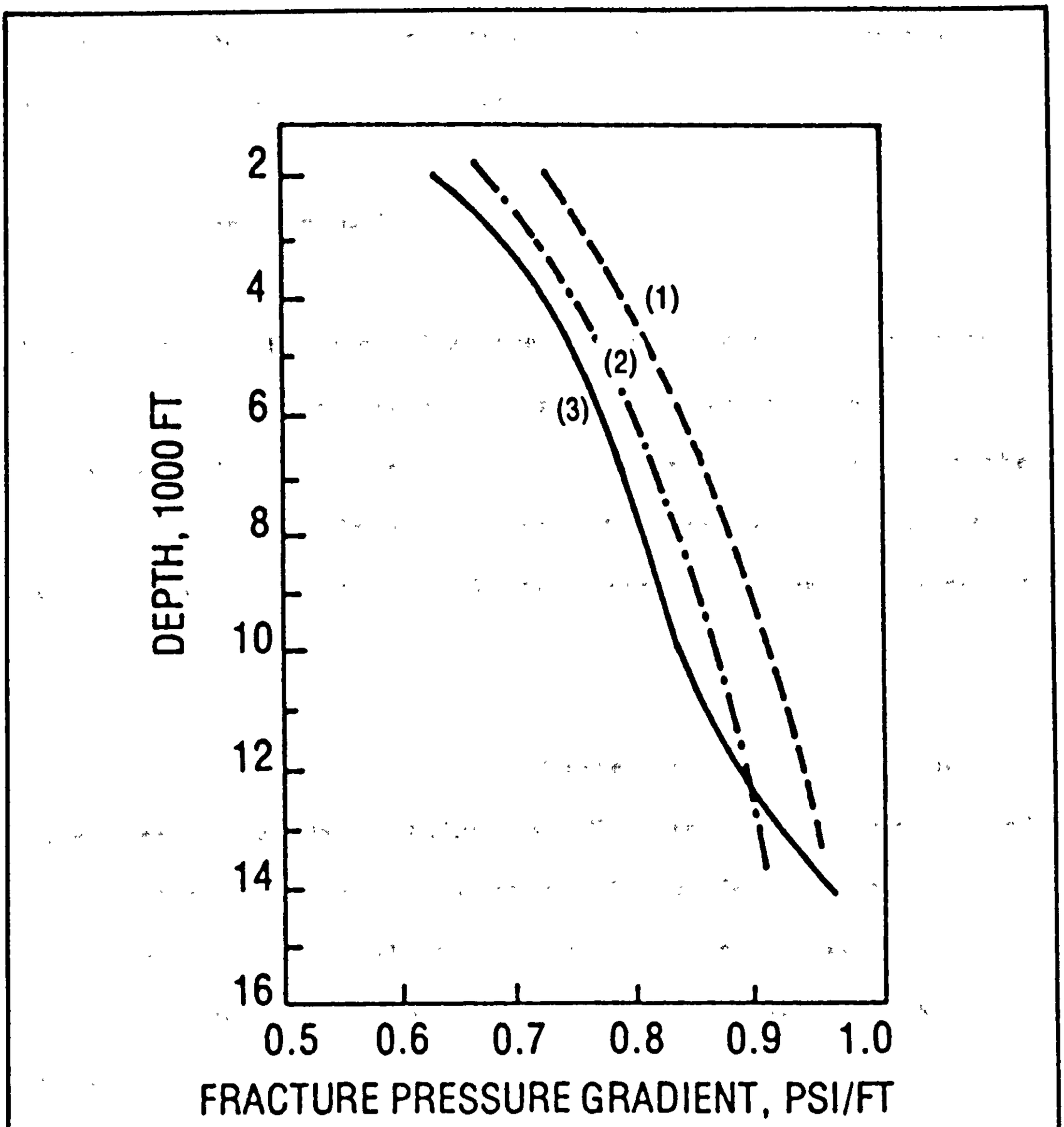

Figure 1.18 : Comparison of Several Fracture Gradient Predictions for the U.S. Gulf Coast

(1) South Texas (after Matthews & Kelly [50])
(2) Louisiana Gulf Coast (ditto [50])
(3) Average Empirical Trend for 10 Offshore Fields (after MacPherson & Berry [52])

Figure 1.18 shows the average trend of their field data compared to the results of other investigations.

1.6.4 Theoretical Approach

The majority of the theoretical prediction methods employ classical elasticity theory.in which the stresses are redistributed in the manner described by Kirsh's solution as modified to include the effective stress principle. More recently however, investigators have been considering elastic-plastic theory when examining borehole failure in tension.

A criterion for the initiation and extension of vertical fractures was presented in 1967 by Haimson and Fairhurst [53]. They assumed the formation was elastic, porous and included the effect of the fluid flow into the formation. Their solutions are essentially those which have become associated with classical hydraulic fracturing theory.

Their criterion for fracture initiation in porous rock was,

$$P_f = \frac{3\sigma_x - \sigma_y + T_o}{2 - \alpha(1-2\gamma)/(1-\gamma)} - P_p \quad .. \quad .. \quad .. \quad .. \quad (1.27)$$

where P_f = Fracture initiation pressure

σ_x = Minimum horizontal compressive stress

σ_y = Maximum horizontal compressive stress

T_o = Tensile strength of the rock

α = poroelastic constant

γ = Poisson's ratio

P_p = Pore Pressure

For rock impermeable to the fracturing fluid the above equation was reduced to

$$P_f = 3\sigma_x - \sigma_y + T_o - P_p \quad .. \quad .. \quad .. \quad .. \quad .. \quad (1.28)$$

Haimson and Fairhurst showed that the effect of a penetrating fluid was to reduce the tangential stress acting on the hole periphery and therefore reduce the wellbore pressure necessary to initiate a fracture. They stated that the reason for this discrepancy was that in the case of a penetrating injection fluid, the pore pressure at the wellbore boundary would be P_w [Figure 1.19(a)], while in the non-penetrating case, there would be no flow into the formation and consequently the pore pressure would be Pp everywhere [Figure 1.19(b)]. Hubbert and Willis [6] reached the same conclusion at an earlier date, however, they did not examine the situation in as much detail.

Bradley [31] disregarded the tensile strength of the rock in his criterion for tensile failure, in which he stated 'when the effective fracturing stress is less than or equal to zero, tensile failure will occur'. His analysis did not consider fluid flow into the formation and accordingly his solutions were that for a non-penetrating fluid; however, he did provide information about fracture pressures of deviated boreholes which hitherto had not been

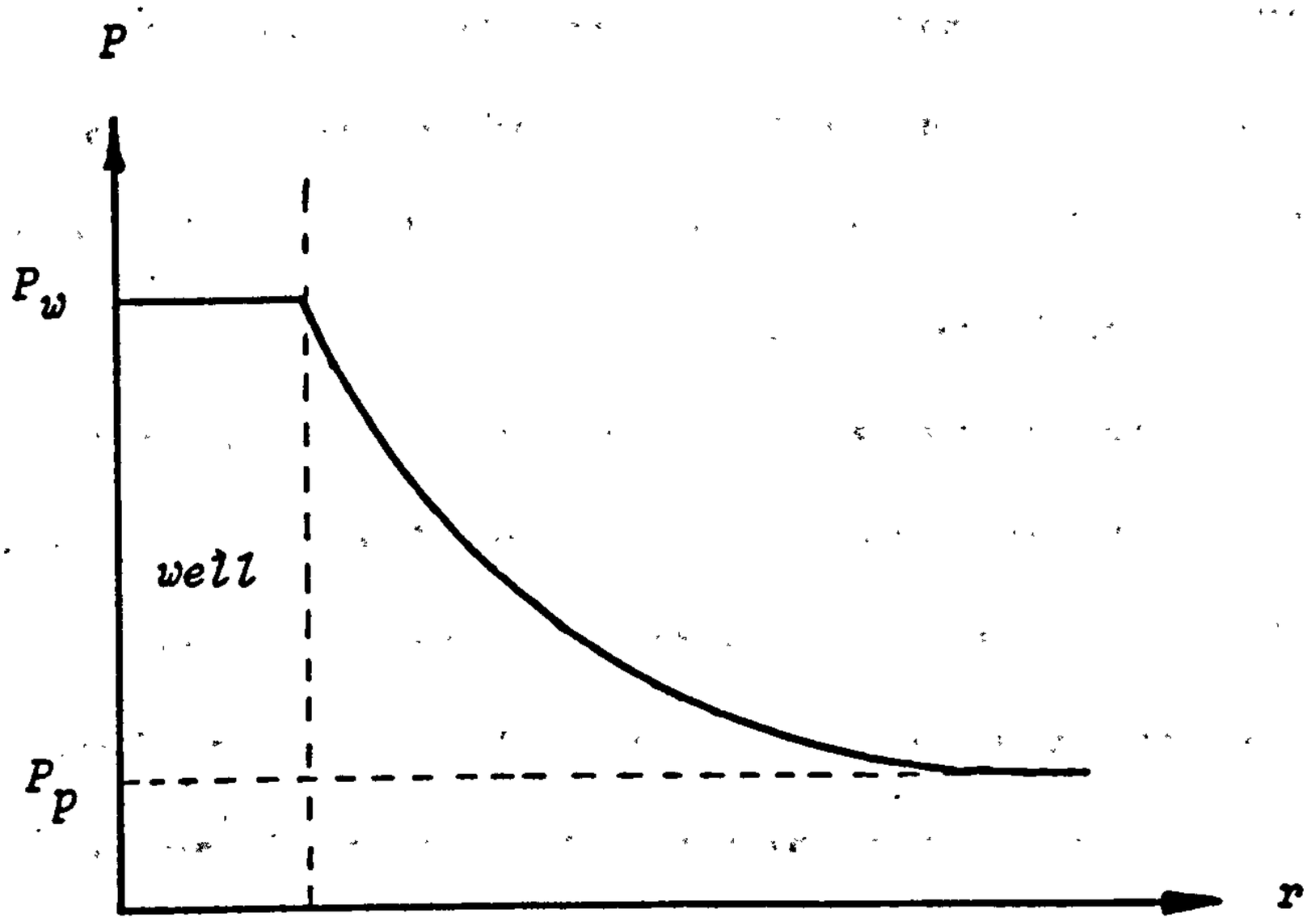

Figure 1.19(a) : Radial Pore Pressure Distribution for a Penetrating Fluid [53]

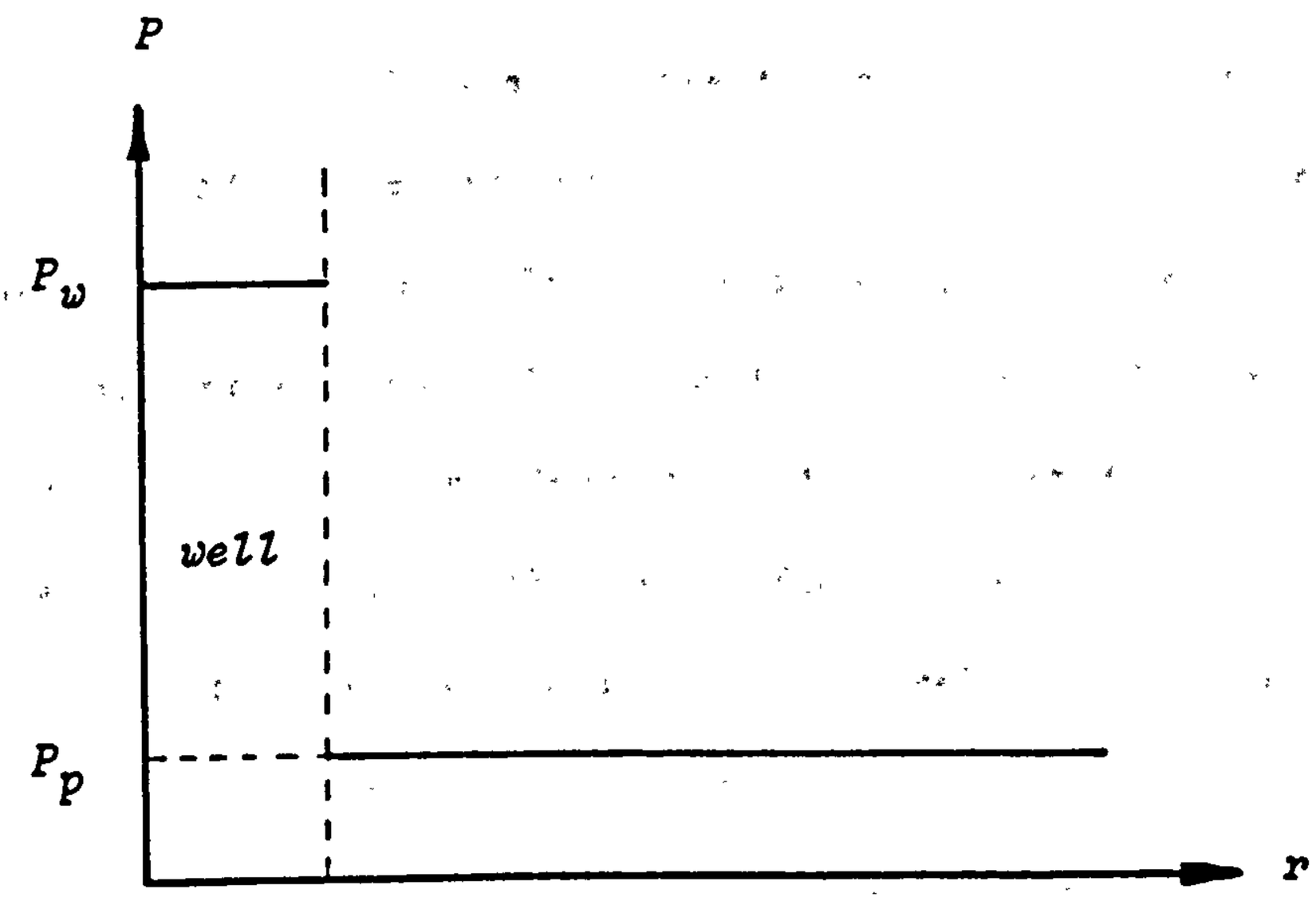

Figure 1.19(b) : Radial Pore Pressure Distribution for a Non-Penetrating Fluid [53]

reported. Bradley illustrated that the inclination of the borehole had an effect on fracture initiation pressure (Figure 1.20). As indicated by curve A, it can be seen that an inclined borehole in a normally stressed formation will fracture at a lower wellbore pressure than a vertical well. This effect was found to be more pronounced in tectonically active zones, as shown by curve B. In the case illustrated,. the wellbore pressure required to initiate fracturing is seen to decrease appreciably as the hole inclination increases. Bradley concluded by stating that fracture gradients measured in inclined holes need to be corrected for the effect of borehole inclination to obtain true values. He went on to state that fracture extension pressures were unaffected by borehole angle.

Geertsma [34], in his study of hydraulic fracture initiation pressures included a term for the tensile strength of the rock material which he modelled as a poroelastic solid. His results were similar to that of Haimson and Fairhurst for the case of a penetrating fracturing fluid. In his analysis, Geertsma realised that the poroelastic approach can only hold true when the rock behaves in an elastic manner. Geertsma stated that for competent rock this would usually be the case for tensile failure but suggested that if the rock surrounding the borehole had at any time behaved in a plastic manner it was no longer possible to apply elastic theory in order to predict fracture initiation pressure.

Medlin and Masse [54] studied fracture initiation in the laboratory and compared this with the results from a theory which was based on poroelastic behaviour. Their conclusions, published in 1979, were

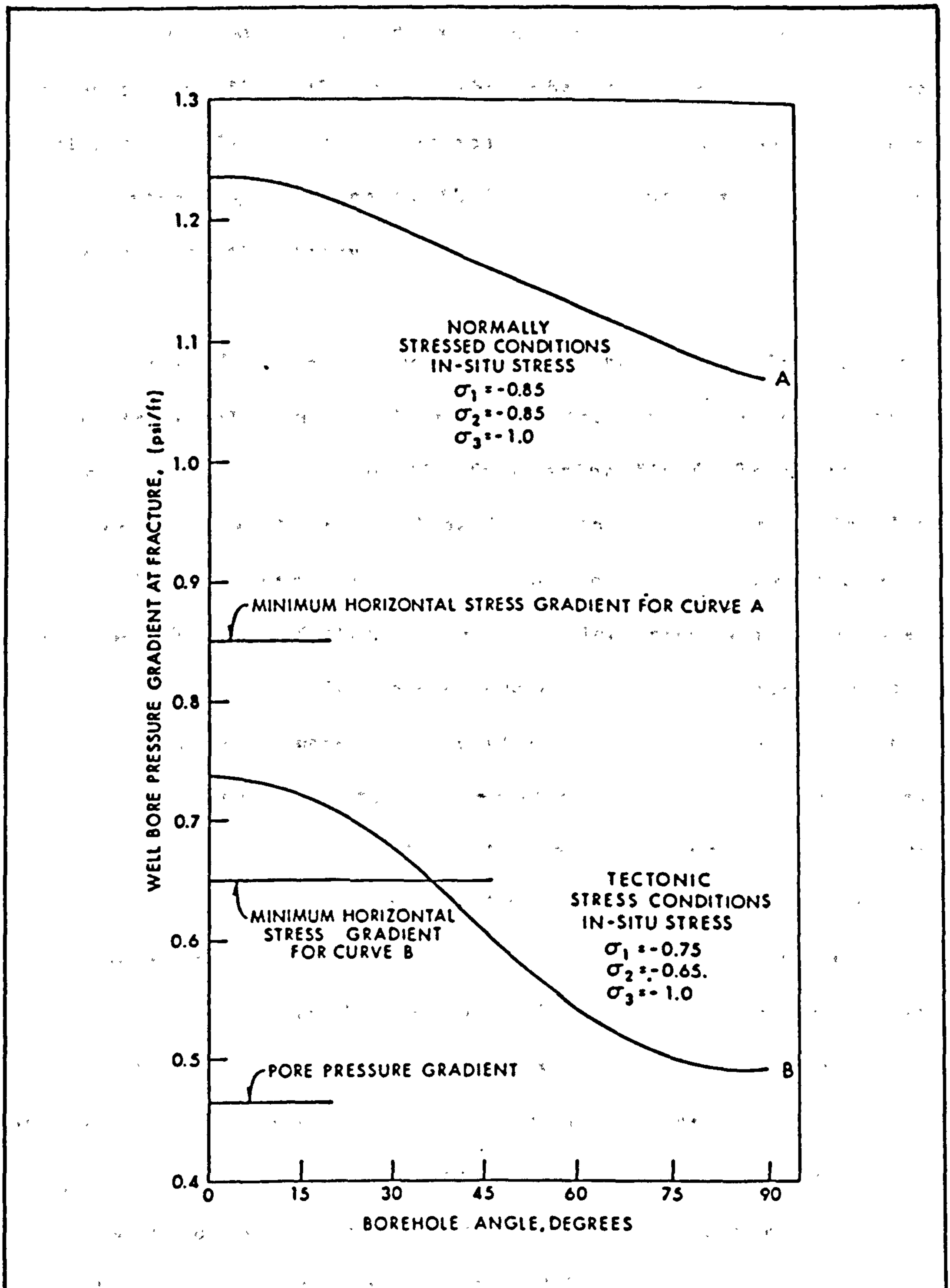

Figure 1.20 : Effect of Borehole Inclination on Fracture Initiation Pressure (after Bradley [31])

restricted to results for hydrostatic stress conditions. For the non-penetrating fluid they found that when the stresses exceed the elastic range, failure pressures would be lower than predicted. For the penetrating fluid case, their results were not completely consistent with the theory.

Horsrud et al [55], were the first to show how a plastic zone surrounding a well could influence the stress distribution around a wellbore during injection of the fracturing fluid. They extended their previous work on solid particle influx [37] to hydraulic fracturing by considering the effect of fluid flow into the formation. They showed that if the injection pressure was increased the plastic zone could increase or decrease in size depending on the rock properties; however, they stated that if the radius of the plastic zone decreased, the rock would not return to its original state. Horsrud et al went on to state that in a poorly consolidated sand, fractures would therefore be initiated in a plastically strained material and that the fracture initiation pressures calculated when taking this into consideration could be lower than those calculated using elastic theory. The difference depended on the initial state of stress and the rock properties and was found to be greatest when the sand was poorly consolidated and the stress ratio and Poisson's ratio were low. The difference was then typically in the order of magnitude of 10%.

1.6.5 Discussion of Fracture Gradient Prediction Methods

In the U.S. Gulf coast and other areas that have undergone extensive drilling, fracture initiation pressures are predicted using the empirical formulae presented earlier. These can be applied with confidence in other areas of similar geological and tectonic regime only when sufficient drilling has allowed calculation of the necessary empirical constants. The absence of any method for predicting fracture pressures outside these areas has necessitated the use of those empirical formulae, with the general result that actual fracture pressures can be very different from calculated pressures [56]. Accordingly, none of the empirical formulae can accurately predict stresses in poorly explored regions. An examination of the empirical formulae derived from well logs indicates that they essentially estimate the value of the minimum horizontal stress. Therefore, the empirical approach appears to underestimate the effect of the stresses around the wellbore due to penetration of the injected fluid into the porous formation. The estimation of fracturing pressures from pure elastic theory, however, has the tendency to predict higher gradients as the stress concentration around the hole is taken into consideration.

1.7 EFFECT OF CLOSURE STRESS ON A PROPPED FRACTURE

1.7.1 Proppant Selection

The selection of a proppant is mainly governed by the fracture conductivity needed for a desired production rate. This, in turn, is

related to the in-situ proppant permeability and concentration of proppant within the fracture. Each individual reservoir requires specific design criteria which dictates the physical properties of the proppant to be used. These physical properties, such as strength and density, vary with each proppant type, therefore a wide range of reservoir conditions can be satisfied. Qualitively, the comparable strengths and densities of each proppant is as follows:

PROPPANT	STRENGTH	DENSITY
Frac Sand	Weakest	Lightest
Intermediate	Medium	Medium
Bauxite	Strongest	Heaviest

1.7.2 Determination of Closure Stress

The strength required and permeability of a proppant are dictated by the anticipated closure stress. As previously mentioned, when a hydraulic fracture is created the in-situ stresses must be overcome to open and propagate the fracture. The same stresses tend to close the fracture and remain to act on the proppant. This is often referred to as the closure stress. If the proppant is not strong enough to withstand the closure stress of the fracture, it will be crushed and the permeability of the fracture will be drastically reduced.

The closure stress may be represented by the equation [57] :

$$CS = (P_{fg}D) - BHPP \quad .. \quad .. \quad .. \quad .. \quad .. \quad (1.29)$$

where CS = Closure Stress (psi)

P_{fg} = Fracture Gradient (psi/ft)

D = Depth of Fracture (ft)

BHPP = Bottom-Hole Producing Pressure (psi)

From the above relationship it is clear that the stress acting on a proppant is controlled or influenced by the producing pressure. It is common practice, however, to use the initial fracture gradient and the reservoir abandonment pressure to calculate the maximum closure stress on the proppant. As the reservoir pressure is depleted, both the fracture gradient and bottom-hole pressure are reduced, but at different rates. The net result is an increase in the effective stress on the proppant with time [58]. The most severe closure stress condition can happen early in the life of the well and close to the wellbore, because the amount of stress required to open the fracture is at the highest value. During cleanup and testing operations, the flowing pressure at the wellbore is often reduced to zero. Therefore, consideration should be given to this increase in closure stress when selecting the optimum proppant for a specific formation.

1.7.3 Effect of the Borehole on Closure Stress Estimation

Almost without exception, the stress concentration effects caused by the borehole are ignored in the calculation of closure stress [10].

It was indicated in the previous section that the empirical methods of predicting fracture gradients from well data appear to underestimate the effect of the stress concentration around the well due to penetration of the injection fluid into the porous formation. The formation integrity or leak-off test, which is most often used to give an indication of the fracture gradient, is not always straight forward to interpret, especially in permeable formations. Accordingly, these techniques are used to provide minimum fracture initiation pressures equal to, or slightly greater than the minimum horizontal stress. This is desirable to avoid problems of lost circulation, but to use the same method of determining fracture gradient to arrive at a realistic estimate of closure stress is questionable.

When the well is in production, fluid no longer penetrates into the formation but flows from it. This causes a pore pressure drawdown in the formation towards the wellbore and will accordingly increase the closure stress; however, the stress concentration induced by the borehole remains to act on the fracture. If the rock surrounding the borehole behaves in an elastic manner, the stress concentration is at a maximum at the hole periphery and will diminish some three to four radii from the hole (Section 1.3.3). If a plastic zone is induced around the well, however, the maximum stress concentration no longer acts on the wall of the borehole but on the face of the propped fracture at a radial distance dictated by the mechanical properties of the surrounding rock. Although this stress abutment, which will henceforth be termed the maximum closure stress, is localised, it may act to form a 'bottleneck' and accordingly

restrict the flow of fluid through the propped fracture when the well is produced. This will have the adverse effect of decreasing fracture conductivity and reduce the longterm effectiveness of the fracturing treatment.

1.8 DISCUSSION AND CONCLUSIONS

In the foregoing chapter, an attempt has been made to illustrate the factors which have to be taken into consideration when predicting the mechanical stability of a wellbore. Particular emphasis has been placed on understanding the rock mechanical factors that influence rock failure, which involved a detailed review of failure criteria. An extensive literature search was conducted in order to establish the present state-of-the-art knowledge on the rock mechanical aspects of borehole stability in compression as well as in tension. From the variety of papers reviewed, however, it is evident that the rock mechanical principles that affect borehole stability - the uncontrollable factors - are not fully understood.

The area in which there is greatest interest but also the greatest confusion is in the prediction of borehole failure in compression. There is general agreement on the occurrence of a plastic zone around a borehole; however, the majority of earlier workers have simplified the problem by examining a vertical well under a hydrostatic state of stress. More recent investigators, still making the unrealistic assumption of hydrostatic conditions, have introduced further complexities into their stress solutions as to make them over- complicated and difficult to apply to a field

situation. The case of a borehole in a nonhydrostatic problem has been investigated using elastic theory, but it has yet to be analysed using elastoplastic theory. It can be concluded that it is not possible to arrive at a totally mathematical solution to the problem, and as such, rock properties must be taken into consideration.

As regards borehole failure in tension, a lot more work has been carried out on this subject, mainly due to the fact that it is the same mechanism that is involved in hydraulic fracturing. Consequently, there is far more agreement over the causes of hydraulically induced lost circulation than is the case for compressional failure.

For the case of inclined holes, less information is known, although it is clear that a lower than usual wellbore pressure is required to prevent fracture initiation while at the same time a higher than usual wellbore pressure must be applied to prevent compressive failure. The approach used by Bradley [31] appears to be most applicable to field situations. However, an extended approach to include plasticity effects for inclined holes would greatly enhance the applicability of this theoretical work to real situations. Therefore, for inclined boreholes, further theoretical investigations into the effects of a plastic zone is required for a complete and accurate assessment of the state of stress when a well is excavated. This has to be coupled with laboratory and field testing to verify or disprove the theory. Promising moves in this direction was Geertsma's attempt to correlate compressive failure

with indentation results [34] while Bradley's use of well records to predict the state of stress and the rock strength regionally by applying stability theory warrants further investigation.

None of the approaches reviewed can lay claim to be the panacea to the problems of borehole instability. They all suffer to some extent from lack of testing in the laboratory or field. It is difficult to simulate field conditions in the laboratory and this makes it difficult to relate such studies to field conditions. Properties of formation samples inevitably change on transportation to the surface and accurate simulation of downhole conditions is costly, as is carrying out the tests. It is clear that in the interests of greater control over borehole stability, much more practical work has to be undertaken.

The foregoing analysis has exposed the following areas which require either further or exploratory research.

(1) The state of stress around inclined boreholes should be investigated by a physical modelling method, such as the photoelastic technique, in order to confirm that inclined holes are indeed less stable than vertical boreholes. The results of this analysis could then be applied to develop or enhance existing analytical methods to arrive at a better understanding of the induced state of stress and to provide more reliable stability predictions.

(2) There is ample scope for research into the stability of inclined boreholes in a non-hydrostatic stress regime using elastoplastic theory. Such an investigation should consider flow of fluid into and out of the formation and the effect of an altered permeability in the plastic zone with the objective of predicting maximum and minimum mud weights which can be carried in the wellbore.to prevent instability. In order to apply these findings to a field situation, mechanical property tests would have to be performed on reservoir core to provide information on rock deformation failure criteria. Therefore, a great deal of rock mechanical testing is indicated.

(3) If the concept of a plastic zone surrounding a well is accepted, it follows that the direct effect of such a zone on the maximum closure stress acting on a propped fracture should be investigated. Such an analysis has not previously been dealt with in the literature although realistic estimates of closure stress are essential in order to optimise proppant selection.

CHAPTER TWO

EXAMINATION OF THE INDUCED STATE OF STRESS AROUND INCLINED BOREHOLES USING THE PHOTOELASTIC TECHNIQUE OF STRESS FREEZING

2.1 INTRODUCTION

The intention of this chapter was to investigate the induced state of stress produced around deviated boreholes in a triaxial stress field by means of the three-dimensional photoelastic technique of stress freezing.

A photoelastic model containing inclined boreholes was prepared and a loading frame designed and fabricated to provide triaxial loading to the model. Stress analysis was performed using a polariscope while the secondary principal stresses were separated by the Shear Difference method. The effect of wellbore or 'mud' pressure was not considered in this analysis. Although this loading in a homogeneous, isotropic, perfectly elastic medium did not actually simulate the stress state around an oil well in a porous, non-homogeneous, anisotropic medium, it was felt that it was an experimental step which would lead to useful information about the actual state of stress around the vicinity of an inclined hole.

2.2 THE PHOTOELASTIC TECHNIQUE

2.2.1 The Development of Photoelasticity

Photoelasticity is an experimental technique which enables the stress concentrations produced within a loaded, transparent model to be measured. It is one of the more useful methods for making quantitative stress analysis in both two and three-dimensions. Even though the method is experimental, the assumptions and principles of

the theory of elasticity are required to translate the measured optical effects into terms of stress. It is not possible, however, to directly observe the separate maximum and minimum principal stresses, σ_1 and σ_2 - termed P and Q in two-dimensional photoelastic analysis, within a stress field. It is therefore necessary to utilise further techniques in order to determine the magnitude and direction of these stresses.

The optical phenomenon upon which the science of photoelasticity is based is the quasi-crystalline behaviour of certain stressed, transparent materials. This effect was first discovered by Sir David Brewster in 1816 when he noted that glass when stressed or strained became double refracting. He further noticed that the degree of optical anisotropy was proportional to the applied stress or strain. It has since been found that this property is present to some degree in most transparent solids.

Little progress was made, however, towards the application of photoelasticity to general engineering problems. With the introduction of celluloid as a model material, Filon and Coker [59] developed and applied the technique to such problems and published their findings in their Treatise on Photoelasticity.

Prior to 1952, the photoelastic method was limited to analysis of two-dimensional surface stress distributions, except in special cases of symmetry. At this time, Frocht and Guernsey [60] showed that it was possible to determine interior stresses thus solving the 'general space' problem. This was accomplished by extending the

shear difference method to cover three dimensions and by employing a technique known as 'Stress Freezing'. Accordingly, this technique has been utilised for the purpose of this study.

Today, photoelasticity is a well established science, and as such, there are many text books which deal with the subject admirably [61-63]. Accordingly, only a brief discussion of the theory of photoelasticity is given, followed by an account of the essential photoelastic apparatus and an explanation of the photoelastic effect.

2.2.2 Photoelastic Theory

Photoelastic theory is founded on two subjects, namely optics and stress/strain analysis. The application of these two subjects to birefringence is defined as the 'Stress-Optic Law' [63].

Certain transparent materials such as glass, Araldite, Bakelite, Solithane 113 and other plastics are optically isotropic when unstressed. When stressed, however, they become anisotropic and behave like a uniaxial crystal. In general, a plane-polarised wave entering a stressed plate of one of these materials is split into two components which are plane polarised in the directions of the principal stresses at that point [62]. These components are not transmitted with the same velocity, so that upon leaving the plate they have a relative path retardation. The magnitude of this relative retardation is directly proportional to the difference between the principal stresses, (P-Q), and the thickness of the

plate, while being inversely proportional to the wavelength of the light. Hence,

$$R = \frac{C_\sigma t}{\lambda} (P-Q) \qquad .. \quad .. \quad .. \quad .. \quad .. \quad (2.1)$$

where R = Relative retardation in the plane of P and Q

P = Maximum principal stress at point of interest

Q = Minimum principal stress at point of interest

λ = Wavelength of the light

t = Thickness of the plate (model)

C_σ = The relative stress optical coefficient

2.3 ESSENTIAL PHOTOELASTIC APPARATUS AND THE PHOTOELASTIC EFFECT

2.3.1 Introduction

A complete photoelastic analysis can only be performed using a polariscope. A polariscope is an instrument which is used to measure the relative retardation produced when polarised light is passed through a stressed material. There are two types of polariscope which may be used for photoelastic analysis. They are respectively known as the Plane Polariscope and the Circular Polariscope.

2.3.2 The Plane Polariscope

A Nicol prism, or any other polarising prism, will convert ordinary light into plane polarised light. Figure 2.1 shows two polarising prisms with coinciding centre lines parallel to the path of a ray of

natural light emanating from a nearby source.

The prism or plate nearest the light source will be referred to as a polariser, the other, as an analyser. It is evident that the effect of the analyser upon the light emerging from the polariser depends on the relative position of the principal planes. Two cases are of special interest: one when the principal planes are parallel as shown in Figure 2.1(a), and the other when they are perpendicular or crossed with respect to each other as indicated in Figure 2.1(b). In the first case, all the light will pass through while in the second, no light will get through.

In a crossed, plane polariscope, there exists a plane polarised beam which is completely extinguished by the analyser, yielding a dark background when a stressed medium is placed within its field.

2.3.2 The Circular Polariscope

This optical arrangement is shown schematically in Figure 2.2 and consists of four elements, two polarising plates and two quarter-wave plates. The polariser and analyser are in a crossed position as are the optical axes of the quarter-wave plates which are set at 45° to the principal plane of the polariser.

If a beam of natural light enters the polariser the optical transformation will be as symbolically indicated in Figure 2.2(a). The polariser, as before, will convert the natural light beam into plane polarised light. On entering the first quarter wave plate,

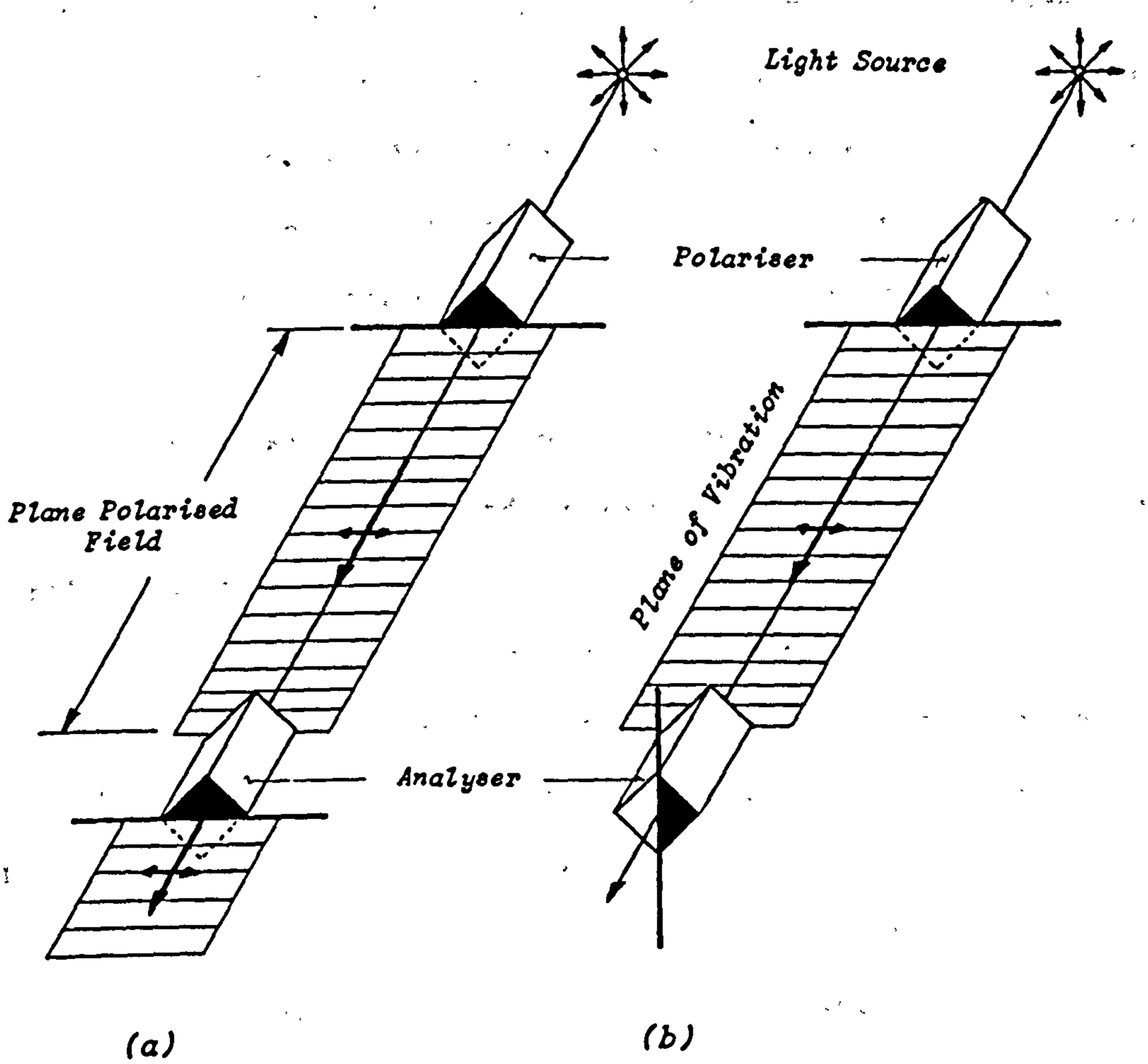

Figure 2.1 : The Plane Polariscope (after Frocht [63])

this ray is split into equal components and will emerge as a beam of circularly polarised light. From the preceeding paragraph it follows that the effect of the second quarter-wave plate, which is crossed with respect to the first, will be to restore the circular polarised light to a plane polarised beam. The analyser, being crossed with respect to the polariser, will therefore prevent this beam emerging from the analyser. If the optical axes of the quarter-wave plates are set parallel with the axes of the polariser and the analyser respectively, the instrument will behave as a plane polariscope.

The circular polariscope set-up described above effectually stops the light from the source and is used when a dark background is desired. Sometimes, however, it is preferable that the polariscope transmit rather than stop the light. This can be accomplished by crossing the Nicols and paralleling the quarter-wave plates, or by paralleling the Nicols and crossing the quarter-wave plates. In order to obtain circularly polarised light, the principal plane of the first quarter-wave plate must be set at 45° to the principal plane of the polariser. In both cases, the analyser will transmit a beam of plane-polarised light. Such an arrangement is illustrated in Figure 2.2(b), and is used when stress patterns against light backgrounds are required instead of the usual dark backgrounds i.e. to produce half-order isochromatic fringes.

The circular polariscope is used when it is desirable to eliminate the isoclinics from the isochromatic fringes - the birefringence exhibited in a stressed medium.

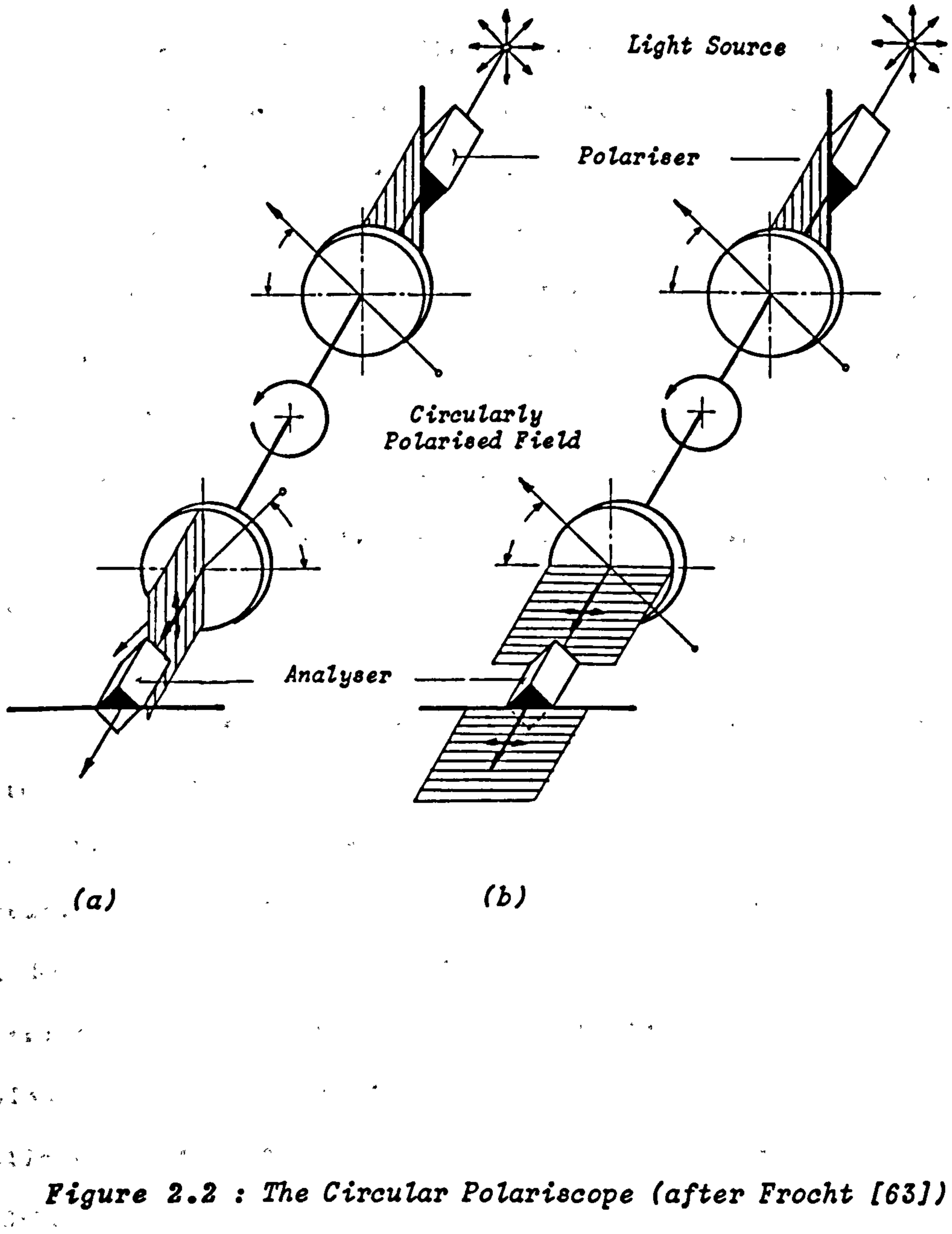

Figure 2.2 : The Circular Polariscope (after Frocht [63])

2.3.3 The Isoclinic Fringe

As stated previously, when a photoelastic model is stressed, it produces a fringe pattern when viewed in a plane polariscope. When one of the principal stress directions is parallel to the principal plane of the polariser, the transmitted intensity is zero. A continuous, dark band called an isoclinic fringe will be observed to pass through all points in the stress field where this occurs. The isoclinic fringe is thus the locus of points at which one or other of the principal stresses is parallel to the polarising axis of the polariser. The sharpness of the isoclinic fringe depends upon and indicates the rate of change of the principal stress directions over the field. The greater the rate of change, the greater the degree of the isoclinic.

It is usual to refer the principal stress directions to a suitable datum line on the model, such as an edge or an axis of symmetry. The angle between this line and the direction of the algebraically greater principal stress is referred to as the isoclinic parameter θ. For any given setting of the crossed plane polariscope, a corresponding isoclinic pattern can be observed. As the crossed polariser and analyser are rotated together, usually in an anticlockwise direction, the isoclinic pattern changes. In a given model, there will be an isoclinic line corresponding to every value of θ between 0° and 180°. Successive isoclinics can be recorded photographically or traced by hand from a projection screen to provide a map of the principal stress directions. Stress

trajectories, which indicate the direction of the principal stresses, may then be constructed graphically from the isoclinic map [64]. The isoclinics produced in a stressed 'elbow' are illustrated in Figure 2.3(a).

2.3.4 The Isochromatic Fringe

If a stressed model is viewed in white light, coloured lines or fringes are observed where the retardation and principal stress differences are constant, i.e. lines of constant (P-Q). The colour depends on the degree of retardation and is the complement of that extinguished by interference. These coloured fringes are called isochromatics.

If monochromatic light is used, a dark fringe will appear where the retardation is a multiple of the wavelength of the light used. These lines are called monochromatic fringes and are generally very distinct. Most photoelastic analysis is conducted using this type of light source as accurate measurements can be made from well defined monochromatics. The monochromatic fringe pattern obtained from a stressed 'elbow' joint is illustrated in Figure 2.3(b).

2.3.5 Distinction Between Isoclinic and Isochromatic Fringes

From the foregoing analysis, it is evident that when a stressed model is placed in the field of a plane polariscope, two different systems of fringes appear simultaneously, namely the isoclinics and isochromatics. If white light is used, they can be easily

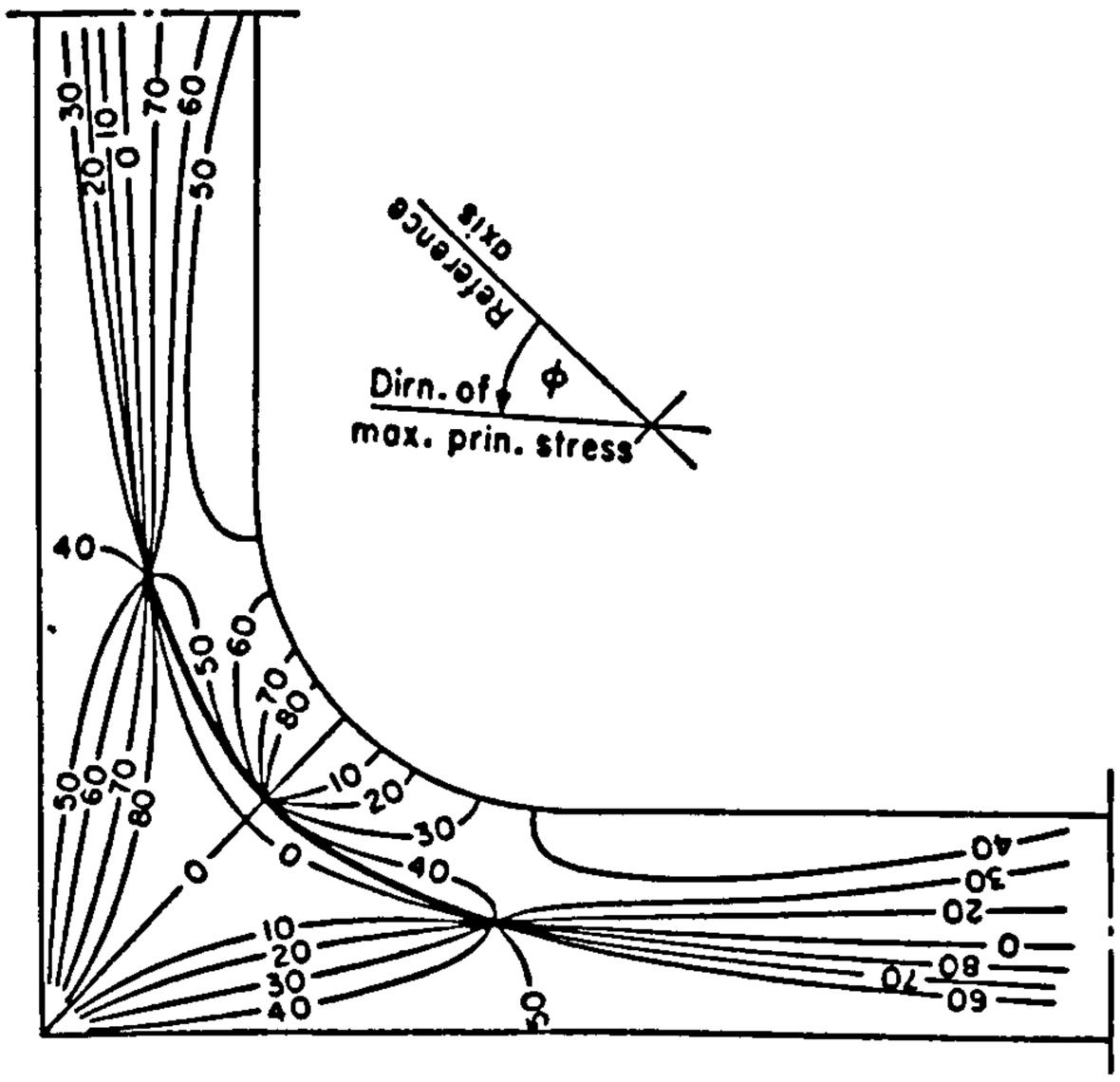

Figure 2.3(a) : Isoclinics Produced in a Stressed Elbow (after Hendry [61])

Figure 2.3(b) : Isochromatics Produced in a Stressed Elbow (after Hendry [61])

distinguished from each other as the isoclinics are black while the isochromatics, with the exception of the zero fringe, are coloured. With monochromatic light both sets of fringes are black; however, the monochromatics are nevertheless distinguishable as they are more sharply defined. Accordingly, if a circular polariscope is used, the isoclinics are optically removed.

2.3.6 The Tardy Method of Compensation

In photoelastic stress analysis, it is often necessary to determine the fringe orders at various points in the model. Points that do not lie on fringe lines have fractional values of fringe order N. The Tardy method of Compensation [65], provides a means of obtaining fractional fringe orders by rotation of the analyser. Consider a point in a model lying between fringe orders of N and (N+1), the following steps are taken to determine the fractional fringe order:

(1) With a plane polariscope arrangement, the polariser and analyser are rotated until an isoclinic fringe passes through the point in question.

(2) The quarter-wave plates are then inserted and rotated to attain a crossed circular polariscope arrangement, taking care not to adjust the polariser or analyser.

(3) The analyser is then rotated until an isochromatic fringe coincides with the point. The angle θ through which the analyser is rotated should then be noted.

(4) If the (N+1) fringe order moves to the point as the analyser is rotated through the angle θ, then the fringe order at that point, say P, is given by:

$$N_p = (N+1) - \frac{\theta}{180} \qquad .. \quad .. \quad .. \quad .. \quad .. \quad (2.2)$$

(5) If the N^{th} order fringe moves to the point as the analyser is rotated, then the fringe order at the point is:

$$N_p = N + \frac{\theta}{180} \qquad .. \quad .. \quad .. \quad .. \quad .. \quad (2.3)$$

When the analyser is rotated through 90°, then the half-order fringes appear. Maximum light is transmitted in this position i.e. a light field transmission.

The Tardy Method provides a simple means of determining fractional fringe orders. It does not, however, provide values of the integral fringe orders. In models where the values of the integral fringe orders are not known, an alternative method of compensation is required to provide firstly the integral fringe order and secondly, the fractional fringe order. Two methods exist, colour matching techniques [66] and the use of an optical element, such as the Babinet Compensator [67]. These procedures are well described in the literature and will not be reproduced here.

2.4 THREE-DIMENSIONAL PHOTOELASTICITY

2.4.1 The Frozen Stress Method

Three-dimensional photoelasticity is based on the fact that it is possible to produce frozen stress patterns in certain photoelastic materials. This is accomplished by means of the Frozen Stress Method [68]. A frozen stress pattern is one that remains in the material after the load is removed. At room temperature the fringe pattern disappears upon removal of the load, the same is true at high temperatures. If the load is applied at high temperature, however, and maintained constant while the temperature of the material is cooled slowly to room temperature, the fringe pattern remains and effectively becomes 'frozen' in the model. Removal of the load at room temperature does not remove the fringe pattern. Once the fringes are frozen in a model they are unaffected by changing its shape by cutting, milling or filing, provided these operations do not raise the temperature of the model above its softening or critical temperature.

The load may be applied to the model either before or after reaching the critical temperature, although in practice, the former procedure is usually adopted. Extreme accuracy is required to ensure that the model is subjected to the correct loading as even small loading errors can cause a large discrepancy in the frozen stress pattern. Overloading could result in excessive deformations in the model due to the low rigidity of the material at elevated temperatures. The heating of the model is best carried out at a steady rate and

adequate time must be allowed before commencing the cooling process to ensure that the softening point has been reached in the centre of the model. Cooling must be carried out slowly to avoid the formation of thermal stresses.

When a frozen stress model is viewed in a polariscope, a complex fringe pattern is observed which is not readily analysable. In this condition, however, the model can be sliced without modifying the fringe patterns. These slices may then be analysed individually as in the manner of two-dimensional photoelasticity. In interpreting the isochromatic fringe pattern in an arbitrarily oriented slice viewed normally, a general form of the stress optic law is used with the principal stresses P and Q replaced by secondary principal stresses in the plane of the slice.

2.4.2 The Scattered Light Method

A more recent development of stress analysis in three-dimensions is the Scattered Light Method. This technique, originally proposed by Weller [69] in 1939 and subsequently developed by Jessop [70] and Srinath [71], opened up the possibility of observing the effects of stress in a three-dimensional model without slicing and therefore without resorting to the freezing process. In practice however, it is usually applied to the measurements of stresses at a free boundary or in a plane of symmetry.

The scattered light theory is well described in the literature and will not be reproduced here. The construction, within the Department

of Mineral Resources Engineering, University of Strathclyde of a modified polariscope as required for scattered light photoelasticity, is detailed by the doctorial thesis of Davies [72].

2.5 STRESS ANALYSIS

2.5.1 Separation Of The Principal Stresses

The isochromatics produced in a two-dimensional photoelastic model represent the loci of points of constant principal stress difference. In slices obtained from three-dimensional models, however, the isochromatics generally represent loci of constant secondary principal stress difference. Several methods have been devised to separate the principal stresses. These include the Filon's Graphical Integration method [73], the Oblique Incidence Method [74], Frocht's Shear Difference Method [75], and methods of determining the isopachics. The latter includes graphical and numerical methods [76], and also experimental procedures using lateral extensometers.

In three-dimensional photoelasticity, the two most widely used methods are by Shear Difference and Oblique Incidence. For the purpose of this investigation, the Shear Difference Method was chosen to separate the principal stresses as it is readily adaptable to computer application and offers good results if the isoclinic lines are located with sufficient accuracy. The application of the technique is given below.

2.5.2 The Shear Difference Method

This method utilises the isochromatics and isoclinics to calculate the normal and tangential stresses along an arbitrary line [75].

Referring to Figure 2.4(a), OX is an imaginary line in a photoelastic model along which it is desired to calculate the normal and tangential stresses, OY is the axis normal to OX. If an integration is performed along OX and using lines of finite length, the differential equations of equilibrium are accordingly transformed into equations of finite differences, thus

$$\sigma_{x_n} = \sigma_{x_o} - \int_o^n \frac{\partial \tau_{xy}\, \partial x}{\partial y} \qquad .. \;\; .. \;\; .. \;\; .. \;\; .. \;\; (2.4)$$

If $\partial y = \partial x$, then the above equation expressed in finite difference form is reduced to:

$$\sigma_{x_n} = \sigma_{x_o} - \sum_o^n \Delta\tau_{xy} \qquad .. \;\; .. \;\; .. \;\; .. \;\; .. \;\; (2.5)$$

The shear difference, $\Delta\tau_{xy}$, may then be determined from photoelastic data. In order to determine the rate of change of τ_{xy} with sufficient accuracy, the shear stress value should be calculated at corresponding points along two auxiliary lines A-A and B-B, equidistant from line OX. This is performed by the following relationship:

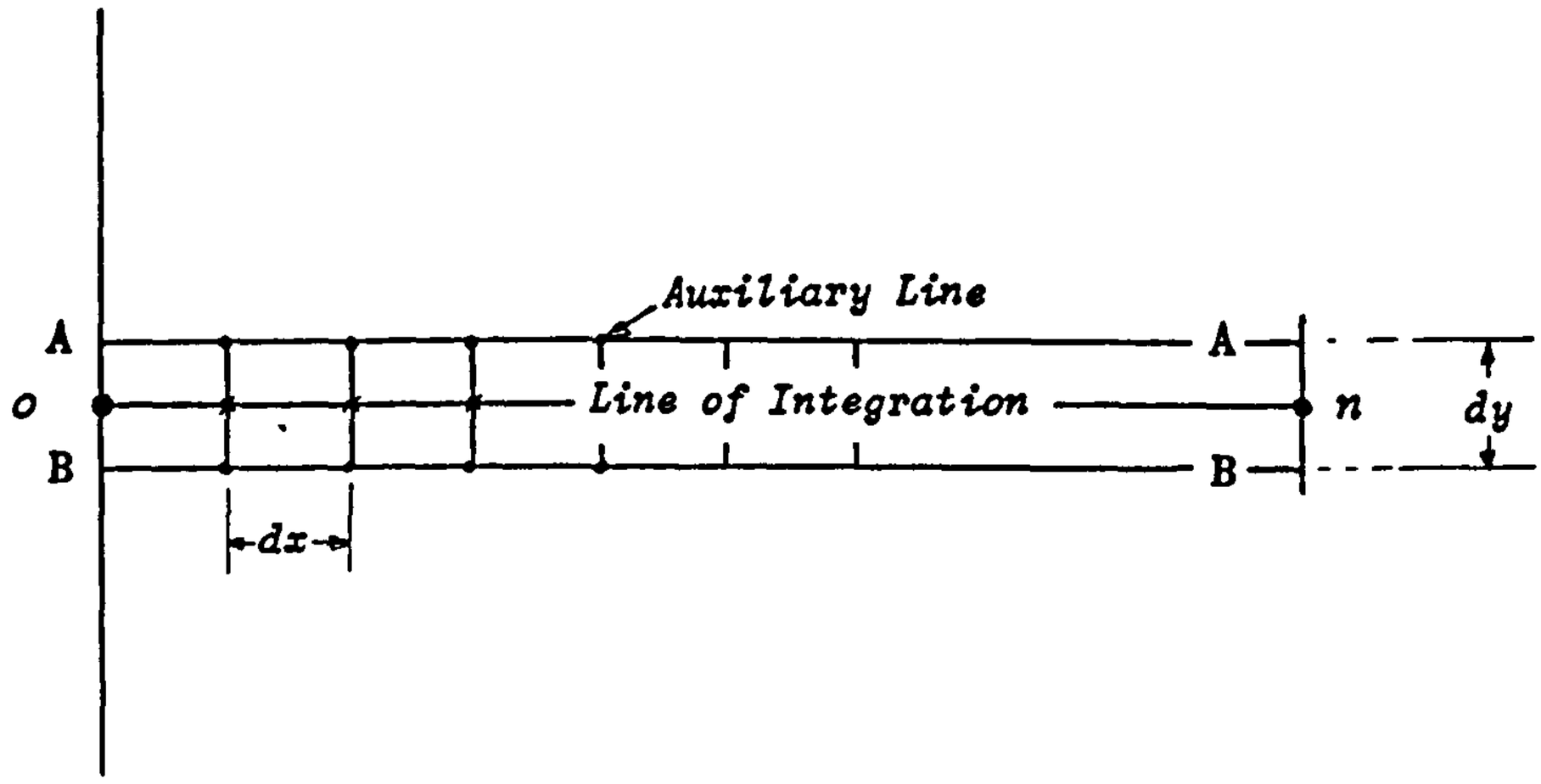

Figure 2.4(a) : The Shear Difference Method

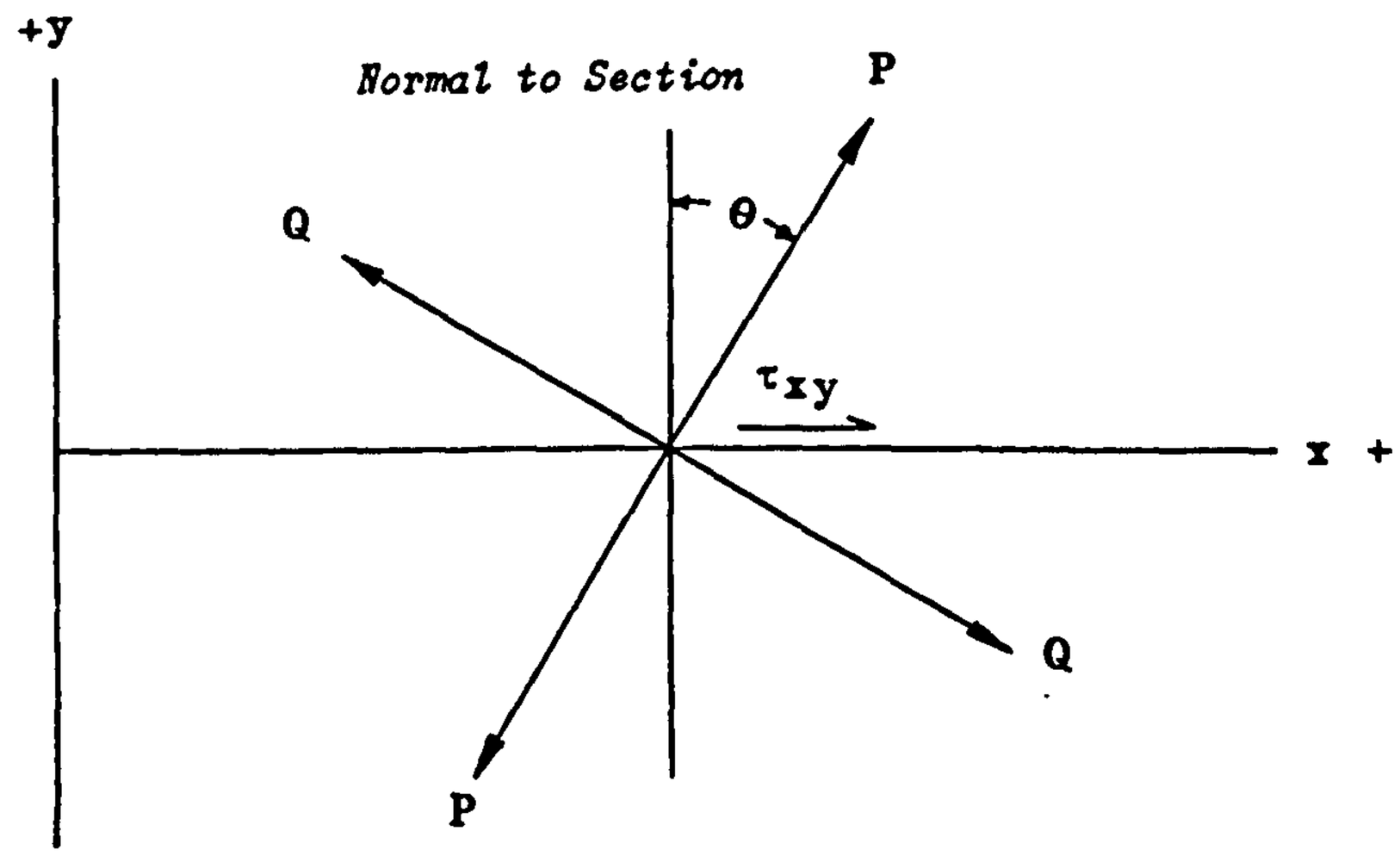

Figure 2.4(b) : Sign Convention for Shear Difference Method

$$\tau_{xy} = \frac{(P-Q)}{2} \text{ Sin } 2\theta \qquad .. \quad .. \quad .. \quad .. \quad (2.6)$$

The Shear difference is therefore:

$$\Delta\tau_{xy} = (\tau_{xy})_{A-A} - (\tau_{xy})_{B-B} \qquad .. \quad .. \quad .. \quad (2.7)$$

In practice, line OX and auxiliary lines A-A and B-B are divided into elements of equal length by a perpendicular system of lines as indicated in Figure 2.4(a). The shear difference is then calculated at each point along line OX. The normal stress acting in the X-direction σ_x, may then be obtained by means of equation (2.4), commencing the integration from a point on a free boundary where $\sigma_x = 0$ or from a point where σ_x is known.

The isoclinic parameter θ is measured clockwise between the normal to the section of integration and the direction of the greater principal stress. The sign convention used for the shear difference method is shown in Figure 2.4(b). To avoid errors in computation, this convention must be strictly adhered to.

Knowing the value of σ_x, the normal stress acting in the Y-direction σ_y, may then be obtained from the standard equation:

$$\sigma_y = \sigma_x + [(P-Q)^2 - 4\tau_{xy}^2] \qquad .. \quad .. \quad .. \quad (2.8)$$

The positive sign before the root is taken if $\sigma_y > \sigma_x$, as is the case when the algebraically greater stress P makes an angle of less than 45^0 with the normal to the section. The principal stresses P

and Q may then be obtained from,

$$P,Q = \frac{(\sigma_x - \sigma_y)}{2} \pm \frac{(P-Q)}{2} \qquad .. \quad .. \quad .. \quad (2.9)$$

The normal stress to the x-y plane, σ_z, can then be obtained from the plane strain formula, where $\gamma = 0.5$ for Araldite CT200 at stress freezing temperatures, viz.

$$\sigma_z = \gamma \ (\sigma_x + \sigma_y) \qquad .. \quad .. \quad .. \quad .. \quad .. \quad (2.10)$$

The shear difference method involving stress components in three-dimensions is more complex, involving the determination of the slopes of shear stress in two mutually perpendicular planes and may involve the use two similar models or sub-slicing techniques. The expansion of the shear difference method into three-dimensions is well documented by Frocht and Guernsey [60] and will not be reproduced here.

Thus, the shear difference method can be applied to both two and three-dimensional problems. The accuracy of the method depends significantly on the precision in determining the values of the isoclinic parameter, due to the term Sin2θ. In models where the isoclinics are easily deliniated, the shear difference method will provide an accurate means of determining the separate principal stresses.

2.6 CONSIDERATIONS IN MODEL DESIGN

2.6.1 Properties of Photoelastic Materials

The essential properties of a transparent material suitable for frozen stress photoelasticity models may be summarised as follows [77] :-

(1) The material must not show any double refraction before the application of external loads.

(2) The stress-strain and stress-retardation relationships should be linear.

(3) The fringe pattern must be retained in the material without alteration for a reasonable length of time.

(4) The material must have a well defined softening temperature.

(5) The material must have adequate mechanical strength and must be easy to machine without chipping or developing machining stresses. Good casting properties are of great value.

(6) The material must be moderate in cost and readily avaliable.

2.6.2 Choice of Material

The selection of a photoelastic material is governed by the individual problem to be investigated, the data required and the procedure to be employed.

Epoxy resins are today the most widely used photoelastic materials, being suitable for both two and three-dimensional investigations and for use as birefringent coatings. They possess good mechanical properties, are only slightly susceptible to edge effects and are avaliable at comparitively low cost.

Epoxy resins suitable for photoelastic use are commercially avaliable under the trade names of Araldite CT200 and Araldite MY753 [78]. The former is highly recommended for photoelastic models as it has reasonable transparency, is readily machinable and exhibits little creep at room temperatures. For this reason, Araldite CT200 was chosen as the transparent medium for the purpose of this study.

2.6.3 Model design and Preparation

A solid block of Araldite CT200 was obtained direct from the manufacturers, Sharples Mechanics Ltd. Receiving the material pre-cast prevented the difficult task of mixing the araldite resin and hardener without the entrapment of air bubbles, as reported by Karim [79].

The araldite block was squared off in a milling machine to form a true cube of 150 mm side length. To avoid chipping, moderate speeds and sharp tools were required. It was found that the use of cooling fluid made little difference to the production of machining stresses; however, it was retained as a means of removing cuttings. Throughout the above operations, the recommendations of Dixon [79] with respect to the machining of photoelastic materials were closely followed.

The positioning of the boreholes was the next consideration. The original intention was to examine three boreholes:- one vertical, one horizontal and the other inclined at 45°. As the main object of this investigation, however, was to investigate the stress concentrations around deviated wells, it was decided to include two further inclined holes at respective angles of 25° and 60° to the vertical.

The disadvantage in drilling a large number of holes in close proximity was the danger of stress interference between the simulated boreholes. It was established in the preceeding chapter that for a circular hole in an elastic medium under biaxial compression, the maximum stress concentration would be 2σ and that this stress concentration diminishes some three to four radii form the hole periphery. Although this simplification is valid only for two-dimensional circular openings, it was felt that it gave a reasonable indication of the possible stress effects.

All dimensions in millimetres

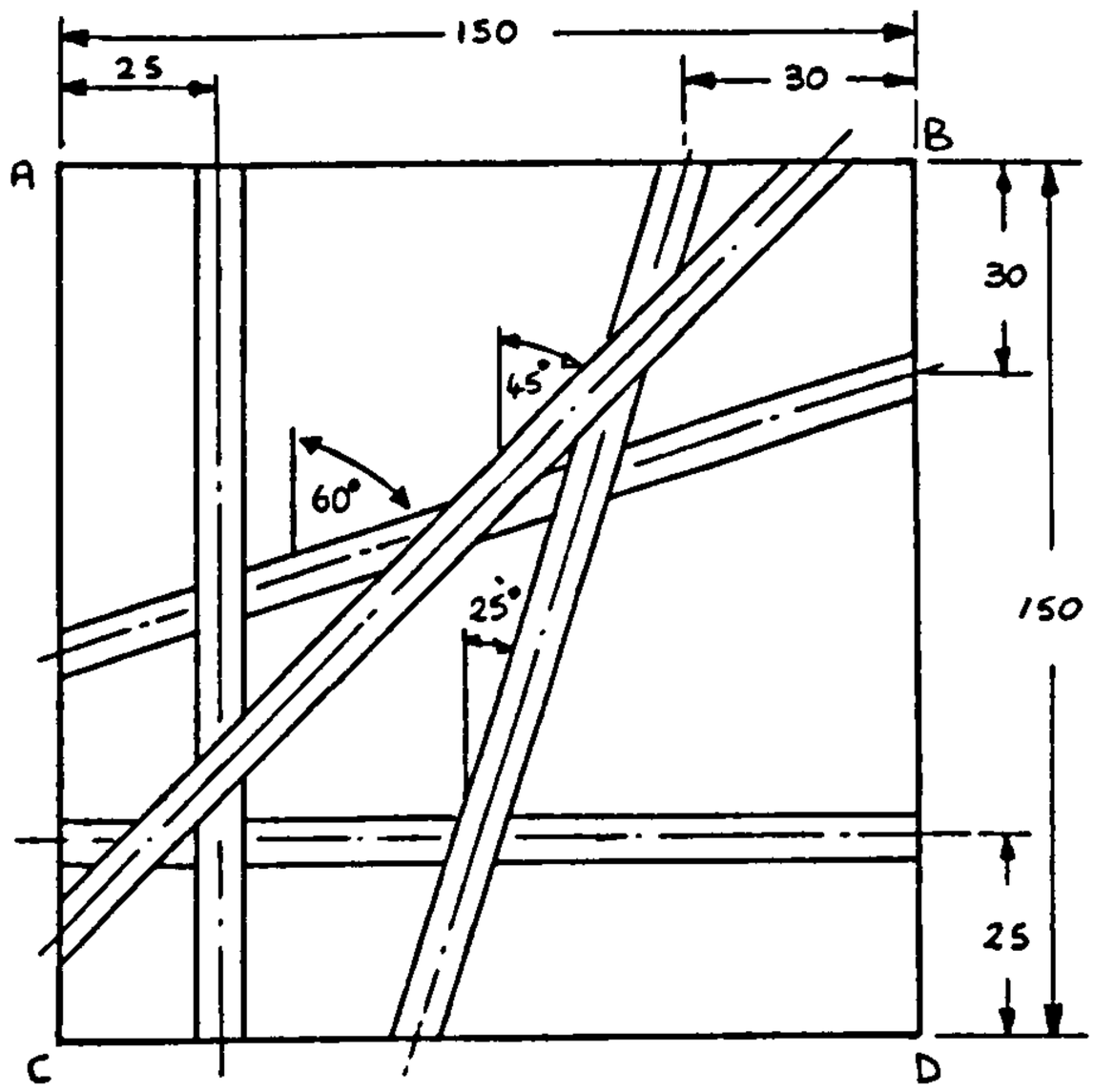

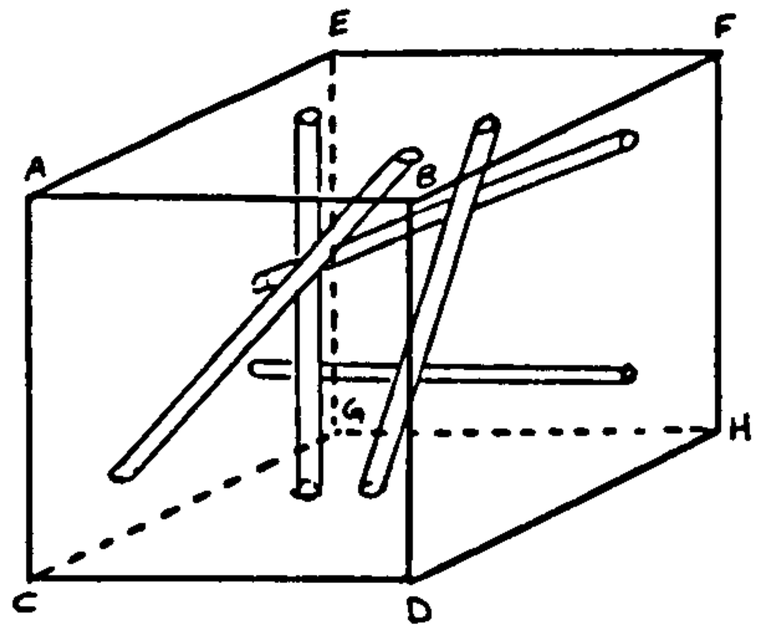

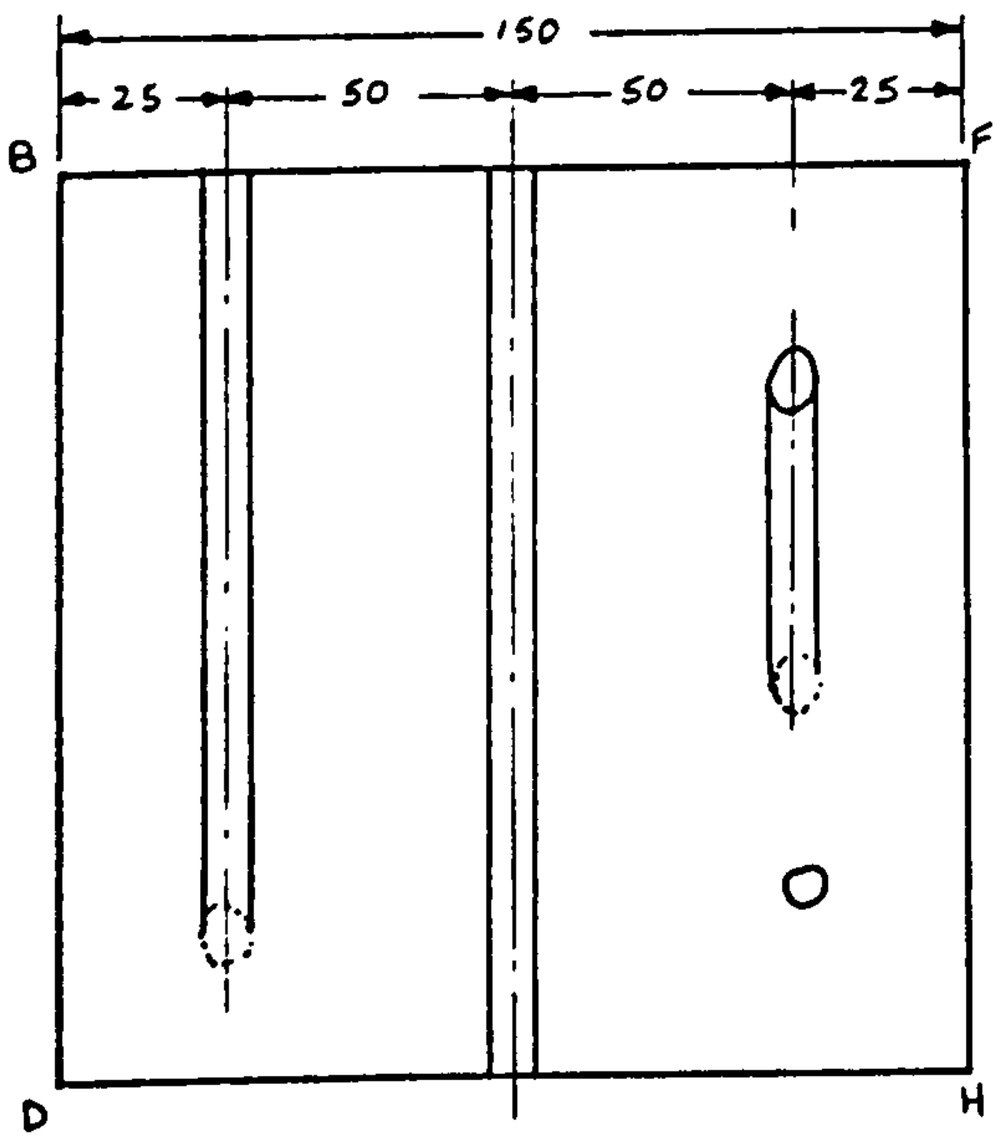

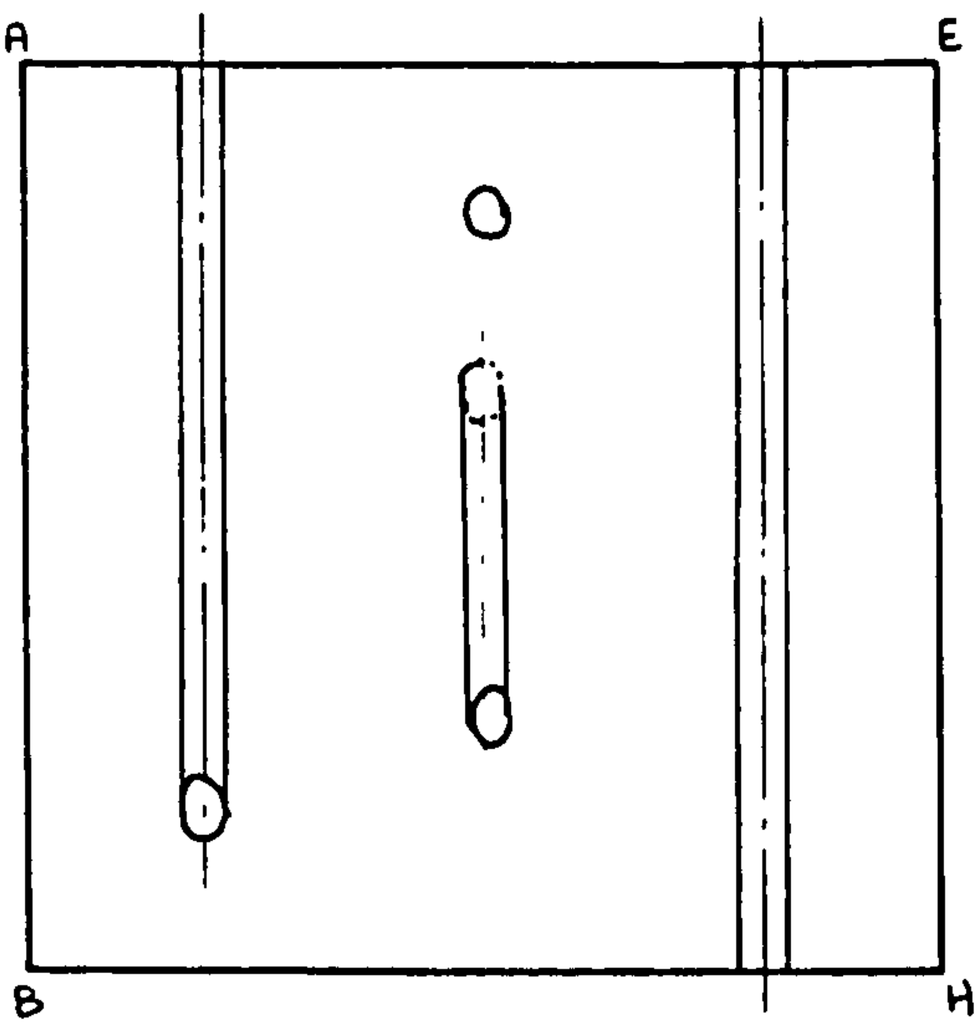

Figure 2.5 : Diagram of Borehole Layout in Photoelastic Model

The bit used to drill the holes in the araldite block had a diameter of 6 mm, thereby producing a hole of radius 3 mm. The minimum planer spacing was therefore specified at 36 mm (2 x 18 mm). A diagram of the borehole layout is given in Figure 2.5.

On examination of the model in a circular polariscope, it was found to contain appreciable machining stresses. It was therefore necessary to anneal the unloaded model by passing it through through repeated stress freezing cycles (outlined in Section 2.8.3) to remove the undesired stresses.

2.7 DESIGN AND CONSTRUCTION OF A SUITABLE LOADING FRAME

2.7.1 Loading Requirements

As the photoelastic model was to be loaded in a manner as near in situ conditions as possible, it was required to construct a loading frame which would be able to :-

(1) Simulate the three-dimensional state of stress, as occurs at great depth (Figure 2.6(a)).

(2) Simulate plane strain loading.

(3) Have the facility to alter the vertical to horizontal stress ratio.

As the loading frame and model were required to be inserted into the stress freezing oven, the limiting factors in the design were temperature, physical size and the method of applying the desired load. It was not considered practically possible to attempt to simulate 'mud weight' by applying air pressure to the wellbore as the requirement for three-dimensional loading necessitated that the model be surrounded by a loading frame and accordingly the provision of wellbore air-supply lines would overcomplicate the frame design.

2.7.2 Design Considerations

Three different designs were considered,

(a) The most basic design, as indicated in Figure 2.6(b), proposed that loading would be effected by three pairs of tapered confining plates, the load being applied by tightening bolts to a specified torque.

(b) A more advanced method consisted of loading the model on all six faces by a pressurised rubber membrane within a steel jacket, as shown in Figure 2.6(c).

(c) An alternative design to the above proposed loading the model on all six faces by means of separate air-bags confined within a steel jacket, as shown in Figure 2.6(d).

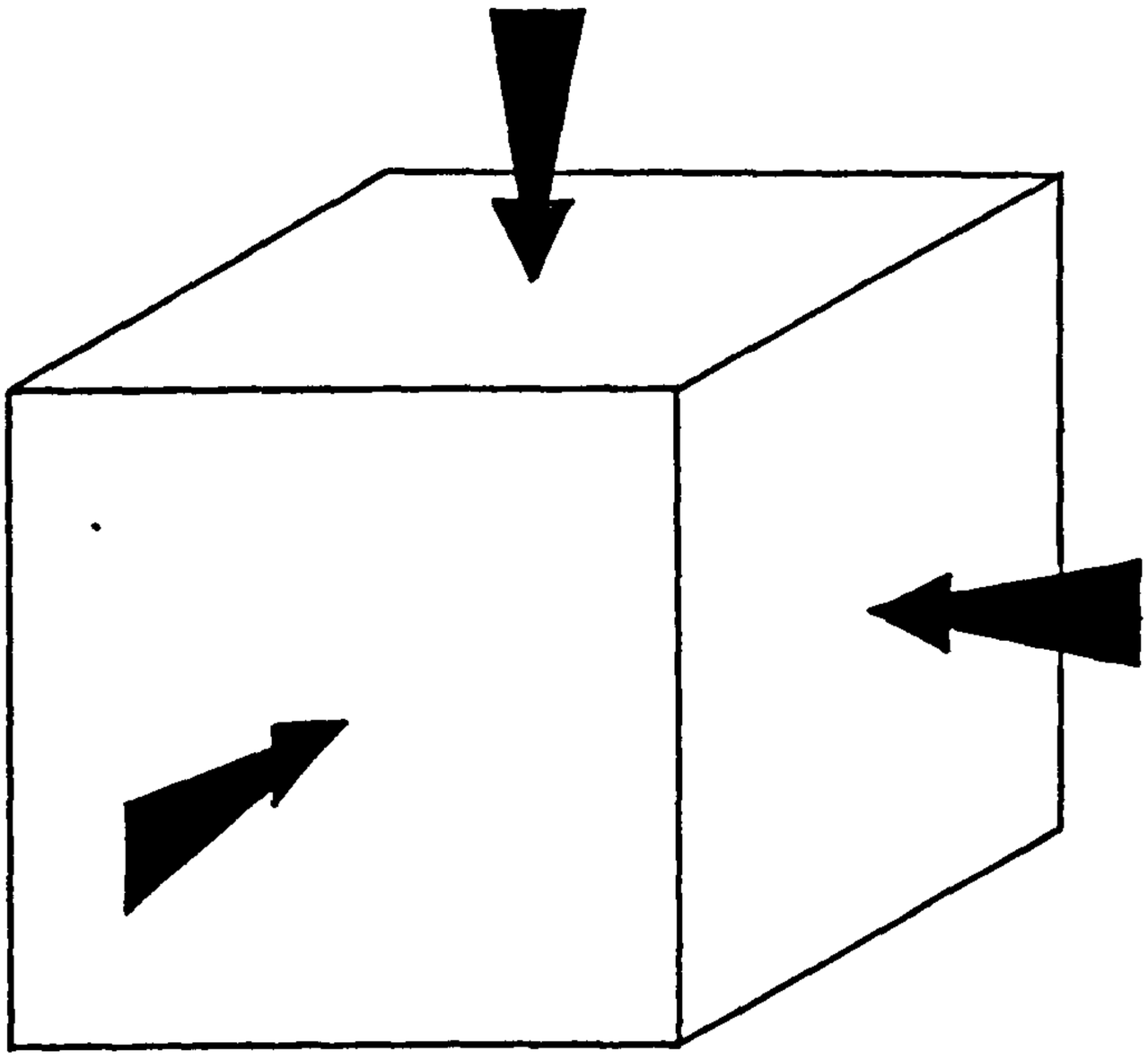

Figure 2.6(a) : Three-dimensional Loading

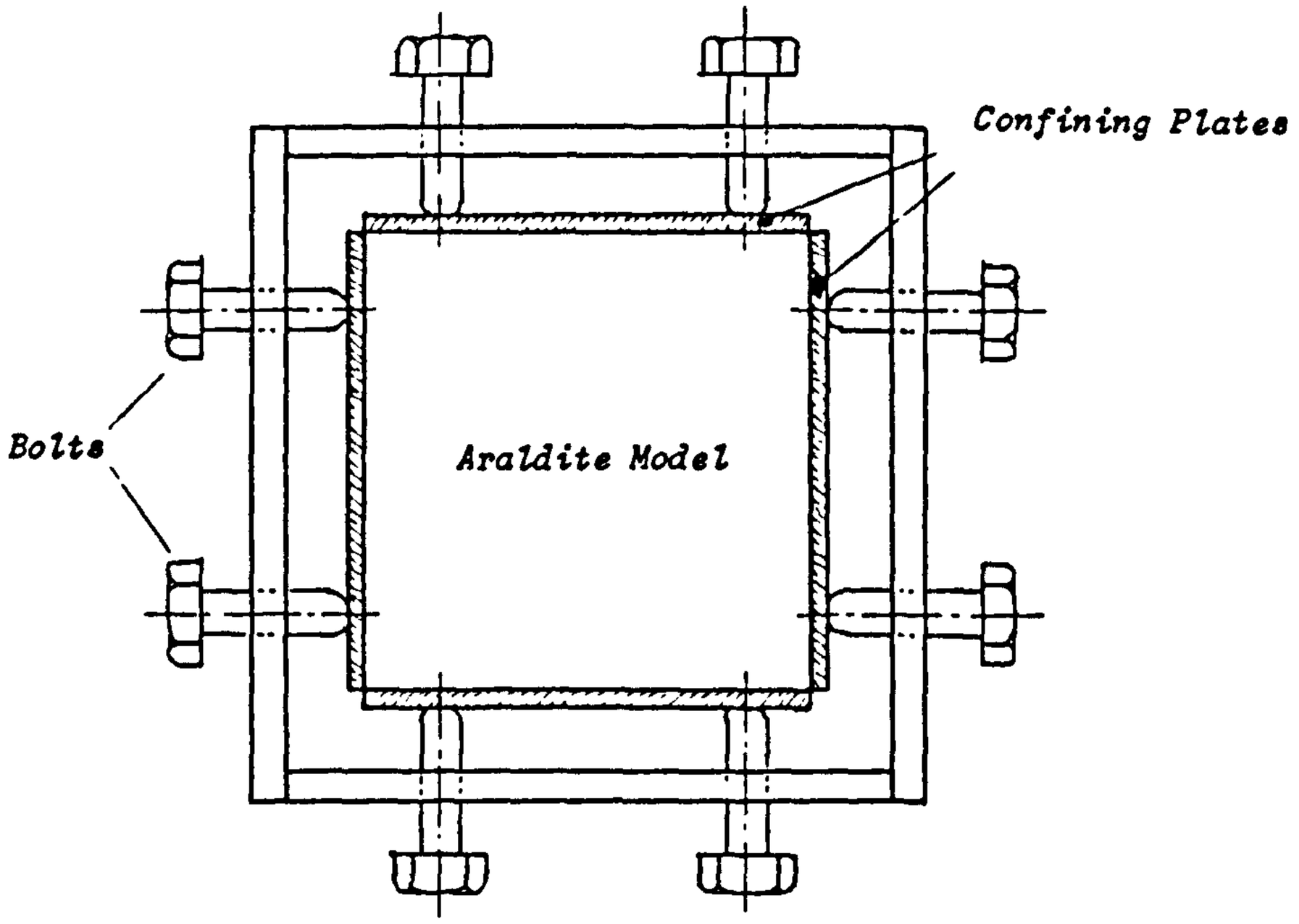

Figure 2.6(b) : Loading Frame Design #1

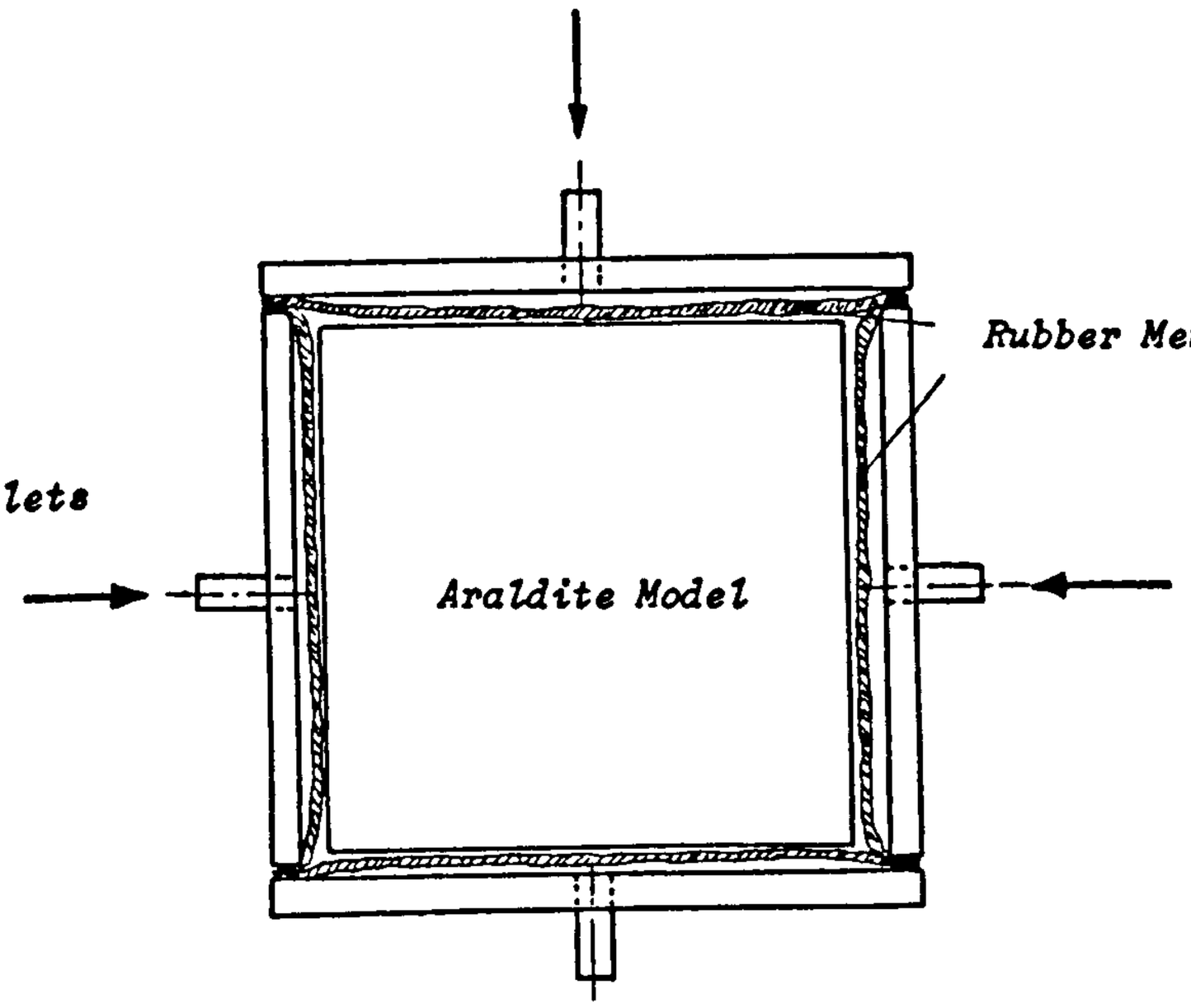

Figure 2.6(c) : Loading Frame Design #2

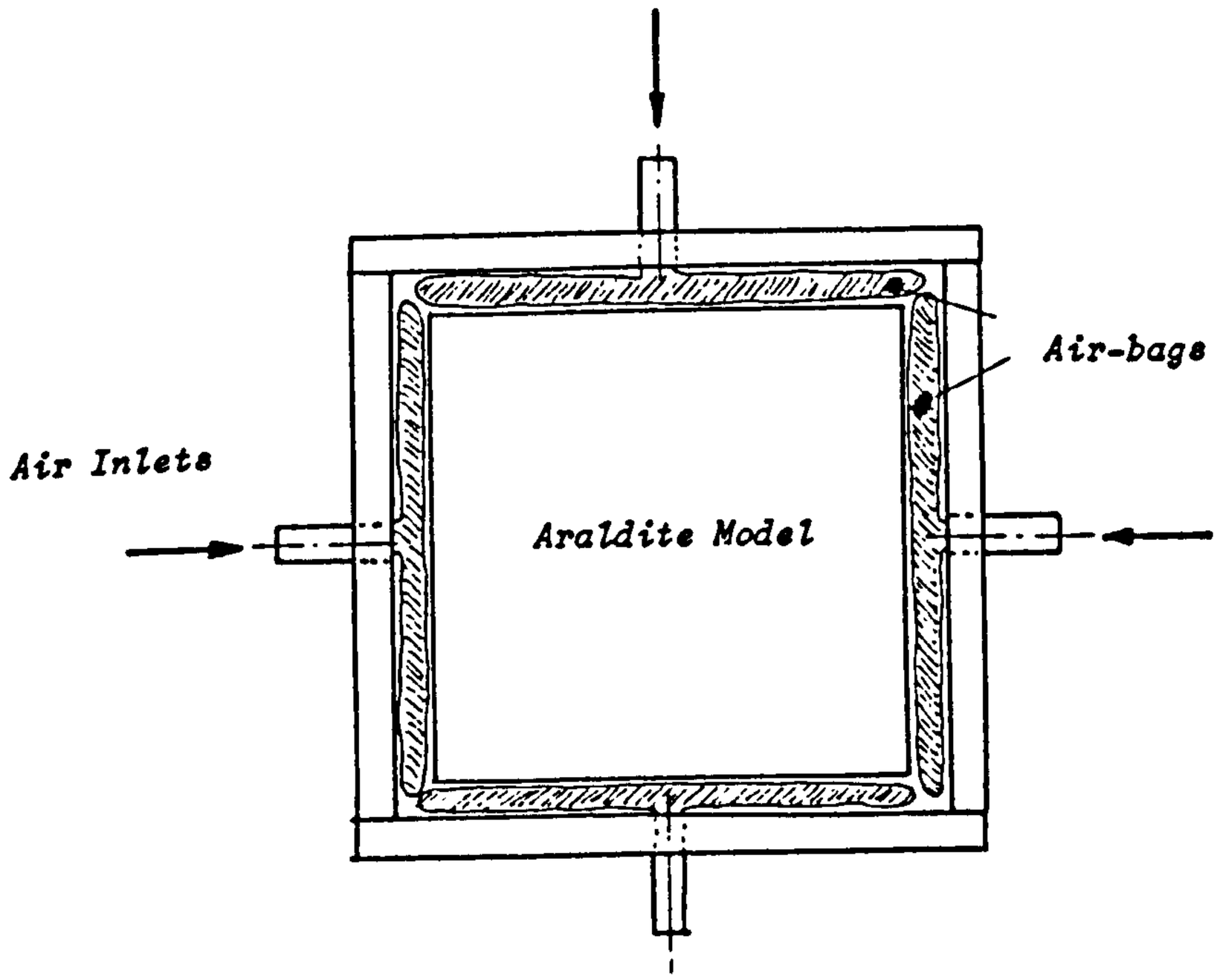

Figure 2.6(d) : Loading Frame Design #3

After discussions and testing [80], the confining plate method was rejected as it would not produce a constant rate of loading. Additionally, problems were anticipated regarding the calibration of the torquing operations.

The method of loading which employed a rubber membrane appeared more feasible than the confining plate method. A complex system of gaskets would, however, be required to maintain an air tight seal, thus the subsequent increase in design and technician time deemed the method impractical.

The remaining option, utilising air-bags appeared to solve the above problems but offered its own. Namely, obtaining air-bags capable of withstanding the elevated temperatures involved in stress freezing.

2.7.3 Final Frame Design

A sample air-bag made from a reinforced nylon material, glued at each edge and incorporating a rubber inlet tube was supplied by MFC Survival Ltd., North Wales. Deflated, its dimensions were 155 mm square The manufacturers rated the unconfined bag at 69 kPa (10 psi) at a maximum temperature of 80°C [81]. It was therefore necessary to test the sample air-bag to the requirements dictated by the stress freezing process.

To simulate loading conditions, the air-bag was inflated between two steel confining plates. An expansion of 7 mm was allowed as shown in Figure 2.7. Air pressure was supplied from a nitrogen bottle. A

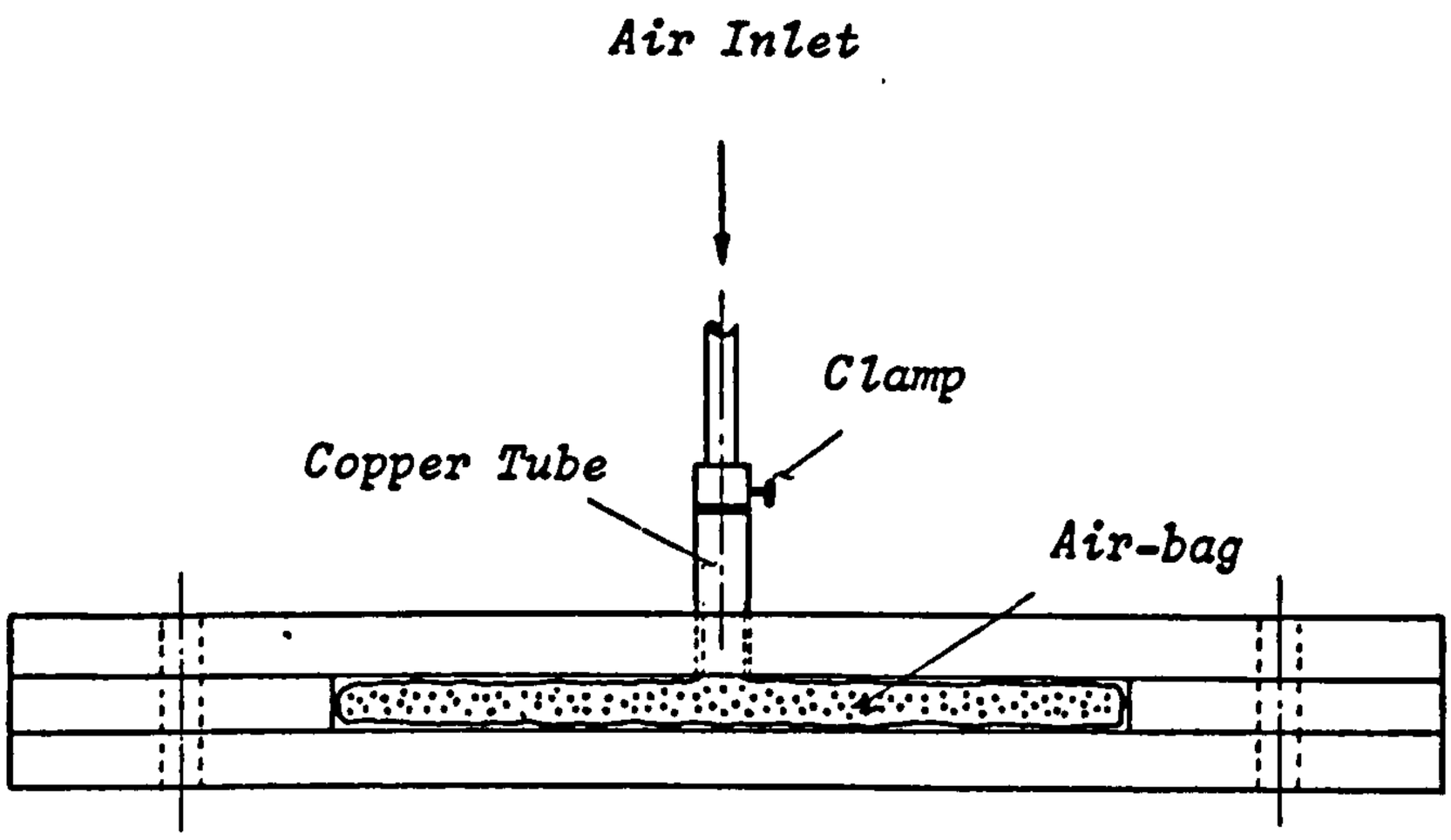

Figure 2.7 : Air-bag Test Rig

Test 1 : Pressure maintained at 345 kPa (50 psi) Temperature increased at 5°C/hr to 135°C Result : Rubber inlet failed after 3 hrs at 135°C
Test 2 : Rubber inlet confined with copper tube, clamped and sealed with silicone rubber Pressure increased to 485 kPa (70 psi) Temperature maintained constant at 135°C Result : Air-bag held pressure for 15 hours
Test 3 : Repeat test Pressure increased to 550 kPa (80 psi) Temperature increased to 145°C Result : Air-bag held pressure for 10 hours Pressure then increased to 825 kPa (120 psi) and maintained for 30 mins without failure
Test 4 : Air-Bag tested over full duration of the stress freezing cycle Result : Air-Bag held pressure without failure

Table 2.1 : Results of Air-Bag Test

pressure regulator, calibrated to 1035 kPa (150 psi) was connected to the supply, thus ensuring a constant pressure acted on the test rig throughout the test period. The bag was tested under various temperature and pressure conditions, the results are presented in Table 2.1.

In general, the performance of the air-bag was satisfactory. The initial failure of the rubber tube was caused by expansion of the inlet tube, thus exposing a section of unprotected rubber. This problem was solved by enclosing the rubber inlet within a short length of copper pipe. The air-bag proved, during the testing stage, that it was capable of withstanding pressures and temperatures in excess of that required for the stress freezing cycle. On this recommendation, a total of eight identical air-bags were ordered and the steel frame was designed to accept six of these bags.

A schematic of the loading frame is presented in Figure 2.8. It can be seen that the frame consisted of three pairs of steel plates which were bolted together to form a cube. Each plate had a central hole to allow the air-bag supply tube to pass through. A short length of copper pipe was used to protect the rubber supply line. Fluro-Silicone rubber provided an air tight seal between the rubber and brass inlet pipe. The top and bottom air inlets were connected together and the outlet to a manifold, as were the four side or 'horizontal' inlets. This allowed the facility to alter the vertical to horizontal stress ratio. Copper tubing and brass connections were used throughout. The frame was supported by four adjustable legs to allow the loading frame to be levelled.

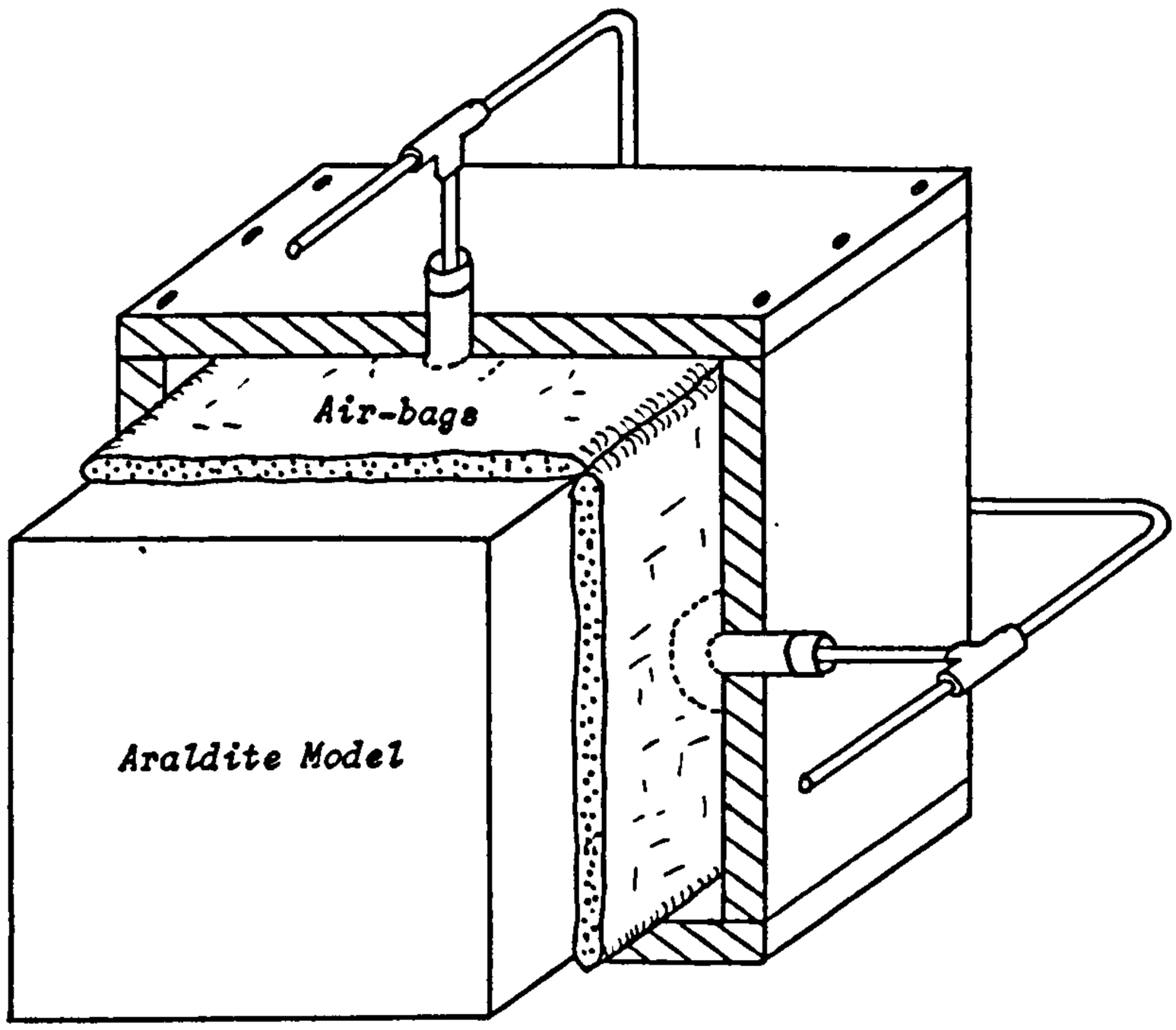

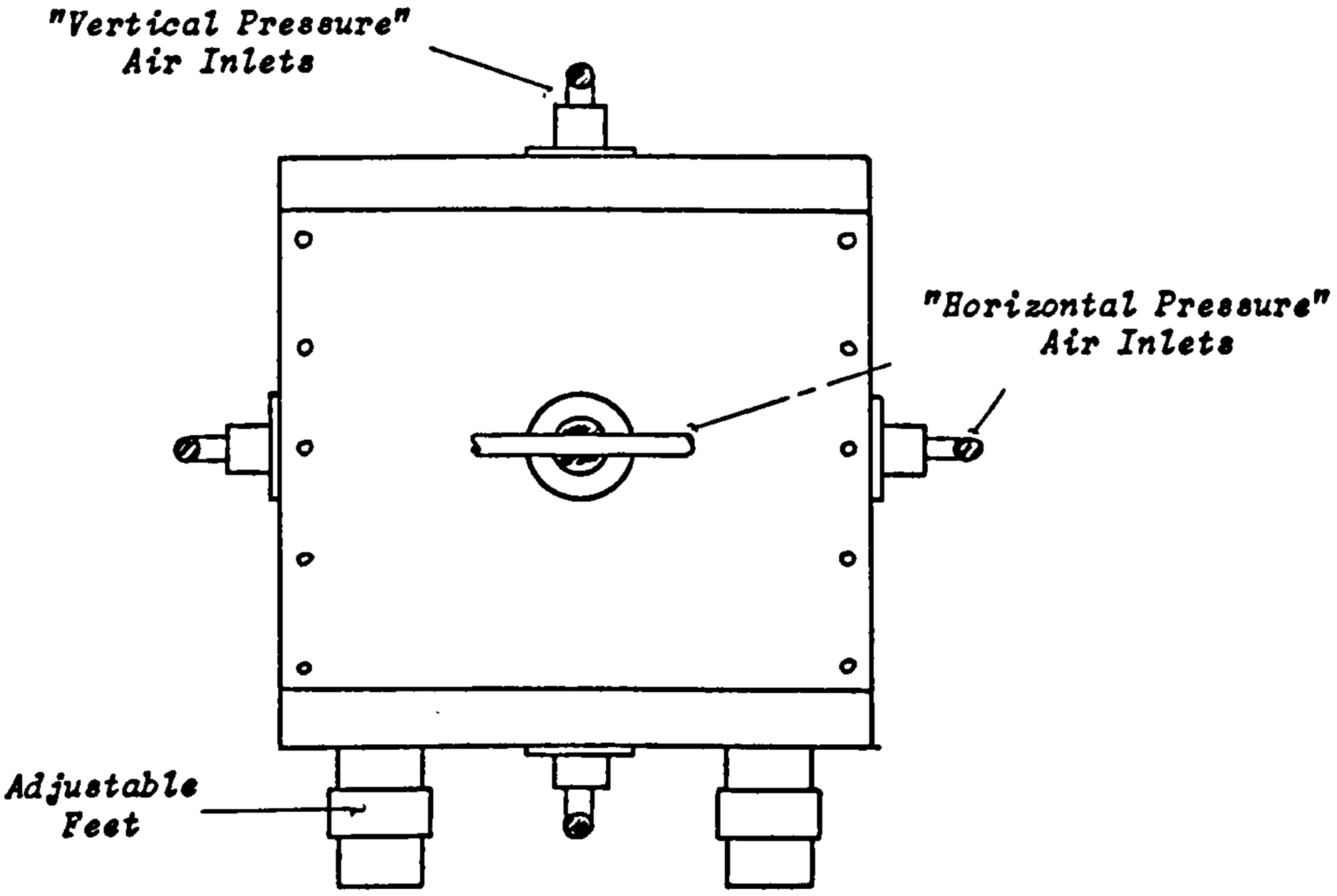

Figure 2.8 : Schematic Diagram of Loading Frame

2.8 EQUIPMENT REQUIRED FOR STRESS FREEZING PHOTOELASTICITY

2.8.1 Required Equipment

The equipment required to perform and analyse the stress freezing experiment consisted of a polariscope, a camera for recording the isochromatic fringes, an oven large enough to accommodate the model and loading frame, and some means of controlling the rate of change of temperature. It was also necessary to design a 'stress freezing cycle', detailing the rate of heating and cooling which the model was to be subjected to.

2.8.2 Oven and Programme Controller

The oven used for the stress freezing experiment was a fan circulated, LTE oven with an internal capacity of 157 litres. It had an operational temperature capability of 300°C. It's features included a West Gardian programme controller (set to a maximum of 150°C), glass door, internal light and two vents on either side as a provision for tubes or wires. The vents could be closed with asbestos flaps when not in use.

The programme controller, which had a variable time scale from 1 hr/rev to 16 days/rev, was set at 72 hrs/rev to correspond with the duration of the freezing cycle.

2.8.3 Stress Freezing Cycle

The conditions of stress freezing are primarily governed by the requirements such as that on heating, no parts of the model should become overstressed by reason of differential expansions or of internal load transfer from parts that are above the softening point. Secondly, adequate time must be allowed before commencing the cooling process to ensure that the softening or critical point has been reached not only on the surface of the model but also in the centre. Cooling should be carried out slowly to avoid thermal stresses. The 'soaking' period and rate of cooling required for varying thicknesses of Araldite CT200 are indicated respectively in Figures 2.9(a) and 2.9(b). Accordingly, considering the thickness of the model, the stress freezing cycle illustrated in Figure 2.10 and detailed in Table 2.2 was devised.

2.8.4 Cam Profiling

The stress freezing cycle was then transformed onto a cam which would be used to control the heating process. Blank cams were avaliable, comprising of a circular aluminium plate with a central fixing hole. Referring to Figure 2.11, temperature and time lines were printed on the surface of the cam. The temperature lines being concentric circles spaced at 5°C intervals, while the time markers were curved and ran across the temperature lines. A total of 72 lines were included, each corresponding to one hour of the programme cycle.

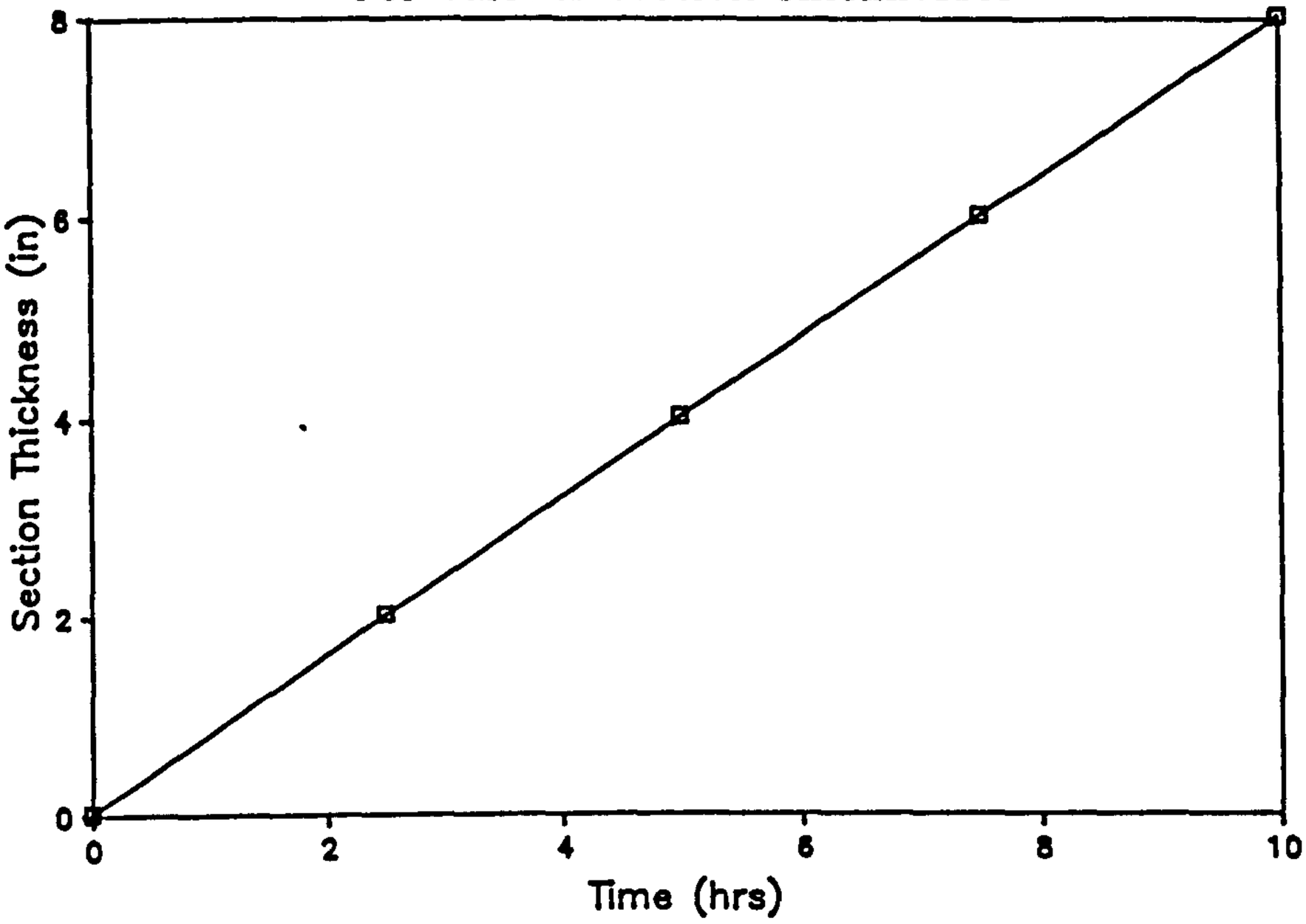

Figure 2.9(a) : after Karim [78]

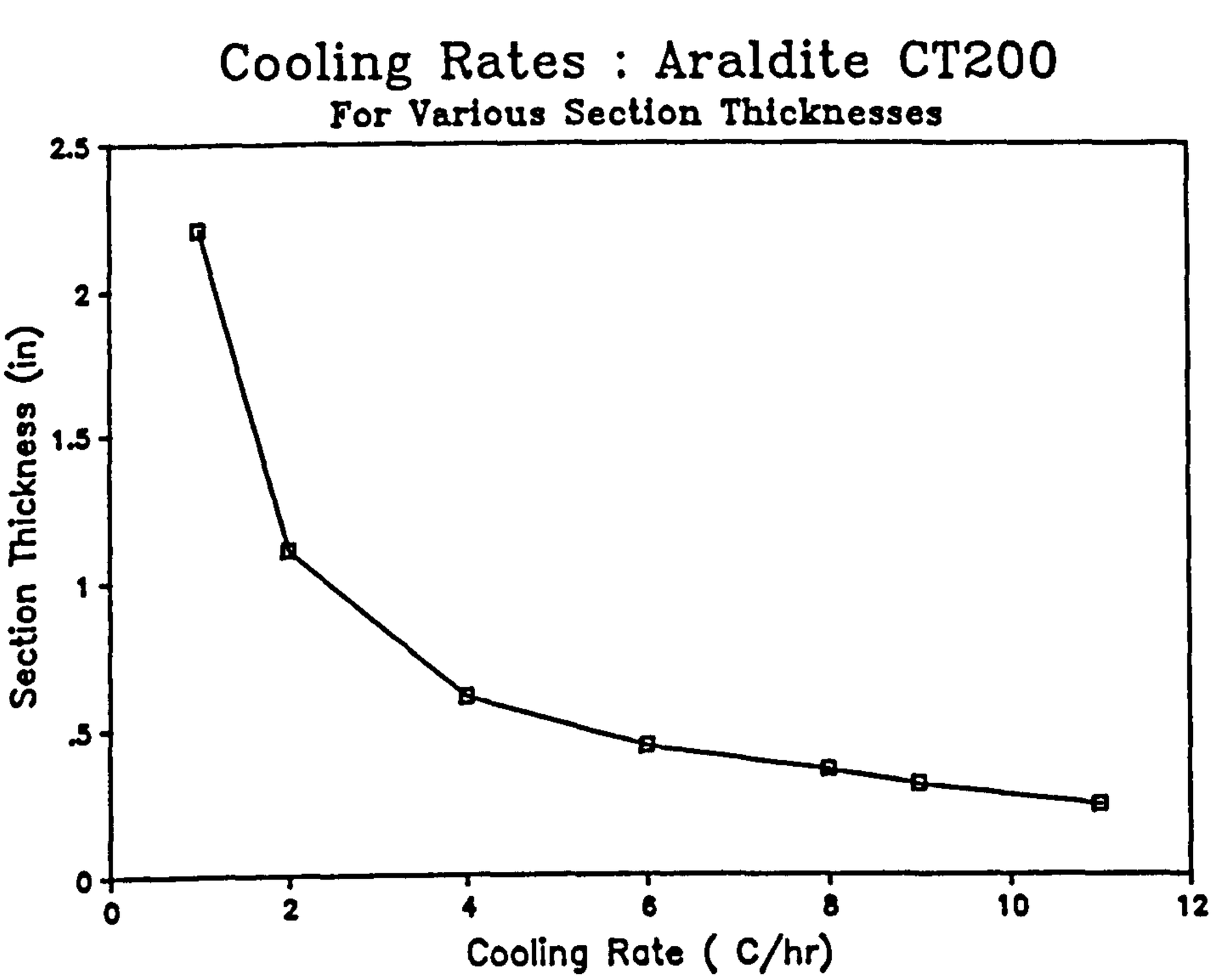

Figure 2.9(b) : After Karim [78]

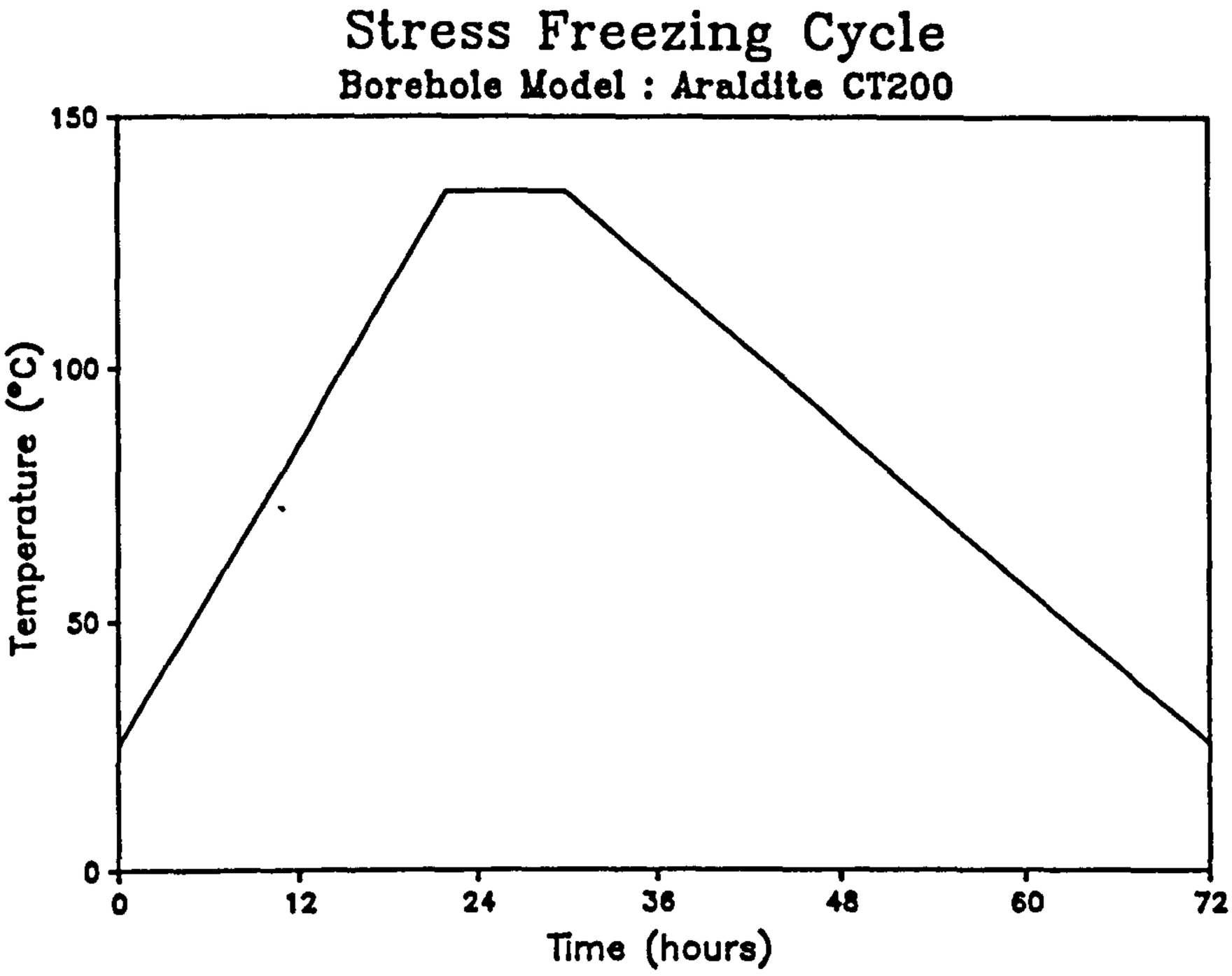

Figure 2.10 : Stress Freezing Cycle for Borehole Model

Heat model from 25°C to 135°C at 5°C/hr	22 hours
Maintain maximum temperature of 135°C	8 hours
Cool model from 135°C to 25°C at 2.5°C/hr	42 hours
Total Cycle Time	72 hours

Table 2.2 : Stress Freezing Cycle

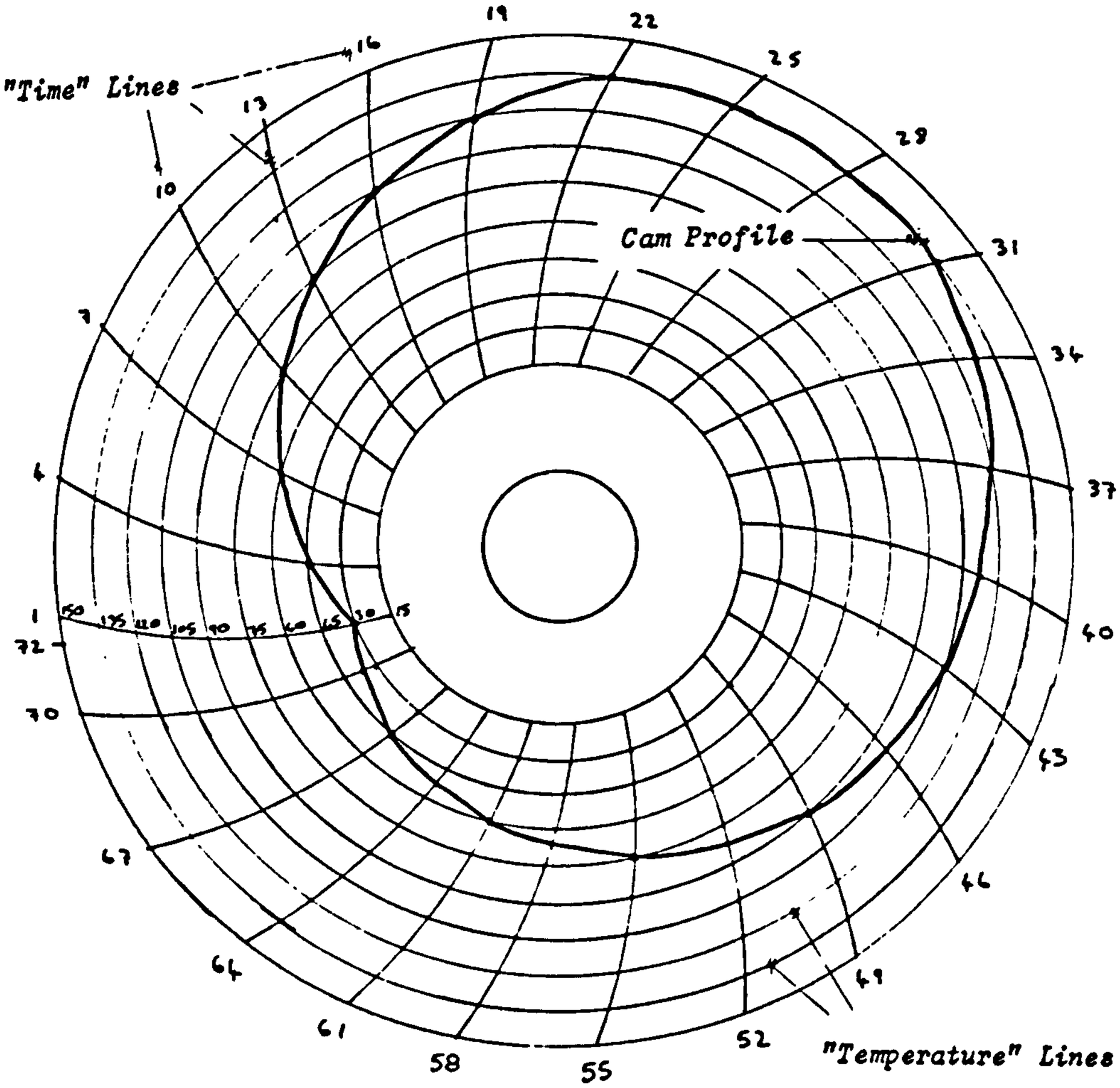

Figure 2.11 : Method of Cam Profiling

The stress freezing cycle was then 'plotted' onto the cam, the method of marking being as illustrated in the diagram. After the profile was cut the cam was inserted into the programme controller and its accuracy confirmed.

2.8.5 Polariscope

The photoelastic bench used was a Sharples combined transmission and diffused light polariscope. The unit was compact, built around a wooden storage cabinet and incorporated a mercury vapour and a tungsten filament light source, loading frame, projection screen, camera stand and the necessary optical arrangements (as detailed in Section 2.3.2). Full instructions as to the operation of the polariscope may be found in the Sharples Instruction Manual [82].

2.8.6 Photography

The camera used for black and white photography was an Olympus OM2 SP, f1.8, automatic and manual over-ride SLR with a spot metering facility. For close-up work, an 80-210 f 3.8 macro zoom was used. This was found to yield better results than conventional close-up lenses. All the isochromatic fringe photographs were taken under sodium monochromatic light using the diffused light arrangement of the crossed circular polariscope. The film used was Kodalith, ASA 12, which being a lith film, reproduced only black and white colours i.e. without any grey tones.

In photographing the isochromatics, the maximum aperture was used as the only advantage to be gained by employing smaller apertures was less critical focusing. The exposure times varied with the quality of surface finish and thickness of the slice, however, an average exposure time of 8 secs was established for a 4-5 mm slice smeared with Benzyl Benzoate.

2.9 CALIBRATION OF ARALDITE CT200 SPECIMENS

2.9.1 Theory

Photoelastic materials normally display some variation in mechanical and optical properties from one batch to another. It is therefore necessary to calibrate the material to be used. The calibration specimens were obtained from the same batch of Araldite CT200 as used for the borehole model. The two parameters normally required in the calibration of the photoelastic materials are the Material Fringe Value (F) and the modulus of elasticity (E). For the purpose of this investigation, only the material fringe value was required. From the stress optic law:

$$P-Q = FN/t \qquad .. \quad .. \quad .. \quad .. \quad .. \quad (2.11)$$

therefore,

$$F = (P-Q)\ t/N \qquad .. \quad .. \quad .. \quad .. \quad .. \quad (2.12)$$

Thus, for calibration specimens of known thickness in which the principal stress difference is known (using elastic theory), it is possible to calculate the material fringe value. The disk in diameteral compression is the most useful method commonly used for calibration of epoxy resin specimens. From the theory of elasticity, the principal stresses P and Q at the centre of the disk under applied load L are:

$$P = 6L/\pi dt \quad \text{and} \quad Q = -2L/\pi dt \qquad .. \quad .. \quad (2.13)$$

The principal stress difference is therefore,

$$P-Q = 8L/\pi dt \qquad .. \quad .. \quad .. \quad .. \quad .. \quad (2.14)$$

From Eqn (2.12), it follows that,

$$F = 8L/\pi dN \qquad .. \quad .. \quad .. \quad .. \quad .. \quad (2.15)$$

The material fringe value can therefore be expressed quite simply in terms of the load, diameter and fringe order at the centre of the disk.

2.9.2 Loading Device for Disk in Diameteral Compression

The loading device used for the calibration is shown in Figure 2.12 and was first used by Karim [78]. The unit operates by the application of weights placed upon a circular platform attached to a

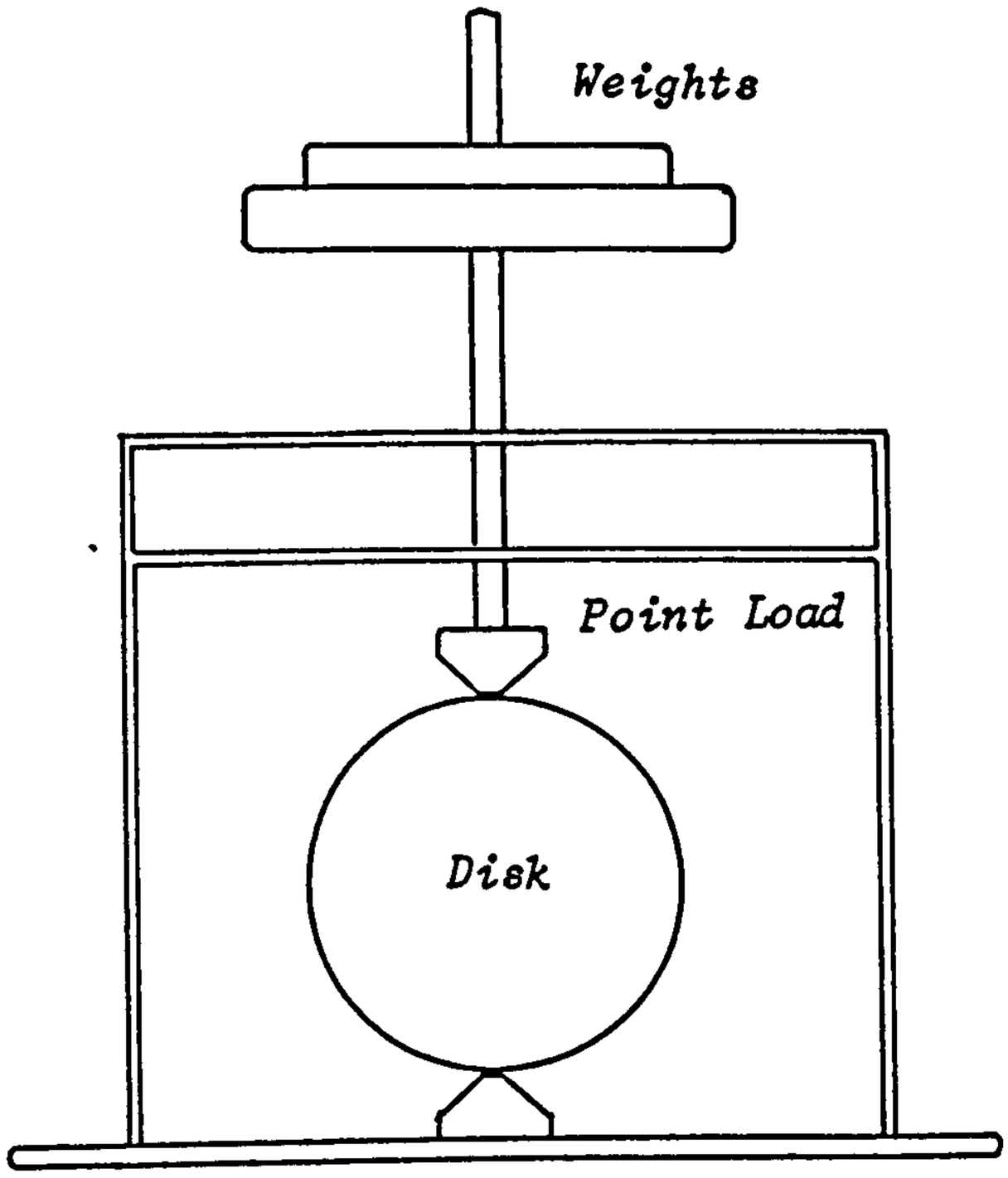

Figure 2.12 : Calibration Rig for Disk in Diametral Compression

Test Number	Material Fringe Value kPa/fr/m	psi/fr/in
#1	0.274	1.58
#2	0.254	1.44
#3	0.246	1.40
Average	0.258	1.47

Table 2.3 : Calibration Results

brass rod, one end of which carries a brass wedge. A similar wedge was located on the base of the loading device. A load of 2.73 kg was placed on the circular platform. The weight of the platform, brass rod and attached wedge amounted to 0.25 kg, thus the total applied load was 2.98 kg. Two disks were prepared for calibration, the diameter and thickness of each disk were 45 mm and 15 mm respectively.

2.9.3 Results of Calibration

After each disk was subjected to the stress freezing cycle, it was examined using a crossed circular polariscope. The zero fringe order, which was identified as a black fringe, was located at the edge of the disk. The integral fringe order was determined by counting the successive fringes towards the centre of the disk. The Tardy Method of compensation was used to give the exact value of fringe order at the centre of the disk. The material fringe value was calculated using equation (2.15) and the results are presented in Table 2.3.

2.10 STRESS FREEZING EXPERIMENT : GENERAL PROCEDURE

2.10.1 Loading the Model

The loading rig, containing the model was placed in the stress freezing oven and leveled using the adjusting feet. Two lengths of copper tubing were led through an inlet on the side of the oven, one was connected to the vertical and the other to the horizontal

pressure input manifolds. An initial pressure of 69 kPa (10 psi) was applied in order to centre the model within the rig.

A vertical to horizontal stress ratio of 1.0 : 0.8 was chosen, which was felt to represent a normal in-situ ratio. Accordingly, a vertical pressure of 345 kPa (50 psi) in conjunction with a horizontal pressure of 275 kPa (40 psi) was applied to the model and maintained by regulators. The air supply was provided by two nitrogen bottles, the arrangement being as indicated in Figure 2.13.

The model was then passed through the stress freezing cycle, as described in section 2.8.3.

2.10.2 Slicing Plan

The model was initially divided into three sections with a large band saw, as shown in Figure 2.14. Slices perpendicular to the axes of the boreholes were then taken from the centre of the model, away from the effects of the confining bags, as illustrated in Figure 2.15. Slicing was carried out by means of a diamond cutting wheel, water being used as a lubricant. The thickness of the slices produced varied from approximately 4 mm to 6 mm.

The slices were then ground smooth on sheets of wet and dry sandpaper to remove the cutting marks invariably left by the diamond wheel and to obtain a uniform thickness. Polishing was not necessary as the slices were to be immersed in Benzyl Benzoate, a fluid of matched refractive index.

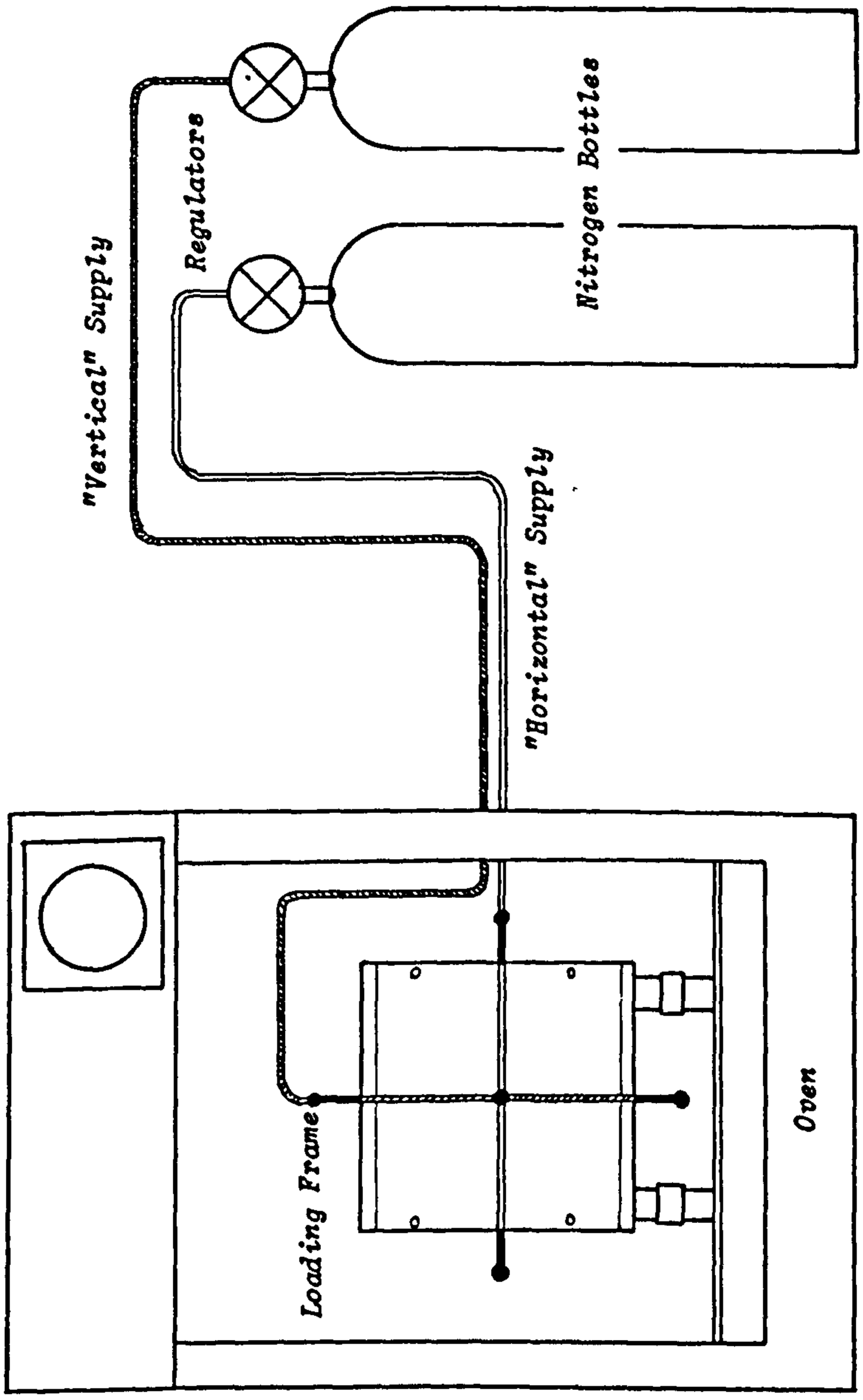

Figure 2.13 : Schematic Diagram of Test Equipment

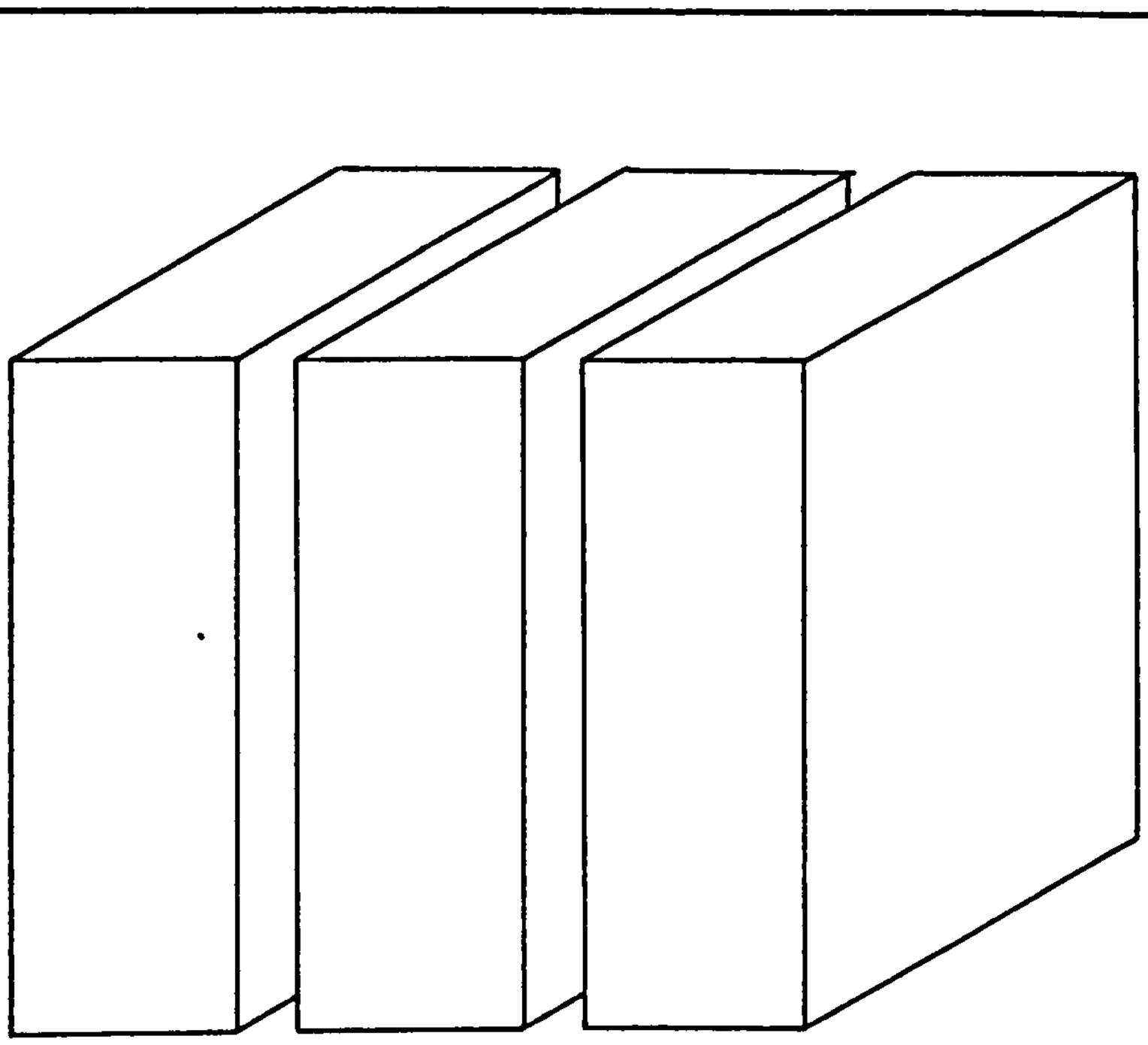

Figure 2.14 : Model Sliced into Three Sections

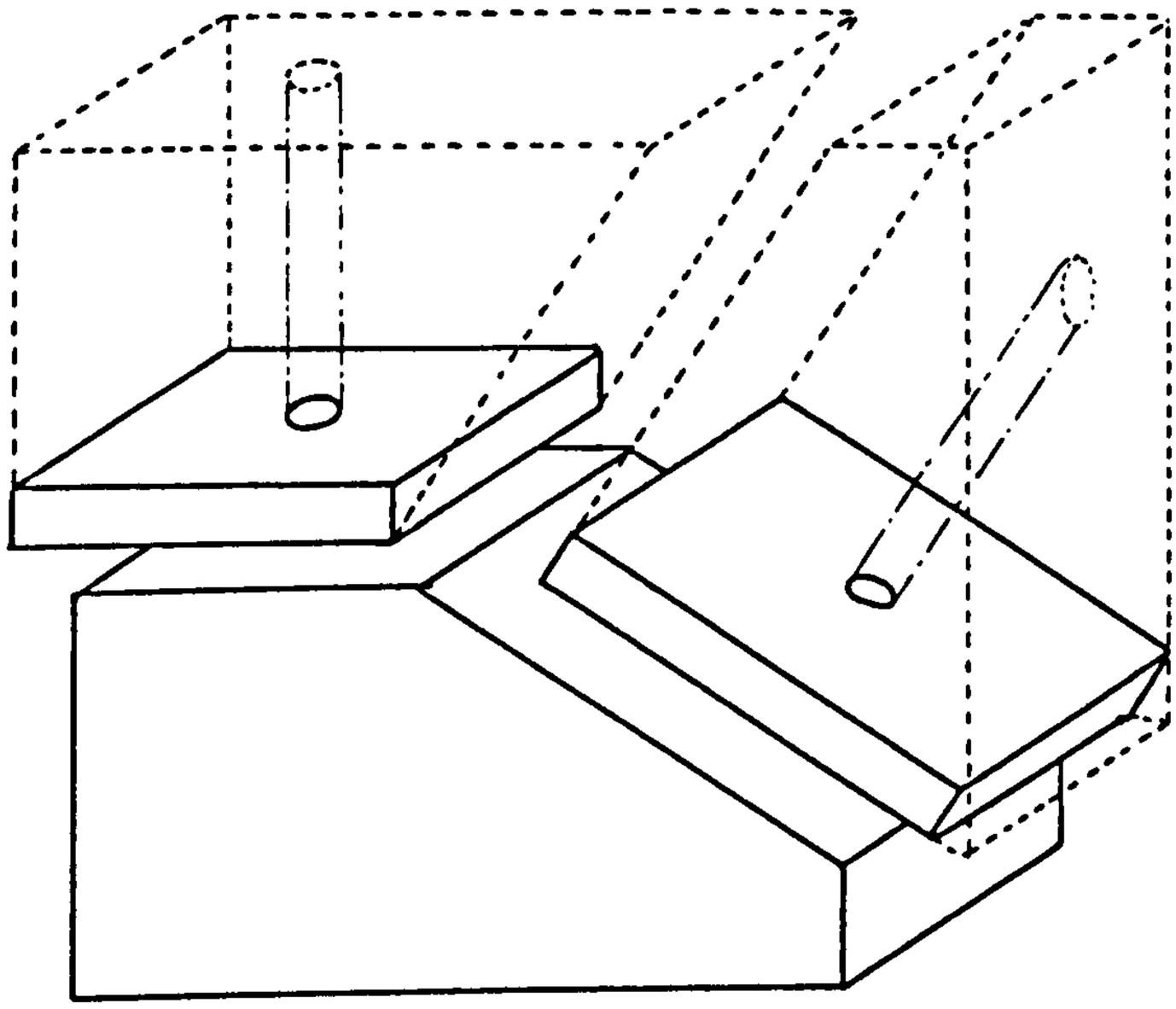

Figure 2.15 : General Slicing Method

The isoclinics and isochromatics frozen into each slice will remain unchanged for several years with a minimal amount of creep recovery. Time-edge-effect caused by moisture absorption can be removed by heating the slices at a temperature between 60-70°C for 24 hours. Alternatively, the slices may be stored in a desiccator.

2.10.3 Examination of Slices

From both theory and experiment, it can be shown that the stresses in the direction of propagation of plane polarised light produce no photoelastic effect upon the light [75]. Thus, if the direction of light is in the z-direction, i.e. along the borehole axis, the components of stress having the subscript z have no photoelastic effect, namely σ_z, τ_{rz} and $\tau_{\theta z}$. Therefore, the only components that gave rise to secondary principal stresses are σ_r, σ_θ and $\tau_{r\theta}$, which can be determined by a two-dimensional approach. The procedure of analysis was as follows:

(1) The isochromatic fringes were photographed.

(2) The integral fringe orders were then determined from the photograph and by colour matching techniques [66].

(3) The isoclinics were projected and traced at 10° intervals.

(4) A grid was drawn along sections of interest to obtain point-to-point data.

(5) The isoclinic parameter θ was noted at each point of interest.

(6) The fractional fringe order at each point of interest was determined by the Tardy method of compensation [65].

(7) The principal stresses were then determined using the Shear Difference Method [70].

2.11 DATA ANALYSIS

2.11.1 Separation of the Principal Stresses

This was accomplished by means of the Shear Difference method, as described in Section 2.5.2. The principal stresses were separated along two sections of the slice, the horizontal (OX) axis and vertical (OY) axis. For the purpose of this analysis, the borehole axis is considered as the z-axis, regardless of the hole inclination.

Referring to Figure 2.16, two lines A-A and B-B were drawn with a fine lead pencil 1.5 mm appart on either side of the horizontal line OX. Similar lines, C-C and D-D, were drawn 1.5 mm apart on either side of the vertical line OY. OX and OY represented the lines along which the principal stresses were to be separated. Each set of lines were equally divided into eight divisions, 1.5 mm apart. As the radius of the simulated borehole was 3 mm, the radial depth of

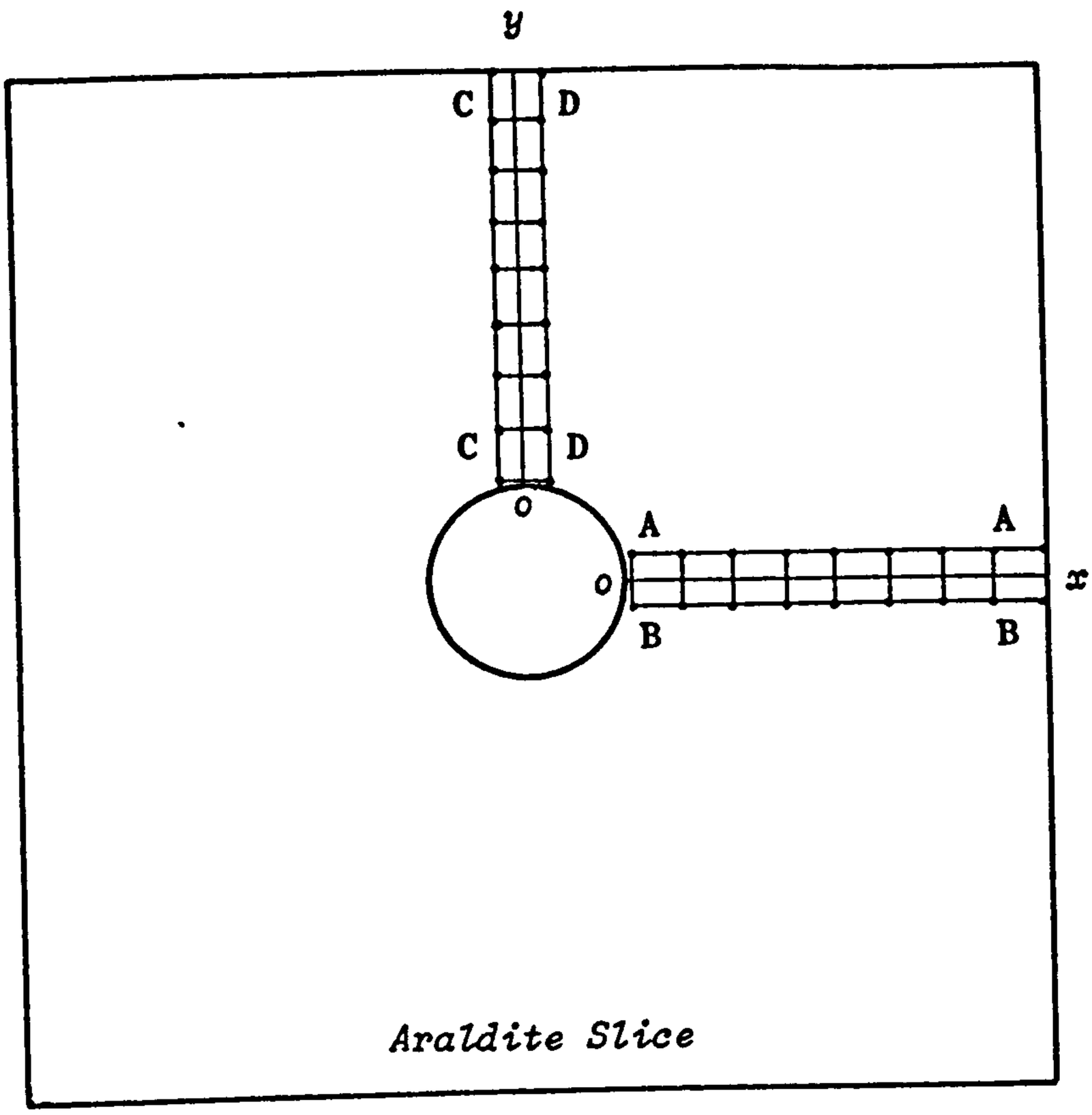

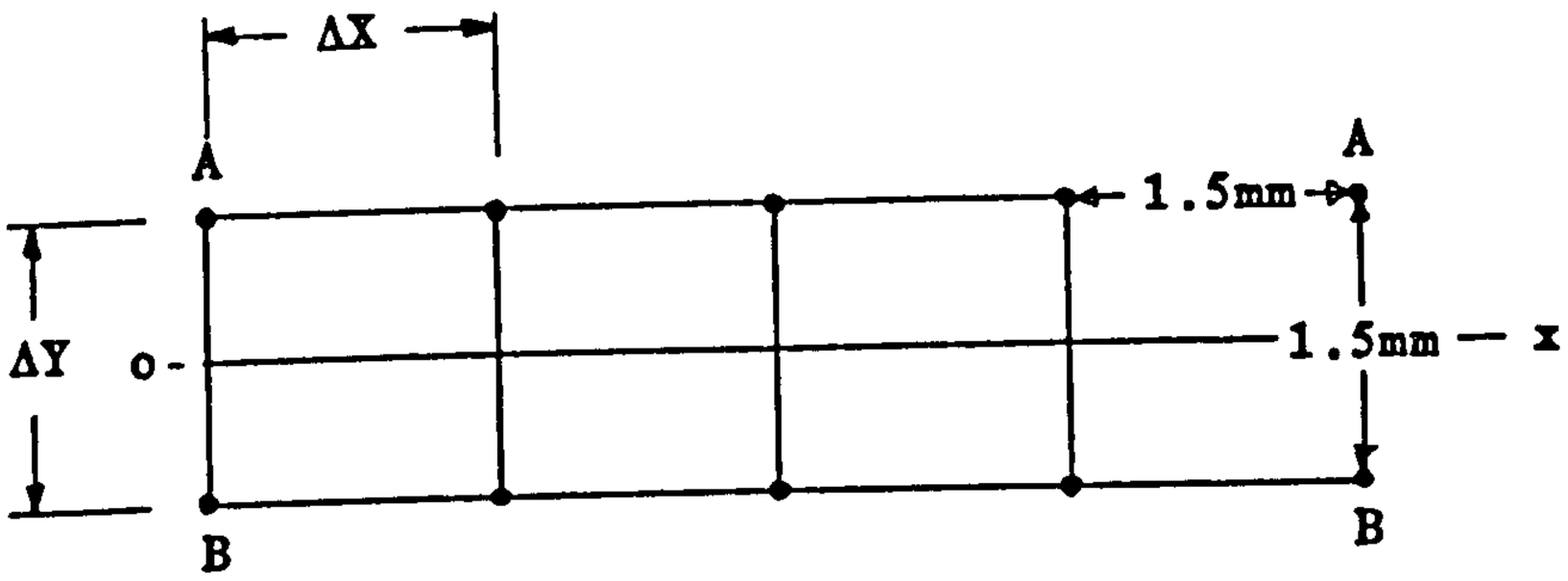

Figure 2.16 : Lines of Principal Stress Separation

investigation was therfore four times the borehole radius. The isoclinic parameter θ was obtained directly from the slice viewed in a plane polariscope arrangement for each data point along lines A-A and B-B, and similarly along C-C and D-D. Having obtained the isoclinic parameters, the slice was then viewed in a circular polariscope arrangement and the fractional fringe orders were determined for each data point using the Tardy Method of compensation.

The shear stress was then calculated at each data point by means of equation (2.6). The shear difference $\Delta\tau_{r\theta}$, was then calculated for each point, as indicated in equation (2.7). Commencing from point O on the free boundary of the hole where $\sigma_r = 0$, $\Delta\tau_{r\theta}$ was summated from point to point along OX. This procedure was repeated along OY. The tangential stress σ_θ, at each point was then calculated using equation (2.8).

Having obtained the secondary principal stresses σ_r'' and σ_θ'', as a function of radial distance, the principal stresses P and Q (σ_θ and σ_r) were then obtained from equation (2.9). The axial stress σ_z was then calculated from elastic theory using equation (2.10).

The above calculations were performed on an Apricot F1 micro-computer using Supercalc 3, a commercially available spreadsheet package.

2.11.2 Presentation of Results

The isochromatics and isoclinics obtained from each slice are presented in diagrammatic form. Accordingly, a tracing of the fringe pattern is presented in place of the photograph, as it was considered that a fringe diagram gave a clearer illustration of the fringe orders. The isoclinics have been traced at 10° intervals.

The values of the secondary principal stresses σ''_r, σ''_θ and $\tau''_{r\theta}$ are given in terms of the parameters of the isochromatics (N). The principal stresses, however, are presented in stress units. To obtain values in terms of stress units, the isochromatic parameter N for the principal stress were mutiplied by the conversion factor, which was obtained by dividing the material fringe value obtained from the calibration procedure (Section 2.9.3) by the thickness of the slice, i.e. F/t. A positive sign in the table denotes compression. The principal stresses measured from the horizontal and vertical sections are also presented graphically to allow a visual comparison of the results.

2.12 RESULTS

2.12.1 Vertical Borehole

The isochromatic and isoclinic fringe traces for the vertical borehole are illustrated in Figure 2.17. An examination of the symmetrical fringe pattern produced indicated that correct loading had occurred. The maximum isochromatic parameter was observed at the

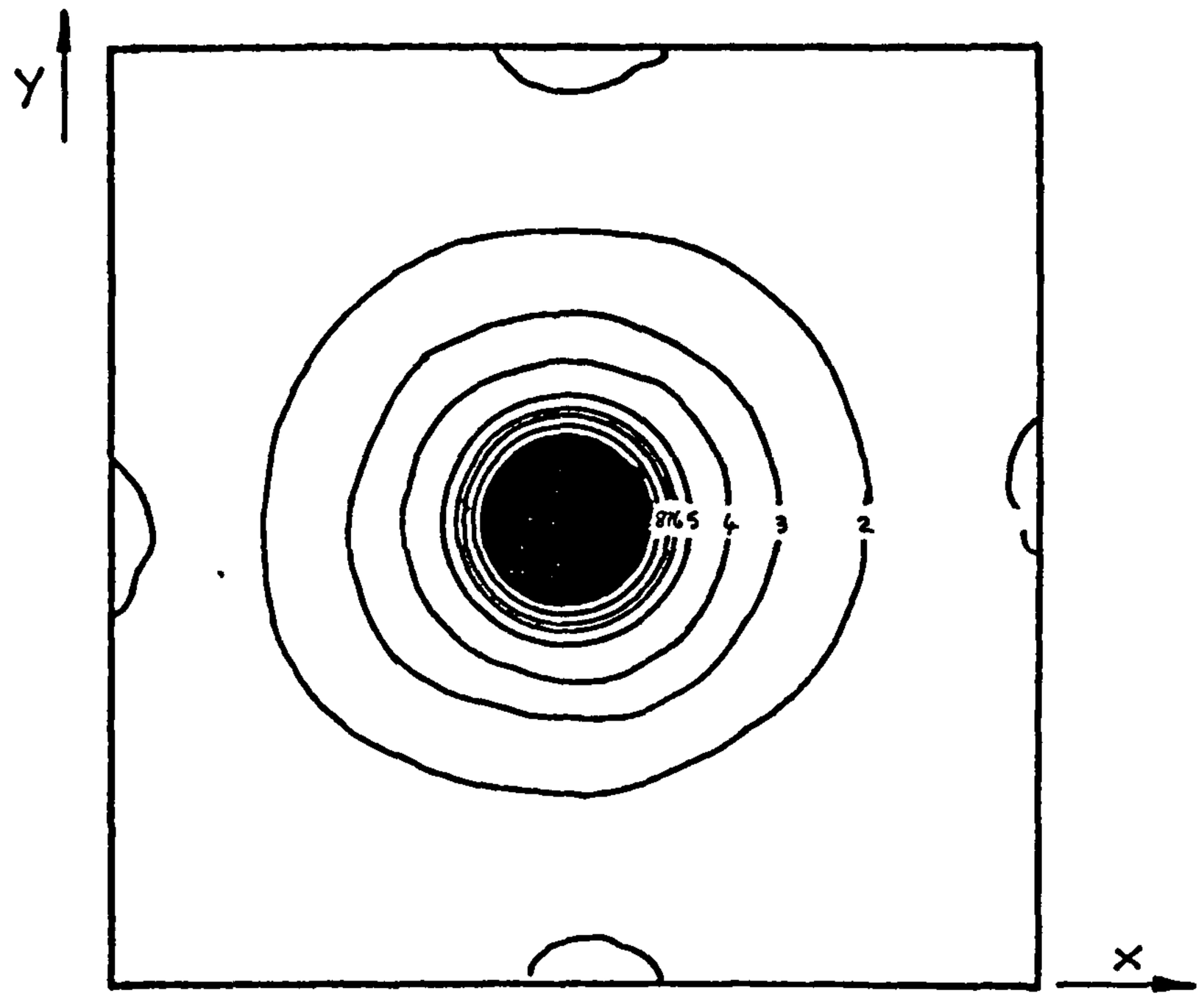

Isochromatics - Vertical Hole

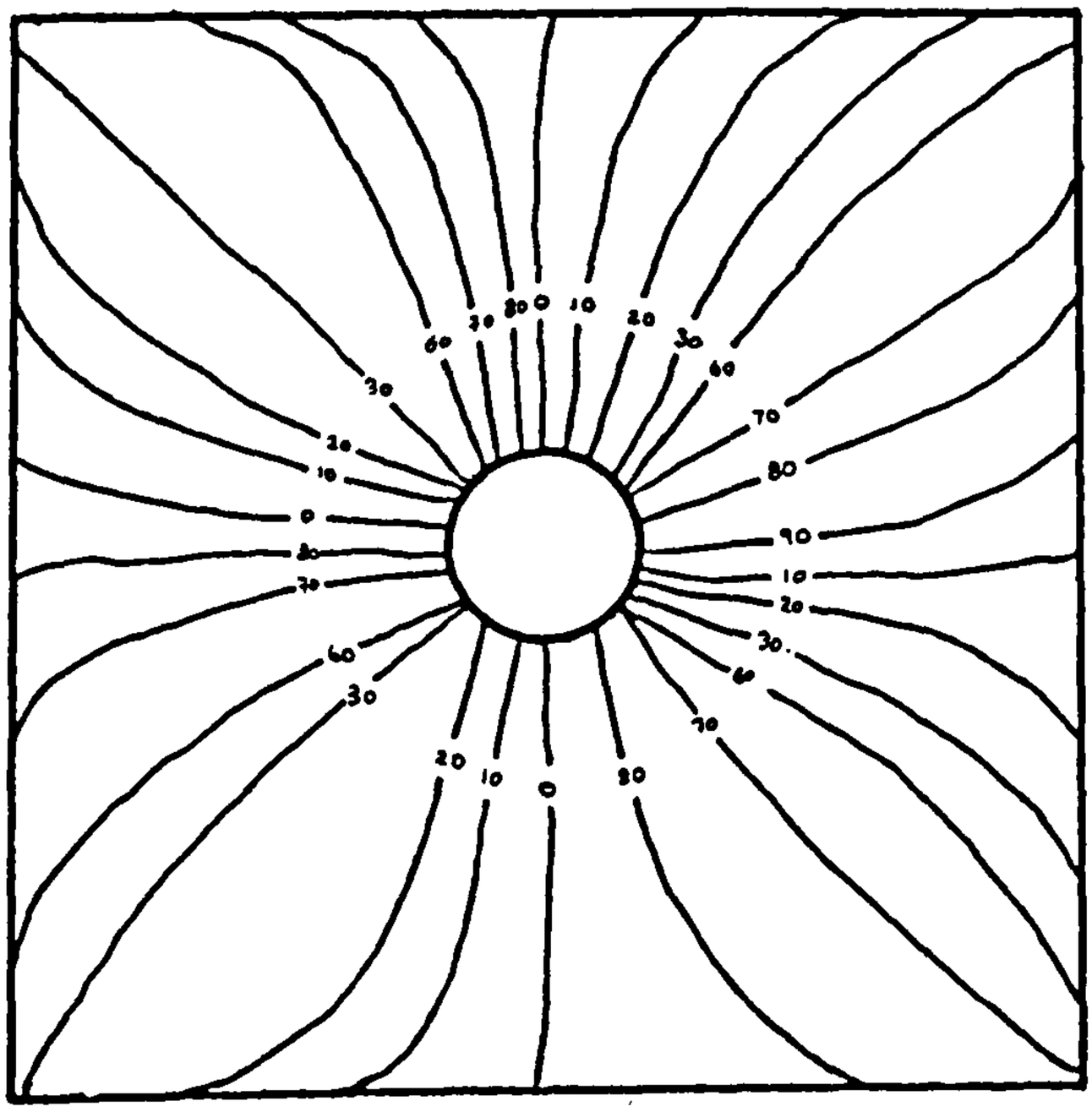

Isoclinics - Vertical Hole

Figure 2.17 : Vertical Borehole - Isochromatics & Isoclinics

Radial Dist.	Fringe Number	Isoclinic A-A	Isoclinic B-B	Mean Shear Difference	Min 2nd Principal Stress	Max 2nd Principal Stress	Shear Stress
1.0	8.00				.00	8.00	.00
1.5	3.50	-14.0	30.0	-2.3371	2.34	5.84	.00
2.0	1.89	-12.0	21.0	-1.0167	3.35	5.24	.00
2.5	1.15	-4.0	6.0	-.1996	3.55	4.70	.01
3.0	.89	-2.0	3.0	-.0776	3.63	4.52	.00
3.5	.61	-3.0	3.0	-.0638	3.69	4.30	.00
4.0	.55	-1.0	2.0	-.0288	3.72	4.27	.00
4.5	.38	-1.0	2.0	-.0199	3.74	4.12	.00
5.0	.25		1.0	-.0044	3.75	4.00	.00

Table 2.4(a)

Radial Dist.	Fringe Number	Isoclinic C-C	Isoclinic D-D	Mean Shear Difference	Min 2nd Principal Stress	Max 2nd Principal Stress	Shear Stress
1.0	8.00				.00	8.00	.00
1.5	3.60	-15.0	34.0	-2.5689	2.62	6.22	.00
2.0	1.95	-8.0	12.0	-.6653	3.25	5.20	.00
2.5	1.30	-4.0	7.0	-.2477	3.48	4.78	.01
3.0	.92	-3.0	4.0	-.1121	3.59	4.51	.00
3.5	.60	-3.0	3.0	-.0627	3.66	4.26	.00
4.0	.55	-2.0	3.0	-.0479	3.70	4.25	.00
4.5	.40	-1.0	3.0	-.0279	3.73	4.13	.00
5.0	.25		2.0	-.0087	3.74	3.99	.00

Table 2.4(b)

Radial Distance r/a	Radial Stress (kPa)	Hoop Stress (kPa)	Axial Stress (kPa)
1.0	0	504	252
1.5	147	368	257
2.0	211	330	271
2.5	224	296	260
3.0	229	285	257
3.5	233	271	252
4.0	235	269	252
4.5	236	260	248
5.0	236	252	244

Table 2.4(c)

Radial Distance r/a	Radial Stress (kPa)	Hoop Stress (kPa)	Axial Stress (kPa)
1.0	0	504	252
1.5	165	392	278
2.0	205	328	266
2.5	219	301	260
3.0	226	284	255
3.5	230	268	249
4.0	233	268	251
4.5	235	260	248
5.0	236	251	244

Table 2.4(d)

Vertical Borehole

Table 2.4(a) Secondary Principal Stresses - Line OX
(b) Secondary Principal Stresses - Line OY
(c) Principal Stresses - Line OX
(d) Principal Stresses - Line OY

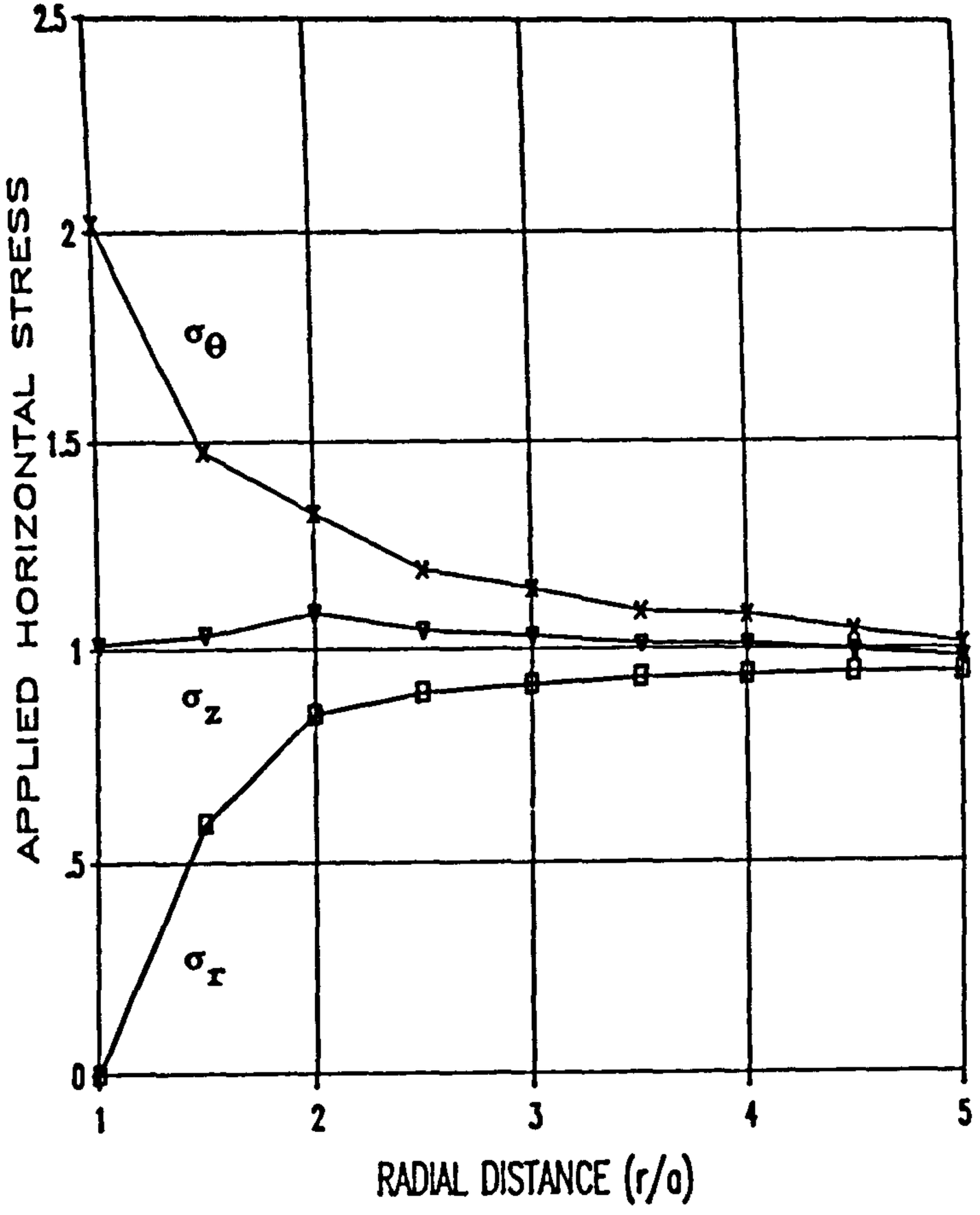

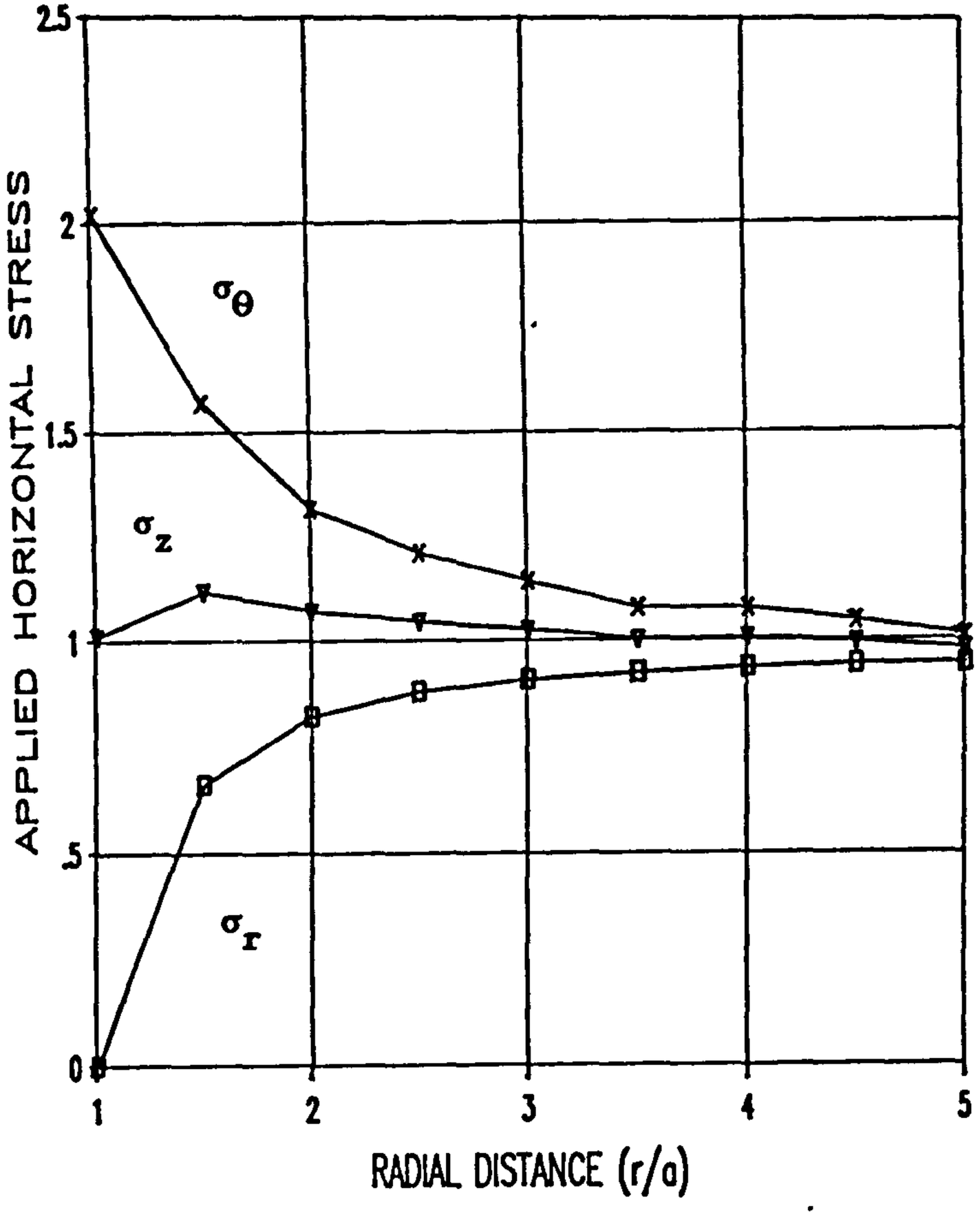

Figure 2.18 : Vertical Hole - Principal Stresses along Lines OX and OY

borehole wall and had a value of 7.5 fringe units. The isoclinics, which were traced in intervals of 10°, were found to extend radially from the borehole. The thickness of the slice was measured and found to be 4.09 mm, thus the conversion factor (F/t) was 63 kPa fr.

Although the fringe isochromatics appeared symmetrical around the borehole, the secondary principal stresses were separated along both the OX and OY axes to confirm that the desired horizontal loading had occurred. Accordingly, the input parameters and the computed secondary principal stresses for lines OX and OY are displayed in Tables 2.4(a) and 2.4(b) respectively. No shear stresses were measured along either line as the slice was taken from a plane of principal stress. Therefore the secondary principal stresses measured were identical to the principal stresses.

The principal stresses measured along line OX are presented in Table 2.4(c) and in graphical form in Figure 2.18. The maximum hoop stress acting on the periphery of the borehole was found to be 504 kPa (2.02 σ_{app}). This value decreased to 368 kPa (1.47 σ_{app}) at r/a = 1.5 before further decreasing to a value of around 252 kPa (1.01 σ_{app}) at the maximum radius of investigation. The radial stress increased from zero at r/a = 1 to 147 kPa (0.59 σ_{app}) at r/a = 1.5 before reaching a value of 236 kPa (0.95 σ_{app}) at the maximum radius of investigation. The difference between the radial and hoop stress at this radial distance was 16 kPa. The axial stress varied from 244 kPa (0.98 σ_{app}) to 271 kPa (1.08 σ_{app}).

The principal stresses measured along line OY are given in Table 2.4(d) and illustrated graphically in Figure 2.18. The maximum hoop stress acting on the periphery of the borehole was measured to 504 kPa (2.02 σ_{app}). This value decreased to 382 kPa (1.57 σ_{app}) at r/a = 1.5 before reaching a value of about 251 kPa (1.0 σ_{app}) at the maximum radius of investigation. The radial stress increased from zero at the periphery to 165 kPa (0.66 σ_{app}) at r/a = 1.5 and reached a value of 236 kPa (0.95 σ_{app}) at the maximum radius of investigation. The difference between the radial and hoop stress at this radial distance was 15 kPa. The axial stress varied from 244 kPa (0.98 σ_{app}) to 278 kPa (1.11 σ_{app})

2.12.2 25° Borehole

The isoclinics and isochromatics obtained from the 25° borehole slice are illustrated in Figure 2.19. The fringe orders at the periphery of the borehole were found to be 8 and 7 fringe units on the OX and OY axes respectively. The isoclinics were traced at 10° intervals. Two isotropic points were identified (i.e. regions where the two principal stresses were equal), each on the horizontal axis on either side of the borehole at a radial distance of approximately 4.5 radii. As the slice thickness was 4.23 mm, the conversion factor (F/t) was 61 kPa fr.

The input parameters and the resulting secondary principal stress values for section lines OX and OY are given in Tables 2.5(a) and 2.5(b) respectively. As the slice was not taken along a plane of principal stress, shear stresses were present along each section of

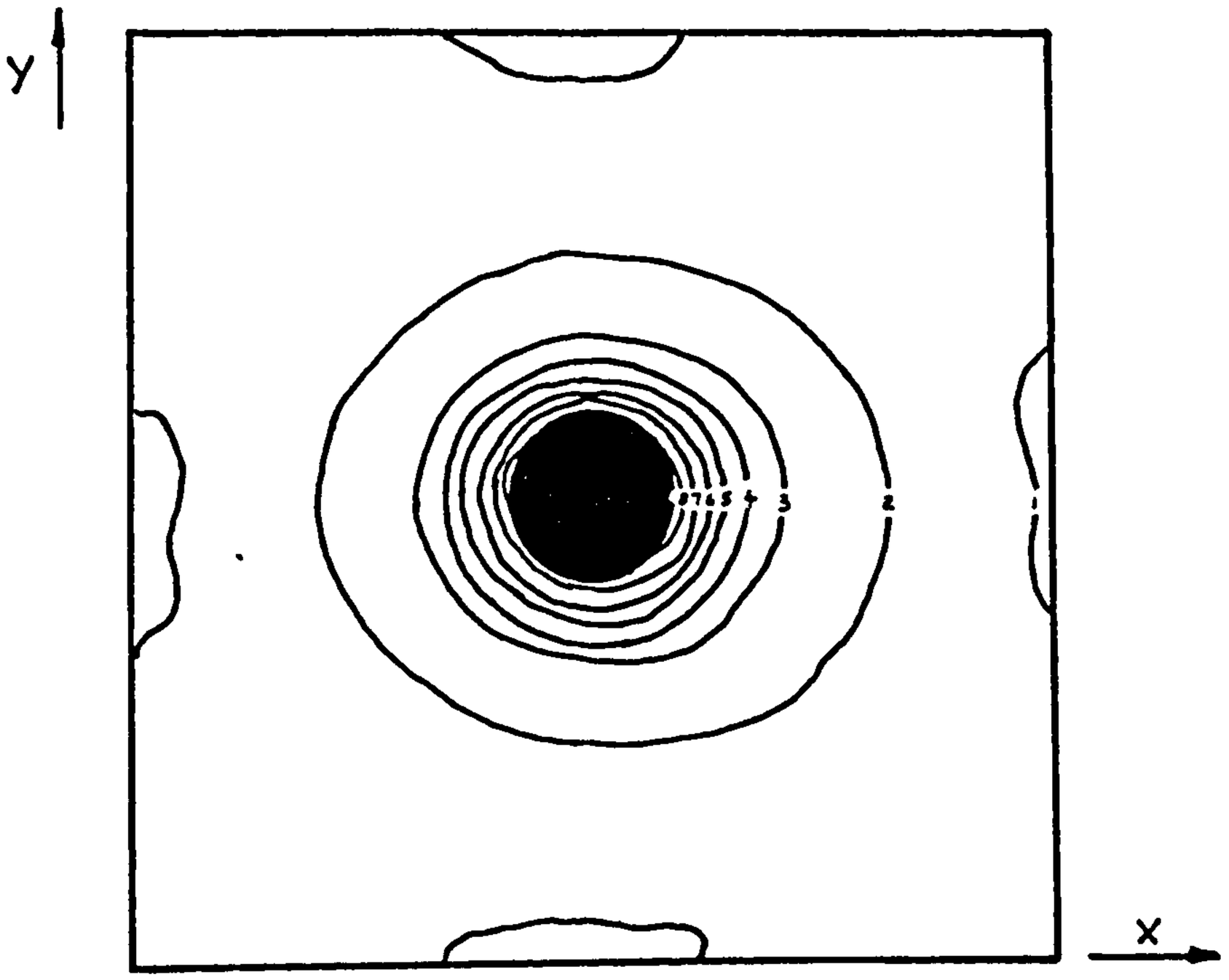

Isochromatics - 25° Hole

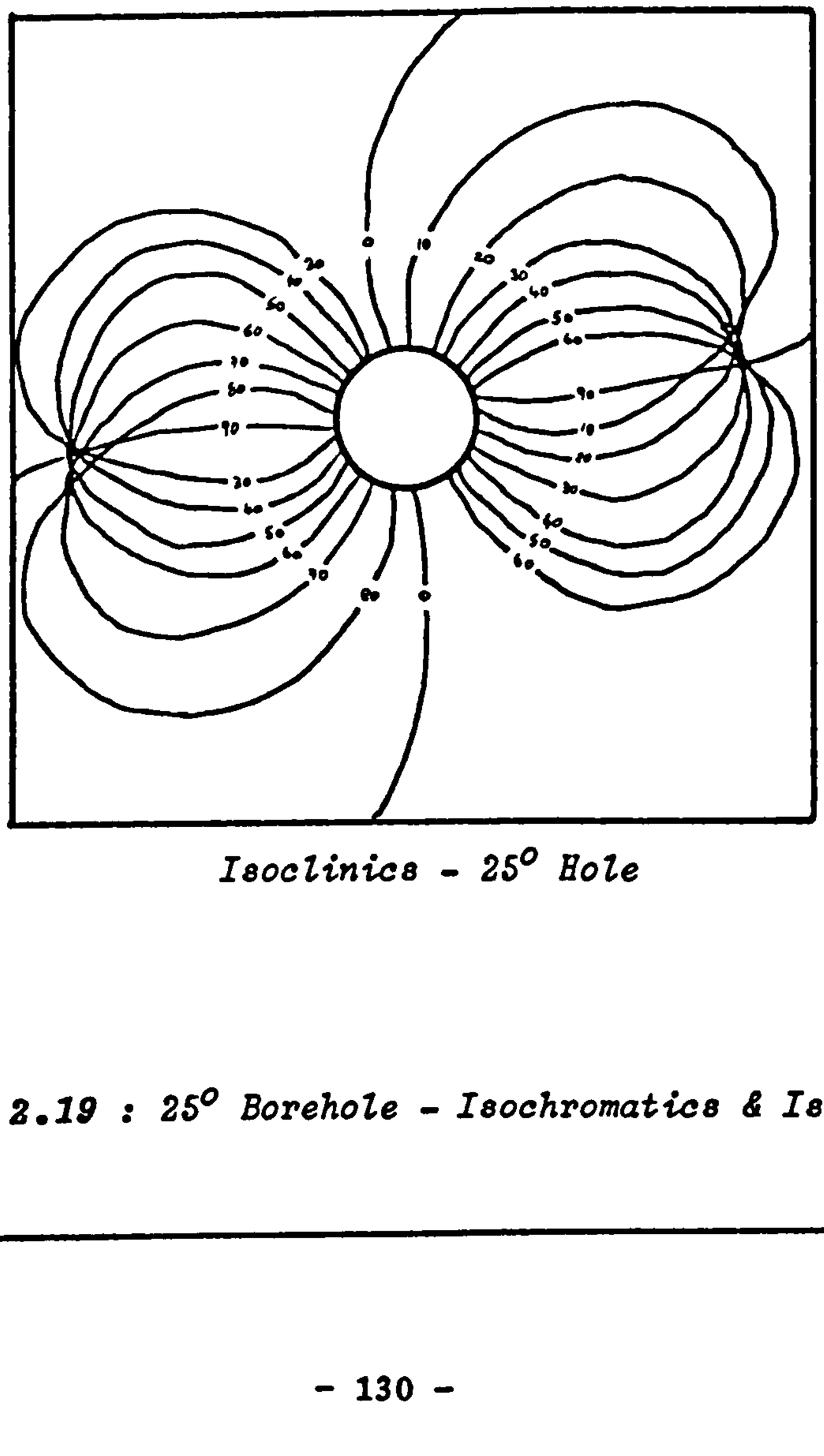

Isoclinics - 25° Hole

Figure 2.19 : 25° Borehole - Isochromatics & Isoclinics

Radial Dist.	Fringe Number	Isoclinic A-A	Isoclinic B-B	Mean Shear Difference	Min 2nd Principal Stress	Max 2nd Principal Stress	Shear Stress
1.0	8.00				.00	8.00	.00
1.5	3.75	-26.0	14.0	-2.3578	2.36	5.99	-.47
2.0	2.25	-16.0	4.0	-.7527	3.11	5.30	-.25
2.5	1.36	-18.0	-2.0	-.3523	3.46	4.75	-.22
3.0	.90	-20.0	-10.0	-.1353	3.60	4.39	-.22
3.5	.85	-22.0	-18.0	-.0454	3.64	4.32	-.26
4.0	.76	-26.0	-23.0	-.0261	3.67	4.19	-.28
4.5	.70	-28.0	-25.0	-.0220	3.69	4.20	-.24
5.0	.50	-30.0	-28.0	-.0092	3.70	4.15	-.11

Table 2.5(a)

Radial Dist.	Fringe Number	Isoclinic C-C	Isoclinic D-D	Mean Shear Difference	Min 2nd Principal Stress	Max 2nd Principal Stress	Shear Stress
1.0	7.00				.00	7.00	.00
1.5	3.56	-6.0	45.0	-2.1501	2.15	5.67	.28
2.0	1.85	-4.0	28.0	-.8956	3.05	4.88	.13
2.5	.95	-1.0	20.0	-.3219	3.37	4.30	.10
3.0	.65	-1.0	18.0	-.2024	3.57	4.21	.06
3.5	.45	2.0	16.0	-.1035	3.67	4.12	.04
4.0	.25	3.0	15.0	-.0494	3.72	3.97	.03
4.5	.15	4.0	15.0	-.0271	3.75	3.90	.02
5.0	.10	5.0	15.0	-.0163	3.77	3.87	.00

Table 2.5(b)

Radial Distance r/a	Radial Stress (kPa)	Hoop Stress (kPa)	Axial Stress (kPa)
1.0	0	512	256
1.5	140	387	264
2.0	188	341	265
2.5	209	306	258
3.0	216	284	250
3.5	217	282	249
4.0	217	276	246
4.5	219	275	247
5.0	224	267	246

Table 2.5(c)

Radial Distance r/a	Radial Stress (kPa)	Hoop Stress (kPa)	Axial Stress (kPa)
1.0	0	448	224
1.5	147	364	256
2.0	197	313	255
2.5	219	276	248
3.0	227	270	248
3.5	228	264	246
4.0	227	254	241
4.5	230	249	240
5.0	235	247	241

Table 2.5(d)

25^{o} Borehole

Table 2.5(a) Secondary Principal Stresses - Line OX
(b) Secondary Principal Stresses - Line OY
(c) Principal Stresses - Line OX
(d) Principal Stresses - Line OY

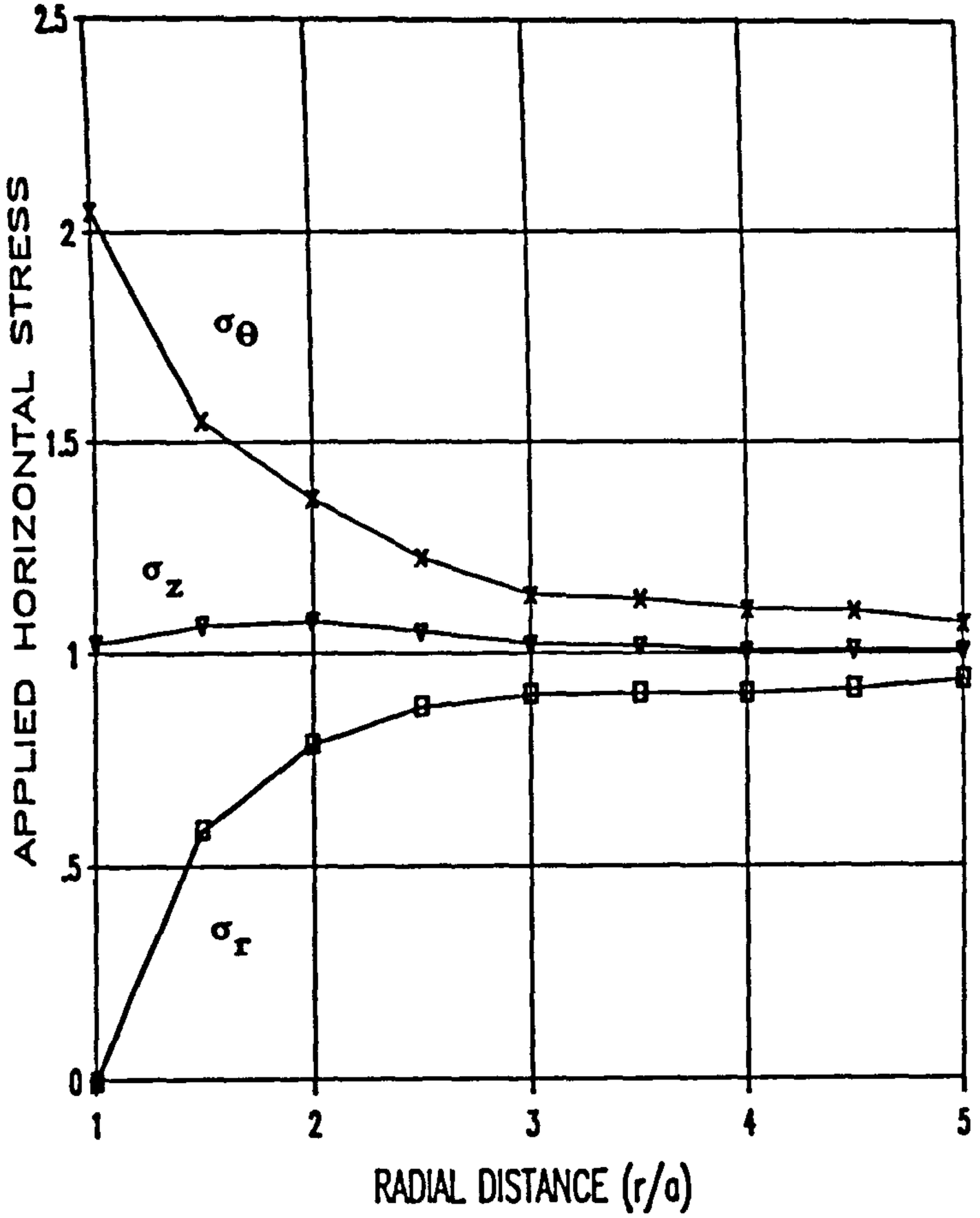

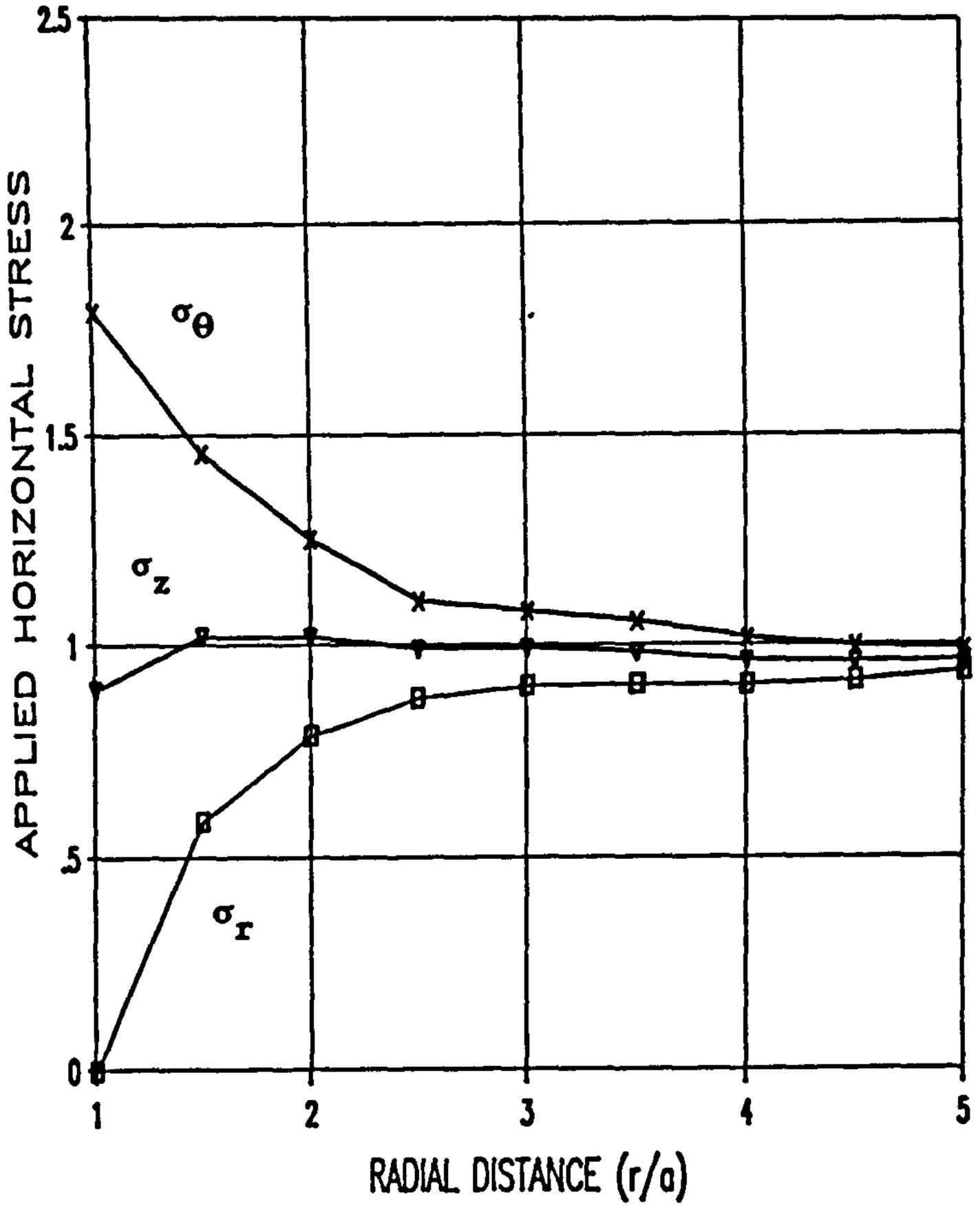

Figure 2.20 : 25° Hole - Principal Stresses along Lines OX and OY

interest and were found to be at a maximum in the region adjacent to the borehole periphery. The shear stresses measured along the horizontal OX line were tensile, while the shear stress values along the vertical OY line were found to be compressive.

The principal stresses acting in the plane of the slice along line OX are presented in Table 2.5(c) and illustrated in Figure 2.20. The hoop stress acting on the OX axis had a value of 512 kPa (2.05 σ_{app}) at the borehole wall which decreased to 267 kPa (1.06 σ_{app}) at r/a = 5, the maximum radius of investigation. The radial stress, which was zero at the periphery, increased rapidly to 224 kPa (0.9 σ_{app}) at the maximum radius of investigation. The axial stress was found to vary from 246 to 265 kPa (0.98 to 1.06 σ_{app}).

The principal stresses for line of interest OY are given in Table 2.5(d) and in Figure 2.20. The hoop stress at the periphery was found to be 448 kPa (1.79 σ_{app}) which reduced to 247 kPa (0.99 σ_{app}) at r/a = 5. The radial stress increased from zero at the periphery to 235 kPa (0.94 σ_{app}) at the maximum radius of investigation. The axial stress was found to vary from 224 to 256 kPa (0.9 to 1.02 σ_{app}) and was at a maximum in the region adjacent to the periphery of the hole.

2.12.3 45° Borehole

The isoclinics and isochromatics for the 45° slice are illustrated in Figure 2.21. It is seen that the maximum fringe orders obtained from the OX and OY axes were 9 and 8 units respectively. The

isoclinics which were traced at 10° intervals, were observed to converge at two isotropic points on either side of the borehole on the OX axis at a radial distance of about 5 radii. A slice 4.45 mm thick was examined, therefore a conversion factor of 58 kPa fr was used.

The secondary principal stresses acting along axes OX and OY are displayed in Tables 2.6(a) and 2.7(b). Referring to Table 2.6(a), the shear stress values along the OX axis were found to be tensile and at a maximum value in the immediate vicinity of the borehole, before tending towards zero as the radial distance increased. The shear stresses acting on the OY axis were compressive, as indicated in Table 2.6(b). Again, the shear stress was at a maximum close to the borehole periphery.

The principal stresses acting on line OX are presented in Table 2.6(c) and graphically in Figure 2.22. The maximum hoop stress measured at the periphery was found to be in the order of 552 kPa (2.21 σ_{app}). This value decreased to 392 kPa (1.57 σ_{app}) at r/a = 1.5 before reaching a value of 305 kPa (1.22 σ_{app}) at r/a = 5. The radial stress increased from zero to 233 kPa (0.93 σ_{app}) at the maximum radius of investigation. The difference between the radial and hoop stress at that point was 72 kPa. The computed axial stress was found to have an average value of 270 kPa (1.08 σ_{app}).

The principal stresses calculated along line OY are displayed in Table 2.6(c) and also in Figure 2.22. In this case, the hoop stress at r/a = 1 was measured at 464 kPa (1.85 σ_{app}) and was seen to

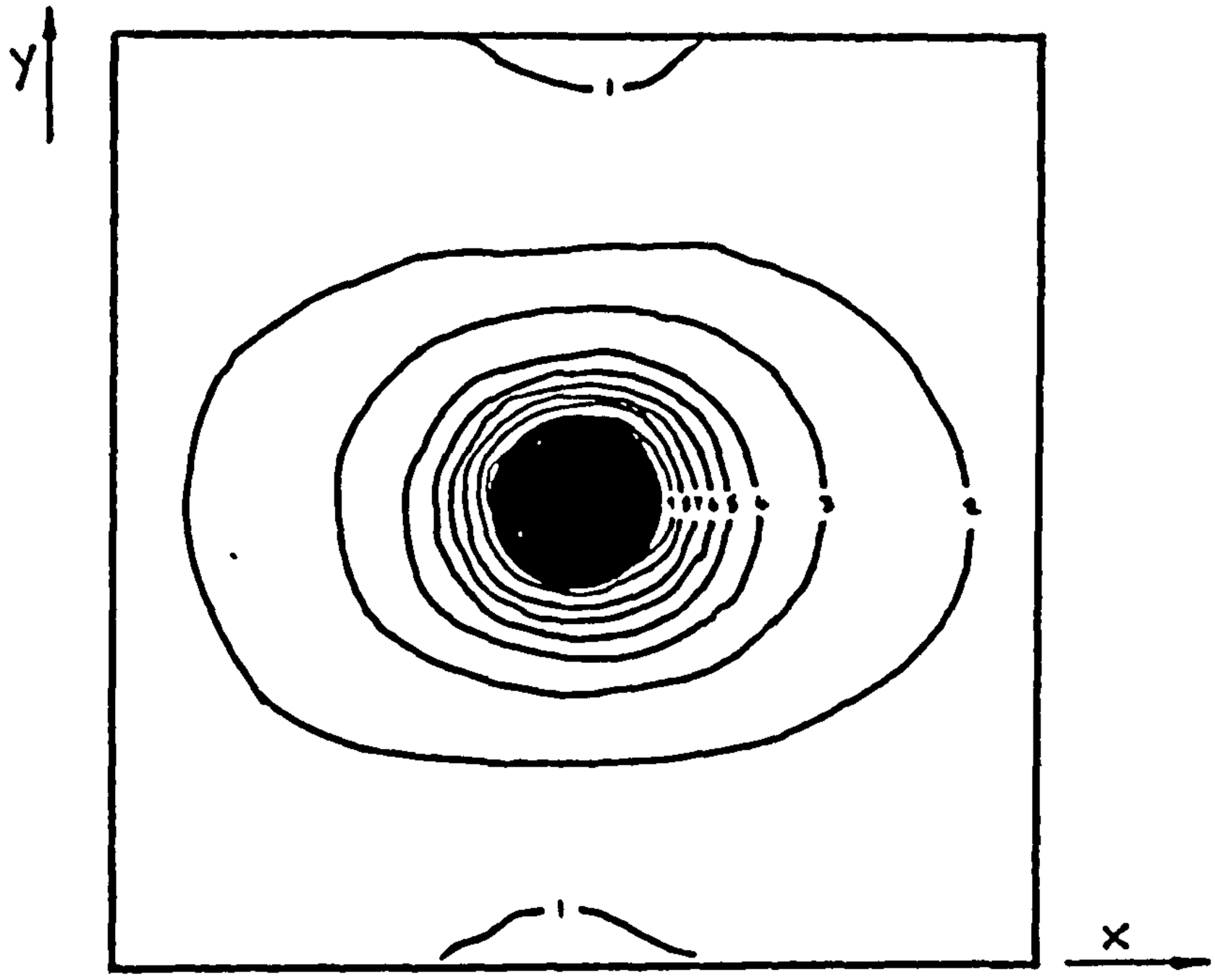

Isochromatics - 45° Hole

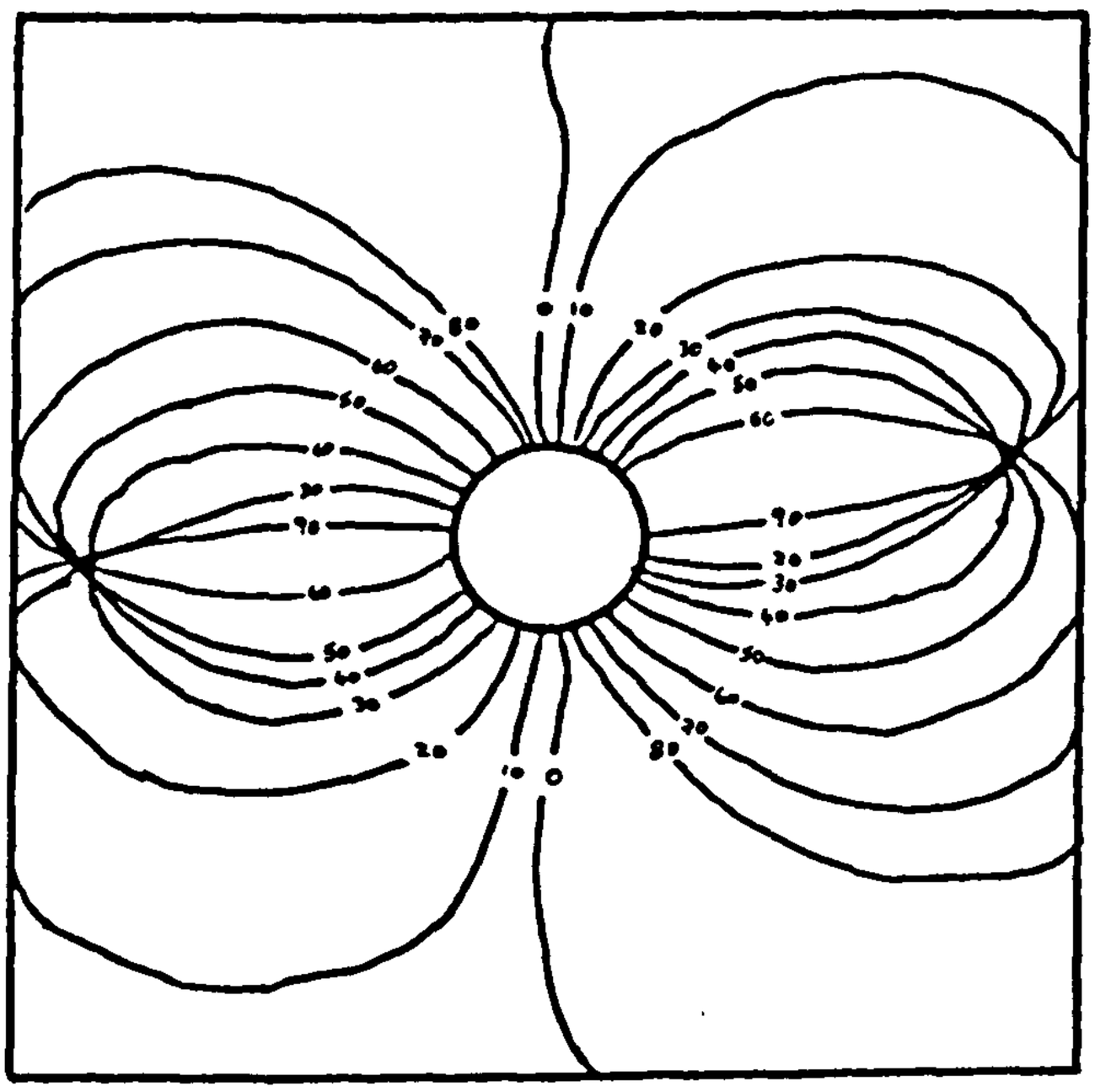

Isoclinics - 45° Hole

Figure 2.21 : 45° Borehole - Isochromatics & Isoclinics

Radial Dist.	Fringe Number	Isoclinic A-A	Isoclinic B-B	Mean Shear Difference	Min 2nd Principal Stress	Max 2nd Principal Stress	Shear Stress
1.0	9.00				.00	9.00	.00
1.5	4.25	-25.0	13.0	-2.5594	2.56	6.70	-.48
2.0	3.05	-8.0	4.0	-.6326	3.19	6.23	-.14
2.5	2.15	-5.0	3.0	-.2990	3.49	5.64	-.04
3.0	1.85	-4.0	2.0	-.1933	3.68	5.53	-.03
3.5	1.75	-3.0	2.0	-.1525	3.84	5.59	-.02
4.0	1.56	-3.0	1.0	-.1088	3.95	5.50	-.03
4.5	1.43	-2.0		-.0499	4.00	5.42	-.02
5.0	1.25	-2.0	-1.0	-.0218	4.02	5.27	-.02

Table 2.6(a)

Radial Dist.	Fringe Number	Isoclinic C-C	Isoclinic D-D	Mean Shear Difference	Min 2nd Principal Stress	Max 2nd Principal Stress	Shear Stress
1.0	8.00				.00	8.00	.00
1.5	3.85	-8.0	46.0	-2.4544	2.45	6.27	.24
2.0	2.04	-6.0	32.0	-1.1288	3.58	5.58	.20
2.5	1.36	2.0	26.0	-.4884	4.07	5.39	.17
3.0	.75	12.0	35.0	-.1999	4.27	4.94	.17
3.5	.40	14.0	47.0	-.1056	4.38	4.69	.12
4.0	.30	15.0	64.0	-.0432	4.42	4.68	.08
4.5	.20	18.0	60.0	-.0278	4.45	4.63	.04
5.0	.05	69.0	65.0	-.0024	4.45	4.50	.01

Table 2.6(b)

Radial Distance r/a	Radial Stress (kPa)	Hoop Stress (kPa)	Axial Stress (kPa)
1.0	0	522	261
1.5	145	392	269
2.0	185	362	273
2.5	202	327	265
3.0	214	321	267
3.5	223	324	273
4.0	229	319	274
4.5	232	315	273
5.0	233	305	269

Table 2.6(c)

Radial Distance r/a	Radial Stress (kPa)	Hoop Stress (kPa)	Axial Stress (kPa)
1.0	0	464	232
1.5	141	365	253
2.0	207	325	266
2.5	235	314	274
3.0	245	289	267
3.5	251	275	263
4.0	255	273	264
4.5	258	269	263
5.0	258	261	260

Table 2.6(d)

45° Borehole

Table 2.6(a) Secondary Principal Stresses - Line OX
(b) Secondary Principal Stresses - Line OY
(c) Principal Stresses - Line OX
(d) Principal Stresses - Line OY

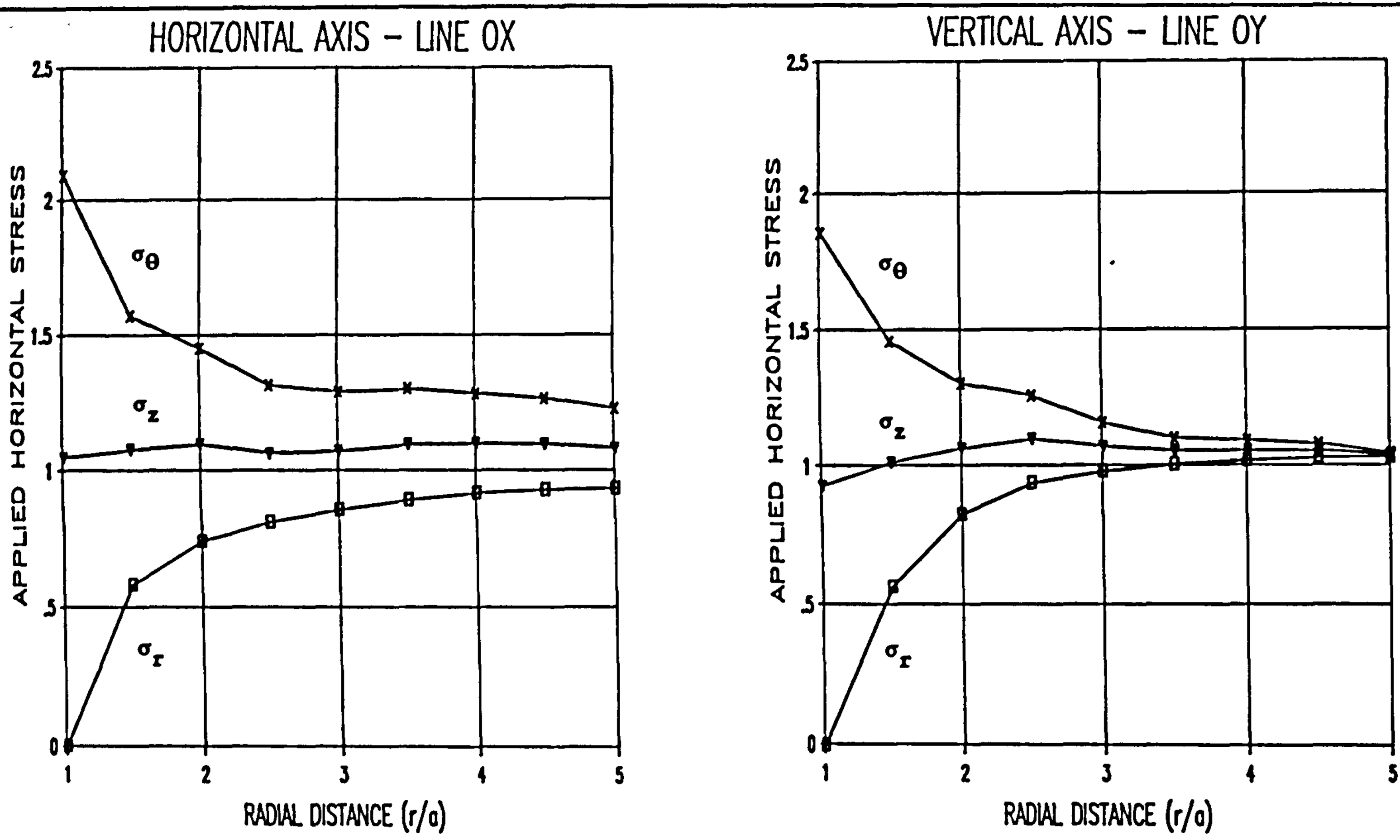

Figure 2.22 : 45° Hole - Principal Stresses along Lines OX and OY

decrease to a value of 261 kPa (1.04 σ_{app}) at r/a = 5. The radial stress increased from zero at the periphery to a maximum of 258 kPa (1.03 σ_{app}) at r/a = 5. The difference between the radial and hoop stress at that point was 3 kPa. The axial stress varied from 232 kPa (0.93 σ_{app}) at the periphery to 274 kPa (1.1 σ_{app}) at r/a = 2.5.

2.12.4 <u>60° Borehole</u>.

The isochromatics and isoclinics for the 60° borehole slice are displayed in Figure 2.23. The maximum isochromatic parameter observed at the periphery of the borehole on the OX and OY axes were 6.5 and 5 fringe units respectively. Two isotropic points were identified from a plot of the isoclinics, each on the OX axis at a radial distance of approximately 4 radii on either side of the borehole. Slice thickness was 3.04 mm, therefore F/t was 85 kPa fr.

The input parameters and the computed secondary principal stresses along lines OX and OY are displayed in Tables 2.7(a) and 2.7(b). In accordance with the test results obtained for the alternative borehole inclinations, the shear stresses measured along line OX were found to be tensile, while the shear stress values measured along line OY were compressive. In each case the maximum shear stress value was found to occur in the immediate vicinity of the borehole.

The principal stresses acting on the horizontal line OX are given in Table 2.7(c) and in Figure 2.24. The hoop stress acting on the periphery of the borehole was found to be 559 kPa (2.24 σ_{app}). Away

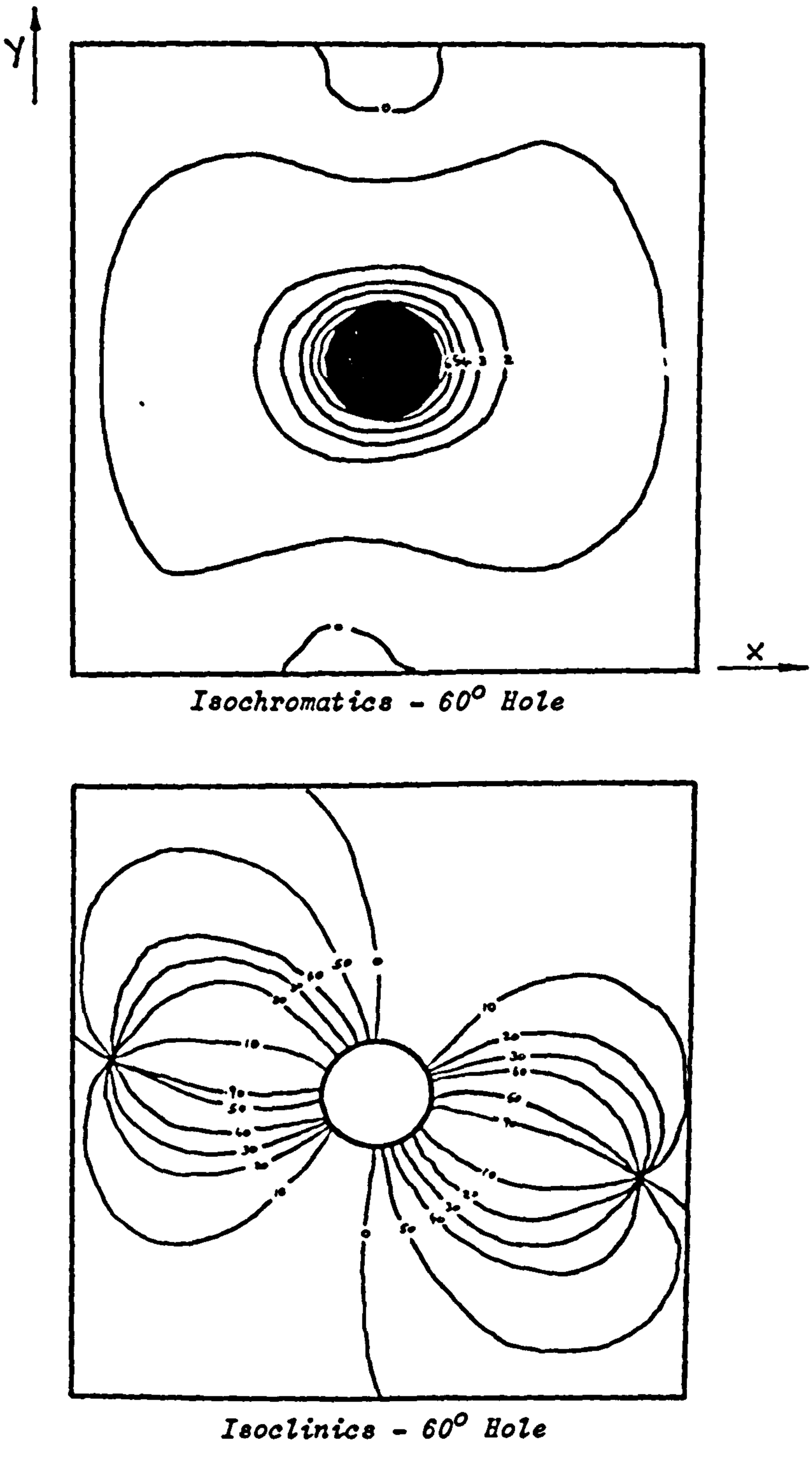

Figure 2.23 : 60° Borehole - Isochromatics & Isoclinics

Radial Dist.	Fringe Number	Isoclinic A-A	Isoclinic B-B	Mean Shear Difference	Min 2nd Principal Stress	Max 2nd Principal Stress	Shear Stress
1.0	6.50				.00	6.50	.00
1.5	3.12	-17.0	10.0	-1.4059	1.41	4.48	-.27
2.0	1.89	-11.0	7.0	-.5826	1.99	3.87	-.09
2.5	1.42	-10.0	4.0	-.3416	2.33	3.74	-.08
3.0	1.10	-7.0	3.0	-.1905	2.52	3.62	-.04
3.5	.95	-6.0	3.0	-.1484	2.67	3.62	-.03
4.0	.84	-3.0	2.0	-.0732	2.74	3.58	-.01
4.5	.81	-2.0	1.0	-.0424	2.78	3.59	-.01
5.0	.80	-2.0	1.0	-.0419	2.83	3.63	-.01

Table 2.7(a)

Radial Dist.	Fringe Number	Isoclinic C-C	Isoclinic D-D	Mean Shear Difference	Min 2nd Principal Stress	Max 2nd Principal Stress	Shear Stress
1.0	5.00				.00	5.00	.00
1.5	2.59	-9.0	49.0	-1.6826	1.68	4.26	.11
2.0	1.25	-4.0	40.0	-.7025	2.39	3.59	.17
2.5	.86	5.0	32.0	-.3118	2.70	3.52	.12
3.0	.38	4.0	25.0	-.1191	2.82	3.18	.05
3.5	.20	1.0	20.0	-.0608	2.88	3.07	.02
4.0	.10	2.0	12.0	-.0168	2.89	2.99	.01
4.5	.10	3.0	12.0	-.0151	2.91	3.01	.00
5.0	.01	4.0	9.0	-.0008	2.91	2.92	.00

Table 2.7(b)

Radial Distance r/a	Radial Stress (kPa)	Hoop Stress (kPa)	Axial Stress (kPa)
1.0	0	559	279
1.5	119	387	253
2.0	171	333	252
2.5	200	322	261
3.0	217	311	264
3.5	229	311	270
4.0	236	308	272
4.5	239	309	274
5.0	243	312	277

Table 2.7(c)

Radial Distance r/a	Radial Stress (kPa)	Hoop Stress (kPa)	Axial Stress (kPa)
1.0	0	430	215
1.5	144	367	256
2.0	203	311	257
2.5	230	304	267
3.0	242	274	258
3.5	247	264	256
4.0	249	257	253
4.5	250	259	254
5.0	250	251	251

Table 2.7(d)

60^{o} Borehole

Table 2.7(a) Secondary Principal Stresses - Line OX
(b) Secondary Principal Stresses - Line OY
(c) Principal Stresses - Line OX
(d) Principal Stresses - Line OY

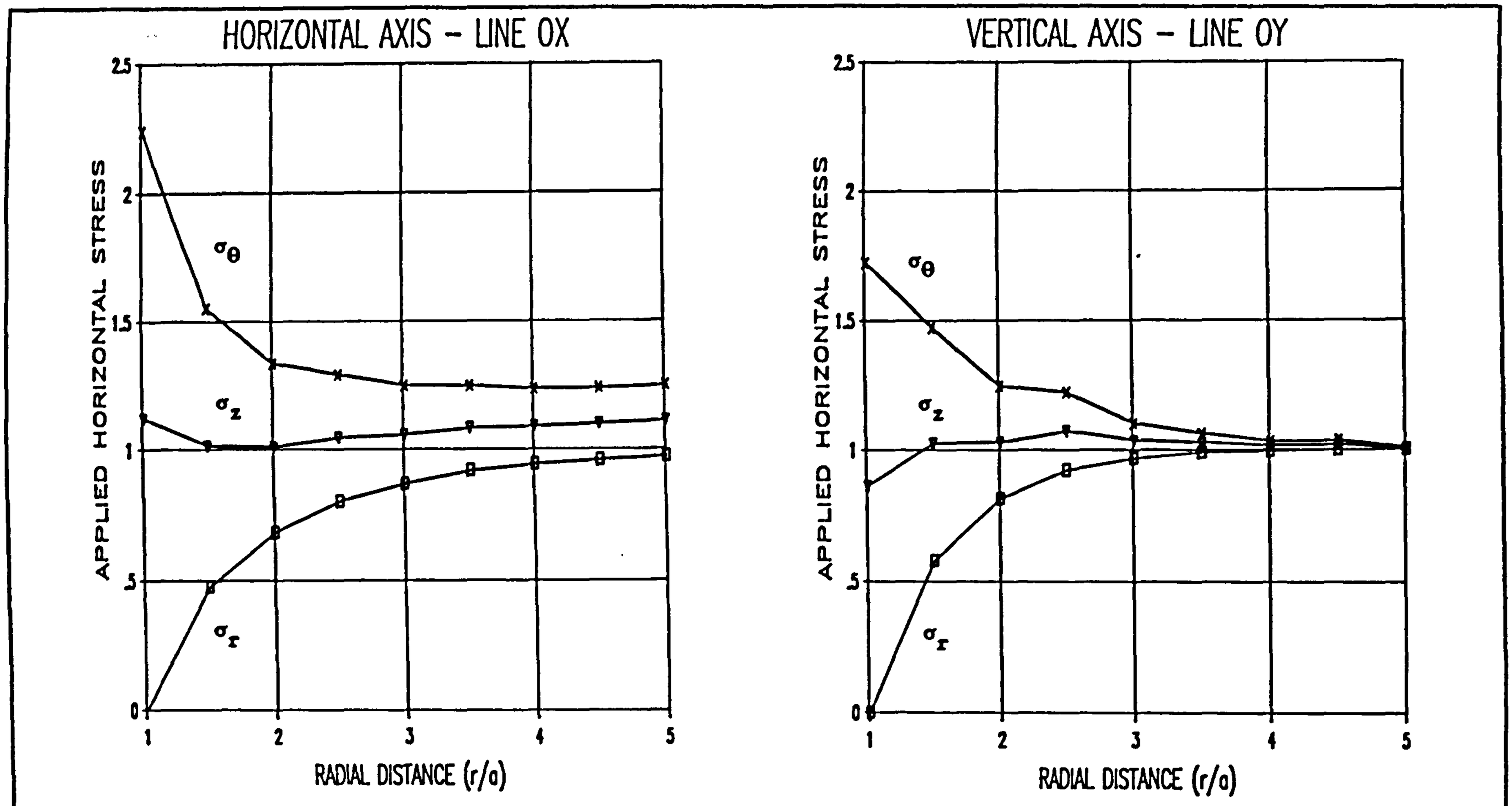

Figure 2.24 : 60° Hole - Principal Stresses along Lines OX and OY

from the effect of the borehole, this value decreased and leveled off at around 311 kPa (1.24 σ_{app}). The radial stress increased from zero at the borehole wall to a maximum of 243 kPa (0.97 σ_{app}) at r/a = 5. The axial stress was found to remain relatively constant at a value of about 270 kPa (1.08 σ_{app}).

The principal stresses for line OY are displayed in Table 2.7(d) and also in Figure 2.24. The hoop stress decreased from a maximum value of 430 kPa (1.72 σ_{app}) at the wall of the borehole to 367 kPa (1.45 σ_{app}) at r/a = 1.5 and reached a minimum value of 251 kPa (1.0 σ_{app}) at r/a = 5. The radial stress increased from zero at the borehole periphery to a value of 144 kPa (0.57 σ_{app}) at r/a = 1.5 before reaching a maximum value of 250 kPa (1.0 σ_{app}) at r/a = 5. The axial stress varied from 215 kPa (0.86 σ_{app}) at the hole periphery to a maximum value of around 267 kPa (1.07 σ_{app}).

2.12.5 Horizontal Borehole

The isoclinics and isochromatics obtained from the 90° borehole slice are illustrated in Figure 2.25. The maximum isochromatic parameter identified at the hole periphery on lines OX and OY were 7 and 4 fringe units respectively. In common with the inclined holes, two isotropic points were identified after a plot of the isoclinics. Each isotropic point occurred on either side of the borehole on the OX axis at a radial distance of about 3 radii. As a slice 3.44 mm thick was examined, the conversion factor was 75 kPa fr.

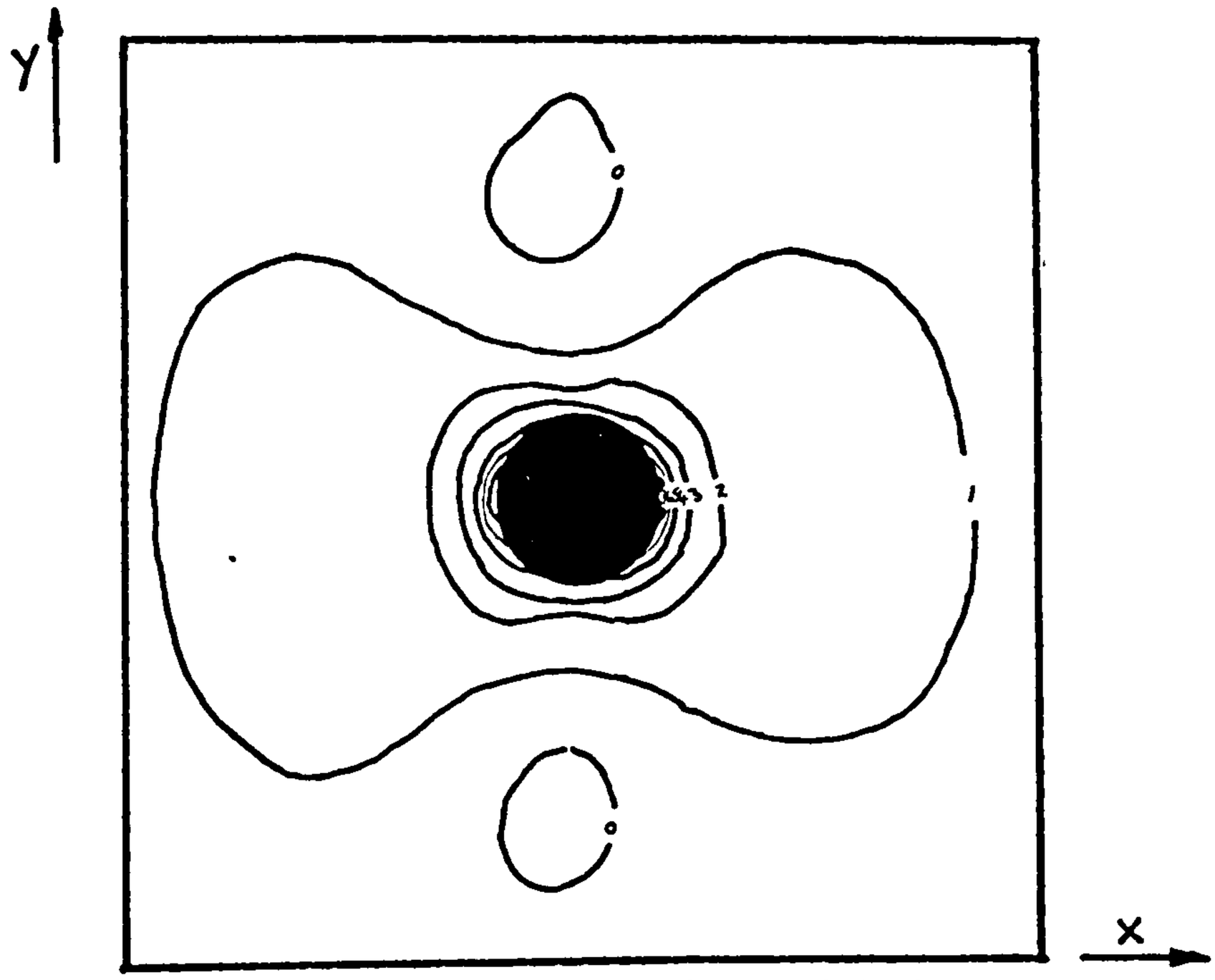

Isochromatics - Horizontal Hole

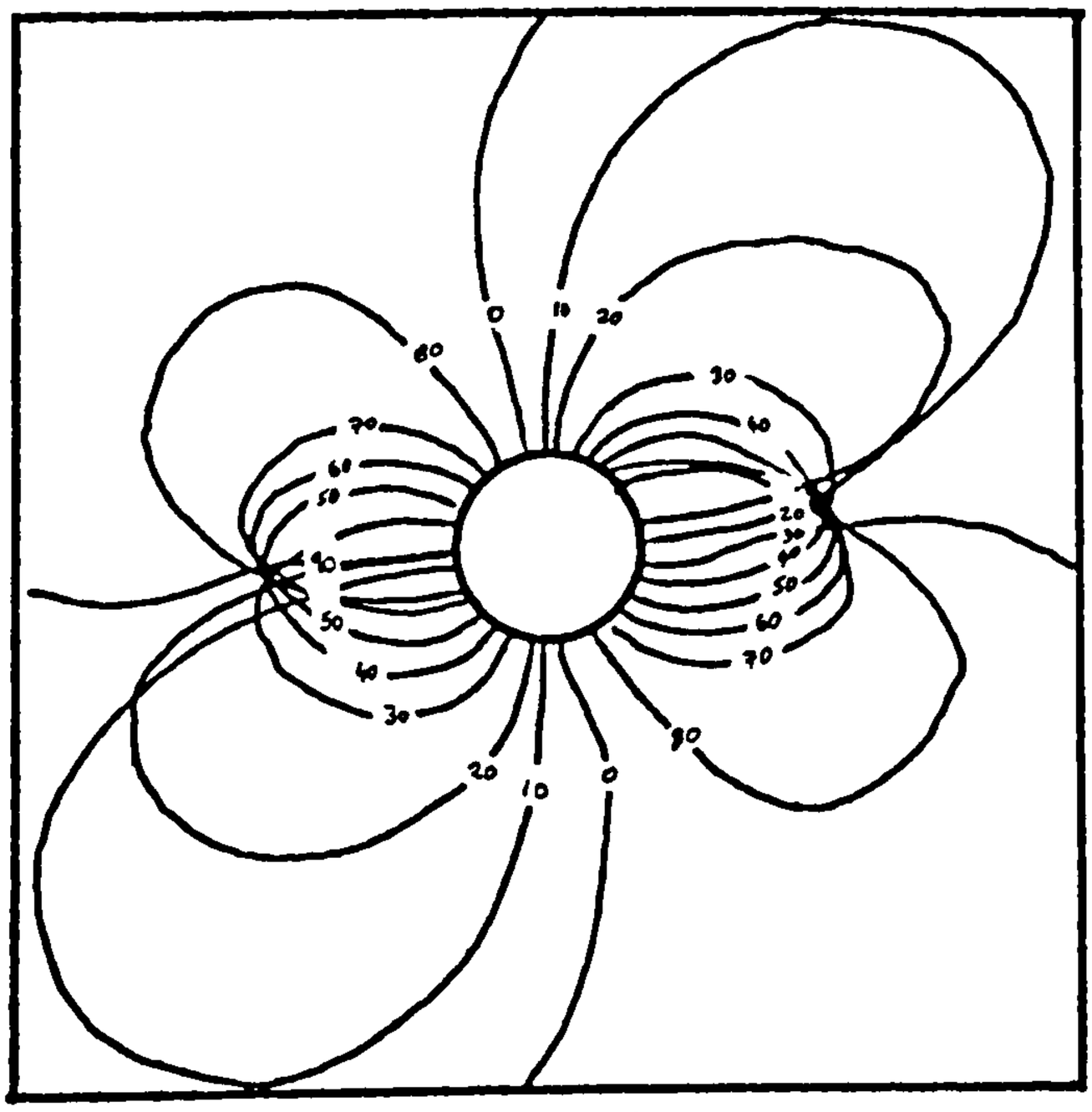

Isoclinics - Horizontal Hole

Figure 2.25 : Horizontal Borehole - Isochromatics & Isoclinics

Radial Dist.	Fringe Number	Isoclinic A-A	Isoclinic B-B	Mean Shear Difference	Min 2nd Principal Stress	Max 2nd Principal Stress	Shear Stress
1.0	7.00				.00	7.00	.00
1.5	3.58	-10.0	18.0	-1.6644	1.66	5.24	.01
2.0	2.12	-9.0	13.0	-.7922	2.46	4.58	.01
2.5	1.56	-8.0	11.0	-.5072	2.96	4.52	.00
3.0	1.12	-7.0	8.0	-.2898	3.25	4.37	.00
3.5	1.02	-3.0	3.0	-.1066	3.36	4.38	.00
4.0	.91	-3.0	3.0	-.0951	3.46	4.37	.00
4.5	.85	-2.0	2.0	-.0593	3.51	4.36	.00
5.0	.73		1.0	-.0127	3.53	4.26	.00

Table 2.8(a)

Radial Dist.	Fringe Number	Isoclinic C-C	Isoclinic D-D	Mean Shear Difference	Min 2nd Principal Stress	Max 2nd Principal Stress	Shear Stress
1.0	4.00				.00	4.00	.00
1.5	1.89	-15.0	46.0	-1.4169	1.42	3.31	.01
2.0	.98	-10.0	32.0	-.6080	2.02	3.00	.01
2.5	.42	-8.0	12.0	-.1433	2.17	2.59	-.01
3.0	.21	-7.0	10.0	-.0613	2.23	2.44	.00
3.5	.15	-6.0	5.0	-.0286	2.26	2.41	.00
4.0	.10	-6.0	3.0	-.0156	2.27	2.37	.00
4.5	.08	-4.0	2.0	-.0084	2.28	2.36	.00
5.0	.01	-4.0	2.0	-.0010	2.28	2.29	.00

Table 2.8(b)

Radial Distance r/a	Radial Stress (kPa)	Hoop Stress (kPa)	Axial Stress (kPa)
1.0	0	602	301
1.5	126	399	263
2.0	187	348	267
2.5	225	344	285
3.0	247	332	290
3.5	255	333	294
4.0	263	332	297
4.5	267	332	299
5.0	268	324	296

Table 2.8(c)

Radial Distance r/a	Radial Stress (kPa)	Hoop Stress (kPa)	Axial Stress (kPa)
1.0	0	304	152
1.5	108	251	180
2.0	154	228	191
2.5	165	197	181
3.0	169	185	177
3.5	172	183	177
4.0	173	180	177
4.5	173	180	176
5.0	174	174	174

Table 2.8(d)

Horizontal Borehole

Table 2.8(a) Secondary Principal Stresses - Line OX
(b) Secondary Principal Stresses - Line OY
(c) Principal Stresses - Line OX
(d) Principal Stresses - Line OY

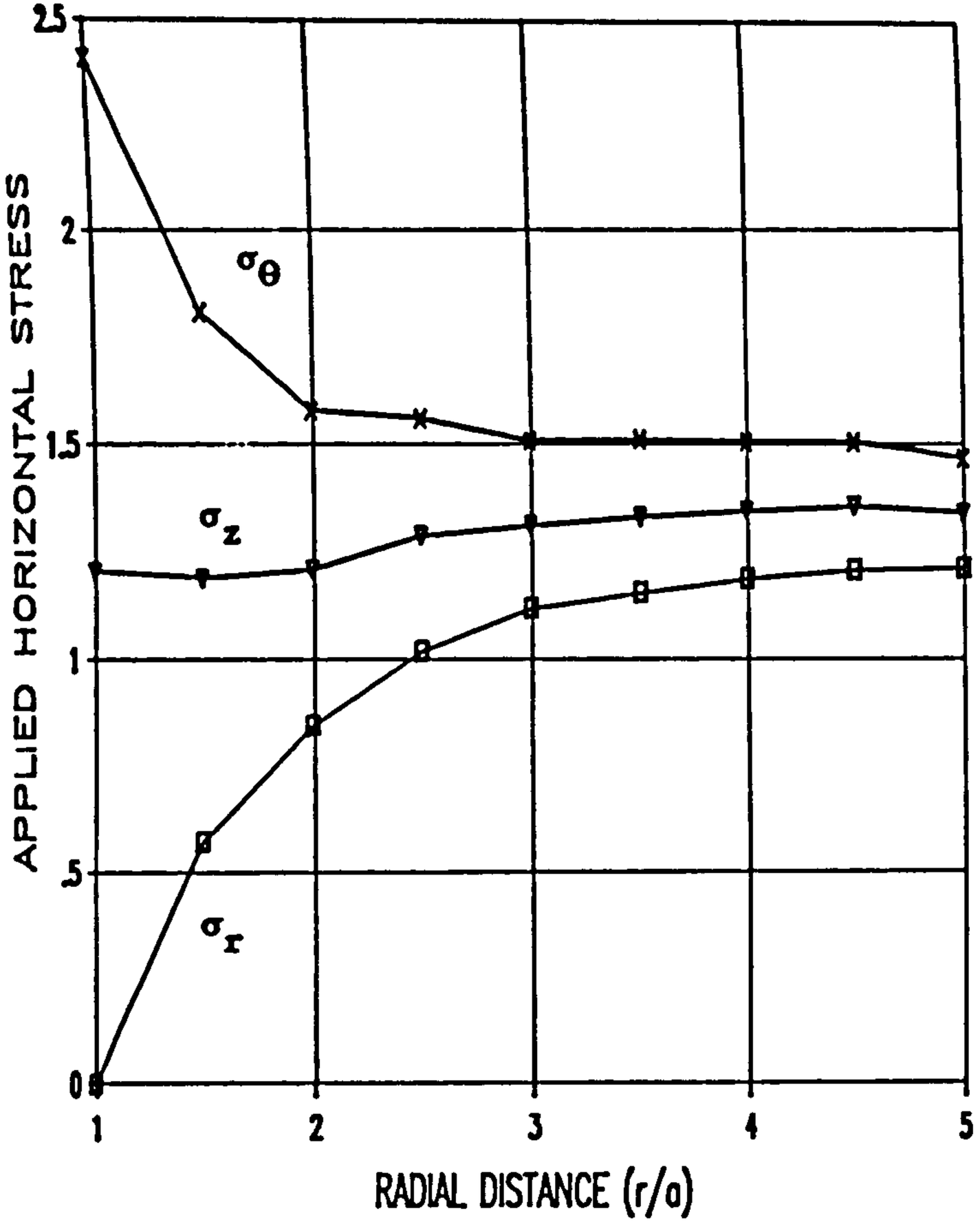

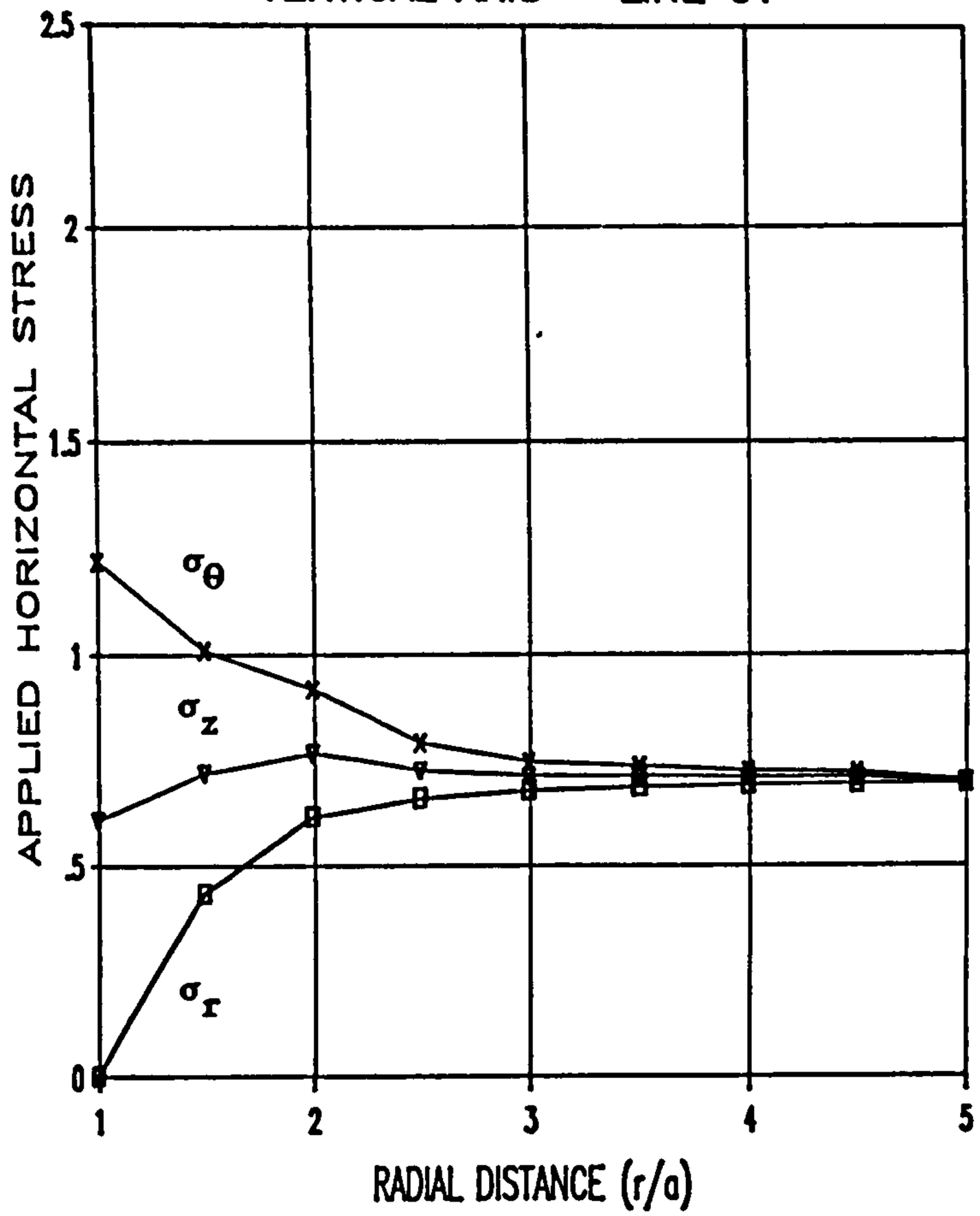

Figure 2.26 : Horizontal Hole - Principal Stresses along Lines OX and OY

The input parameters and the secondary principal stresses calculated along lines OX and OY are displayed in Tables 2.8(a) and 2.8(b) respectively. As the slice was taken from a plane of principal stress, no shear stresses were measured along each of the lines of interest. The principal stresses acting in the plane of the slice were therefore identical to the measured secondary principal stresses.

The principal stresses acting along line OX are presented in tabular form in Table 2.8(c) and graphically in Figure 2.26. It can be seen that the hoop stress measured at the borehole wall was 602 kPa (2.41 σ_{app}). This value decreased to 399 kPa (1.35 σ_{app}) at r/a = 1.5 before reaching a minimum value of 324 kPa (1.3 σ_{app}) at the maximum radius of investigation. The radial stress increased from zero at the hole periphery to 126 kPa (0.5 σ_{app}) at r/a = 1.5 and reached a maximum value of 268 kPa (1.07 σ_{app}) at the r/a = 5. The calculated axial stress varied from 263 to 301 kPa (1.05 to 1.2 σ_{app}).

The principal stresses measured along line OY are given in Table 2.8(d) and in Figure 2.26. In this case, the maximum hoop stress measured at the hole periphery and at r/a = 5 was 304 kPa (1.22 σ_{app}) and 174 kPa (0.7 σ_{app}) respectively. The radial stress increased from zero at the boundary of the borehole to a value of 174 kPa (0.7 σ_{app}) at r/a =5. The axial stress varied from 152 kPa (0.61 σ_{app}) at the hole periphery to 191 kPa (0.76 σ_{app}) at r/a = 2.

2.13 CONSIDERATIONS OF ACCURACY

The accuracy of the results obtained depended on several factors, the foremost of which was the accuracy of loading. As the loading was applied by means of separate air-bags, each acting on one face of the model, it was important to confirm that the air-bags remained air tight and provided the desired load. The circular fringe distribution obtained for the vertical borehole confirmed that the horizontal loading was correctly applied while an examination of the symmetrical fringe pattern produced by the horizontal borehole gave an indication the desired vertical pressure had been provided. The poor results obtained from the horizontal hole, however, suggests that it may have been positioned too near the side of the model.

Another factor was the degree of flatness of the model faces. This was dependant on the accuracy of machining. Accordingly, the flatness, squareness and general surface finish of the model was checked prior to loading and found to be satisfactory.

The third factor influencing the accuracy of the results was the determination of the isoclinic parameter θ. This could only be determined to an accuracy of about 2°. The transition between the isoclinic parameters was not always clearly defined as the isoclinics tended to occur as bands rather than as sharply defined lines. This was especially true for the isoclinics measured as the radius of investigation increased. The isoclinic parameters were double-checked to attain the best accuracy possible, nevertheless, the determination of θ represented an inherent source of error.

Measurement of the fractional fringe order however, did not constitute a problem. The Tardy method of compensation has a potential accuracy of 0.01 of a fringe, and an estimated practical accuracy of 0.05 of a fringe order (corresponding to an analyser rotation of 9°). Any errors resulting from the measurement of the fractional fringe orders was therefore small and not considered to be significant.

The fourth factor was a consideration of the direct applicability of the results of the calibration. As the calibration specimens were prepared from the same cast as the material used for the model and the calibration constant gave the correct order of magnitude of the stresses, this factor was not considered to have caused any significant errors in the conversion calculations from terms of isochromatic parameters to stress units.

Finally, the accuracy of the axial stress derived from elastic theory may be questionable. To calculate this value from the values of σ_r and σ_θ a Poisson's ratio of 0.5 was assumed; however, Poisson's ratio for the batch of Araldite CT200 used was measured and consequently this may be a source of error.

2.14 CONCLUSIONS

The results of the photoelastic analysis have revealed several characteristics in the stress distribution around both vertical and inclined boreholes.

For the case of the vertical borehole, the tangential stress was found to be constant at all points around the periphery of the hole and had a value of twice the horizontal in-situ stress. This was in accordance with elastic theory.

The effect of inclining the borehole was to decrease the tangential stress acting on 'roof' of the hole (i.e. the OY axis) and to increase the tangential stress acting at the 'side' of the borehole (i.e. the OX axis). This effect was more apparent with the higher angle holes. This leads to the conclusion that, under normal in-situ stress conditions, the 'roof' of an inclined borehole is more likely to fail in tension while the 'side' of the hole is more likely to fail in compression.

Although the effect of mud weight was not considered in this initial analysis due to difficulties in applying wellbore pressure within the loading frame, the investigation has proved beneficial as it has experimentally demonstrated the varying state of stress around inclined boreholes and has identified regions of maximum potential instability.

As regards the choice of Araldite CT200 for the model material, it may be concluded that it is an ideal material for photoelastic analysis, but care must be taken during machining operations to avoid the production of undesirable thermal stresses.

The inclusion of the 25° and 60° borehole in the photoelastic model did not affect the stress concentrations around the other boreholes and provided extra data on the induced state of stress around inclined boreholes

The loading frame employed in the stress freezing experiment provided an effective and efficient method of applying pressure to the model in three-dimensions. As the loading frame has the capability to apply polyaxial loading, i.e. $\sigma_1 \neq \sigma_2 \neq \sigma_3$, it has the potential to be used in future examinations to simulate tectonic conditions.

The application of computer analysis to separate the secondary principal stresses using the shear difference method eliminated the tedious, repetitive calculations as reported in the literature. It can therefore be concluded that the frozen stress technique, when used in conjunction with the shear difference method, provides a useful approach to the analysis of three-dimensional stress analysis of inclined boreholes.

CHAPTER THREE

THE DETERMINATION OF ROCK MECHANICAL PROPERTIES AND THE APPLICATION OF THE BRINELL HARDNESS TEST TO ROCK

3.1 INTRODUCTION

In rock mechanical stress analysis, the logical progression from a physical modelling technique is to extend the investigation to analytical methods. Such a mathematical analysis would allow the inclusion of failure criteria and enable the prediction of wellbore failure in compression. The opportunity to simulate mud weight and the facility to alter variables such as hole angle and in-situ stress conditions would also be possible, if the necessary equations were available. Before conducting such an analysis, however, an extensive laboratory rock testing programme would be required to provide input parameters as such equations would necessarily be empirical.

The intention of this chapter was threefold:- to investigate the validity of the Brinell hardness test applied to rocks, to establish if a relationship exists between Brinell hardness and the mechanical properties of rocks and to provide failure criteria and physical property data for the analytical borehole stability analysis developed in Chapter 4.

3.2 THE APPLICATION OF THE BRINELL HARDNESS TEST TO ROCK

3.2.1 Concept of a Hardness Test

The hardness of a mineral is directly related to its chemistry and atomic structure, and reflects to some extent the physical and

mechanical properties of the mineral. Hardness is a quality which is readily appreciated but not easily described quantitatively. Various tests have been developed to assess hardness, most of which measure the resistance of the material to scratching or indentation.

In 1824, Mohs proposed a scale of hardness employing a standard set of ten minerals to which relative hardness numbers were allocated [82]. The hardness of a test object is assessed by observing whether or not it is scratched by one of the mineral standards. Scratch hardness may be a useful tool for a quick but rough assessment and has the advantage that no instrumentation is required; however, it leaves much to be desired as a basis for quantitive measurement and is rarely used in engineering.

The instrumentation used in determining rock hardness has been developed from indentation techniques for measuring hardness in metals, minerals and other materials that are assumed to be homogeneous. Hardness is expressed in arbitrary units depending on the design and application of the measuring instrument. The NCB Cone Indenter [83] has been used in the field of rock mechanics to give an indication of rock hardness. Correlations of compressive strength and hardness of Coal Measure rocks has been performed by Szlavin [84] who related uniaxial compressive strength with cone indenter hardness. Investigations into the experimental criteria for classification of rock substances conducted by Coates [85] suggested the possibilty of using some empirical test, such as a hardness or rebound test, to estimate rock strength. Accordingly, Van der Vlis [35] applied the Brinell hardness test, well known in mechanical

engineering [86], to rock samples and showed that it could be used as a practical criterion for rock classification. He went on to suggest the existence of an empirical relationship between the Brinell hardness number and the elastic moduli of rock. Ball-point penetrometer tests on rock, previously applied by Huitt and McGlothlin [87] in studies of the deformations occurring during the propping of hydraulic fractures, also point to hardness as a useful indicator to rock properties. As reviewed in the opening chapter, Geertsma [34] proposed that the Brinell hardess test may also be used to assess particle-influx risk.

The determination of rock hardness is therefore an important concept in rock mechanics. Brinell hardness, however, is not a fundamental property of a material, it has no qualitative value except in terms of a specified load applied in conjunction with a specific diameter of ball indenter.

3.2.2 Test Theory

The Brinell Hardness of a rock may be measured in the same way as that of metals, namely subjecting a sample of the material to a predetermined load via a spherical steel indenter and measuring the diameter or depth of the resulting indentation. The Brinell Hardness Number (BHN) is defined as the ratio L/A, where L is the applied load in kilogrammes and A is the spherical surface area of the indentation in square millimetres. This ratio is constant for a given material only when the applied load and indenter diameter are constant.

Referring to Figure 3.1, the spherical surface area is determined by either measuring the diameter or the depth of the indentation. The brinell hardness number may then be calculated from the following relationships :

$$BHN = \frac{L}{\frac{\pi D}{2}\left(D - \sqrt{D^2 - d^2}\right)} \quad .. \quad .. \quad .. \quad .. \quad (3.1)$$

or

$$BHN = \frac{L}{\pi D h} \quad .. \quad .. \quad .. \quad .. \quad (3.2)$$

where BHN = Brinell Hardness Number (kg/mm²)

L = Applied Load (kg)

D = Diameter of Ball Indentater (mm)

d = Diameter of Indentation (mm)

h = Depth of Indentation (mm)

3.2.3 Development of Brinell Test Apparatus and Procedures

To apply the Brinell hardness test to rock, lower loads than would be used for testing metal are required while the diameter of the ball indenter is also generally smaller. Accordingly, the use of a standard Brinell tester would not be suitable for testing small samples of rock. As a standard Brinell tester was not available for modification, it was therefore necessary to either design or modify existing departmental equipment for use as a Brinell tester. Two items of equipment appeared suitable for modification: these being an NCB cone indenter which was modified for use as a portable

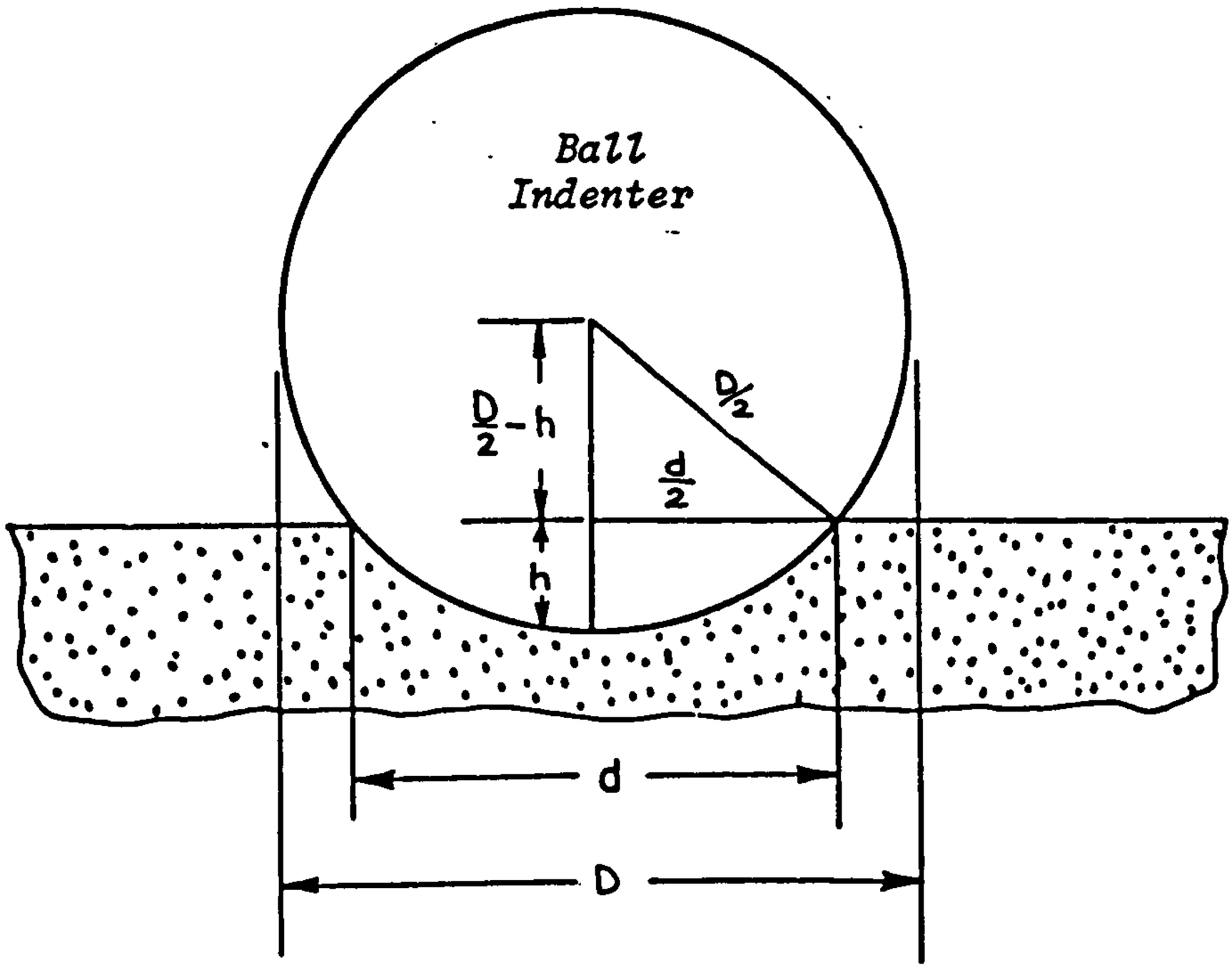

Figure 3.1 : Relationship Between Depth and Diameter of an Indentation [87]

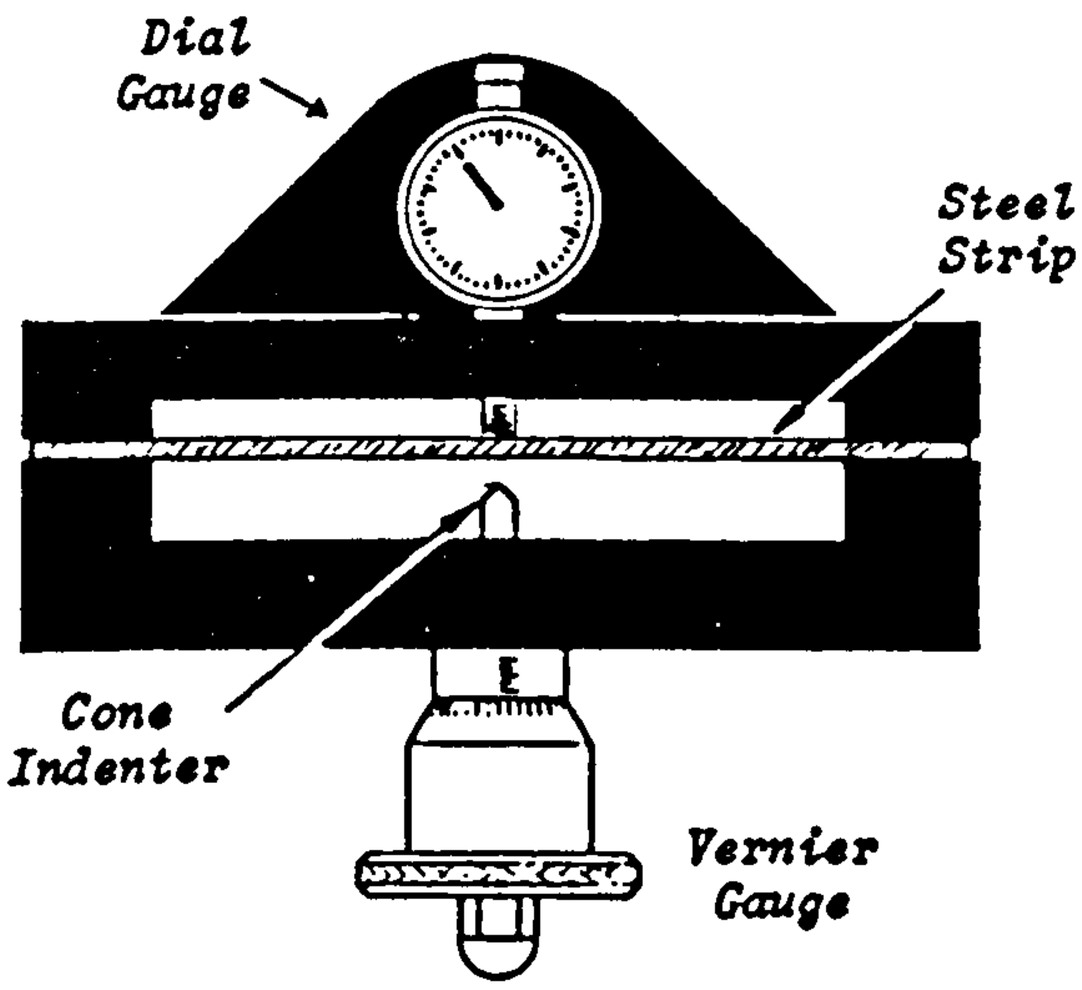

Figure 3.2 : NCB Cone Indenter [83]

tester, and an oedometer which was adapted for use as a laboratory tester. The necessary modifications to these instruments and the test procedures developed are given below.

3.2.3.1 Modified NCB Cone Indenter

The instrument in its original form measures the penetration of a tungsten carbide tipped cone into a rock fragment under a constant force. The applied load is measured by the deflection of a calibrated steel strip clamped within a steel frame (Figure 3.2). The penetration of the cone into the sample is measured and used to give a 'cone indenter number' which is related to the compressive strength of the rock under test.

The modification consisted of replacing the conical indenter by a 5.5 mm diameter hardened steel ball. Due to use of an alternative shape of indenter, it was necessary to recalibrate the instrument. This was accomplished by the application of a series of weights to the steel strip via the ball indenter and noting the respective deflections indicated by the dial gauge reading. A thin metal platten was placed between the indenter and the steel strip to simulate the 'bridging' of a rock sample. The calibration rig is shown in Figure 3.3. The rotating vernier gauge on the standard instrument was scaled in divisions of 0.025 mm. To provide greater accuracy in reading indentation depths, these divisions were further divided to produce divisions of 0.005 mm.

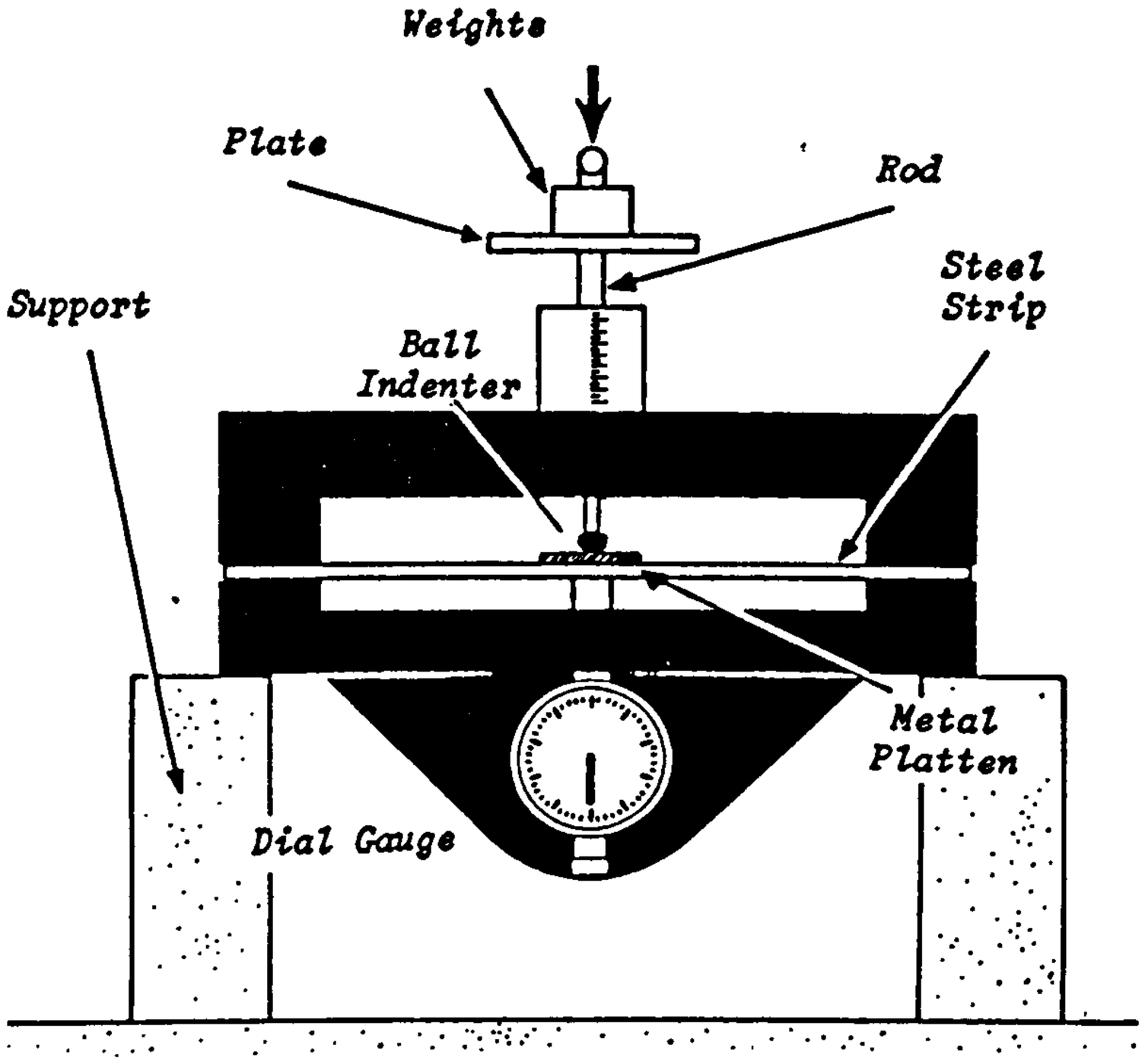

Figure 3.3 : Calibration Rig used for Modified Cone Indenter

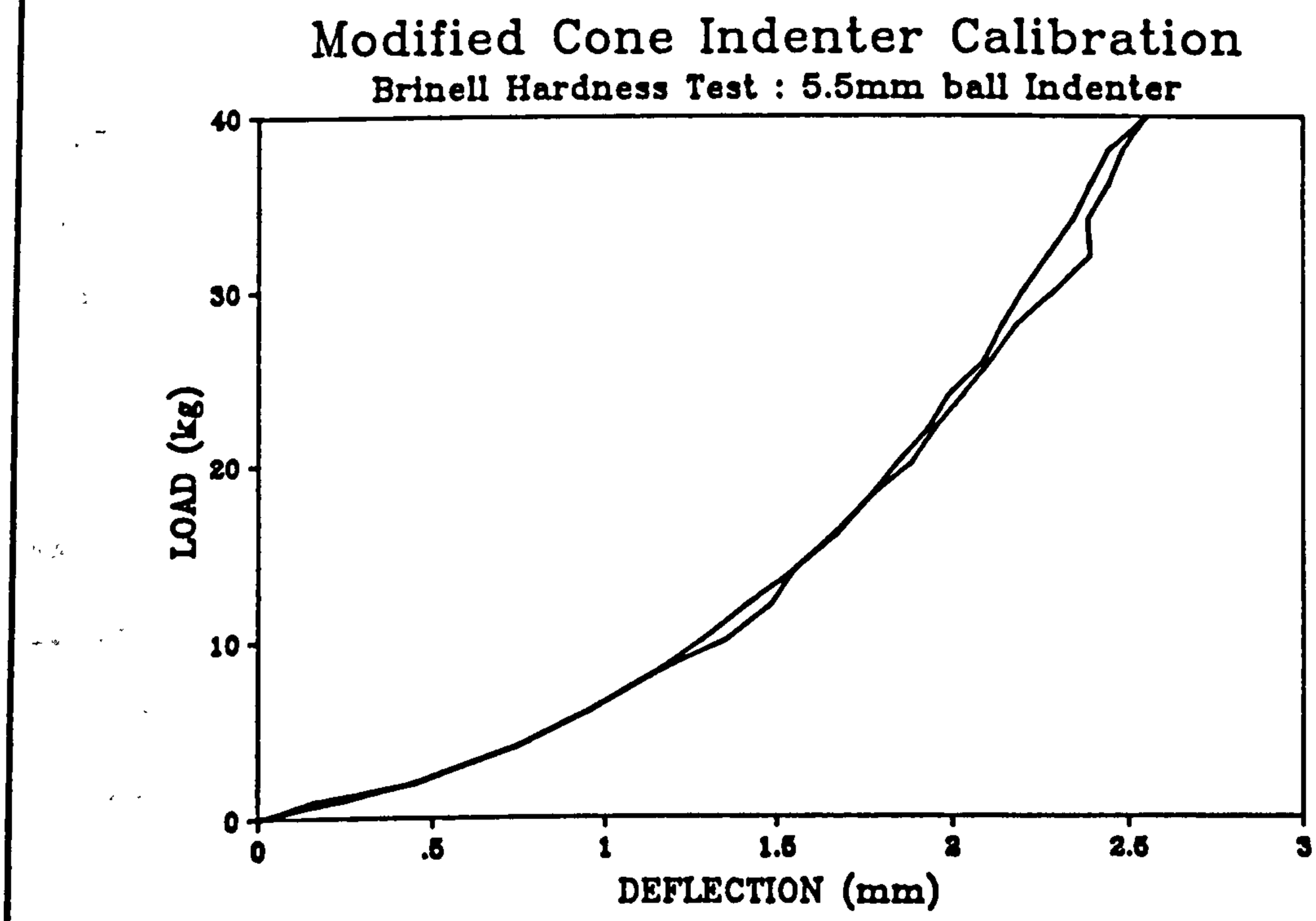

Figure 3.4 : Calibration Graph for Modified Cone Indenter

The unit was calibrated with respect to applied load in stages of 2 kg up to a maximum of 40 kg, the weights applied carefully to reduce the effect of shock loading. The results are presented graphically in Figure 3.4. It can be seen form the graph that the the measured deflection of the steel strip was not linear, the higher load producing a lower rate of change of deflection. This was considered to be due to the steel strip offering a greater resistance to bending at elevated loads. Slight hysteresis was also found to be present at higher loads.

3.2.3.2 Test Procedure

Based on experience gained with the instrument, the following test procedure was established. Sample preparation was minimal with the cut-off sections of the core plugs being used for testing. The only preparation required was to smooth the faces of rock disk with emery paper. It was found that confining the rock disk with a plastic cable tie prevented premature tensile failure when used in conjunction with a thin metal platten, the platten being placed between the sample and the steel strip. Accordingly, this technique was adopted throughout each test. To reduce the effect of surface irregularities, the hardness was determined from the difference in penetration between two load levels. The test procedure was as follows:

(1) The sample and platten were inserted into the device and the ball indenter brought into contact by rotation of the vernier. The dial gauge was zeroed at this point.

(2) The vernier was then slowly and evenly rotated until a reading of 1.28 mm (D_1) was indicated on the dial gauge. This corresponded to a load of 10 kg. The vernier reading (M_1) was noted.

(3) The vernier was gently rotated further until a reading of 2.20 mm (D_2) was indicated on the dial gauge. This corresponded to a load of 30 kg. The vernier reading was again noted (M_2)

(4) The depth of the resulting indentation was obtained from the following relationship:

$$\text{Depth} = (M_2 - M_1) - (D_2 - D_1) \quad .. \quad .. \quad .. \quad .. \quad (3.3)$$

Two further tests were generally performed on each sample, taking care not to place the indenter on the same spot twice. The average indentation depth was then obtained. The Brinell Hardness Number was then calculated from equation (3.2), with L = 20 kg and D = 5.5 mm.

3.2.3.3 Modified Oedometer

An oedometer is an device which is normally used to measure the consolidation of clay or soils over a period of time. The modification to this piece of apparatus consisted of replacing the existing loading arm with an alternative arm incorporating a threaded socket into which a steel ball indenter and holder was

fitted. Three holders incorporating respective ball diameters of 1.59 mm, 3.17 mm and 5.5 mm were made. The modified apparatus is illustrated in Figure 3.5. The standard oedometer dial gauge was replaced by a more accurate gauge reading to 0.002 mm. The loading beam of the oedometer increased the applied load to the sample by a factor of 10:1 (i.e. a weight of 1 kg applied on the pan was equivalent to 10 kg applied to the sample via the loading arm.)

3.2.3.4 Test Procedure

The Brinell hardness tests performed using the modified oedometer were conducted on one inch core plugs which had been prepared for mechanical property testing.

The prepared sample was confined with a plastic cable-tie to reduce the possibility of failure during the test. The sample was placed on the oedometer load plate and the ball indenter rested on the core surface. Care was required to ensure that the loading arm, core sample and dial gauge were in-line with respect to each other. A retaining load of 1 kg (10 kg_{app}, i.e. corresponding to an applied sample load of 10 kg) was placed on the pan and the dial gauge set to zero. This served to reduce the effect of surface irregularities. A 0.5 kg weight (5 kg_{app}) was then added to the pan and the dial gauge reading taken. The load was increased in increments of 0.5 kg (5 kg_{app}) up to a maximum of 4 kg (40 kg_{app}) and the indentation was read after each incremental increase in load.

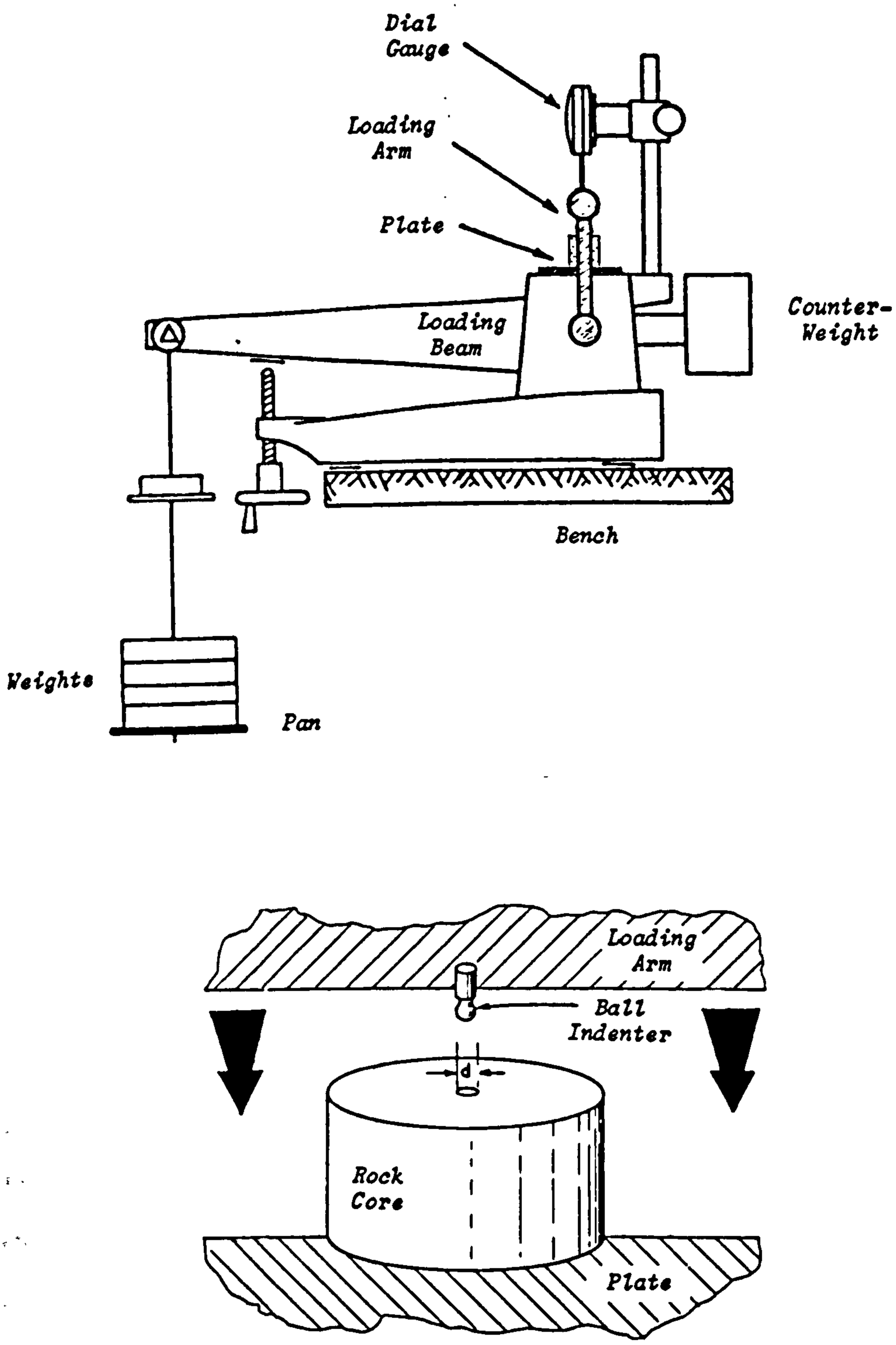

Figure 3.5 : Diagram of Modified Oedometer

In most cases, the penetration of the ball indenter under load into the core samples was not instantaneous. To minimise this source of error, several dial readings were recorded after a load was applied, and when it appeared the reading was constant, that reading was taken as the final depth of indentation.

Each sample was subjected to three indentation tests. The place at which the ball indenter rested was chosen at random; however, no tests were conducted at or near the edge of the core sample as this could result in sample failure. After each test the point of penetration was marked and no subsequent test was made in or adjacent to the marked point.

A 'correction-factor' test was then conducted to determine the deflection inherent in the apparatus without embedment for various loads. In this test, the ball indenter and holder were removed and substituted by an empty holder. The holder was then brought into contact with the load plate and the dial gauge set to zero. The deflection of the apparatus was then determined under the same compressive loads as for the Brinell test. This deflection was then subtracted from the total deflection obtained from the Brinell test to obtain the true depth to which the ball-point had penetrated the core sample. No correction was made for strain in the core sample as this was considered to be negligible.

The BHN for each load increment was calculated from equation (3.2), the average value obtained for each of the indentation tests was again averaged and was designated the Brinell hardness of the rock.

3.2.4 Comparison of Typical Results Obtained from each Instrument

A series of tests were performed on similar rock types to compare the hardness values obtained from the above apparatus. Two types of rock were tested: a red, coarse grained sandstone and a white, fine grained sandstone. Three samples of each rock type were tested on each instrument, three tests being performed on each sample. Both instruments were fitted with a 5.5 mm ball indenter.

3.2.4.1 Results Using Modified Cone Indenter

Red Sandstone : The test results for the three red sandstone samples are presented in Table 3.1. The average Brinell hardness number for this rock type was found to be 21.5.

White Sandstone : The Brinell hardness test results for this rock type are given in Table 3.2. From this table, it can be seen that the average Brinell hardness number using the modified cone indenter was 59.3.

3.2.4.2 Results Using Modified Oedometer

Red Sandstone : The results for the red sandstone are presented in Table 3.3. The average Brinell hardness number for this rock was measured to be 23.9.

	D2 (mm)	D1 (mm)	M2 (mm)	M1 (mm)	Depth (mm)	BHN
Test #1	2.20	1.28	3.174	2.205	.049	23.62
Test #2	2.20	1.28	3.410	2.435	.055	21.05
Test #3	2.20	1.28	3.398	2.420	.058	19.96
Test #4	2.20	1.28	3.278	2.305	.053	21.84
Test #5	2.20	1.28	3.325	2.355	.050	23.15
Test #6	2.20	1.28	3.375	2.400	.055	21.05
Test #7	2.20	1.28	3.535	2.565	.050	23.15
Test #8	2.20	1.28	3.315	2.335	.060	19.29
Test #9	2.20	1.28	3.311	2.335	.056	20.67
Red Sandstone : Average Brinell Hardness Number = 21.50						

Table 3.1 : Brinell Hardness Results for Red Sandstone Using a Modified NCB Cone Indenter

	D2 (mm)	D1 (mm)	M2 (mm)	M1 (mm)	Depth (mm)	BHN
Test #1	2.20	1.28	3.395	2.455	.020	57.87
Test #2	2.20	1.28	3.484	2.545	.019	60.92
Test #3	2.20	1.28	3.490	2.550	.020	57.87
Test #4	2.20	1.28	3.165	2.225	.020	57.87
Test #5	2.20	1.28	3.293	2.355	.018	64.31
Test #6	2.20	1.28	3.439	2.500	.019	60.92
Test #7	2.20	1.28	3.093	2.154	.019	60.92
Test #8	2.20	1.28	3.136	2.195	.021	55.12
Test #9	2.20	1.28	3.165	2.225	.020	57.87
White Sandstone : Average Brinell Hardness Number = 59.30						

Table 3.2 : Brinell Hardness Results for White Sandstone Using a Modified NCB Cone Indenter

	Load (kg)	Depth of Indentation (mm) Test 1	Test 2	Test 3	BHN
SAMPLE #1	5	.007	.009	.013	30.70
	10	.029	.035	.025	19.41
	15	.043	.043	.038	21.09
	20	.050	.052	.045	23.69
	25	.058	.061	.056	24.83
	30	.069	.072	.075	24.07
SAMPLE #2	5	.008	.010	.011	29.94
	10	.030	.029	.027	20.19
	15	.041	.043	.040	21.00
	20	.049	.052	.048	23.32
	25	.057	.062	.056	24.81
	30	.070	.073	.074	24.00
SAMPLE #3	5	.009	.010	.012	28.00
	10	.028	.031	.023	21:17
	15	.042	.044	.038	21.09
	20	.052	.053	.045	23.15
	25	.060	.060	.057	24.52
	30	.071	.072	.069	24.55
Average Brinell Hardness Number					23.86

Table 3.3 : Brinell Hardness Results for Red Sandstone Using a Modified Oedometer

	Load (kg)	Depth of Indentation (mm) Test 1	Test 2	Test 3	BHN
SAMPLE #1	5	.004	.004	.004	71.64
	10	.009	.009	.009	62.69
	15	.013	.013	.013	68.39
	20	.018	.017	.017	65.41
	25	.021	.020	.020	71.64
	30	.032	.024	.025	63.57
SAMPLE #2	5	.005	.004	.005	62.01
	10	.010	.010	.009	59.87
	15	.014	.014	.013	63.52
	20	.019	.019	.018	62.01
	25	.023	.022	.022	64.78
	30	.027	.026	.025	66.78
SAMPLE #3	5	.004	.004	.004	72.34
	10	.009	.008	.010	64.31
	15	.013	.014	.014	63.52
	20	.019	.018	.019	62.01
	25	.023	.023	.024	62.01
	30	.028	.027	.028	62.76
Average Brinell Hardness Number					64.96

Table 3.4 : Brinell Hardness Results for White Sandstone Using a Modified Oedometer

White Sandstone : The results for the white sandstone are given in Table 3.4 where an average Brinell hardness number of 65 was indicated.

3.2.4.3 Discussion of Results and Conclusions

From the results presented above, and from numerous unpublished tests, it was apparent that the modified cone indenter provided a lower Brinell hardness number than the modified oedometer, i.e. for the same sample and applied load, the penetration depth measured by the modified cone indenter was greater than the oedometer. The size of sample used in the modified cone indenter could be a contributory factor as a small rock 'disk' as used in this test would generally be weaker than a larger sample and therefore be more susceptible to indentation. The main source of error, however, was considered to be in the reading of the vernier gauge. In the standard form, the vernier read to 0.025 mm. The addition of a secondary scale provided an accuracy of 0.005 mm; however, reading to a greater accuracy required visual estimation. Accordingly, the modified cone indenter required a degree of operator experience to obtain satisfactory results. This effect was more apparent with harder samples where the measurement of penetration depth was more critical.

A source of error with the modified oedometer test was in the application of additional weights to the pan. If care was not taken during this operation, the ball indenter could be 'shock loaded' which would have the effect of prematurely increasing the depth of indentation and would therefore provide unrealistic results.

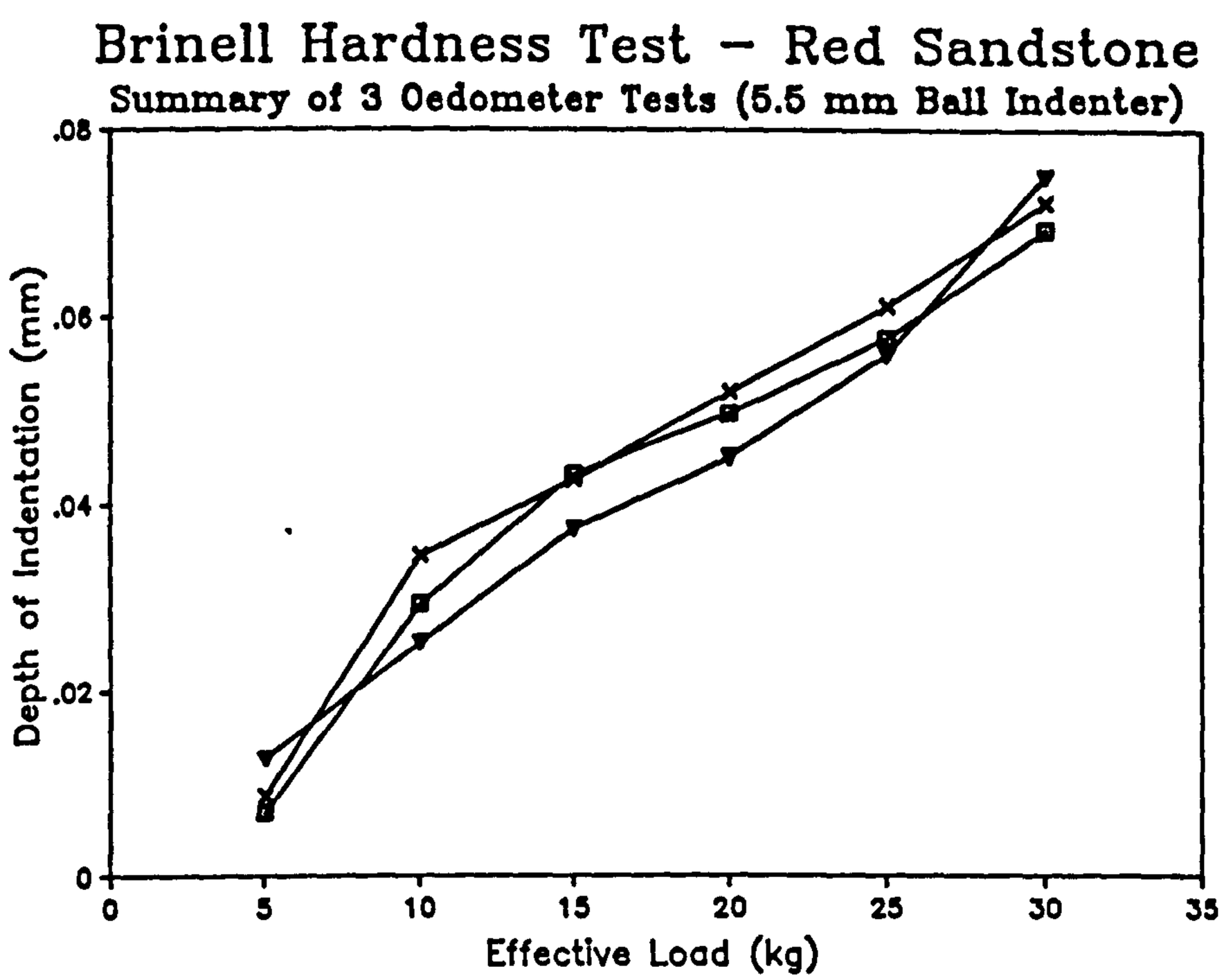

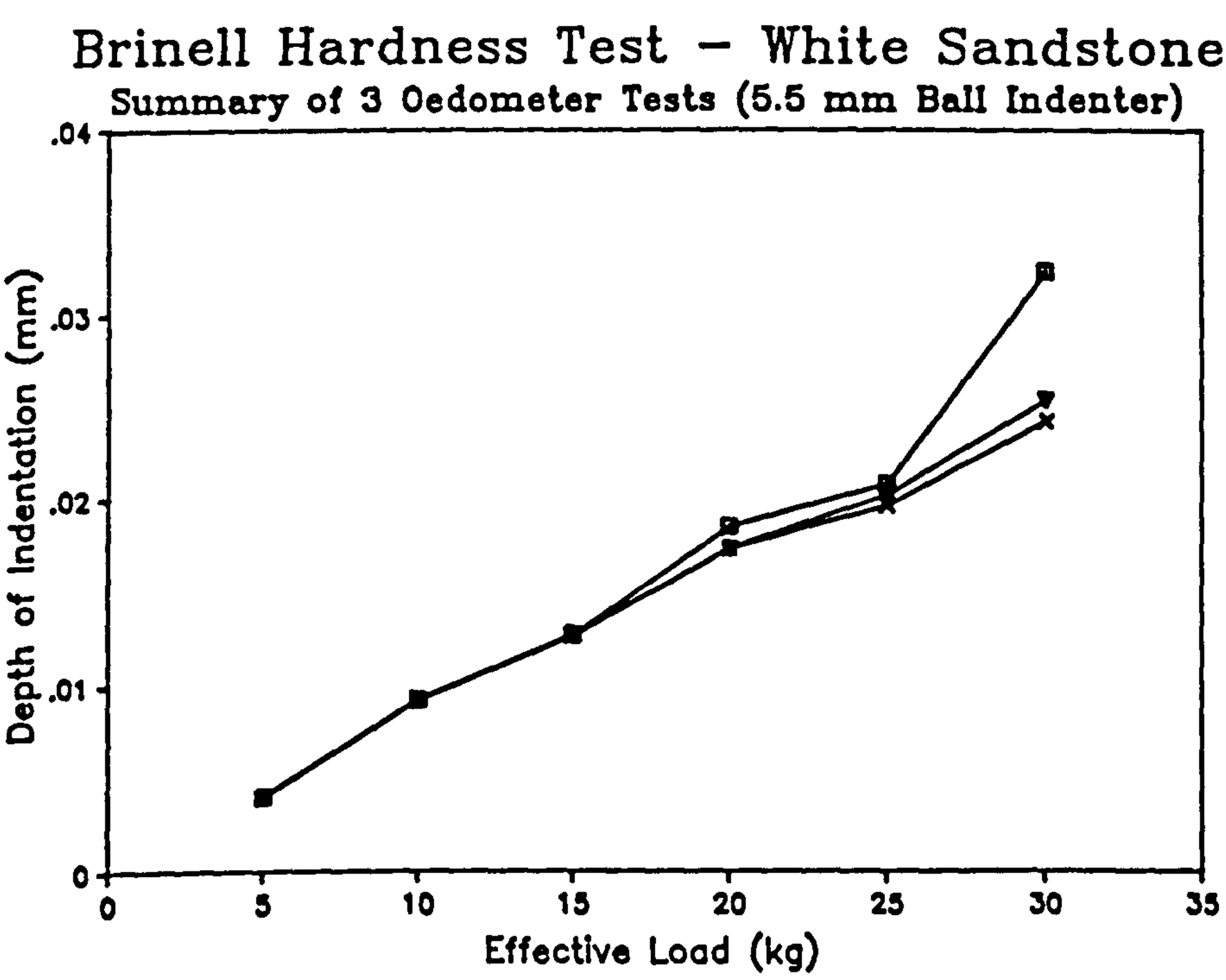

Figure 3.6 : Repeatability of Brinell Hardness Results Using a Modified Oedometer

From the above results, it can be concluded that the modified oedometer provided more repeatable results than the modified cone indenter. In general, however, the repeatability of the test measurements depended on the homogeneity of the sample which was tested. Figure 3.6 illustrates a set of typical modified oedometer test results for both the white and red sandstone samples. It can be seen that test repeatability was superior with the fine grained white sandstone than with the coarser grained red sandstone.

Although the modified oedometer provides more repeatable results, the modified cone indenter is nevertheless a useful instrument for determining Brinell hardness as it is portable and easy to use, the test samples need little preparation and the results are comparable with the modified oedometer.

3.3 DETERMINATION OF MECHANICAL PROPERTIES

3.3.1 Introduction

Sandstone core samples from two North Sea wells were available for analysis, these being from sectors 47/14 and 11/30 respectively. Accordingly, the following tests were conducted :-

(a) Density

(b) P-Wave Velocity

(c) Multi-Failure-State Triaxial tests on strain gauged samples, giving a Mohr's envelope, Static Young's Modulus

and Poisson's Ratio at a range of effective confining stress values.

(d) Brinell Hardness

3.3.2 Sample Preparation

The mechanical property tests described in this section were performed using one inch diameter plugs which were obtained from the industry standard 4 inch diameter core. During the laboratory coring operations water was used as a lubricant for sandstone samples while an air-flush was used for the shale samples. The ends of the core plugs were trimmed with a diamond saw mounted on a surface grinder before being ground smooth on a lapping machine. A specimen length to diameter ratio of 2.5:1 was used throughout while the tolerances recommended by Hawkes and Mellor [88] and by the International Society of Rock Mechanics [89] were closely adhered to (Table 3.5). The controls on specimen geometry were intended to ensure that under the action of the testing machine, a predictable, uniform stress was induced in the central section of the specimen, remote from the end effects at the plattens.

3.3.3 Density

Rock density was determined from measurements of test specimen volume and weight. The length and diameter of the cylindrical specimens were measured using a digital vernier gauge reading to 0.01 mm, enabling their volume to be determined. The specimens, air dried for 7 days after trimming, were also weighed on a precision

balance reading to 0.001 g. Specimen density was then determined by dividing weight by volume.

3.3.4 P-Wave Velocity

P-Wave velocity was determined from the time taken for P-wave transmission through the specimen. The equipment shown schematically in Figure 3.7 was utilised [90], the transmission time being interpreted from the oscilloscope trace shift of the received P-wave caused by introducing the specimen between the transmitting and receiving transducers.

3.3.5 Multi-Failure-State Triaxial Tests (Specimen Strain Gauged)

These tests were conducted using a standard Hoek Triaxial Cell rated to 10000 psi (69000 kPa), confining pressure being developed with a hand pump and the axial load being developed by a servo-controlled hydraulic testing machine.

Each specimen was strain gauged with diametrically opposed pairs of active vertical and horizontal strain gauges. External dummy gauges on a sandstone core were used to complete the the bridges, strain being read on digital meters via strain gauge amplifiers. Connections to the active gauges were made with strips of brass rather than insulated leads as normally used. This system worked well and overcame some of the difficulties experienced with premature lead failure, enabling strains to be monitored in some cases up to 6500 psi (45000 kPa).

Parameter	Specification or Tolerance	
	Hawkes and Mellor	International Society of Rock Mechanics
Length/Diameter ratio l/d	2.0 < l/d < 4	
Flatness of ends	flat to within 0.0025 mm to 0.0125 mm depending on strength and modulus of rock	flat to within 0.02 mm
Parallelness of ends	to within 0.001 x diameter	-
Squareness of ends	to within 0.001 radians	to within 0.001 radians
Generators of Clyndrical Surfaces	straight to within 0.025 mm	straight to within 0.3 mm
Diameter	should not vary by more than ± 0.025 mm over length of specimen	specimen should be smooth and free from irregularities

Table 3.5 : Recommendations for Specimen Geometry [88,89]

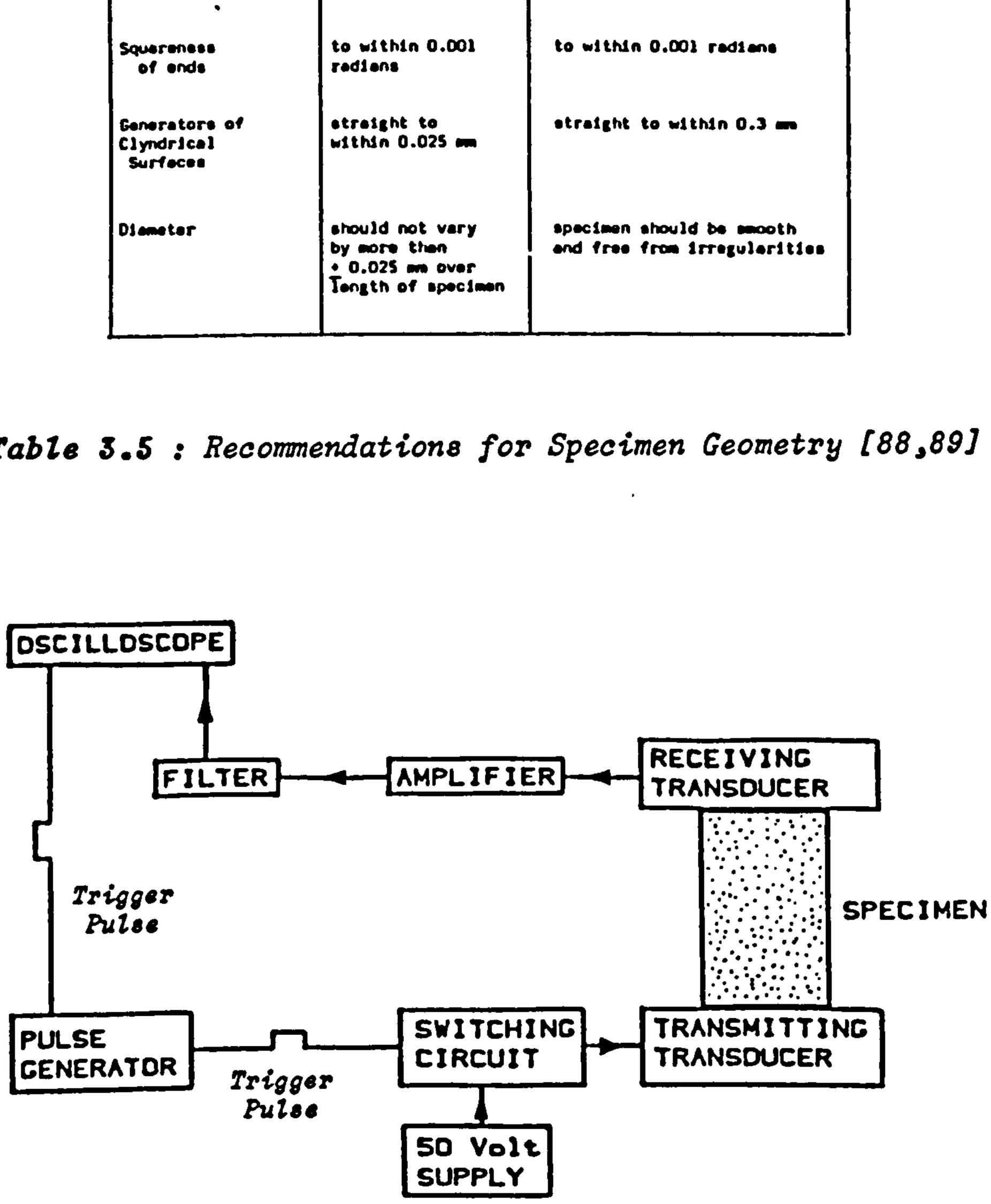

Figure 3.7 : Schematic Diagram of Equipment Used to Measure P-Wave Velocity [90]

3.3.5.1 Specimen Testing Procedure

A confining pressure was applied and held constant, while the axial load was increased, the resulting axial strain in the specimen being detected by a linear displacement transducer measuring closure between the loading plattens of the testing machine. The output of the transducer was fed to the X axis of an XY recorder, while the axial load applied to the specimen was fed to the Y axis. Strain softening caused flattening of the curve traced. This indicated the onset of failure, and the axial load was noted. The confining pressure was then increased and the axial load increased again until strain softening was detected. Repetition of this procedure up to a confining pressure of 5000 psi (34500 kPa) enabled several failure states to be obtained for each specimen, as shown in Figures 3.8(a) and 3.8(b).

The procedure was usually continued with the confining pressure being reduced in increments to 2500 psi (17250 kPa), along with a comparable decrease in axial load. The specimen axial load was then increased to cause failure and to produce a residual strength value at a confining pressure of 5000 psi (34500 kPa).

3.3.5.2 Internal Angle of Friction and Projected Cohesion

The multi-failure-state strength data was analysed graphically by the computer program MC-PLOT which was purposely written by the author. The input to the program consisted of the peak strength and

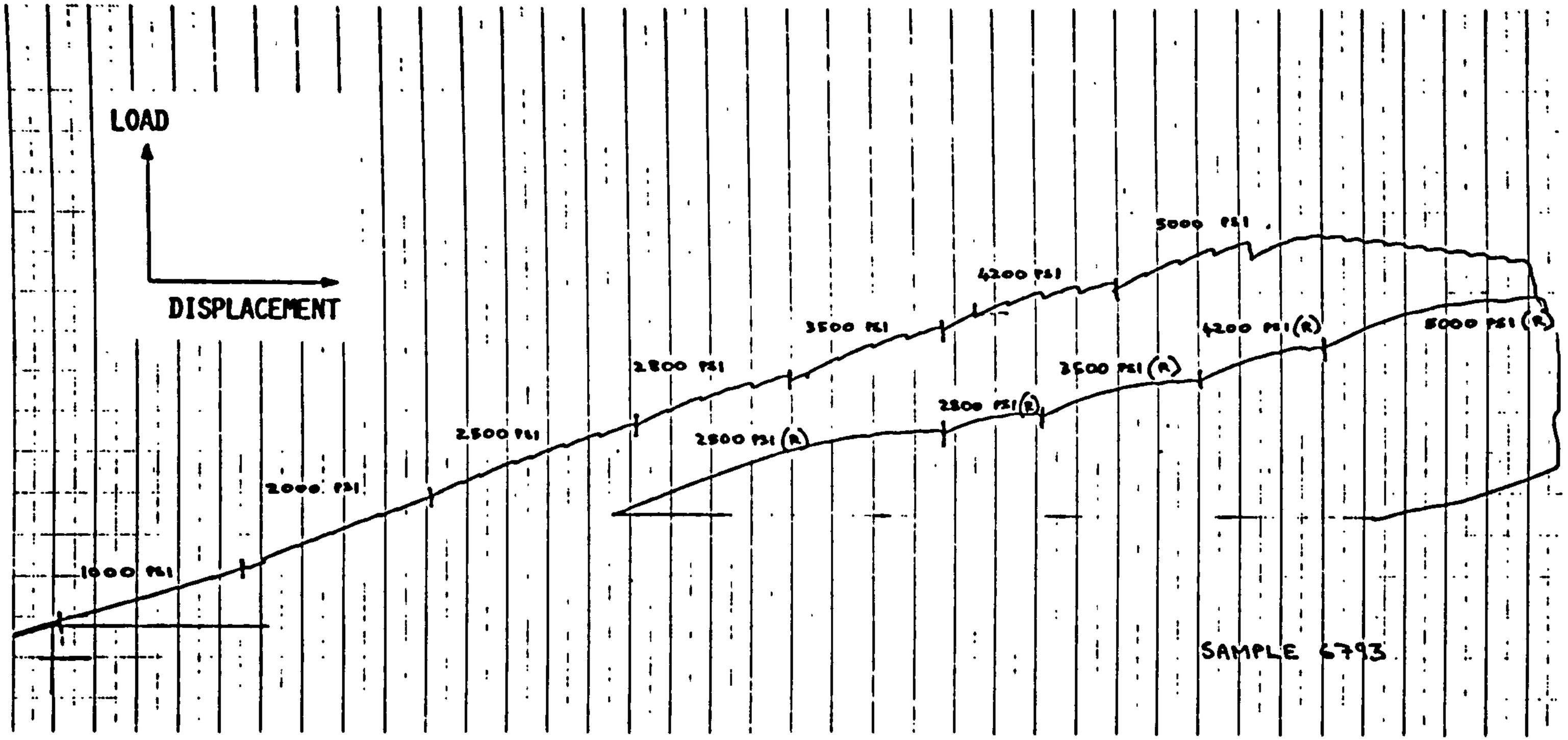

Figure 3.8(a) : Graphical Analysis of Multi-Failure Triaxial Results

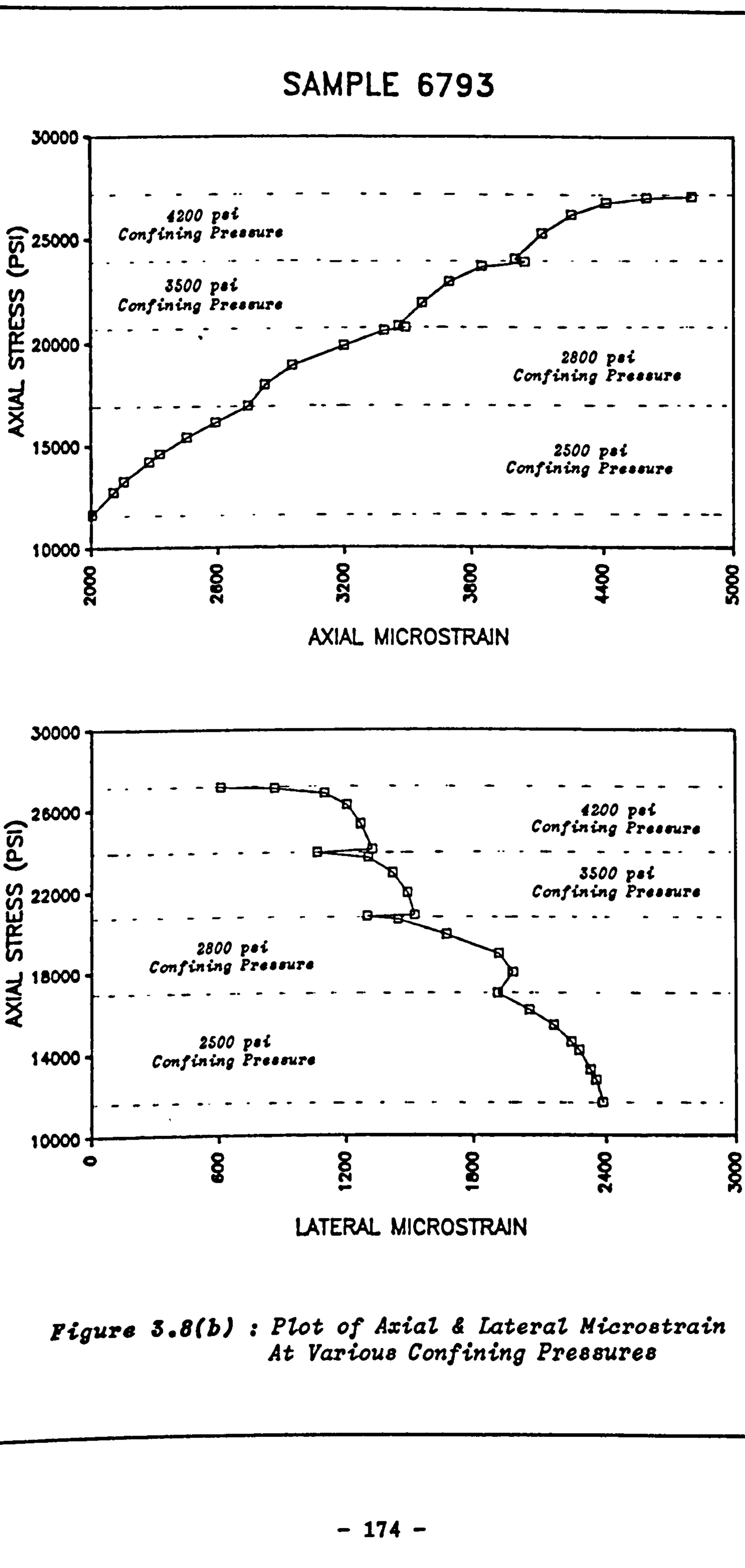

Figure 3.8(b) : Plot of Axial & Lateral Microstrain At Various Confining Pressures

confining pressure values for the various failure states which were obtained directly from the XY plot. A failure envelope was then constructed by plotting a series of Mohr's Circles. A typical MC-PLOT output is presented in Figure 3.9. The angle of internal friction was measured directly from computer plot while the apparent cohesion was obtained from the intersection of the failure envelope with the shear strength axis.

3.3.5.3 Triaxial Stress Factor

The triaxial stress factor is possibly one of the most important parameters in assessing the behaviour of soft rocks around an excavation [91], it is defined by the following equation:

$$\sigma_1 = \sigma_0 + K\sigma_3 \qquad .. \quad .. \quad .. \quad .. \quad .. \quad (3.4)$$

where σ_0 = Unconfined Compressive Strength

σ_1 = Failure Load

σ_3 = Confining Pressure

K = Triaxial Stress Factor

and is related to the angle of internal friction (α) by the expression:

$$K = \frac{1 + \text{Sin } \alpha}{1 - \text{Sin } \alpha} \qquad .. \quad .. \quad .. \quad .. \quad .. \quad (3.5)$$

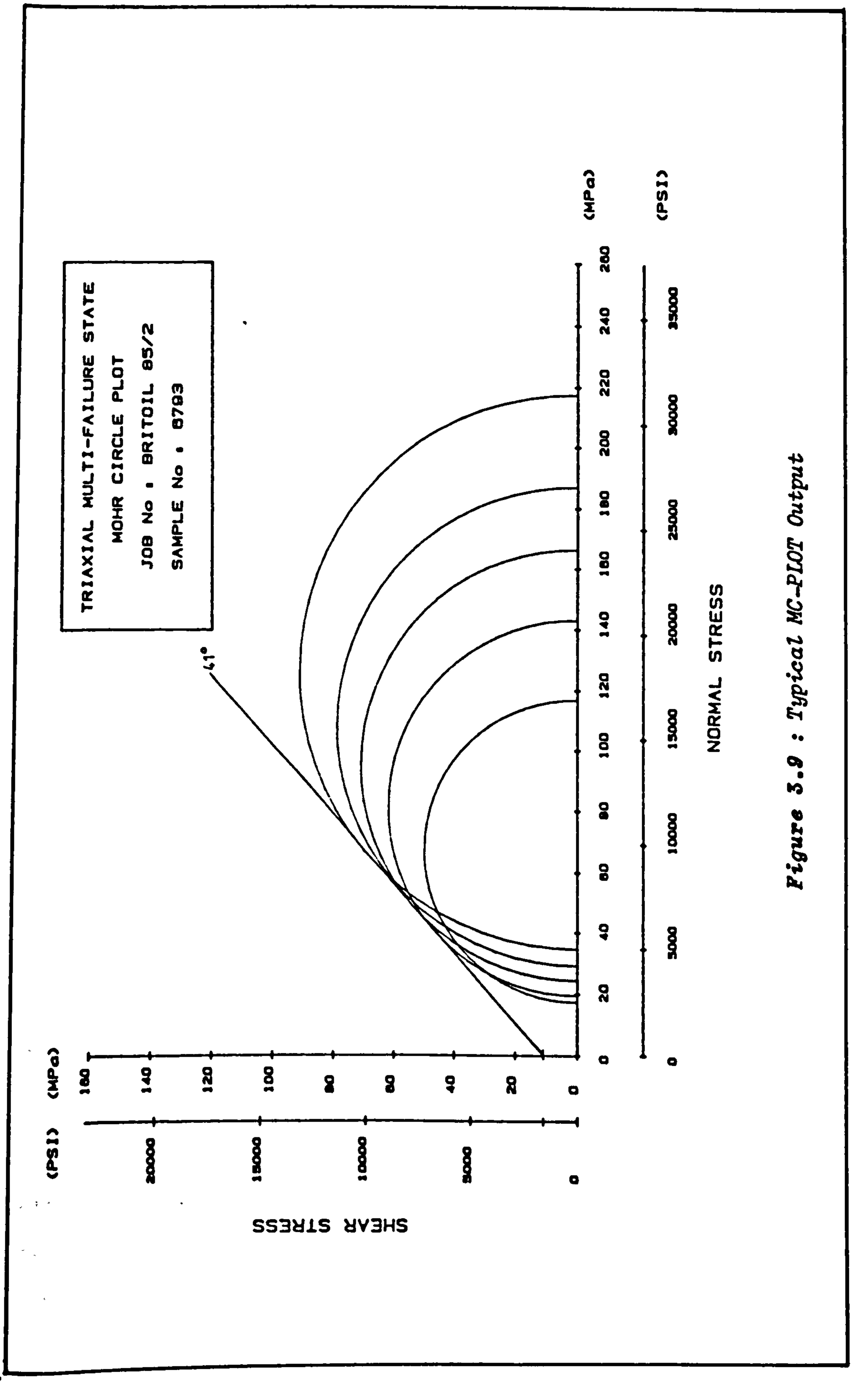

Figure 5.9 : Typical MC-PLOT Output

The triaxial stress factor for each sample was calculated from the above equation using the angles of internal friction determined from Section 3.3.5.2.

3.3.5.4 Uniaxial Compressive Strength

Due to insufficient core samples available for testing, values of Uniaxial Compressive Strength were derived from the Mohr-Coulomb relationship [41], viz.

$$C_0 = S_0 \frac{2 \cos \alpha}{1 - \sin \alpha} \qquad .. \quad .. \quad .. \quad .. \quad .. \quad (3.6)$$

where S_0 = The Cohesion of the rock.

C_0 = Uniaxial Compressive Strength

3.3.5.5 Young's Modulus and Poissons Ratio.

Specimen strain data obtained in conjunction with the multi-failure triaxial tests was processed using a spreadsheet program, the following theory being used to determine Static Young's Modulus and Poisson's Ratio.

Consider the change in strain from ξ_{z_1} to ξ_{z_2} that occurs in the Z direction (i.e. along the axis of the test specimen) due to a change in stress from σ_{z_1} to σ_{z_2}, the confining stress $\sigma_x = \sigma_y$ being held constant.

Given that,

$$\xi_{z_1} = \frac{1}{E} (\sigma_{z_1} - \gamma(\sigma_x + \sigma_y)) \quad .. \quad .. \quad .. \quad .. \quad (3.7)$$

$$= \frac{1}{E} (\sigma_{z_1} - 2\gamma\sigma_x) \quad .. \quad .. \quad .. \quad .. \quad .. \quad (3.8)$$

where E = Young's Modulus

γ = Poisson's Ratio

and that similarly,

$$\xi_{z_2} = \frac{1}{E} (\sigma_{z_2} - 2\gamma\sigma_x) \quad .. \quad .. \quad .. \quad .. \quad .. \quad (3.9)$$

then the change in strain

$$\xi_{z_2} - \xi_{z_1} = \frac{1}{E} (\sigma_{z_2} - 2\gamma\sigma_x) - \frac{1}{E} (\sigma_{z_1} - 2\gamma\sigma_x) \quad .. \quad (3.10)$$

i.e

$$E = \frac{\sigma_{z_2} - \sigma_{z_1}}{\xi_{z_2} - \xi_{z_1}} \quad .. \quad .. \quad .. \quad .. \quad .. \quad (3.11)$$

Now consider the change in strain in the X direction due to a change in σ_z, $\sigma_x = \sigma_y$ = constant.

Given that

$$\xi_{x_1} = \frac{1}{E} (\sigma_x - \gamma(\sigma_y + \sigma_{z_1})) \quad .. \quad .. \quad .. \quad .. \quad (3.12)$$

and that

$$\xi_{x_2} = \frac{1}{E} (\sigma_x - \gamma(\sigma_y + \sigma_{z_2})) \quad .. \quad .. \quad .. \quad .. \quad (3.13)$$

then the change in strain

$$\xi_{x_2} - \xi_{x_1} = \frac{\gamma}{E} (\sigma_{z_1} - \sigma_{z_2}) \qquad .. \quad .. \quad .. \quad .. \quad (3.14)$$

i.e.

$$\gamma = \frac{E (\xi_{x_2} - \xi_{x_1})}{\sigma_{z_1} - \sigma_{z_2}} \qquad .. \quad .. \quad .. \quad .. \quad .. \quad (3.15)$$

Plotting graphs for ξ_x for increasing σ_z with $\sigma_x = \sigma_y$ = constant as shown in Figure 3.10 enabled the linearity of the stress-strain relationships assumed in the above equations to be confirmed, and equations (3.11) and (3.15) to be applied to the determination of Static Young's Modulus and Poisson's Ratio.

3.3.5.6 Brinell Hardness

As the modified oedometer was not fully commissioned when this testing programme was conducted, a modified NCB cone indenter fitted with a 5.5 mm ball indenter was used to determine Brinell hardness. The experimental procedure outlined in Section 3.2.3.2 was followed. The off-cuts of the core plugs were used to provide disks for testing. Due to the short length of the core plugs, however, four of the nine samples from well 47/14a-8 were not tested, as top priority was given to obtaining the recommended triaxial specimen length.

3.4 Mechanical Property Results

The results for the above tests are presented in Tables 3.6 and 3.7 for wells 47/14a-8 and 11/30a-A6 respectively.

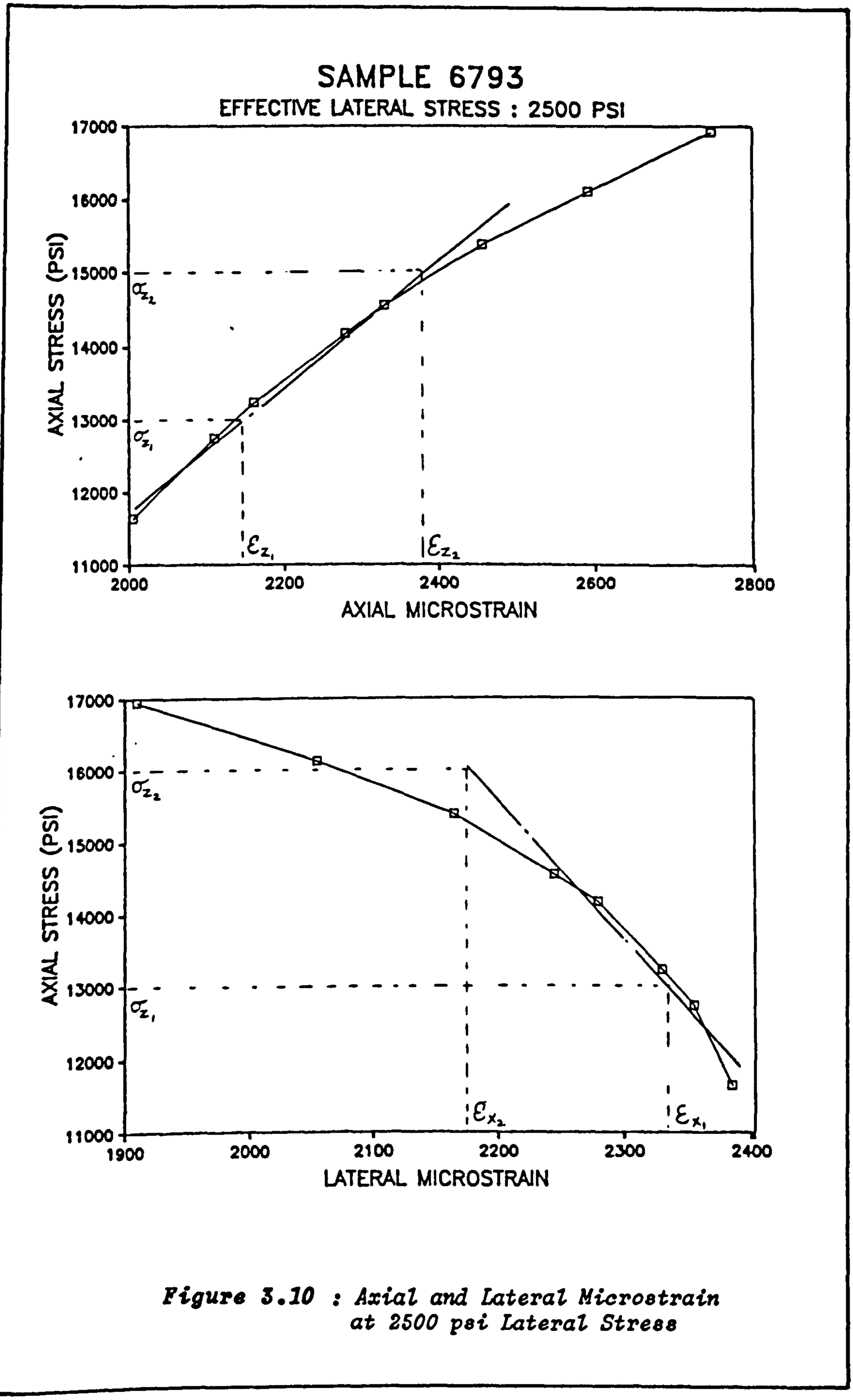

***Figure 3.10** : Axial and Lateral Microstrain at 2500 psi Lateral Stress*

Sample Depth (ft)	Sample Density (lb/ft^3)	P-Wave Velocity (ft/s)	Young's Modulus (psi)	Poisson's Ratio	Internal Angle of Friction	Triaxial Stress Factor	Apparent Cohesion (psi)	Uni Comp Strength (psi)	Brinell Hardness (kg/mm^2)
9078	134.5	5317	3.4e6	.43	27.0	2.66	1233	4024	4.1
9090	133.5	4572	2.1e6	.26	29.5	2.94	1305	4475	4.6
9103	127.6	2359	3.1e6	.49	19.5	2.00	290	821	1.5
9111	132.2	4837	3.1e6	.29	25.0	2.46	1450	4552	7.9
9117	143.8	4676	4.3e6	.47	28.0	2.77	3048	10145	
9121	150.9	8080	5.4e6	.49	32.5	3.32	2393	8724	8.9
9133	145.6	4550	4.8e6	.15	30.0	3.00	2248	7787	
9137	142.3	5353	3.7e6	.29	35.0	3.69	1015	3900	
9142	141.4	5036	4.1e6	.31	31.0	3.12	1523	5384	

Table 3.6 : Mechanical Property Test Results - Well 47/14a-8

Sample Depth (ft)	Sample Density (lb/ft^3)	P-Wave Velocity (ft/s)	Young's Modulus (psi)	Poisson's Ratio	Internal Angle of Friction	Triaxial Stress Factor	Apparent Cohesion (psi)	Uni Comp Strength (psi)	Brinell Hardness (kg/mm^2)
6777	153.8	5717	6.2e6	.25	22.0	2.20	2590	7680	23
6789	145.1	5193	7.5e6	.49	43.0	5.29	1657	7622	11
6793	143.4	4706	7.7e6	.37	41.0	4.81	1554	6820	24
6796	142.3	4399	4.1e6	.31	40.0	4.60	1657	7107	7
6820	142.2	4453	5.5e6	.38	36.0	3.85	2072	8133	12
6835	142.9	4827	9.1e6	.39	38.0	4.20	3940	16156	27
6842	136.4	3757	6.2e6	.33	37.0	4.02	1657	6647	17
6845	145.5	3797	5.7e6	.29	38.0	4.20	2279	9345	12
6856	138.8	4760	6.1e6	.32	34.0	3.54	3522	13248	17

Table 3.7 : Mechanical Property Test Results - Well 11/30a-A6

3.4.1 Discussion of Results : Well 47/14a-8

The density of the sandstones tested ranged from 126.6 lb/ft³ to 150.9 lb/ft³, a variation of 15%. This small variation together with the similarity in grain size of the specimens tested and depth of origin (9078 ft - 9142 ft) suggested from previous work that properties of all specimens should be similar [92]. Examination of all test results suggests this to be broadly true. P-wave velocity depends on rock type, porosity, degree of consolidation and the fluid in the pore spaces. Density has been taken as an indication of porosity, the other parameters being assumed constant.

A plot of P-wave velocity against density is shown in Figure 3.11. There appears to be a logical trend, P-wave velocity increasing with density. Sample density was also plotted against apparent cohesion (Figure 3.12) and general trend was apparent.

The relationship between P-wave velocity and Brinell hardness is illustrated in Figure 3.13 and a logical trend is evident, P-wave velocity increasing with density. This suggested that a relationship should exist between Brinell hardness and apparent cohesion; however, no such correlation was found. There was also little correlation between Brinell hardness and sample density. This may be in some part due to the reduced number of Brinell hardness results obtained. A plot of Young's Modulus against Brinell hardness is shown in Figure 3.14. From an examination of this graph it was evident that a greater number of Brinell hardness values would be

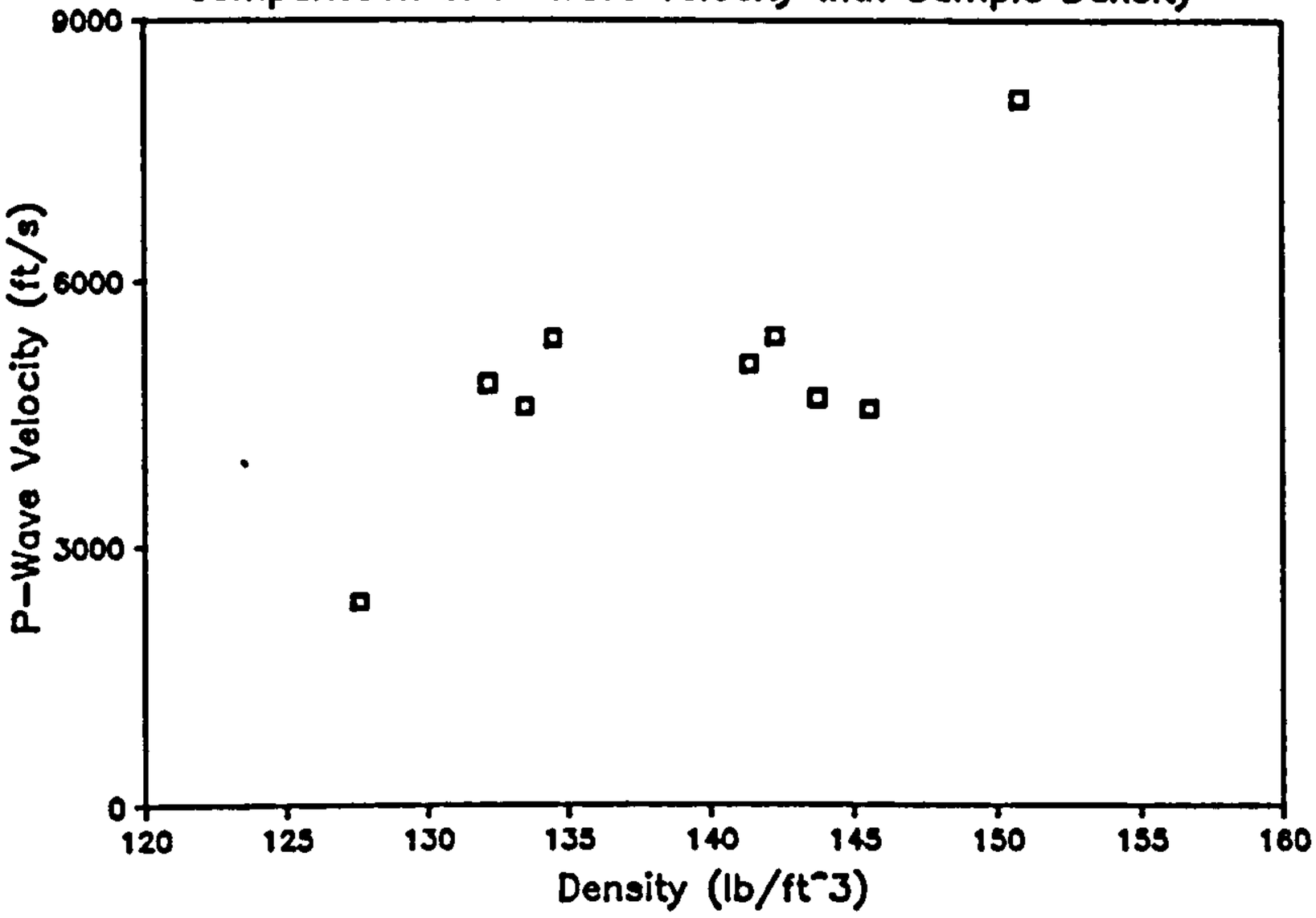

Figure 3.11

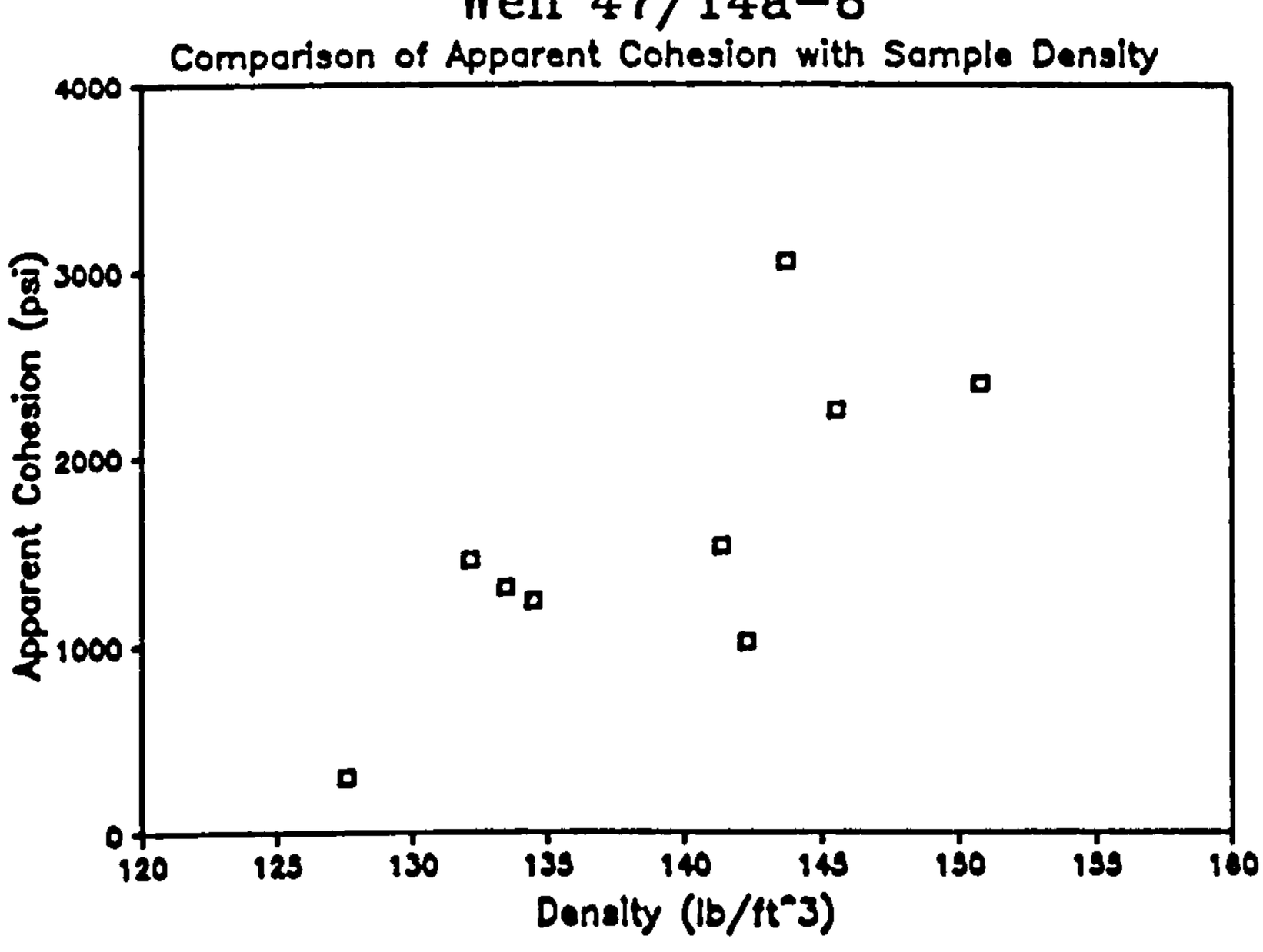

Figure 3.12

Figure 3.13

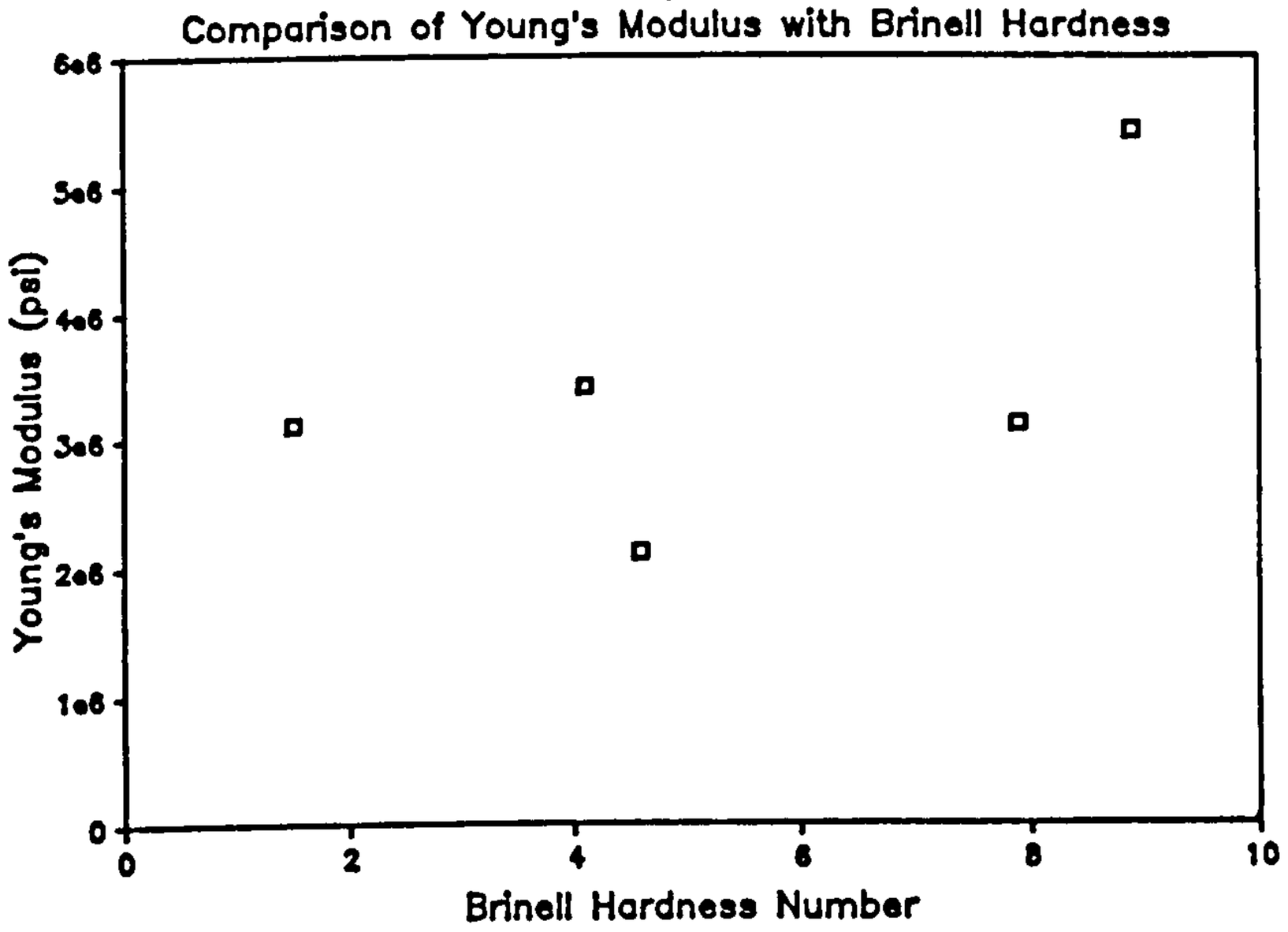

Figure 3.14

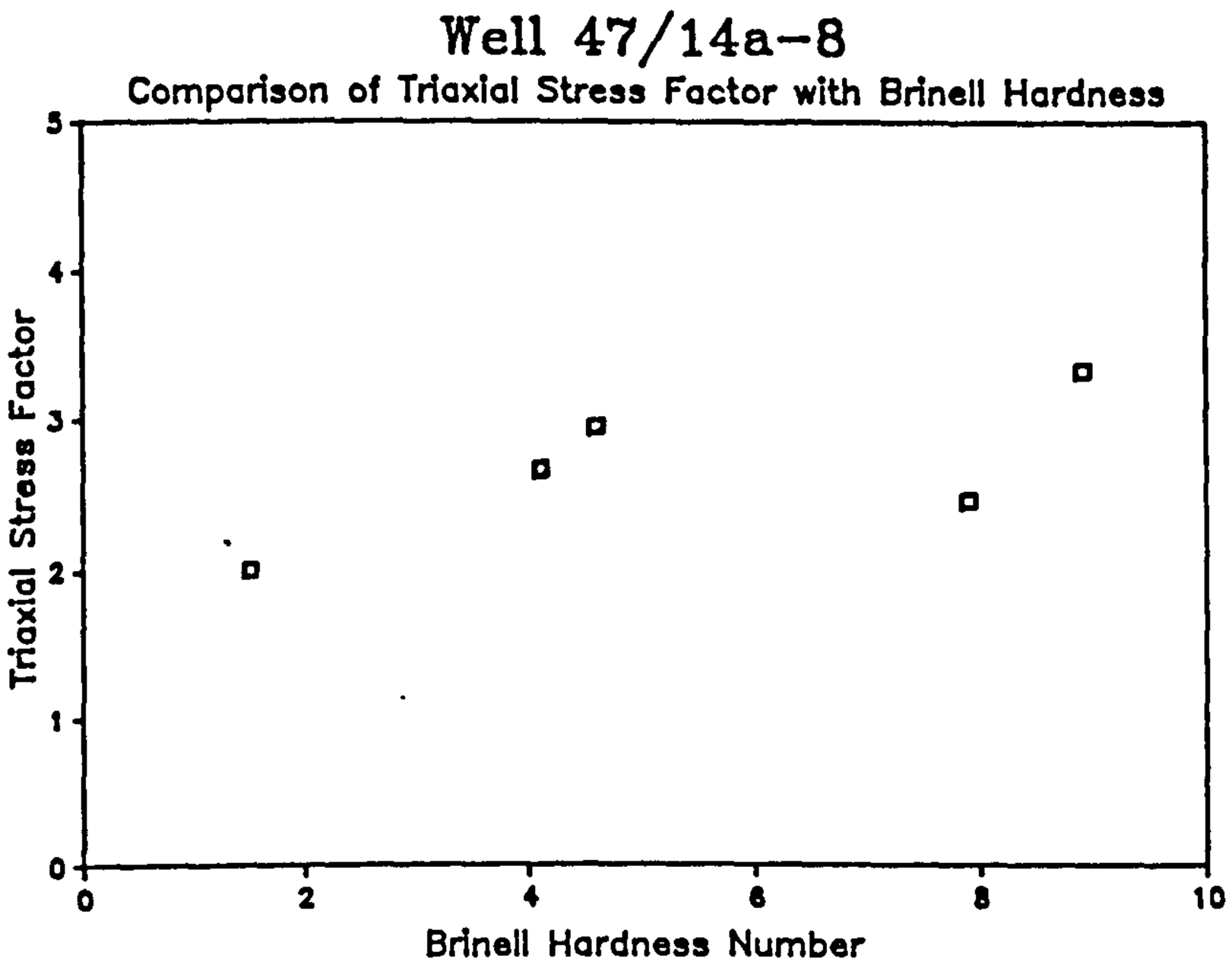

Figure 3.15

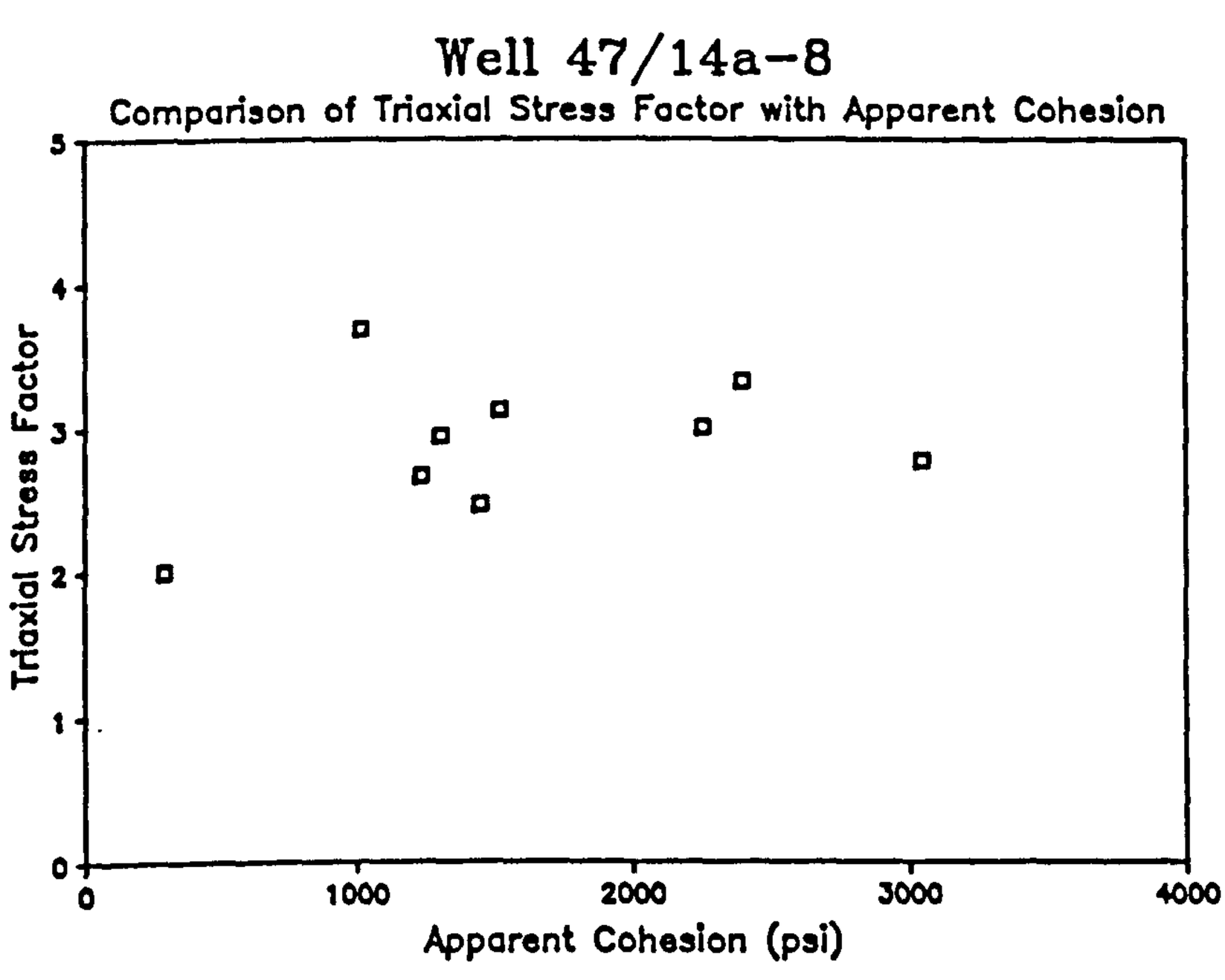

Figure 3.16

required before a relationship could be shown.

A plot of Brinell hardess against the 'triaxial stress factor', as shown in Figure 3.15, suggested the existence of a relationship. The correlation between the triaxial stress factor and apparent cohesion, however, was less conclusive (Figure 3.16).

In general, the values of Young's Modulus and angle of internal friction appeared to be reasonable. There was no apparent correlation between any of these properties with themselves or sample density.

3.4.2 Discussion of Results : Well 11/30a-A6

The density of the rock samples tested ranged from 136.4 lb/ft^3 to 153.8 lb/ft^3, a variation of 12%. In general, sample density increased with clay content. The relationship between P-wave velocity and sample density is presented in Figure 3.17 and a logical trend is apparent. It can be seen from Figure 3.18, that in this case, no correlation between sample density and apparent cohesion was evident.

There appears to be little relationship between P-wave velocity and Brinell hardness, as evident in Figure 3.19. A plot of Brinell hardness against Young's Modulus (Figure 3.20) indicated a definite relationship, the modulus increasing linearly with Brinell hardness. Two samples exhibiting a high clay content were found to deviate from this trend.

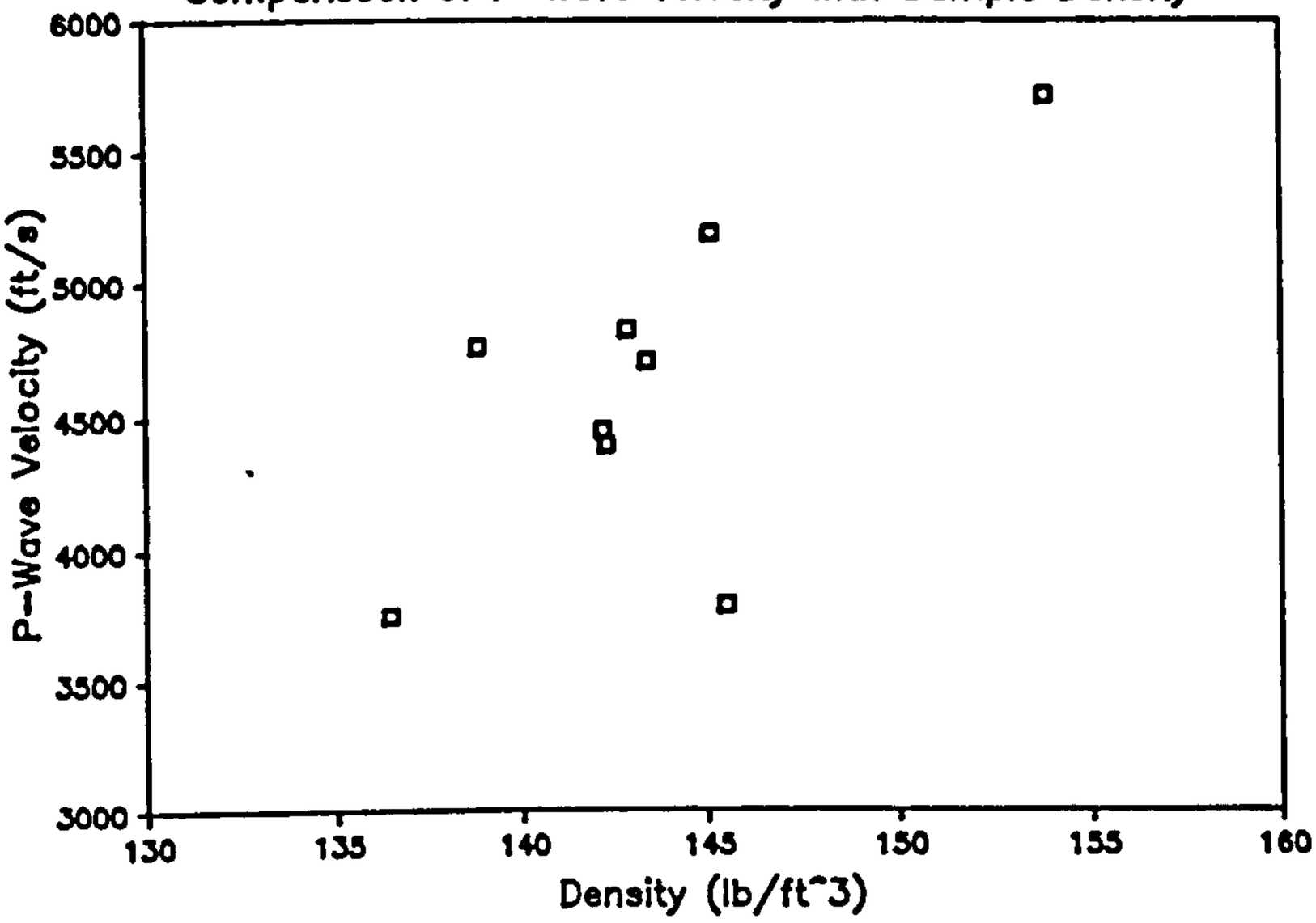

Figure 3.17

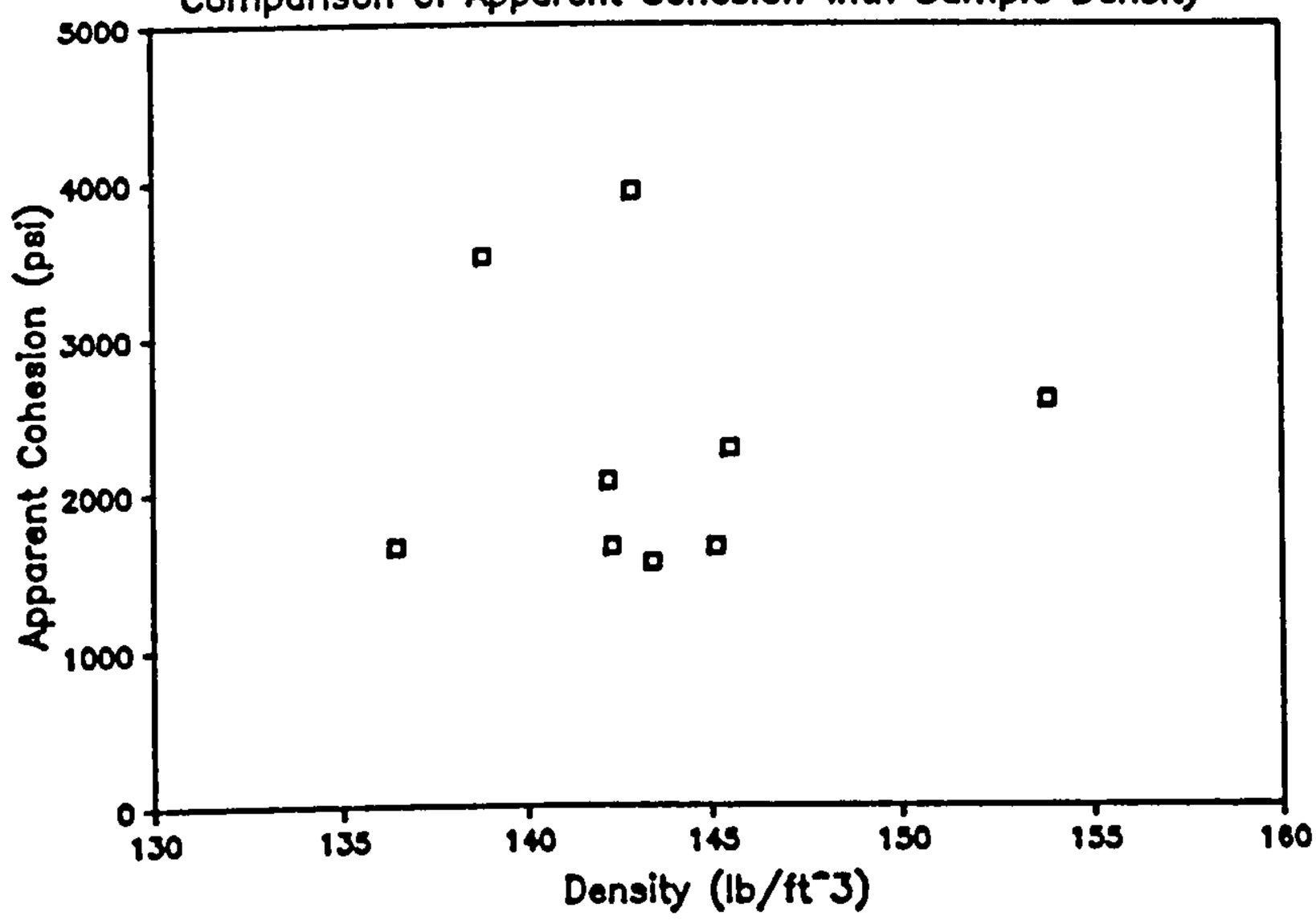

Figure 3.18

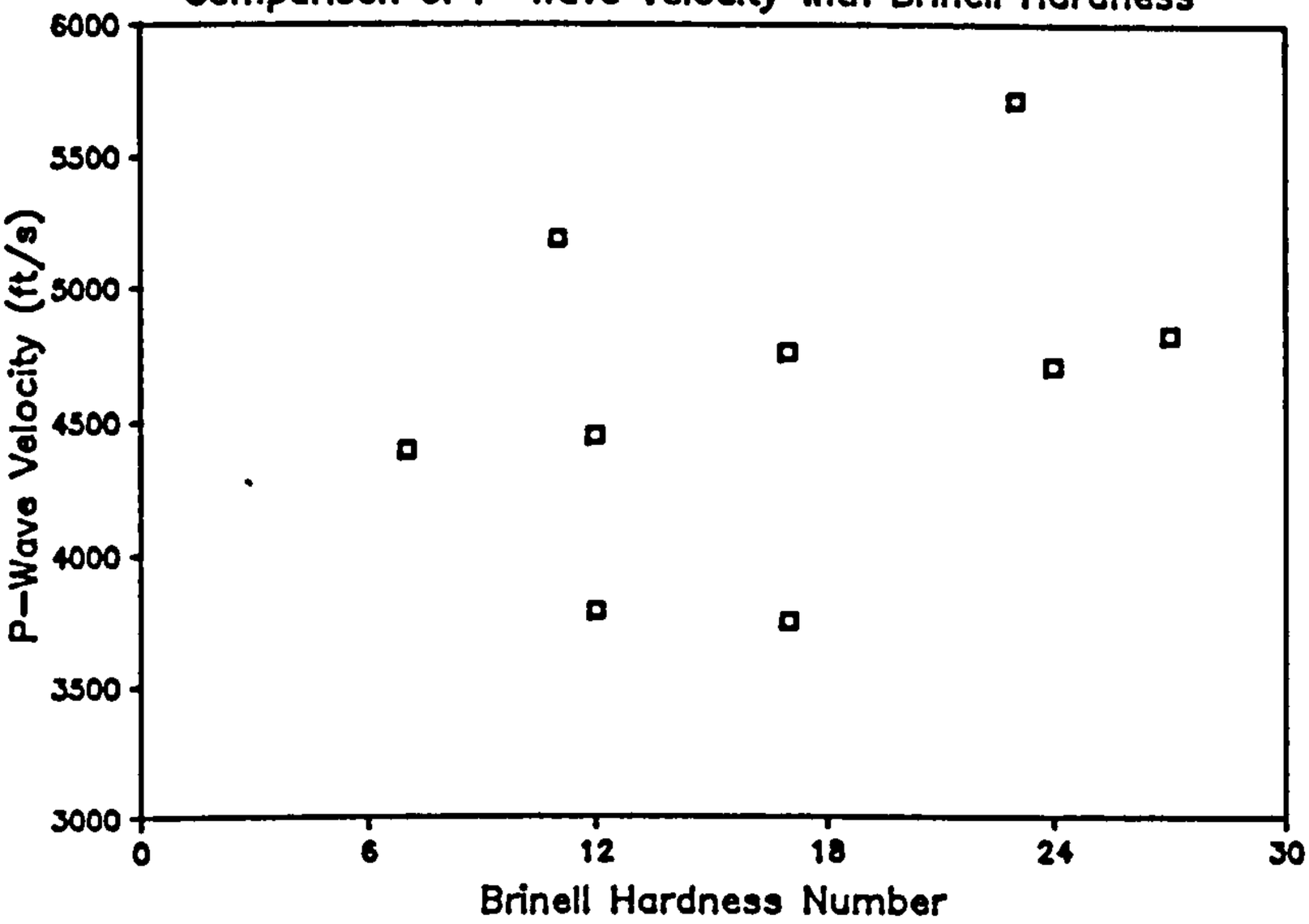

Figure 3.19

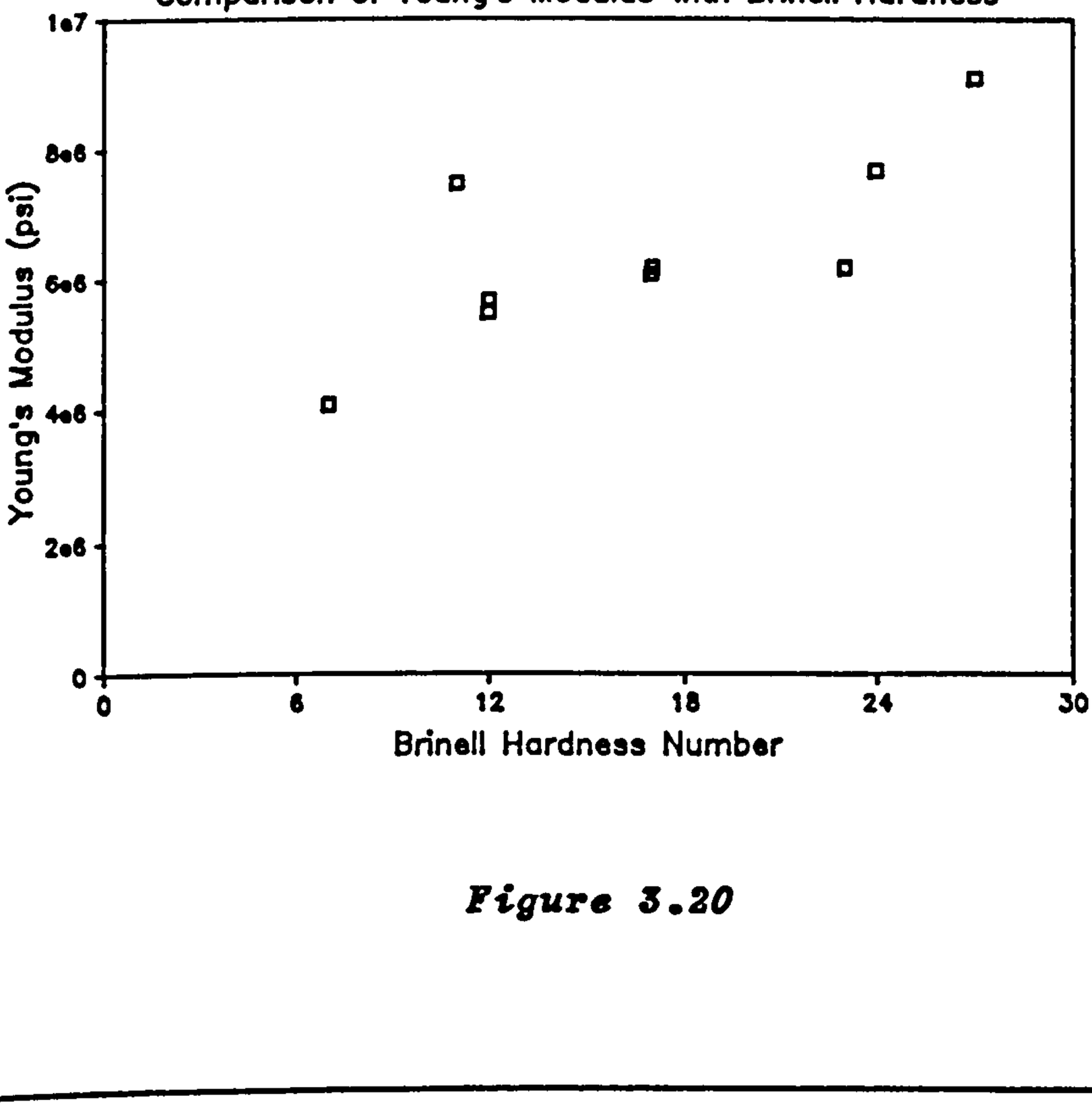

Figure 3.20

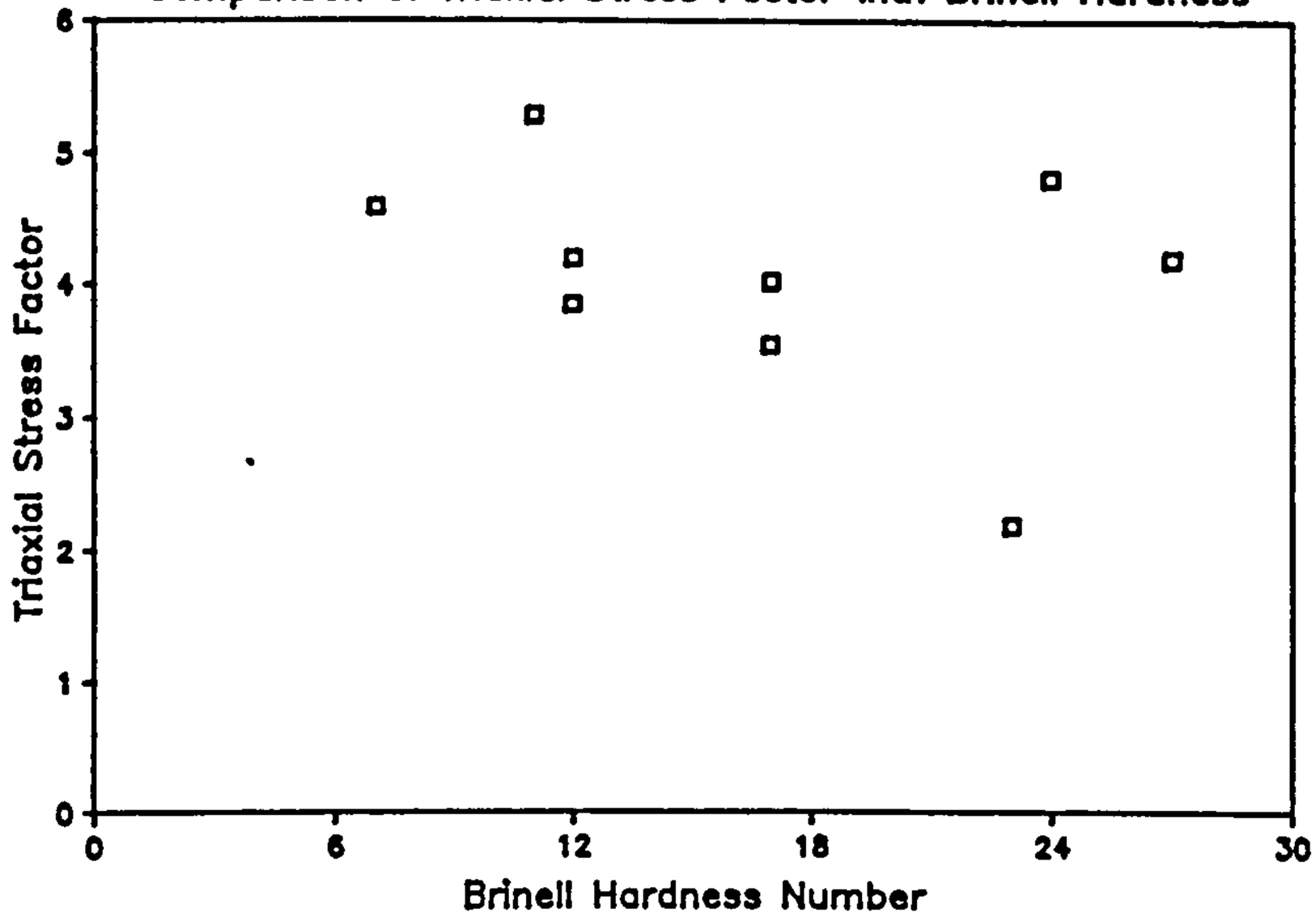

Figure 3.21

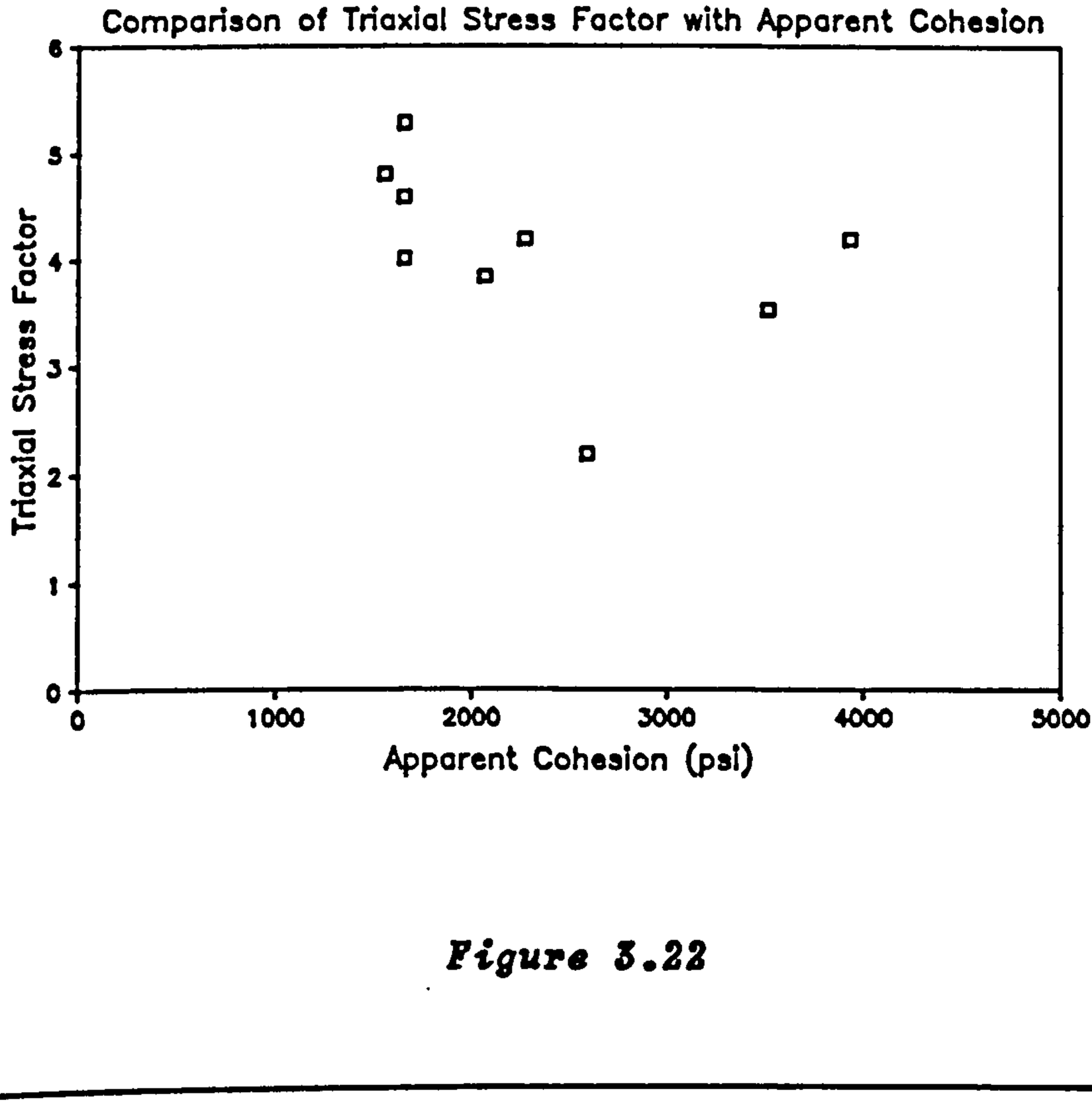

Figure 3.22

No correlation was found to exist between the triaxial stress factor and Brinell hardness (Figure 3.21), while the scatter of results obtained from a plot of the triaxial stress factor against apparent cohesion illustrated the absence of a relationship (Figure 3.22).

The values of Young's Modulus and angle of internal friction were of a higher order than the corresponding values from well 47/14a-8. As with the previous test results, no correlation was found to exist between any of values themselves or with density.

3.5 CONCLUSIONS

It may be concluded that the Brinell hardness test is a quick and simple method of assessing the properties of a rock. In general, the above results appear to corroborate the existence of a relationship between Brinell hardness and the elastic moduli of rock. A relationship between sample density and P-wave velocity can also be reported, although this is less apparent. As for the other mechanical properties, no direct conclusions can be drawn.

The values of Uniaxial Compressive Strength were derived from the Mohr's envelope for each specimen. Ideally, these parameters should have been determined from separate tests. Due to the apparent difficulties in obtaining reservoir core in sufficient quantities to conduct such tests, the results quoted may be considered to give a good indication of the respective properties.

The flattening of the stress-strain curve at different confining pressures [Figure 3.8(b)] suggests that Young's Modulus and Poisson's Ratio should be determined independently from the Multi-Failure test as it is desirable to obtain stress-strain data from the linear sections of the graph. This, however, would require an additional core sample per test and the availability of such may not always be possible.

The accuracy of the Brinell hardness test may be reduced with samples displaying a high clay content. This is possibly due to the variation in sample grain size which, in the case of samples from well 11/30a-A6, had the effect of reducing test repeatability.

The repeatability and linearity of the initial results using the modified oedometer indicate that the instrument is capable of producing accurate hardness values. The attraction with the technique developed is that a prepared core sample can be tested using the apparatus without damage prior to mechanical property testing and has the advantage of increasing the likelihood of generating consistent and meaningful results.

The modified NCB cone indenter, although not as accurate as the modified oedometer, is nevertheless of value as a brinell tester as it is pocket-sized, easy to use and can accept small samples of rock. The instrument is therefore suitable for field use and as the test does not require prepared core samples, it is feasible that it could be used for providing estimates of rock hardness from drill

cuttings or other small fragments of rock.

The mechanical property results detailed in this chapter were used to develop failure criteria for the analytical analysis presented in the following chapter.

CHAPTER FOUR

ANALYTICAL ANALYSIS OF THE STABILITY OF INCLINED BOREHOLES UNDER NON-HYDROSTATIC STRESS CONDITIONS

4.1 INTRODUCTION

The photoelsatic analysis detailed in Chapter Two illustrated that, under 'normal' in-situ stress conditions, the 'roof' of an inclined borehole is more likely to fail in tension while the 'side' of the hole is more likely to fail in compression. Although proving beneficial, this physical modelling approach neglected the effect of internal wellbore pressure and, of course, provided solutions based on elastic theory. It was also a laborious technique which could only provide information about a limited number of hole angles and would have required a number of subsequent models to provide comprehensive data. It was therefore apparent that a more rigorous method of analysis was required. The purpose of this chapter was to investigate the induced state of stress surrounding inclined boreholes by analytical methods. The rock properties determined in the preceding chapter were used to develop failure criteria which were applied to existing analytical elastic solutions. This approach was then extended to investigate the post-failure stress distribution as a function of radial distance.

4.2 ELASTIC STRESS ANALYSIS

4.2.1 Introduction

The object of this section was to examine the magnitude of the stresses surrounding a wellbore under the assumption of elastic conditions and to study the effect of hole inclination and wellbore pressure on the induced state of stress. This investigation was

necessary in order to determine the possiblity of maintaining the rock in the neighbourhood of the wellbore in an elastic condition and to predict the onset of borehole failure.

4.2.2 State of Stress Acting on the Borehole Wall

If the material surrounding a borehole is assumed to behave in a perfectly elastic manner and if the material is stressed beyond its elastic limit, failure will occur at the wall of the hole. Therefore, to assess the state of stress required to induce failure, it is necessary to have an understanding of the theoretical stress concentrations which act on the borehole wall. Stress solutions as a function of of radial distance were discussed in Section 1.3.3. Including the effect of wellbore pressure P_w, and considering compressive stresses and fluid pressure as positive, the effective stresses acting on the wall of the borehole are as follows [31]:

$$\sigma_r = P_w \quad .. \quad .. \quad .. \quad .. \quad (4.1)$$

$$\sigma_\theta = (\sigma_x+\sigma_y-P_w) - 2(\sigma_x-\sigma_y)\mathrm{Cos}2\theta - 4\tau_{xy}\mathrm{Sin}2\theta \quad .. \quad (4.2)$$

$$\sigma_z = \sigma_{zz} - \gamma[2(\sigma_x-\sigma_y)\ \mathrm{Cos}\ 2\theta + 4\tau_{xy}\mathrm{Sin}2\theta] \quad .. \quad .. \quad (4.3)$$

$$\tau_{\theta z} = 2(\tau_{xz}\mathrm{Cos}2\theta - \tau_{xz}\mathrm{Sin}2\theta) \quad .. \quad .. \quad .. \quad .. \quad (4.4)$$

$$\tau_{r\theta} = \tau_{rz} = 0 \quad .. \quad .. \quad .. \quad .. \quad (4.5)$$

where σ_y and σ_x are respectively the maximum and minimum in-situ

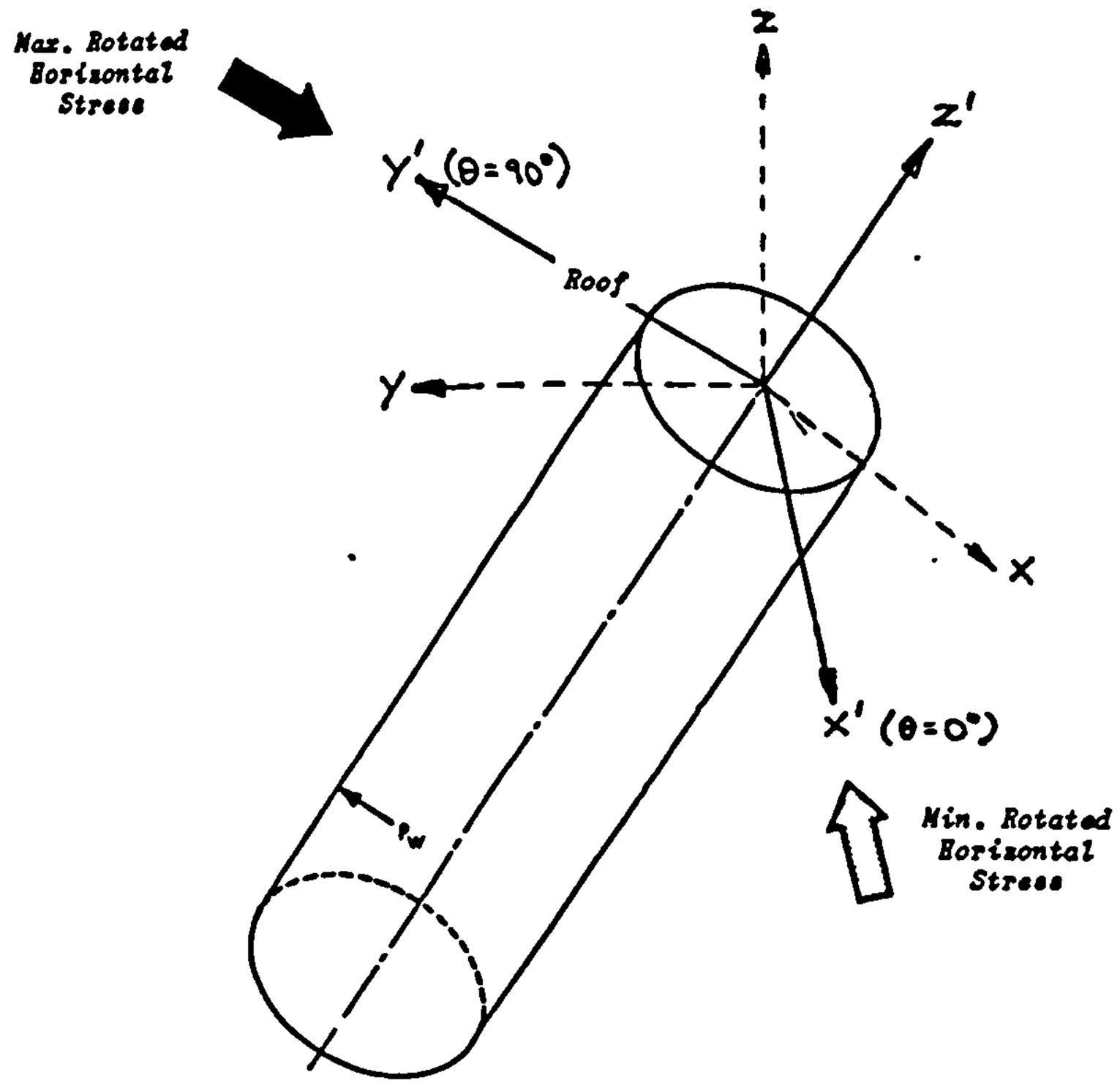

Figure 4.1 : Manner of Borehole Inclination

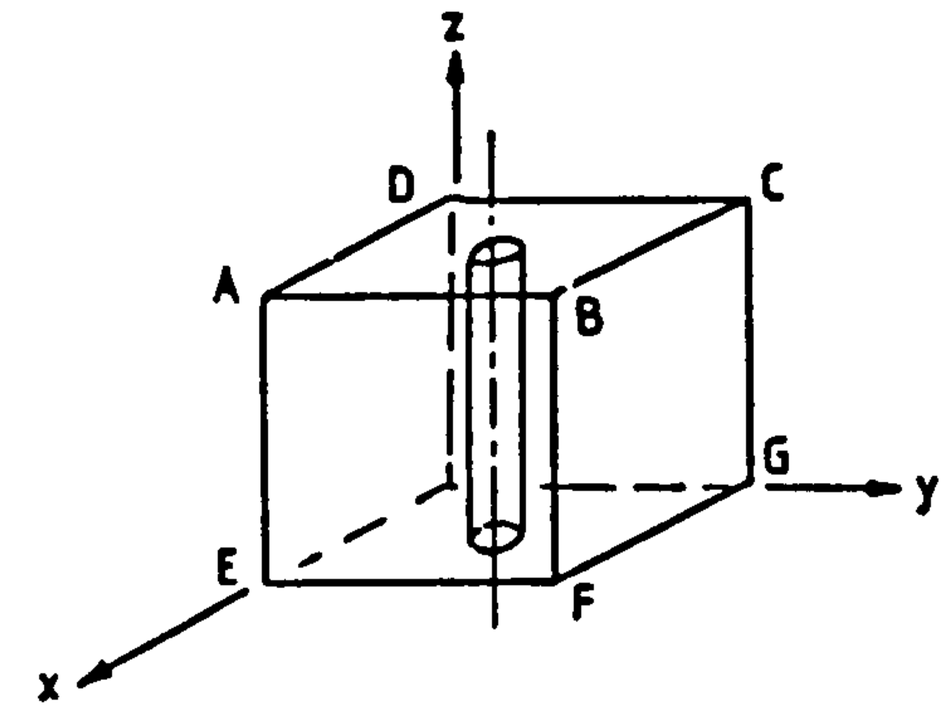

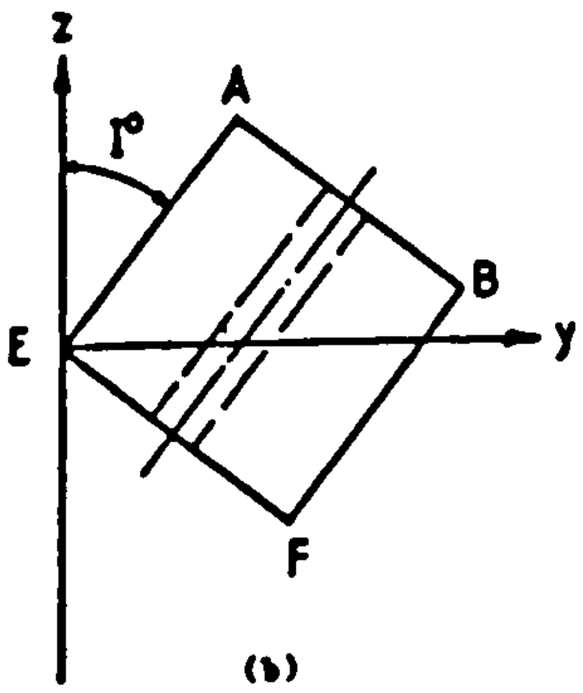

Figure 4.2(a)

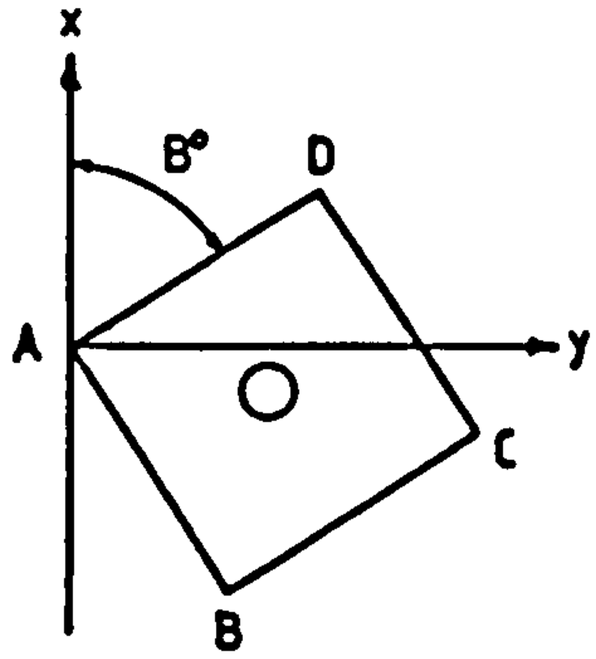

Figure 4.2(b)

stress components acting normally to the axis of the borehole and θ is the angular position around the wall of the borehole, the other parameters are as defined in Section 1.2.

For a non-vertical borehole or a hole that is not lined up with one of the principal in-situ stresses, it is necessary to transform the principal stresses into the coordinate frame of the borehole to obtain the in-situ stress components required for the above set of equations. This may be accomplished by mathematically rotating the principal stresses by the use of direction cosines [32].

If the principal stresses acting at a point in a borehole with its centre line bisecting that point and with its orientation x, y, z known, it is possible to determine the stresses acting on any other borehole passing through the same centre but with different orientation x', y', z'. The manner in which the borehole is orientated is shown in Figure 4.1. The angles between the rotated borehole axis and the x, y, z axes are called 'direction angles' and their cosines, $l = \cos a$, $m = \cos b$, $n = \cos c$, are termed the 'direction cosines' of the rotated borehole axis. They are related by the expression $l^2 + m^2 + n^2 = 1$ [4].

Referring to Figure 4.2(a) and noting that the z-axis is the borehole axis, to define an increase in borehole inclination, the plane perpendicular to the z-axis, i.e. the xy-plane, is rotated around the x-axis by the required inclination, I^o. This yields the following set of direction cosines which relate each rotated axis to its previous centre.

l_1 = Cos 0° m_1 = Cos 90° n_1 = Cos 90°

l_2 = Cos 90° m_2 = Cos I° n_2 = Cos (90°+I°)

l_3 = Cos 90° m_3 = Cos (90°-I°) n_3 = Cos I°

If the horizontal principal stresses are equal, borehole direction or azimuth has no effect on the rotated stress values. Therefore, the above direction cosines may be inserted into equations (4.7)-(4.12) to obtain the rotated stresses for a particular hole inclination.

To define a specific borehole azimuth when tectonic conditions are present, it is necessary to orientate the cube so as the new z-axis frame has the same azimuth as the borehole [Figure 4.2(b)]. The following direction cosines define this situation, the xy-plane being orientated around the z-axis while the x-axis is held horizontal, by the required azimuth, B°.

l_1'= Cos B° m_1'= Cos (90°-B°) n_1'= Cos 90°

l_2'= Cos (90°+B°) m_2'= Cos B° n_2'= Cos 90°

l_3'= Cos 90° m_3'= Cos 90° n_3'= Cos 0°

The direction cosines of the borehole axis may then be calculated by determining the angle (η) between the two sets of x', y', z' axis frames whose direction cosines are defined above. This may be accomplished using the following relationship [92].

$$\text{Cos } \eta = ll' + mm' + nn' \quad .. \quad .. \quad .. \quad (4.6)$$

Expansion of equation (4.6) yields a full set of direction cosines which are then applied to the folowing equation set to obtain the transformed rectangular coordinates.

$$\sigma_x = l_1^2\sigma_1 + m_1^2\sigma_2 + n_1^2\sigma_3 \quad .. \quad .. \quad .. \quad (4.7)$$

$$\sigma_y = l_2^2\sigma_1 + m_2^2\sigma_2 + n_2^2\sigma_3 \quad .. \quad .. \quad .. \quad (4.8)$$

$$\sigma_z = l_3^2\sigma_1 + m_3^2\sigma_2 + n_3^2\sigma_3 \quad .. \quad .. \quad .. \quad (4.9)$$

$$\tau_{xy} = l_1l_2\sigma_1 + m_1m_2\sigma_2 + n_1n_2\sigma_3 \quad .. \quad .. \quad .. \quad (4.10)$$

$$\tau_{yz} = l_2l_3\sigma_1 + m_2m_3\sigma_2 + n_2n_3\sigma_3 \quad .. \quad .. \quad .. \quad (4.11)$$

$$\tau_{zx} = l_3l_1\sigma_1 + m_3m_1\sigma_2 + n_3n_1\sigma_3 \quad .. \quad .. \quad .. \quad (4.12)$$

The rotated in-situ coordinates are then inserted into equations (4.1)-(4.5). Therefore, using the above theory, the state of stress acting on the borehole wall can be determined for any combination of borehole inclination and azimuth.

4.2.3 Effect of Mud Weight and Hole Inclination on the Solutions

Among the factors which may be controlled during the drilling of a well are the mud weight, and the inclination and direction of the wellbore. To investigate the effect of varying these parameters on the induced stress acting on the borehole wall the above set of equations were applied to a hypothetical situation. In this analysis, the effect of both a high and a low mud weight in wells of various inclinations was examined. The horizontal to vertical principal stress ratio was assumed to be 0.8:1.0. As the horizontal principal stresses σ_2 and σ_3 were assumed to be equal, the effect of

hole direction had no effect on the induced stress concentrations.

The results of this analysis are presented graphically in Figures 4.3(a) and 4.3(b). It can be seen that the trends of the respective curves illustrated in both figures were identical, the only effect of varying wellbore pressure was to vary the magnitude of the respective values, (i.e. the respective curves were moved either up or down the effective stress axis).

Figure 4.3(a) illustrates the effective stresses which would be induced at the borehole wall if a low mud weight was used in wells inclined at 45° and 90° (i.e. horizontal). The solutions for a vertical well are also shown for comparison. As expected, the hoop stress acting on the wall of the vertical well was found to be constant around the borehole, as was the radial stress. For the inclined wells, however, the hoop stress concentrations were observed to vary around the periphery of the hole and had a maximum value at an angular position of 0° (i.e. the σ_x direction, or the 'side' of the borehole) and a minimum value at 90° (i.e. the σ_y direction, or the 'roof' of the borehole - see Figure 4.1).

Figure 4.3(b) shows the effect of using a high mud weight in boreholes of the same inclination. It can be seen that the radial stress increased in value (equivalent to the effective mud weight), while the respective hoop stress concentrations reduced in value. More specifically, in the case of the horizontal borehole, the minimum hoop stress value was observed to approach zero at an angular position of 90°, thus indicating that tensile failure was

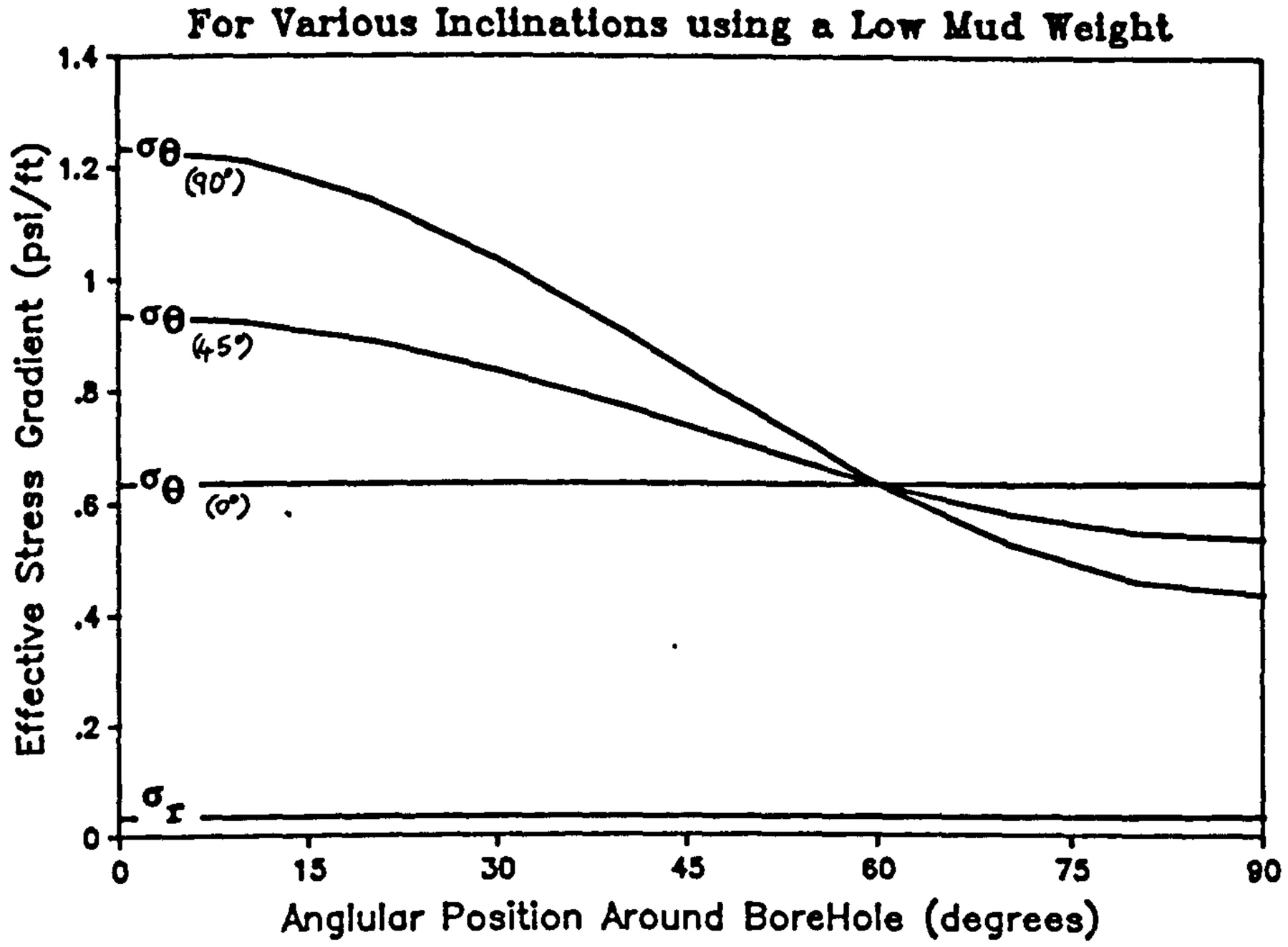

Figure 4.3(a) : Effect of a Low Mud Weight on the Stress acting at the Periphery of a Borehole

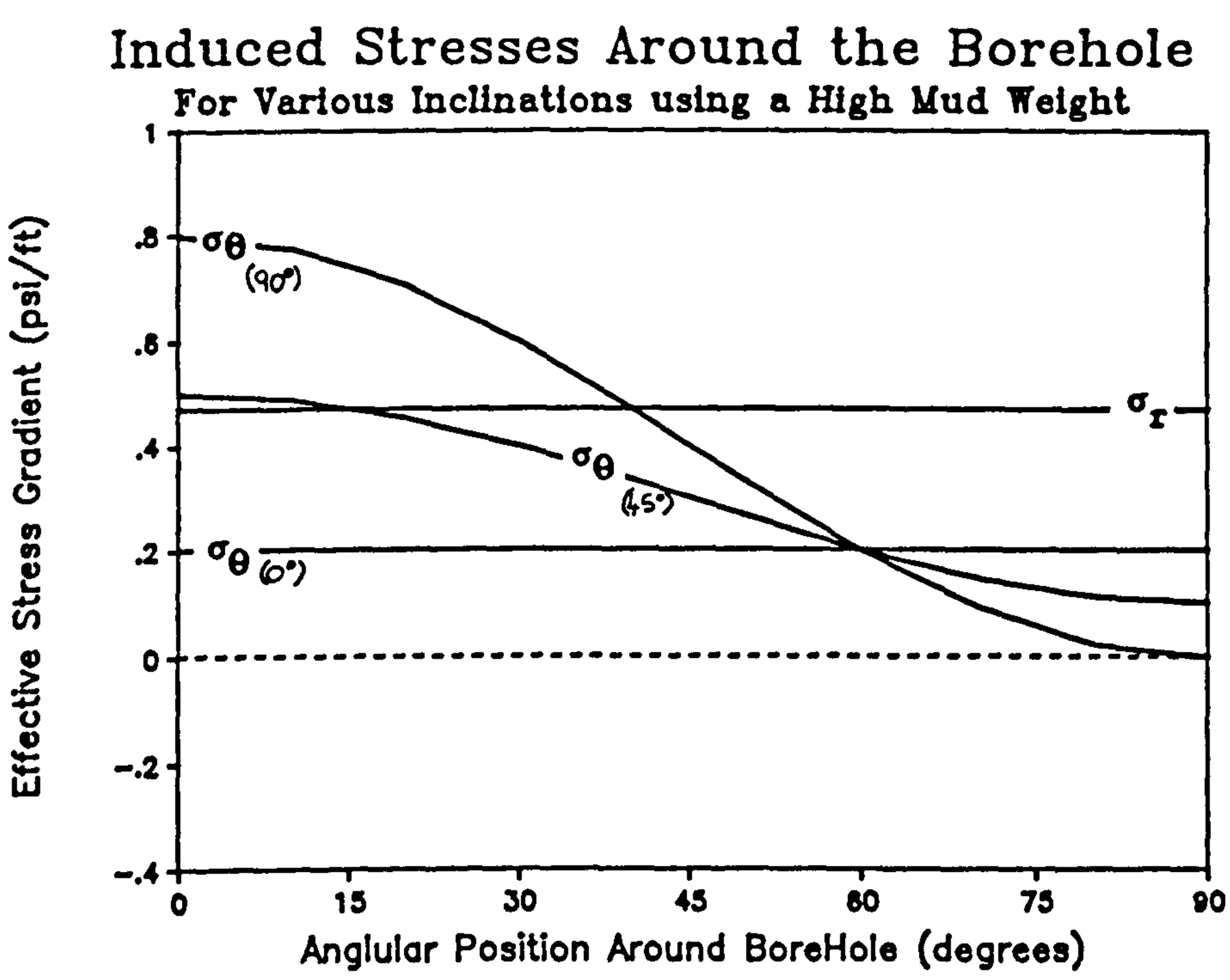

Figure 4.3(b) : Effect of a High Mud Weight on the Stress acting at the periphery of a Borehole

probable. This confirms that inclined boreholes are more likely to fail in tension than a vertical well and that the fracture will be initiated in a plane perpendicular to the least principal stress, i.e. in the σ_y direction.

The general stability of the borehole is dictated by the difference in the maximum and minimum stresses acting on the borehole wall, i.e. $\sigma_\theta - \sigma_r$. The region where this difference is greatest marks the onset of compressional failure. From an examination of both figures, it can be seen that $\sigma_\theta - \sigma_r$ was greatest for the high angle holes and occurred at an angular distance of 0°. This effect is more apparent in Figure 4.3(a) where a low mud weight was used. Again, this confirms that inclined boreholes have a reduced ability to resist compressional failure, however, failure criteria would have to be applied to determine the onset of instability.

From the above analysis, assuming normal in-situ stress conditions, it is apparent that compressional and tensile failure will be initiated at 90° to each other. Therefore, when assessing the state of stress around the well the respective maximum and minimum limiting values must be used as input parameters for the failure criteria.

The Mohr's circle approach is an ideal method to illustrate in graphical terms, the stress relationships at the borehole wall brought about by varying the wellbore pressure. To construct a Mohr's circle using polar coordinates, the effective radial and hoop stresses are plotted on the x-axis and a circle is drawn through

these points with the centre midway between them. The top of the circle represents the maximum shear stress. From Figure 4.4(a), it can be seen that if the mud weight (wellbore pressure) is decreased, the value of σ_r decreases and the hoop stress increases, thus enlarging the Mohr's circle. If this circle bisects a specified failure criterion, borehole failure in compression will occur. To reduce the radius of the circle and therefore avert collapse, the mud weight is increased. This will increase the value of σ_r which effectivly reduces σ_θ. As a result of this, the circle becomes smaller and its periphery moves away from the failure curve. Increasing the mud weight too much, however, will lead to the radial stress exceeding the hoop stress [Figure 4.4(b)]. Subsequently, if the hoop stress becomes tensile, the borehole will fail in tension thus a fracturing and lost circulation condition will exist.

4.2.4 Development of Failure Criteria

Rocks behave differently in tension than in compression and as a result, a separate failure criterion is required to describe each type of failure. In this investigation, classical fracturing theory was applied to predict tensile failure while the Mohr-Coulomb and the three-dimensional Griffith failure criteria were applied to predict hole collapse. The development of the criteria is given below.

4.2.4.1 Tensile Failure

The tensile failure criterion adopted for this analysis was that

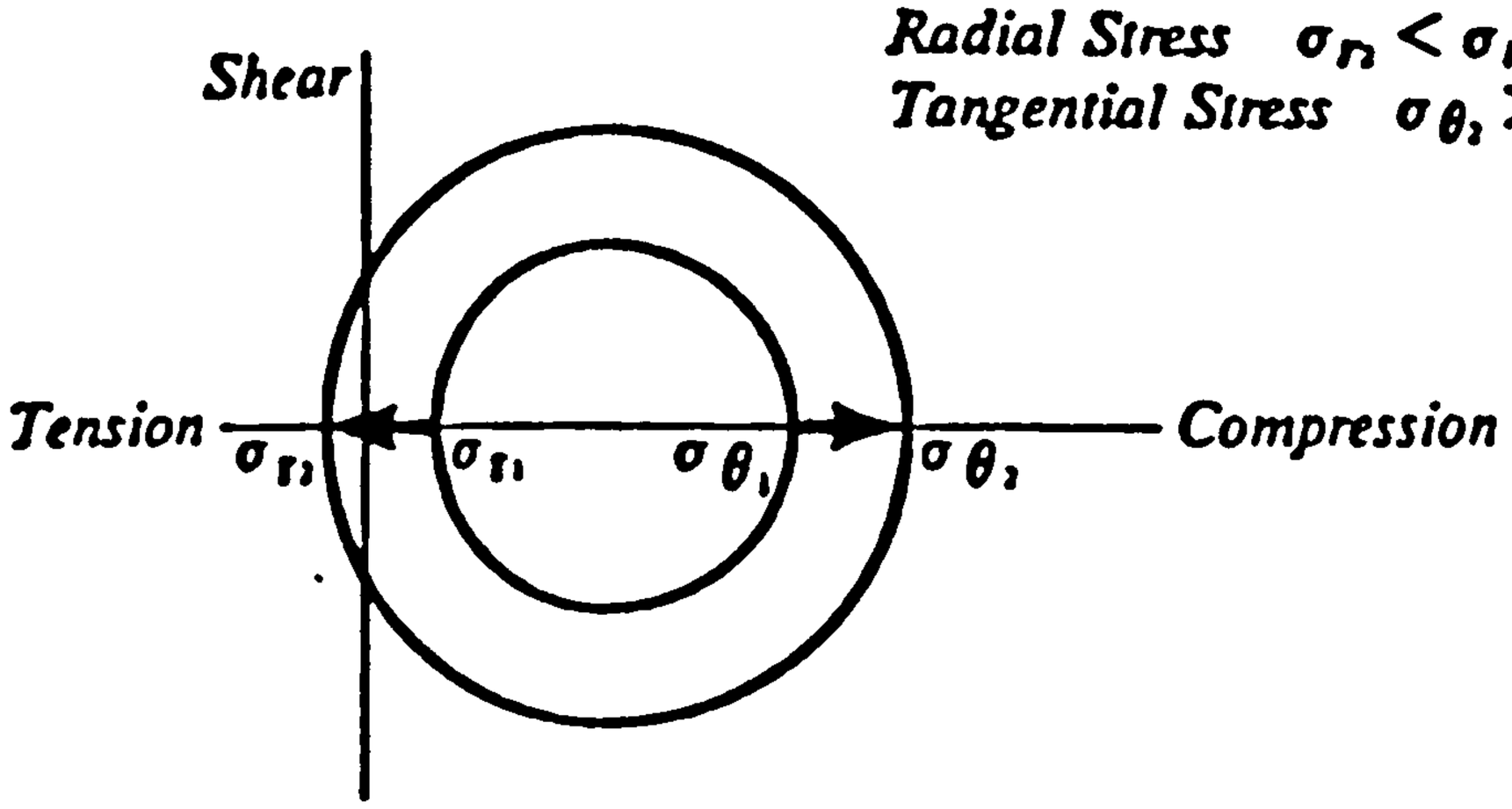

Figure 4.4(a) : Effect of Decreasing Mud Weight on Mohr's Circle

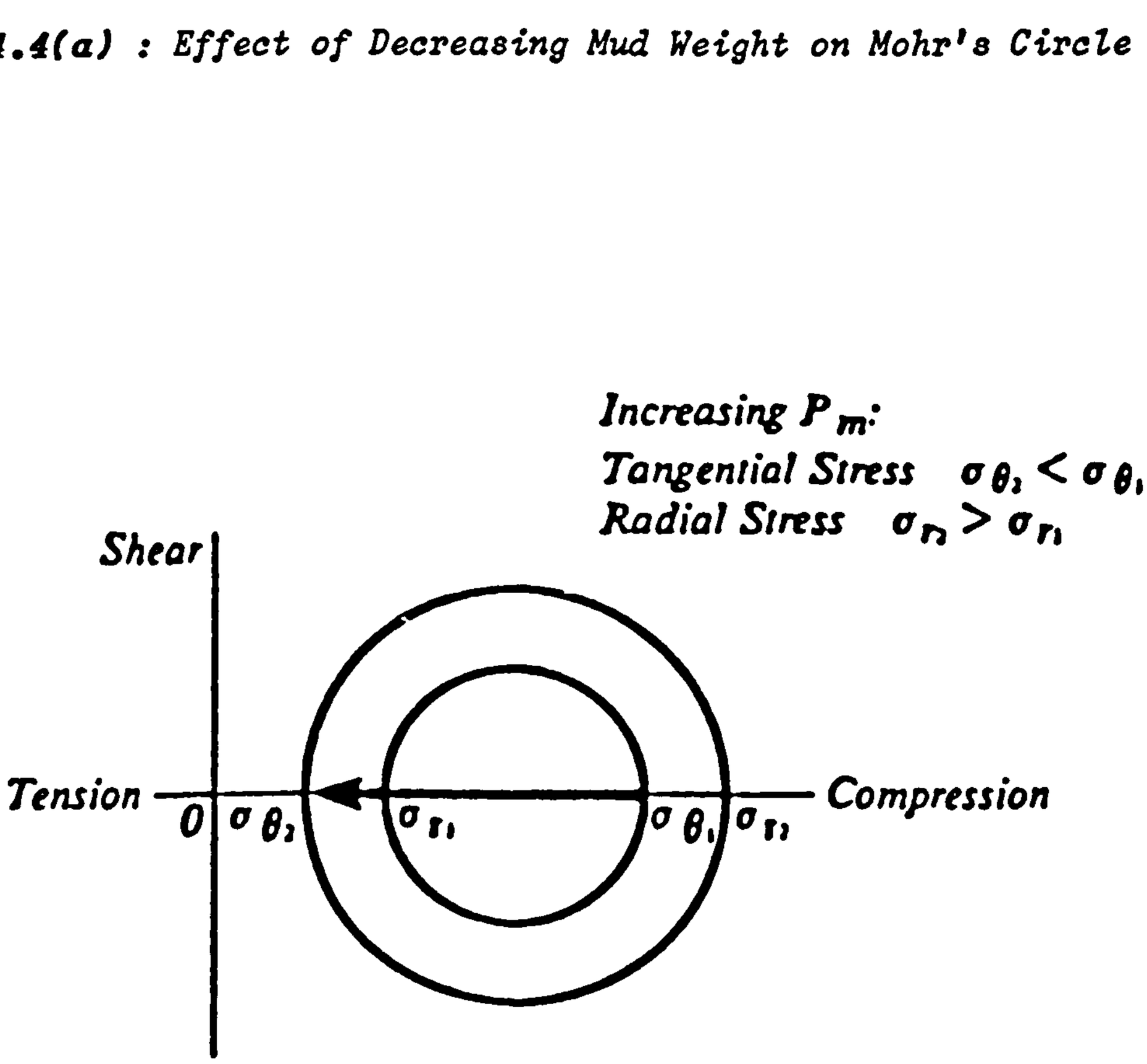

Figure 4.4(b) : Effect of Increasing Mud Weight on Mohr's Circle

lost circulation/hydraulic fracturing would occur when the borehole pressure exceeded the effective tangential or hoop stress σ_θ acting on the borehole wall. In this examination, the tensile strength of the rock was considered to be zero. This assumption has been applied by Bradley [31] and others [56], and appears to be justified as it is assumed that a fracture initiates at a joint, flaw or existing fracture. Therefore, in accordance with classical elastic fracturing theory (Section 1.5.2), the borehole pressure required to initiate tensile failure at the borehole wall (assuming a non-penetrating fluid) is :

$$P_f = 3\sigma_x - \sigma_y - P_p \qquad .. \quad .. \quad .. \quad .. \quad (4.13)$$

4.2.4.2 Compressive Failure : Mohr-Coulomb Model

As shown in Section 1.3.4.3 and as discussed above, the relationship between the shear and principal stress acting in a plane can be described by the Mohr-Coulomb Failure Criterion. The Coulomb failure line is a linear approximation of the Mohr failure envelope. It is depicted as follows:

$$\tau_m = \sigma_m \text{ Sin } \alpha + S_0 \text{ Cos } \alpha \qquad .. \quad .. \quad .. \quad (4.14)$$

where $\tau_m = 1/2(\sigma_\theta - \sigma_r)$ .. .. (4.15)

and $\sigma_m = 1/2(\sigma_\theta + \sigma_r)$ .. .. (4.16)

which are the maximum shear stress and the mean stress in the plane σ_1, σ_3. The mean stress σ_m is to be distinguished from the

three-dimensional mean stress $(\sigma_1+\sigma_2+\sigma_3)/3$.

The effective stresses acting on the borehole wall considering the effect of pore pressure (P_p) and borehole pressure (P_w) are:

$$\sigma_r = P_w - P_p \quad .. \quad .. \quad .. \quad .. \quad (4.17)$$

$$\sigma_\theta = 3\sigma_x - \sigma_y - P_w - P_p \quad .. \quad .. \quad .. \quad .. \quad (4.18)$$

To obtain τ_m and σ_m in terms of σ_x, σ_y, P_p and P_w, σ_r and σ_θ were substituted into equations (4.15) and (4.16), viz,

$$\tau_m = 1.5\sigma_x - 0.5\sigma_y - P_w \quad .. \quad .. \quad .. \quad .. \quad (4.19)$$

$$\sigma_m = 1.5\sigma_x - 0.5\sigma_y - P_p \quad .. \quad .. \quad .. \quad .. \quad (4.20)$$

By inserting τ_m and σ_m from the above into equation (4.14), and solving for P_w, the critical borehole pressure (P_c) required to induce failure using the Mohr-Coulomb criterion was as follows,

$$P_c = (1.5\sigma_x-0.5\sigma_y) - (1.5\sigma_x-0.5\sigma_y-P_p)\mathrm{Sin}\alpha - S_o\mathrm{Cos}\alpha \quad .. \quad (4.21)$$

where α is the Internal Angle of Friction and S_o is the Cohesion or the Initial Shear Strength of the rock.

3.4.2.3 Compressive Failure : Three-Dimensional Griffith Model

The three-dimensional Griffith failure criteria considers all three effective stresses acting on the borehole wall. The total hydrostatic stress at the hole periphery is therefore :

$$S = 1/3(\sigma_z + \sigma_\theta + \sigma_r) \qquad .. \quad .. \quad .. \quad .. \quad (4.22)$$

To simplify the solution, it was assumed that $\sigma_\theta = \sigma_z$, therefore, the stresses at the surface of the borehole where S is applied are :

$$\sigma_r' = P_w \, . \qquad .. \quad .. \quad .. \quad .. \quad (4.23)$$

$$\sigma_z' = \sigma_\theta' = 1.5S - 0.5P_w \qquad .. \quad .. \quad .. \quad .. \quad (4.24)$$

As detailed in Section 1.3.4.5, the 3D Griffith failure envelope may be mathematically defined using cylindrical coordinates in the following manner :

$$(\sigma_z'-\sigma_\theta')^2 + (\sigma_z'-\sigma_r')^2 + (\sigma_\theta'-\sigma_r')^2 = 2C_o(\sigma_z'+\sigma_\theta'+\sigma_r') \qquad .. \quad (4.25)$$

The effective stress values of σ_z, σ_θ and σ_r were then substituted into the 3D Griffith equation which yielded a quadratic equation of the form,

$$P_w = \frac{-b \pm \sqrt{b^2 - 4ac}}{2a} \qquad .. \quad .. \quad .. \quad .. \quad (4.26)$$

where $a = 6.75$

$b = 13.5xS$

$c = 6.75xS^2 - 6xC_oxS$

Of the two P_w values obtained from the quadratic formula, the higher value was rejected as it wrongly predicted that a borehole with a

high compressive strength (C_o) would be less stable than with a low value of C_o, while the lower P_w value gave the opposite, and more realistic, relationship. Therefore, the lower P_w value was designated P_c, i.e. the critical wellbore pressure for shear failure using the 3D Griffith approach.

4.2.5 Application of Failure Criteria to predict Stability

4.2.5.1 Method of Analysis

Both the Mohr-Coulomb and the 3D Griffith failure criteria developed above were applied to wells 11/30a-A6 and 47/14a-8 to provide estimates of the minimum and maximum mud weights which could be carried in the well to prevent wellbore collapse. The mechanical properties detailed in the preceeding chapter were used to provide failure criteria for each well. The technique was also applied to predict whether the formation would collapse under normal drawdown conditions. In a producing well, 'drawdown' is the difference between the flowing bottom hole pressure and the static bottom hole pressure. In this case, 'predicted drawdown' refers to the drawdown at failure calculated by either the Mohr-Coulomb or the 3D Griffith criteria. This value is the difference between the pressure in the wellbore at which failure would occur, and the static bottom hole pressure, which, for this analysis, was assumed to be equal to the pore pressure. The following additional assumptions were made to enable the compressive failure criteria to be applied to the wells examined.

(1) The formation around the borehole was modelled as a linear elastic solid under a condition of plane strain along the axis of the borehole.

(2) The medium obeyed a definable failure criterion.

(3) The voids in the rock matrix were filled with a fluid and the pore pressure (P_p) acted equally in all directions. A 'normal' pore pressure gradient of 0.465 psi/ft was assumed.

(4) The rock was incompressible.

(5) The overburden pressure (σ_1) was considered to be the dominant stress and acted vertically on the rock at depth. A 'normal' overburden gradient of 1 psi/ft was assumed.

(6) The two horizontal stresses (σ_2 and σ_3) were assumed to be equal and related to the overburden stress by the following relationship:

$$\sigma_2 = \sigma_3 = \frac{\gamma}{1 - \gamma} (\sigma_1 - P_p) - P_p \qquad .. \quad .. \quad .. \quad (4.27)$$

Over the section of interest, the laboratory measured values of Poisson's ratio (γ) for each horizon were averaged and the mean value was used to arrive at a constant horizontal to vertical stress ratio.

(7) Plane Strain conditions were assumed

The respective P_c values for the various horizons in each well were calculated using a spreadsheet package and plotted with respect to the total vertical depth, regardless of the hole inclination. Although the various data points were connected to form a line graph, it should be noted that the respective graphs represent a general trend and no direct conclusions could be drawn from areas between the data points.

4.2.5.2 Mohr-Coulomb Analysis

Well 11/30a-A6 : The critical mud weight vs depth curve at selected horizons of this well is presented in Figure 4.5(a). From an examination of this figure, it can be seen that the critical mud weight which could be carried without compressive failure was less than the minimum possible mudweight of 8.95 lb/gal. (i.e. a mud weight equivalent to the pore pressure). It was therefore concluded that compressive failure over this section of the well would be unlikely under normal drilling conditions. The critical wellbore pressure and the maximum predicted drawdown over this section are illustrated in Figure 4.5(b). It was evident that over this section, the well may be subjected to a pressure drawdown in the order of 500 psi (3450 kPa) before the onset of compressional failure and subsequent sand production.

Over the section of interest, the P_c curve was observed to vary consderably. An examination of the core plugs tested indictated that

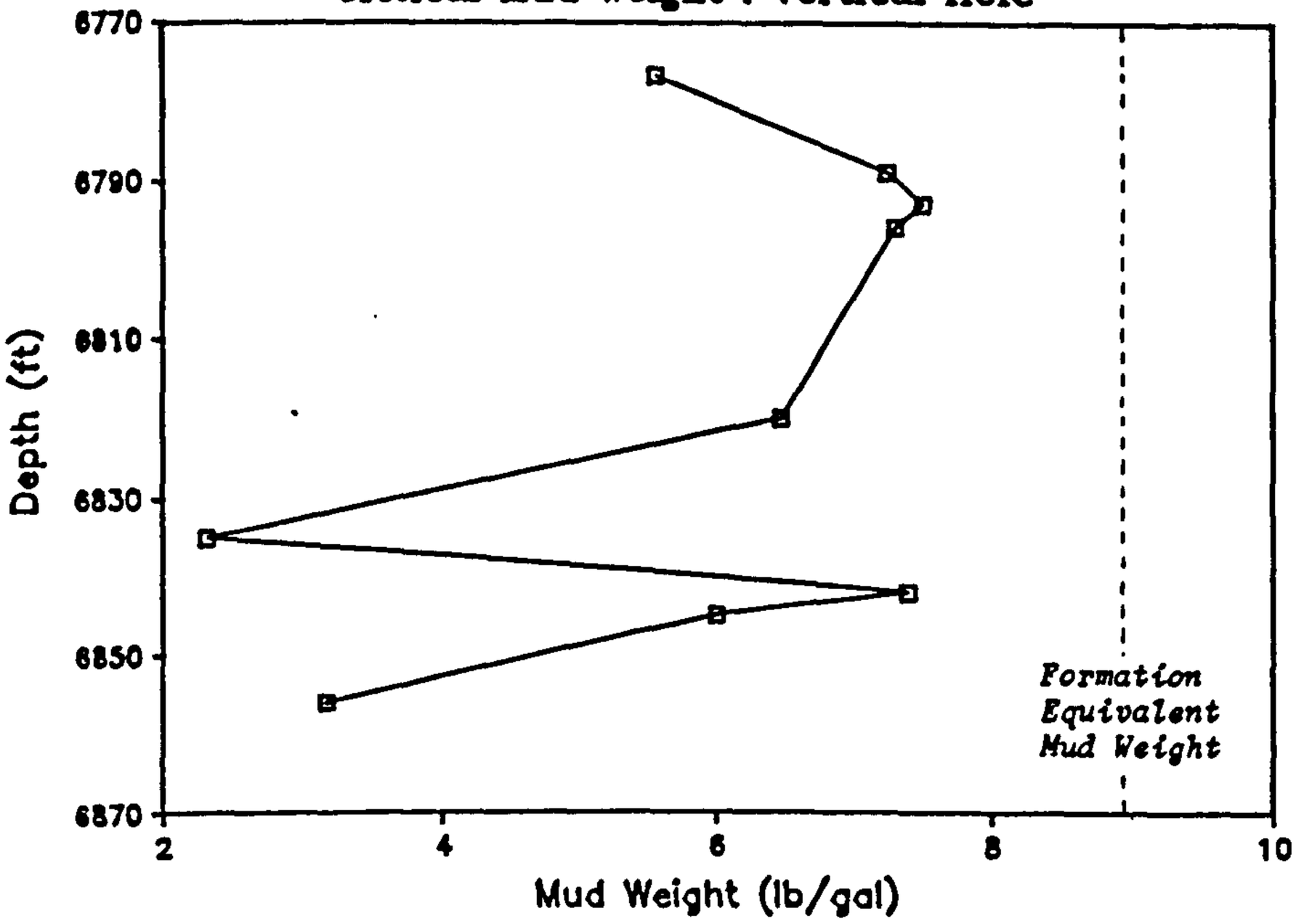

Figure 4.5(a) : Well 11/30a-A6 - Critical Mud Weight Mohr/Coulomb Failure Analysis

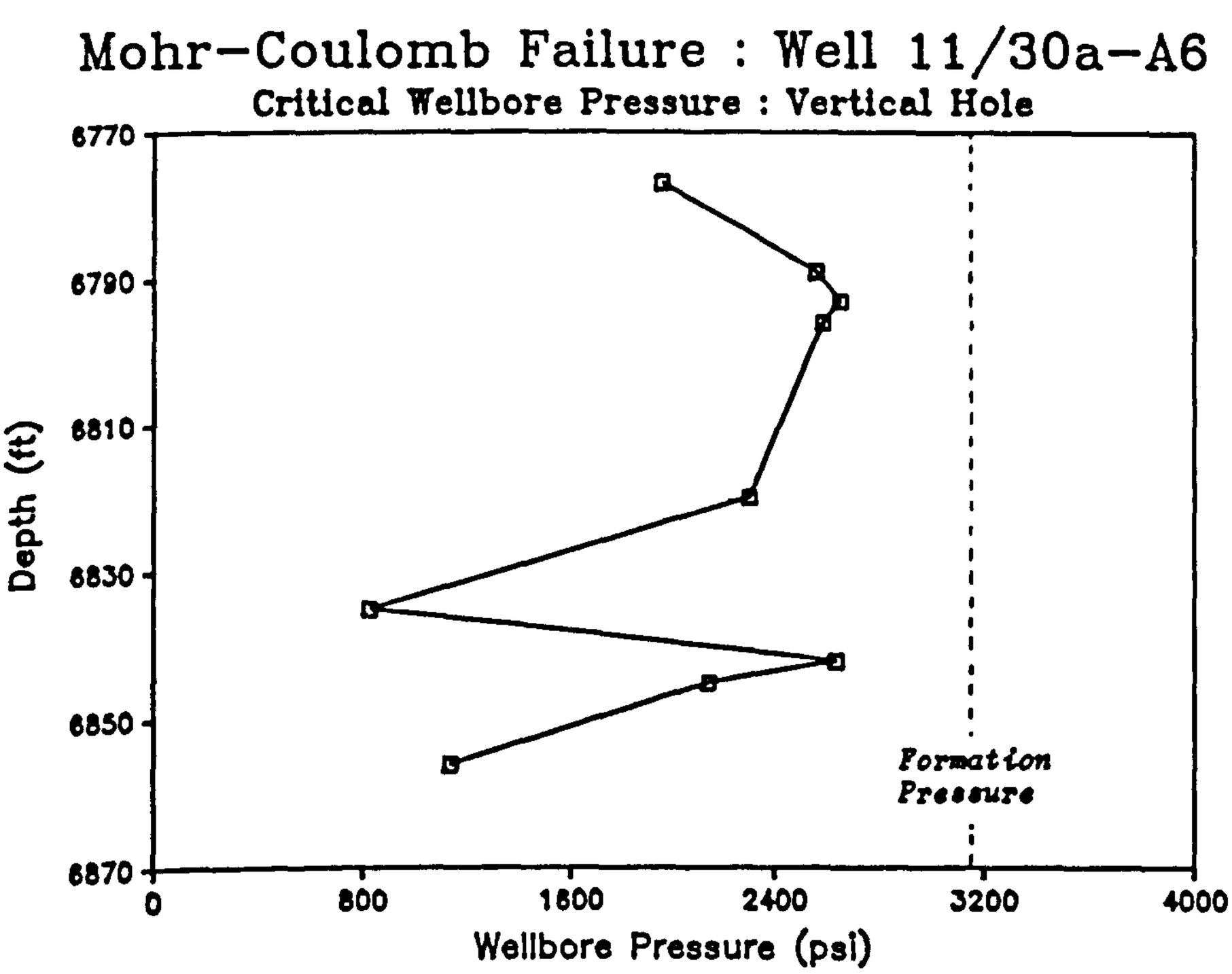

Figure 4.5(b) : Well 11/30a-A6 - Critical Wellbore Pressure Mohr/Coulomb Failure Analysis

with increased depth, the rock type varied from pure shale to sandy shale to fairly clean sandstone. In general, the P_c values predicted for the horizons displaying a high shale content were found to be higher than that of the cleaner sandstone horizons. A swing of around 5 lb/gal or a wellbore pressure of 1800 psi (12420 kPa) was observed between the two extremes of rock type.

Well 47/14a-8 : The critical mud weight vs depth curve for this well is given in Figure 4.6(a). From an analysis of this figure, it was evident that over certain horizons the critical mud weight was greater than the 'equivalent' pore pressure, and as such, the use of a 'balance' mud weight while drilling a vertical well through this region could result in compressive failure. Therefore, to avoid the possibility of well collapse, a mud weight of 12 to 13 lb/gal would be required. The critical wellbore pressure to prevent failure is illustrated in Figure 4.6(b) and the shaded regions in this figure represent zones of potential formation collapse. Therefore in this section of the well, only a selected horizon could be produced without compressive failure and sand production, alternatively, gravel packing could be employed to prevent or minimise sand production.

The P_c curve was observed to vary considerably over the section of interest. As regards rock type, the core samples indicated that the sanstone was clean and homogeneous. However, there was a fairly wide variation in cohesive strength while the internal angles of friction were generally low, thus indicating weak rock. A visual examination of the rock samples from the horizons displaying particularly high

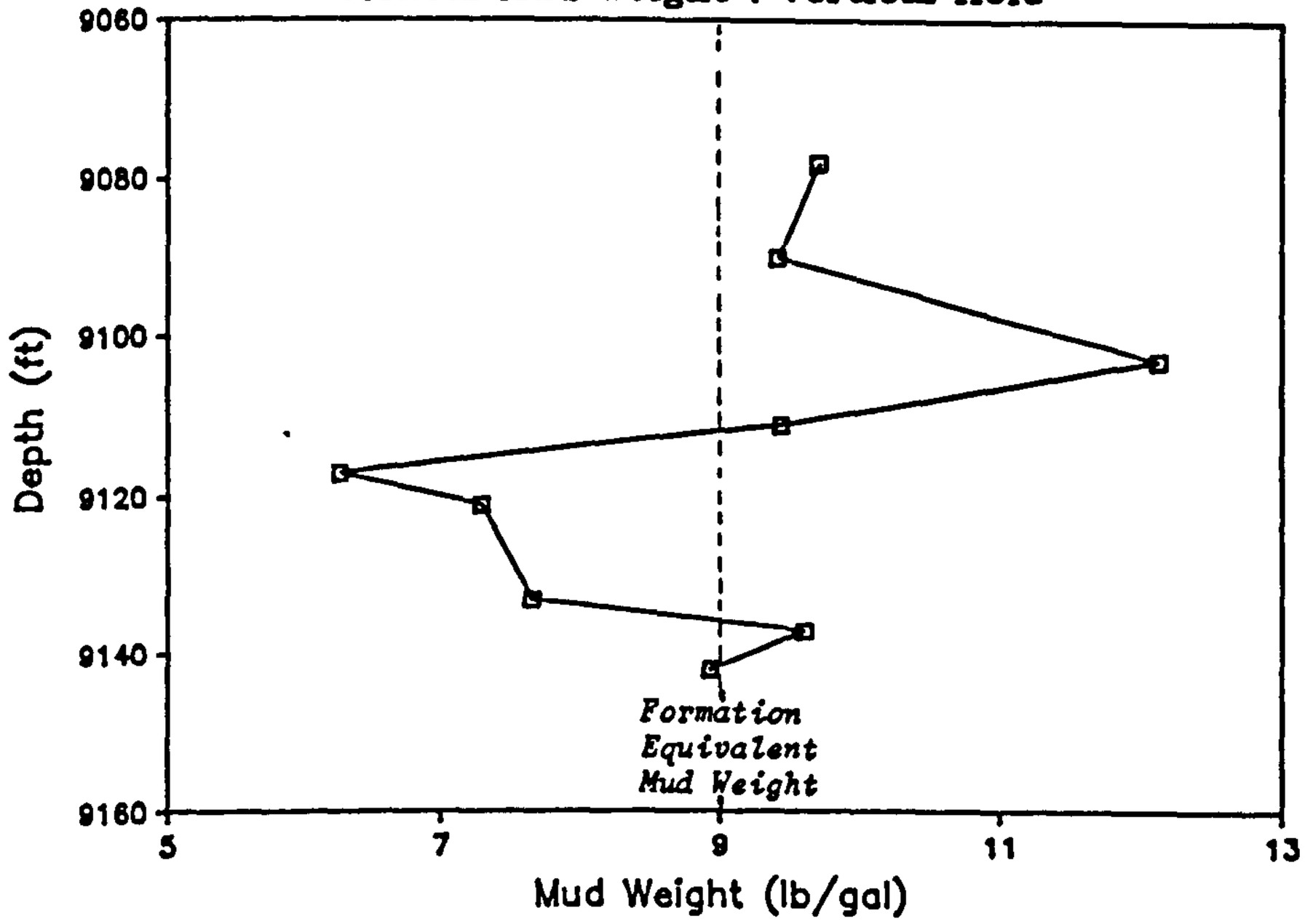

Figure 4.6(a) : Well 47/14a-A8 - Critical Mud Weight Mohr/Coulomb Failure Analysis

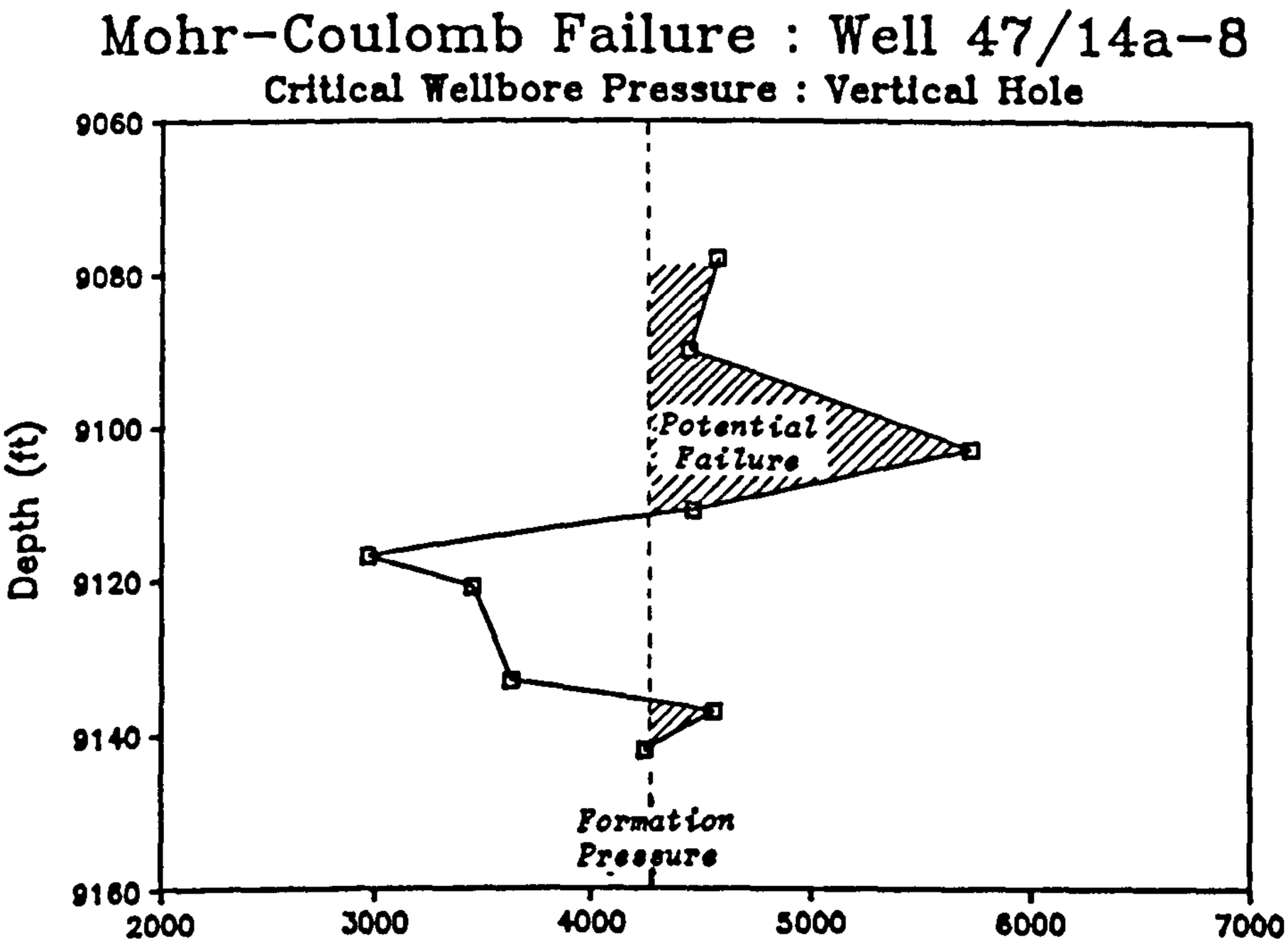

Figure 4.6(b) : Well 47/14a-8 - Critical Wellbore Pressure Mohr/Coulomb Failure Analysis

critical wellbore pressures indicated that they were loosely cemented and therefore more susceptible to compressive failure.

4.2.5.3 3D Griffith Analysis

Well 11/30a-A6 : The critical mud weight to prevent compressional failure in well 11/30a-A6 using the 3D Griffith approach is given in Figure 4.7(a). An examination of this figure indicated that a 'negative' critical mud weight was predicted, while a plot of the critical wellbore pressure, as shown in Figure 4.7(b), suggested that the bottom-hole pressure could be reduced to zero without inducing compressive failure or sand production.

Well 47/14a-8 : Figure 4.8(a) shows the critical mud weight predicted for well 47/14a-8. It can be seen that the majority of the P_c curve found to be less than the pore pressure, and as such, would be stable under normal drilling conditions. However, to prevent compressive failure of the region around 9100 ft (2775 m), it would be necessary to increase the mud weight to around 15 lb/gal. The critical wellbore pressure is presented in Figure 4.8(b) and the shaded region illustrates the zone of potential formation collapse.

4.2.5.4 Comparison of Failure Prediction Results.

The most striking difference in the prediction results using the two failure criteria was the low values of P_c calculated using the 3D Griffith model.

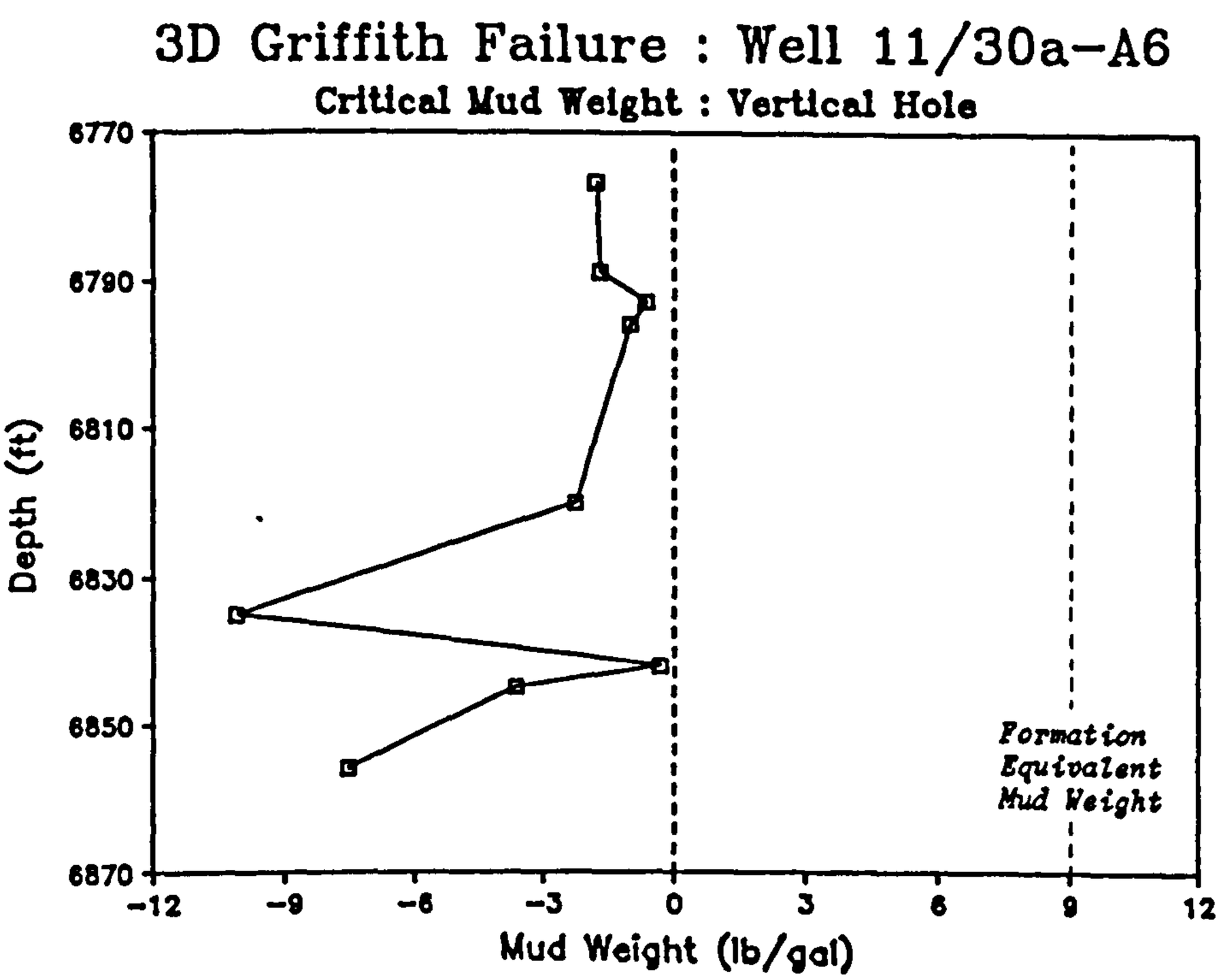

Figure 4.7(a) : Well 11/30a-A6 - Critical Mud Weight 3D Griffith Analysis

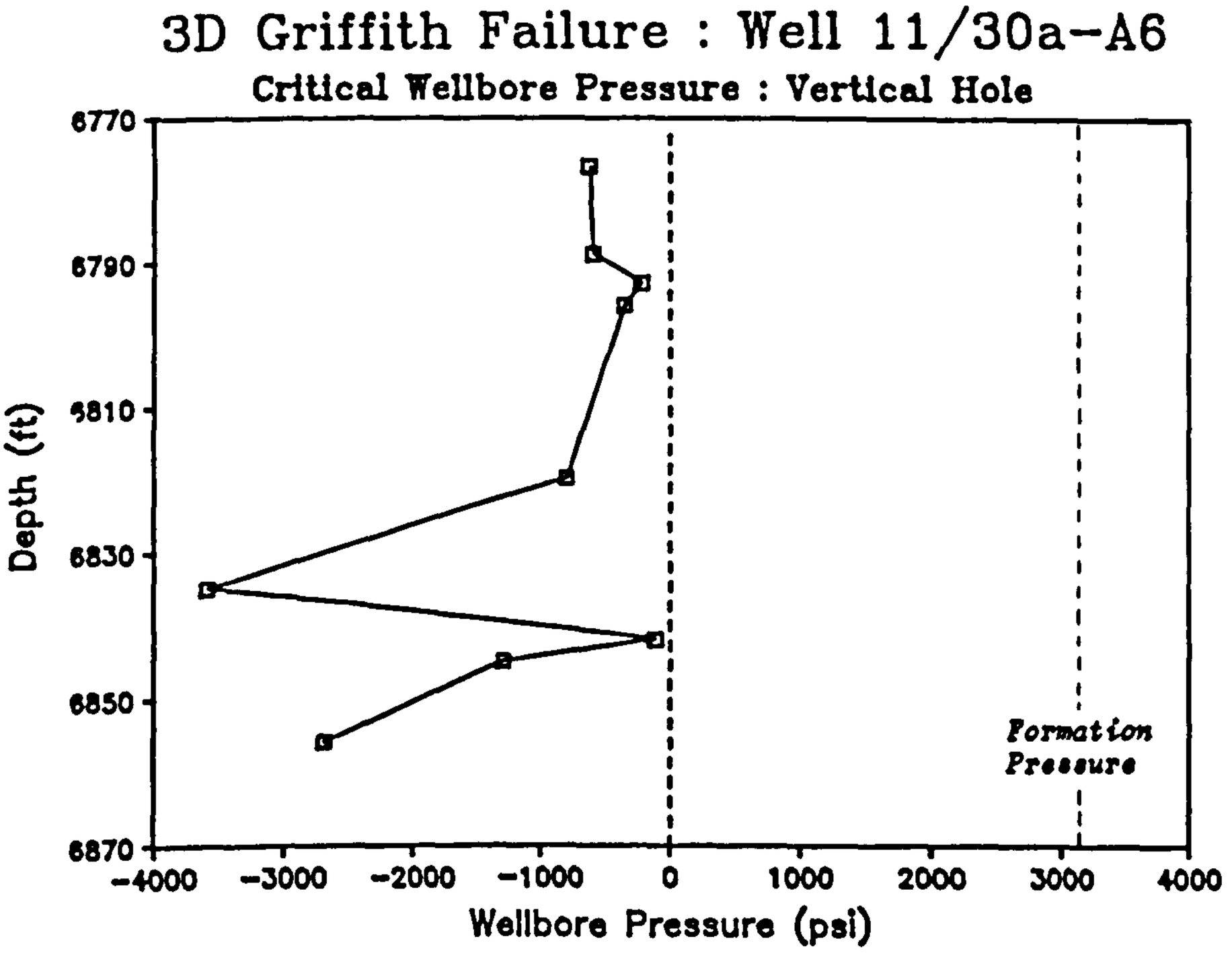

Figure 4.7(b) : Well 11/30a-A6 - Critical Wellbore Pressure 3D Griffith Analysis

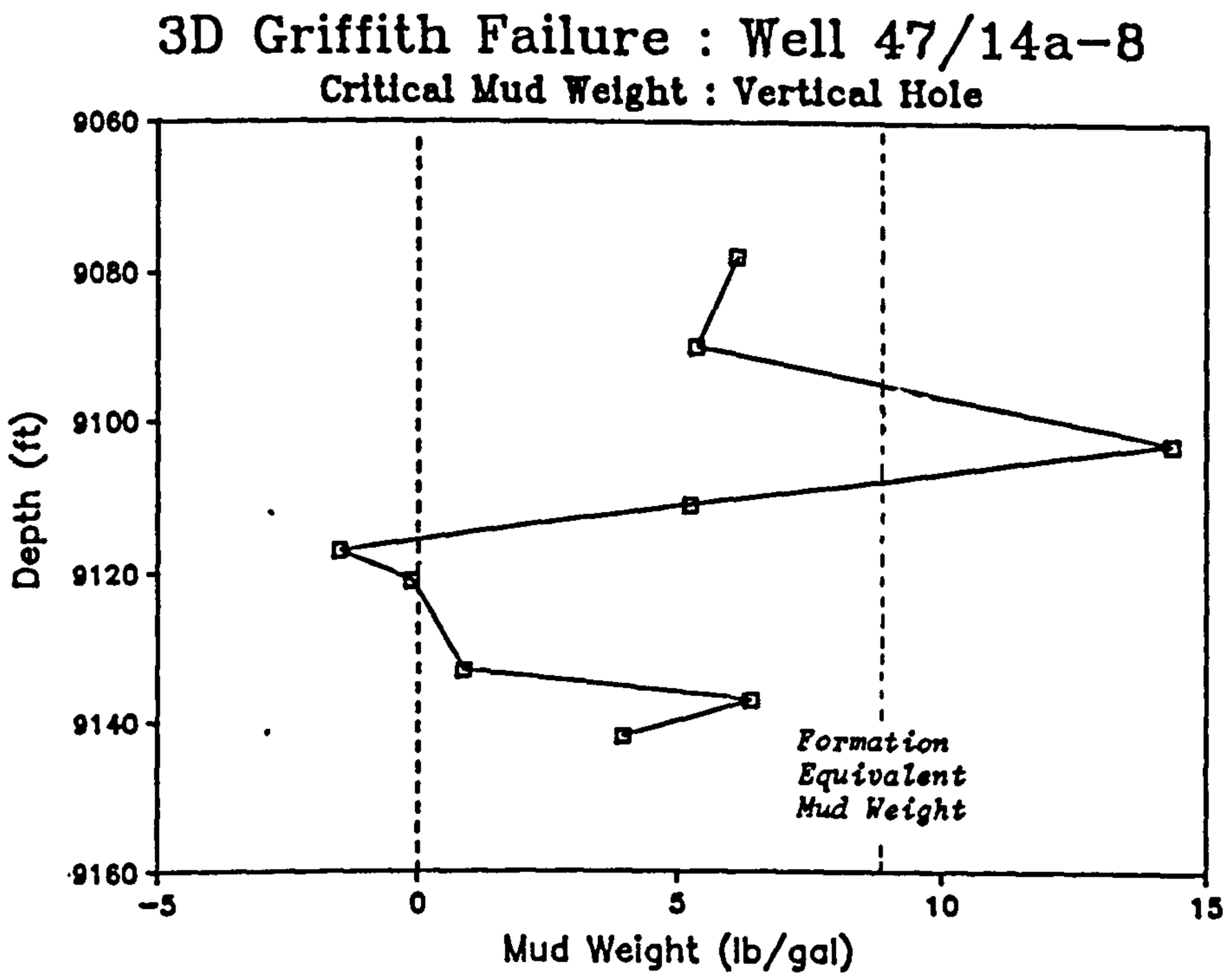

Figure 4.8(a) : Well 47/14a-8 - Critical Mud Weight 3D Griffith Analysis

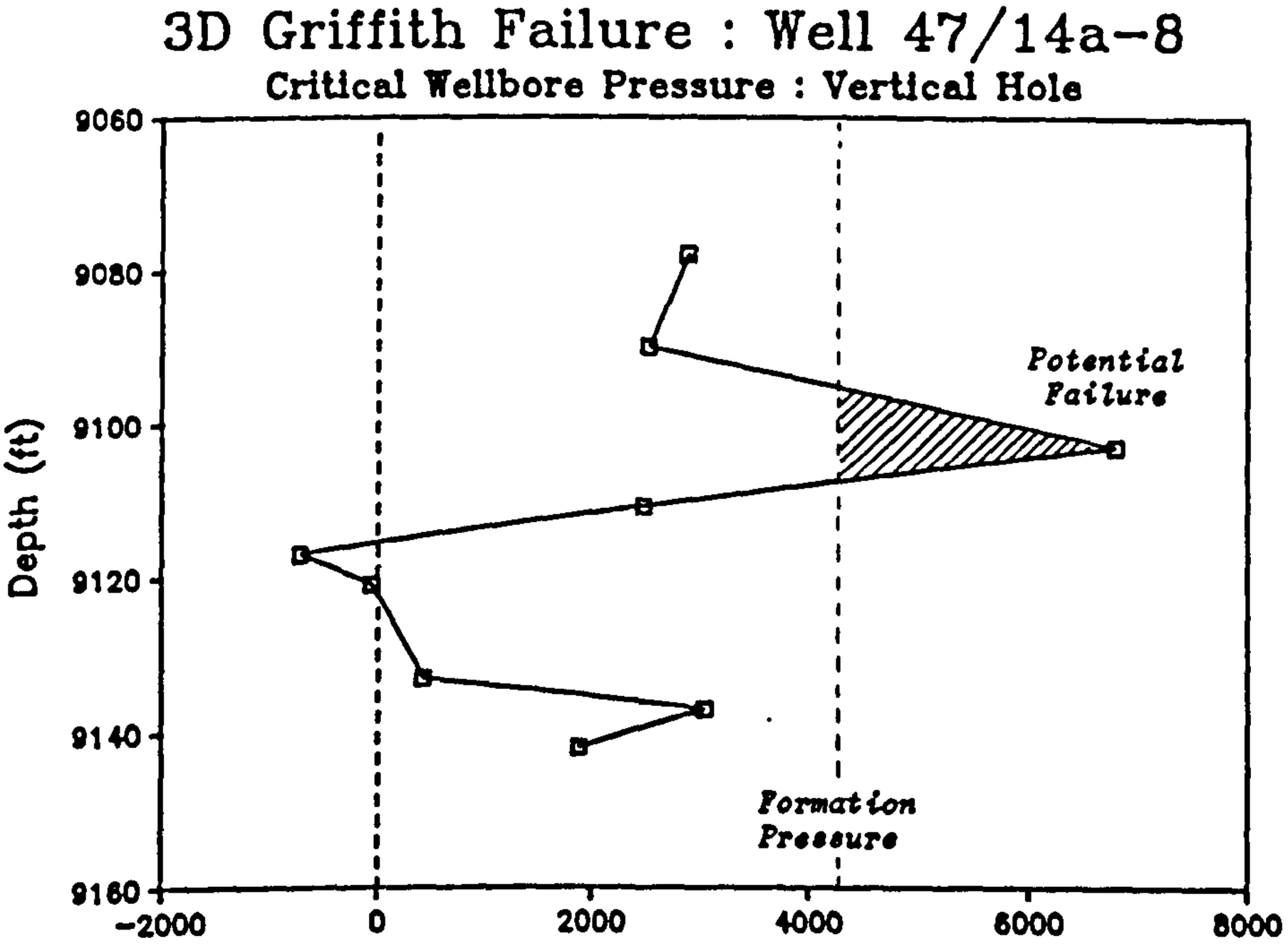

Figure 4.8(b) : Well 47/14a-8 - Critical Wellbore Pressure 3D Griffith Analysis

With the exception of Poisson's ratio, the only rock parameter which was input to the Griffith model was the unconfined compressive strength. As explained in Section 4.3.2.3, this parameter was not directly measured but derived from the respective values of cohesion and internal angle of friction. In the two wells examined, the calculated compressive strengths varied from 820 psi (5658 kPa) to over 16000 psi (110400 kPa), such values were not considered to be unrealistic of laboratory values. However, it was apparent that the C_o values, especially for well 11/30a-A6, were too high and accordingly the Griffith model predicted critical pressures which were considered to be too low when compared to that of the Mohr-Coulomb model. When rock properties are required for empirical roadway deformation formulae in the field of mining engineering, it is argued that the laboratory values of compressive strength are heavily biased 'on the strong side' and are converted to in-situ values by dividing the latter by an appropriate factor [5]. Accordingly, an investigation into the effect of reducing the compressive strength on the P_c prediction was conducted.

Figure 4.9 shows the effect of reducing the laboratory compressive strength by respectively dividing the parameter by a factor, f, of 1 to 5. It can be seen that a reduction in compressive strength had the effect of increasing the critical mud weight. It is interesting to note that in the case of well 11/30a-A6, dividing the C_o by 3 yielded a 3D Griffith P_c curve of similar magnitude and trend to that obtained using the Mohr-Coulomb model (Figure 4.10).

3D Griffith Failure : Well 11/30a-A6

Critical Mud Weight : Vertical Hole

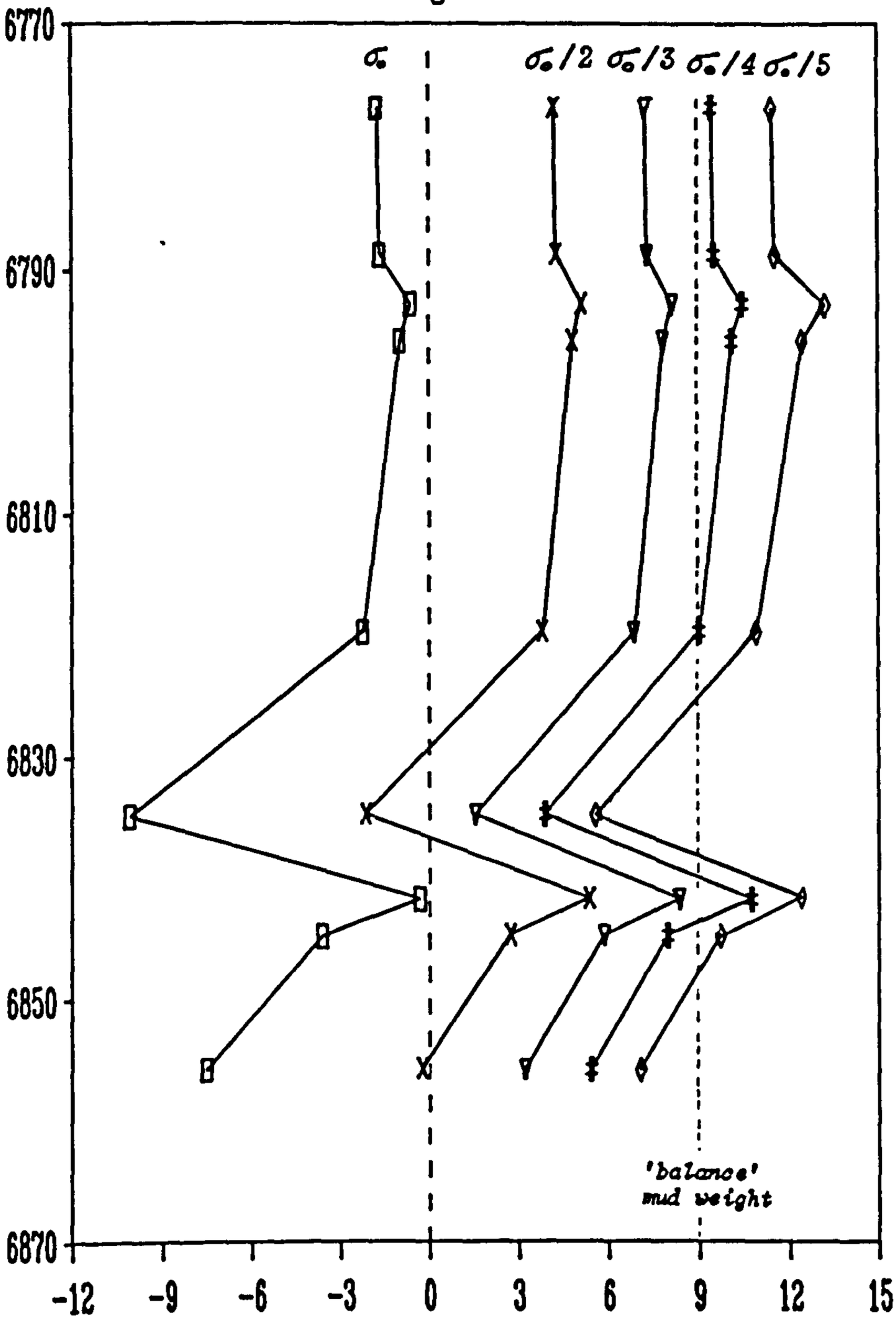

Figure 4.9 : Effect of Reducing Compressive Strength on the Prediction of Critical Mud Weight using the 3D Griffith Model

Critical Mud Weight Curve : Well 11/30a-A6

Comparison of Mohr-Coulomb & Modified Griffith Models

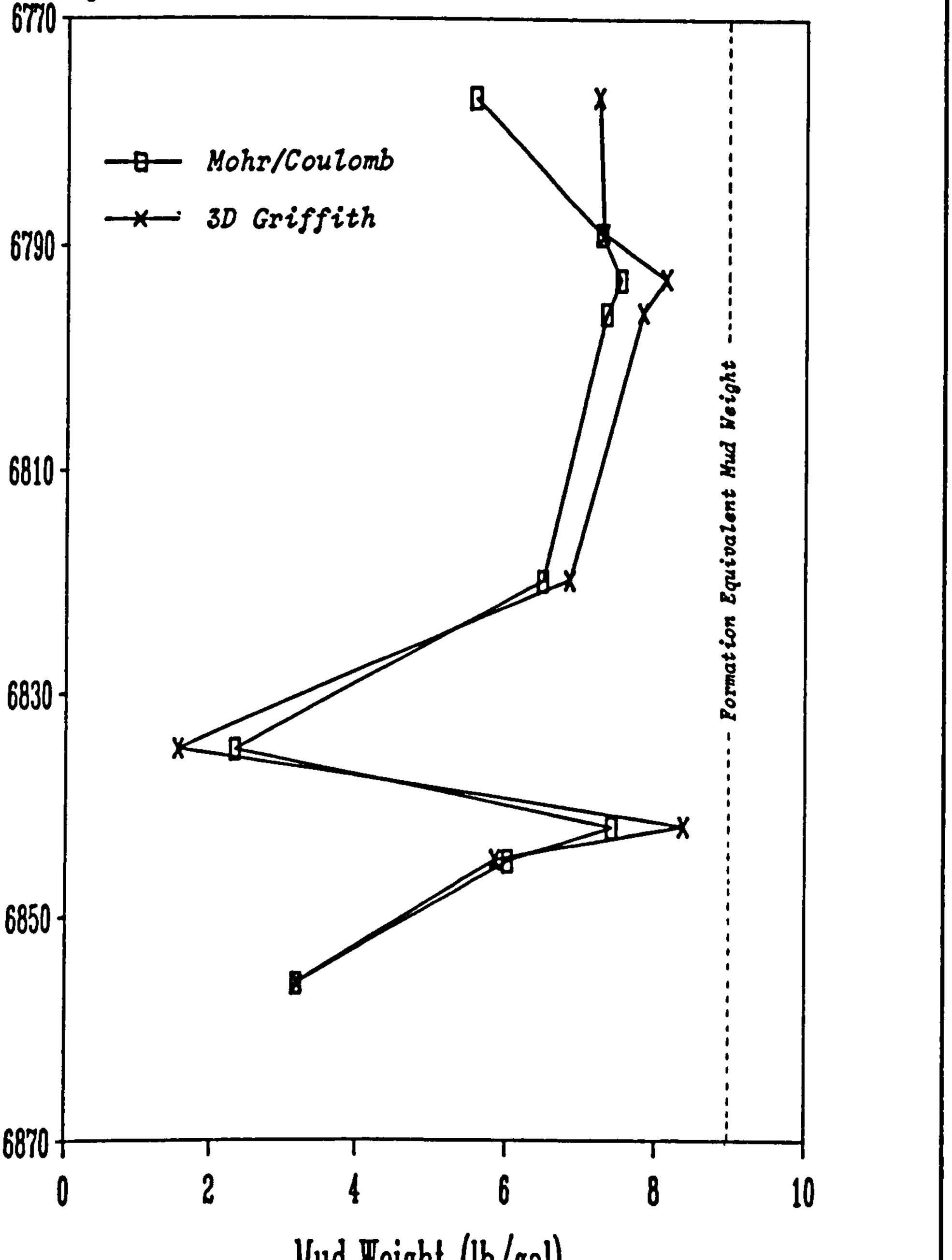

Figure 4.10 : Comparison of the Mohr/Coulomb and the 'Modified' 3D Griffith Modele for Well 11/30a-A6

4.2.5.5 Effect of Hole Inclination

Only the Mohr-Coulomb failure criteria was applied to investigate the effect of borehole inclination as the 3D Griffith model involved the simplifying assumption of $\sigma_r = \sigma_\theta$.

Critical mud weights for well 11/30a-A6 were calculated for borehole inclinations of 0°, 30°, 45°, 60° and 90° and the resulting P_c curves are presented in Figure 4.11. From an analysis of this graph, it was evident that the effect of increasing borehole inclination from vertical to horizontal was to increase the minimum mud weight required to prevent compressive failure. It can be seen that most of the P_c values were below the minimum possible mud weight and under normal drilling conditions boreholes drilled through this section up to an angle of 60° would remain stable; however, higher angle boreholes would require a mud weight of at least 10.5 lb/gal to prevent failure.

Similar curves were produced for well 47/14a-8 and are displayed in Figure 4.12. Again it was apparent that the effect of increasing hole inclination was to increase the minimum mud weight which could be carried without inducing compressive failure. In this example, increasing the borehole angle from 0° to 60° would require an average increase in mud weight of around 3 lb/gal. From an examination of Figure 4.12 it was apparent that fairly high mud weights would be required to maintain the stability of highly inclined boreholes drilled through this section. The region around 9100 ft (2775 m) would present most problems.

Mohr-Coulomb Failure : Well 11/30a-A6

Critical Mud Weight @ Various Hole Inclinations

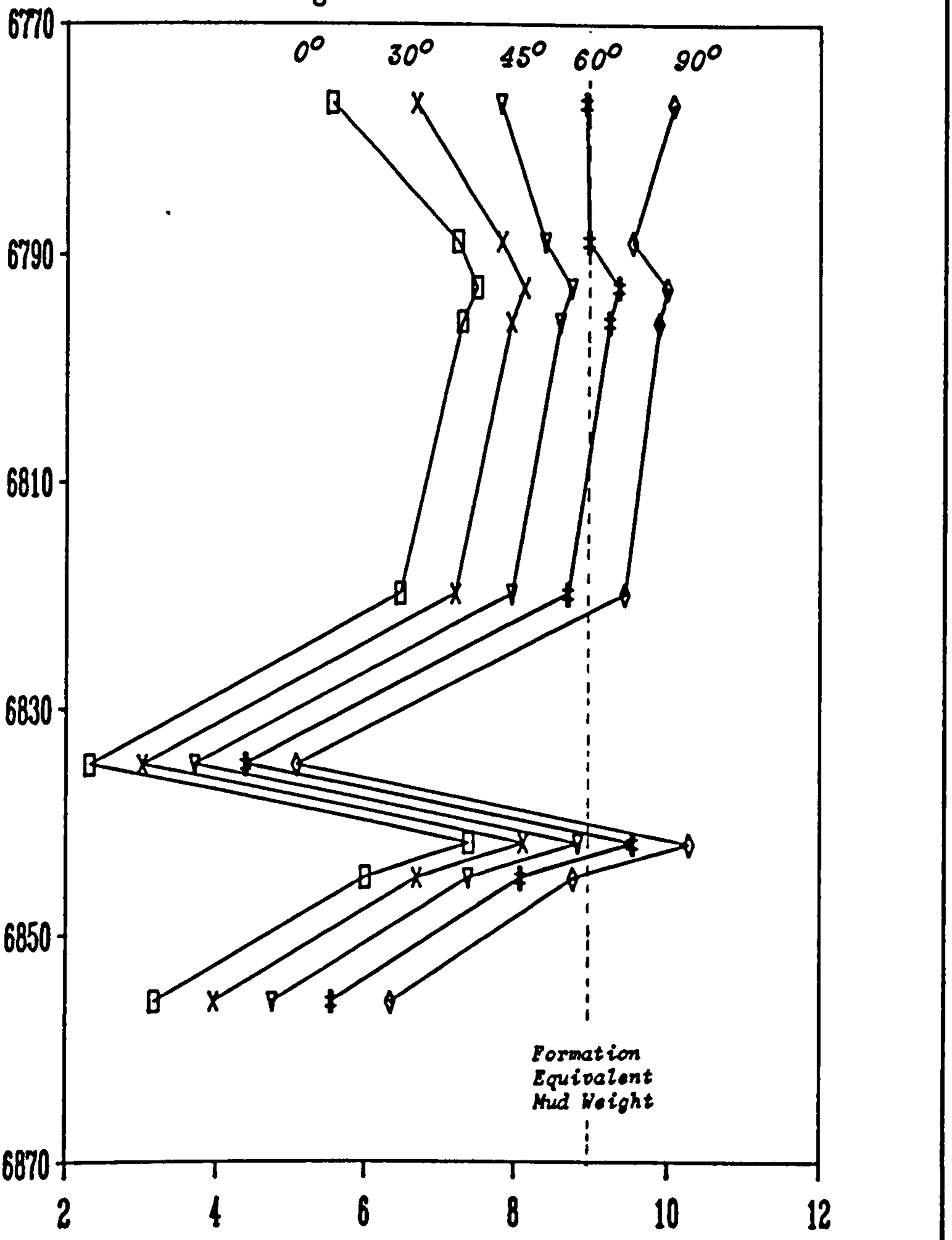

Figure 4.11 : Effect of Hole Inclination - Well 11/30a-A6 Mohr/Coulomb Model

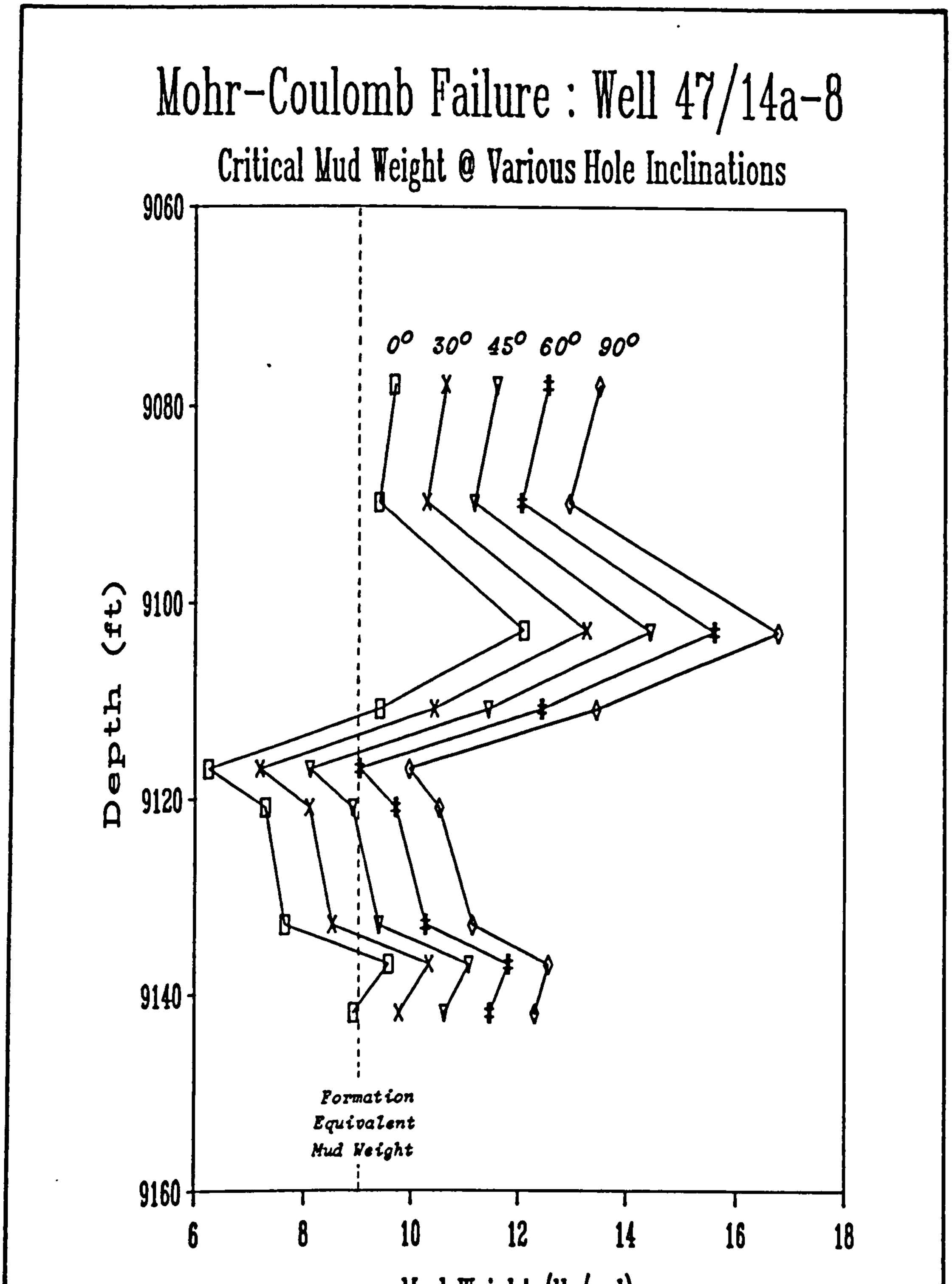

Figure 4.12 : Effect of Hole Inclination - Well 47/14a-8

Although not illustrated, increasing the borehole angle has the additional effect of lowering the maximum drawdown which may be applied to a well and accordingly increasing the zones of potential formation collapse during production.

4.2.6 Prediction of Maximum and Minimum Mud Weight Limits

Using the failure criteria developed, it was then possible to provide estimates of the theoretical maximum and minimum mud weights which could be carried in each of the two wells under investigation as a function of hole angle. For this analysis, the simplifying case of a non-penetrating fluid was assumed to estimate the upper mud weight limit, while the Mohr-Coulomb criteria was applied to predict the critical mud weight to prevent compressive failure.

Figures 4.13(a) and 4.13(b) show the calculated mud weight operating curves for wells 11/30a-A6 and 47/14a-8 respectively. For the purpose of this analysis, the P_c values calculated at each depth were averaged to give a 'typical' value over the section of interest. If required, it would have been equally possible to produce similar curves for each horizon from which rock property data was available. Referring to these figures, the region between the upper and lower lines represent the stable region. It can be seen that for each well, increasing the hole angle had the effect of decreasing the mud weight which could be carried in the well before fracturing and lost circulation would occur. In this case, inclining the hole from the vertical through 90° predicted a reduction in the

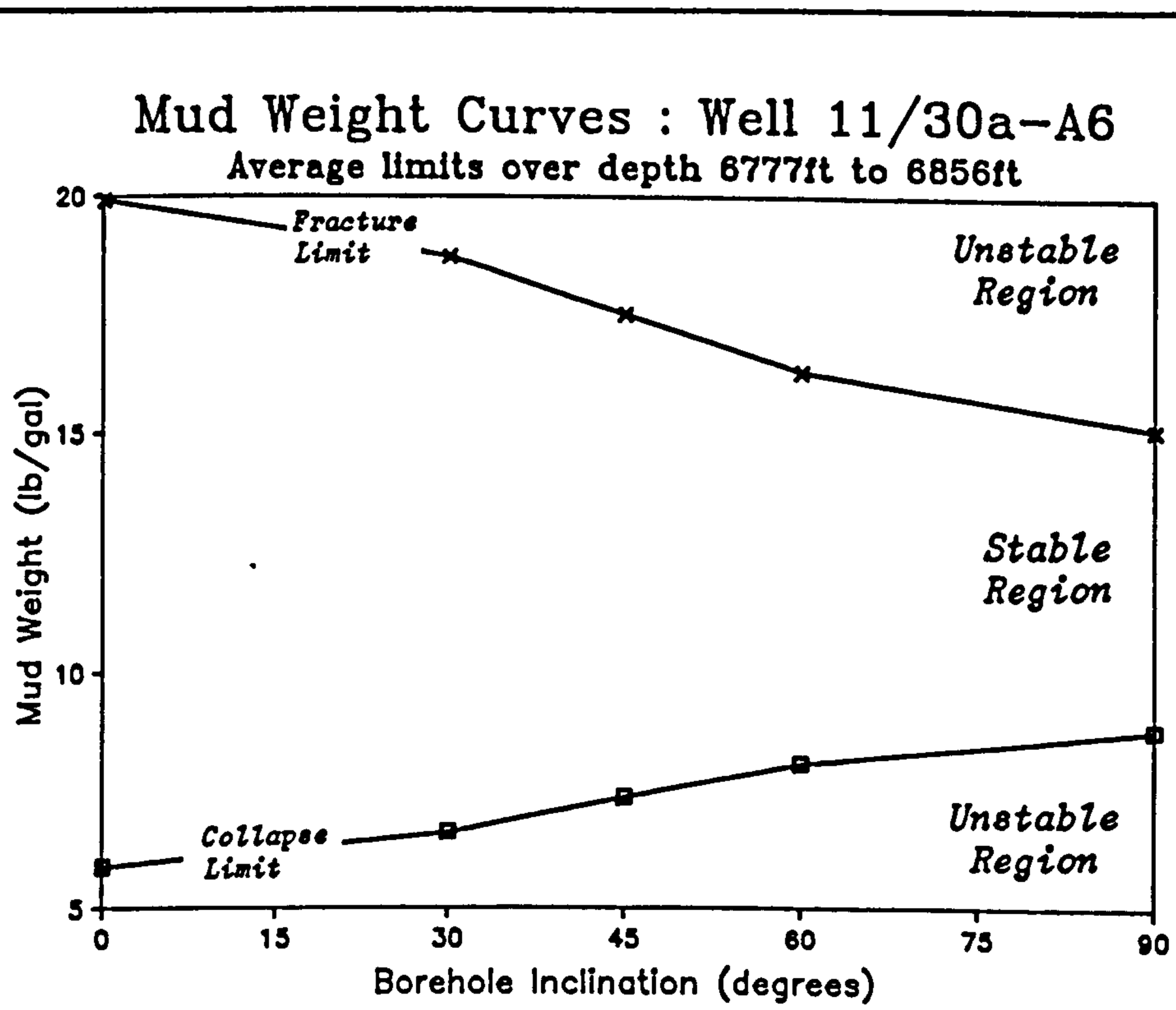

Figure 4.13(a) : Mud Weight Operating Curves - Well 11/30a-A6

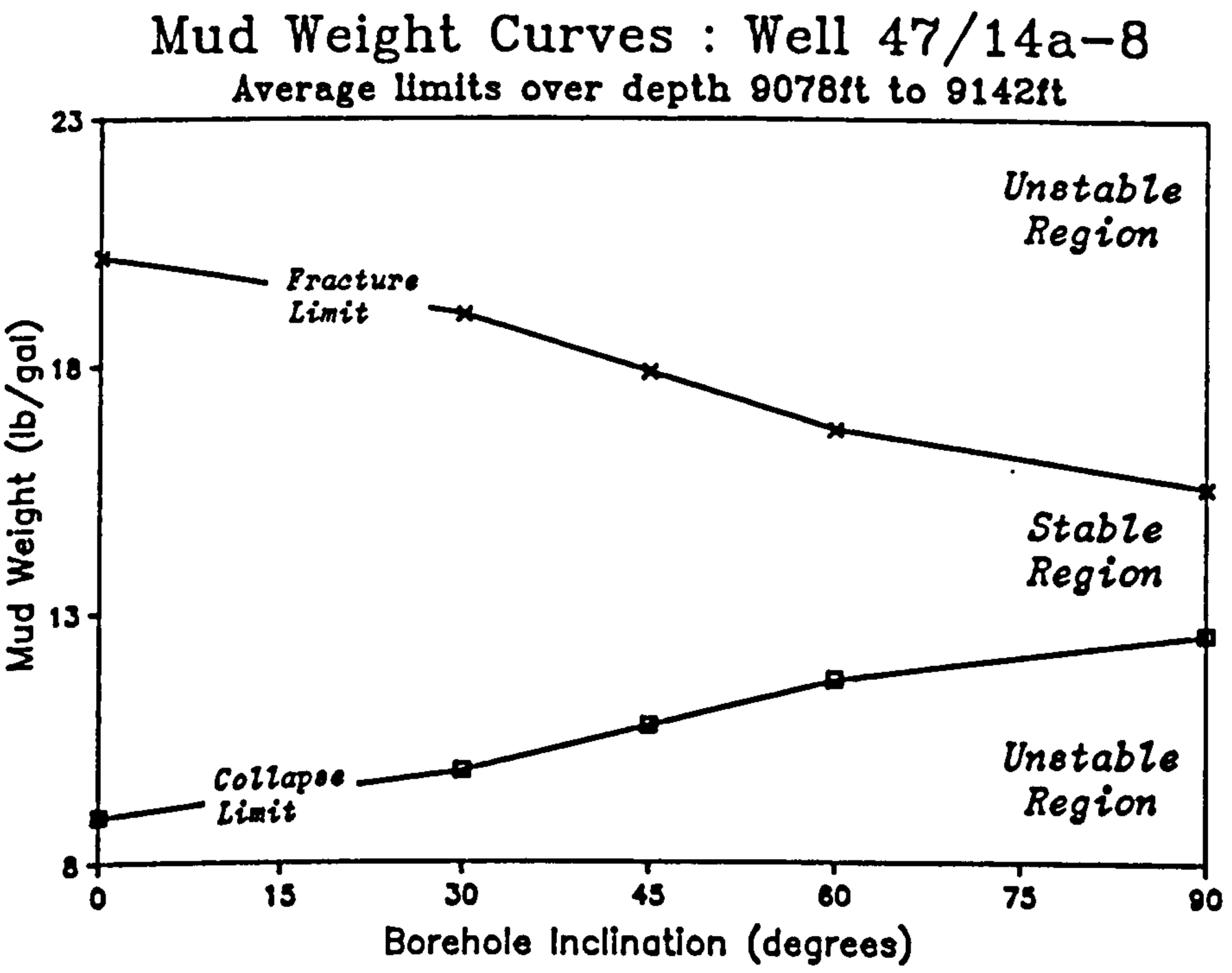

Figure 4.13(b) : Mud Weight Operating Curves - Well 47/14a-8

fracture initiation gradient of around 4 lb/gal. It was also evident that the higher angle holes required higher mud weights to prevent compressive failure. In the case of well 11/30a-A6, if the hole was drilled using a 'balance' mud weight (i.e. a mud weight equal to the formation pressure), there should be problems regarding hole stability as the P_c curve was always less than this limiting value. Well 47/14a-8 could be drilled vertically using a 'balance' mud weight. However, a 12.5 lb/gal mud would be required to drill a horizontal borehole in this formation.

From a comparison of the two graphs, it was clear that more care would be required to prevent stability problems with the latter well. Indeed, for the higher angle holes, the theoretical difference between the maximum and minimum mud weights had been reduced to around 3 lb/gal. It should be stated that the fracture initiation predictions represent the upper limit as they are solutions for a non-penetrating fluid. If flow into the formation was considered, the result would be to decrease the fracture gradient curve by a degree proportional to the penetrating quality of the rock. Such an analysis, as presented, is nevertheless useful as it is possible to predict stability limits for various horizons in the reservoir, providing, of course, that the necessary input parameters are known.

4.2.7 Discussion and Conclusions re Elastic Analysis

The analytical analysis based on elastic theory as presented in this section has shown that for an inclined borehole in a normal stress regime, tensile and compressional failure will initiate at 90° to

each other. This work also illustrated that the minimum rotated tangential stress occurs at the 'roof' (and 'floor', i.e. $\theta = 90°$ and 270°) of an inclined borehole. Thus it can be concluded that tensile failure will be initiated in this direction. After the stress concentration effects of the hole are passed, the fracture will, of course, propagate in a manner perpendicular to the direction of the least principal stress. As the maximum rotated tangential stress acts on the 'side' of the hole, ($\theta = 0°$ and 180°) it may be concluded that hole collapse will be initiated in the direction of the least principal stress.

Mohr-Coulomb and three-dimensional Griffiths failure relationships have been developed and applied to provide estimates of the optimum mud weight to prevent hole collapse for a specific well. The approach can also be used to provide an indication of the maximum drawdown pressure before hole collapse. Of the two criteria applied, the 3D Griffith criterion appeared to predict mud weights which were too low. The suggested reason for this was the compressive strength parameter, which was the only rock property input, was considered to drastically affect the results. A modification was proposed which involved decreasing the compressive strength by a factor to enable results of the same order of the Mohr-Coulomb theory to be obtained.

It may be concluded that the critical mud weight/wellbore pressure (P_c) line graphs are a clear and simple way of illustrating, in graphical terms, the regions of instability in a well as a function of depth and hole inclination. In the examples given, the data points were often far apart and accordingly no direct conculsions

could be made from the areas between the data points. However, they were primarily intended to demonstrate the method and enable a comparison to be drawn between the two wells. To obtain a more detailed picture of the stability limits of the well, formation rock samples would be required to be taken at intervals of no more than 10 ft (3.05 m).

One factor which can have a marked effect on stability predictions is the relationship between the horizontal and vertical in-situ stresses. The writer has resisted the temptation to apply Eaton's in-situ stress data as it was empirically derived for the U.S Gulf Coast (see Chapter 1). As stated the primary objective was to demonstrate the method used and as in-situ stress is a variable input parameter to the relationships, an alternative value could be inserted if it was known with confidence.

This analysis has also confirmed that inclined boreholes have a reduced ability to withstand high mud weights before fracturing while they require increased mud weight to prevent hole collapse.

4.3 THE APPLICATION AND EXTENSION OF THE YIELD ZONE CONCEPT TO PREDICT THE STABILITY OF INCLINED BOREHOLES UNDER NON-HYDROSTATIC CONDITIONS

4.3.1 Introduction

It was found in the previous section that under certain conditions, high mud weights were required to theoretically maintain the rock

surrounding the borehole in an elastic condition. The elastic approach, however, gives no indication of the post failure characteristics of the material as it merely predicts catastophic failure. As discussed in the opening chapter, it has become accepted that under such conditions, a zone of plastically deformed rock would form around the borehole which reduces the localised stress concentration. This assumption of perfect plasticity may be valid for rocks such as salt or shale which display plastic behaviour. However, for rocks such as sandstone or limestone which do not readily exhibit plastic behaviour, this assumption may be questionable. In the field of mining engineering, and also in civil engineering to some extent, the post failure characteristics of the rock surrounding an overstressed opening are considered to be that of a granular material. This is considered to be more representative of the failed rock in-situ. The failure, or yielding of the rock results in a decrease in the in-situ strength and another redistribution of the stresses, which in turn leads to the creation of a failed zone around the hole. This region has been referred to as a 'yield zone' by Wilson [5] and others [91,94] who have developed a working hypotheses for the behaviour of the yielded rock. One drawback with this approach, however, is that it deals with total stresses and employs the unrealistic, but common assumption of hydrostatic conditions.

As previous elastoplastic research has been limited to the analysis of vertical boreholes, the purpose of this section was to determine if the 'yield zone' approach could be applied to predict the stability of inclined boreholes situated under non-hydrostatic

conditions. To apply such an approach to an oilfield situation, it was necessary to modify the existing 'yield zone' equations to take into consideration the effect of pore pressure and non-hydrostatic conditions.

4.3.2 Concept of a Yield Zone

From classical elastic theory, a circular opening in a hydrostatic stress field q will have a tangential stress around its circumference of 2q. In soft rocks at depth, this value will generally be greater than the in-situ compressive strength of the rock and the opening will fail. If the broken rock at the boundary is held in place by a restraining force, friction within the broken rock will allow the pressure which can be withstood to build up as distance from the opening increases. Eventually, the resistance of the 'yielded' material is sufficient to prevent yield in the first place, and the 'abutment peak' will then be reached and thereafter the stress will diminish according to the laws of elasticity. As stated, this approach differs from perfect plasticity as the post failure characteristics of the material are assumed to be that of a granular material.

4.3.3 Yield Zone Hypothesis : Review of Formulae

The yield zone hypothesis developed by Wilson [5] and Airey [91] assumed that the redistributed stresses around a circular opening in soft rock exceed its strength. Failure was assumed to occur at the wall of the opening and was assumed to extend into the surrounding

rock to a position where the rock can support the stresses. Beyond this boundary, the rock was considered to be below its failure limit and the laws of elasticity could be applied. The failed material within the boundary was considered to be a yield zone and the post failure mechanical properties of the rock were those of a granular material.

The basic assumptions were:

(a) the opening had a circular cross-section

(b) the surrounding rock was homogeneous and isotropic

(c) plane strain conditions

(d) the virgin horizontal and vertical stresses were equal

Assumptions were also made as to the failure criteria both in the yield zone and in the elastic zone beyond. Wilson stated that although the relationship between the stress at failure (σ_1) and the confining pressure (σ_3) was frequently curved [95], an approximate linear relationship of the following form could be assumed for unbroken rock:

$$\sigma_1 = \sigma_0 + K\sigma_3 \qquad .. \ .. \ .. \ .. \ .. \ (4.28)$$

where σ_0 was the unconfined compressive strength and K was a constant for the particular rock in question and was referred to as the 'triaxial stress factor' (see Section 3.3.5.3 for a definition).

A similar criterion was also assumed in the failed rock within the

yield zone, i.e.

$$\sigma_i' = \sigma_0' + K\sigma_3 \qquad .. \quad .. \quad .. \quad .. \quad .. \quad (4.29)$$

In this case, σ_i' was the strength required to cause movement in the broken material when confined to a pressure σ_3 and σ_0' in the corresponding stress at zero confinement.

Therefore, if a circular opening in a hydrostatic field is considered and the failure criterion in the yield zone is taken as $\sigma_1 = K\sigma_3$ and in the elastic zone as $\sigma_1 = K\sigma_3 + \sigma_0$, then the resulting formulae may be transcribed as below [5]:

(a) <u>Stress Solutions within the Yield Zone</u>

$$\sigma_r = (p + p')\ [r/a]^{K-1} - p' \qquad .. \quad .. \quad .. \quad (4.30)$$

$$\sigma_\theta = K(p + p')\ [r/a]^{K-1} - p' \qquad .. \quad .. \quad .. \quad (4.31)$$

where a is the radius of the opening, p the restraint on its boundary and $p' = \sigma_0'/(k-1)$.

(b) <u>Stress Solutions at the yield/elastic boundary</u>

$$\sigma_{re} = \frac{2q - \sigma_0}{K + 1} \qquad .. \quad .. \quad .. \quad .. \quad .. \quad (4.32)$$

$$\sigma_{\theta y} = \frac{K(2q - \sigma_0)}{K + 1} + \sigma_0' \qquad .. \quad .. \quad .. \quad .. \quad .. \quad (4.33)$$

$$\sigma_{\theta e} = \frac{K(2q - \sigma_o)}{K + 1} + \sigma_o \qquad .. \quad .. \quad .. \quad .. \quad .. \quad (4.34)$$

where q is the hydrostatic stress field remote from the opening, while $\sigma_{\theta y}$ and $\sigma_{\theta e}$ are the hoop stresses acting immediately on either side of the yield and elastic boundary.

(c) <u>Stress Solutions within the elastic zone</u>

$$\sigma_r = q - A\,(a/r)^2 \qquad .. \quad .. \quad .. \quad .. \quad .. \quad (4.35)$$

$$\sigma_\theta = q + A\,(a/r)^2 \qquad .. \quad .. \quad .. \quad .. \quad .. \quad (4.36)$$

$$\text{where } A = \left[\frac{(K-1)q + \sigma_o}{K + 1}\right] x \left[\frac{2q - \sigma_o + p'(K+1)}{(p+p')\quad(K+1)}\right]^{\frac{2}{K-1}} \qquad .. \quad (4.37)$$

In a recent paper, Fama developed a new constitutive equation for a Coulomb material [96]. In his analysis, he presented more workable solutions expressing the state of stress in the elastic zone. They are given as follows,

$$\sigma_r = q - (q - \sigma_{re})\,[r_e/r]^2 \qquad .. \quad .. \quad .. \quad (4.38)$$

$$\sigma_\theta = q + (q - \sigma_{re})\,[r_e/r]^2 \qquad .. \quad .. \quad .. \quad (4.39)$$

where σ_{re} is the value of σ_r at $r = r_e$ and may be obtained from equation (4.32)

The width of the yield zone, $r = r_e$, may be found from the condition of continuity of σ_{re} at the yield/elastic boundary, viz.

$$r_e = a\left[\frac{2q - \sigma_\theta + p'(K+1)}{(p+p')\ (K+1)}\right]^{\frac{1}{K-1}} \qquad .. \quad .. \quad .. \ (4.40)$$

Units : The above equations require consistent units for the input parameters. Wilson stated that all stress values should be input in MPa while the radius values are input in metres.

The general form of the stress distribution is shown in Figure 4.14. Wilson stated that the parameter σ_θ appearing in the final form of the equations should be taken as the in-situ unconfined strength of the rock in the elastic zone and should not be confused with the unconfined compressive strength as determined in the laboratory. This value can be obtained from the unconfined compressive strength of a laboratory tested specimen by dividing the latter by an appropriate factor, f. This factor, which takes into account the in-situ structural characteristics of the rock in question. The values for the factor are [5]:

f = 1 for strong, massive unjointed rock

2 for widely spaced joints or bedding planes in rock

3 for more jointed but still massive rock

4 for well jointed and weaker rocks

5 for unstable seatearth and closely cleated rock such as coal or may be used when the general conditions are unknown

6 and 7 for for weak rocks in the neighbourhood of fault zones

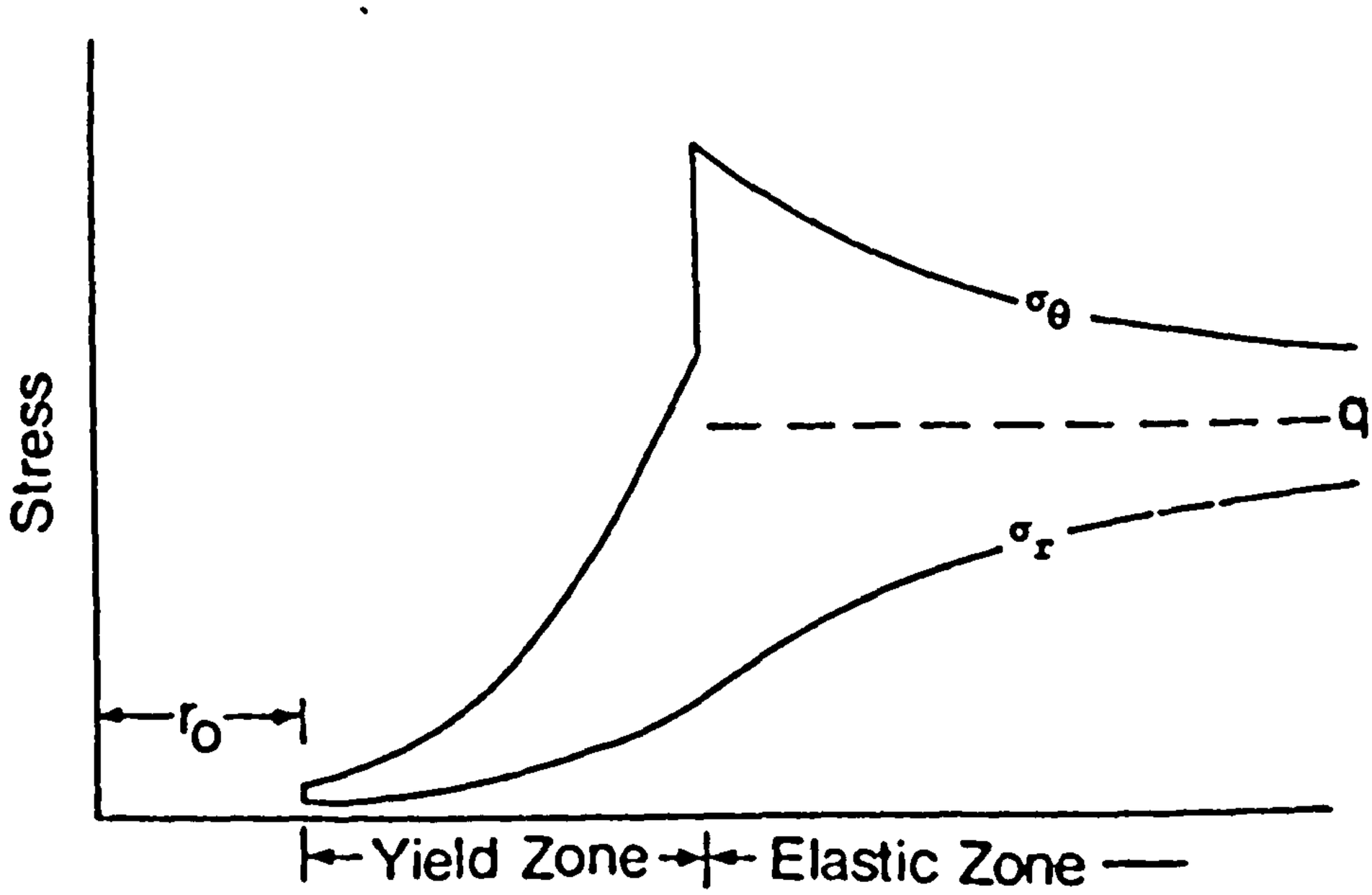

Figure 4.14 : Stress Distribution in the Yield and Elastic Zones Surrounding a Mine Roadway [5]

4.3.5 Application of the Yield Zone Concept to an Oilfield Situation

To apply the yield zone concept to an oilfield situation it was necessary to modify the above formulae to include the effect of pore pressure and mud weight, and to extend the hypothesis to consider non-hydrostatic stress conditions in order to examine inclined boreholes. Further modifications were also necessary to include the effect of fluid flow into or out of the formation.

4.3.5.1 Effect of Pore Pressure

The effective stress concept (Section 1.3.2.1) was introduced to the equations and used throughout the calculations. In the yield zone, the σ_r and σ_θ parameters were already defined in effective stress terms as they were derived from laboratory failure criteria at zero pore pressure. For the yield/elastic boundary and elastic zone, the pore pressure (P_p) was subtracted from the in-situ principal stress values.

4.3.5.2 Effect of Mud Weight

The mud pressure in a borehole provides the same function as the lining resistance (p) in the above equations, i.e. it applies internal pressure to the walls of the opening to prevent collapse. As effective stresses were used in the modified approach, a zero value of p was equivalent to a mud/pore pressure balance. Therefore the lining resistance was considered to be the difference between

the mud pressure and the pore pressure and was designated P_m in the modified set of equations.

The p' parameter (the augmentation to lining resistance) was considered to have a value of 690 psi (100 kPa) in accordance with Wilson [5].

4.3.5.3 Application to Non-Hydrostatic Stress Conditions

In the original formulae, the 2q parameter was equivalent to the tangential or hoop stress acting at a point on the wall of the opening. It was therefore required to determine the hoop stress acting around the periphery of an inclined hole.

This was accomplished by rotating the principal stresses to the borehole coordinate frame by means of direction cosines in the manner described in Section 4.2.3. The respective in-situ rotated horizontal stresses were then inserted into equation (4.2) to obtain the hoop stress which acted tangentially at the point under consideration. The tangential stress value at the point of interest was termed σ_t, and for the case of a horizontal hole under hydrostatic conditions, was equivalent to the value, 2q. As the σ_t parameter was expressed as total stresses, it was necessary to subtract pore pressure to obtain σ_t in terms of effective stress, i.e. $(\sigma_t - P_p)$

The equations describing behaviour at the yield/elastic boundary and in the elastic region required modification in the manner σ_t was

calculated. For biaxial loading, elastic theory reveals that the hoop stress diminishes to the far field value of in-situ stress acting at 90°, while the radial stress increases to the in-situ stress value acting in the same direction. Thus, the radial stress acting in the σ_x direction (i.e. the side of the hole) is dependent on the in-situ stress σ_x, but the hoop stress acting along the σ_x direction is dependent on the in-situ stress σ_y. Similar modifications are required for the 'roof' of the hole. Therefore, this has to be taken into account when calculating the tangential stress, σ_t.

For example, if the stress distribution in the radial direction along the σ_x axis (i.e. $\theta = 0°$) is to be calculated, the procedure required to calculate σ_t would be as follows. To determine the radial stress at the yield/elastic boundary, the σ_t value obtained from setting $\theta = 0°$ in equation (4.2) would be used to calculate σ_{re} [from equation (4.43)]. This σ_{re} value would then be inserted into equation (4.46) to calculate the radial stress in the elastic zone. To determine the hoop stress at the yield/elastic boundary, the σ_t value obtained from setting $\theta = 90°$ in equation (4.2) would be used. To calculate the hoop stress in the elastic zone, this σ_t value would be inserted into equation (4.43) to obtain a value for σ_{re} which would then be substituted into equation (4.47). Alternatively, if the stress distribution along the σ_y axis was desired, θ would be set to 90° to calculate σ_t for the radial stress and set to 90° to determine the σ_t input parameter required to calculate the hoop stress.

The σ_t input parameter required to calculate the radius of the yield zone is obtained by taking $\theta = 0°$ if the width at the 'side' of the hole is required, $\theta = 90°$ if the width at the 'roof is required.

4.3.5.4 Modified Stress Solutions

(a) Modified Stress Solutions within the Yield Zone

$$(\sigma_r - P_p) = (P_m + p')\ [r/a]^{K-1} - p' \qquad .. \quad .. \quad .. \ (4.41)$$

$$(\sigma_\theta - P_p) = K(P_m + p')\ [r/a]^{K-1} - p' \qquad .. \quad .. \quad .. \ (4.42)$$

(b) Stress Solutions at the yield/elastic boundary

$$(\sigma_{re} - P_p) = \frac{(\sigma_t - P_p) - \sigma_\bullet}{K + 1} \qquad .. \quad .. \quad .. \ (4.43)$$

$$(\sigma_{\theta y} - P_p) = \frac{K[(\sigma_t - P_p) - \sigma_\bullet]}{K + 1} + \sigma_\bullet' \qquad .. \quad .. \quad .. \ (4.44)$$

$$(\sigma_{\theta e} - P_p) = \frac{K[(\sigma_t - P_p) - \sigma_\bullet]}{K + 1} + \sigma_\bullet \qquad .. \quad .. \quad .. \ (4.45)$$

(c) Stress Solutions within the elastic zone

$$(\sigma_r - P_p) = (q_r - P_p) - [(q_r - P_p) - \sigma_{re}]\ [r_e/r]^2 \qquad .. \ (4.46)$$

$$(\sigma_\theta - P_p) = (q_\theta - P_p) + [(q_\theta - P_p) - \sigma_{re}]\ [r_e/r]^2 \qquad .. \ (4.47)$$

where $q_r = [0.5(\sigma_x+\sigma_y) + (\sigma_x-\sigma_y)Cos2\theta]$ .. .. (4.48)

$q_\theta = [0.5(\sigma_x+\sigma_y) - (\sigma_x-\sigma_y)Cos2\theta]$ .. .. (4.49)

Note: σ_x and σ_y are the rotated in-situ principal stresses and O is the angular position around the wall of the borehole and is measured from the σ_x axis.

The modified formula for the radius of the yield zone is,

$$r_e = a\left[\frac{(\sigma_t-P_p) - \sigma_\theta + p'(K+1)}{(P_m+p')\ (K+1)}\right]^{\frac{1}{K-1}} \quad .. \quad .. \quad .. \quad (4.50)$$

Units : To avoid complicating the above formulae further by including conversion factors, the input parameters have been left in metric units (see Section 4.3.3).

4.3.6 Implications of Modified Formulae

To fully explore the significance of these modified formulae, specific values for the parameters have been taken. Three typical rocks having the following properties were considered:

weak rock : $K = 2.5$, $\sigma_\theta = 5$ MPa (725 psi)

medium rock : $K = 3.5$, $\sigma_\theta = 15$ MPa (2175 psi)

strong rock : $K = 4.5$, $\sigma_\theta = 25$ MPa (3625 psi)

Unless otherwise indicated, an overburden stress of 1 psi/ft (22.6 kPa/m) was assumed, the pore pressure gradient was considered to be 0.465 psi/ft (10.5 kPa/m) and the horizontal to vertical principal stress ratio was assumed to be 0.825:1 (corresponding to $\gamma = 0.4$). This stress ration may appear to be unrealistic at very shallow depths when compared to Eaton's data (see Section 1.6.3). However, as with the elastic investigation, the writer considered that employing a constant stress ratio would reduce the number of uncertain variables involved, which would allow clearer conclusions to be drawn. As stated, the in-situ stress ratio is a variable in the yield zone equations and if the regional in-situ stress ratio was known, alternative curves could be reproduced using the same technique. In this investigation, the radius of the borehole (a) was maintained dimensionless, while r/a should be taken as the dimensionless radial distance and r = a at the periphery of the hole.

4.3.6.1 Effect of Mud Weight

The effect of using a 9, 9.5, 10 and 10.5 lb/gal mud weight on the width of the yield zone at various depths was examined. These values were then inserted into equation (4.50) to produce the graphs shown in Figure 4.15.

Referring to this figure, which is only applicable to a vertical well, it was evident that if a 'balance' mud weight was used (i.e. 9 lb/gal) while drilling through weak rock, at depths below 1000 ft (305 m) a yield zone would form and would extend a considerable

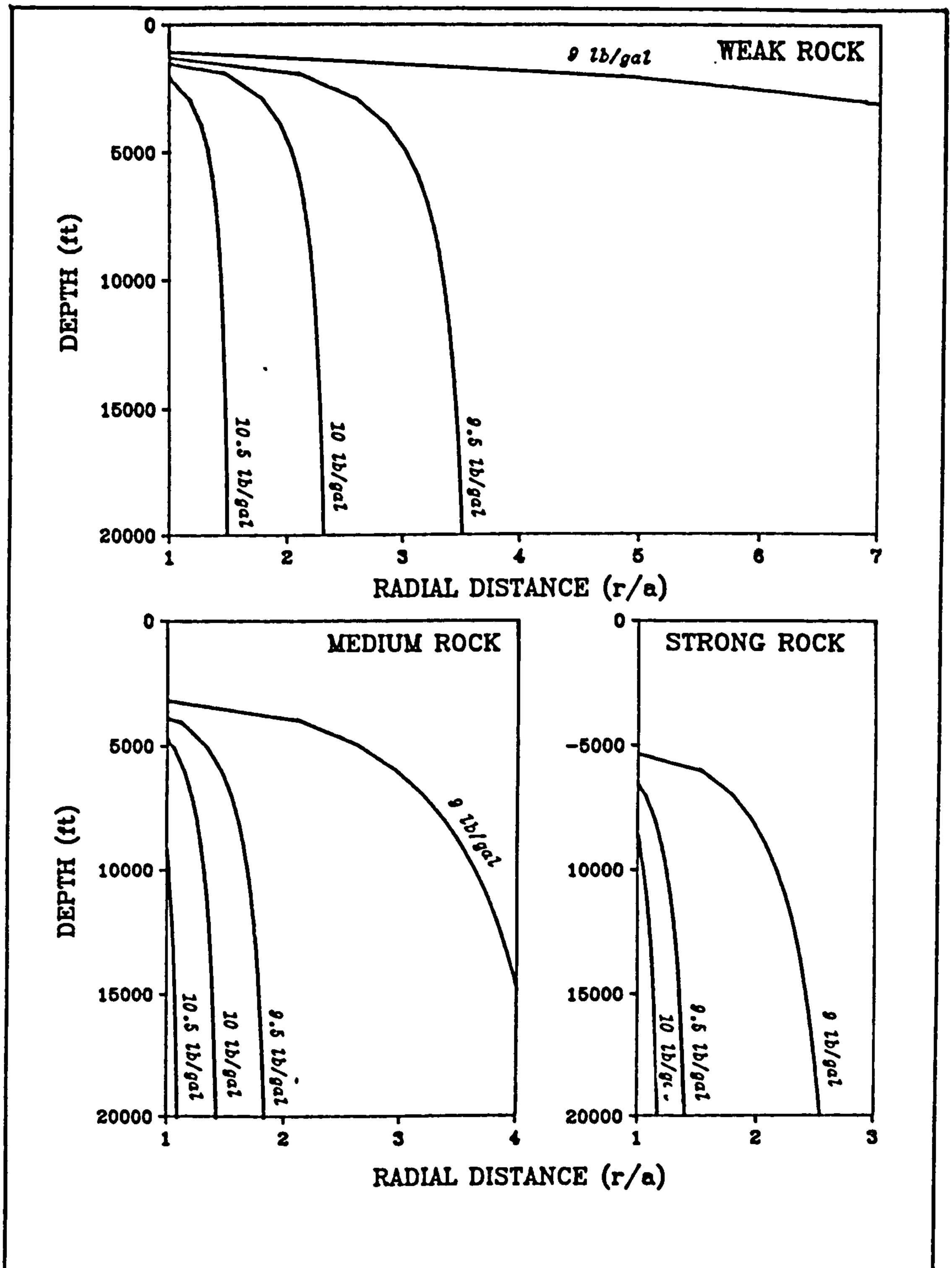

Figure 4.15 : Effect of Mud Weight on the Width of a Yield Zone

distance into the formation. However, increasing the mud weight to 9.5 lb/gal, had the effect of reducing the radius of the yield zone to between r/a = 3 to 3.5. Increasing the mud weight to 10 and 10.5 lb/gal respectively had the effect of reducing the radial extent of the yield zone even further.

In medium strength rock, it was apparent that a yield zone would not develop until a depth of around 3500 ft (1225 m) if the well was drilled in balance. From this figure, it can be seen that the radius of the yield zone using this mud weight was appreciably smaller than the yield radius calculated for the weaker rock. Again, increasing the mud weight had the desired effect of reducing the yield radius while allowing greater depths to be drilled without the formation of such a zone. If the well was drilled using a 10.5 lb/gal mud, a yield zone would only exist at depths below 9000 ft (2745 m). The benefit to be achieved by increasing the mud weight further would be small.

With strong rock, a yield zone would not develop at depths below 5000 ft (1525 m) if the well was drilled in balance. Even then, the yield zone would only extend a small distance into the formation. As can be seen from the graph, only the 9.5 and 10 lb/gal mud weight curves are additionally shown as it was calculated that a 10.5 lb/gal mud would maintain the strong rock within its elastic limit.

From the above analysis, it is clear that rock strength plays a major role in determining the stability of a wellbore. It is also apparent that a sufficient mud weight can be used to limit the

extent or to prevent the formation of a yield zone forming around the hole. As the curves tend to become almost vertical with depth, it can be concluded that at great depth, it is the mechanical properties of the rock which dictates the stability of the hole.

4.3.6.2 Effect of Borehole Inclination

It has been established that for an inclined borehole under non-hydrostatic stress conditions, compressional failure will be initiated in the direction of the least principal stress (i.e. the σ_x direction in this analysis). As a yield zone is initiated due to compressive failure, it was therefore apparent that the shape of a yield zone around an inclined hole would not be circular. To investigate the development of a yield zone around inclined holes, the radius of the yield/elastic boundary was calculated at pre-determined angular intervals around the periphery of the hole. The hole was assumed to remain circular throughout. This analysis was accomplished by calculating the effective tangential stress acting on the periphery of the borehole at the point of angular interest using equation (4.2), the in-situ stresses being rotated into the borehole coordinate frame in the usual manner. The respective values of effective tangential stress were then inserted into equation (4.50) to arrive at a series of values for the radius of the yield zone. As these values were in polar coordinate form, it was necessary to transform the data to rectangular coordinates to facilitate plotting by computer (see Section 1.2.6).

To illustrate the development of a yield zone around an inclined

hole under non-hydrostatic conditions, the above procedure was followed for the case of a 60° hole situated in medium strength rock. The various stages of development were obtained by reducing the mud weight in the borehole by increments. The resulting graphical outputs are shown in Figure 4.16.

Figure 4.16(a) shows the rock surrounding the hole at its elastic limit. In this example, an 11.5 lb/gal mud weight was used. Compressive failure is initiated where the difference between the tangential and radial stress is the greatest. As this was an inclined hole, the greatest stress concentration acted in the σ_x direction, therefore this was the region where the yield zone would initiate. Figure 4.16(b) shows what will be termed the first stage of yielding. The 11 lb/gal mud weight was sufficient to prevent yielding in the 'roof' of the hole, but insufficient to prevent yielding in the 'side' of the hole. The first yield stage is therefore characterised by the growth of two separate yield domains. Figure 4.16(c) shows the effect of further decreasing the mud weight to 10 lb/gal and the onset of the second stage of yielding. It can be seen that the two yield regions coalesce as to form a continuous elliptical yield zone around the hole, with the greater radius being in the direction of the least principal stress. The yield zone was found to increase in size with further reduction in the mud weight.

As the tangential stress acting on the hole periphery changes with hole inclination, it was apparent that the shape of the yield zone would change accordingly. To investigate this effect, the shape of the yield zone was determined for boreholes of angles 0°, 30°, 60°

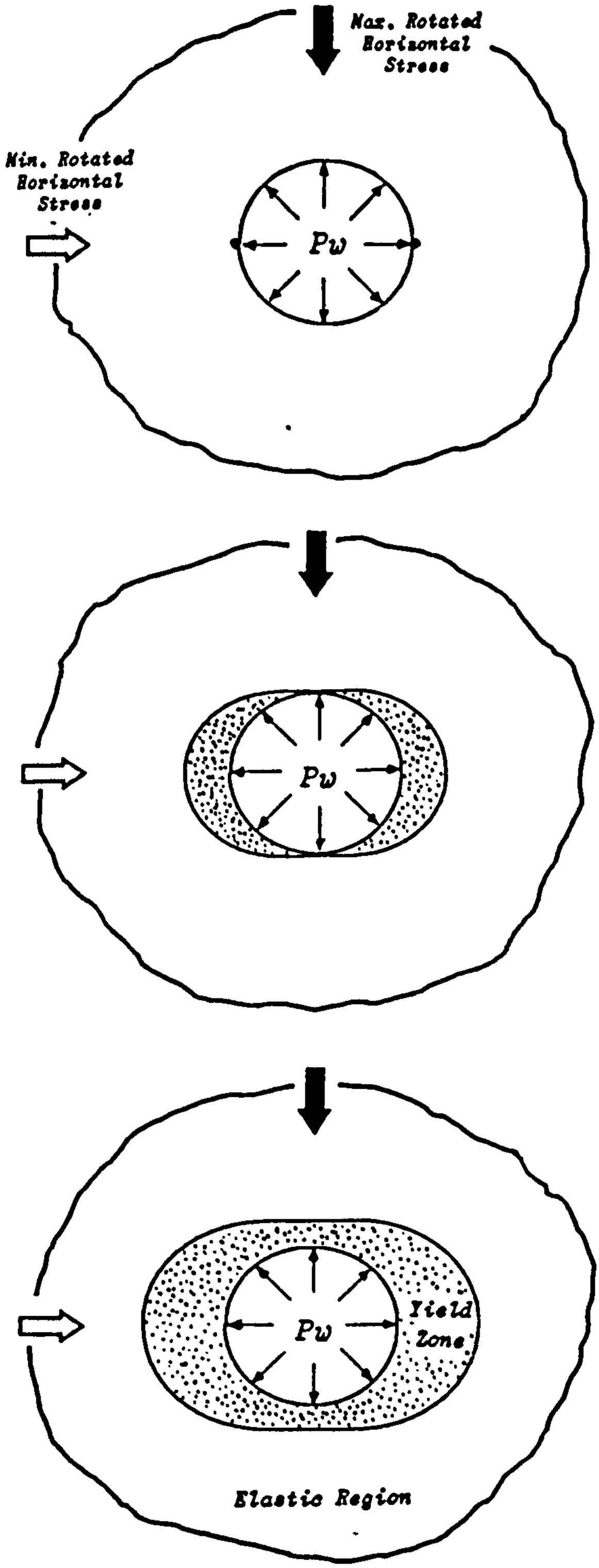

(a) Elastic Limit

(b) First Stage of Yielding

(c) Second Stage of Yielding

Figure 4.16 : *The Development of a Yield Zone Around an Inclined Borehole*

and 90°. The ratio of the horizontal to vertical stress also affects the tangential stress and therefore the shape of the yield zone. To allow for this, two stress ratios were chosen. These were termed a 'low' horizontal to vertical stress ratio (0.75:1) and a 'high' horizontal to vertical stress ratio (0.825:1). Such values were obtained by inserting Poisson's ratio equal to 0.35 and 0.4 repectively into equation (4.27). A normal pore pressure was assumed. The results are shown graphically in Figure 4.17. The 'low' stress ratio results are given in the left-hand column while the results using a 'high' stress ratio are presented in the right-hand column.

For the vertical hole, it can be seen that the yield zone was larger with the higher stress ratio. This was to be expected as, according to theory, the radius of a yield zone is proportional to the tangential stress acting on the periphery of the hole. With the 30° hole, the yield zone for each stress ratio was observed to be elliptical in shape and had increased in size in the σ_x direction. Inclining the hole to 60° produced an interesting effect for the low stress ratio hole. It was found that the radius of the yield zone in the σ_y direction had reduced in size, thus indicating that the hole was becoming more likely to fail in tension if the mud weight was excessive. A similar effect was observed with the high stress ratio hole, although it appeared more ovaloidal in shape. The yield radius in the σ_y direction was observed to reduce even further with the horizontal hole and the low stress ratio. Again this was due to the reduced tangential stress acting on the periphery at this point. With the high stress ratio, the yield zone shape was still ovaloidal except for a slight reduction in the radius at the top of the hole.

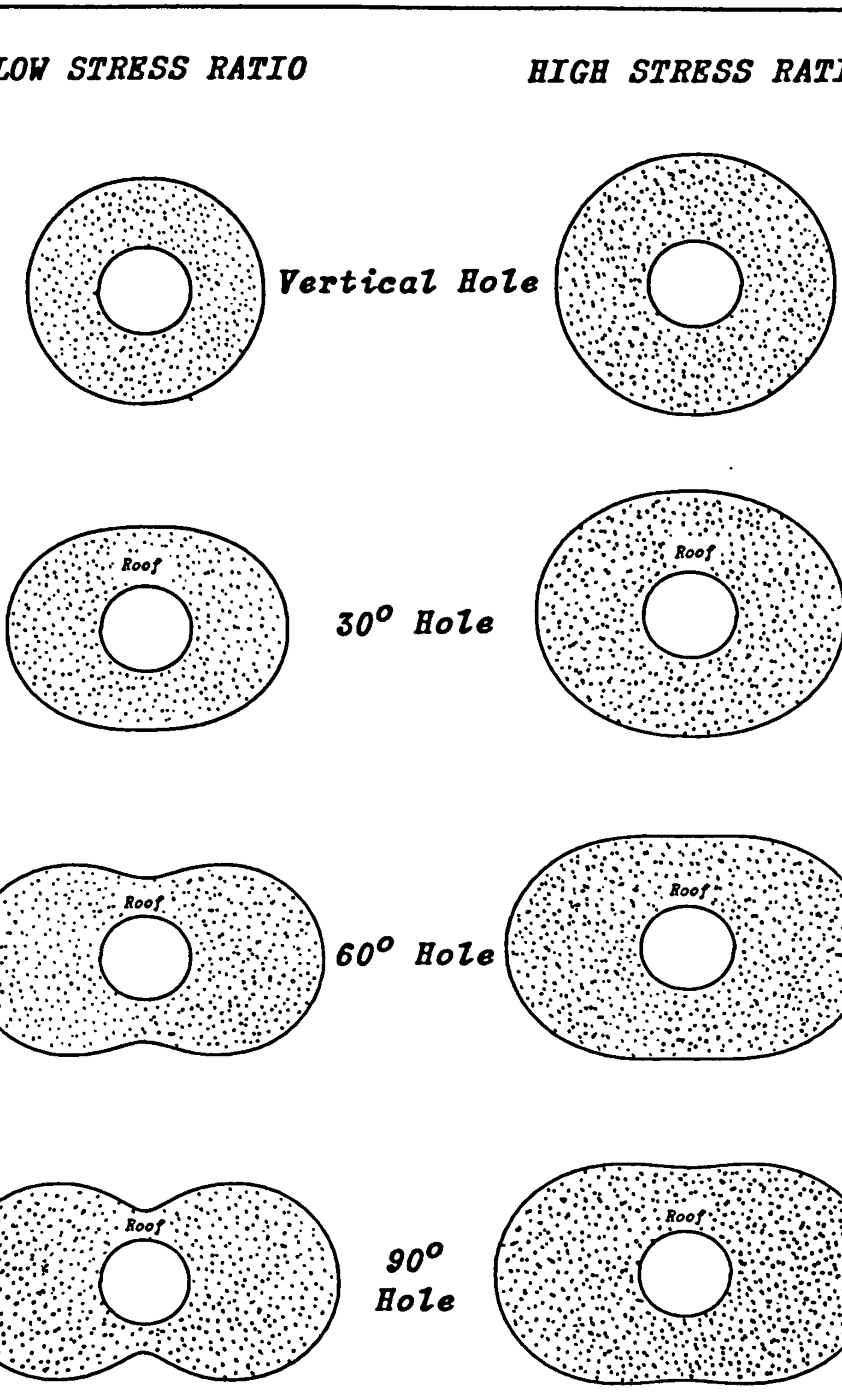

Figure 4.17 : The Shape of a Yield Zone Around Holes of Various Inclinations

It may therefore be concluded that the shape of the yield zone around an inclined hole not only depends upon the hole inclination but is affected by the regional in-situ stress ratio. It has been shown that the lower stress ratio produces the more distorted yield zone boundary.

In the above analysis, the shape of the hole was assumed to remain circular otherwise the equations could not have been applied. In the field, however, the borehole may not be circular. It has been shown that the greatest compressive stress acts at the 'side' of an inclined borehole, i.e. in the direction of the minimum rotated horizontal stress. This induces shear failure which may cause hole break-out [Figure 4.18(a)]. There is field evidence that the direction of the minimum horizontal stress can be inferred from break-out orientation [97]. Applying the yield zone concept, if the yielded material is assumed to fall into the hole, then the hole break-out will feasibly occur in the manner discussed above [Figure 4.18(b)].

There is also field experience with inclined holes to the contrary which indicates that the hole is elongated in the direction of the greatest rotated horizontal stress, i.e. the 'roof' of the hole [98]. This may again be explained using the yield zone concept if the failed material is assumed to be held in place by the mud cake and the weight of mud in the hole. Wilson [93] developed an empirical equation which may be used to predict the closure of mine roadways as a result of the formation of a yield zone. The writer,

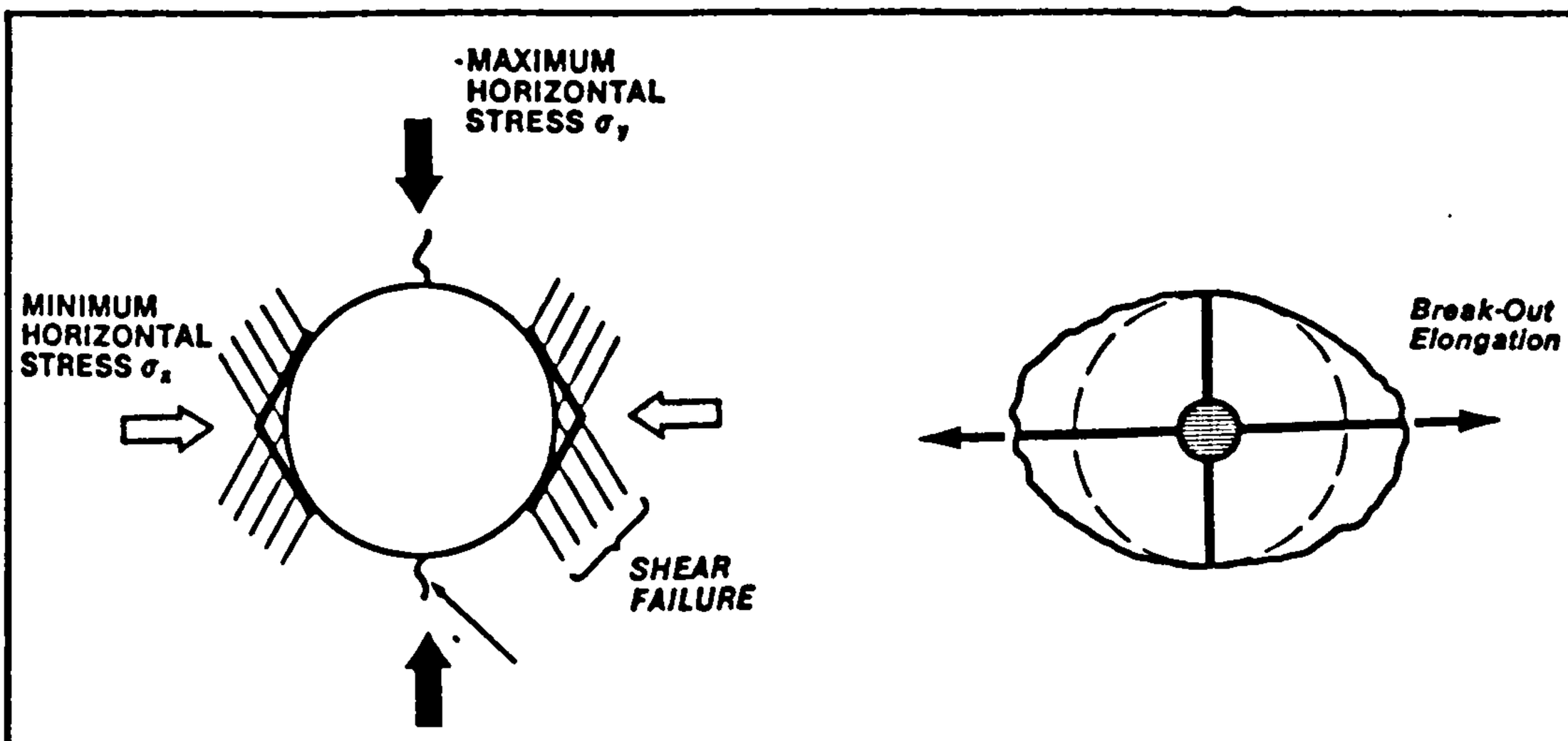

Figure 4.18(a) : Breakout orientation Produced by Elastic Failure [41]

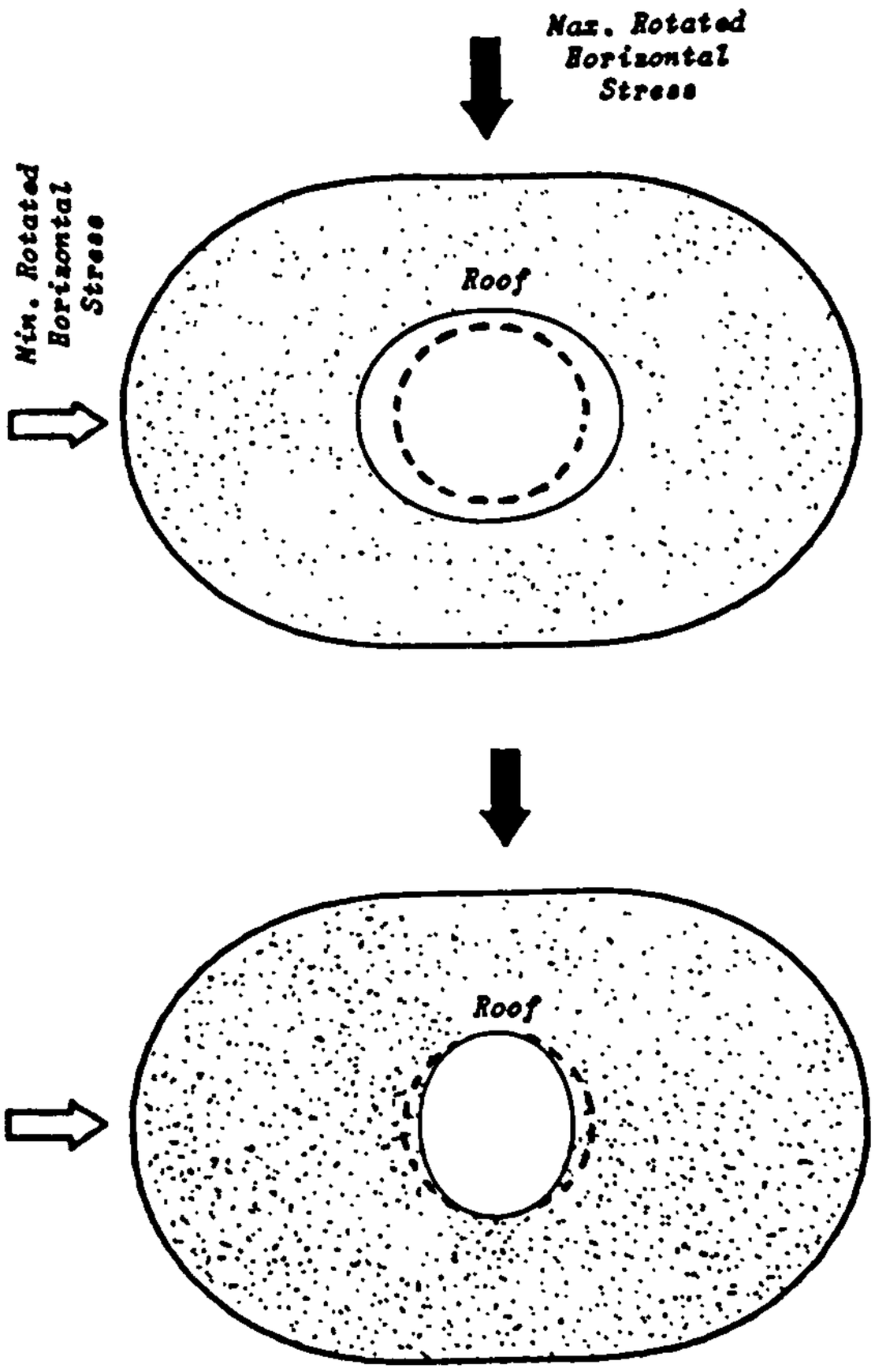

(i) Failed material assumed to fall into borehole

(ii) Failed Material assumed to remain in place

Figure 4.18(b) : Possible Borehole Shapes as a Result of a Yield Zone Around an Inclined Well

however, has resisted the temptation to blindly apply this relationship to estimate the magnitude of inclined borehole closure as it was reasoned that other downhole factors may affect the hole shape, i.e. drillstring errosion, swelling shale etc. The basis of roadway closure prediction is that the closure experienced is directly proportional to the width of the yield zone. For inclined boreholes, under normal in-situ stress conditions, it has been shown that the width of the yield zone is greatest in the direction of the minimum rotated in-situ stress. It therefore follows that the greatest amount of closure will be predicted to occur in this direction, if the failed material remains in place. Thus, the shape predicted is that of an elliptical borehole, but with its long axis in the direction of the maximum rotated horizontal stress (the 'roof'). This is shown in Figure 4.18(b).

Therefore the yield zone hypothesis may be used to explain each of the above occurrences, depending on whether the failed material is considered to remain in place after yielding is initiated, or is considered to fall into the borehole.

4.3.6.3 Stress Distribution in the Yield and Elastic Zones

The nature of the stress distribution around an opening under the assumption of hydrostatic conditions is well understood:- the major principal stress grows from a low value to a peak at the abutment, which is the edge of the yield zone, then decays to its in-situ value. However, the nature of the stress distribution around inclined holes in a non-hydrostatic stress regime is less well

understood. The modified equations were applied to demonstrate the stress distribution as a function of radial distance. A weak-medium rock system was modelled (K = 3, σ_o = 10 Mpa (1450 psi)). A horizontal to vertical stress ratio of 0.825:1 was chosen and the total vertical depth of the section of interest was taken to be 10000 ft (3050 m).

Figure 4.19(a) shows the stress distribution acting radially outwards from the 'side' of the hole, i.e. in the direction of σ_x and $\theta = 0°$. As established above, it can be seen that the effect of increasing the borehole inclination was to increase the width of the yield zone. Also evident from this figure was the increase in the abutment stress with hole angle. This was due to the rotated in-situ stress σ_y, which was equal to the horizontal stress for the vertical hole, but tended to the value of the vertical stress as the borehole angle increased towards 90°. It can be seen that after the peak stress abutment, the radial stress went on to increase to the far field value of σ_x while the hoop stress decreased towards the far field value of σ_y (noting that in this analysis, σ_y and σ_x were the respective maximum and minimum rotated in-situ stresses).

Figure 4.19(b) shows the stress distribution as a function of radial distance in the σ_y direction, or the 'roof' of the hole ($\theta = 90°$). Note that the vertical 'depth' scale for this figure is different than the previous figure. These graphs were the most striking of the two sets. Again, the distribution around a vertical hole is given to allow a comparison. It can be seen that for the 45° hole, the hoop stress and radial stress have crossed over, with σ_r tending towards

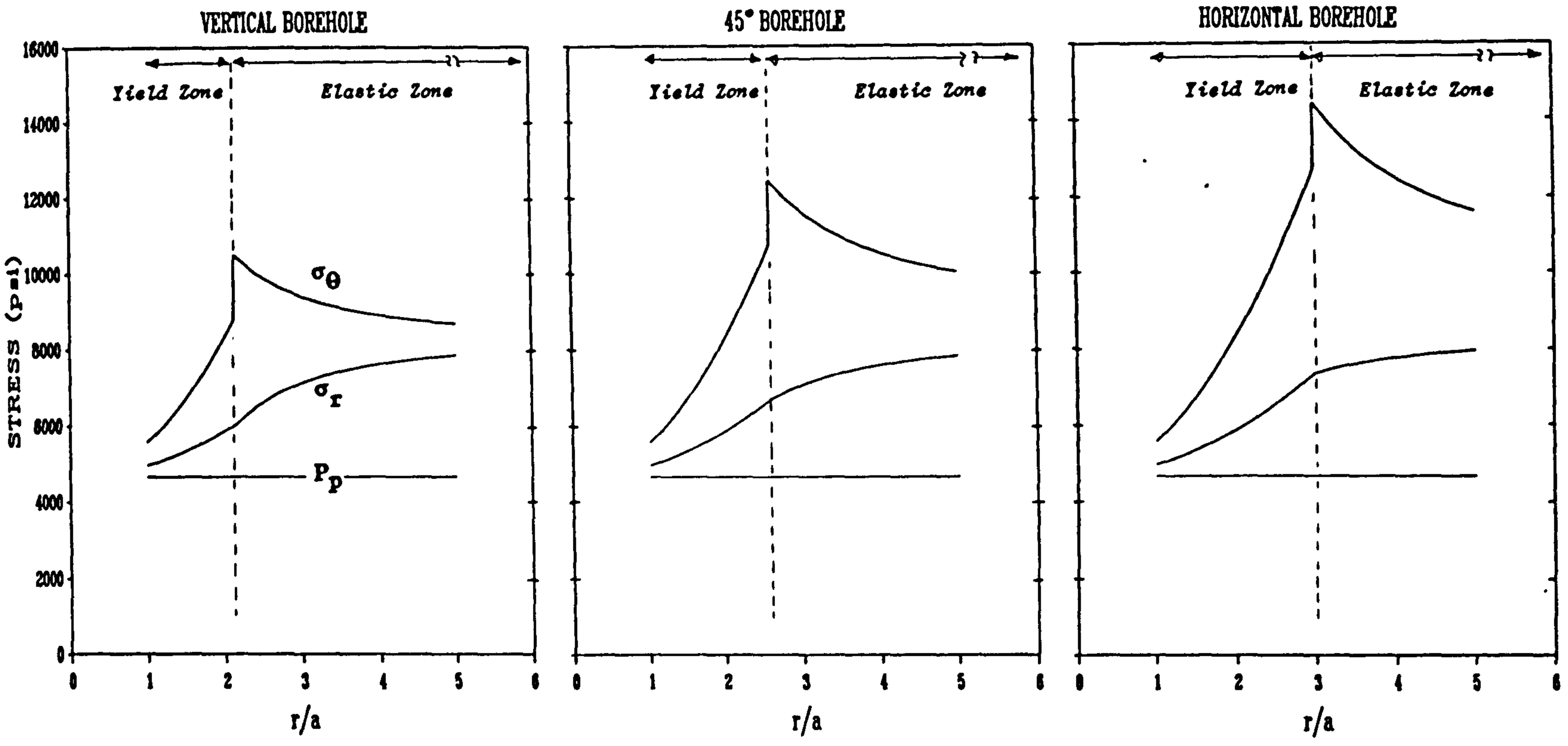

Figure 4.19(a) : Stress Distribution in the Yield and Elastic Zones in the Direction of the Minimum Rotated Stress i.e. the 'side' of the hole

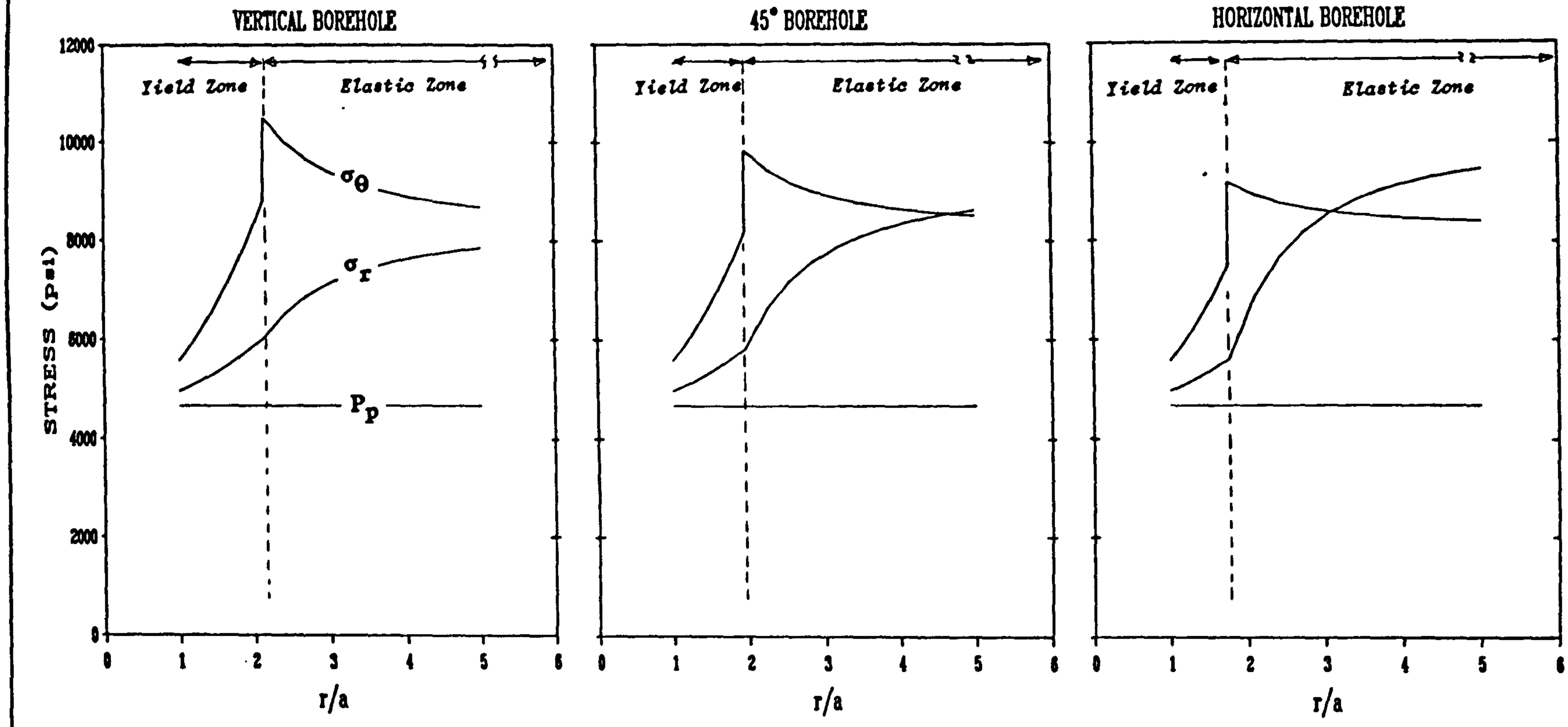

Figure 4.19(b) : Stress Distribution in the Yield and Elastic Zones in the Direction of the Maximum Rotated Stress i.e. the 'roof' of the hole

the far field value of σ_y while σ_θ decreased to the far field value of σ_x. This effect was more obvious with the horizontal hole. These graphs also show that the abutment peak at the yield/elastic boundary reduced with increased hole angle and consequently, the width of the yield zone at the 'roof' of the hole was found to be smaller with the higher angle holes. It is of note that it is this value of stress abutment which remains to act on a hydraulic fracture as the closure stress. The significance of which will be discussed later.

A picture has therefore developed about the stress distribution as a function of radial distance for inclined holes in a non-hydrostatic stress field. The shape, width of yield zone and peak abutment will of course change with different input data; however, the graphs produced illustrate for the first time the effect of hole inclination on the stress distribution around a bore hole surrounded by a yield zone under non-hydrostatic stress conditions.

4.3.6.4 Estimation of Mud Weight to Prevent a Yield Zone

Theoretically, it is possible to predict a sufficient mud weight which, depending on rock properties and the local in-situ state of stress, will prevent the formation of a yield zone around an inclined borehole. In the modified formulae set, equation (4.43) allows the calculation of the radial stress at the yield/elastic boundary. Therefore, this value of radial stress must be provided by the mud in the borehole to maintain the rock surrounding the hole in an elastic condition. Equation (4.43) was applied to construct mud

weight curves which illustrated the theoretical mud weight to prevent the first stage of yielding (i.e. $\theta = 0°$) around holes of various inclinations in weak, medium and strong rock. These curves, which are presented in Figure 4.20, were generated by assuming an overburden gradient of 1 psi/ft (22.6 kPa/m), a formation pressure gradient of 0.465 psi/ft (10.5 kPa/m) and a horizontal to vertical stress ratio of 0.825:1. The respective mud weights were plotted against total vertical depth.

To read the graphs, the depth of interest should be chosen and a horizontal line drawn across until it bisects the desired mud weight curve with respect to hole inclination. Dropping a vertical line from the intersection point will allow the theoretical mud weight to prevent the first stage of yield to be read directly from the axis. As can be seen from the graphs, mud weight curves were generated at hole inclinations of 0°, 30°, 45°, 60° and 90°. The vertical dashed line represents the equivalent mud weight of the formation pressure.

The obvious conclusion which was made from a comparison of these graphs was that weaker rock required a higher mud weight to prevent the formation of a yield zone. This has been established earlier. The graphs also illustrate that vertical holes may be drilled deeper than inclined holes before a yield zone will develop. Also apparent from these graphs was that only a marginal increase in mud weight would be required to prevent yielding at great depth. From an examination of the effect of borehole angle, it was evident that the increase in mud weight required to prevent the onset of yield was independent of depth.

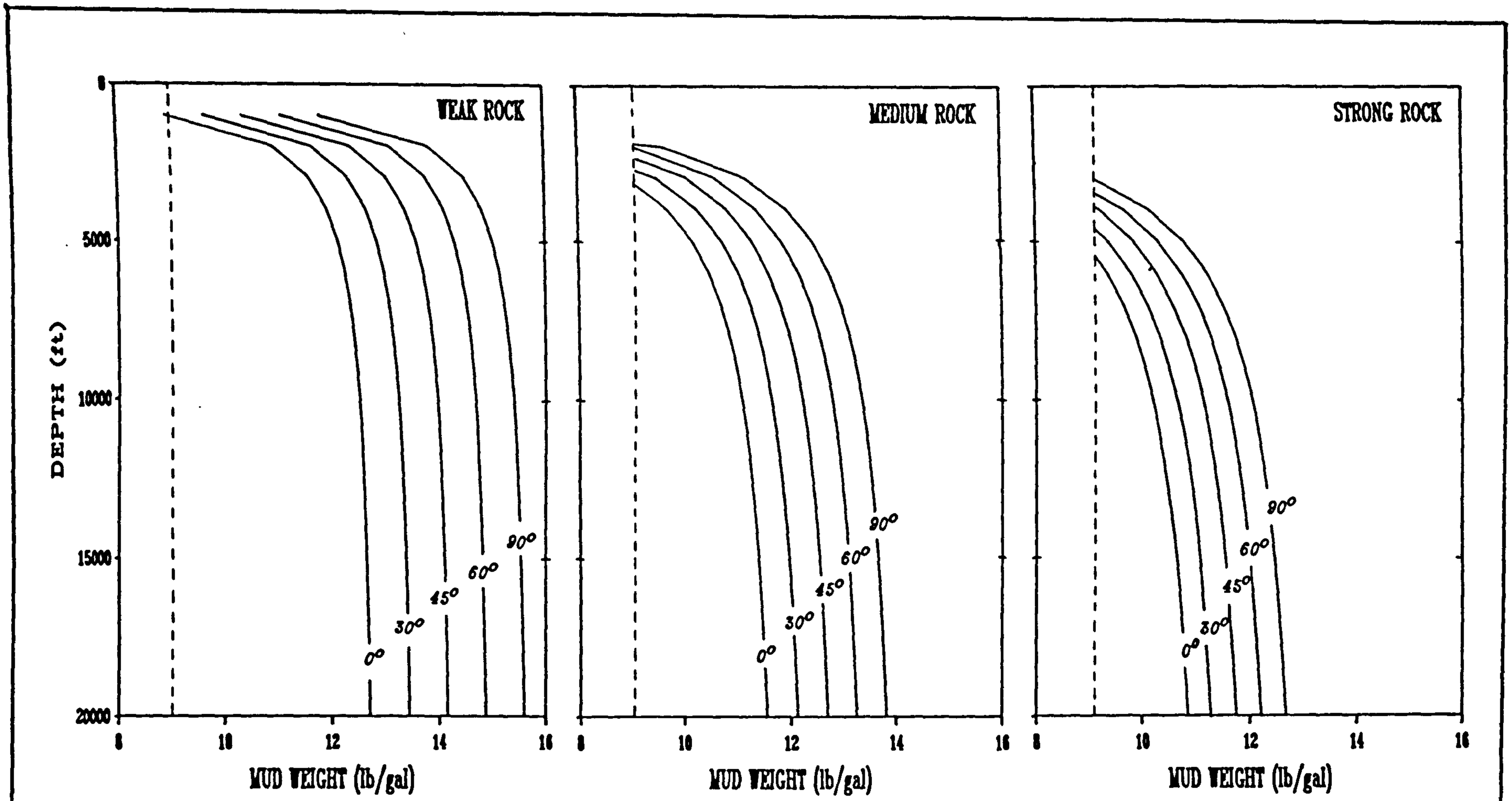

Figure 4.20 : Mud Weight Required to Prevent the Formation of a Yield Zone for Various Hole Angles

4.3.7 Effect of Fluid Flow

To include the effect of drawdown on the extent of the yield zone, Darcy radial flow theory was applied to allow the prediction of the pore pressure at various points in the reservoir during production.

4.3.7.1 Flow Model

With respect to flow conditions in the yield and elastic zones, it was reasoned that the flow into the wellbore would be exactly balanced by fluid flow across the yield/elastic boundary and accordingly, the flow regime in the yield zone could be assumed to be steady state. To make the flow model more realistic, the flow regime in the elastic zone was assumed to be semi-steady state.

For this analysis, it was assumed that the formation was homogeneous and had an effective permeability, k_e in the elastic zone. Rinses et al [36] suggested that the permeability in a plastic zone surrounding a wellbore could be reduced. The author is in agreement with this for the following reason. If a yield zone of granular material is develops around a wellbore, the granular material will initially by more permeable than the neighbouring rock. It is postulated that the mud weight over-balance will easily force mud filtrate etc into the granular material which will in turn reduce the permeability of the yield zone to below that of the elastic material. Therefore, it may be reasoned that after a period of time, the permeability in the yield zone will be lower than the effective

permeability of the reservoir. More discussion on this subject is given in Section 4.7.3.3. The permeability in the yield zone was therefore assumed to have been altered so that the average value in this region was k_y. The boundary of the reservoir was taken to be 1000 times that of the hole radius, while the height of the producing zone was taken to be 3.28 ft (1 m). The inflow equations appropriate for the pressure distribution shown in Figure 4.21 is therefore [99],

$$p_r - p_{wf} = \frac{Q\,\mu}{2\pi k_y h} \ln\,(r/a) \qquad a<r<r_e \quad .. (4.51)$$

$$p_r - p_a = \frac{Q\,\mu}{2\pi k_e h}\left[\ln\frac{r}{r_e} - \frac{r^2}{2r_e^2}\right] \qquad r_e<r<r_a \quad .. (4.52)$$

In particular,

$$p_a - p_{wf} = \frac{Q\,\mu}{2\pi k_y h} \ln\,(r/a) \qquad .. \;\; .. \;\; .. (4.53)$$

and

$$p_e - p_a = \frac{Q\,\mu}{2\pi k_e h}\left[\ln\frac{r}{r_e} - \frac{1}{2}\right] \qquad .. \;\; .. \;\; .. (4.54)$$

At $r = r_e$, there is continuity of pressure, therfore, adding the above equations the total drawdown $(p_a - p_{wf})$ is defined, viz.

$$p_a - p_{wf} = \frac{Q\,\mu}{2\pi k_e h}\left[\ln\frac{r_a}{a} - \frac{1}{2} + \left(\frac{k_e}{k_y} - 1\right)\ln\frac{r_e}{r_w}\right] \quad .. (4.55)$$

The above equation yielded a pore pressure curve which described the pore pressure distrbution as a function of radial distance. The flow

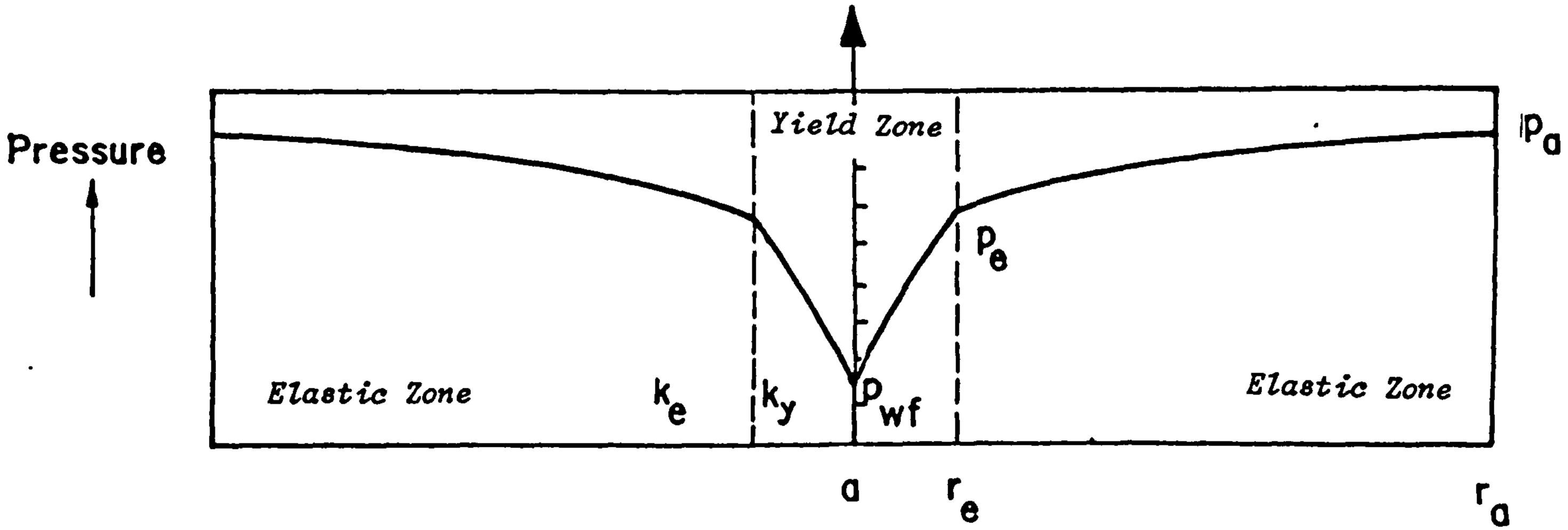

***Figure 4.21** : Radial Pore Pressure Distribution*

model was integrated into the modified yield zone equation set by substituting the respective pore pressures into the yield zone equations. This altered the localised effective stresses which were in turn used to generate the stress distribution curves.

Units : The above equations require Darcy units, as specified by Dake [99]. The values chosen were: Q = variable (cc/s), μ = 1 cp, k_y = 0.1 Darcy or 0.01 Darcy, k_e = 0.1 Darcy and h = 100 cm. These values were used to calculate the total drawdown and the respective pore pressures in atmospheres which were then converted to MPa to enable them to be input to the modified yield zone equations. For continuity with the other analytical results, the final stress solutions were converted to psi. The radius of the borehole, a, was maintained dimensionless, while r/a is the dimensionless radial distance and r = a at the periphery of the hole.

4.3.7.2 Stress Solutions around an Open Hole

The effect of fluid flow into an open hole is shown in Figure 4.22. For this initial example, a uniform permeability was assumed while the rock properties were that of a strong rock. The borehole was considered to be vertical and the horizontal to vertical principal stress ratio was set at 0.825:1. The depth of interest was 10000 ft (3048 m). The graphs were generated by maintaining the other input parameters constant while the flow rate was varied. No specific flow rates have been given as this analysis was intended to be purely qualitative.

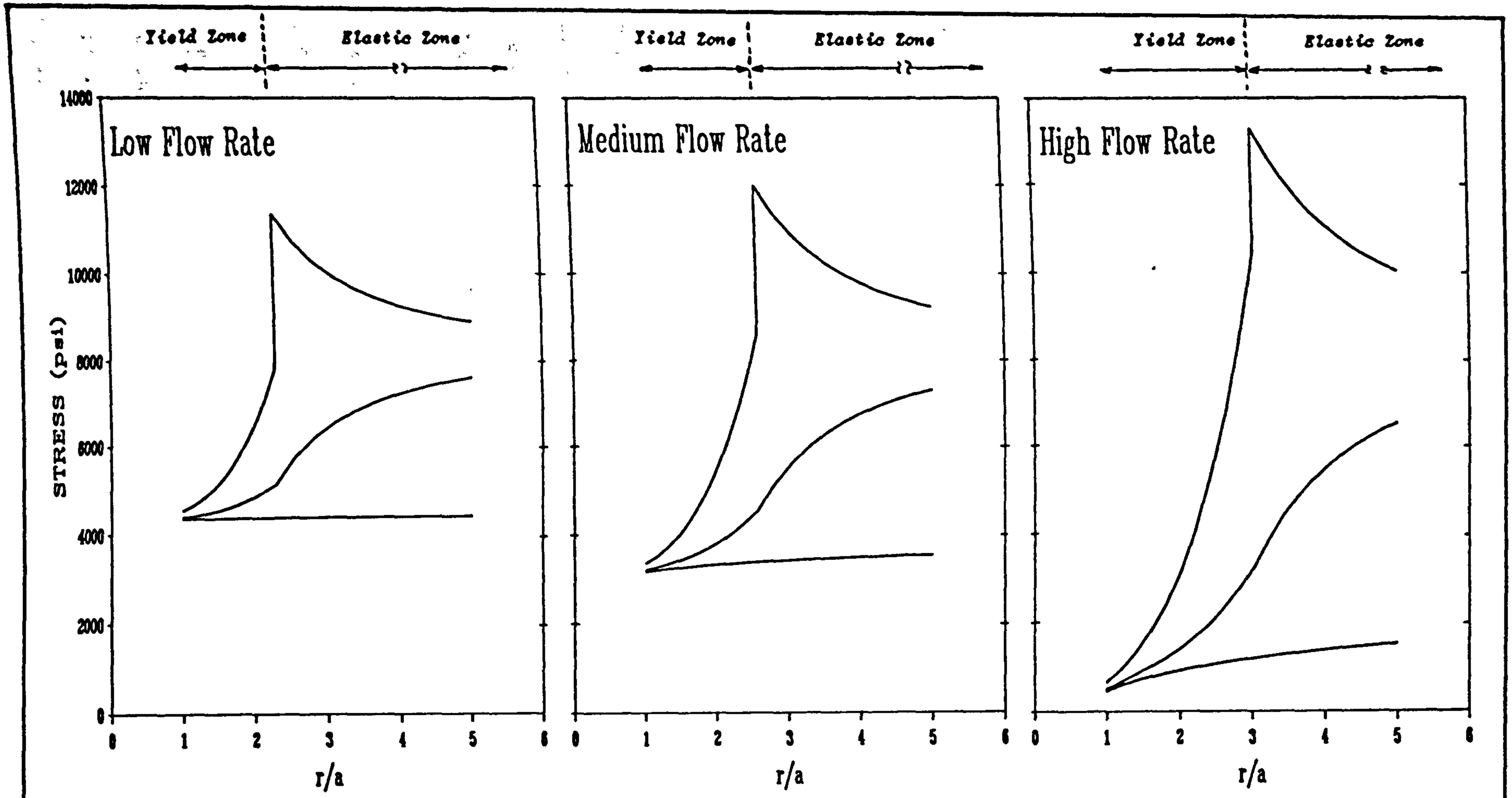

Figure 4.22 : Effect of Flow Rate on the Stress Distribution Around a Vertical Well - Uniform Permeability

It can be seen that the obvious effect of producing the well was to increase the width of the yield zone. It has already been established that the extent of the yield zone around a vertical well is dependent on the mechanical properties of the rock. Therefore, the width of the yield zone with weaker rock would be greater. Indeed, for very weak rock, it may not be possible to produce the well without a yield zone of excessive width forming. The peak stress or abutment was also observed to increase proportionally with fluid flow. The reason for the above effect was due the reduction in pore pressure in the region surrounding the wellbore which had the result of increasing the localised effective stress.

4.3.7.3 Stress Solutions around a Cased Hole

When a casing is set and cemented, the cement column in the well will cause an increase in pressure acting against the wall of the borehole. The pressure exerted by the casing therefore has a similar function to the mud weight. To estimate the stress distribution around a cased hole, the pressure applied by the casing was substituted for the mud weight (p_m) in the modified formulae set. The effect of variable permeability was also examined. The graphs were generated using the same input criteria as above unless otherwise stated.

Uniform Permeability : Figures 4.23(a) and 4.23(b) respectively show the theoretical stress distribution for an open hole and a cased hole with a uniform permeability, i.e. $k_y = k_e$. From a comparison of the two graphs, it was evident that the width of the yield zone was

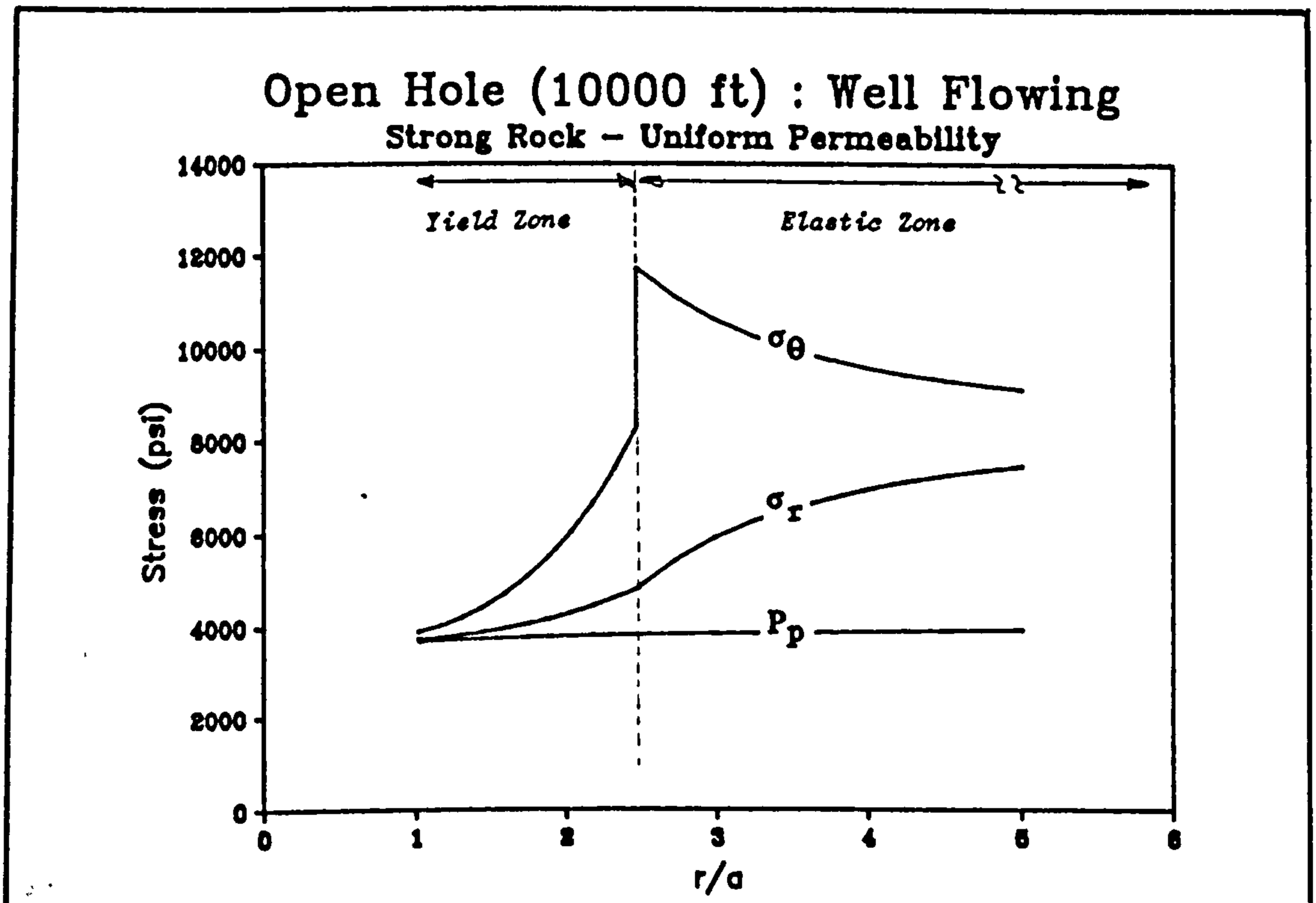

Figure 4.23(a) : Stress Distribution Caused by Fluid Flow into an Open Hole - Uniform Permeability

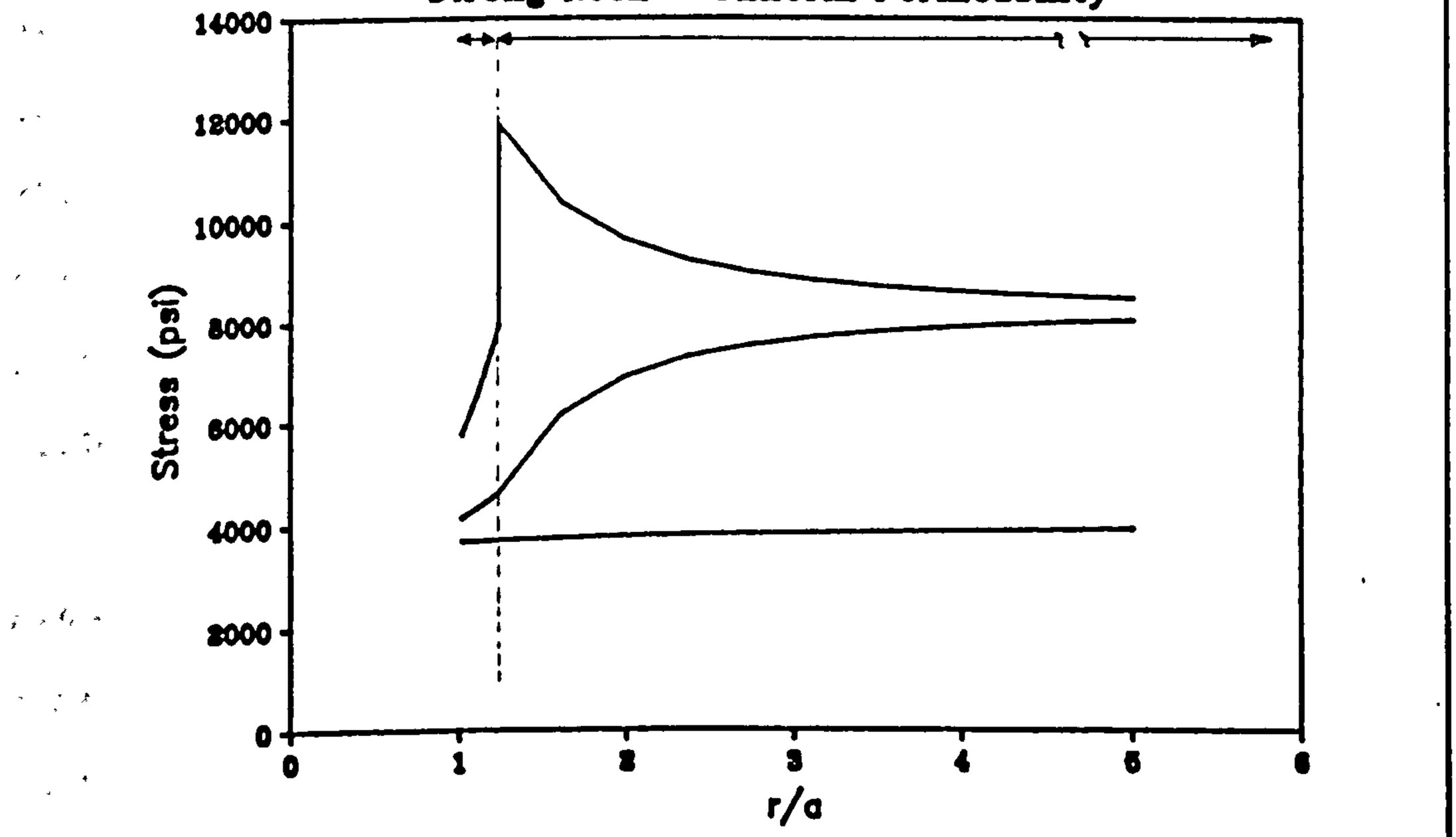

Figure 4.23(b) : Stress Distribution Caused by Fluid Flow into a Cased Hole - Uniform Permeability

drastically reduced as a result of casing the well.

Reduced Permeability in the Yield Zone : As stated, the yield zone surrounding the wellbore could possibly be a zone with reduced permeability, compared with that of the elastic region. It is also likely that the permeability may be variable throughout the yield zone due to mud filtrate and size variations in the granular material. However, this relationship is presently unknown and would require extensive laboratory permeability testing of granular material to obtain such a function. To give an indication of the effect of a reduced permeability in the yield zone, the above example was repeated using the same numerical values with the exception that the permeability in the yield zone was assumed to be constant and had a value of one tenth of the permeability in the elastic region. The results for the open and cased holes are shown in Figures 4.24(a) and 4.24(b) respectively. From these figures, it can be seen that the width of the yield zone was greatly reduced by the casing, while the effect of a reduced yield zone permeability was apparent from an examination of the pore pressure curve. It can be seen that the majority of the pressure drawdown occurred in the yield zone.

From a comparison of Figures 4.23 and 4.24, the width of the yield zone assuming a reduced permeability was found to be slightly larger than that predicted using the uniform permeability approach. It was also apparent that a greater drawdown pressure would be required to produce the reduced permeability well at a similar rate.

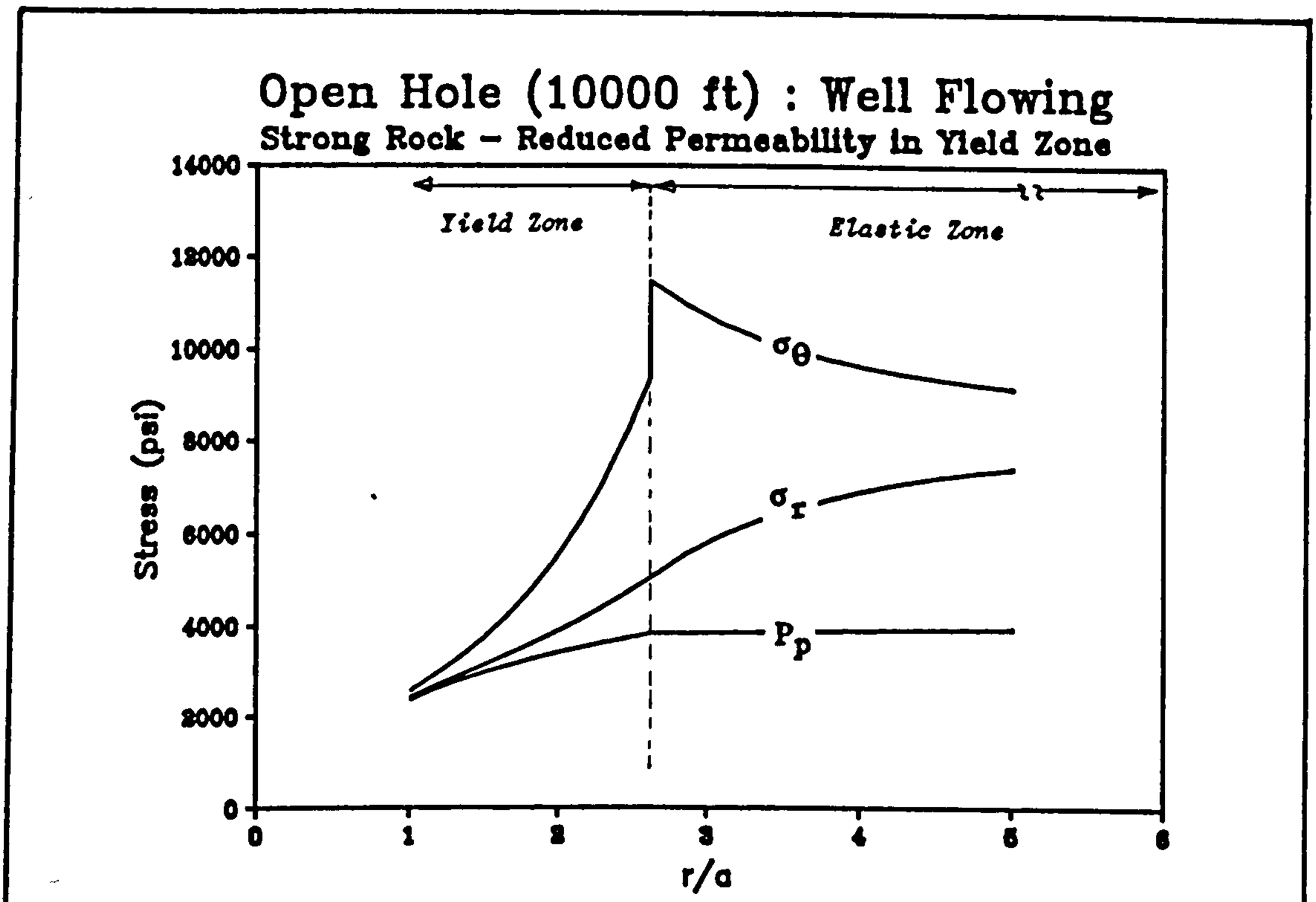

Figure 4.24(a) : Stress Distribution Caused by Fluid Flow into an Open Hole - Reduced Permeability

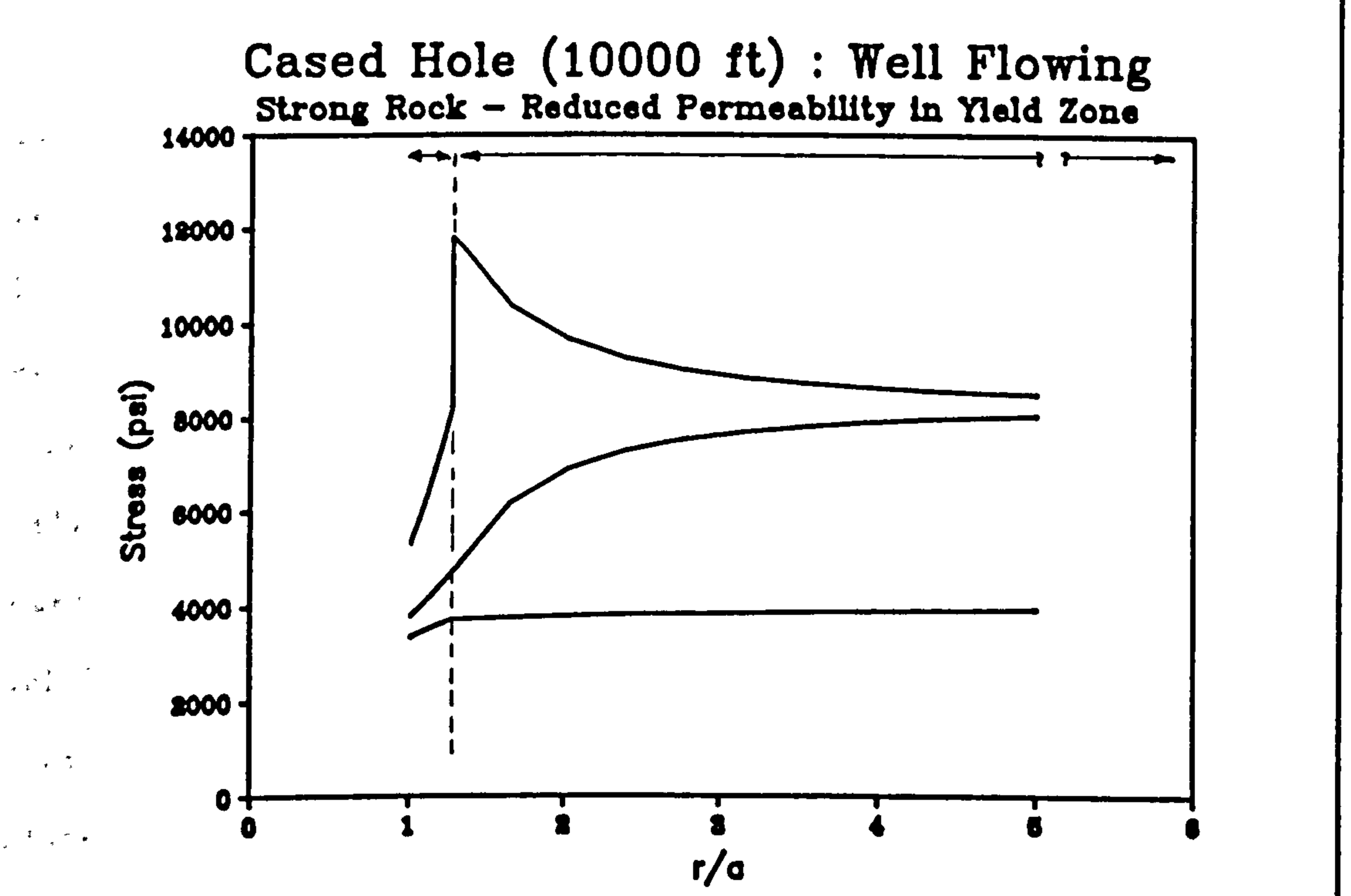

Figure 4.24(b) : Stress Distribution Caused by Fluid Flow into a Cased Hole - Reduced Permeability

It can therefore be concluded that the effect of casing was to reduce the width of the yield zone. Therefore, if a larger yield zone had previously existed, most of the originally yielded material apparently returns to an elastic state of stress. However, although the material theoretically behaves in an elastic manner, the mechanical properties of the rock will most probably be different from the originally elastic material. It is therefore clear that considering the effect of fluid flow using the yield zone hypothesis in open and cased wells is complicated by many variables. If further research indicates that the yield zone is in fact a zone of reduced permeability, then this may have implications on the manner that the 'skin' or 'damaged region' surrounding a well is assessed.

4.3.8 Application to a Specific Case

The yield zone approach was applied to the two wells which were examined in the previous section, namely 11/30a-A6 and 47/14a-8. For this analysis, the values of uniaxial compressive strength were reduced by a factor of 5 to arrive at a realistic in-situ value. This was in accordance with Wilson [5]. The overburden stress gradient was assumed to be 1 psi/ft (22.6kPa/m). Over the section of interest, the laboratory measured values of Poisson's ratio (γ) for each horizon were averaged and the mean value was used to arrive at a constant horizontal to vertical stress ratio. The average value of Poisson's ratio for each well was 0.35, therefore a horizontal to vertical stress ratio of 0.75:1 was used throughout. The a 'normal' pore pressure gradient of 0.465 psi/ft (10.5 kPa/m) was assumed. The effect of water depth was not considered.

4.3.8.1 Mud Weight to Prevent Formation of Yield Zone

Well 11/30a-A6 : The mud weight to prevent the formation of a yield zone for hole inclinations of 0°, 30°, 45°, 60° and 90° were plotted against total vertical depth for the TVDs between 6777 and 6856 ft (2067 and 2091 m), as shown in Figure 4.25. From an analysis of this graph, it was apparent that a yield zone would exist at all data points if the well was drilled in balance. For the vertical hole, a mud weight of around 10.5 lb/gal would prevent the rock from yielding, except at the top of the section of interest. This sample [at 6777 ft (2067 m)], was a shale and had a triaxial stress factor of 2.2. Thus, if the well was drilled with a 10.5 lb/gal mud weight, the shale section would yield and reduce the diameter of the hole at this depth. The curves for each hole inclination were all seen to follow a similar trend. Over most of the section of interest, with the exception of the shale region, increasing the hole angle from 0° to 60° would require an increase in mud weight of around 2 lb/gal.

Well 47/14a-8 : Similar mud weight curves were generated and plotted against total vertical depth for well 47/14a-8 between depths of 9078 and 9142 ft (2768 and 2788 m). They are presented in Figure 4.26. Increasing the hole angle from 0° to 60° would require an increase in mud weight of around 3 lb/gal. One section [at 9103 ft (2776 m)] which had a triaxial stress factor of 2 and a very low compressive strength, stood out as being the weakest region. At this depth, a mud weight of 12 lb/gal would be required to prevent yield in a vertical hole. With a horizontal hole, however, a mud weight of

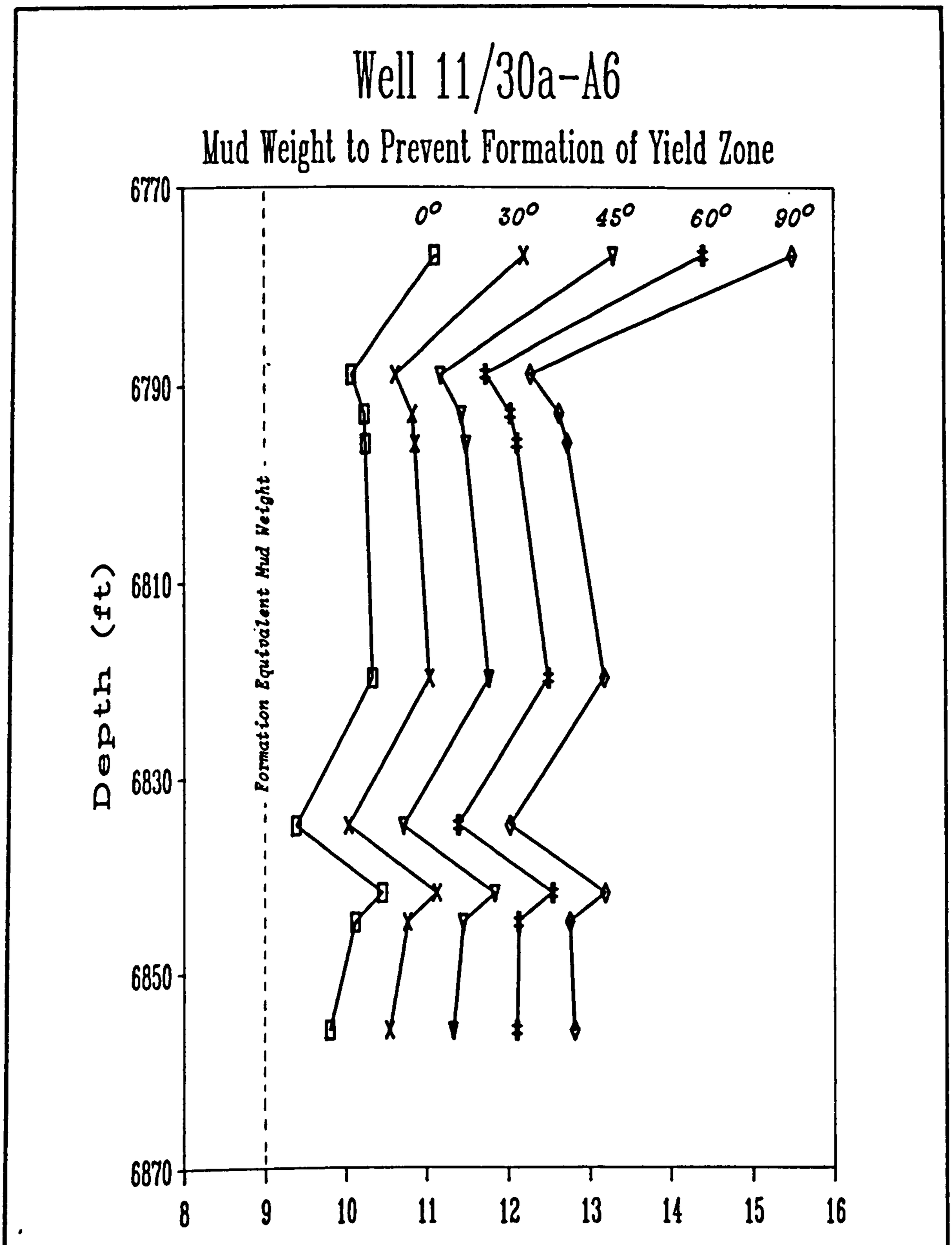

Figure 4.25 : Mud Weight Required to Prevent the Formation of a Yield Zone around Well 11/30a-A6

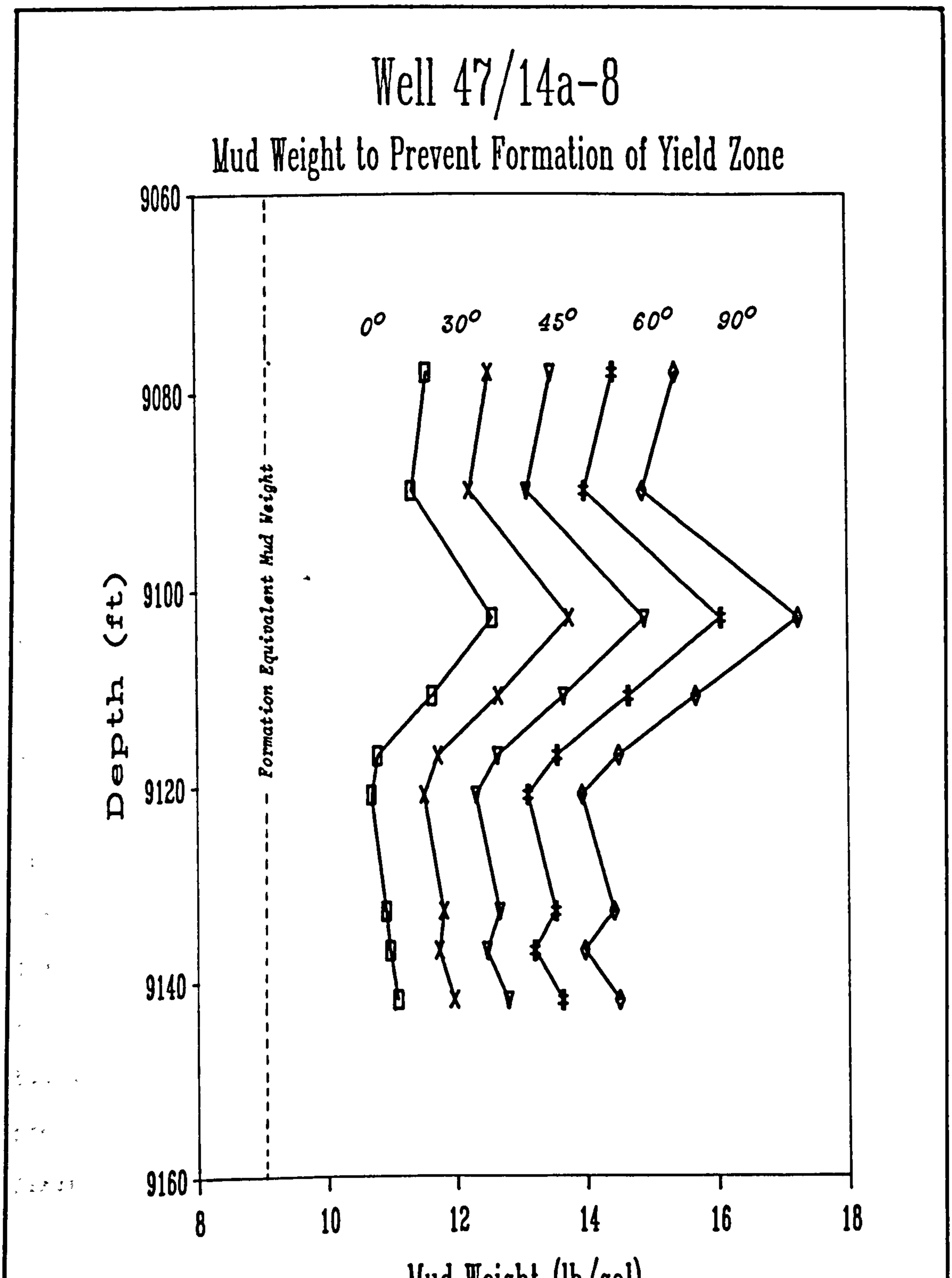

Figure 4.26 : Mud Weight Required to Prevent the Formation of a Yield Zone around Well 47/14a-8

over 17 lb/gal would be required to maintain this section in an elastic condition.

4.3.8.2 Prediction of Maximum and Minimum Mud Weights

The yield zone approach may be applied to estimate fracture initiation pressure. The effective tangential stress acting on the 'roof' wall of the borehole is given by equation (4.45). Therefore, using the same tensile failure criterion as outlined in Section 4.2.4.1 (i.e. zero tensile strength concept), the fracture initiation pressure may be calculated from the sum of the effective tangential stress at the borehole wall and the pore pressure (termed $\sigma_{\theta_{frac}}$). As fluid flow into the formation was not considered, the solution was therefore that of a non-penetrating fluid.

Figures 4.27(a) and 4.27(b) show the calculated mud weight operating curves as a function of hole inclination for wells 11/30a-A6 and 47/14a-8 respectively. For this application, the σ_{re} and the $\sigma_{\theta_{frac}}$ values were averaged to give a 'typical' value over the section of interest. Also given in these figures is the fracture initiation pressure for the various hole inclinations calculated from classical fracturing theory.

A comparison of the fracture initiation pressures calculated from classical elastic theory with that of the yield zone hypothesis indicated that the latter approach predicted lower values. The difference between the respective values for each well, however, was not constant. As hole inclination increased, this difference was

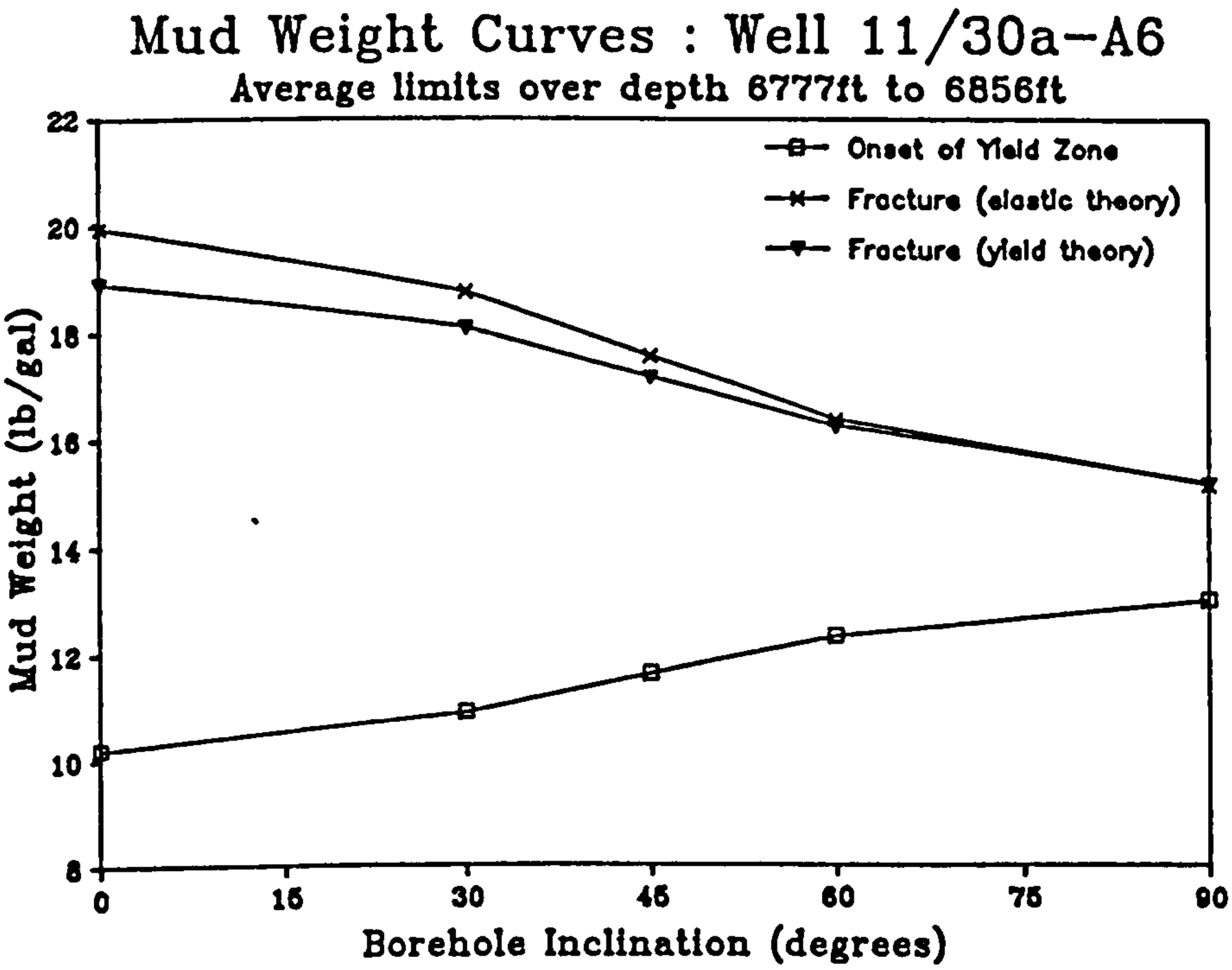

Figure 4.27(a) : Mud Weight Operating Curves - Well 11/30a-A6

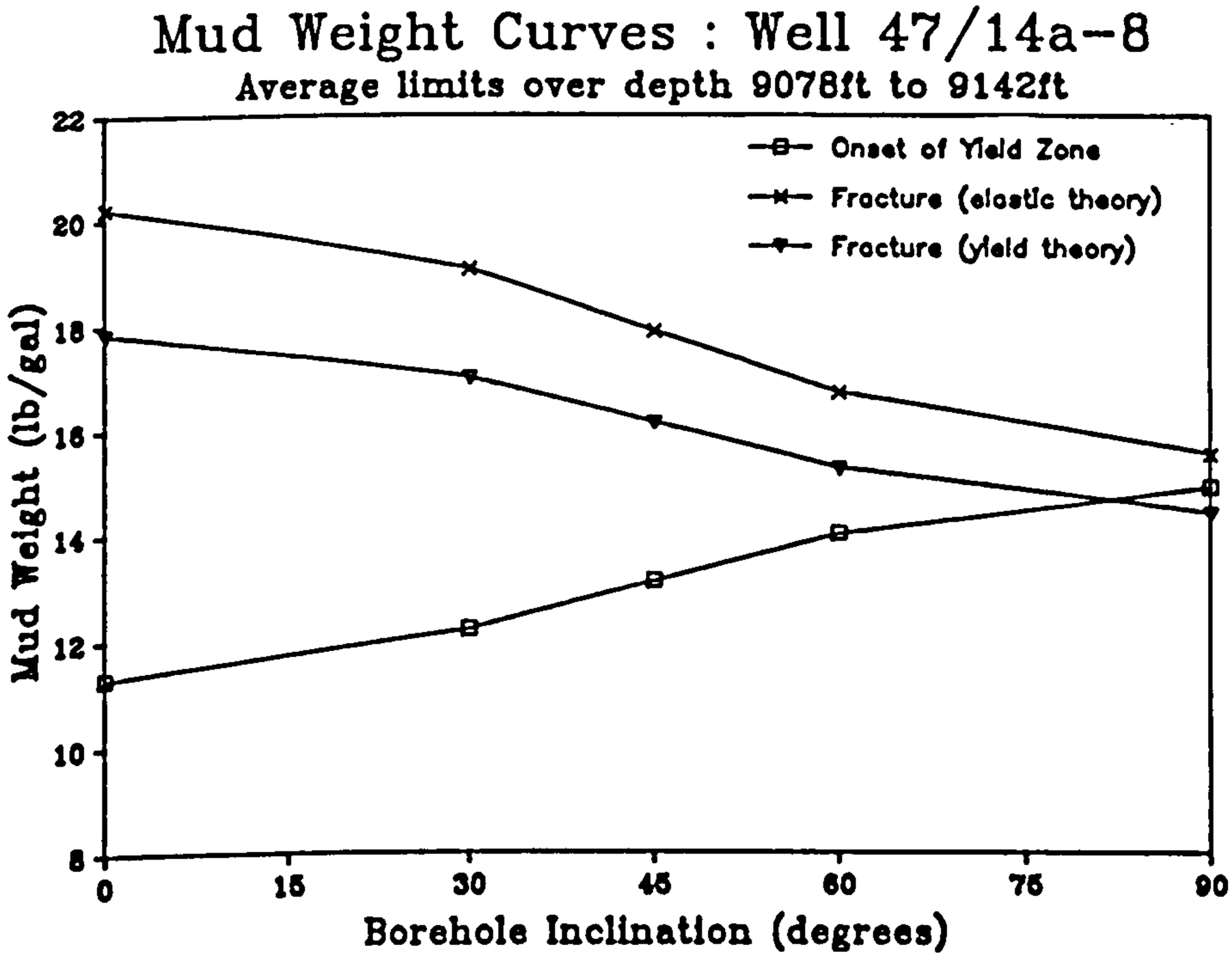

Figure 4.27(b) : Mud Weight Operating Curves - Well 47/14a-8

found to decrease. It can also be seen from the graphs that the difference in fracture pressure estimations was greatest for well 47/14a-8. It has been established that the rock samples tested from this well were generally weaker than that of well 11/30a-A6. Therefore, it can be concluded that rock strength plays a major part in the fracture pressure predictions using the yield zone concept - the weaker rock being easier to fracture. This appears to be a logical conclusion and one that is not apparent from classical fracturing theory.

With well 47/14a-8 [Figure 4.27(b)], it can be seen that the maximum and minimum mud weight curves intersect at a borehole angle of about 80°. This suggests that holes above this angle could not be drilled without either inducing lost circulation or the formation a yield zone.

4.3.9 Discussion and Conclusions re Yield Zone Analysis

It has been shown that the yield zone approach can indeed be applied to predict the stability of both vertical and inclined boreholes under non-hydrostatic stress conditions.

It can be concluded that rock strength, but more especially the triaxial stress factor, plays a major role in the stability or instability of an inclined borehole. The simple rule being, the higher the triaxial stress factor, the more stable the borehole. From the mud weight vs depth curves produced for various rock strengths, it can be concluded that, at great depth, it is the

mechanical properties which dictate hole stability.

The development of a yield zone around an inclined hole has been illustrated. It has been established that the 'first stage' of yielding occurs at the 'side' of an inclined hole, i.e. in the direction of the minimum rotated horizontal stress. Thus, it can be concluded that although a small yield zone may exist at the 'side' of an inclined borehole, the rock at the 'roof' of the hole may be within its elastic limit, and therefore stable.

It can also be concluded that the shape of a yield zone around an inclined hole depends not only upon the hole inclination, but on the regional in-situ horizontal to vertical stress ratio. It has been shown that the lower stress ratio produces the more distorted yield zone radius, while higher stress ratios produce a more ellipical yield zone. It has also been postulated that the yield zone hypothesis can explain why some boreholes are not circular.

The effect of fluid flow has been examined by the application of simple Darcy flow equations and assuming steady state conditions in the yield zone with semi-steady state conditions applying beyond. It can be concluded that the effect of increasing the flow rate from an uncased well increases the width of the yield zone. It can also be concluded that casing the well has the effect of reducing the width of the yielded region. Therefore, it can be concluded that effective casing allows the well to be produced at a greater rate without either the development of a yield zone, or the formation of a yield zone of excessive width. The effect of a reduced permeability in the

yield zone has been examined. This analysis indicated that the width of the yield zone would increase in the direction of the minimum rotated horizontal stress, but decrease in the direction of the maximum rotated in-situ stress. If further research indicates that the yield zone is in fact a zone of reduced permeability, then this may have implications on the manner that the 'skin' or 'damaged region' surrounding a well is assessed.

The approach has also been applied to draw up mud weight curves for the wells whose rock properties were determined in Chapter Three. It was shown that fracture initiation pressures, assuming a non-penetrating fluid, calculated by the yield zone hypothesis predicted values which were lower than estimated using classical fracturing theory. Thus it can be concluded that rock strength has an effect on fracture pressures, i.e. the softer rock fracturing at lower pressures. This appears to be a logical conclusion, but one which is not apparent from classical elastic fracturing theory.

4.4 CONCLUSIONS

The state of stress induced around both vertical and inclined wells has been examined and stability predictions made by the application of failure criteria to existing analytical solutions.

The yield zone hypothesis developed by Wilson [5] has been extended to cover non-hydrostatic stress conditions and the effect of pore pressure. This allowed an analysis of the stability of inclined boreholes surrounded by a zone of yielded rock.

It can be concluded that the yield zone analysis generally predicted that a higher mud weight would be required than that predicted by the elastic analysis. This was due to the fact that an 'in-situ' value of compressive strength was used for the yield zone analysis, while the laboratory values were used for the Mohr-Coulomb and three-dimensional Griffith approach.

Therefore, it can be concluded that one possible area of error when applying the yield zone approach is in the estimation of the 'f' factor by which to reduce the laboratory value of uniaxial compressive strength to obtain a realistic in-situ value. As stated, the uniaxial compressive strength was reduced by a factor of 5 in the above application. To examine the effect of various 'f' reduction factors on the mud weight predictions for zero yield, a series of curves were generated using strength reduction factors of 1, 2, 3 and 5. The example shown in Figure 4.28 refers to a vertical hole using the rock properties of well 47/14a-8. With no strength reduction factor applied, the trend of the curve was similar to that of the vertical mud weight curve shown in Figure 4.12 which was produced using the Mohr-Coulomb theory. This result was hardly surprising as the yield zone approach employs a linear Coulomb failure criterion. Indeed, it confirmed the accuracy of the method. Decreasing the uniaxial compressive strength by a factor of 2 had the effect of increasing the mud weight for zero yield. Dividing the uniaxial compressive strength by respective factors of 3 and 5 had the effect of further increasing the mud weight required to prevent the formation of a yield zone. Overall, the general trend of the

Well 47/14a-8 : Vertical Hole

Mud Weight to Prevent Formation of Yield Zone

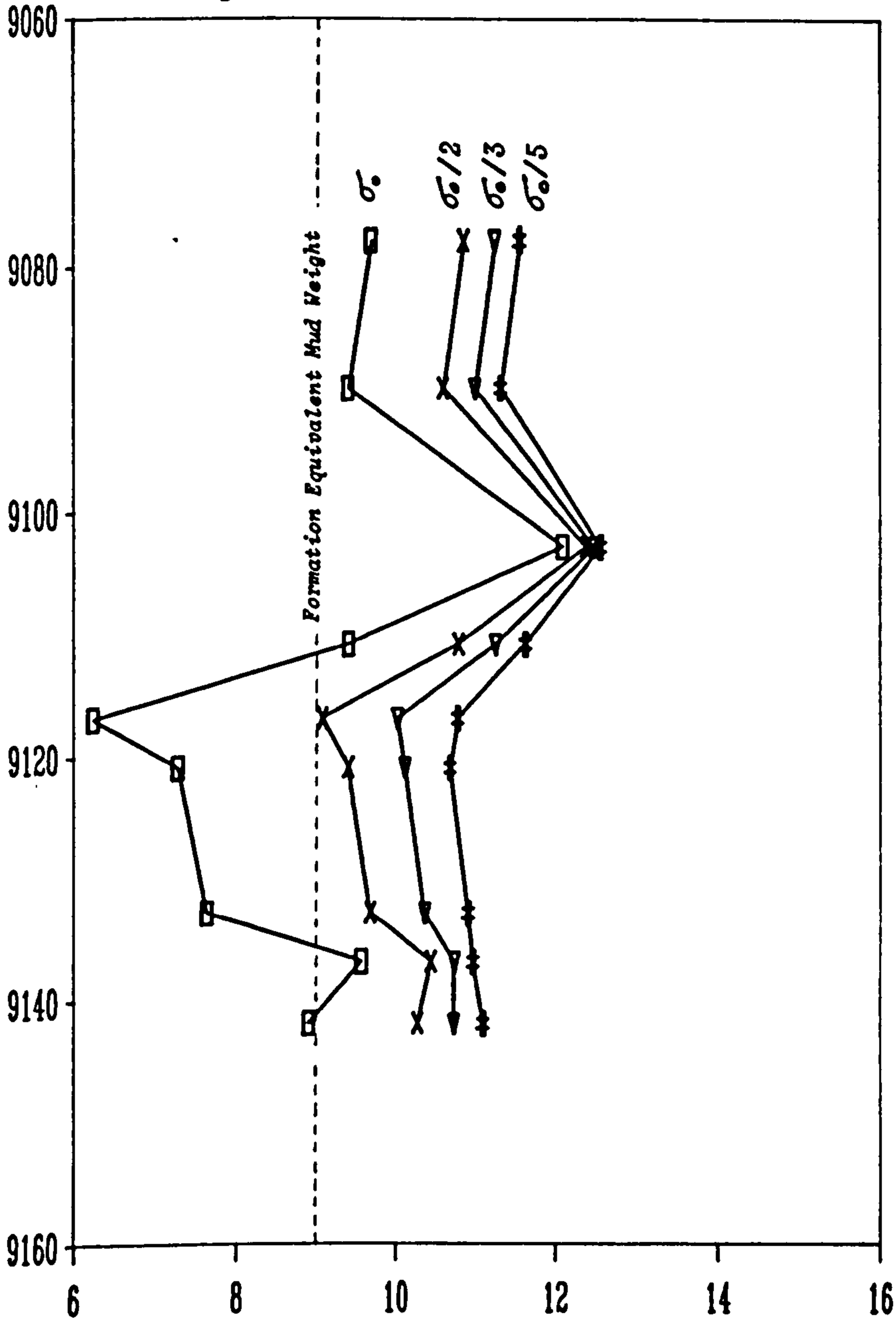

Figure 4.28 : Effect of the Compressive Strength Reduction Factor on the Yield Zone Width

curves were similar. However, the greatest difference between each curve occurred with the samples which had the higher values of uniaxial compressive strength.

CHAPTER FIVE

THE DEVELOPMENT OF A LABORATORY TECHNIQUE FOR THE MEASUREMENT OF FRACTURE PERMEABILITY/CONDUCTIVITY

5.1 INTRODUCTION

It was established in the opening chapter that the minimum fracture initiation pressure is often taken to be equal to, or slightly above, the value of the minimum horizontal principal stress. The stress acting to close a hydraulic fracture is calculated by subtracting the bottom hole producing pressure from the fracture initiation pressure. To err on the side of safety, the minimum bottom hole producing pressure is taken to be zero, thus the closure stress is also considered to be equal to, or slightly above the minimum horizontal stress. Consequently, the effect of the stress concentration around the borehole is generally ignored in the calculation of closure stress.

It was shown in the previous chapter that if the wellbore is surrounded by a yield zone, the maximum closure stress will act on the fracture face at a radial distance from the hole dictated by the mechanical properties of the rock. Thus, the proppant selected must be strong enough to withstand this increased closure stress if a marked reduction in conductivity is to avoided. To investigate the effect of a such a yield zone on fracture conductivity estimations and proppant optimisation required the facility to measure the conductivity of a simulated propped fracture as a function of closure stress.

The aim of this chapter was to develop a laboratory technique which could be used to determine a realistic value of fracture conductivity at various levels of closure stress. The intention of this

research programme, which was sponsored by Britoil plc, was to set up a data base outlining the properties of various commercially available proppants which could be used by the company to select the optimum proppant for use in a specific formation. The procedure was required to simulate both proppant crushing and embedment, therefore required the use of formation core to simulate the fracture face.

This chapter details the design and in-house manufacture of the specialised equipment required to measure fracture conductivity in the laboratory, the development of experimental procedures, the various test results and the conclusions drawn from them. A literature search of previous work into fracture conductivity was also conducted. Before an analysis of such a review, a thorough understanding of certain fundamental concepts concerning the physical properties of a porous medium was required. Finally, the direct effect of a yield zone on the estimation of closure stress and on the selection of a proppant was examined.

5.2 FUNDAMENTAL CONCEPTS OF A POROUS MEDIUM

5.2.1 Porosity

From a reservoir engineering aspect, one of the most important rock properties is porosity (ϕ), a measure of the space available for storage of hydrocarbons. Absolute porosity is defined as the ratio of total volume of void space in the rock to the total bulk volume of the rock. This can be expressed in mathematical form as a percentage, viz.

$$\phi = \frac{\text{Total Volume of Void Space}}{\text{Total Bulk Volume}} \times 100 \quad .. \quad .. \quad (5.1)$$

If the calculation of porosity is based upon the volume of interconnected voids, the quantity is termed the effective porosity. In reservoir engineering calculations, it is the effective porosity which is of interest. In the case of calculating the porosity of a proppant pack however, the absolute value is required.

5.2.2 Specific Surface / Wetted Surface Area

The specific surface (S) of a porous material is defined as the ratio of the total interstitial surface area of the voids or pores (A_v) to the bulk volume (V_b) of the porous medium:

$$S = A_v/V_b \quad .. \quad .. \quad .. \quad .. \quad .. \quad (5.2)$$

For example, the specific surface or wetted surface area of a porous material comprising of spherical particles of radius r is,

$$S = 4\pi r^2/(2r)^3 = \pi/2r \quad .. \quad .. \quad .. \quad .. \quad .. \quad (5.3)$$

It is therefore apparent that a fine material will exhibit a much greater specific surface than a coarse material occupying the same volume. The specific surface area may also be defined with respect to unit pore volume or with repect to a unit weight of the material. Thus, the specific surface of a porous material is affected by the porosity, mode of packing, grain size and the shape of the grains.

5.2.3 Permeability

Permeability is a measure of the ease of flow of a fluid through a porous medium. The permeability of an oil reservoir is as important as the porosity, for not only is the actual oil in place important, but the rate at which the oil will flow through the reservoir is equally important. In a propped hydraulic fracture however, the permeability of the fracture is of paramount importance as this, in conjunction with the propped fracture width, dictates the conductivity of the fracture and therefore its specific flow capacity.

5.2.4 Fracture Conductivity

The ability of a propped fracture to allow fluid flow is dependent on the permeability of the proppant bed (k), and the propped fracture width (W_f). Fracture conductivity (kW_f), is therefore defined as the product of the propped fracture width and the fracture permeability, and is commonly expressed in units of darcy-feet (D*ft).

5.2.5 Relationship Between Permeability and the Porous Media.

Several investigators have attempted to establish empirical correlations to link permeability with other physical properties of a porous material such as porosity and specific surface area. Since permeability depends upon continuity of pore space, there is not, in

theory (nor in practice), any unique relation between porosity and permeability. As a consolidated porous medium which may exhibit secondary porosity is impossible to simulate, various 'models' representing an unconsolidated porous medium have been developed in an attempt to derive the motion equations from the basic principles underlying the theory of hydrodynamics. A review of such models and theories is given by Scheidegger [100]; one of these theories, namely the hydraulic radius theory, is briefly described below.

This theory is based on the assumption that an unconsolidated porous medium is equivalent to a series of channels. By the use of the fundamental observation that permeability, in absolute units, has a dimension of an area or length squared, it may be argued that the length of the channels should be a characteristic for the permeability. Such a length may be called the hydraulic radius of the porous medium, and is linked with the hypothetical channel to which the porous medium is thought to be equivalent. An example of the hydraulic radius is the ratio of the volume of a conduit filled with fluid to its wetted surface area.

One of the most widely accepted derivations based on the hydraulic radius theory, in which the permeability is related to other porous media properties, is that proposed by Kozeny [101]. In this theory, the porous media is treated as a group of capilary tubes of equal length, but not necessarily of circular cross-section. By solving the Navier-Stokes equations for slow, steady flow through such a system he obtained the permeability equation in the form,

$$k = C\phi^3/S^2 \qquad .. \quad .. \quad .. \quad .. \quad .. \quad (5.4)$$

Where ϕ is the porosity, S is the specific surface of the tube, C is the Kozeny constant which is a dimensionless quantity dependent on the geometrical form of the capillary tube cross-section and k, the permeability, is expressed in units of tube length squared.

Numerous modifications to the Kozeny equation have been proposed. A much used modification is that postulated by Carmen [102], who expressed the permeability as,

$$k = \frac{\phi^3}{C_k S^2 (1-\phi)^2} \qquad .. \quad .. \quad .. \quad .. \quad .. \quad (5.5)$$

Using earlier work by Carmen, Darin and Huitt [103] showed that,

$$C_k = C_o \frac{L_e}{L_b} \qquad .. \quad .. \quad .. \quad .. \quad .. \quad (5.6)$$

where C_k = Kozeny-Carmen constant

C_o = Flow shape factor (2.5 for a bed of spheres).

L_b = Length of bed of porous medium.

L_e = Length of path taken by fluid traversing L_b.

These investigators and Wyllie and Gregory [104] showed that (L_e/L_b) was dependent upon the shape of particles in a bed, and should be about 2 for unconsolidated porous media, and C_k should therefore have a value of 5.

In order to determine the fracture conductivity, the propped

fracture width (W_f) has to be introduced to the relationship. Thus, if C_k is assigned a value of 5, the conductivity of a propped fracture may be defined as follows:

$$kW_f = \frac{W_f}{5S^2} \times \frac{\phi^3}{(1-\phi)^2} \qquad .. \quad .. \quad .. \quad .. \quad .. \quad (5.7)$$

Transforming from darcy units into field units, we obtain a modified Kozeny-Carmen equation, viz

$$kW_f = 1.1x10^{7} \times \frac{W_f}{S^2} \times \frac{\phi^3}{(1-\phi)^2} \qquad .. \quad .. \quad .. \quad (5.8)$$

where kWf = Fracture Conductivity (Darcy-ft)

Wf = Fracture width (in)

S = Wetted surface area (in^2/in^3)

ϕ = Proppant porosity (fraction)

Therefore, for an unconsolidated porous material, such as a bed of proppant, it is possible to establish a relationship between permeability, porosity and specific surface or wetted surface area by means of the modified Kozeny-Carmen equation.

5.3 PROPPANT SELECTION

5.3.1 Factors Affecting Fracture Conductivity

The selection of a proppant is mainly governed by the fracture conductivity required for a desired production rate. This, in turn, is related to the in-situ pemeability, porosity and concentration of

the proppant within the fracture. The physical properties of a propping agent that will affect the resulting fracture conductivity are [105]: strength, grain size, grain-size distribution, proppant density, roundness and sphericity, and proppant quality (amount of fines and impurities). Fracture conductivity is also dependent upon formation properties (i.e. proppant embedment) and, of course, closure stress. Figure 5.1 indicates the effect of proppant crushing and embedment on the porosity of a propped fracture. The drawdown rate may also affect the conductivity. As the reservoir is depleted, both the fracture gradient and bottom hole pressure are reduced, but at different rates. This has the effect of increasing the effective stress acting on the proppant, therefore reducing conductivity. As shown in Chapter 4, if the wellbore is surrounded by a yield zone, the maximum closure will no longer be on the borehole wall but will act on the fracture face at a radial distance from the hole dictated by the mechanical properties of the rock. Thus, the proppant selected must be strong enough to withstand this increased closure stress if a marked reduction in conductivity is to be avoided.

5.3.2 Propping Agents

As stated in the opening chapter, the function of a propping agent is to artificially hold a hydraulic fracture open and thus provide conductivity. The amount of proppant necessary to accomplish this will depend, of course, on the height, width and length of the created fracture.

PROPPANT EVALUATION ....

Measurement of Hydraulic Fracture Conductivity

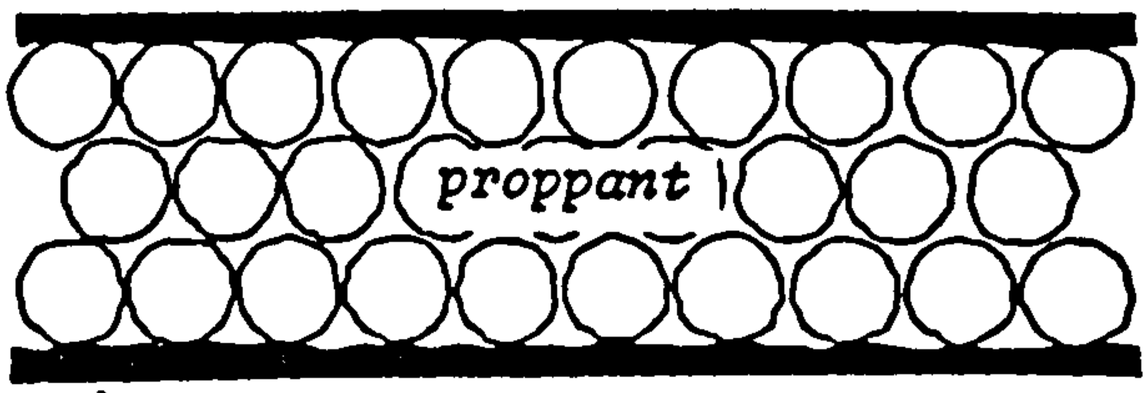

High strength proppant, hard formation ....
high fracture conductivity

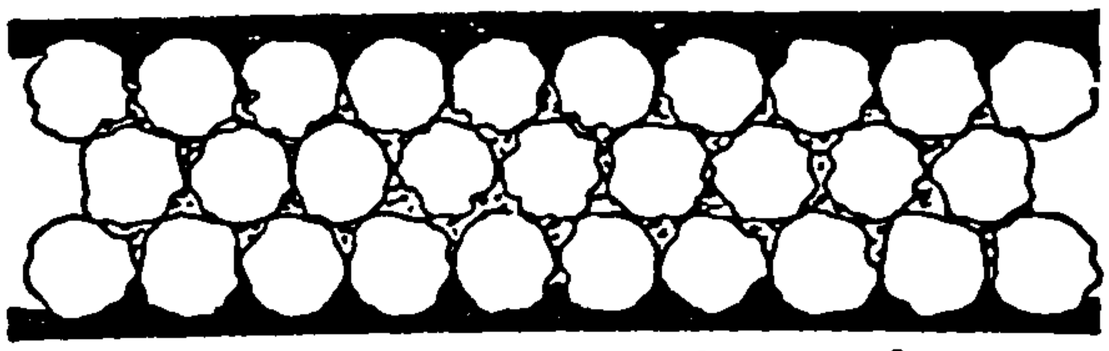

Low strength proppant, soft formation .....
low fracture conductivity

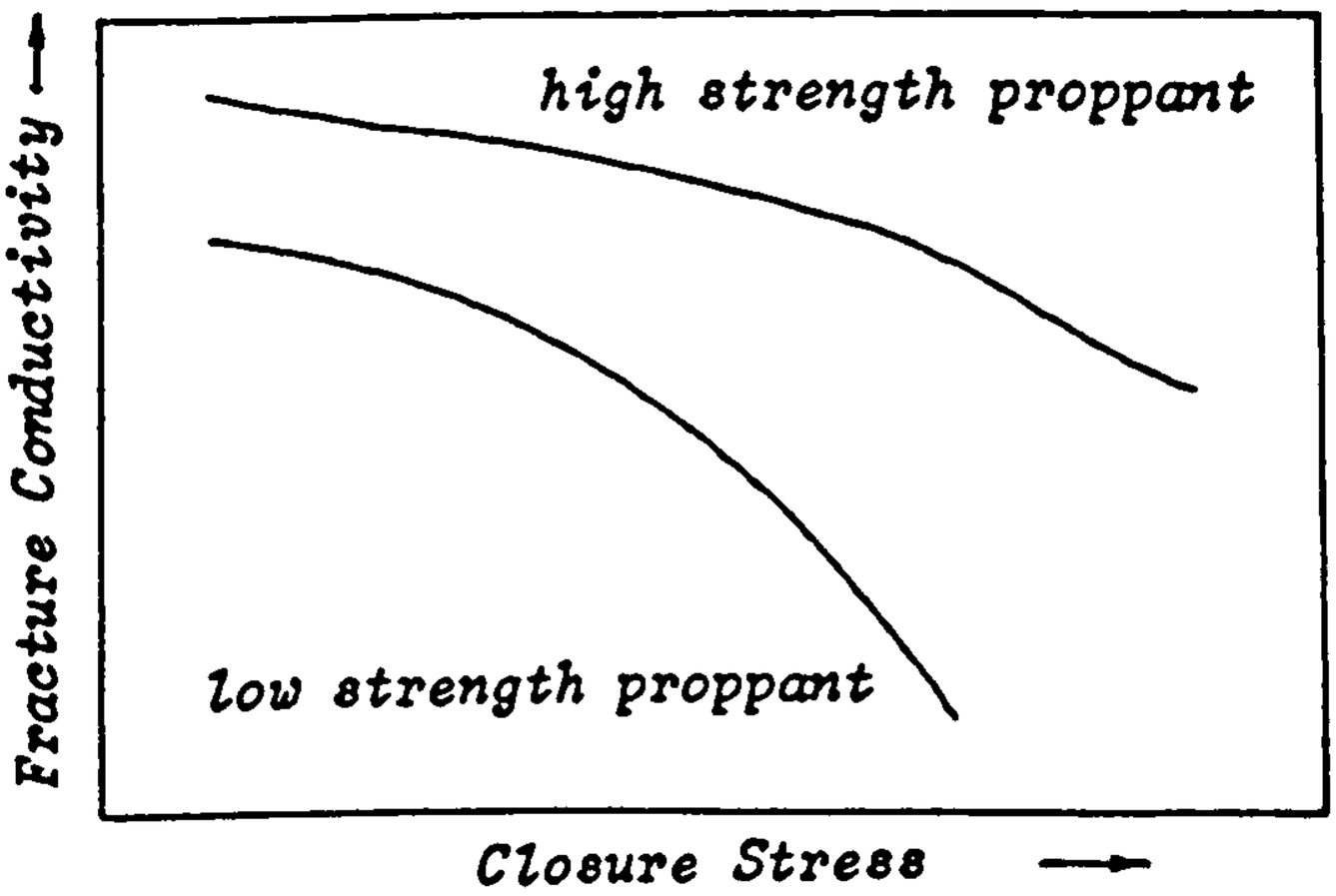

EFFECT OF STRESS ON FRACTURE CONDUCTIVITY

Figure 5.1 : Effect of Proppant Crushing and Embedment on the Porosity of a Propped Fracture

Some of the earlier materials used as propping agents included sand, steel shot, aluminium pellets, plastic beads and ground walnut shells. With the exception of sand, the above pioneering materials were proven unreliable [57]. Ceramics, such as glass beads, were then introduced and widely accepted for use as high strength propping agents. Such materials were found to resist crushing in the laboratory up to closure stresses of 6000 psi (41000 kPa). If these proppants, however, were scratched or damaged when pumped downhole during a fracturing treatment or exposed to high temperature brine, they would lose most of their compressive strength and therefore become ineffective in maintaining conductivity. For these reasons, and due to high manufacturing costs, glass beads are no longer used in the industry.

Sand is the most often used proppant, especially in wells with low closure stress. Due to the large quantities and wide variety of proppants used today, the American Petroleum Institute has established test procedures for several proppant properties to distinguish the quality and usefulness of each proppant [106]. There are currently four reliable propping agents available for hydraulic fracturing purposes: API quality frac sand, resin-coated sand, intermediate strength proppants and sintered bauxite. The following is a brief overview of their properties and applications.

5.3.2.1 API Quality Frac Sand

Frac sands can be sub-divided into groups of excellent, good and substandard grades, and typically have a specific gravity of about

2.65. The term excellent quality is derived from the material strength or crush resistance properties. In terms of fines generated, crush resistance for these sands is less than half of the maximum value recommended by API RP56 [106]. Good quality sand meets or exceeds the recommendations of API while substandard grades fail to meet the API recommendations.

Silica or quartz sand provides several advantages and has been proven to be successful for all reservoir types with certain depth limitations. Frac sand is less expensive than other types of proppants and it is readily available in most areas. When sand crushes, it breaks into fragments that still maintain some permeability which may be adequate for production under certain circumstances. Currently no other low cost proppant material is available in quantity that offers the roundness, strength and chemical resistance of sand. The disadvantages of sand are that it will begin to crush at very low closure stress and substantial crushing is evident at about 4000 psi (28000 kPa). Therefore, in deep formations the fracture conductivity may be reduced by tenfold or more [57].

5.3.2.2 <u>Resin Coated Sand</u>

Resin coated sand, which has a specific gravity of around 2.55, is made by coating frac sand with an organic resin which is partly polymerised. Two types of resin coated sand are used as fracture proppants, curable and precured. Both curable and precured variaties are manufactured by the same process that is used to produce coated

sand for the foundry industry.

Curable resin coated sand was originally patented by Exxon Production Research for use in gravel packing operations. Precured proppants became available in 1982, about nine years after the first curable product was used in fracturing operations. When subjected to stress, the precured resin coated sands have higher conductivity and are stronger than conventional sands. This is due to the resin coating which helps to spread the stress over a larger area of the sand grain and reduces point loading. When the grains do crush, the resin coating helps to encapsulate the crushed portions of the grains and prevents them from migrating and plugging the pore channel and reducing the permeability. The curable resin coated sands are used mainly to prevent flowback of proppant near the wellbore. Figure 5.2 illustrates that uncoated frac sand begins to lose permeability at about 4000 psi (28000 kPa). Fully cured resin coated sand is seen to lose permeability at about 6000 psi (41000kPa). At 10000 psi (69000 kPa), the fracture permeability of both uncoated and resin coated sand are similar.

As the resin occupies pore space, the permeability of the resin coated pack is necessarily lower than that of uncoated proppant prior to crushing. Although a resin coating may be added to any type of proppant, there is less demand for coating the higher strength proppants.

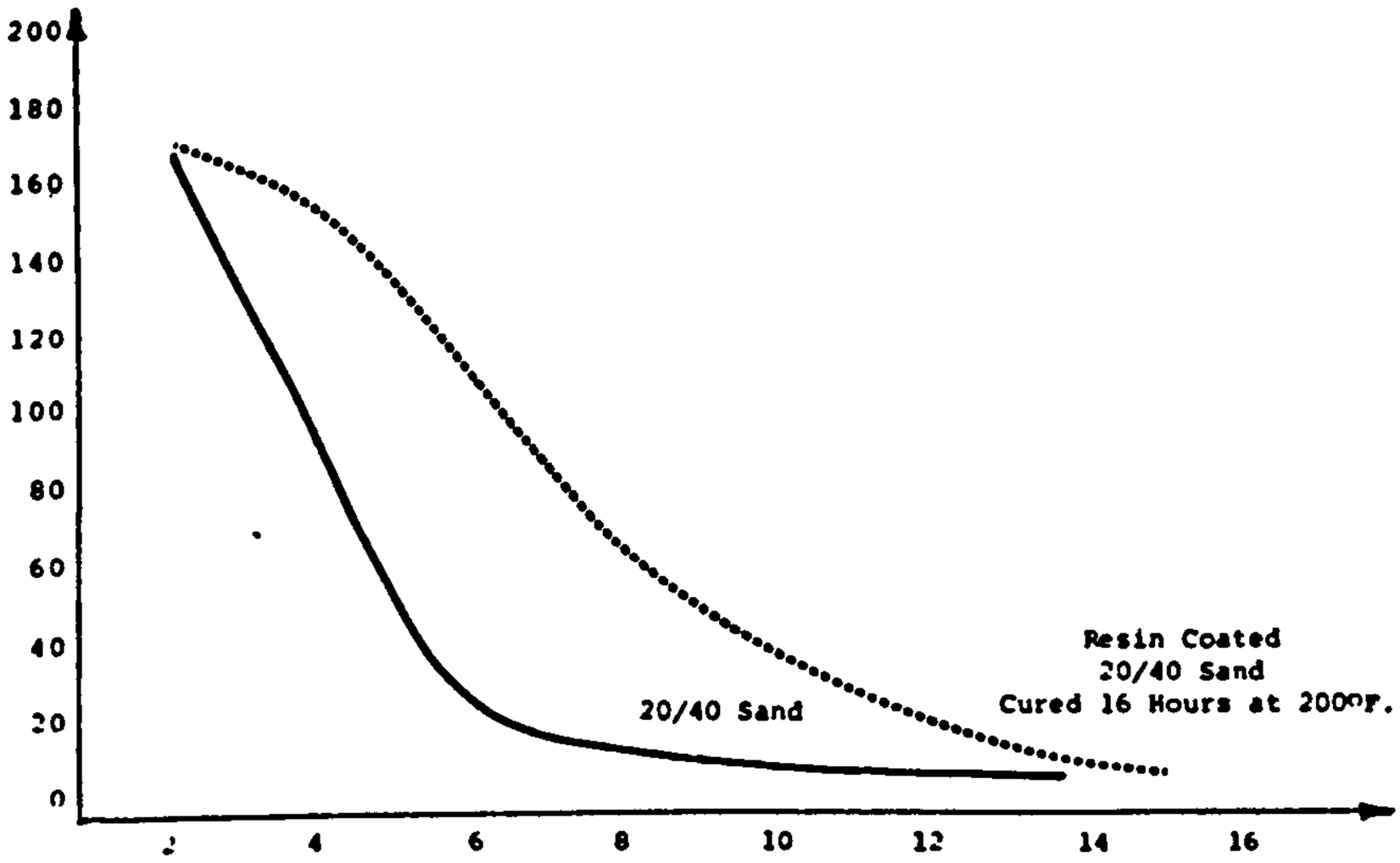

Figure 5.2 : Effect of Resin Coatings on Propping Agents

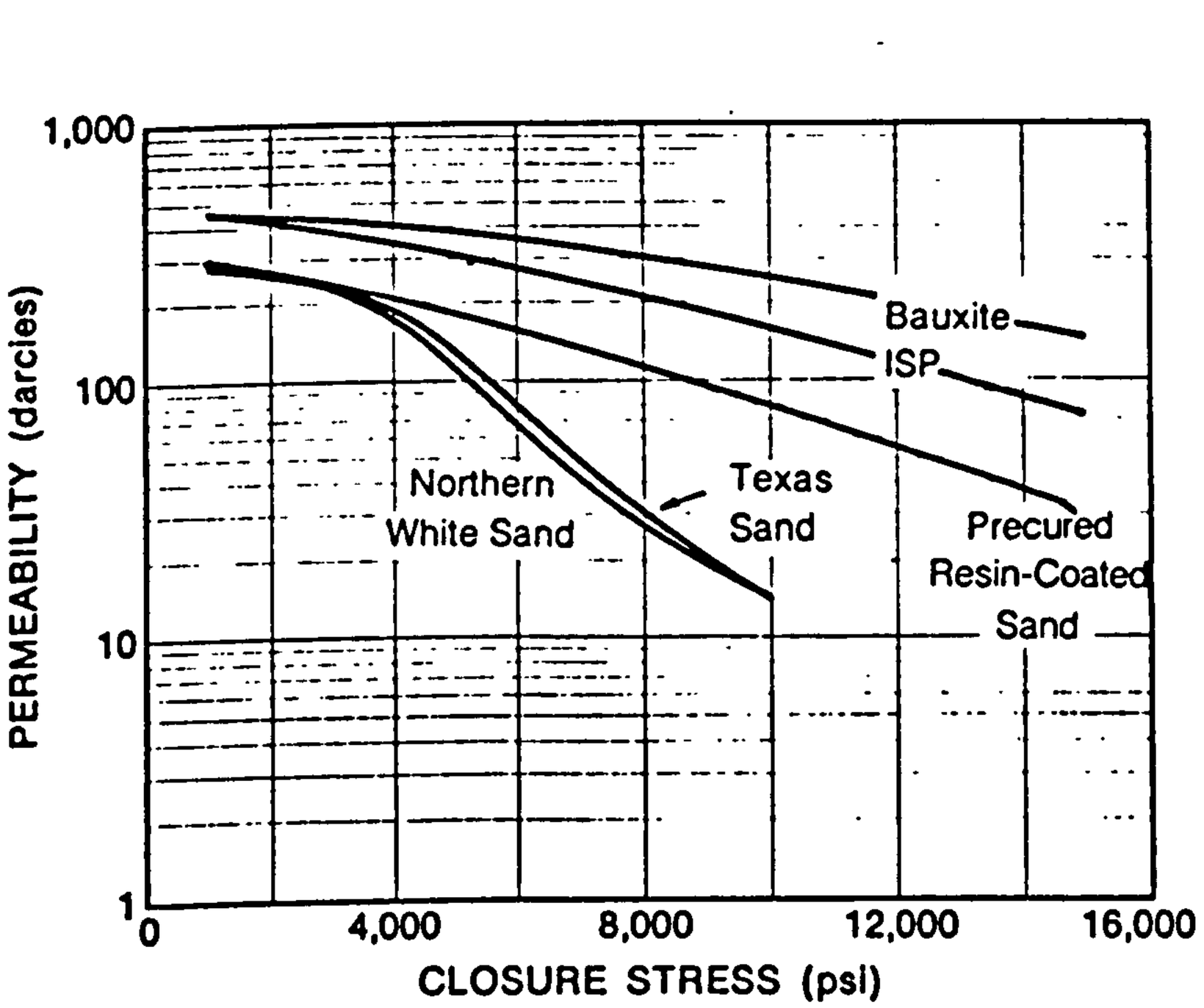

Figure 5.3 : Permeability vs Closure Stress for Various 20/40 U.S. Mesh Proppants [57]

5.3.2.3 Intermediate Strength Proppants

Intermediate strength proppants (ISP), also referred to as intermediate density proppants, are fused ceramic proppants that have a specific gravity of approximately 2.7 to 3.3. The lower specific gravity is representative of the raw materials used to make the proppant. The absence of continuous crystaline shear planes produces high strength and exceptional crush resistance. Crushing of ISPs produces large particles which are still capable of providing good flow capacity. Their roundness and sphericity are similar to the best frac sands, while their bulk density is only slightly higher. In spite of these similarities, the load bearing properties of intermediate strength proppants are far superior to those of frac sand. Intermediate strength proppants are mainly used in the closure stress ranges between 6000 psi (41000 kPa) where frac sand fails, 10000 to 12000 psi (69000 to 83000 kPa), where it begins to fail.

5.3.2.4 Sintered Bauxite

Sintered Bauxite, developed and patented by the Exxon Production Research Company, is a high strength propping agent with a specific gravity of about 3.4 or greater. It is manufactured from the high temperature sintering of high alumina bauxite ore which has been ground into particles of the desired shape and size. The colour of the final product can vary from black to brown or grey.

Corundum, the major component of Sintered Bauxite, is one of the hardest materials known to man. It measures nine on the Moh hardness

scale. For comparison, quartz is seven and diamond is ten. When crushed, bauxite does not shatter as completely as do the sands. It simply splits into large pieces which are still capable of providing flow capacity. This crush resistance is due in part to bauxite's elastic properties, which allow slight deformation before failure at high stress.

The first bauxite products were angular in shape, causing abrasion and failure of pumping equipment, treating lines and chokes. Process improvements have produced a material with roundness and sphericity which are better than the best quality frac sands. Although currently available only in limited quantities, Sintered Bauxite has become the standard against which all other proppants are measured. Figure 5.3 illustrates Sintered Bauxite's superiority as compared to other proppants in maintaining high conductivity under extreme pressure.

5.4 LABORATORY MEASUREMENT OF FRACTURE CONDUCTIVITY

5.4.1 Review of Previous Work

In the past, fracture conductivity has been measured in the laboratory by placing a bed of proppant between slabs of reservoir rock or different metals, applying mechanical stress to the proppant and flowing a fluid through the proppant bed to measure the fluid conductivity.

Much conflicting data has been presented on the subject of fracture

conductivity. Often, the choice of test parameters or cell design have been responsible for these discrepancies. There are two basic cell types which have been used to determine fracture conductivity. In early investigations, a radial conductivity cell was used [Figure 5.4(a)]. As oil or gas flow in a fracture is generally linear, results provided by such tests were therefore unrepresentive of in-situ conditions.. The advantage with this type of cell however, is that formation samples may be easily inserted in place of steel pistons and accordingly such a cell can be used to measure the combined effect of proppant crushing and embedment. Alternatively, a linear flow cell can be used which simulates the in-situ flow regime found in hydraulic fractures, as illustrated in Figure 5.4(b). The disadvantage with this approach is that it only measures proppant crushing, as steel pistons are used to apply the closure stress. Formation samples may be inserted into such a cell but the preparation time required to shape the samples to fit the linear flow cell is usually prohibitive.

Service companies providing commercially available proppants are the main source of fracture conductivity information [57,107]. In general, these tests are conducted using steel pistons as the simulated fracture face and therefore do not consider the effect of proppant embedment. The conductivities and permeabilities reported by them should only be used to provide relative comparisons and require to be adjusted for use in job design based on a knowledge of embedment, pack damage and multi-phase flow.

In the 1970s, Cooke published several papers on the subject of

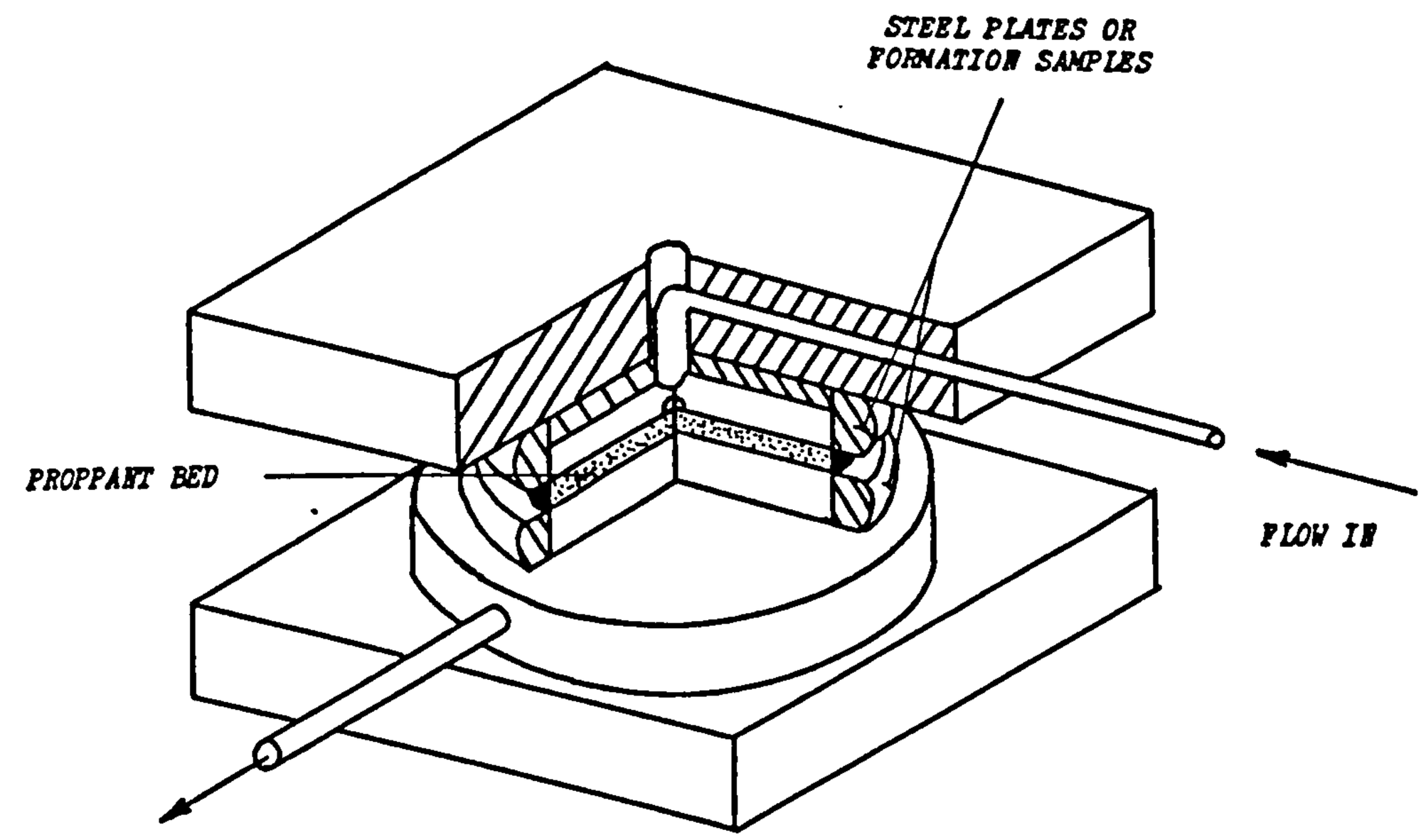

(A) RADIAL FLOW CELL

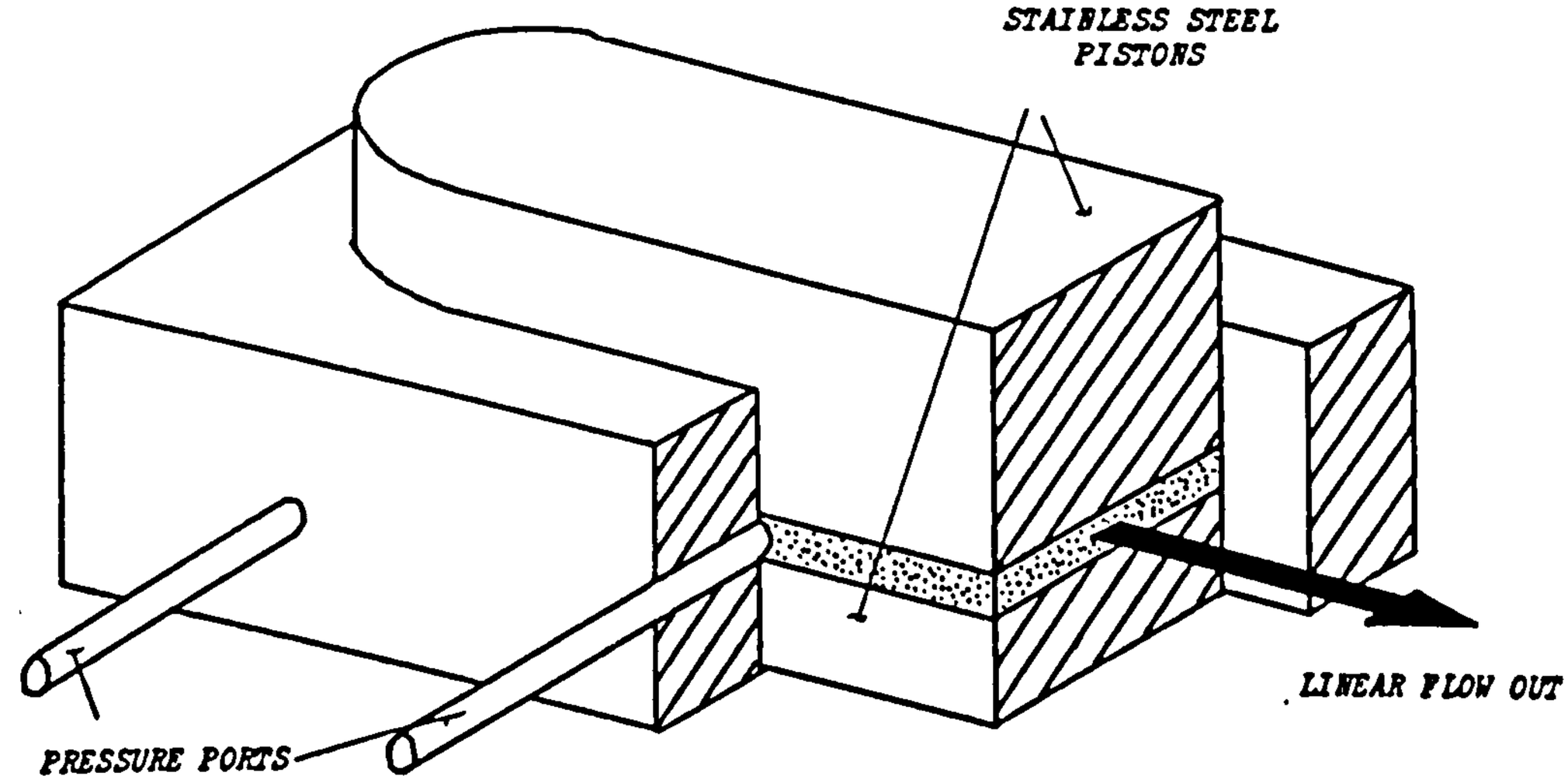

(B) LINEAR FLOW CELL

Figure 5.4 : Example of Typical Designs of Conductivity Cell

fracture conductivity. The first of which presented data on the effect of the testing environment on the conductivity of a multi-layer of brittle proppant under stress and the effect of flow rate (deviation from Darcy's law) on the flow resistance of the proppants [108]. He concluded that the permeability of multiple layers of frac sand under stress can be affected by the presence of high temperature brine. He went on to state that all the proppants tested showed a marked difference in permeability/stress behaviour in the presence of oil and water at 250°F. Cooke also identified the need for improved materials to use as propping agents. The second of his papers examined the effect of fracturing fluid on fracture conductivity [109]. He stated that the factors which determined conductivity reduction from a fracturing fluid were the concentration of proppant in the fluid, the amount of gel residue in the fluid, the porosity of the proppant, and the fraction of gel residue retained in the fracture as the fluid leaks off. In a later paper, Cooke introduced the industry to high-strength sintered bauxite by demonstrating its superior crush resistance to other proppants in laboratory tests [110].

Cutler et al [111] conducted a laboratory comparison of commercially available and experimental proppants at intermediate and high closure stresses. Their analysis, while providing a considerable amount of data, only considered the effect of proppant crushing. Although an early type of linear flow cell was used to generate the data, the pressure drop was not measured within the linear flow section of the cell and thus may have had a detrimental effect on the results.

Brown and Much [112] performed a laboratory evaluation of four commonly used proppants using a similar cell. They concluded that the conductivity of a propped fracture decreases with time because of the interaction between the proppant and its environment. In long term tests, intermeadiate strength proppants showed only a minor loss of conductivity versus time while frac sands lost most of their initial conductivity. They stated that stress activated corrosion was believed to be an important factor in proppant failure. Brown and Much went on to conduct further research into the effects of stress corrosion [113] and concluded that the long term stability of a proppant is a function of its composition, surface and internal flaws, and the environment where it is used.

McDaniel [114] developed a non-commercial approach to measure fracture conductivity in the laboratory to assist operators in the selection of proppants for high temperature and high stress hydraulic fracturing operations. In his work, he investigated the effects of extended time at different test conditions, the variation between ambient and elevated temperature testing and the effects of brine flow at high temperature and closure stress. His results, which indicated that short-term, ambient temperature conductivity testing usually results in optimistic results, are summarised in Table 5.1. The right hand column of this table shows the ratio of the final conductivity to the original low temperature conductivity that was measured at the same stress prior to heating. McDaniel termed this value the 'Conductivity Correction Factor' which could be used to correct low temperature test data. He went on to state

Combined loss of conductivity during the test period as a result of 8,000 psi [55.2 MPa] stress, 275°F [135°C], and 2% KCl brine flow for 10 to 14 days

Proppant	Conductivity @ 75°F [24°C] (D-ft)	Final Conductivity @ 275°F [135°C] (D-ft)	Conductivity Correction Factor
Ottawa Sand	0.840	0.063	.07
Ottawa Sand*	2.080	0.158	.08
RC Sand	2.590	0.438	.17
ICP	4.990	2.482	.47
ISB	5.070	2.655	.53
HSB	4.950	2.686	.54

* This data is for a proppant concentration of 4.0 lb/ft^2 while all other data in this table is for 2.0 lb/ft^2. The values in this table represent an average from 2 or 3 tests.

Table 5.1 : Summary of McDaniel's Conductivity Results Showing the Concept of A Conductivity Correction Factor [114]

that the values in the table were not intended to be universal in application and that in a specific oilfield application, a lower or higher formation temperature or closure stress would possibly give a different correction factor. The approach developed by McDaniels has provided good data on the effect of high temperature and stress on selected proppants, however, his analysis does not consider the effect of proppant embedment.

Wendorff [115], in his examination of fracture conductivity took into account the effect of proppant embedment by means of incorporating formation samples in the test procedure. He developed a fracture porosimeter, which was in effect, a conventional Hoek-Franklin triaxial cell to apply confining pressure and closure stress to a bed of proppant sandwiched between two core samples. Wendorff reasoned that the conductivity of a propped fracture under down-hole conditions could be determined using a modified Kozeny-Carmen equation (see Section 5.2.5). With this relationship, fracture conductivity at stress can be calculated when proppant wetted surface area, porosity and fracture width are known. He constructed a data-base which consisted of wetted surface areas and permeabilities of proppants over a range of closure stresses. The data was generated using a linear flow cell, while the fracture porosimeter was used to measure the amount of proppant embedment and therefore the respective reduction in porosity. He concluded by stating that his results were in general agreement with field experience and with limited fracture conductivity data obtained on rock-proppant systems, thus indicating that the method was reliable for determining the conductivity of propped formations under stress.

He went on to propose that the use of a Hoek triaxial cell as a fracture porosimeter allowed both closure and confining stresses to be applied to the rock-proppant systems, thus better simulating downhole stress conditions.

The method developed by Wendorff appears, at present, to be the most realistic for the laboratory determination of fracture conductivity as it considers the combined effect of proppant crushing and embedment. The validity of the Kozeny-Carmen equation was investigated in Section 5.2.5 and was found to be applicable. It is for these reasons that Wendorff's approach was adopted for the basis of this analysis and a fuller account of the theory is given below.

5.4.2 Theoretical Basis to the Project

5.4.2.1 Set up of Proppant Data Base

Using the linear flow test unit, the fracture conductivity of a bed of proppant compressed between steel pistons may be calculated using a modified Darcy's equation.

$$kW_f = \frac{0.008\ Q\mu l}{\Delta P b} \qquad \ldots\ldots\ldots\ldots\ldots (5.9)$$

where, kW_f = Fracture conductivity (darcy-ft)

Q = Flow rate of test fluid (cc/min)

l = Length between pressure ports (in)

ΔP = Differential pressure between ports (psi)

b = Breadth of test unit (in)

μ = Viscosity of test fluid (cp)

In order to determine the wetted surface area of a proppant, it is necessary to determine the width of the propped fracture and the porosity of the proppant bed. The fracture width is determined by subtracting the length of the pistons and shims at closure stress (L_p), from the length of the pistons, shims and proppant bed measured at closure stress ($_{Lpo}$).

$$W_f = L_{po} - L_p \qquad \text{.. .. .. (5.10)}$$

The porosity of the proppant bed is obtained by subtracting the absolute volume of the proppant from the test unit volume and dividing by the test unit volume, viz.

$$\phi = 100\,\frac{(W_f a - V)}{W_f a} \qquad \text{.. .. .. (5.11)}$$

and, $$V = 0.061(M/D) \qquad \text{.. .. .. (5.12)}$$

where, ϕ = Proppant Porosity (%)

Wf = Fracture width (in)

a = Test unit area (in^2)

V = Absolute volume of proppant (in^3)

M = Weight of proppant tested (g)

D = Absolute density of proppant (g/cc)

The wetted surface area of the proppant may then be determined from the above data by solving equation (5.8) for S, as follows :

$$S = \sqrt{\frac{1.1\times10^{7}}{kW_f}\, W_f \frac{\phi^3}{(1-\phi)^2}} \qquad .. \quad .. \quad .. \quad .. \quad (5.13)$$

Flow cell permeability may be calculated by dividing the fracture conductivity by the width of propped fracture,

$$k = \frac{12(kW_f)}{W_f} \qquad .. \quad .. \quad .. \quad .. \quad .. \quad (5.14)$$

5.4.2.2 Application of Proppant Data Base to Formation Samples

Using the above data and utilising a triaxial fracture porosimeter, a value for fracture conductivity allowing for proppant embedment may now be obtained provided the width of the proppant bed (W_f) between two formation cores is known. This can be determined the following relationship:

$$W_f = L_t - L \qquad .. \quad .. \quad .. \quad .. \quad .. \quad (5.15)$$

where L_t = Length of plattens, core plugs and propped fracture at given stress (in)

L = Length of plattens and core plugs at given closure stress (in)

Knowing the propped fracture width between formation samples, the porosity at closure stress of the simulated fracture may be calculated using equation (5.11).

Finally, using ϕ and W_f determined from the fracture porosimeter and S from the data base, the fracture conductivity, taking into account

the effect of proppant embedment, may be found using the Modified Kozeny-Carmen equation (5.8).

As before, the permeability of the simulated propped fracture may be found from equation (5.13) by substituting kW_f and W_f determined from the fracture porosimeter.

5.4.3 Equipment Required for the Laboratory Determination of Fracture Conductivity/Permeability

The following equipment was identified as being required for the laboratory measurement of fracture conductivity :

(a) Linear flow cell

(b) Permeameter system

(c) Triaxial cell

(d) Compression Machine

The linear flow cell and permeameter system were specialised items which were not commercially available. It was therefore necessary to design and manufacture the required equipment within the Department of Mineral Resources Engineering. Full details of the design and manufacturing stage are given in Section 5.6.

5.5 PRELIMINARY FRACTURE PERMEABILITY INVESTIGATIONS USING A NITROGEN PERMEAMETER AND TRIAXIAL CELL

5.5.1 Introduction

During the early stages of the linear flow cell and oil permeameter manufacture, a series of fracture permeability/conductivity tests were performed by the author in conjunction with Grant [116]. These tests, using a gas permeameter, triaxial cell and rock cores with simulated propped, vertical fractures, were intended to examine the combined effect of proppant crushing, embedment, formation crushing and formation permeability at various closure stress values. As this investigation was conducted to provide a preliminary indication of proppant performance, the nitrogen permeability values obtained were not converted to Klinkenberg liquid permeabilities.

5.5.2 Equipment

5.5.2.1 Nitrogen Permeameter

The E.D.P.S. nitrogen permeameter [117] has been designed to eliminate many of the potential sources of error which can occur with conventional gas permeameters. It is a highly accurate instrument intended for both academic and industrial use.

The instrument operates by flowing nitrogen at a known rate through a rock core and measuring the resulting pressure drop by means of a differential pressure transducer. Upstream pressure, flow rate and

nitrogen temperature are also monitored to allow the calculation of rock permeability. The permeameter is provided with a B.C.D. socket which may be easily interfaced with most microcomputers enabling real time permeability calculations to be performed using electronic flow, pressure and temperature data. Rock cores are held in a rubber sleeve within a Hassler type cell and confined under a maximum pressure of 150 psig. The design of the core holder enables rapid sample changeover, a simple release lock mechanism provides a seal for both the confining pressure and core pressure.The core holder provided accepts 1 inch diameter cores up to 3 inches long.

The instrument is capable of measuring accurate flow and pressure parametres for cores with permeabilities ranging from 0.1 mD to in excess of 20 Darcies.

5.5.2.2 Modifications to the Nitrogen Permeameter System

The major modification to the nitrogen permeameter system was the inclusion of a triaxial cell to allow in-situ stress to be applied to the core sample. Accordingly, longer inlet and outlet nitrogen flow lines were required to allow the nitrogen permeameter to be connected to the plattens of the the triaxial cell. Gas flow through the plattens and sample was provided by the use of perforated plattens [118].

During initial testing it was suggested that a leak in the triaxial cell could allow hydraulic oil to enter the nitrogen flow lines, and if left unchecked, could cause irrepairable damage to the more

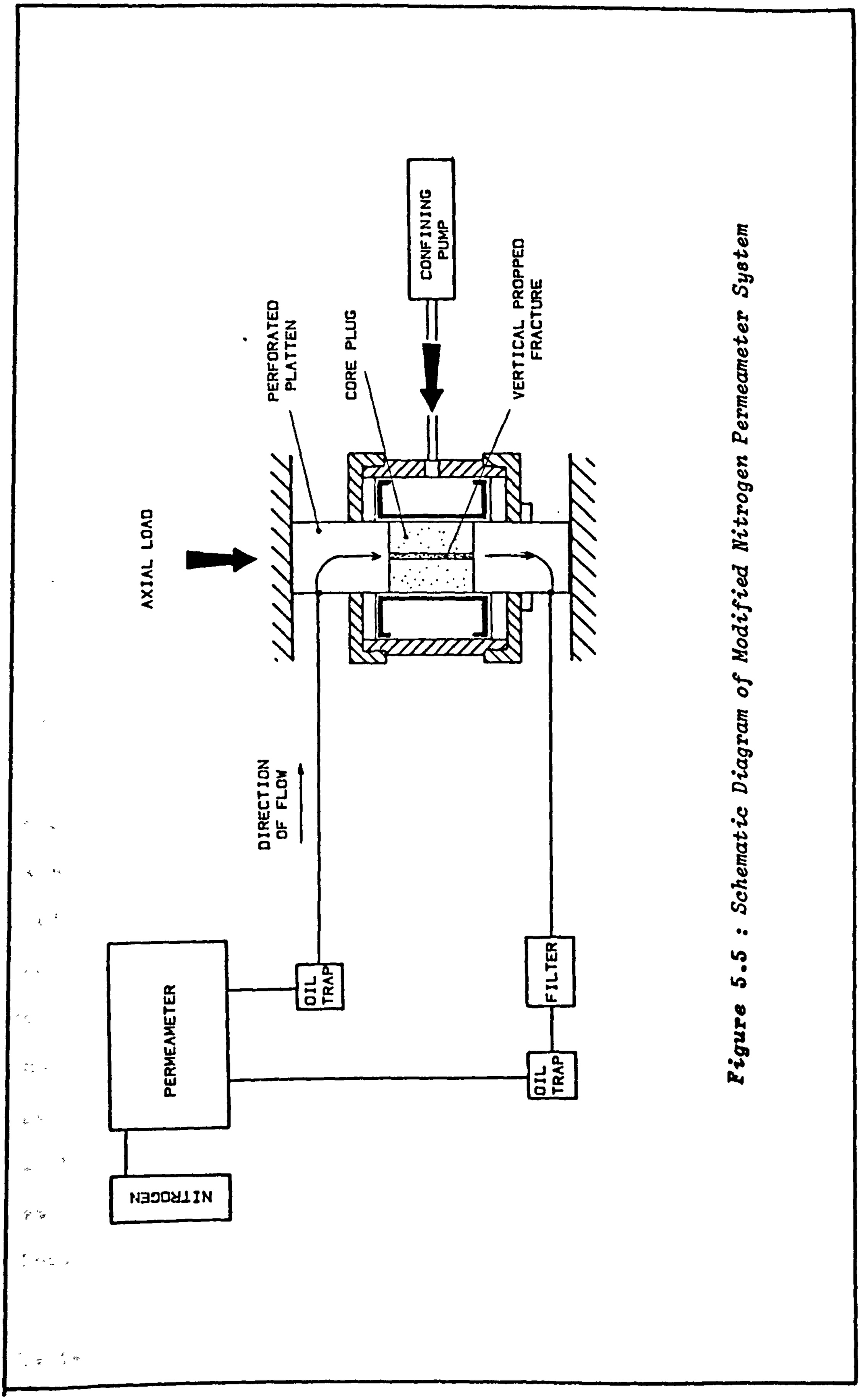

Figure 5.5 : Schematic Diagram of Modified Nitrogen Permeameter System

sensitive electronic components of the nitrogen permeameter. In order to safeguard these components, two oil traps were manufactured and included in the system. An in-line filter was connected to the core outlet flow line to trap any fines produced. The modified nitrogen permeameter system is depicted in Figure 5.5.

5.5.3 Testing Programme

Two different sandstones were tested. These being a soft, red sandstone displaying a coarse grain texture (Brinell hardness = 24), and a hard, fine grained white sandstone (Brinell hardness = 65). In order to obtain a comparison, both rock types were tested with 20/40 Sintered Bauxite and 12/20 frac sand.

5.5.3.1 Sample Preparation

Core samples were obtained from blocks of red and white sandstone using a 38.1 mm (1.5 in) I.D. core barrel, water being used as a coolant. After the cores were produced, they were cut to the required length of 76.2 mm (3 in) by means of a diamond saw. Unlike conventional core preparation, the use of a lapping machine to smooth the core faces was avoided as this would damage the pore spaces at the core ends and therefore seriously reduce permeability. As the simulated fracture was required to be vertical, the diamond saw was again used to half the core along its vertical axis, as shown in Figure 5.6(a).

The two core halves were then taped together, the simulated fracture

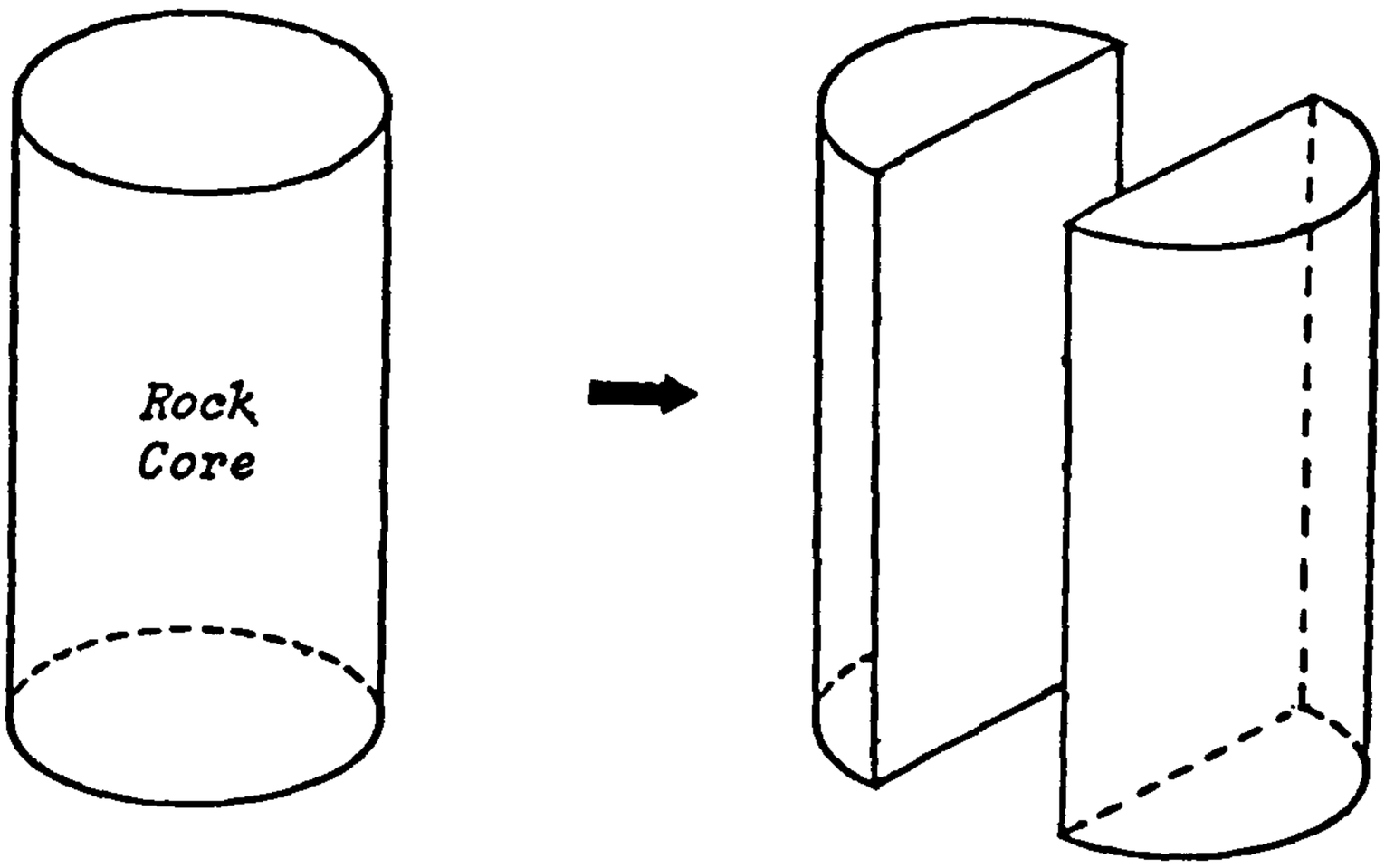

Figure 5.6(a) : Rock Sample Preparation

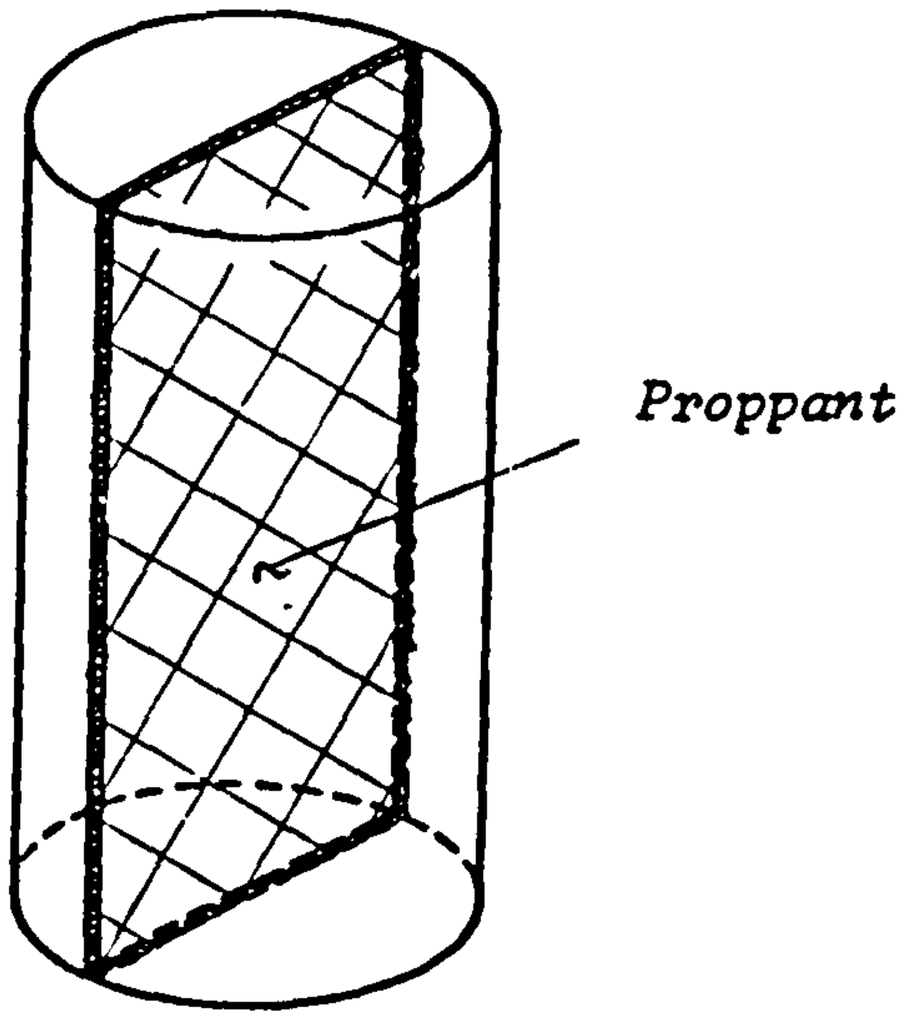

Figure 5.6(b) : Proppant Filled Fracture - Sample Ready to Test

being held open with two metal 'spacers' wedged at either end of the sample. The spacers were then removed and one fracture end sealed with tape. The desired proppant was then poured into the open fracture [Figure 5.6(b)]. During this stage, care was taken to ensure an even concentration of proppant was obtained. On completion, the other end of the fracture was sealed with tape until ready for testing. Prior to testing, the prepared cores were stored horizontally to minimise proppant settling.

5.5.3.2 Test Procedure

The prepared sample was then inserted into the triaxial cell and the fracture ends untaped before the insertion of the perforated plattens. A low confining pressure was applied to hold the sample and plattens in place. The cell was then inserted into a compression machine and a low axial stress was applied.

The axial and confining/closure stress were then increased simultaneously to their respective starting values of 2500 psi and 2000 psi (17250 kPa and 13800 kPa). Upstream pressure, nitrogen temperature, flow rate and differential pressure readings were taken before the axial and closure stress were increased to the next desired level. A vertical:horizontal stress ratio of 1.0:0.8 was maintained throughout the test. After the maximum closure stress of 7000 psi (48500 kPa) had been reached, the respective stresses were reduced in similar intervals and the respective permeameter parameters recorded.

5.5.4 Results

As stated previously, tests were conducted on samples of a soft, red sandstone and a hard, white sandstone, using 20/40 Sintered Bauxite and 12/20 sand in each case. The fracture pemeability values obtained were not converted into conductivity data as it was not possible to determine the change in fracture width at the various closure stress levels.

Tests were also run on complete cores of each type of sandstone in order to compare nitrogen permeabilities. The results obtained for the red sandstone are presented with the corresponding fracture permeability data. Flow through the white sandstone, however, was unable to be measured and was therefore considered impermeable.

5.5.4.1 Red Sandstone Tests

The results of the Sintered Bauxite and sand proppants with respect to the red sandstone tests are depicted in Figure 5.7.

From an examination of this figure, it can be seen that both proppants behaved in a similar manner and that the nitrogen permeability of the Sintered Bauxite was greater than that of the sand. The most striking aspect of this test was that the difference in nitrogen permeability between the proppants was not greater. The Sintered Bauxite nitrogen permeability was seen to decrease at a constant rate up to a closure stress of around 6500 psi (44850 kPa), where it fell steeply. An examination of the sand curve indicated a

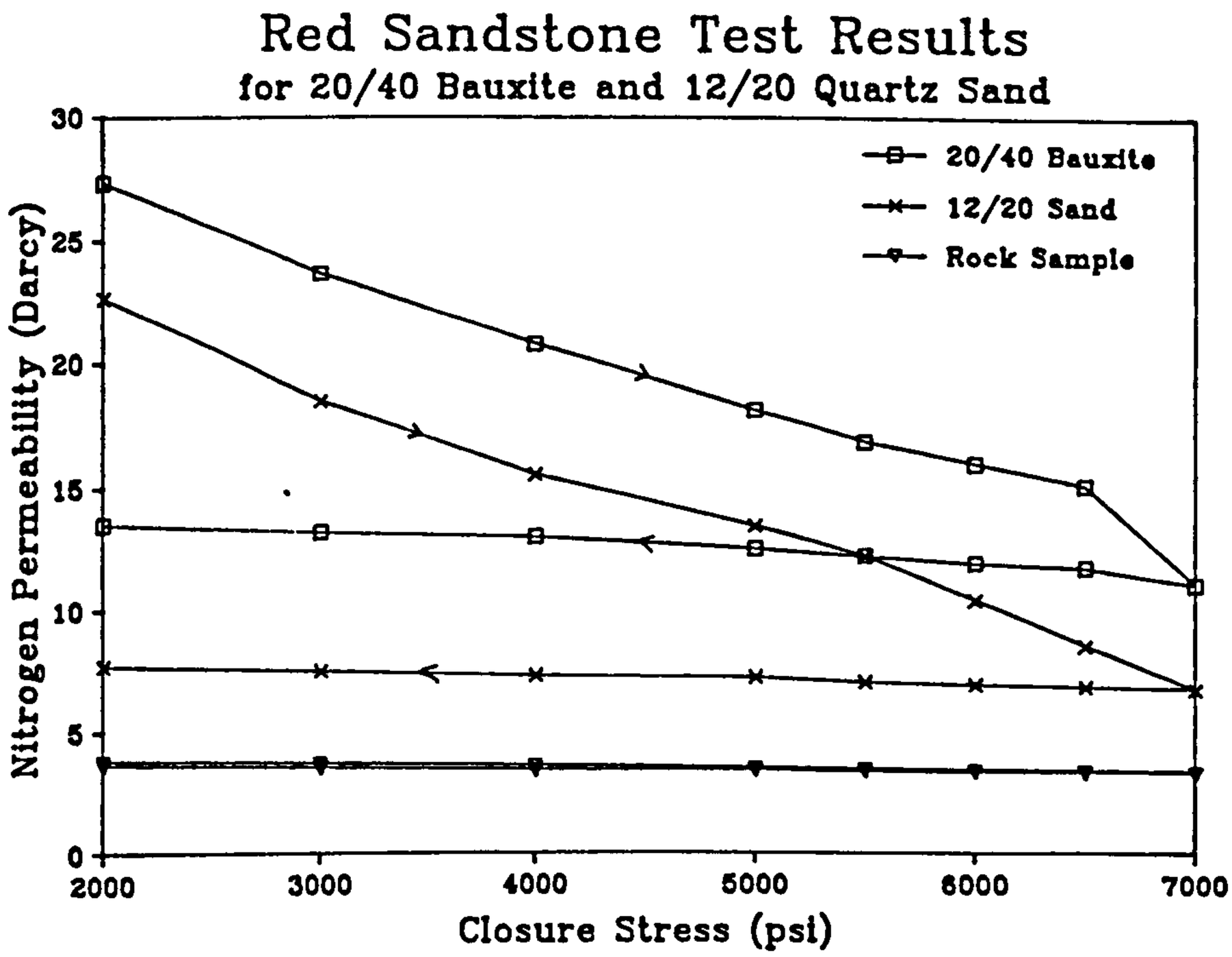

Figure 5.7 : Test Results for Red Sandstone Fracture Propped with 20/40 Bauxite and 12/20 Sand

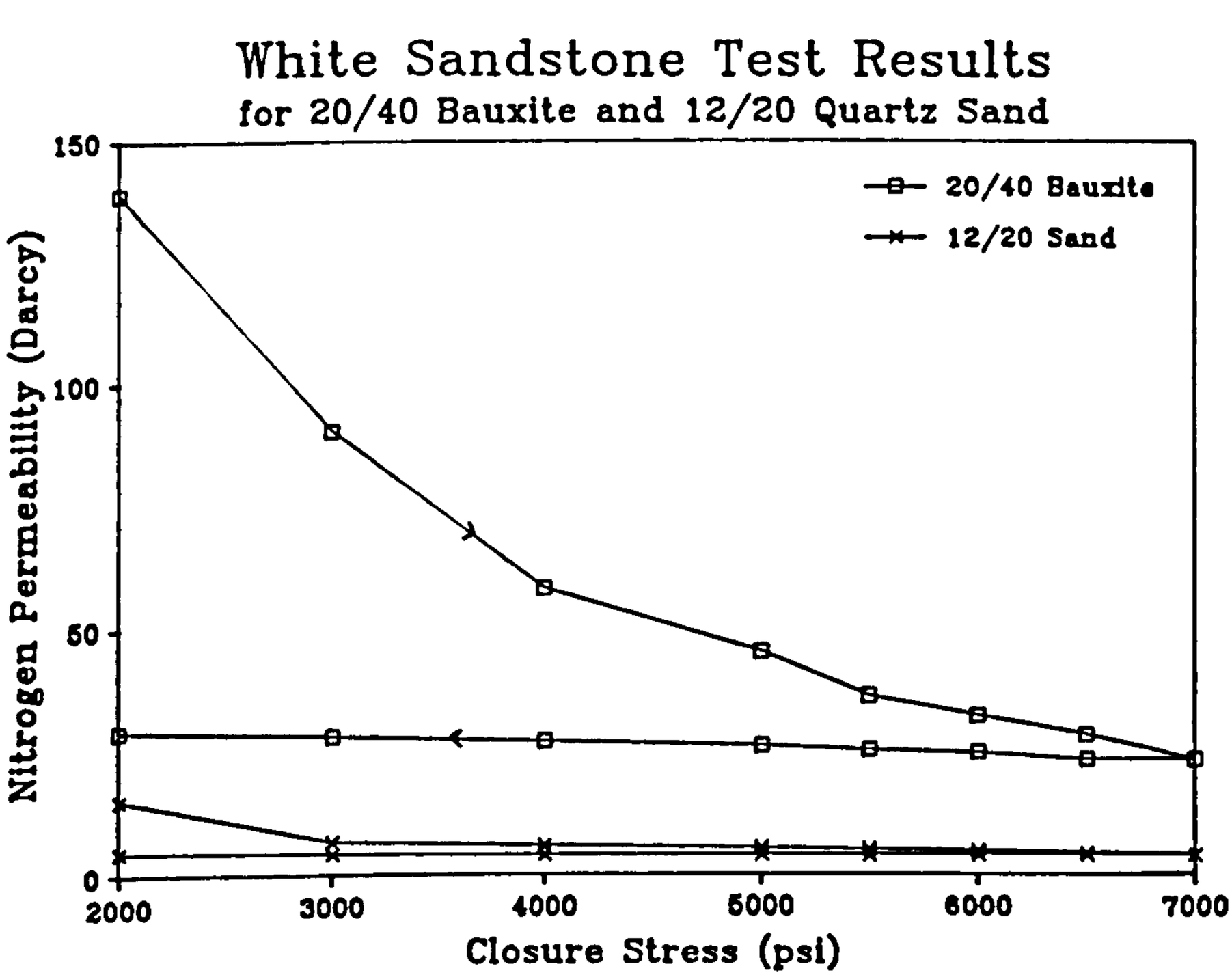

Figure 5.8 : Test Results for White Sandstone Fracture Propped with 20/40 Bauxite and 12/20 Sand

constant reduction in nitrogen permeability with closure stress values up to 4000 psi (27600 kPa), where the curve was seen to level off before again following a downward trend. At the maximum closure stress of 7000 psi (48300 kPa), it was evident that the nitrogen permeability of the Sintered Bauxite fracture was twice that of the sand fracture. In both cases, nitrogen permeability readings were also taken while the closure and axial stress were being removed. In both cases, it was evident that the fracture permeability was essentially irrecoverable.

5.5.4.2 White Sandstone Tests

The results of the white sandstone tests with both proppant types are displayed in Figure 5.8.

The Sintered Bauxite proppant curve displayed a high initial nitrogen permeability which decreased rapidly until a closure stress of around 4000 psi (27600 kPa) was reached where it was observed to decrease at a constant level. The sand curve however, had a low initial nitrogen permeability which decreased at a relatively constant level. At the maximum closure stress, it was apparent that the nitrogen permeability of the sintered bauxite was in the order of six times greater than the sand propped fracture. As in the case of the red sandstone tests, permeameter readings were taken as the respective stress values were decreased and similarly, it was observed that fracture permeability was essentially irreversable.

5.5.4.3 Discussion and Comparison of Results

The most striking difference between the two sets of test results was the difference in nitrogen permeabilities of the fractures propped with Sintered Bauxite, the white sandstone yielding the higher values. As an examination of the red sanstone fracture faces indicated that severe embedment had occurred while minimal proppant crushing was observed, it was most likely that the difference was due to the 'soft' nature of the sample. With the harder, white sandstone however, the Sintered Bauxite would have tended to deform rather than embed as little evidence of embedment was observed in the fracture face.

A comparison of the permeabilities obtained from the sand propped fractures indicated that the red sandstone sample displayed a higher fracture permeability, with an overall average of twice that of the white sandstone. An examination of both sample fracture faces indicated that while proppant embedment had occurred in both cases, it was most apparent in the red sandstone fracture. An analysis of the proppant grains however, indicated that although crushing was evident in both instances, the proppant removed from the white sandstone fracture was more severely crushed. Therefore, in this case, it appeared that proppant crushing was the major factor in permeability reduction.

5.5.5 Conclusions

This investigation was intended to demonstrate the importance of using the most suitable type of proppant with respect to a specific formation. It can be therefore be concluded that the use of a high strength proppant, such as Sintered Bauxite, in conjunction with a soft, friable formation is not economical, while the use of a low strength proppant, such as sand, in conjunction with a hard formation will lead to excessive crushing and consequent reduction in fracture permeability. It is therefore clear that the physical properties of the formation to be fractured must be taken into consideration when estimating the required fracture conductivity.

5.6 EQUIPMENT DESIGN AND MANUFACTURE

5.6.1 Linear Flow Cell

The test cell described below is based on a design proposed by Cooke [108]. It is a linear flow cell capable of testing a proppant pack 7 in. long, 1.5 in. across and of varying width. It is sometimes referred to as an API cell although the design has never been finalised by the American Petroleum Institute committee [119]. The linear flow cell has a test area of 10 in^2 and has been machined from 304 stainless steel. The cell is capable of withstanding in excess of 15000 psi (103500 kPa) closure stress. A diagrammatic representation of the cell is given in Figure 5.9.

With reference to Figure 5.10, the linear flow cell comprises of

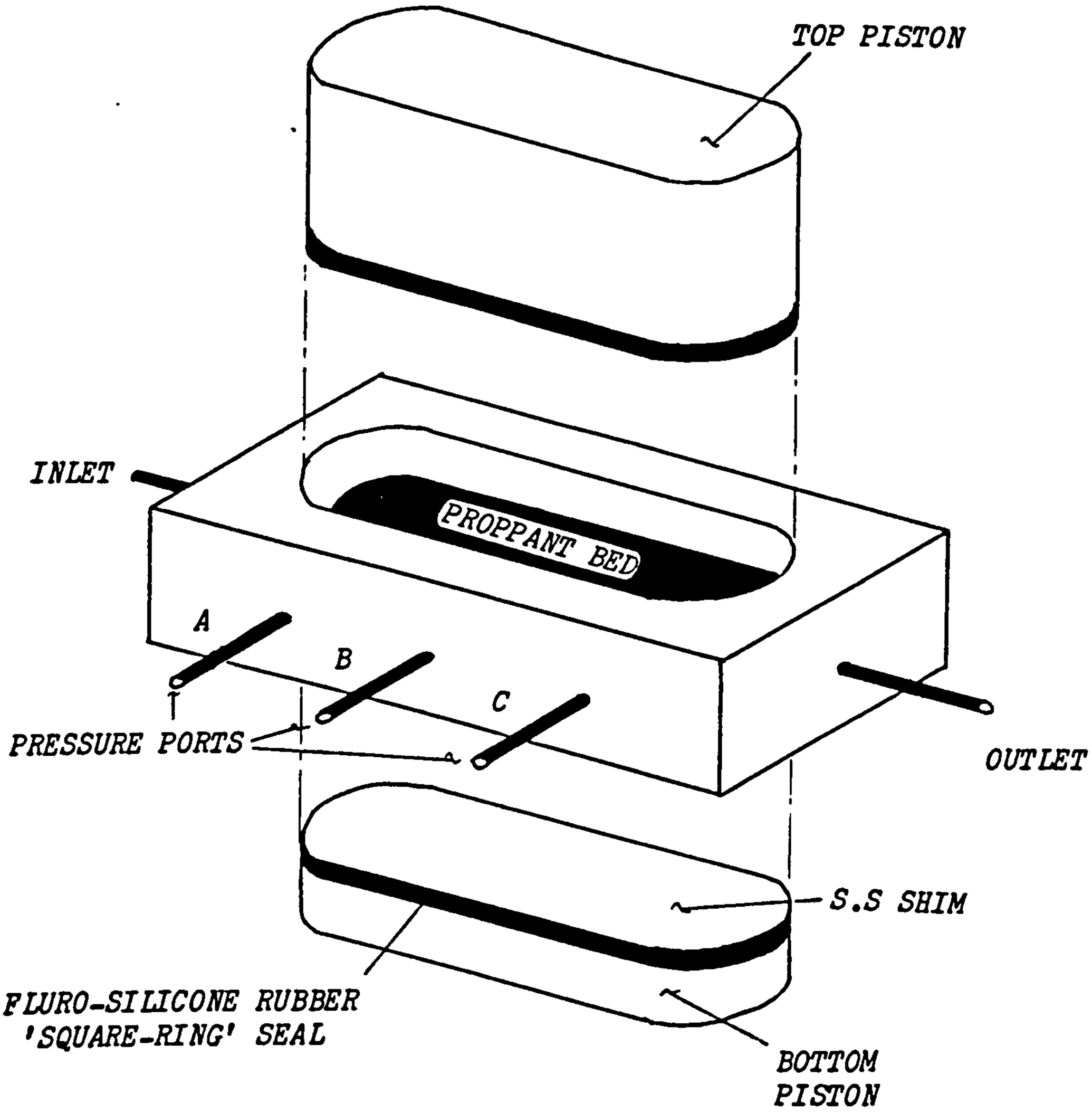

Figure 5.9 : Diagramatic Representation of the Linear Flow Cell

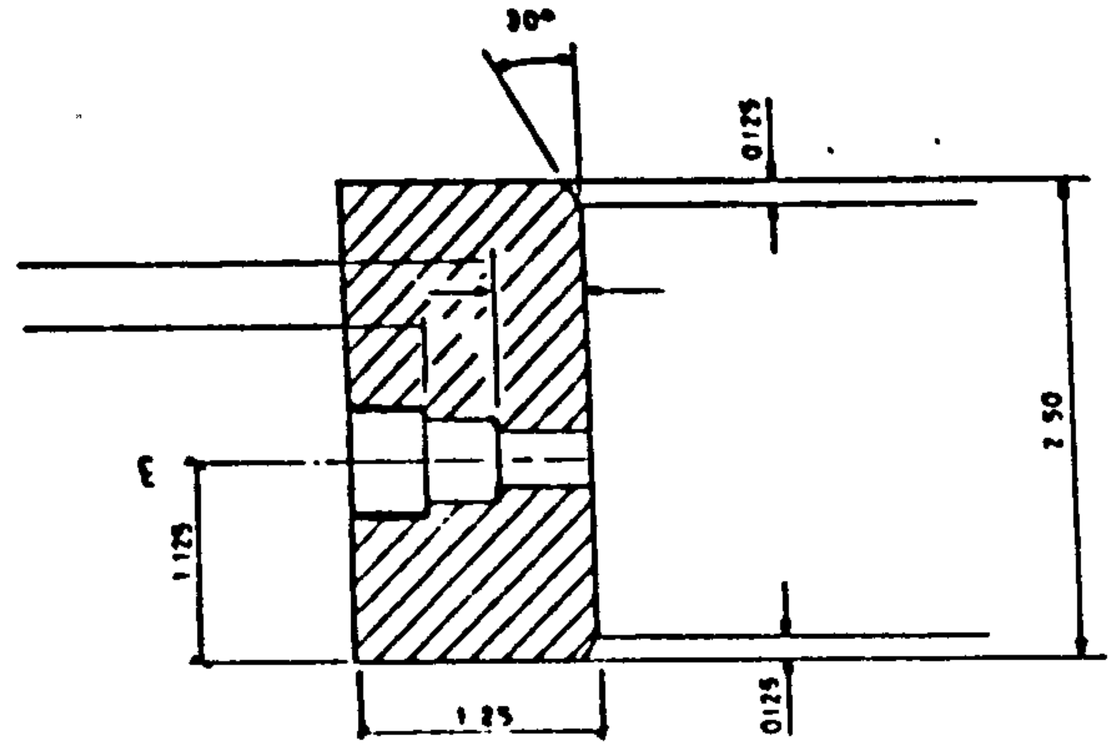

TYPICAL CROSS SECTION

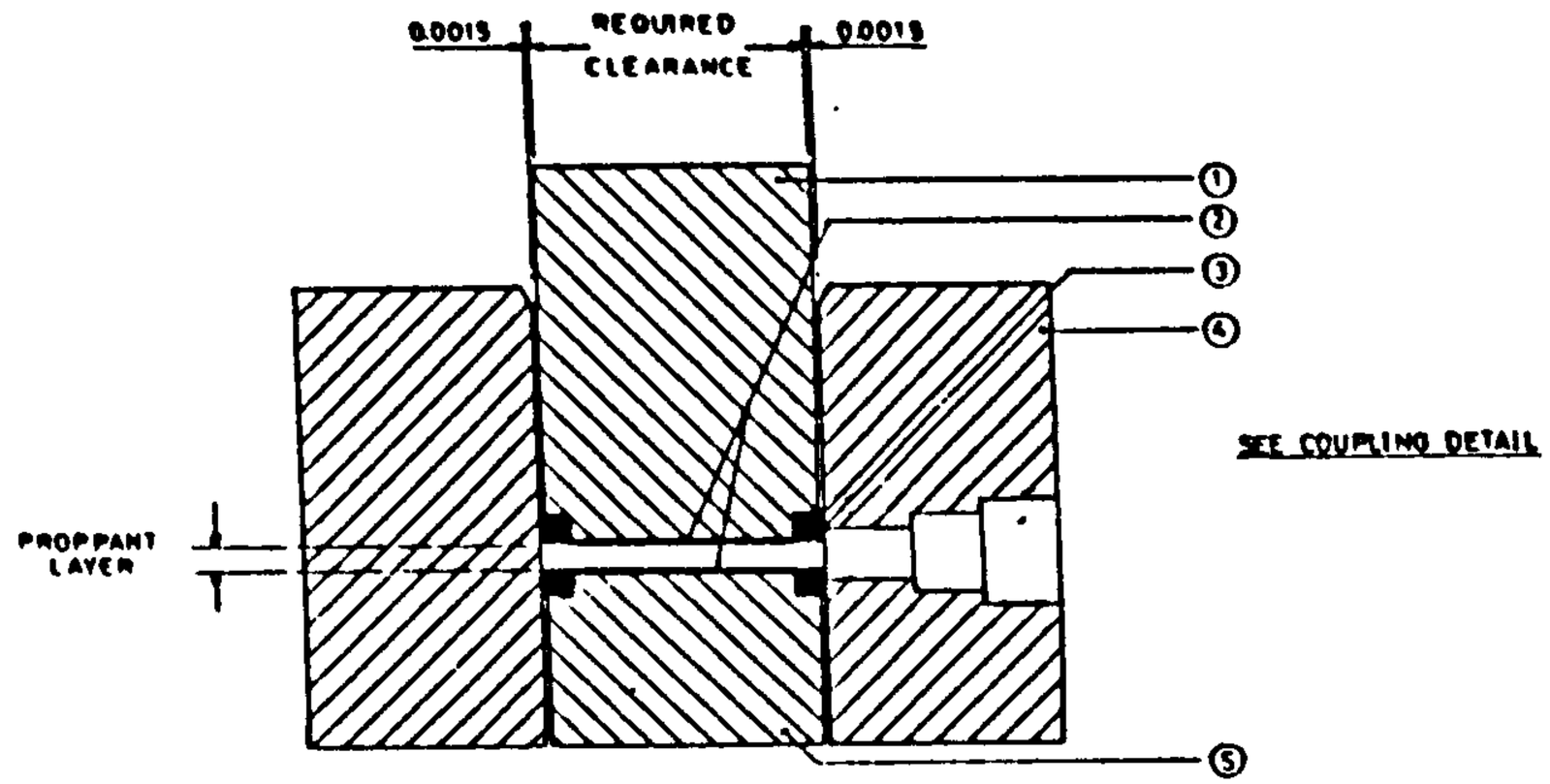

ASSEMBLED SECTIONAL VIEW

1. TOP PISTON
2. SHIMS (0.035 in)
3. SILICONE RUBBER SEAL
4. TEST CHAMBER
5. BOTTOM PISTON
6. FILTER (60 micron)
7. FILTER HOLDER
8. HYDRAULIC COUPLING

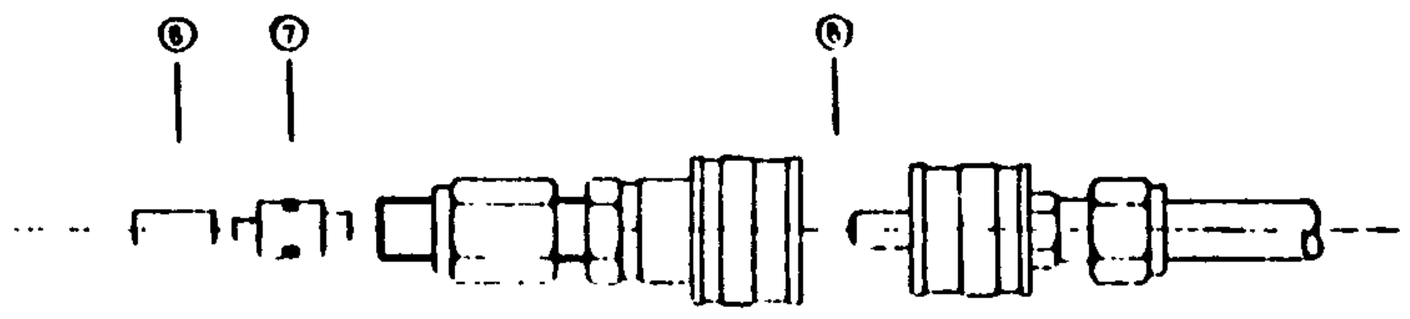

COUPLING DETAIL

Figure 5.10 : The Linear Flow Cell

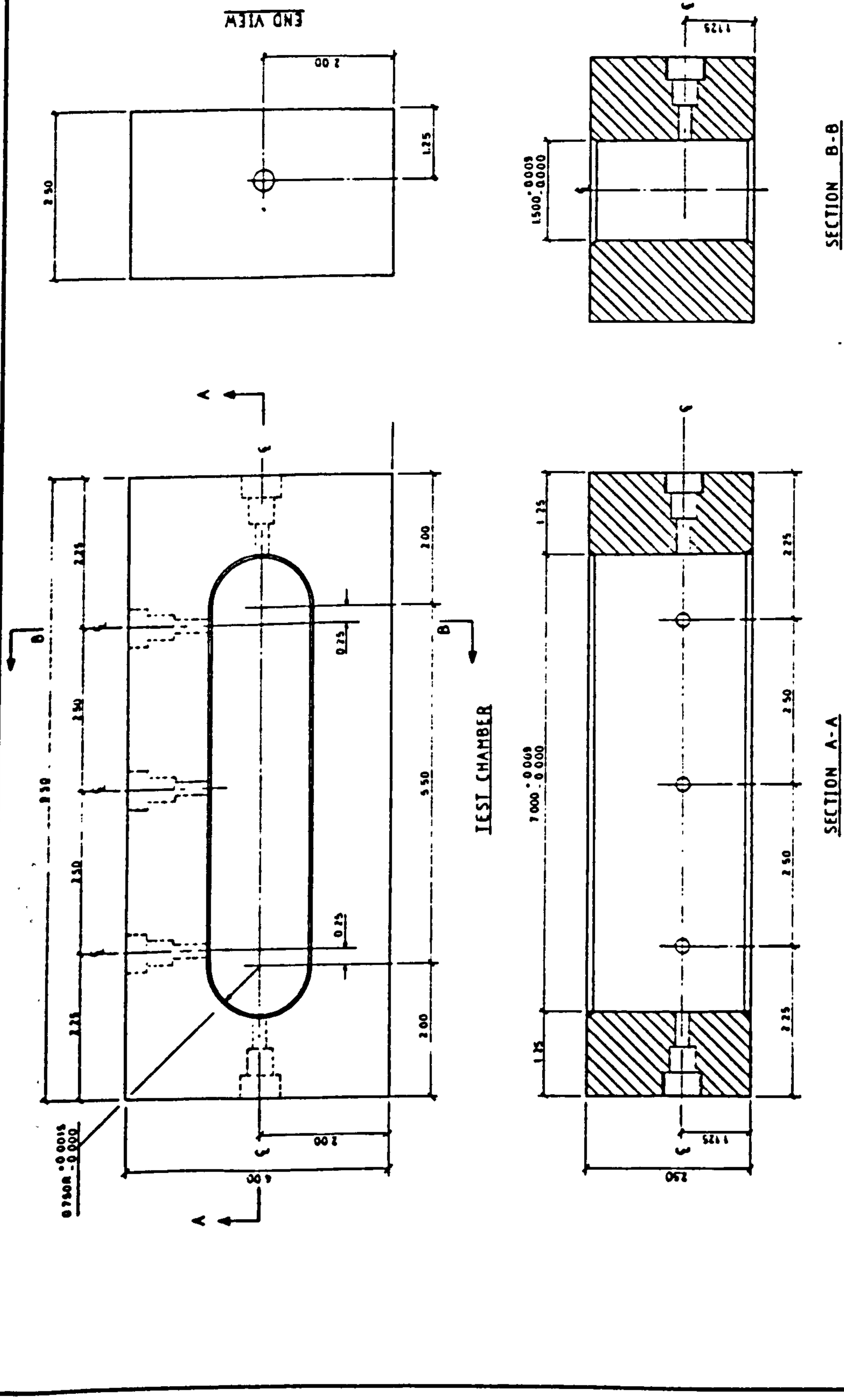

Figure 5.11 : Details of the Linear Flow Cell Test Chamber

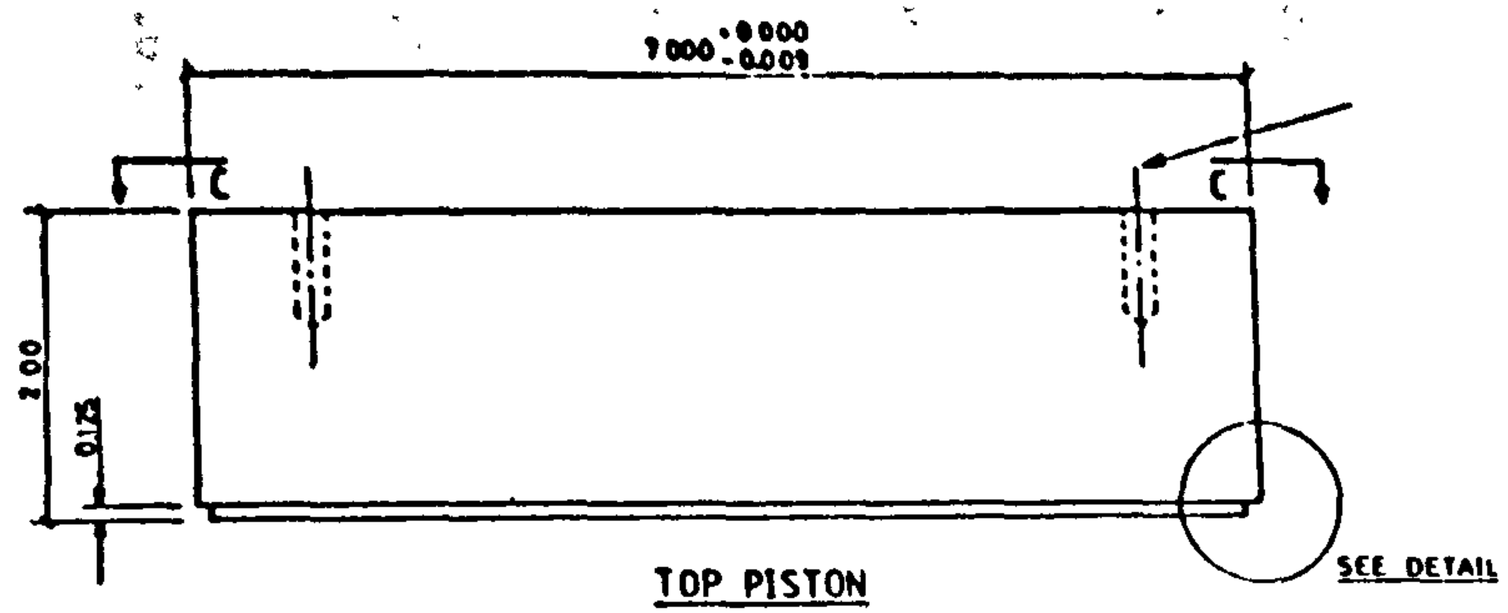

TOP PISTON

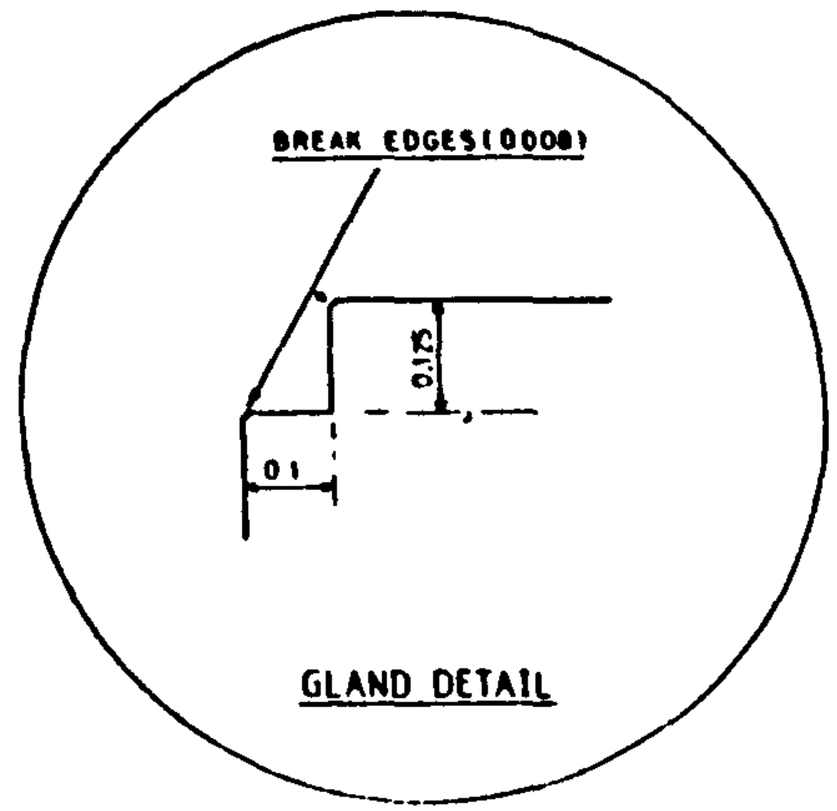

GLAND DETAIL

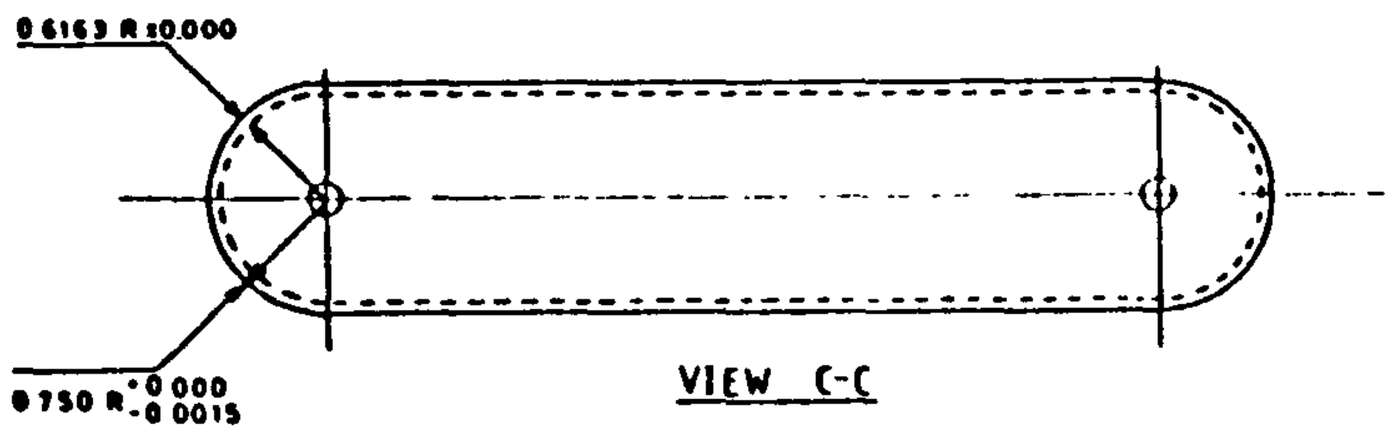

VIEW C-C

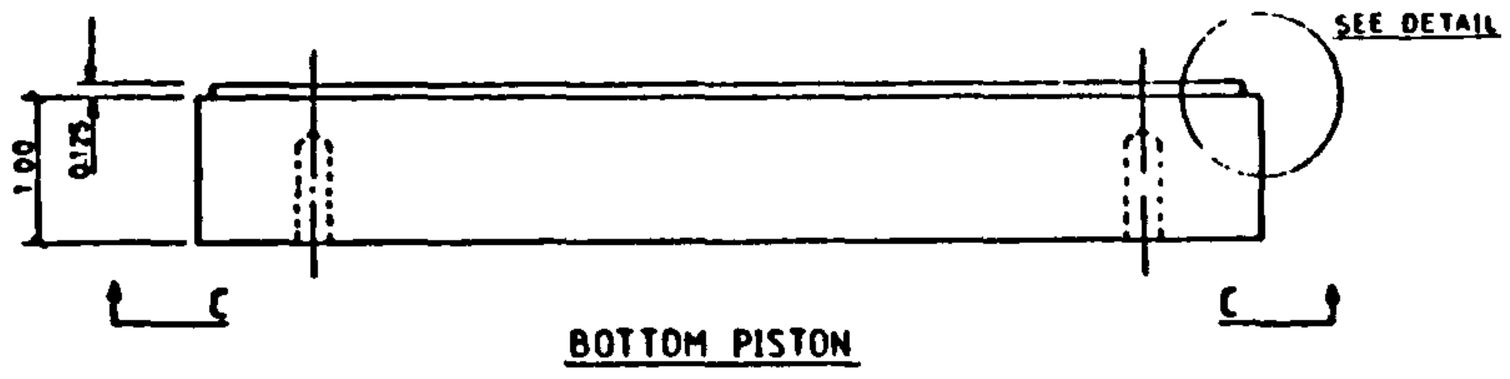

BOTTOM PISTON

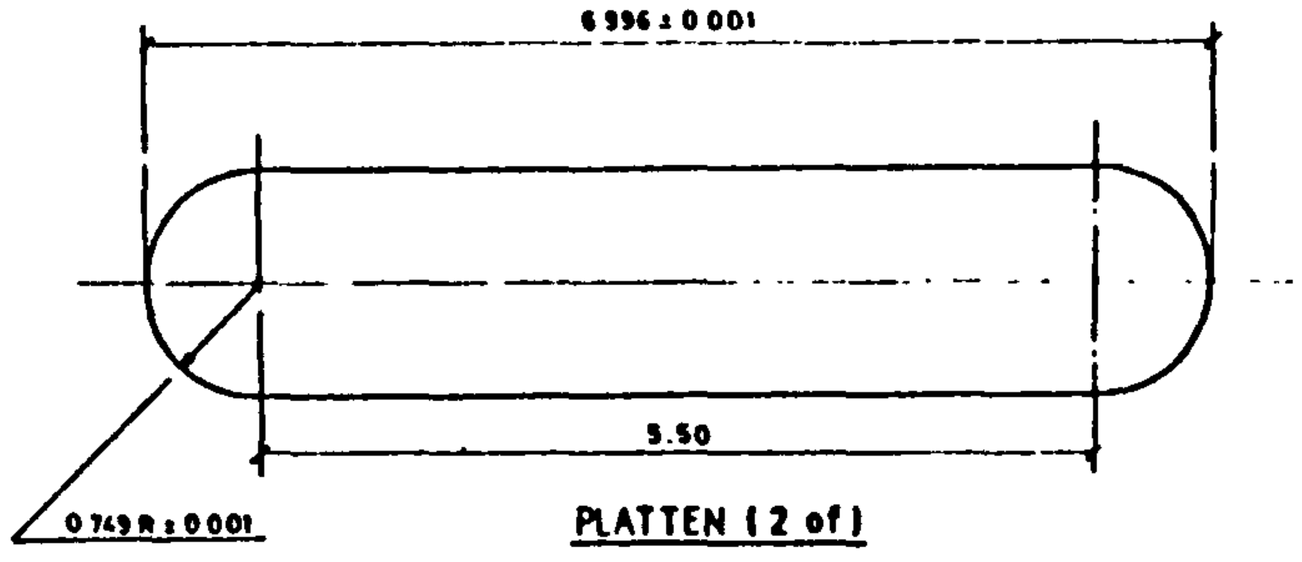

PLATTEN (2 of)

Figure 5.12 : Details of The Linear Flow Cell Pistons

three main components, a test chamber (4) and two pistons (1,5). Detailed drawings of the chamber and pistons are given in Figures 5.11 and 5.12. A fluid seal between the pistons and test chamber is provided by fluro-silicone rubber square rings (3), as shown in Figure 5.10. Stainless steel shims (2) are used to prevent rubber embedment and to provide protection to the faces of the pistons.

Hydraulic connection to the flow cell is made by self-sealing, quick release, stainless steel couplings (9). The inlet, outlet and pressure port couplings are 'keyed' and colour coded to prevent accidental intermixing of flow lines.

Proppant fines are prevented from entering the permeameter system by replacable sintered stainless steel filters (6). The filters have a nominal pore diameter of 60 microns and are connected to the quick release couplings as shown in Figure 5.10.

The facility to measure pressure drop across the linear flow section of the cell is provided by three pressure ports each having 2.5 in. centres, allowing a total measurable linear flow length of 5 in.

5.6.2 Oil Permeameter

5.6.2.1 Considerations in Design

The original design proposal for the oil permeameter system is illustrated schematically in Figure 5.13. The intention was to pump hydraulic oil from a reservoir through the linear flow cell and

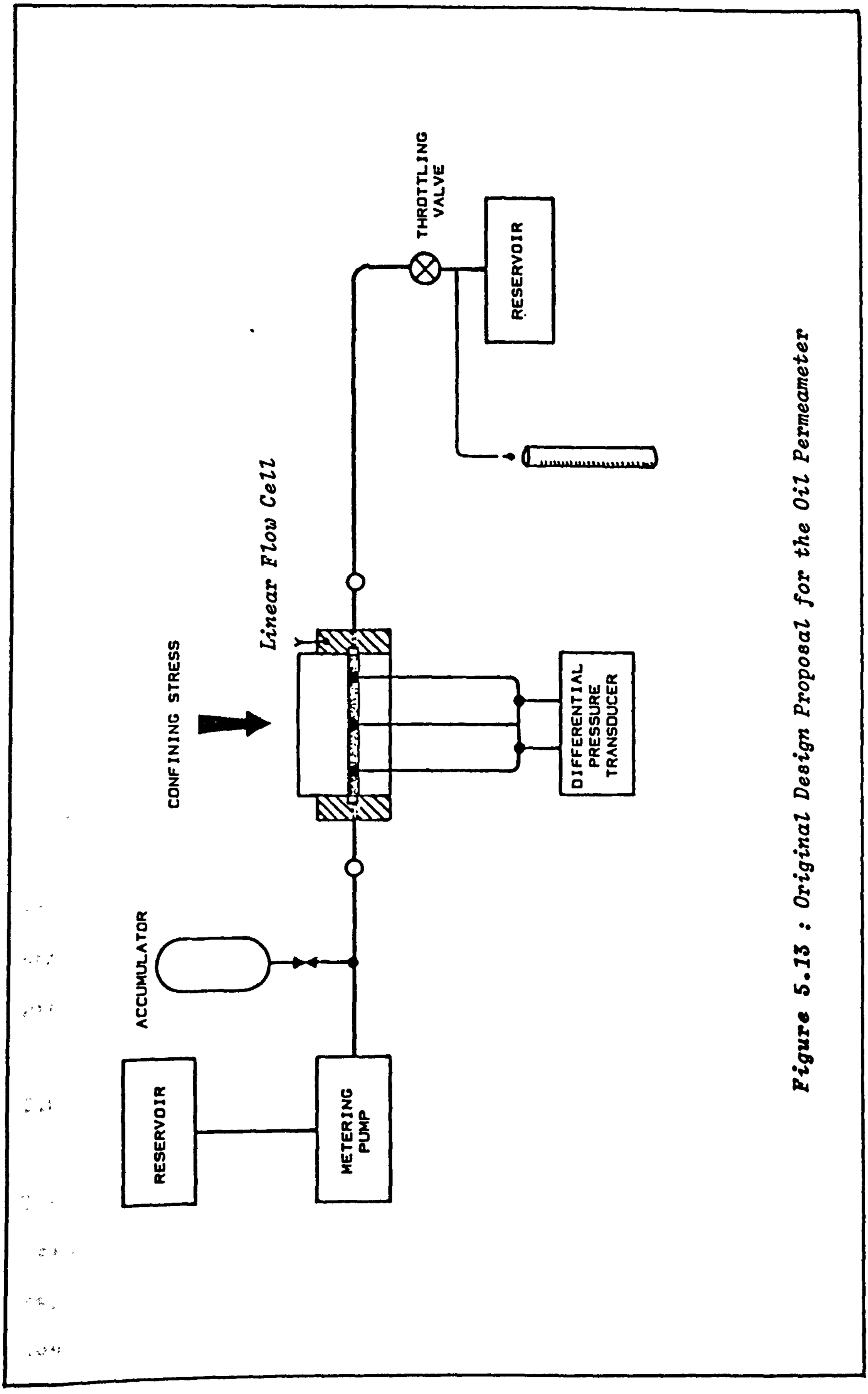

Figure 5.13 : Original Design Proposal for the Oil Permeameter

control the flow rate with a metering pump. A hydro-pneumatic accumulator was included to dampen oil pulsation. The pressure drop across the flow cell was proposed to be measured by a differential pressure transducer. In order to apply a back-pressure to the system, a throttling valve was included in the design. It was also anticipated that a complex series of valves would be required to divert the test fluid to the various measurement points.

Although the literature had recommended the use of brine as the permeant, it was proposed that oil should be used as the flowing medium as the presence of brine in the laboratory environment could damage electrical equipment. The fluid used as the permeant was a highly refined, petroleum base oil known as Shell Tellus No 10. This is a very stable, low viscosity oil, which is normally used in industrial hydraulic systems. It has been used by a number of researchers in the past and proved satisfactory [120,121]. Full technical details are given in reference [122].

After deciding on a basic system design, it was necessary to determine the specifications required for the pump and differential pressure transducer.

5.6.2.2 Pump

Darcy's law represents a linear relationship between the filtration velocity and pressure gradient, moreover, the straight line representing this relationship passes through the origin of the coordinates. Any deviation from this relationship represents

non-Darcian flow. Darcy's law is only true in a certain velocity range (laminar flow), outside of which (turbulent flow) a more general flow equation must be used to describe the flow correctly.

The Reynolds number (R_e), which is a dimensionless quantity expressing the ratio of inertial to viscous forces within a fluid, is used as a criterion to distinguish between laminar and turbulent flow. It may be defined as follows [123] :

$$R_e = dv\rho/\mu \qquad .. \quad .. \quad .. \quad .. \quad .. \quad (5.16)$$

where v = Mean Velocity (cc/sec)

ρ = Density (g/cc)

μ = Viscosity (poise)

d = Size of passageway (cm)

The critical R_e between laminar and turbulent flow in pipes is about 2000 (where d is taken as the pipe diameter). By analogy, a Reynolds number may be defined for flow through porous media. In this case, d is generally taken as an average grain (rather than pore) diameter. With such values of d, it has been found that the transition region lies at values of Reynods number of the order 1 to 10 [123].

In order to determine the maximum flow rate through the proppant pack which would be within the laminar flow region, the following values were inserted into equation (5.16). The lower limit of Reynolds number was chosen, i.e. $R_e = 1$.

d = 0.085 cm (20 mesh)

μ = 0.14 poise

ρ = 0.866 g/cc

The results indicated that oil could be pumped through the proppant pack at a rate of 1.9 cc/sec (114 cc/min) before turbulent flow would be encountered. Although flow rates through the linear flow cell were anticipated to be between 10 to 20 cc/min and therefore well within the laminar flow region, it was decided to obtain a pump which could produce a high flow rate if required. The most suitable pump available for this flow rate was an MPL E2B/365C metering pump. The unit has two pump heads which are driven by a single motor, has a maximum capacity of 6.6 L/hr and can operate with line pressures up to 2000 psi (13800 kPa).

5.6.2.3 Differential Pressure Transducer

The main problem in determining the specifications of the differential pressure transducer was estimating the pressure drop which was likely to occur across the linear flow cell as the literature gave no indication of the magnitude of pressure drop to be expected. This problem was overcome by inserting estimated values of flow rate and fluid viscosity in conjunction with fracture conductivity results obtained from technical catalogues into the modified Darcy formula (equation 5.9), and solving for ΔP. From an analysis of the estimated data, it was proposed that a transducer capable of measuring a differential pressure of 7.25 psi (50 kPa) would be suitable for the range of anticipated flow rates and

conductivities measured. The device was additionally required to withstand the elevated line pressure which were likely to occur system. Accordingly a 0 to 7.25 psi differential pressure transducer was purchased. The transducer was calibrated using a dead weight tester in conjunction with a 24 volt power supply and 5.5 digit electronic multimeter [Figure 5.14(a)]. The calibration graph obtained is presented in Figure 5.14(b).

5.6.3 Triaxial Fracture Porosimeter

This device is a standard Hoek Triaxial cell with the addition of displacement transducers (LVDTs) to monitor the closure of the simulated fracture. Hence, knowing the initial fracture width, the width at any given closure stress could be determined. The triaxial cell was loaded axially in the servo-controlled testing machine, while the confining pressure was generated with a servo-controlled intensifier.

5.6.4 Dry Crush Cell

The dry crush cell was constructed to allow tests following the basic recommendations of API RP56 [ref] to be followed with the exception that the cell crushing area was made equal to that of the linear flow cell, i.e. 10 in^2 (API recommend a maximum cell diameter of 3 in, i.e. 7 in^2). The cell is shown in Figure 5.15. It was decided that the modification to the crushing area was justified as the results from the dry crush cell were to be compared with those from the linear flow cell, which also had an internal test area of

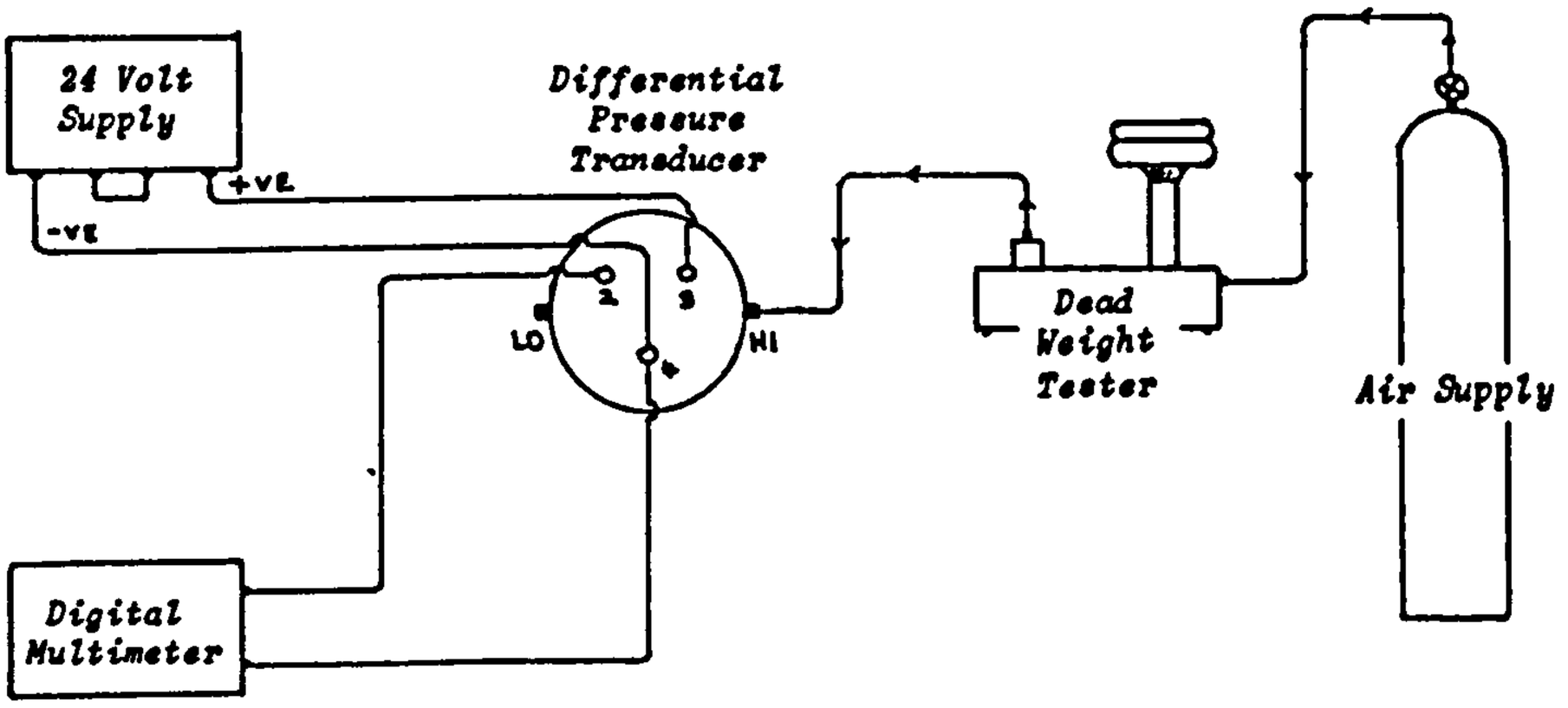

Figure 5.14(a) : Calibration Equipment used for the Differential Pressure Transducer

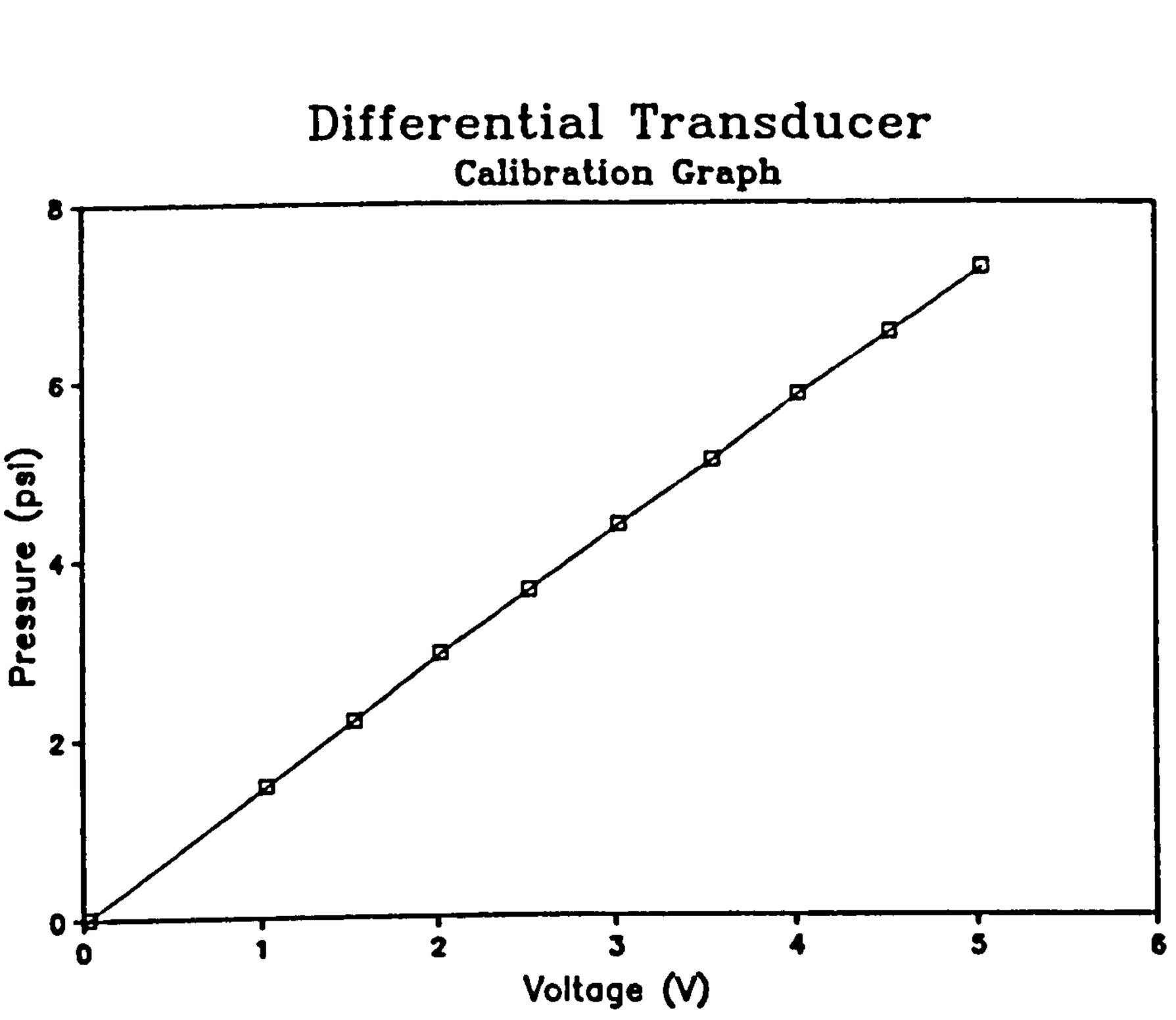

Figure 5.14(b) : Calibration Graph

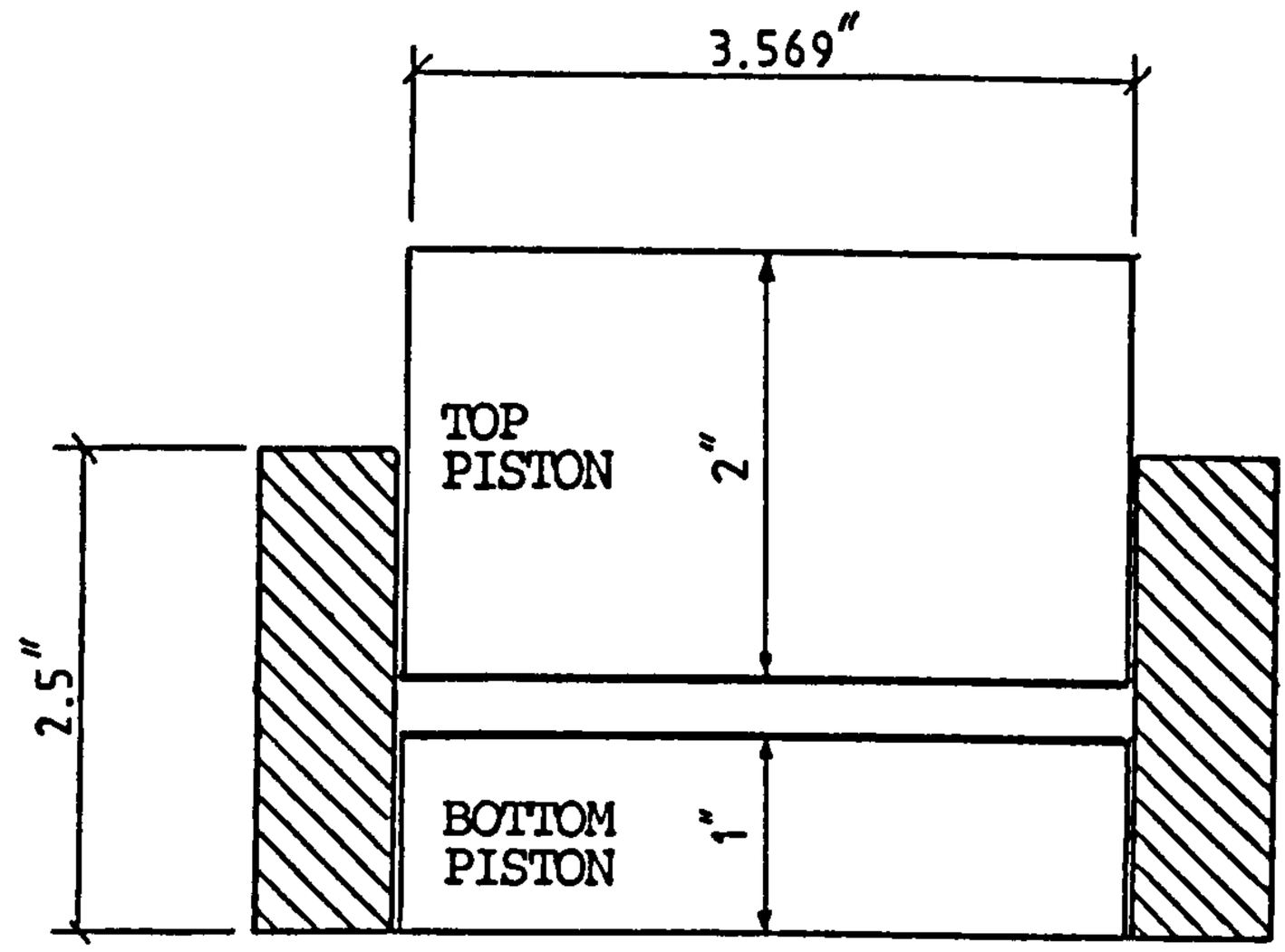

SECTIONAL VIEW ACROSS A-A

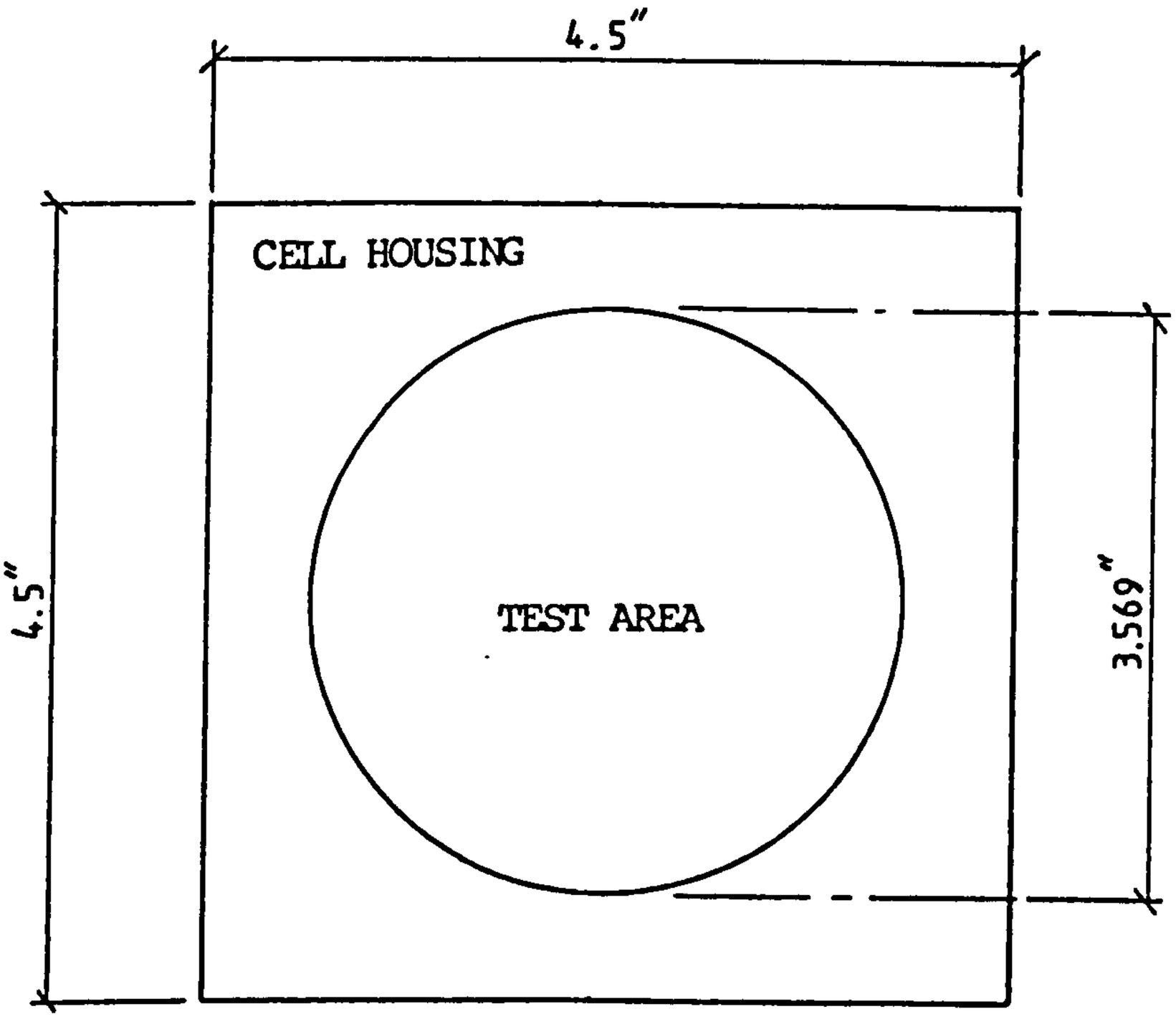

PLAN VIEW OF CELL HOUSING AND PISTONS

Figure 5.15 : Diagram of Dry Crush Cell

10 in².

5.6.5 Servo-Controlled Testing Machine and Intensifier

The testing machine used to generate the compressive forces on the linear flow cell and fracture porosimeter was a 1000 kN 'stiff' servo-controlled machine.

High stiffness (<2 mm machine deflection at full load) combined with the facility to utilise either the load developed on or the compression of the test piece as feed-back in the servo loop enabled 'state-of-the-art' control to be maintained during the experiments.

Similarly, the servo-controlled intensifier used to generate the confining pressure in the fracture porosimeter enabled this pressure to be held constant irrespective of volume changes within the cell.

5.7 SYSTEM TESTING AND DEVELOPMENT

5.7.1 Introduction

This section deals with initial testing of the original permeameter system, the procedure for its operation, preliminary results and an account of the various modifications performed to the system.

5.7.2 Pump Performance

During initial system testing, it was found that the metering pump

produced a severe line pulsation when working against a back-pressure. Additionally, the magnitude of the pulsation was found to be proportional to the flow rate.

To examine the efficiency of the pulsation dampening provided by the accumulator, a series of upstream pressure readings were taken. A pressure transducer was inserted in-line between the accumulator and inlet port of the linear flow cell. The transducer output was connected to an oscilloscope to examine the wave form produced and to a chart recorder for a permanent record.

Two tests were conducted: the first set of readings were taken with the flow by-passing the linear flow cell, the second set with the flow through the cell. A constant back-pressure of 300 psi (2070 kPa) was maintained in conjunction with an applied closure stress of 1000 psi (6900 kPa). In both cases, pressure readings were initially taken with the accumulator isolated to measure the magnitude of system fluid pulsation, then the accumulator was brought in-line to examine the dampening effect.

5.7.2.1 Results by-passing Linear Flow Cell

Referring to Figure 5.16(a), it is evident that severe pulsation was present and was found to be in the order of 22 psi (150 kPa). It can be seen that the fluid pulsation was regular and increased rapidly to a maximum before tailing off. Bringing the accumulator in-line had a marked effect. For greater accuracy, chart recordings of the line pressure were taken on two different scales, the upper line

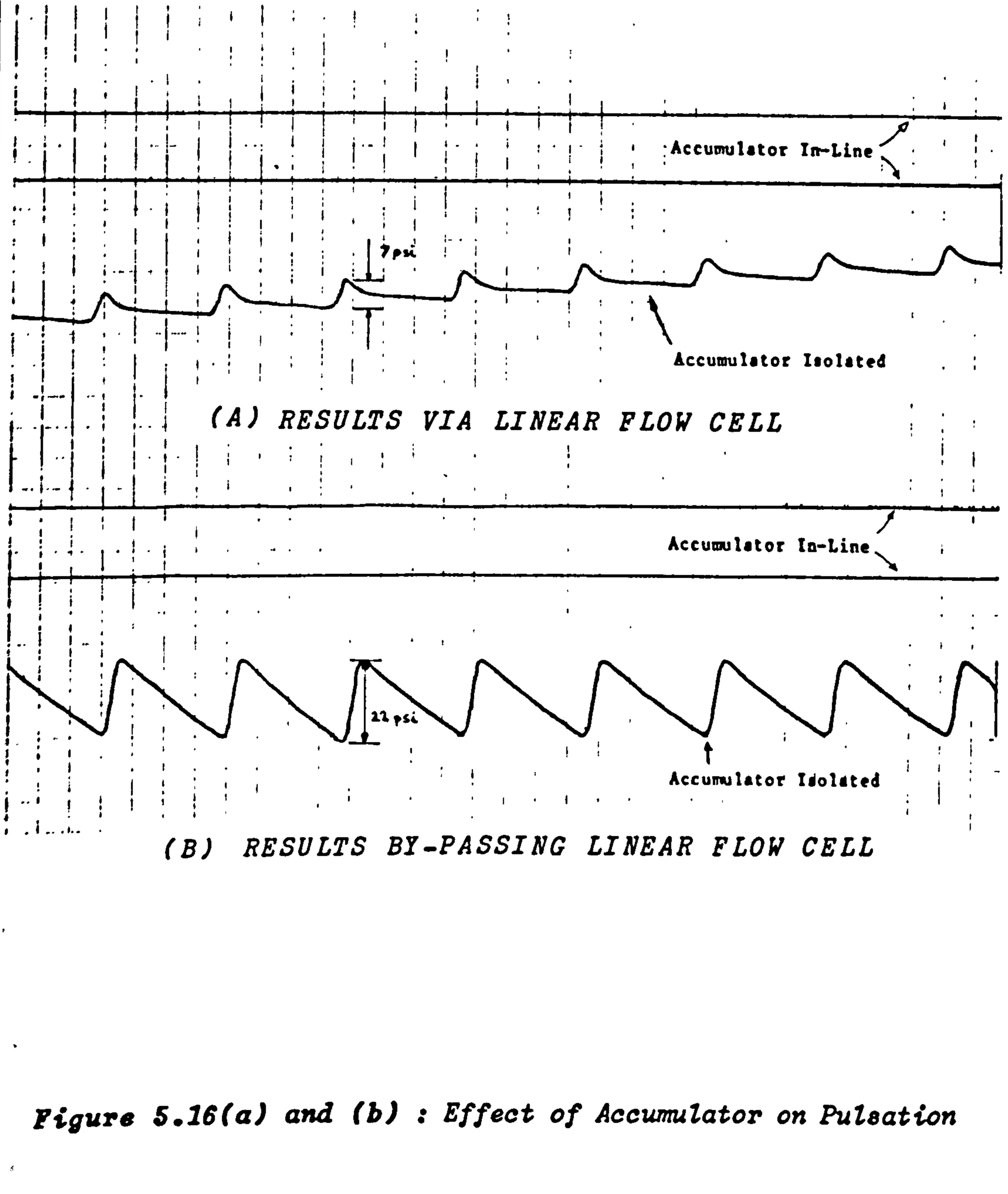

Figure 5.16(a) and (b) : Effect of Accumulator on Pulsation

being the more sensitive. Slight line waver was evident and was found to be less than 0.2 psi (1.4 kPa).

5.7.2.2 Results via Linear Flow Cell

Referring to Figure 5.16(b), it can be seen that the pulsation reduced in magnitude to about 7 psi (48 kPa) when flow was directed through the linear flow cell. The chart recording was observed to step upwards due to a slight increase in back-pressure. The chart reading obtained with the accumulator in-line indicated that the system pulsation had been reduced to a negligible level.

To examine the effect of pulsation with respect to applied stress, the closure stress was increased at regular intervals up to a maximum of 15000 psi (103500 kPa) and chart recordings taken of the line pressures. The results, which are presented in Figure 5.16(c), illustrate that the effect of increasing closure stress had a minimal effect on system pulsation.

5.7.2.3 Overall Performance

It was concluded that the overall performance of the oil permeameter system was satisfactory and ready for preliminary fracture permeability/conductivity testing.

5.7.3 Procedure for the Determination of Flow Cell Conductivity

(1) After the insertion of the bottom piston, 63.2 g of

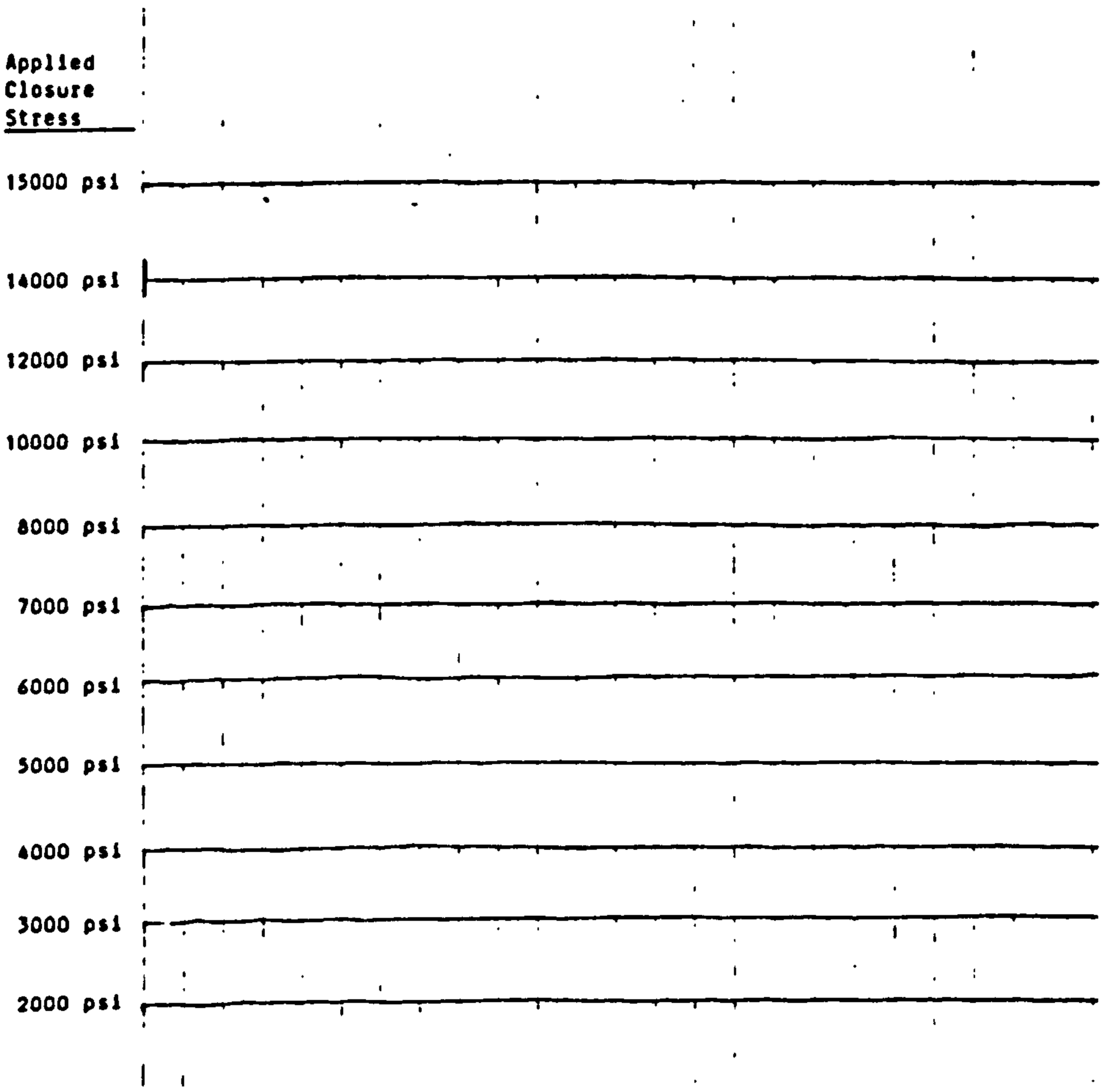

Figure 5.16(c) : Effect of Increasing Closure Stress on Pressure Pulsation

proppant (corresponding to a concentration of 2 lb/ft^2) was poured into the test chamber af the flow cell. The proppant bed was then carefully levelled using a cylindrical plunger device before the insertion of the upper piston.

(2) The prepared linear flow cell was placed in the stiff-testing machine and an initial closure stress of 1000 psi (6900 kPa) applied. Hydraulic connection was then made to the permeameter and oil flow commenced at approximately 10 cc/min. A back-pressure of 200 psi (1400 kPa) was introduced to the system by means of the throttling valve.

(3) The closure stress was then increased and maintained at the required value using the servo-control facility on the testing machine.

(4) Differential pressure readings were then taken across pressure port A-B and the volumetric flow rate was measured by noting the volume of oil returning from the linear flow cell in unit time.

(5) Differential pressure and flow rate measurements were then taken over port A-C.

(6) After satisfactory results were obtained, the closure stress was then increased to the next desired level and the procedure repeated.

5.7.4 Preliminary Results

Flow cell conductivity test results are presented in graphical and tabular form in Figures 5.17 and 5.18. These results, using both 20/40 Sintered Bauxite and 20/40 Quartz Sand show that increased closure stress has a marked effect on conductivity values. Throughout each test, differential pressure readings were taken over ports A-B and A-C. The respective conductivities were seen to differ slightly.

In general, the results show that at closure stresses of 8000 psi (55200 kPa) and above, Sintered Bauxite conductivities were in the order of 4-6 times higher than quartz sand. This was in accordance with Wendorff [115].

With the Sintered Bauxite test, fracture conductivity values were additionally taken for decreasing closure stress. It can be seen that the reduced conductivity was apparently irreversible. This was again in accordance with departmental nitrogen fracture permeability tests (see Section 5.5) and with Cooke [108].

5.7.5 Problems Indentified with the Apparatus

After the preliminary testing was completed, it was concluded that although the basic technique and test equipment were adequate in producing satisfactory results, there were several factors which could be improved in order to obtain a more realistic value for

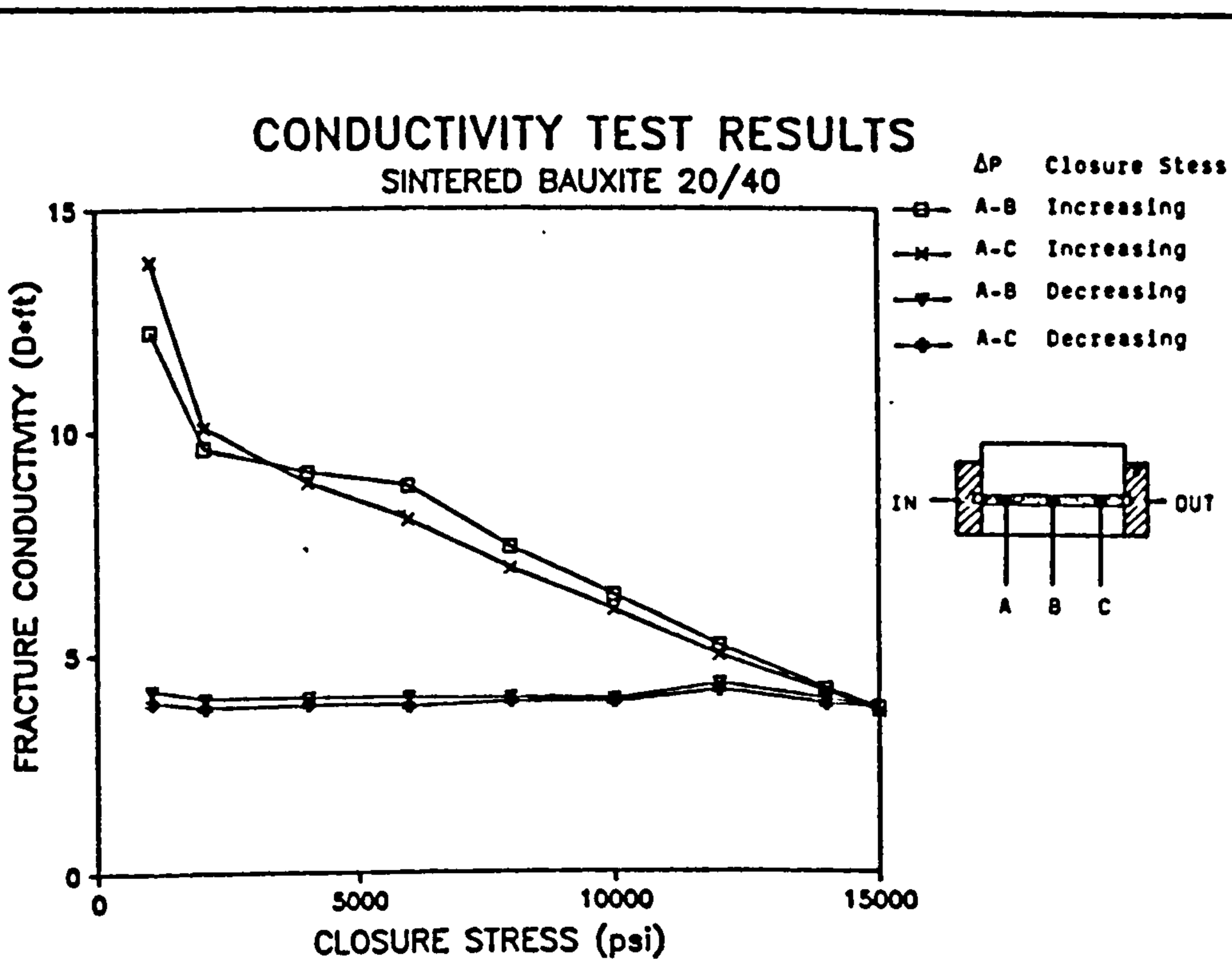

Figure 5.17 : Preliminary Conductivity Results for 20/40 Sintered Bauxite

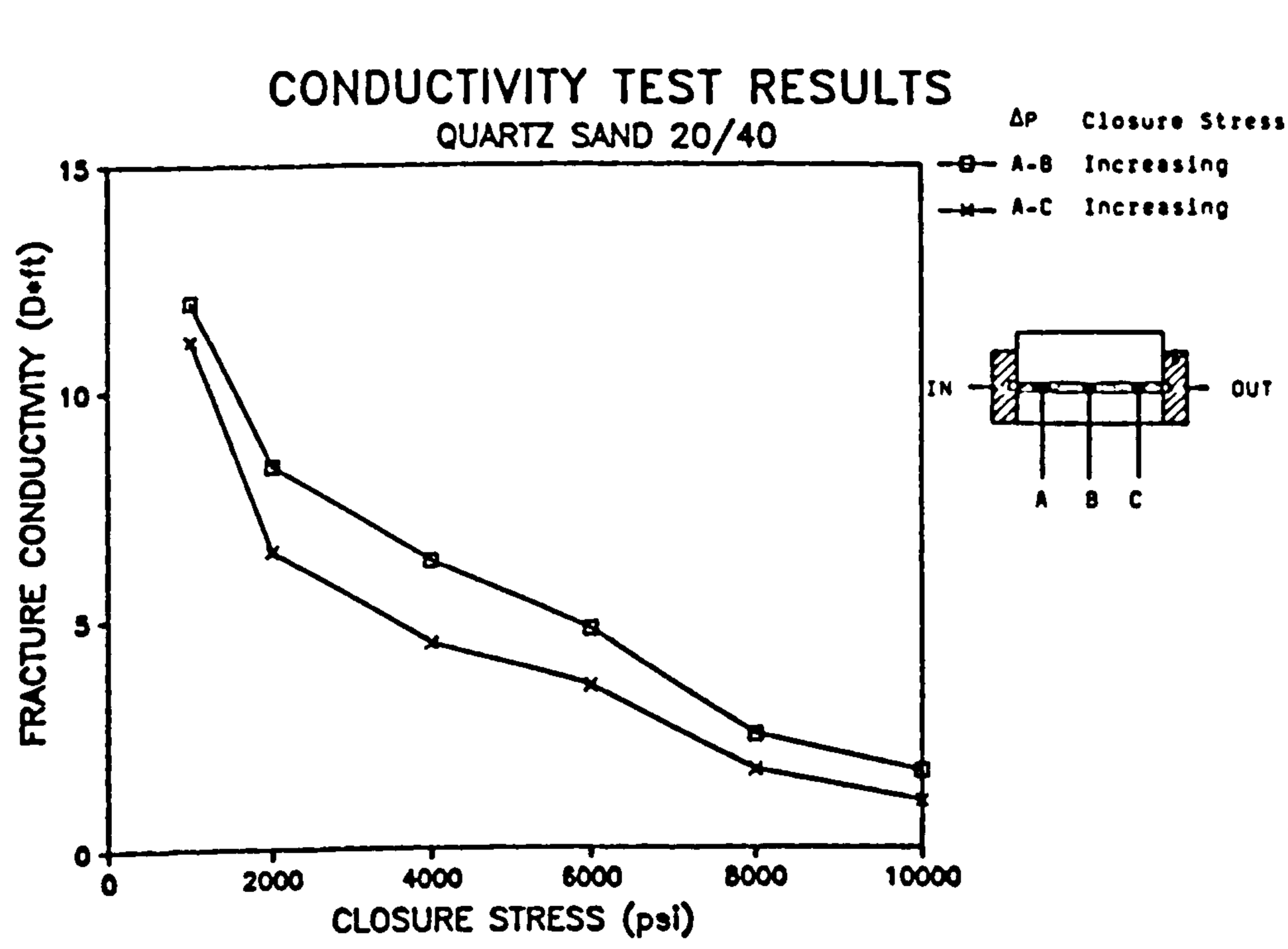

Figure 5.18 : Preliminary Conductivity Results for 20/40 Quartz Sand

fracture conductivity. The following four specific problem areas were identified and selected for special attention.

5.7.5.1 Flow Rate Measurement

The primary source of error in these tests was the measurement of volumetric flow rate which at that stage was achieved by diverting the output from the linear flow cell to a measuring cylinder. It would appear that this method could have been subject to human error in timing the volume of oil collected, while the graduations on the measuring cylinder were also unlikely to be of sufficient accuracy. In addition, there was little opportunity to check or adjust any of the other components of the apparatus while the flow rate measurement was being taken. It was therefore apparent that a more accurate method was required.

5.7.5.2 Variation in Fluid Viscosity

In order to determine the permeability of a propped fracture, it was necessary to have an accurate value for the dynamic viscosity of the test fluid. Unfortunately, the fluid viscosity varied considerably with temperature. According to the manufacture's estimates, a change of 2.8°C in operating temperature would cause a change in the order of 15% in the dynamic viscosity of the oil [121]. As the apparatus in its original form did not allow the temperature of the oil in the flow lines to be measured directly, an accurate measurement of the variation in oil temperature throughout the test was therefore crucial in determining the change in viscosity.

5.7.5.3 Inconsistent Conductivity Values along LFC

During the recording of results for the preliminary tests, it was found that the flow rate could not be maintained constant, while at higher closure stress values, the flow rate decreased to a negligible amount. In addition, it was observed that the fracture conductivity values calculated from the respective permeameter readings across port A-B and A-C were not equal. As this effect had not been previously reported in the literature, it was initially explained as to be most probably due to irregularities in proppant packing along the length of the cell. After a series of tests however, it was evident that this was not the case and that proppant fines had migrated towards the outlet end of the linear flow cell. As the permeameter, at this stage, only allowed differential pressure readings over a combination of two of the three pressure ports, namely over ports A-B and A-C, it was required to modify the permeameter system to enable a measurement to be taken over the remaining option, port B-C.

5.7.5.4 Establishing Equilibrium Conditions

Difficulties were encountered in establishing the stage at which equilibrium conditions had been reached since it was observed that although the closure stress was maintained at a constant level, the fracture width gradually decreased with a resulting drop in flow rate and differential pressure. It was therefore evident that a degree of creep was present and it was necessary to conduct a series

of tests in order to determine the optimum time interval between increasing closure stress and taking oil permeameter readings.

5.7.5.5 Required Action

It was proposed that a series of modifications should be made to the oil permeameter system before investigating the onset of equilibrium conditions and finally performing a test calibration on the linear flow cell.

5.7.6 Modifications to Oil Permeameter System

5.7.6.1 Volumetric Flow Rate Measurement

As there were no commercially available flowmeters which could operate under the viscosity restrictions of Shell Tellus No 10 and accurately measure the extremely low volumetric flow rates, the remaining options were either to construct a capillary flowmeter within the department to obtain electronic flow measurement, or to devise a time dependent volumetric flow rate method which would be of sufficient accuracy. In a previous departmental attempt to construct a capillary flowmeter, Hair [124], reported difficulty in obtaining consistency between experimental and theoretical results. To include a capillary flow meter in the permeameter system would have required the purchase of an additional differential pressure transducer. It was therefore decided to improve the existing volumetric flow rate method. To obtain sufficient accuracy, a graduated burette was substituted in place of the measuring

cylinder. This allowed volumetric flow readings accurate to within 0.02 cc to be obtained. Thus for an average flow rate of 10 cc/min, the error would be in the region of 0.2%. This was felt to be of sufficient accuracy when considering the number of experimental variables involved. Due to the nature of the fluid forces within a burette, oil could not be introduced to the top, as in the normal manner, as the oil would tend to adhere to the walls of the burette. It was therefore necessary to divert the linear flow cell output to the bottom of the burette, which was inverted to allow the correct reading to be obtained. To eliminate any possible errors in reading a value from a miniscus, a flat-topped float was inserted in the burette thereby allowing accurate readings to be taken from it. To allow the burette contents to be emptied, a 3-way valve was included in the flow measurement line which discharged the oil to a small reservoir on the underside of the trolley.

5.7.6.2 Temperature/Viscosity Measurement

The facility to accurately measure in-line fluid temperature was provided by two platinum resistance temperature probes which were mounted immediatly before and after the linear flow cell. The probes were housed in specially adapted 'T-junction'. A pressure seal was effected by means of encasing the upper section of the probe in epoxy resin and fluro-silicone rubber. Protection to the electronics connection onto the probe was provided by a spring which surrounded the lead and prevented excessive flexing. The output from the probes was linearised, reading to 0.1°C on a digital display.

A log-log relationship between kinematic viscosity and temperature for Shell Tellus #10 (formally #15) was obtained experimentally by Abdullah [120] and later confirmed by Thomas [125], viz

$$\eta = 1316.44T^{-1.3537} \quad .. \quad .. \quad .. \quad .. \quad .. \quad (5.17)$$

where η = Kinematic viscosity (centistrokes)

T = Temperature (°C)

Abdullah also obtained a relationship between density, (ρ), in g/cc and temperature.

$$\rho = -5.5812 \times 10^{-4} T + 0.8761 \quad .. \quad .. \quad .. \quad (5.18)$$

At any temperature, the dynamic viscosity (μ) in centipoise is given by product of density and kinematic viscosity, viz.

$$\mu = \eta\rho \quad .. \quad .. \quad .. \quad .. \quad .. \quad (5.19)$$

Therefore, by substituting for η and ρ in the above equation, the dynamic viscosity could be directly related to fluid temperature.

$$\mu = 0.73T^{-0.3537} (1569.80T^{-1} - 1) \quad .. \quad .. \quad (5.20)$$

A comparison between values calculated for dynamic viscosity using the above equation and those found experimentally from density and kinematic viscosity is given in Figure 5.19. A close correspondance between the two sets of data was found. Equation (5.20) therefore

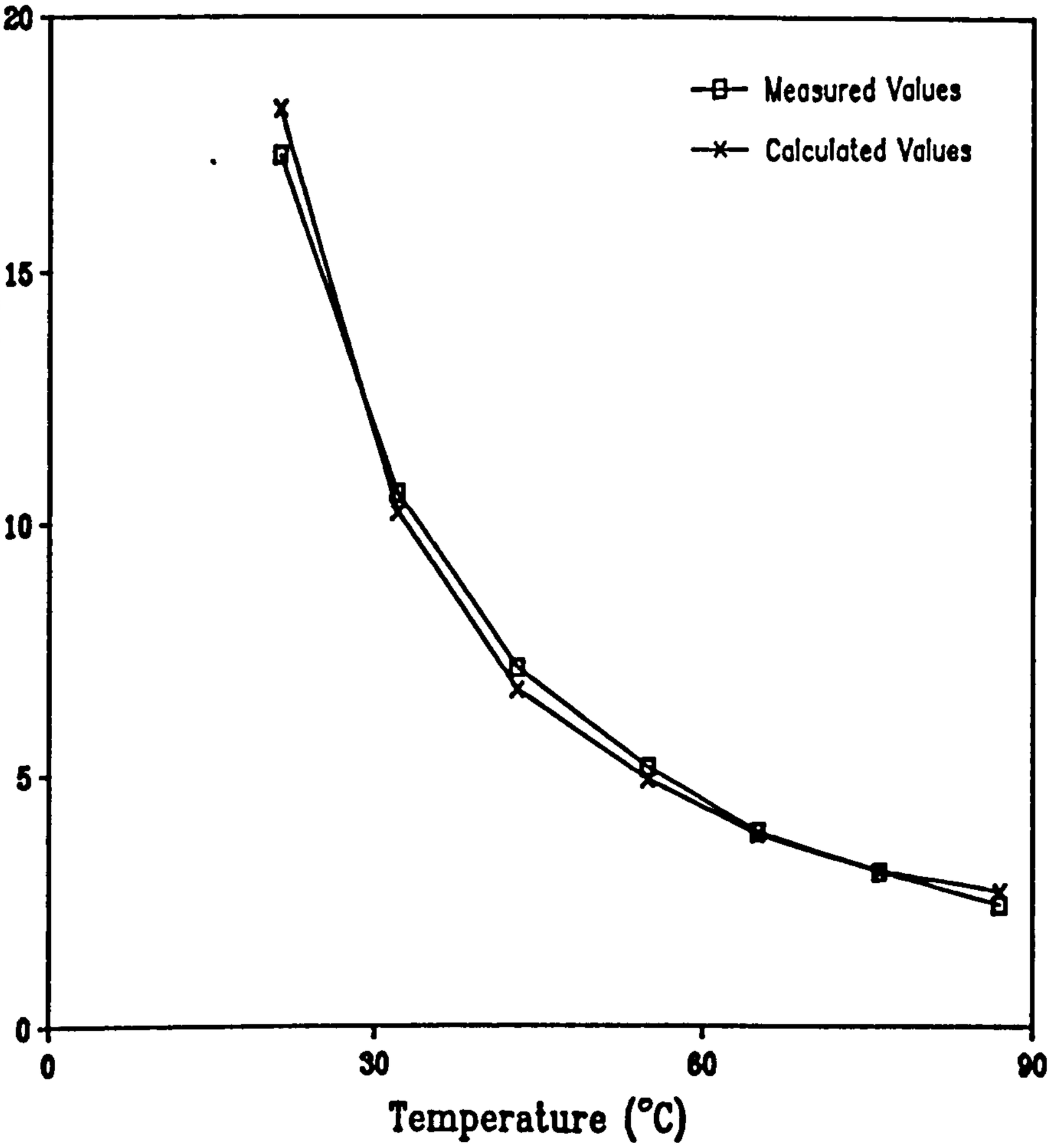

Figure 5.19 : Comaprison of the Measured and Calculated Values of Dynamic Viscosity against Temperature [124]

appears to give a realistic value of dynamic viscosity for any given temperature.

5.7.6.3 Other Modifications

The other modifications which were carried out on the flow cell and permeameter system were as follows:

(a) A slot was cut in the outlet filter of the linear flow cell to prevent excessive back-pressures forming within the cell.

(b) An in-line filter was inserted in the outlet flow line of the cell to prevent the possibility of damage to downstream components.

(c) It was necessary to provide the facility to measure the pressure drop across each pressure port combination, i.e. ports A-B, B-C and A-C. This was accomplished by the insertion of an additional 3-way valve in the differential pressure flow lines and by making port B common to both 3-way valves.

(d) Several 3-way valves were inserted at strategic points in the permeameter flow lines to allow greater control of the system.

5.7.6.4 Description of Modified Oil Permeameter System

The apparatus has been designed as a means of measuring the permeability of a simulated propped fracture using using liquid as the flowing medium. A diagram of the oil permeameter apparatus is given in Figure 5.20 while a flow schematic is presented in Figure 5.21. The permeameter has been assembled on a trolley with the intention of making the system as self-contained and manoeverable as possible. The electronics and digital readouts are incorporated in a console situated on the top of the trolley.

Oil is drawn from the clean reservoir (1) and supplied to the linear flow cell by means of an MPL E2B/356C metering pump (2). The unit has two pump heads which work alternatively and are driven by a single motor. The pump has a maximum capacity of 6.6 L/hr. and can operate with line pressures up to 2000 psi (13800 kPa).

A pressure relief valve (V1) set at 500 psi (3450 kPa) provides overload protection to the tubing used to make all connections. A hydropneumatic accumulator (3), precharged to about line pressure is connected in-line and provides pulsation dampening of the oil flow. An on/off valve (V2) enables the accumulator to be isolated from the system if required.

Flow rate is measured by deflecting the oil outlet from the linear flow cell by means of valve V6 to the bottom of a burette containing a machined float. The volumetric flow is then measured by manually reading the value at the top of the float after a specific time

LEGEND

1. CLEAN OIL RESERVOIR
2. METERING PUMP
3. ACCUMULATOR
4. UPSTREAM PRESSURE GAUGE
5. DOWNSTREAM PRESSURE GAUGE
6. BURETTE RESERVOIR
7. BURETTE
8. DIRTY OIL RESERVOIR
9. DIFF. PRESSURE GAUGE
10. MAX. CELL PRESSURE GAUGE
11. MIN. CELL PRESSURE GAUGE
12. DIFF. PRESSURE TRANSDUCER
13. ELECTRONICS CONSOLE
14. HYDRAULIC PORTS
15. UPSTREAM TEMPERATURE PROBE
16. DOWNSTREAM TEMPERATURE PROBE
17. DIFFERENTIAL PRESSURE PORTS

V1. PRESSURE RELIEF VALVE
V2. ACCUMULATOR IN-LINE
V3. CELL BY-PASS VALVE
V4. FORWARD FLOW/BACK-PRESSURE
V5. THROTTLING VALVE
V6. FLOW RATE MEASUREMENT
V7. BURETTE DISCHARGE
V8. DIFF. PRESSURE VALVE
V9. DIFF. PRESSURE VALVE
V10. SYSTEM SAFE VALVE
V11. EQUALISATION VALVE

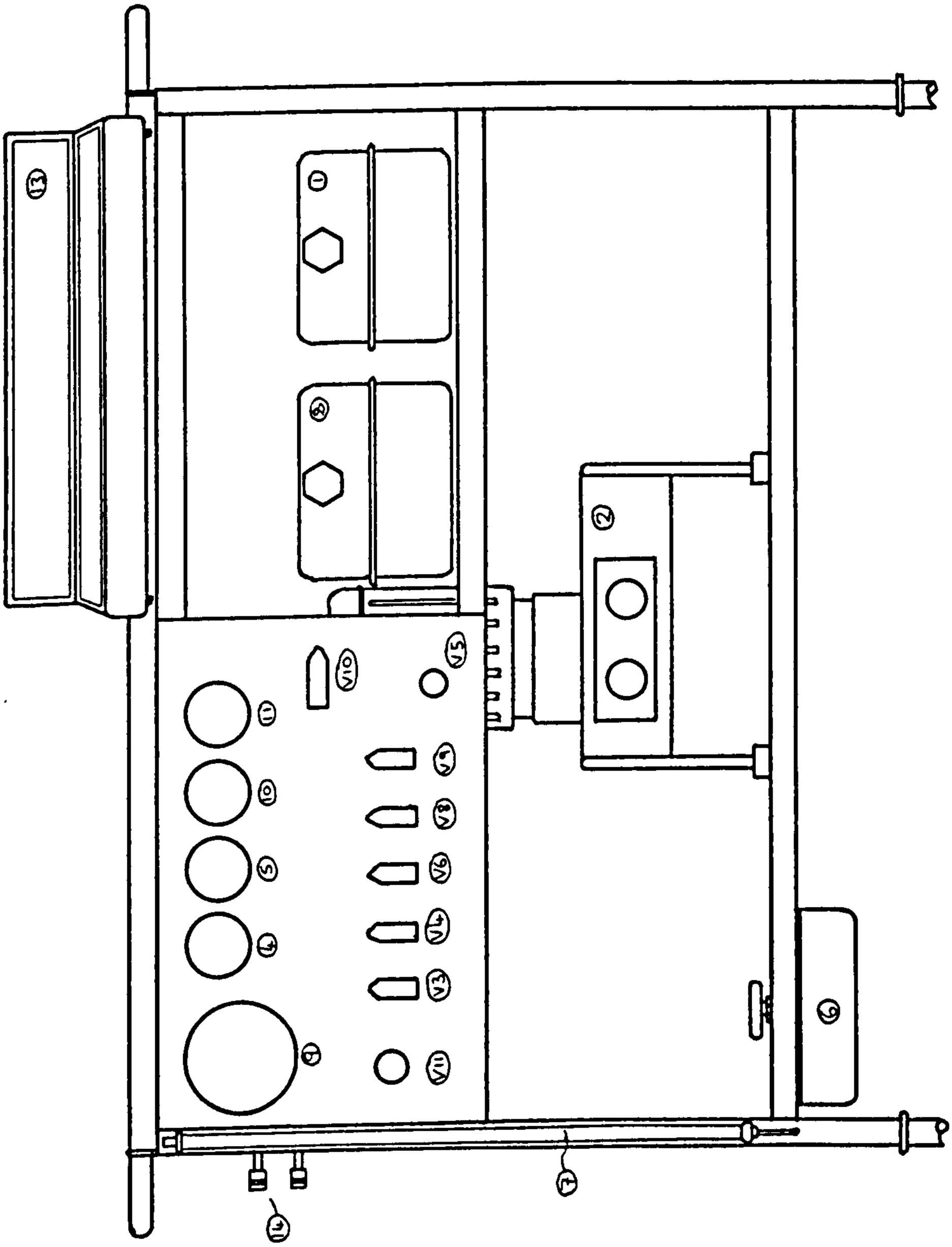

Figure 5.20 : Diagram of Oil Permeameter

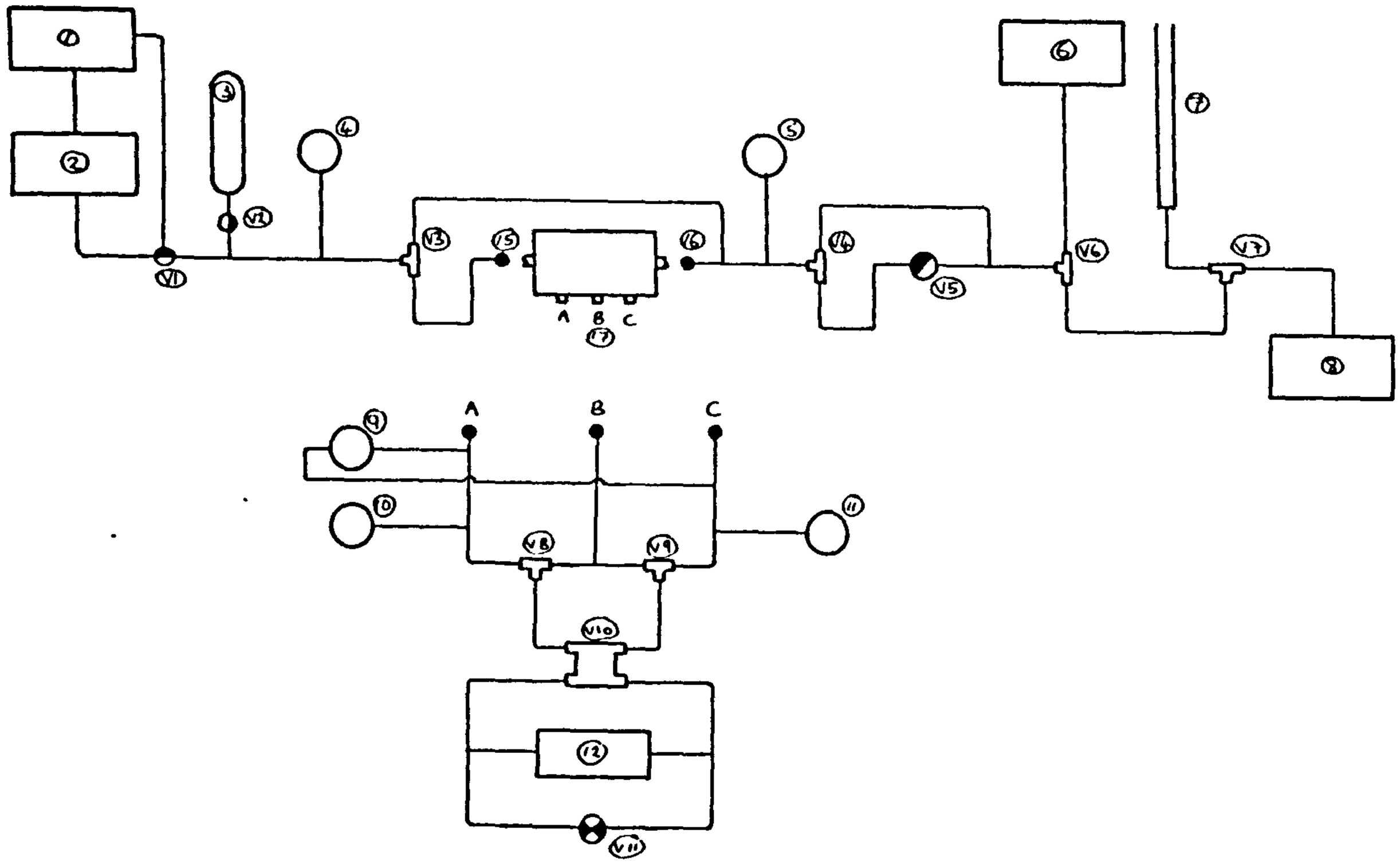

LEGEND

1. CLEAN OIL RESERVOIR
2. METERING PUMP
3. ACCUMULATOR
4. UPSTREAM PRESSURE GAUGE
5. DOWNSTREAM PRESSURE GAUGE
6. BURETTE RESERVOIR
7. BURETTE
8. DIRTY OIL RESERVOIR
9. DIFF. PRESSURE GAUGE
10. MAX. CELL PRESSURE GAUGE
11. MIN. CELL PRESSURE GAUGE
12. DIFF. PRESSURE TRANSDUCER
13. ELECTRONICS CONSOLE
14. HYDRAULIC PORTS
15. UPSTREAM TEMPERATURE PROBE
16. DOWNSTREAM TEMPERATURE PROBE
17. DIFFERENTIAL PRESSURE PORTS

V1. PRESSURE RELIEF VALVE
V2. ACCUMULATOR IN-LINE
V3. CELL BY-PASS VALVE
V4. FORWARD FLOW/BACK-PRESSURE
V5. THROTTLING VALVE
V6. FLOW RATE MEASUREMENT
V7. BURETTE DISCHARGE
V8. DIFF. PRESSURE VALVE
V9. DIFF. PRESSURE VALVE
V10. SYSTEM SAFE VALVE
V11. EQUALISATION VALVE

Figure 5.21 : Flow Schematic of Oil Permeameter System

interval. Valve V7 enables the burette contents to be discharged to a small reservoir situated on the underside of the trolley.

Upsteam and downstream pressures are monitored by two 0-600 psi bourdon tube gauges (4,5). The facility to apply back-pressure to the system is provided by an accurate, micrometer scaled throttling valve (V5). If required, this valve may be by-passed thus allowing a forward flow mode by means of valve V4. To enable oil flow to by-pass the cell, a 3-way valve (V3) has been incorporated in the system.

Platinum resistance temperature probes have been mounted in-line immediately before (15) and after (16) the linear flow cell, enabling accurate viscosities to be calculated and used when determining permeabilities. The probes are linearised, reading to 0.1°C on a digital display.

Two 3-way valves (V8,V9) provide the facility to measure pressure drop across any combination of the three pressure ports on the linear flow cell (17 a,b,c). The maximum differential pressure is initially monitored by a mechanical differential pressure gauge (9), while the cell pressure is monitored by two 0-600 psi gauges (10,11) connected respectively across the high and low pressure lines.

Accurate differential pressure measurements are made across the pressure ports by a differential pressure transducer (12) which has an operational range of 7.25 ± 0.001 psi. The output from the transducer is displayed on an LCD digital display unit situated on

the electronics console.

A 4-way valve (V10) enables the differential pressure transducer to be isolated from the system. A needle valve (V11) is included to provide differential pressure equalisaton when required.

5.7.7 Determination of Semi-Steady State Conditions

5.7.7.1 Intention of Test

The intention of this test was to confirm the existance and to examine the extent of proppant creep within the linear flow cell with a view to determining the optimum time delay between increasing closure stress and taking flow rate, differential pressure and fracture width readings.

5.7.7.2 Test Procedure

(1) For continuity with previous flow tests, a proppant concentration of 2 lb/ft^2 was employed. Accordingly, 63.2 g of proppant was poured into the linear flow cell and levelled before the insertion of the top shim and piston. The cell was the placed in the stiff-testing machine and an initial stress of 100 psi (690 kPa) was applied. The fracture width was then determined and the initial LVDT reading zeroed.

(2) The closure stress was then increased to 1000 psi (6900

kPa) and oil flow commenced at approximately 10 cc/minute while a back-pressure of 200 psi was maintained.

(3) The closure stress was held constant at 1000 psi (6900 kPa) for one hour and the change in fracture width, which was measured to the nearest 0.001 mm by the internal LVDT of the testing machine, was recorded every 5 minutes. Flow rate and differential pressure readings were also taken at this time interval.

(4) Closure was then increased to 2000 psi (13800 kPa) and held at this level for 30 minutes with readings being taken every 5 minutes.

This process was then repeated in steps of 2000 psi (13800 kPa) up to a maximum of 10000 psi (69000 kPa) before reducing the closure stress to zero.

In order to establish the effect of oil flow on creep, it was decided to repeat the above test procedure under non-flowing conditions. Accordingly, the 10 in^2 circular crush cell was used for this purpose.

5.7.7.3 Results

The results of the above tests are presented graphically in Figure 5.22. It is apparent that creep was present and the general trend was similar in both cases. At low closure stresses, the closure

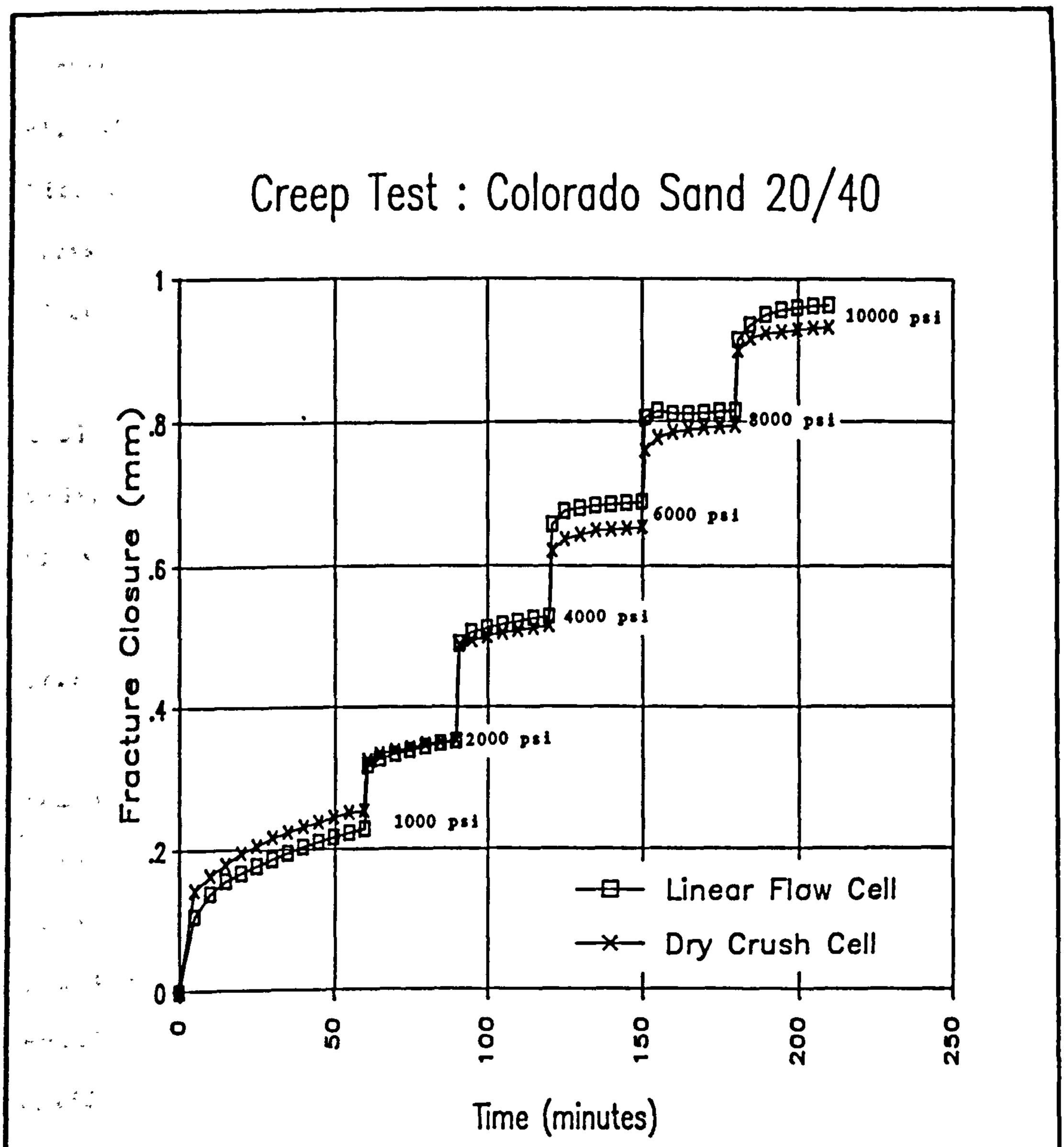

Figure 5.22 : Results of Creep Test - 20/40 Colorado Sand

measured in the crush cell was greater than that of the linear flow cell. This was due to the flow cell operating under a back-pressure, which acts like a pore pressure and effectively reduces closure stress. At higher stress values, this feature can be seen to have a reduced effect.

At closure stresses of 4000 psi (27600 kPa) and above, it was evident that the proppant compaction which occurred in the crush cell was less than that of the linear flow cell.

5.7.7.4 Discussion and Conclusions

From the above results, it can be concluded that creep was present under both flowing and dry test conditions. The magnitude of which was similar in both cases and was at a maximum at the beginning of each test. This was most probably due to the compression machine levelling the proppant bed and at this stage crushing was not considered to be a problem. At higher closure stresses, the creep detected was due to proppant crushing.

Oil flow appears to increase proppant compaction compared to that with no oil flow present. This suggests that the fines generated at higher closure stress values are migrating and filling the pore spaces between the larger proppant particles.

From an analysis of cell conductivity results, it can be concluded that a reasonably steady permeability value is obtained after a period of approximately 15 minutes after the increase in closure

stress.

5.7.7.5 Recommendation

It was therefore proposed to obtain flow rate, differential pressure and fracture width readings some 15 minutes after an increase in closure stress. To minimise the start-up effect, however, it was proposed to maintain the initial closure stress value of 1000 psi (6900 kPa) for a period of one hour to allow the oil permeameter system and linear flow cell to stabilise and reach semi-steady state conditions.

In order to eliminate the effect of the proppant pore pressure, it was proposed to increase the applied closure stress, by the respective amount of back-pressure acting on the cell, to produce an effective closure stress.

5.7.8 Calibration of the Linear Flow Cell System

The intention of this calibration test was to examine the accuracy of the permeability measurements taken with the oil permeameter and the linear flow cell. This was accomplished by a comparison of the actual flow cell permeability with the theoretical permeability of an open fracture.

5.7.8.1 Theory

The permeability of an open slot/fracture is defined as [48],

$$k_{th} = 54 \times 10^{7} \cdot W_f \qquad \ldots\ldots\ldots\ldots\ldots (5.21)$$

where k_{th} = Theoretical Permeability (Darcy)

W_f = Slot/Fracture Width (inches)

The flow cell permeability may then be found from the following relationships (see Section 5.4.2):

$$k_{cell} = \frac{12(kWf)}{Wf} \qquad \ldots\ldots\ldots\ldots\ldots (5.22)$$

and

$$kW_f = \frac{0.008Q\mu L}{\Delta Pb} \qquad \ldots\ldots (5.23)$$

where k_{cell} = Flow Cell Permeability (Darcy)

kW_f = Flow Cell Conductivity (Darcy x Feet)

Q = Flow Rate (cc/min)

μ = Viscosity (cp)

L = Linear Flow Length (inches)

b = Breadth of Flow Cell (inches)

ΔP = Differential Pressure (psi)

5.7.8.2 Calibration Procedure

The empty linear flow cell was inserted in a compression machine. Hydraulic connection was then made to the permeameter and oil flow commenced at approximately 40 cc/mm. The fracture was allowed to open, under internal pressure, until the top platten made contact with the ram of the compression machine. The actual open fracture or

slot width was then determined by measuring the top platten protrusion with a digital micrometer.

A back-pressure of 200 psi (1380 kPa) was then applied to the flow cell and the permeameter system allowed to stabilise before differential pressure, volumetric flow rate and temperature readings were taken. The open fracture width measurement was repeated at this stage.

The flow cell conductivity was obtained from equation (5.23) thus allowing the cell permeability to be calculated from equation (5.22). The flow cell permeability was then compared with the theoretical value obtained from equation (5.21), the same fracture width being used for each calculation.

5.7.8.3 Results

The following is a summary of the permeameter/flow cell readings,

$$\Delta P(A\text{-}C) = 0.002 \text{ psi}$$

$$Q = 40 \text{ cc/min}$$

$$\mu = 18.5 \text{ cp}$$

$$L = 5 \text{ in}$$

$$b = 1.5 \text{ in}$$

$$W_f = 0.132 \text{ in}$$

From equation (5.23), $kW_f = 9867$ Darcy*ft

From equation (5.22), $k_{cell} = 897719$ Darcy

From equation (5.21), k_{th} = 939325 Darcy

5.7.8.4 Discussion

Due to the small pressure drop developed along the 'open' fracture, it can only be claimed that a result of the correct order was obtained. The creation of higher, more easily measured, pressure drops by increasing the flow rate and/or decreasing the open fracture width was considered to be impractical with equipment designed to test the permeability of a proppant-filled fracture.

5.7.9 Conclusions re Test System Performance

The facility to measure and obtain realistic fracture conductivity/ permeability and wetted surface area data has been provided. Initial problems due to equipment and test procedures have been solved and the system is ready for full scale testing.

5.8 PROPPANT TESTING PROGRAMME

5.8.1 Introduction

As stated in the introduction to this chapter, the objective of this testing programme was to set up a data-base outlining the properties of various types of commercially available proppants, such as permeabilities, wetted surface areas, proppant porosities, fracture conductivities and proppant crush resistance in order to select the optimum proppant for a specific formation. This section gives

details of the proppants investigated and the API testing of the proppants as supplied.

5.8.2 Proppants Tested

The proppants tested were 20/40 Sintered Bauxite, 20/40 Interprop I (both supplied by Norton) and 20/40 API quality frac sand (supplied by Colorado Silica Sand U.K.). An overview of the general properties and applications of these proppants may be found in Section 5.3.2.

5.8.3 API Testing of the Proppants as Supplied

Before conducting full scale tests, various physical properties of the proppants were determined. The bulk density and absolute density (specific gravity) of each proppant type was required in order to determine the porosity of the proppant pack. The particle roundness and sphericity was measured and a sieve analysis performed on each proppant to ensure they were within the API RP65 recommendations [ref]. These tests are described below.

5.8.3.1 Bulk Density

The bulk density was determined by weighing a known volume of proppant. A 100 mL volumetric flask was weighed, then filled with proppant and weighed again. The bulk density was then obtained by means of the following equation:

$$BD = \frac{W_{fp} - W_f}{V_f} \qquad .. \quad .. \quad .. \quad .. \quad .. \quad (5.24)$$

where, BD = Bulk Density of Proppant (g/cm^3)

W_{fp} = Weight of Flask and Proppant (g)

W_f = Weight of Flask (g)

V_f = Volume of Flask (cm^3)

5.8.3.2 Apparent Specific Gravity / Absolute Proppant Density

The determination of specific gravity, or the absolute density of a proppant is important because the success of a fracture job depends upon accurate calculation of slurry volumes. The absolute proppant density is also required to determine the porosity of a proppant pack. The specific gravity was determined by filling a volumetric flask with a liquid and measuring their combined weight. One-half of the liquid was removed, then 10g of proppant was added to the flask which was reweighed. The apparent specific gravity was then obtained from the following relationship:

$$SG = \frac{W_p}{V_f - (W_t - W_f - W_p)/\rho_1} \quad \ldots\ldots\ldots\ldots (5.25)$$

where, SG = Apparent Specific Gravity of Proppant (g/mL)

W_p = Weight of Proppant (g)

W_t = Weight of Flask, liquid and Proppant (g)

W_f = Weight of Flask (g)

ρ_1 = Test liquid density (g/mL)

V_f = Volume of Flask (mL)

5.8.3.3 Roundness and Sphericity

Proppant grain roundness is a measure of the relative sharpness of the grain corners, while proppant sphericity is a measure of how close the proppant particle approaches the shape of a sphere. This test was conducted according to the API RP56 specification, i.e. a mono-layer of proppant was collected and particles selected at random. The proppant sample was photographed and printed to obtain a 30X magnification. Twenty proppant grains were then selected at random and the roundness of each grain was compared with Figure 5.23. Next, the sphericity of each grain was assessed by a visual comparison with the chart. The roundness and sphericity values quoted for the proppant was then the average of the values assigned to the selected particles. Sample results are given in Figure 5.24.

5.8.3.4 Size Analysis (By Sieve)

This is one of the oldest method of size analysis and was accomplished by passing a known weight of sample through sucessively finer sieves and then weighing the amount collected on each sieve to determine the percentage weight in each fraction. To be within API specifications, a minimum of 90% should fall between the designated sieve sizes, i.e. -20+40 U.S. mesh in the case of 20/40 proppants. Not over 0.1% should be larger than the first sieve (16 U.S. mesh) and not over 1% should be smaller than the last sieve (50 U.S. mesh). Table 5.2 shows the mesh distributions for the most commonly used proppants [57]. In this analysis, U.S. mesh (A.S.T.M.) sieves were used for continuity.

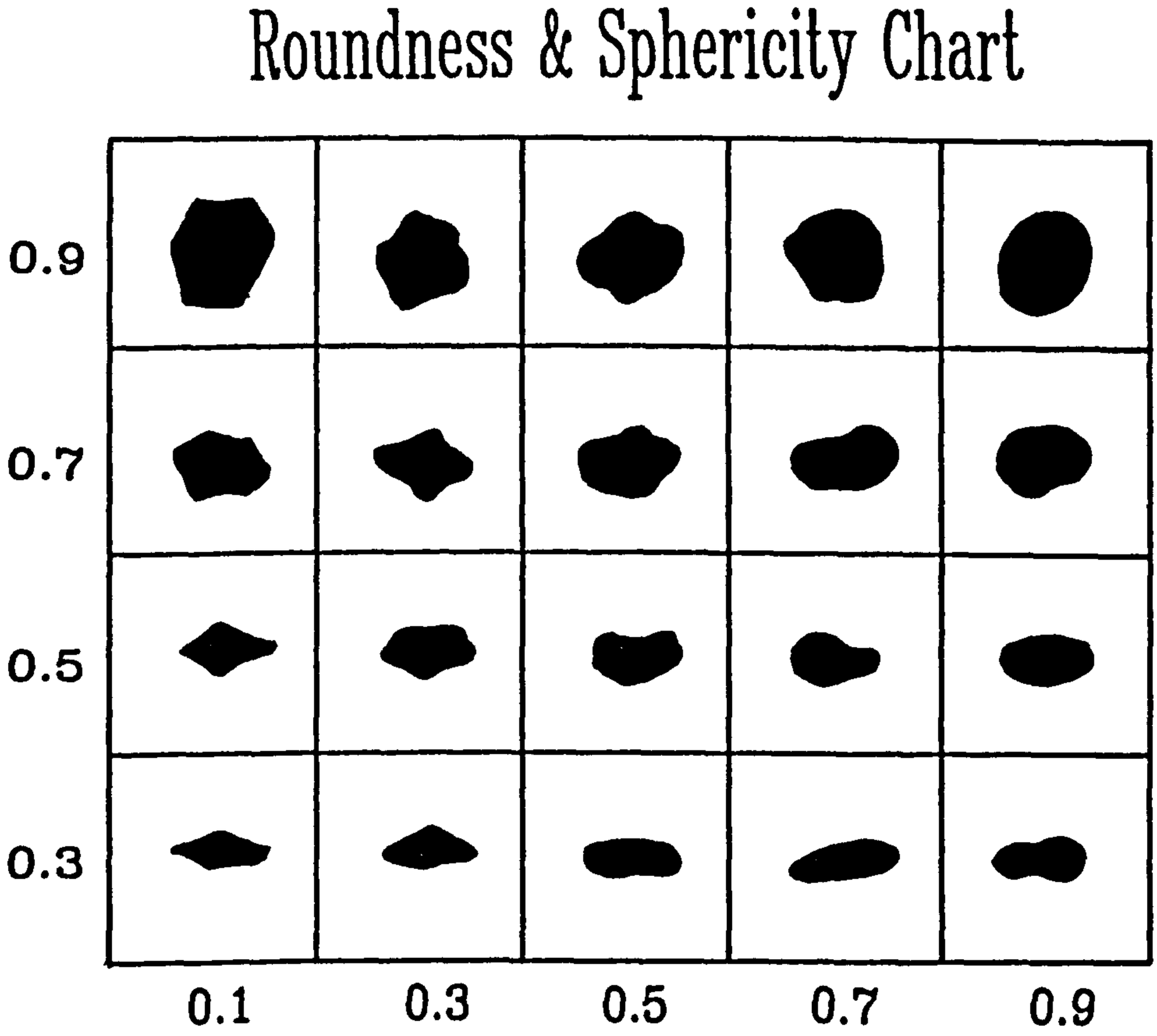

Figure 5.23 : API Roundness and Sphericity Chart [106]

API RP56 Roundness & Sphericity Test

Proppant Type : 20/40 Interprop I
Supplier : Norton

Test Centre : University of Strathclyde
Department of Mining & Petroleum Engineering

Sample Photograph

Grain	Roundness	Sphericity	Grain	Roundness	Sphericity
1	.8	.8	11	.7	.8
2	.8	.9	12	.8	.8
3	.8	.8	13	.8	.9
4	.7	.7	14	.8	.8
5	.9	.9	15	.8	.7
6	.8	.8	16	.8	.8
7	.8	.9	17	.8	.9
8	.7	.7	18	.8	.7
9	.9	.9	19	.9	.9
10	.8	.8	20	.9	.8

Average Roundness : .81 (API Minimum : 0.7)
Sphericity : .82 (API Minimum : 0.7)

***Figure 5.24** : Sample Results - Roundness and Sphericity Test*

5.8.3.5 Test Results

The results of the above tests on 20/40 Sintered Bauxite, 20/40 sand and 20/40 Interprop are given in Table 5.3.

5.8.4 Testing Programme

One of the major problems that complicates the generation of fracture conductivity/permeability data is the variation of sieve distributions that can be encountered. For any given type of proppant, the measured conductivity/permeability will be higher when the average particle size is larger, until proppant crushing becomes significant. When two samples of a '20/40' mesh size proppant have a different distribution of particles within the nominal sieve range, the measured fracture conductivity/permeability will shift accordingly. The above proppants, however, were not resieved to obtain a uniform size prior to performing the following tests since this would have resulted in testing proppants that were not representative of products available in the oilfield.

The following three sections detail the experimental techniques which were applied to construct the data-base of proppant properties, an analysis of the test data, and the application of the data-base to formation samples to arrive at an in-situ value for fracture conductivity.

RECOGNIZED FRAC SAND SIZES

Frac Sand Size Designations	6/12	8/16	12/20	16/30	20/40	30/50	40/70	70/140
	4	6	8	12	16	20	30	40
	6	8	12	16	20	30	40	70
U.S. Sieves	8	12	16	20	30	40	50	100
Recommended	10	14	18	25	35	45	60	120
for Testing	12	16	20	30	40	50	70	140
	16	20	30	40	50	70	100	200
	Pan	Pan	Pan	Pan	Pan	Pan	Pan	Pan

Table 5.2 : U.S. Mesh Sieve Distributions for Common Proppants

Proppant Type / Test	20/40 Bauxite	20/40 Interprop	20/40 Sand
Bulk Density (g/cc)	2.12	1.87	1.61
Specific Gravity	3.64	3.12	2.64
Roundness	0.80	0.81	0.70
Sphericity	0.78	0.82	0.69
Sieve Analysis (U.S Mesh)	% Weight Retained (g)		
-16	0.0	0.1	0.0
-20+30	52.4	74.3	31.5
-30+35	47.4	22.5	42.9
-35+40	4.1	3.1	25.2
-40+60	0.2	0.0	0.3
PAN	0.0	0.0	0.0

Table 5.3 : Test Results of Proppant Properties

5.9 DETERMINATION OF PROPPANT PERMEABILITY AND WETTED SURFACE AREA USING THE LINEAR FLOW CELL

5.9.1 Introduction

This section describes the test procedure and experimental results used to construct the proppant data-base which related the proppant permeability and wetted surface area to closure stress. The tests were conducted using the linear flow cell and oil permeameter, the closure stress being applied by the servo-controlled 'stiff' testing machine. Displacement transducers (LVDTs) were used to monitor the closure of the simulated fracture. Using this equipment and the following test procedure, the determination of simulated fracture conductivity and fracture porosity enabled the Kozeny-Carmen equation to be applied to determine the wetted surface area and the flow cell permeability. A diagram showing the test system is presented in Figure 5.25.

5.9.2 Test Procedure

Based on experience gained with the system, the following test procedure was adopted. This modified procedure was used to generate all the permeability and wetted surface area data which are presented in this section.

(1) After the insertion of the bottom piston and stainless steel shim, 63.2 g of proppant (corresponding to a concentration of 2 lb/ft) was poured into the test chamber

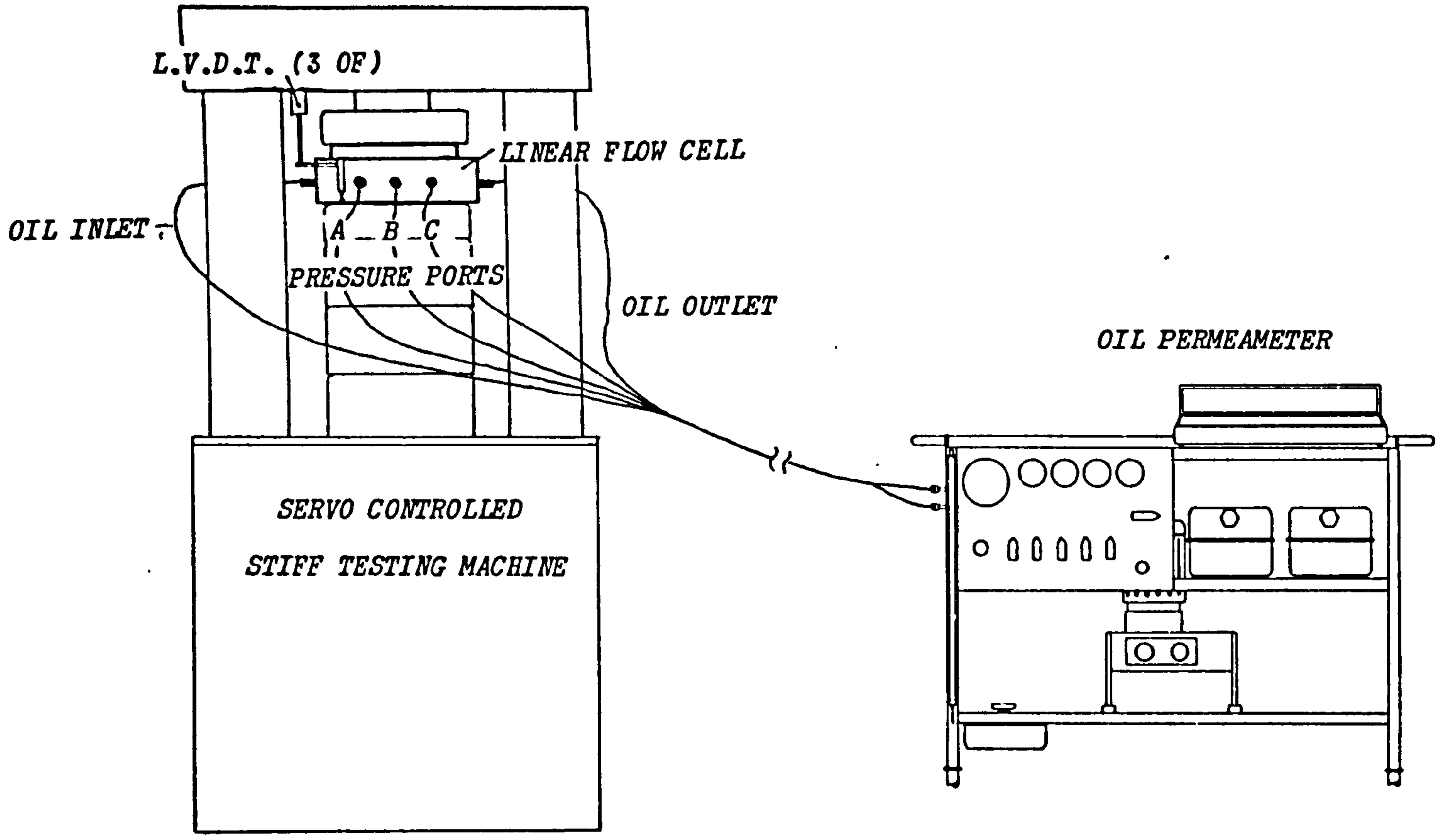

Figure 5.25 : *Test System Comprising of Linear Flow Cell, Oil Permeameter and 'Stiff' Testing Machine*

of the flow cell. The proppant bed was then carefully levelled using a cylindrical plunger device before the insertion of a stainless steel shim and the upper piston. Before proceeding with the test, the protruding ends of the pistons were measured to ensure a constant fracture width had been obtained. If inconsistent readings were obtained, the top piston and shim were removed and the proppant pack re-levelled.

(2) The linear flow cell was then placed in the stiff-testing machine and an initial closure stress of 1000 psi (6900 kPa) applied. Hydraulic connection was then made to the permeameter and oil flow commenced at approximately 10 cc/min. A back-pressure of 200 psi (1380 kPa) was introduced to the system and the closure stress increased to produce an effective pressure of 1000 psi (6900 kPa). The system was then allowed to reach equilibrium for a period of one hour.

(3) Differential pressure readings were then taking across ports A-B while the volumetric flow rate over a period of 30 seconds was measured. The differential pressure was again noted, the two readings being averaged. The initial fracture width was determined by measuring the top platten protrusion while the change in fracture width was recorded by averaging the output from three LVDT position sensors placed at each end and at the centre of the flow cell. Test fluid temperature, thereby allowing the fluid viscosity to

be determined, was then measured by averaging the outputs from the platinum resistance probes.

(4) Differential Pressure, flow rate, fluid temperature and LVDT readings were then taken over pressure ports B-C and A-C.

(5) After satisfactory results were obtained, the effective closure stress was then increased to 2000 psi (13800 kPa) at a rate of 1000 psi/minute and maintained at that value for a period of 15 minutes using the servo-control facility on the testing machine. Fracture width, volumetric flow rate and differential pressure reading were then taken over ports A-B, B-C and A-C.

(6) The above procedure was repeated in pressure increments of 2000 psi (13800 kPa) up to an effective maximum closure of 15000 psi (103500 kPa) for high and intermediate strength proppants or 10000 psi (69000 kPa) for API quality frac sand.

5.9.3 Data Analysis and Presentation - Linear Flow Cell Results

The data was processed using a spreadsheet program. The simulated fracture conductivity (henceforth termed 'flow cell conductivity') at each level of closure stress was calculated from equation (5.9). Knowing the fracture width from the LVDT reading, the permeability (henceforth termed 'flow cell permeability') was then calculated

from equation (5.14). The fracture or proppant porosity was then determined by means of equation (5.11) which allowed the calculation of the wetted surface area from equation (5.13).

As regards presentation of results, the input values of fracture width, differential pressure and flow rate at various closure stresses were displayed in tabular form. The results output indicating wetted surface areas, permeabilities, fracture widths and proppant porosities at various closure stress were given in tabular form on the same data sheet. A brief section stating the proppant data and the description of test conditions was also included. A sample sheet is presented in Figure 5.26. Two tests were conducted on each type of proppant, the results of each test being presented on a separate sheet. Each test was given a reference number, as shown in the figure. To provide an average set of output values for the data-base, a summary sheet, using the same format, was constructed for each proppant which displayed the mean results. As an aid to comparison, the wetted surface areas and flow cell permeabilities as a function of closure stress were also displayed in graphical form.

The data-base files containing the test information were given the extension '.FLO' to enable test identification. For example, the Sintered Bauxite results were stored under the name BAUX.FLO, which contained three data sheets (i.e. the results of the two tests, reference numbers Baux20/40-1 and Baux20/40-2, and the average results set, reference number Baux20/40-AVE). A similar system of naming the Interprop and frac sand data files was used. Further

LINEAR FLOW CELL TEST RESULTS

Proppant Type : 20/40 Interprop I
Supplier : Norton
Reference No : INT20/40-AVE

TEST CONDITIONS

Test Cell Type : 10 sq in Linear Flow Cell (API Spec.)
Proppant Concentration : 2 lbs/sq ft
Proppant Grain Density : 3.120 g/cc
Test Fluid Type : Shell Tellus No. 10
Fracture Width @ 1000 psi : 5.165 mm (.2033 in)

DATA INPUT : Average of 2 Tests

Closure Stress (psi)	Differential Pressure A-B	B-C	A-C	Volumetric Flow-Rate A-B	B-C	A-C	Average Temp.	LVDT Value
1000	27.54	28.13	55.79	13.73	13.67	13.76	25.24	618
2000	30.33	33.42	63.67	13.27	13.47	13.60	25.31	600
4000	33.28	36.75	70.10	13.08	13.25	13.17	25.41	566
6000	34.91	46.28	85.82	12.31	14.00	13.99	25.51	531
8000	43.21	53.18	93.36	13.36	13.49	13.12	25.53	497
10000	42.03	51.14	92.42	10.08	9.73	9.81	25.67	461
12000	49.43	62.07	121.32	10.18	9.89	10.49	25.74	432
14000	67.57	89.18	153.72	10.48	10.44	10.23	25.84	405
15000	73.05	104.63	175.14	9.58	9.77	9.63	25.90	385

RESULTS OUTPUT : Average of 2 Tests

Closure Stress (psi)	Wetted Surface Area A-B	B-C	A-C	Flow-Cell Permeability A-B	B-C	A-C	Frac. Width	Porosity (%)
1000	237.9	240.9	239.1	385.6	375.9	381.7	.2033	39.33
2000	254.0	264.6	257.0	337.4	310.8	329.4	.2033	39.31
4000	264.0	275.6	270.0	302.8	277.8	289.5	.2023	39.03
6000	261.0	281.7	271.4	275.0	235.9	254.2	.1988	37.94
8000	258.5	285.4	271.2	245.5	201.4	223.2	.1951	36.77
10000	267.6	300.5	284.4	193.4	153.4	171.2	.1906	35.29
12000	268.4	305.2	292.9	168.4	130.3	141.4	.1874	34.16
14000	289.6	333.4	312.7	128.0	96.6	109.8	.1845	33.13
15000	294.9	349.4	322.1	109.5	78.0	91.8	.1818	32.14

UNITS : Differential Pressure (mbar) Wetted Surface Area (in^2/in^3)
Volumetric Flow Rate (cc/min) Flow Cell Permeability (Darcy)
Fluid Temperature (Celcius) Fracture Width (in)

Figure 5.26 : Sample Data Sheet - Linear Flow Cell Results

details are given in Appendix 1.

5.9.4 Experimental Results

The test data sheets for the following proppants are given in Appendix 1. A discussion of the test results is given below. To remove the variable of fracture width from the discussion, the permeability rather than the conductivity of the simulated propped fracture was discussed.

5.9.4.1 20/40 Sintered Bauxite

Referring to Figure 5.27(a), it can be seen that the permeability values obtained from ports B-C were lower than those obtained from ports A-B, while the A-C values were found to lie in the region between the two. In general, however, the flow cell permeability values measured over the three port combinations were found to be within 10% of each other.

The flow cell permeability at 1000 psi (6900 kPa) was measured to have an average value of around 300 Darcy. This initial value was found to decrease fairly rapidly as a result of increasing the closure stress to 2000 psi (13800 kPa). This reduction was considered to be due to settling of the proppant pack. As the effective closure stress was increased in increments to 10000 psi (69000 kPa), the flow cell permeability was found to decrease at an average rate of 14 Darcy/1000 psi. Between this region and the maximum closure stress of 15000 psi (103500 kPa), the permeability

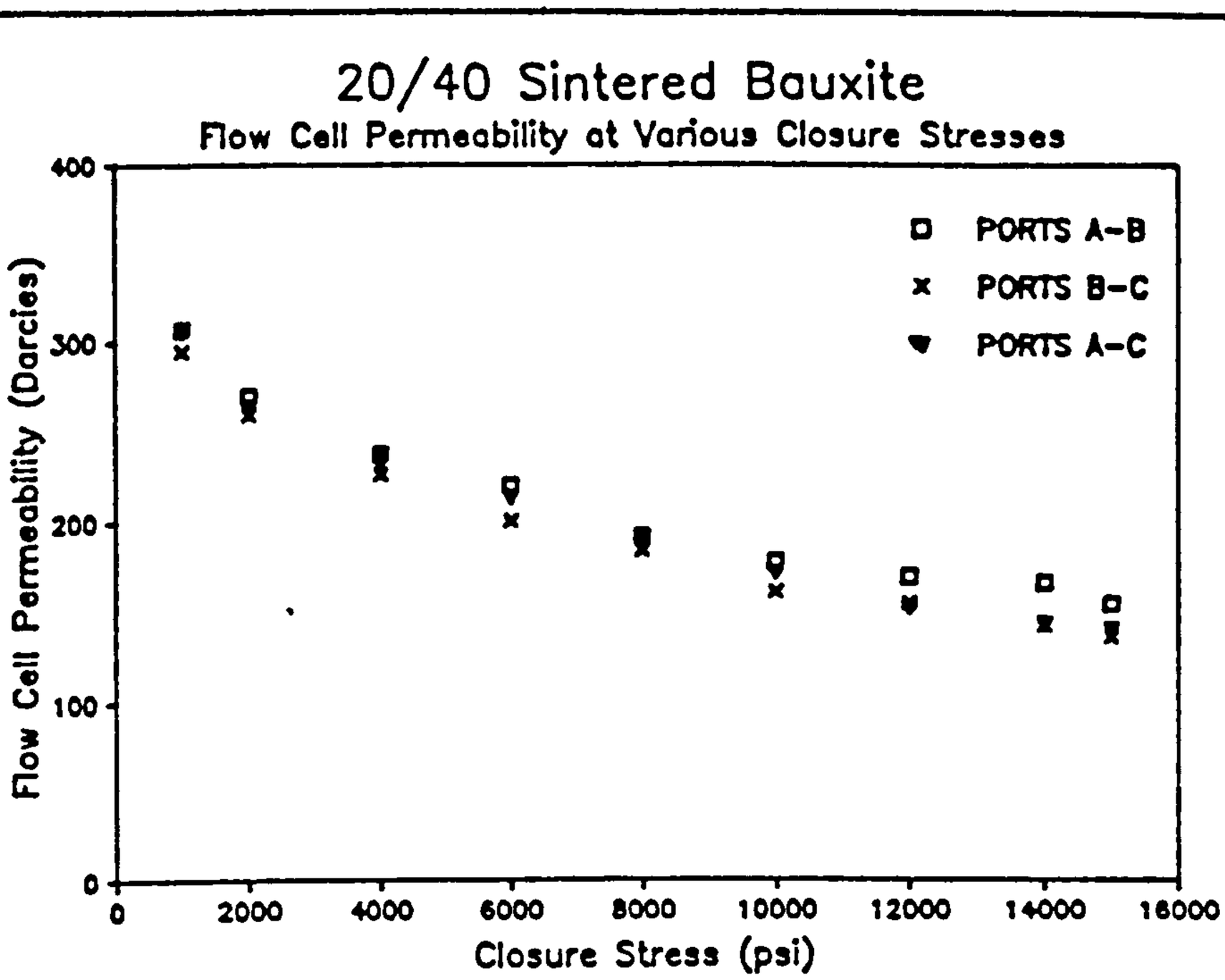

Figure 5.27(a)

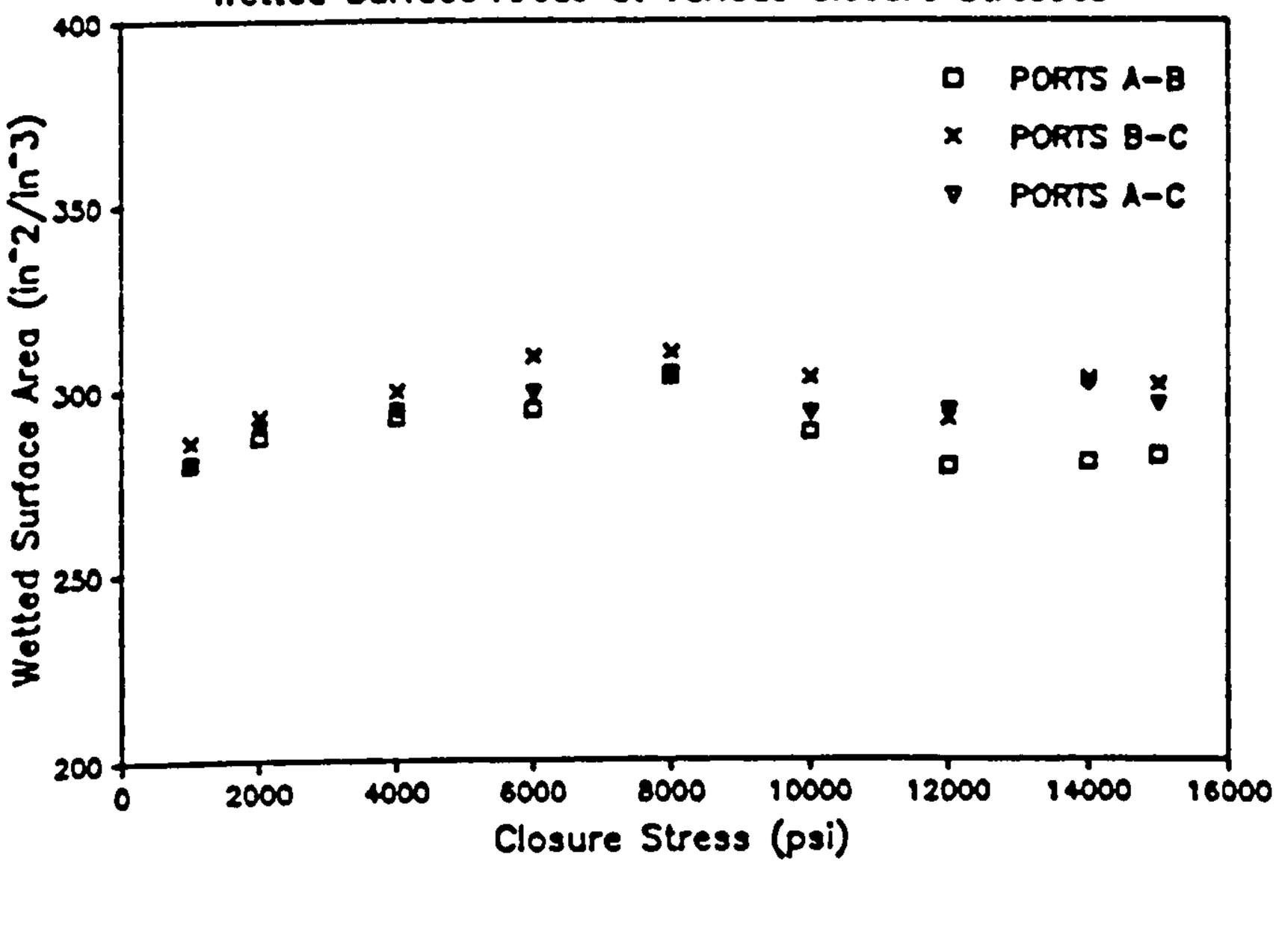

Figure 5.27(b)

decreased at an average rate of 5.3 Darcy/1000 psi. At the maximum closure stress, the average flow cell permeability had decreased to around 45% of the initial value.

The wetted surface area of 20/40 Sintered Bauxite is plotted against closure stress in Figure 5.27(b). In accordance with the flow cell permeability results, the wetted surface area values obtained from ports B-C were seen to differ from the respective values obtained from ports A-B. In this case, however, the B-C values were numerically greater. Again, the wetted surface area results obtained from measurements across the full linear flow length, i.e. ports A-C, were found to lie in the region between the respective values from ports A-B and B-C.

Referring to Figure 5.27(b) it can be seen that the wetted surface area increased proportionally with closure stress until 8000 psi (55200 kPa) where a reduction in surface area was measured. The wetted surface area continued to decrease until a closure stress of 12000 psi (82800 kPa). After this closure value, the wetted surface area increased again, although it never reached its maximum value which occurred at around 8000 psi (55200 kPa). As one would expect surface area to increase proportionally with applied stress, this unexpected trend can be explained either as a result of the high-strength Sintered Bauxite embedding slightly into the stainless steel shims of the linear flow cell, or the proppant grains deforming elastically. In either case, the surface area of the proppant in contact with the fluid would be reduced. An examination of the shims after each test indicated that slight proppant

embedment was most probably the case as their faces were pitted. As the wetted surface area increased until a closure stress of 8000 psi (55200 kPa), it was reasoned that proppant embedment was initiated at or around this closure stress level. Similarly, as the wetted surface area increased with closure stresses above 12000 psi (82800 kPa), it was considered that proppant crushing as well as embedment was present at the higher closure stresses.

5.9.4.2 <u>20/40 Interprop I</u>

The flow cell permeability at various closure stresses for 20/40 Interprop is illustrated in Figure 5.28(a). The initial permeability at 1000 psi (6900 kPa) closure stress was measured to be about 380 Darcy. From an analysis of the graph it can be seen that the flow cell permeability decreased at an average rate of 18 Darcy/1000 psi to an average value of 92 Darcy at the maximum closure stress of 15000 psi (103500 kPa). The final permeability was therefore in the order of 25% of the initial value. As with the Sintered Bauxite tests, the respective Interprop permeabilities measured across the three differential pressure port combinations were observed to vary. The three sets of curves, however, were seen to follow a similar trend. The 'upstream' permeability measurements, i.e. ports A-B, were found to be higher than the 'downstream' permeability measurements, i.e. ports B-C. In accordance with previous tests, the permeabilities measured across ports A-C were found to lie in the region between the respective values from ports A-B and B-C.

The wetted surface areas at various closure stresses are shown in

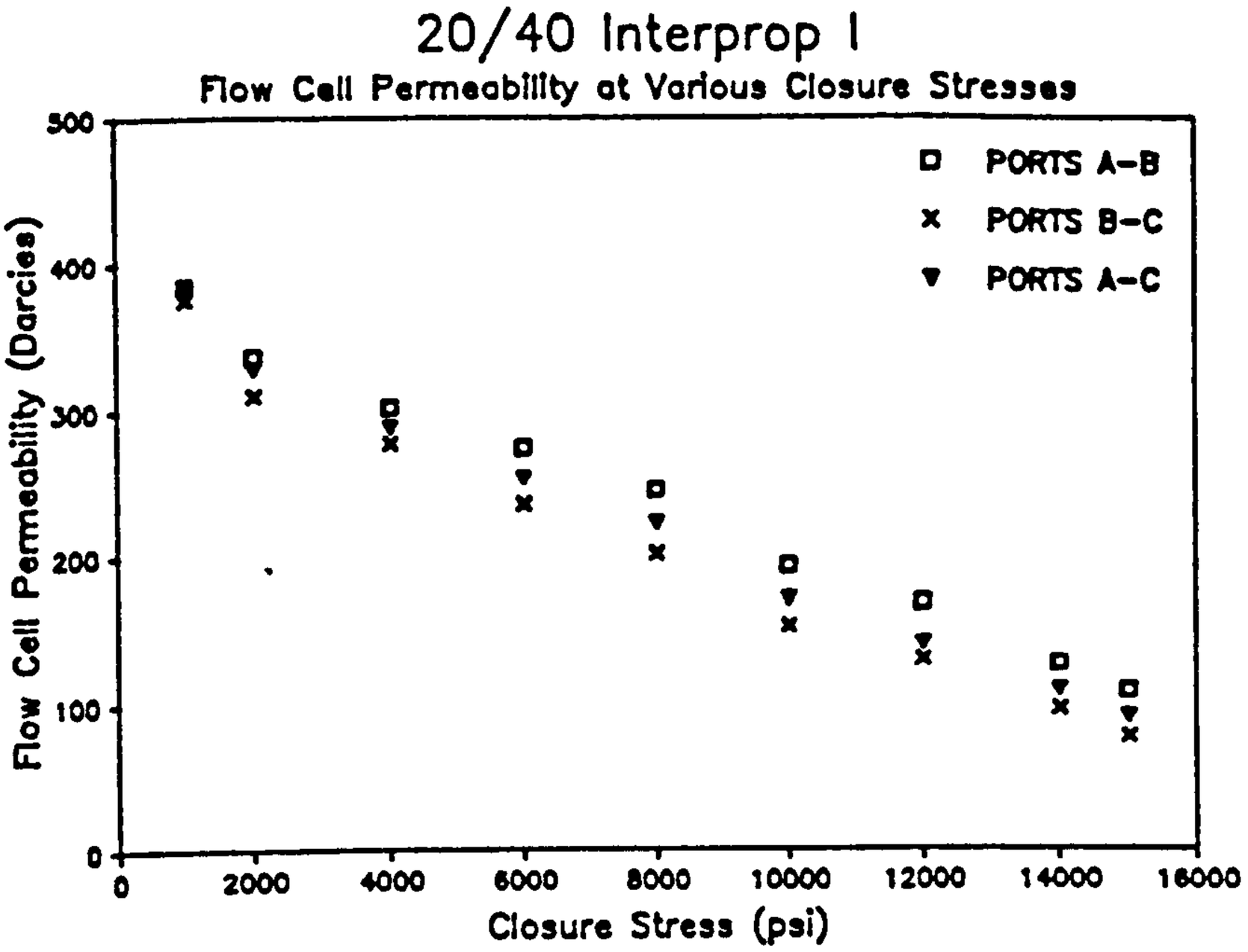

Figure 5.28(a)

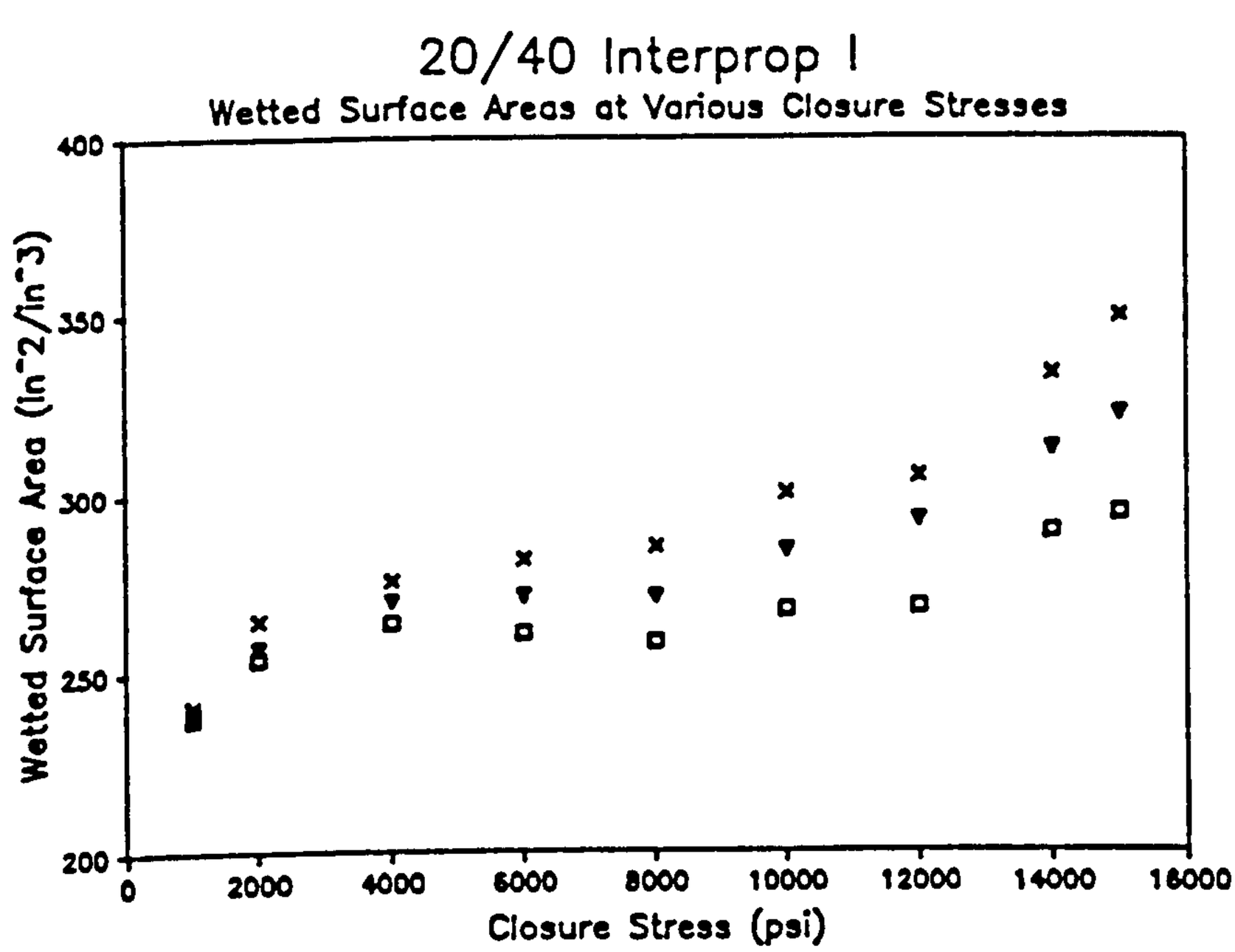

Figure 5.28(b)

Figure 5.28(b). At very low closure stresses, a high increase in wetted surface area with stress was indicated. Between closures of 4000 psi (27600 kPa) and 8000 psi (55200 kPa), the wetted surface area measured over ports A-C remained constant while the calculated wetted surface areas across ports B-C and A-B increased and decreased respectively. After this closure stress value, the wetted surface areas across all port combinations was observed to increase proportionally with applied stress. As indicated on the graph, the difference between the B-C and A-B values were also found to increase with closure stress. As the wetted surface area showed a marked increase with closure stresses of 10000 psi (69000 kPa) and above, it was considered that undesirable proppant crushing probably occurred around this stress level. An examination of the faces of the shims indicated that minimal embedment had occurred.

5.9.4.3 20/40 Sand

The flow cell permeability results for 20/40 frac sand are presented in Figure 5.29(a). At the initial closure stress of 1000 psi (6900 kPa), the average proppant permeability over the three pressure ports was 122 Darcy. As closure stress was increased, the flow cell permeability reduced at a rate of aproximately 8 Darcy/1000 psi until an applied stress of 4000 psi (27600 kPa). After this region, the decreased at an average rate of 12 Darcy/1000 psi until 8000 psi (55200 kPa). The flow cell permeability was then seen to decrease at a lower rate until at the maximum closure stress 10000 psi (69000 kPa), the average permeability had reduced to around 10% of its initial value.

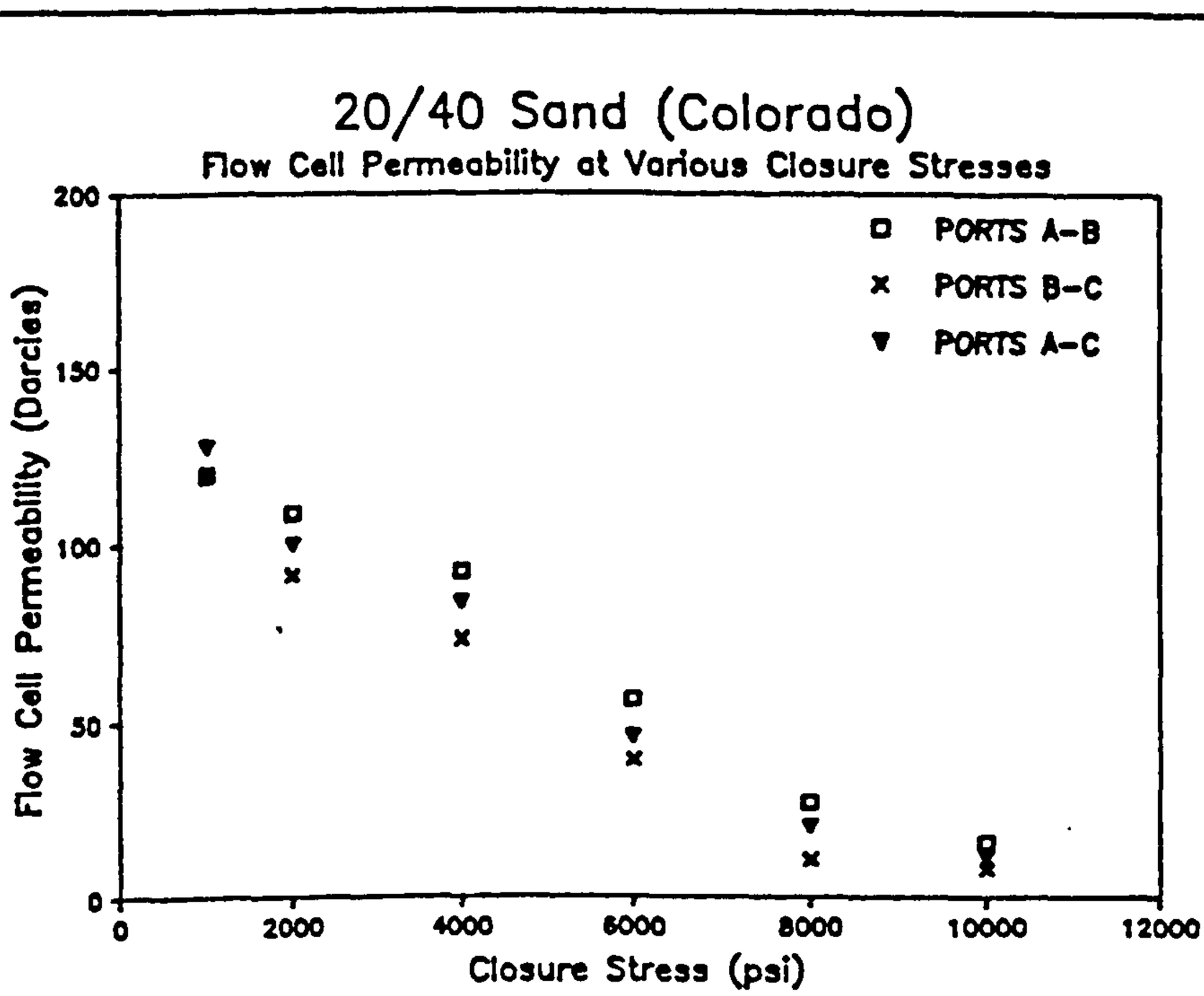

Figure 5.29(a)

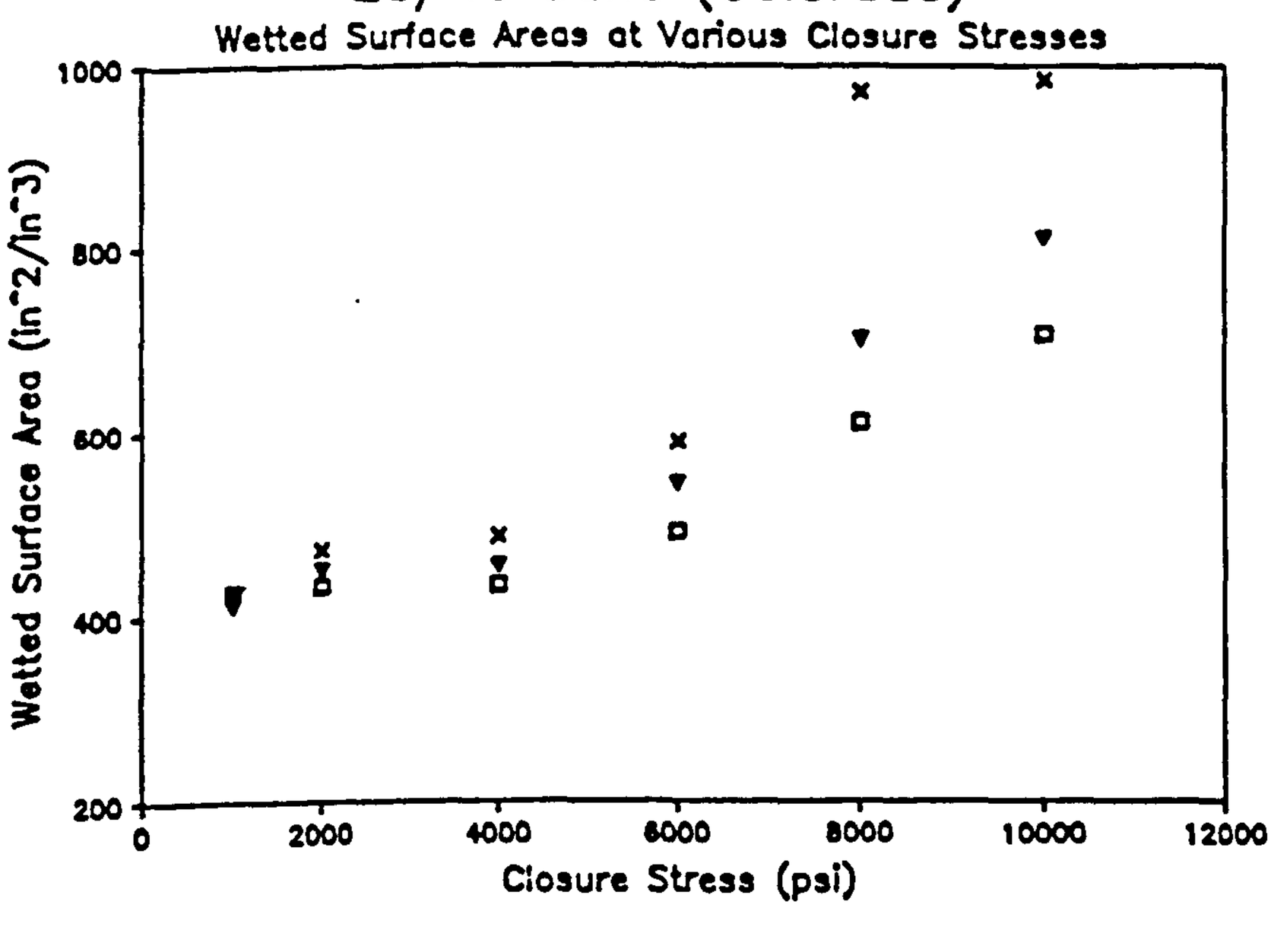

Figure 5.29(b)

The wetted surface area of 20/40 sand at various closure stresses is illustrated in Figure 5.29(b). An examination of this figure indicated that subjecting frac sand to stress greatly increased its wetted surface area. Up to an applied closure stress of 4000 psi (27600 kPa), the wetted surface area increased by only a small amount. As with the other proppants tested, the wetted surface areas calculated from measurements across ports B-C were greater than across ports A-B or A-C. At closure stresses above 6000 psi (41400 kPa) the B-C value increased dramatically, while the A-B and A-C values increased at a constant rate. The greater wetted surface area measured across ports B-C was considered to be due to proppant fines migrating from the upstream to the downstream section of the linear flow cell.

5.9.5 Size Analysis of Samples Retrieved from the Linear Flow Cell to Confirm the Downstream Migration of Fines

As stated above, it was generally found that the differential pressure measured across ports A-B and B-C were not equal, the latter port yielding the higher pressure drop and therefore the lower permeability. This difference in pressure drop was found to be proportional to an increase in closure stress. As the sum of the pressure differentials over ports A-B and B-C was generally within 10% of the value obtained across port A-C, (i.e. the total flow length) it was apparent that a degree of fines migration had occurred. In the case of frac sand, this was confirmed after the completion of the test when the top piston and shim were removed and

a concentration of fines were visible around the outlet port of the linear flow cell.

In order to investigate this phenomenon, the pressure differentials, were plotted against closure stress. A typical graph for frac sand is presented in Figure 5.30. It can be seen that the graph was linear for low closure values up to 2000 psi (13800 kPa). With closure stresses of 4000 psi (27600 kPa) and above, it can be seen that the percentage pressure differential increased rapidly with closure stress and at the maximum stress the pressure difference between ports A-B and B-C was in the order of 200%.

Accordingly, it was decided to confirm that fines migration occurred by sieving samples retrieved from opposite ports A, B and C of the linear flow cell after the completion of each flow test. The proppant samples were cleaned by washing in solvent prior to sieving.

The results are given in Table 5.4 and shown graphically in Figure 5.31. It can be seen that for each type of proppant, the percentage fines increased from port A through port B to port C, i.e. in a downstream direction, thus confirming the downstream migration of fines. Although the literature is aware of fines migration, the author has not detected acknowledgement of this effect when quoting values obtained from the various ports of the linear flow cell.

The result is significant, as fines produced within the fracture remote from the well may accumulate in the zone of increased closure

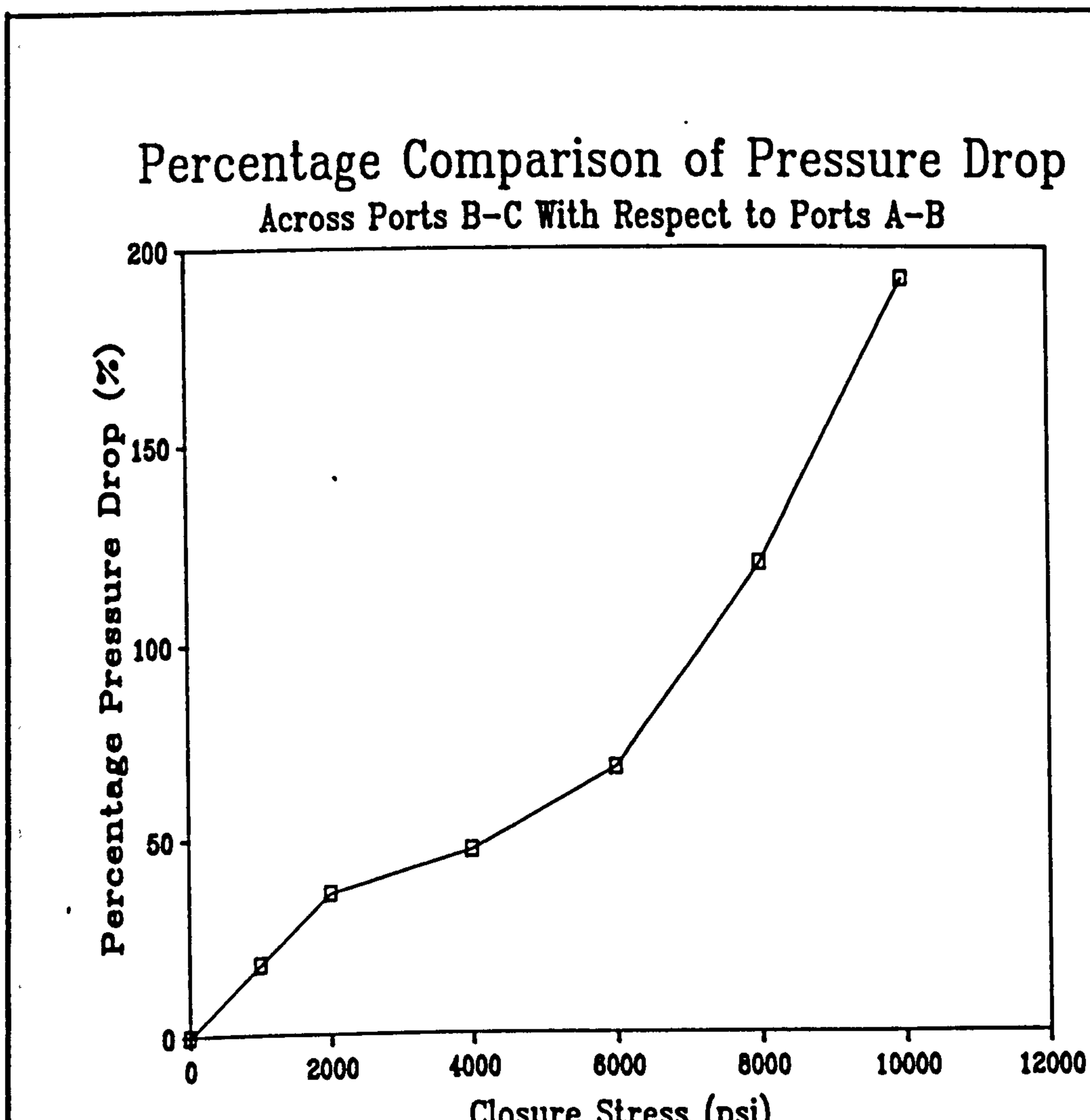

Figure 5.30 : Graph Showing Measured Differential Pressure against Closure Stress

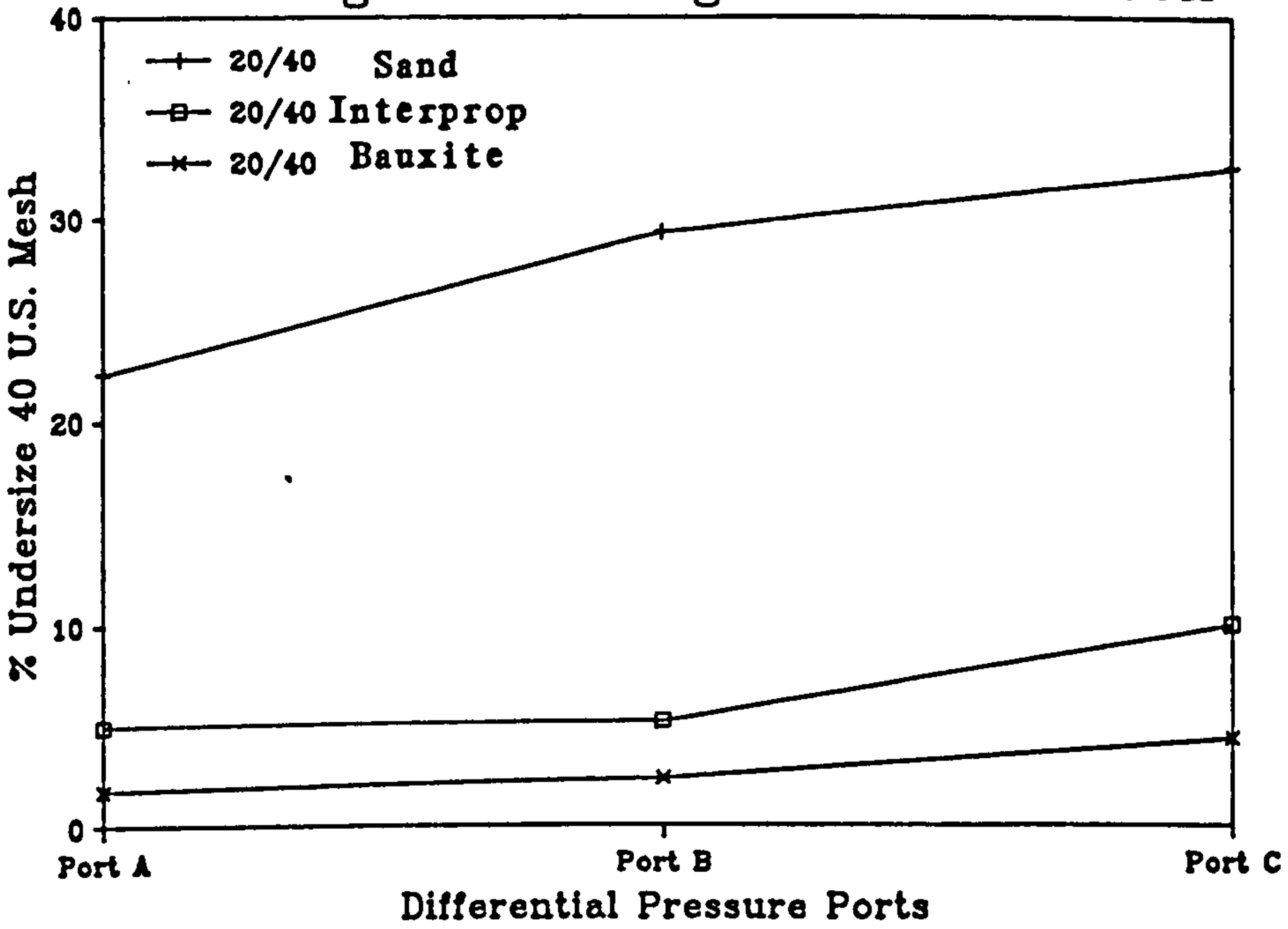

Figure 5.31 : Fines Migration in the Linear Flow Cell

	Proppant Type	Oversize	In Range	Undersize	Recovery
PORT A	Sand	2.41 %	73.12 %	22.23 %	99.76 %
	Interprop	9.85 %	85.04 %	4.91 %	99.80 %
	Bauxite	7.82 %	90.15 %	1.65 %	99.62 %
PORT B	Sand	1.19 %	69.59 %	27.17 %	99.95 %
	Interprop	6.71 %	88.04 %	5.16 %	99.93 %
	Bauxite	6.28 %	91.17 %	2.27 %	99.72 %
PORT C	Sand	1.38 %	65.51 %	32.44 %	99.33 %
	Interprop	6.25 %	83.68 %	9.96 %	99.89 %
	Bauxite	4.46 %	91.12 %	4.36 %	99.94 %

Table 5.4 : Size Analysis of Samples Retrieved from Opposite Ports A, B and C of the Linear Flow Cell

stress in the vicinity of the well. It can therefore be concluded that fines migration does indeed occur. It is consequently proposed that the permeability and wetted surface area values calculated from the differential port B-C may be more realistic for regions immediately around the wellbore, i.e. in the region of fines concentration. The values calculated from port A-B may thus be used for estimates away from the effects of the wellbore, while the values determined between ports A-C may be considered to be an average value.

5.9.6 Discussion of Results and Conclusions

Figure 5.32 shows a comparison of flow cell permeability results obtained for the three proppants tested. The respective curves shown were developed from the average of the results obtained over the total linear flow length, i.e. over ports A-C.

At the lower values of closure stress, it was apparent that Interprop yielded the highest flow cell permeability while the frac sand displayed the lowest. For comparison, 20/40 Interprop had an initial permeability at 1000 psi (6900 kPa) of around 400 Darcy, 20/40 Sintered Bauxite was measured at around 300 Darcy, while the initial permeability of the 20/40 frac sand was found to be in the order of 80 Darcy.

Referring to the Interprop curve, it can be seen that the flow cell permeability decreased linearly with increased closure stress. An examination of the Sintered Bauxite curve indicated that after an

initial sharp drop in permeability, which was attributed to settling of the proppant pack, the permeability decreased gradually and at a constant rate. At closure stresses of 10000 psi (69000 kPa) and above, the superiority of 20/40 Sintered Bauxite over 20/40 Interprop was evident. From an examination of the 20/40 sand curve, it was apparent that the permeability decreased gradually until closure stresses of 4000 psi (27600 kPa) and above where the permeability was observed to decrease at a greater rate. This was considered to mark the onset of undesirable crushing which resulted in the greater reduction in permeability.

The permeability data at low stress values reflected the relative particle sizes of the three proppants. It was established earlier that at low closure stress, the proppant with the larger average particle size yields the higher permeability. Although all three proppants conformed to API specifications, the Interprop was essentially a 20/30 proppant while the sand was essentially 30/40 proppant (see Table 5.3). Subsequent tests on a second batch of 20/40 sand supplied by Colorado Silica Sand UK which had a more uniform size distribution yielded an initial flow cell permeability of around 240 Darcy [126]. The curve produced from this test, denoted 'Silica Sand (Colorado)', has been added to the Figure 5.32. It can be seen that the permeability decreased sharply with increased stress and had a measured permeability of approximately half that of the original sample at the maximum closure stress of 10000 psi (69000 kPa).

A comparison of the wetted surface areas calculated from test data

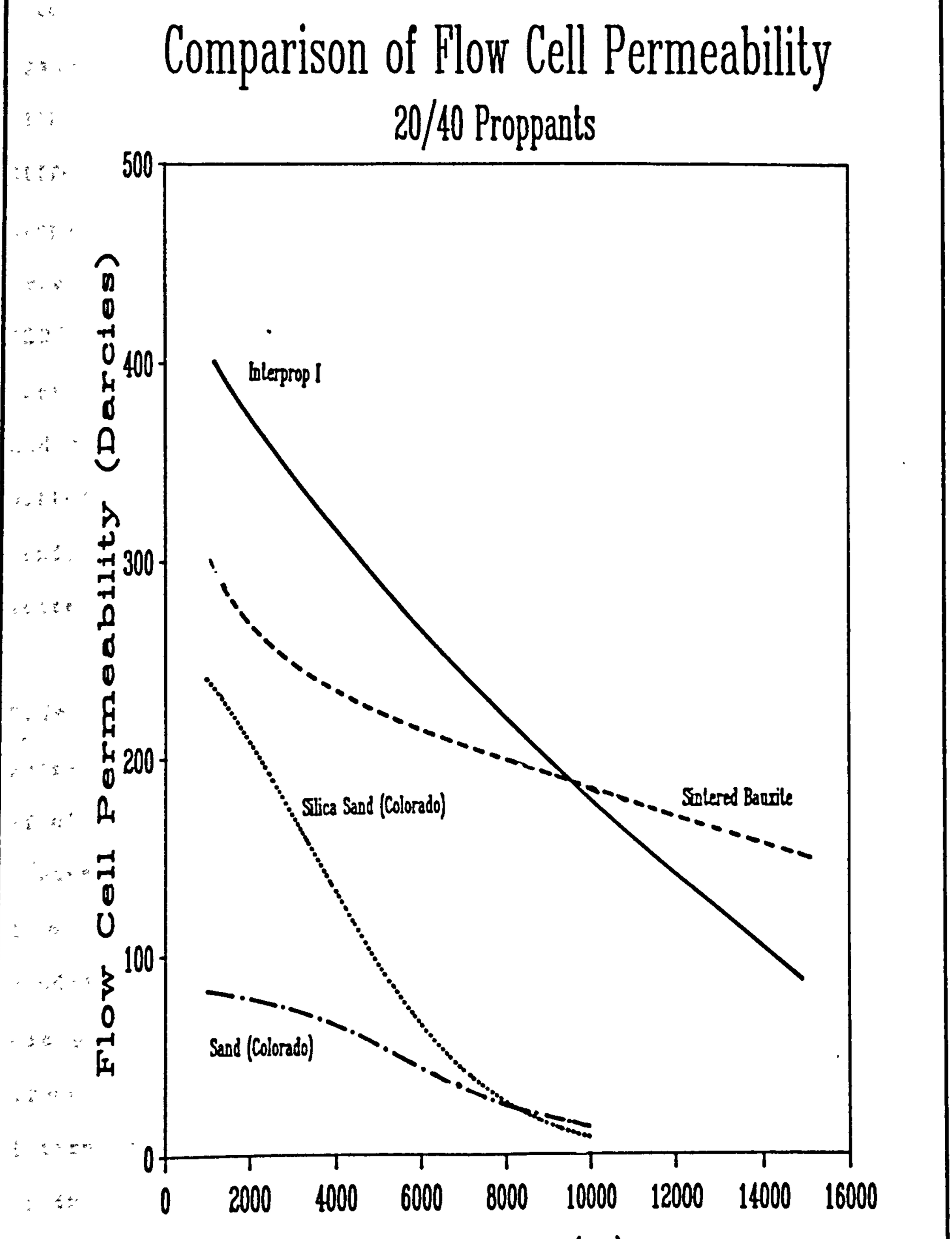

Figure 5.32 : Comparison of Flow Cell Permeability for the Various Proppants Tested

obtained over the total linear flow length is given in Figure 5.33. Again, the 'silica sand' results are provided to allow a comparison with the frac sand. The most striking feature of this graph was the difference between the wetted surface areas of the high-strength proppants (i.e. Sintered Bauxite and Interprop) and the low-strength frac sands. Again the variation in grain size distribution of the '20/40' proppants was emphasised by the calculated value of wetted surface area at the lower values of closure stress. Interprop, which had the largest average grain size was found to have the lower wetted surface area at low stress, while the original batch of frac sand, which had the smallest average grain size yielded the highest wetted surface area.

Referring to the Sintered Bauxite curve, it can be seen that the average wetted surface area increased only marginally over the range of closure stress. This indicated that minimal crushing occurred. However, as stated previously, slight embedment of the grains into the stainless steel shims was detected. As this embedment was condidered to be more severe at higher values of closure stress, it was possible that this contributed to the small and irregular increase in wetted surface area. The wetted surface area of Interprop was seen to increase at a fairly constant rate as a result of increased stress. At both low and high values of closure stress, however, this increase was found to be greater. An examination of the wetted surface area curves of the two batches of frac sand illustrated the effect of grain size variation in the same type of proppant. For the silica sand (2nd batch), the wetted surface area increased gradually up to a closure stress of 4000 psi (27600 kPa).

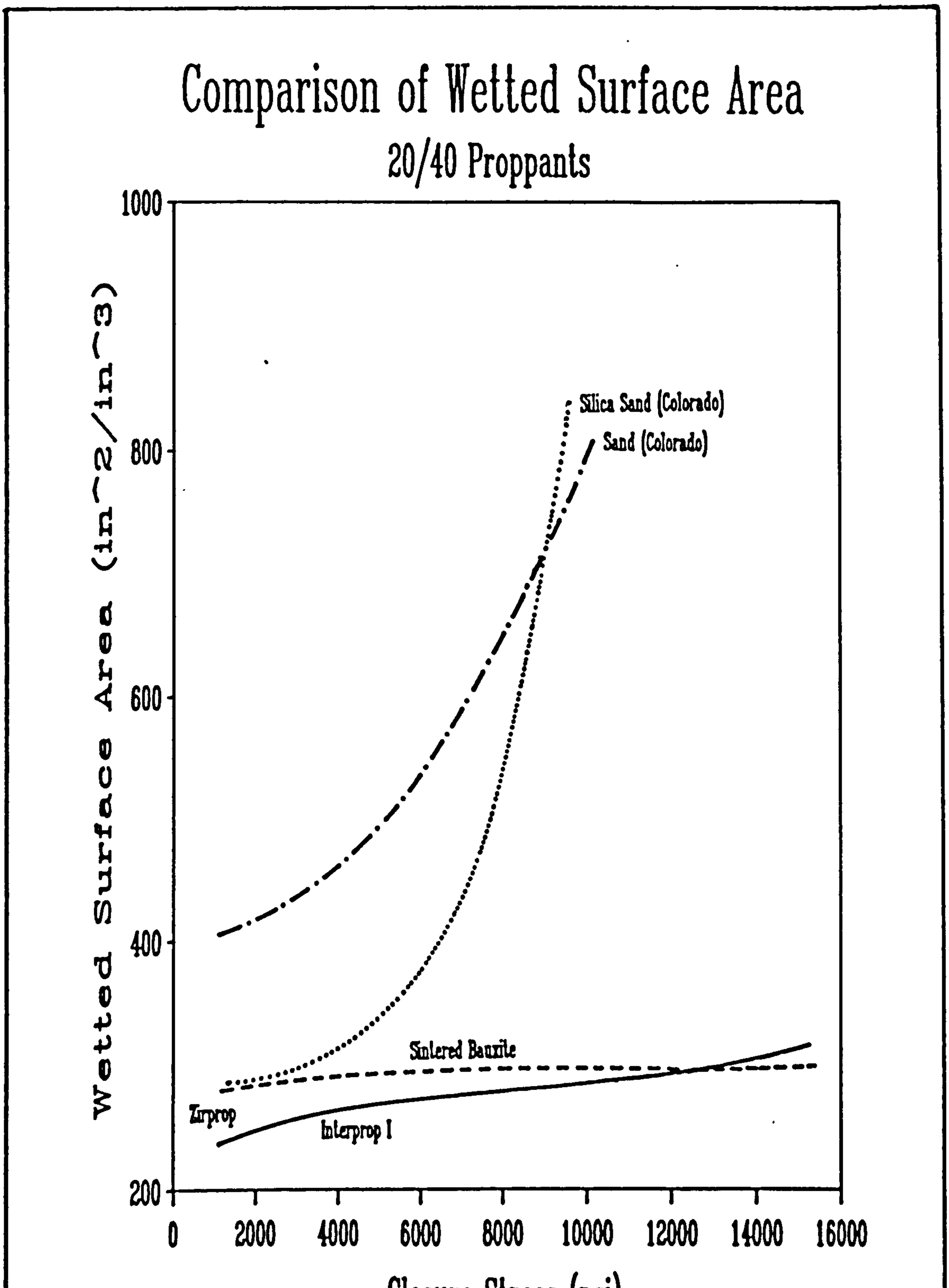

Figure 5.33 : Comparison of Wetted Surface Area for the Various Proppants Tested

After this limiting value, the curve was seen to rise sharply. The wetted surface area of the original sand sample increased at a lower rate and at the maximum closure stress had a lower wetted surface area than that of the silica sand.

In conclusion, the results obtained generally reflected the published properties of the various proppants. viz. the high-strength proppants provide greater permeability/conductivity at higher levels of closure stress.

It has been shown that proppant fines migration does occur in the linear flow cell and the magnitude of which can be measured. In extreme cases (frac sand), upstream (ports A-B) permeabilities up to four times the downstream (ports B-C) values have been measured.

5.10 DETERMINATION OF PROPPANT DRY CRUSH RESISTANCE

5.10.1 Introduction

The crush resistance test indirectly measures the strength of a proppant and its ability to resist erosion or crushing when exposed to pressure.

In the 'Recommended Practices for Testing Sand Used in Hydraulic Fracturing Operations' [106], the American Petroleum Institute described a proppant crush test procedure which stated that the maximum allowable fines for 20/40 proppants was 14% at a closure stress of 4000 psi (27800 kPa). The author considered this test to

be unsatisfactory inasmuch that it only gave crush data at one level of closure stress. Accordingly, it was proposed to investigate the crush resistance of the proppants under investigation at several values of closure stress.

The following extended crush test was introduced to supplement the proppant data-base by including the crush resistance properties of the proppants under investigation as a function of closure stress. From this additional data, it was anticipated that it would be possible to determine the closure stress at which unacceptable proppant crushing and thus fines production commence. The crush cell described in Section 5.6.4 was used. As the data obtained from the crush cell would be compared with that from the linear flow cell, the main design consideration was to reproduce the same test area of the flow cell, i.e. 10 in^2, and thus allow similar concentrations of proppant and fracture widths to be used.

The basic procedure was similar to API RP56 with the exception that the proppant was not sieved to obtain a uniform '-20+40' grade of proppant and a 2 lb/ft^2 concentration was tested with preference to the recommended 4lb/ft^2. The sieve stack used for the extended dry crush analysis is depicted in Figure 5.34.

5.10.2 Test Procedure

The following test procedure was adopted and repeated in stages of 1000 psi (6900 kPa) to a maximum of 15000 psi (103500 kPa) for the high and intermediate strength proppants and 10000 psi (69000 kPa)

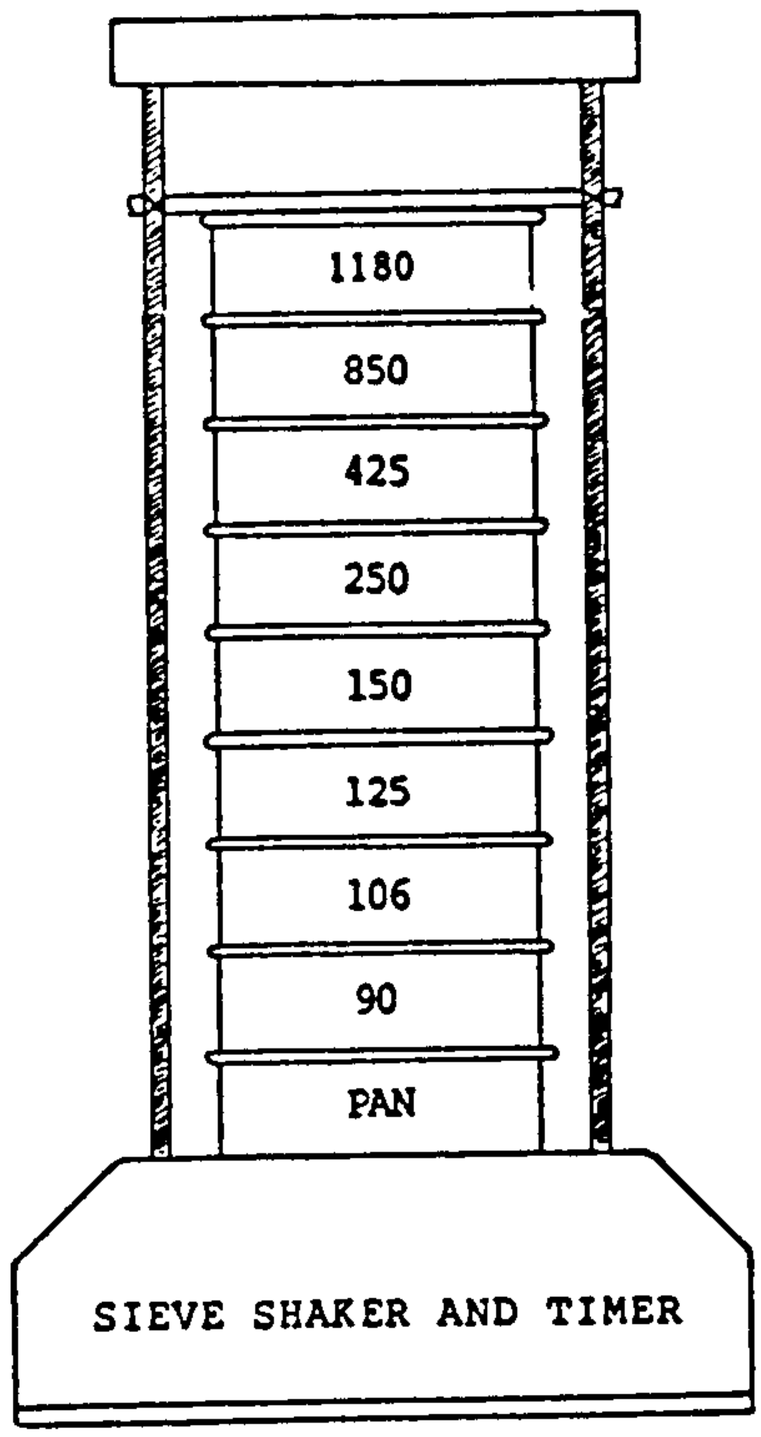

TABLE OF EQUIVALENT MESH MUMBERS

Nominal Aperture (microns)	BS Mesh Number	ASTM Mesh Number
1180	14	16
850	18	20
425	36	40
250	60	60
150	100	100
125	120	120
106	150	140
90	170	170

Figure 5.34 : Sieve Stack Used for the Extended Dry Crush Analysis Tests

for frac sand. A fresh, split sample was used for each test.

(1) The bottom piston was inserted into the cell housing and 63.2 g of proppant (corresponding to a concentration of 2 lbs/ft^2) was poured evenly into the cell. The upper piston was then inserted, uniform levelling was accomplished by the rotation of the piston through 180°.

(2) The crush cell was then placed in the servo-controlled 'stiff' testing machine. The desired closure stress was applied at a rate of 1000 psi/minute and held at that level for 2 minutes before removal of the load.

(3) The pistons were then carefully removed and the cell contents transferred to the uppermost sieve. The sieve stack and pan were then placed on a sieve shaker and sieved for 10 minutes.

(4) The contents of each sieve was then carefully emptied using a fine brush and weighed to within 0.0001 g on an electronic balance.

5.10.3 <u>Data Presentation</u>

The resulting data was processed using a spreadsheet program to provide a full sieve analysis data sheet. A sample data sheet is given in Figure 5.35. It can be seen that the data sheet gives a data-base reference number and indicates the closure stress which

PROPPANT DRY CRUSH TEST RESULTS :
Reference Number : INTER15k
Closure Stress : 15000 psi

PROPPANT DATA

Proppant Type/Size : 20/40 Interprop I
Supplier : Norton
Specific Gravity : 3.12
Bulk Density : 1.87 g/cc
Roundness : 0.82 (Uncrushed)
Sphericity : 0.81 (Uncrushed)

TEST CONDITIONS

Test Cell Type : 10 sq.in. 316 SS (Circular)
Proppant Conc. : 2 lbs/sq.ft.
Closure Stress : 15000 psi

Loading Rate : 1000 psi/minute
Stress Maintained : 2 minutes
Cell Temperature : 21 C (70 F)

SIEVE ANALYSIS OUTPUT

Sample Weight : 62.85 g
Recovered Weight : 62.59 g
Percentage Recovery : 99.58 %

Roundness : *.** (Crushed)
Sphericity : *.** (Crushed)

Percentage Oversize : 5.71 % (+20 Mesh)
Designated Range : 80.18 % (-20+40 Mesh)
Percentage Fines : 14.11 % (-40 Mesh)

U.S. MESH NUMBER	SIEVE FRACTIONS Wt(g)	% Wt	APERTURE (micron)	CUM. % UNDERSIZE	CUM. % OVERSIZE
+16		.00	1180	100.00	.00
-16+20	3.5599	5.69	850	94.31	5.69
-20+40	50.2253	80.25	425	14.06	85.94
-40+60	5.7276	9.15	250	4.91	95.09
-60+100	2.2241	3.55	150	1.36	98.64
-100+120	.2988	.48	125	.88	99.12
-120+140	.1878	.30	106	.58	99.42
-140+170	.2189	.35	90	.23	99.77
PAN	.1451	.23	-90	.00	100.00

Figure 5.35 : Sample Data Sheet - Extended Dry Crush Tests

was applied to the proppant. Other details given on the sheet are the bulk density, roundness and sphericity, specific gravity and the concentration of the proppant. In the sieve analysis output section, the sample weight, recovered weight and percentage recovery are indicated. If a percentage recovery of less than 99.5% was evident, the test was repeated. This was in accordance with API RP56 [106]. The percentage oversize, percentage in-range and percentage fines by weight were also given in this section. The sieve fractions recovered from the respective sieves while the cummulative oversize and undersize were detailed in the data sheet.

In the proppant data-base, the crush test data were given the extension '.CRU' to allow indentification. The files containing the results of Sintered Bauxite tests were named BAUX-**K, with the '**' indicating the level of applied stress (i.e. BAUX-10K indicated 10000 psi (103500 kPa) closure stress). Similarly, the files containing the Interprop and the frac sand results were named INTER-**K and COLOR-**K respectively.

5.10.4 Test Results

To avoid overloading the appendices with data, the results of the extended crush tests have been summarised. If required, the data sheets for the three proppants tested may be found in reference [127]. To give an indication of the progressive crushing of each proppant with increased closure stress, the total percentage fines, percentage oversize and the percentage of proppant grains falling within the designated range were summarised and displayed in

graphical and tabular form. A discussion of the results for each proppant is given below.

5.10.4.1 20/40 Sintered Bauxite

The extended dry crush test results for 20/40 Sintered Bauxite are presented graphically in Figure 5.36 and also in Table 5.5. From an examination of the graph, it was apparent that Sintered Bauxite exhibited extremely good crush resistance. The percentage oversize was found to vary from around 6% at 2000 psi (13800 kPa) closure stress to slightly over 4% at higher stresses. The percentage of proppant particles which were inside the designated range varied from over 94% to 93% at closure stress values up to 13000 psi (89700 kPa). After this value, the percentage in-range decreased slightly to 90.6% at the maximum closure of 15000 psi (103500 kPa). The undersize, or percentage fines produced due to the crushing of the proppant were found to remain at a negligible level up to a closure stress of 9000 psi (62100 kPa). At this closure stress value, the percentage undersize measured was in the order of 1.05%. An examination of Figure 5.36 illustrates that the percentage undersize increased at a constant level due to the effect of increased closure stress. At the maximum closure stress, 4.6% of the proppant was found to be undersize.

5.10.4.2 20/40 Interprop

The sieve fractions at various closure stresses for 20/40 Interprop are given in Figure 5.37 and Table 5.6. As can be seen from the

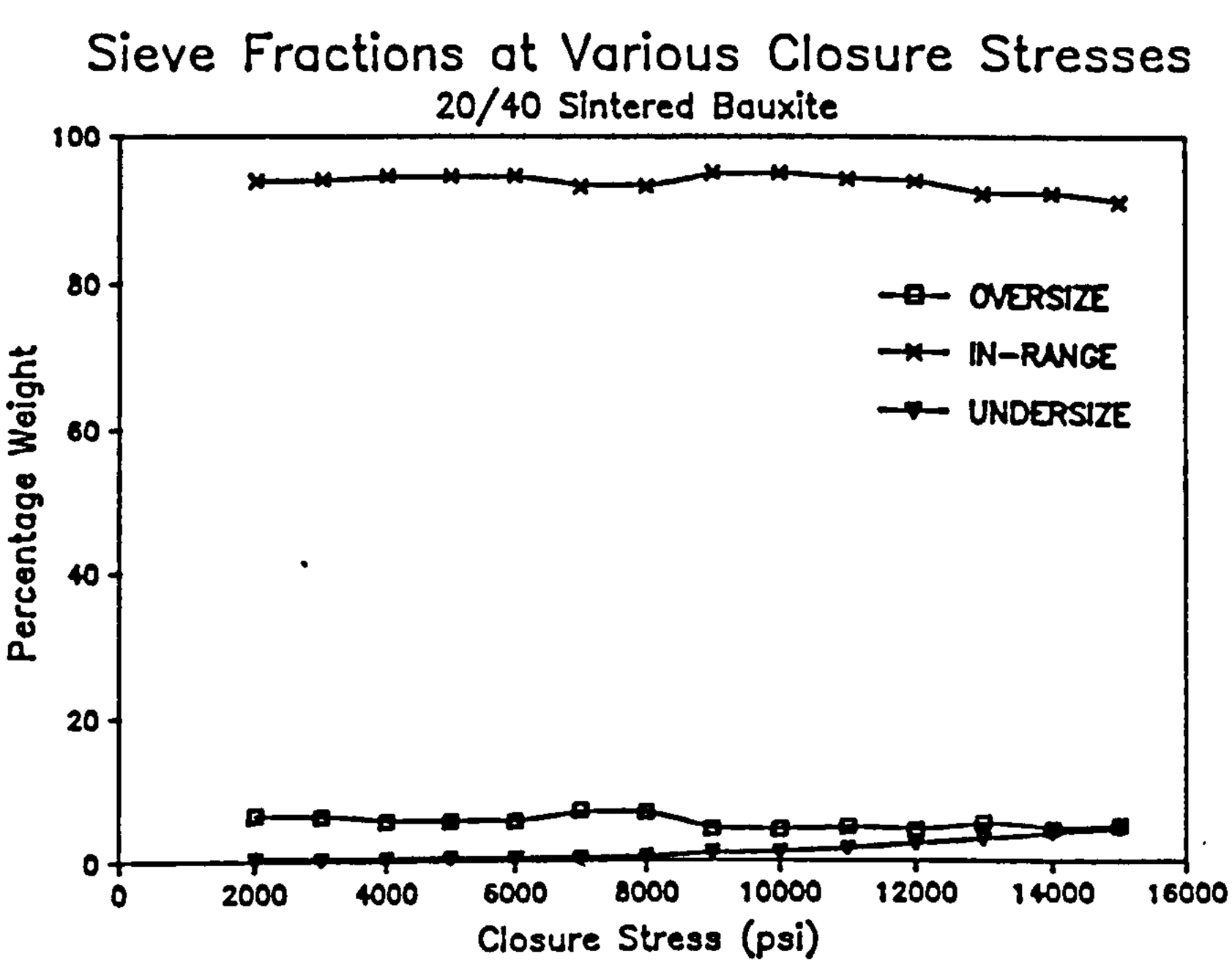

Figure 5.36 : Extended Dry Crush Test Results for 20/40 Sintered Bauxite

Closure (psi)	Oversize (%)	In-Range (%)	Undersize (%)
2000	6.14	93.67	.19
3000	5.99	93.86	.15
4000	5.38	94.33	.29
5000	5.38	94.30	.32
6000	5.36	94.34	.31
7000	6.83	92.84	.33
8000	6.53	92.95	.52
9000	4.20	94.76	1.05
10000	4.13	94.69	1.18
11000	4.53	93.82	1.64
12000	4.13	93.51	2.36
13000	5.19	91.77	3.04
14000	4.31	91.80	3.89
15000	4.81	90.60	4.59

Table 5.5 : Dry Crush Test Results - 20/40 Sintered Bauxite

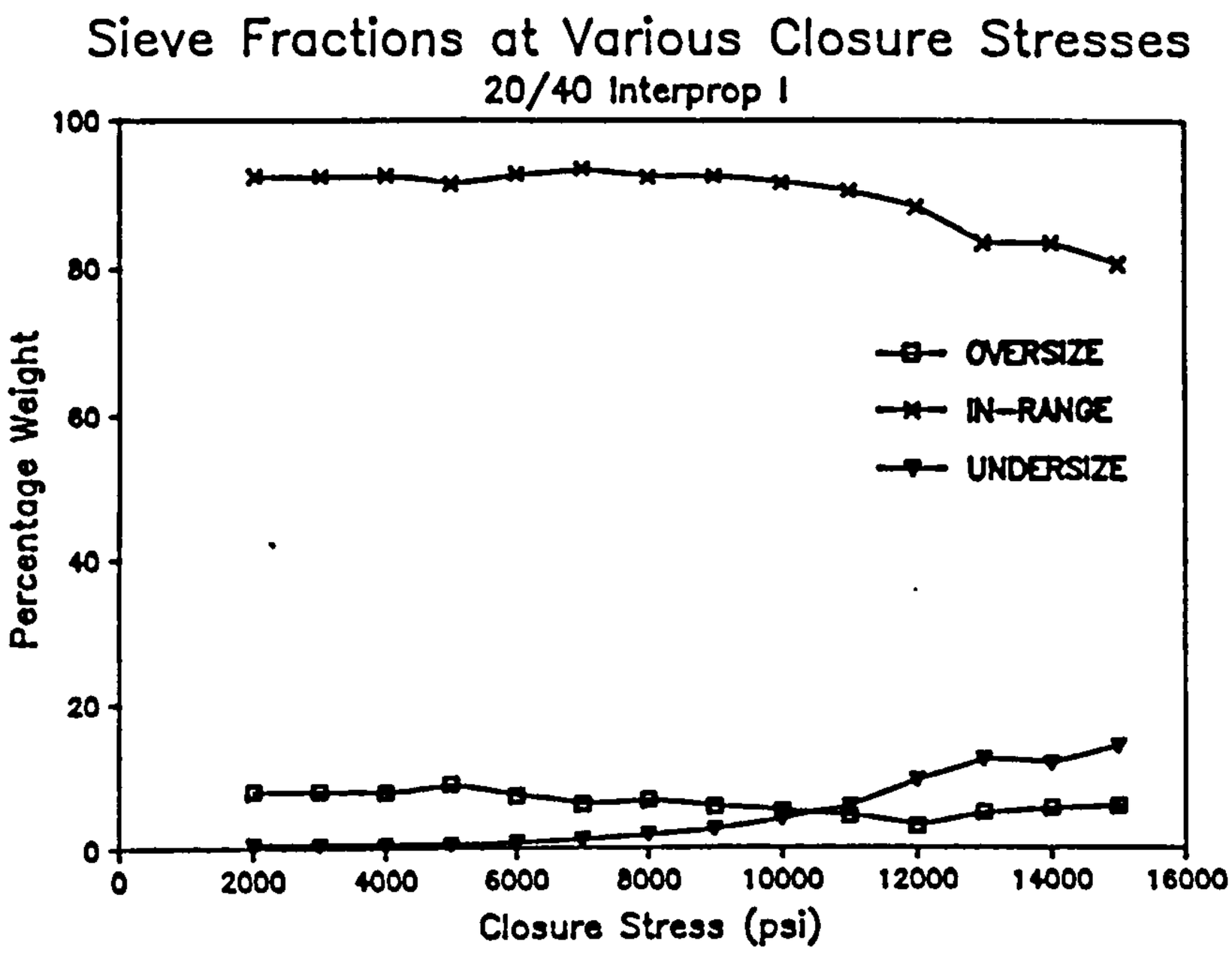

Figure 5.37 : Extended Dry Crush Test Results for 20/40 Interprop

Closure (psi)	Oversize (%)	In-Range (%)	Undersize (%)
2000	7.59	92.07	.34
3000	7.62	92.03	.35
4000	7.49	92.14	.37
5000	8.60	91.01	.38
6000	6.98	92.35	.67
7000	5.83	93.09	1.08
8000	6.39	91.89	1.72
9000	5.47	92.05	2.49
10000	4.92	91.12	3.96
11000	4.26	90.00	5.74
12000	2.82	87.80	9.36
13000	4.78	82.94	12.28
14000	5.43	82.89	11.67
15000	5.71	80.11	14.11

Table 5.6 : Dry Crush Test Results - 20/40 Interprop

table, the percentage oversize was not found to decrease constantly with increased closure stress as it varied between 8.6% at 5000 psi (34500 kPa) to 2.8% at 12000 psi (82800 kPa). As expected, however, the general trend of the curve was downwards. The percentage of 20/40 Interprop measured to be within the designated range remained at over 90% until a closure stress of 11000 psi (75900 kPa), where it was observed to decrease fairly rapidly to around 80% at the maximum closure stress. The percentage undersize remained at a low level of below 1% up to 6000 psi (41400 kPa). After this region, it was seen to increase gradually until a closure stress of 10000 psi (69000 kPa), where almost 4% of the proppant was measured to be undersize. The cross-over point between the percentage undersize and oversize curves occurred between closures of 10000 and 11000 psi (69000 and 75900 kPa). At this point, the percentage of proppant particles within the designated 20/40 range was observed to decrease rapidly, as stated above. This closure stress region indicated the onset of undesirable crushing for this type of proppant. At the maximum stress of 15000 psi (103500 kPa), the percentage undersize was measured to be 14.11%.

5.10.4.3 <u>20/40 Sand</u>

The results of the crush analysis on 20/40 sand are summarised in Figure 5.38 and in Table 5.7. It can be seen that the percentage oversize varied between 5% and 7% until closure stresses of 8000 psi (55200 kPa) and above were reached where the percentage oversize decreased under 4% a closure of 1000 psi (6900 kPa). Examination of the percentage of particles within the 20/40 designated range

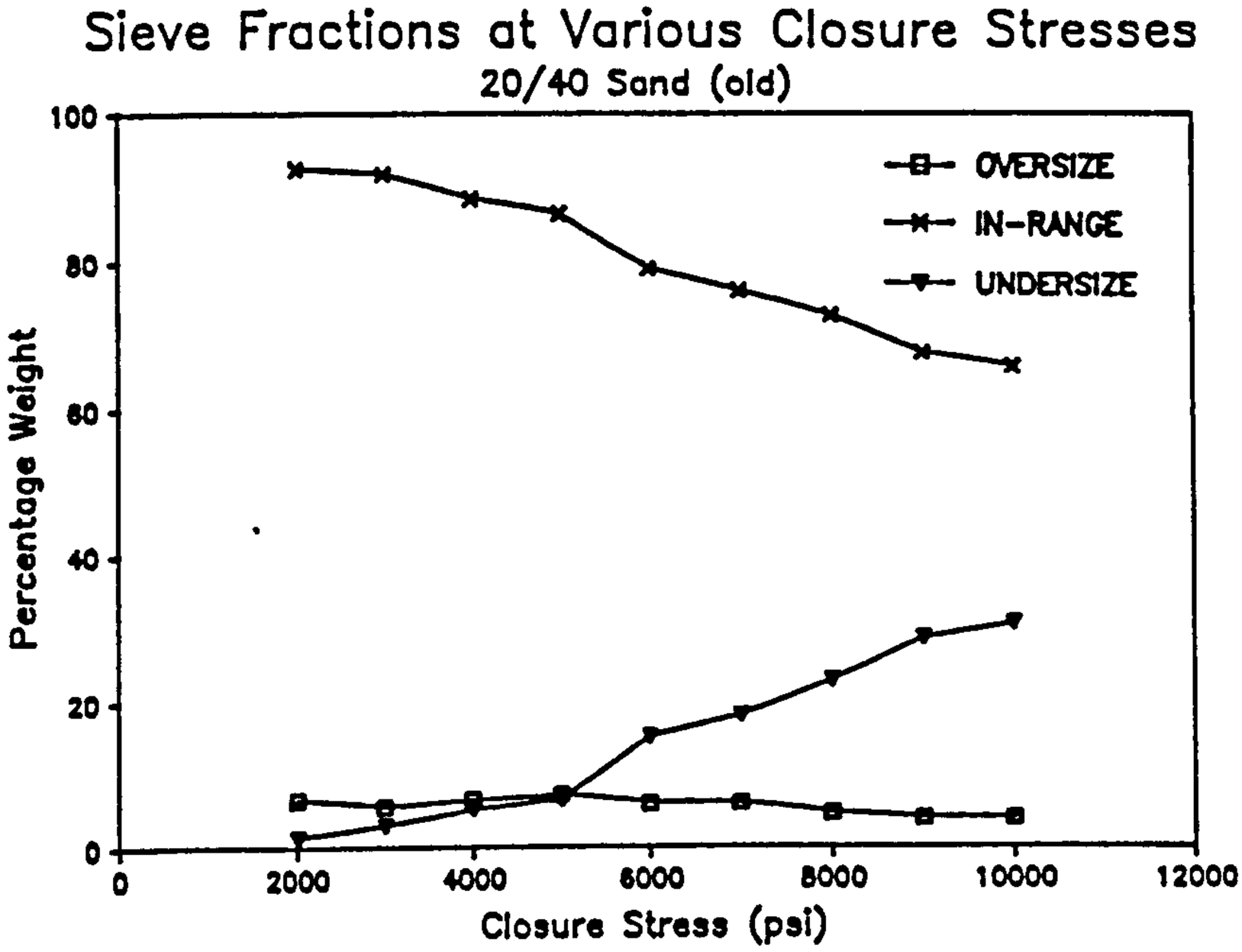

Figure 5.38 : Extended Dry Crush Test Results for 20/40 Sand

Closure (psi)	Oversize (%)	In-Range (%)	Undersize (%)
2000	6.38	92.34	1.28
3000	5.41	91.56	3.03
4000	6.45	88.35	5.20
5000	7.15	86.33	6.53
6000	5.86	78.85	15.28
7000	5.94	75.87	18.19
8000	4.51	72.52	22.97
9000	3.87	67.44	28.69
10000	3.86	65.52	30.62

Table 5.7 : Dry Crush Test Results - 20/40 Sand

yielded a relatively constant value up to 90%. After this region, the amount of proppant particles lying within the specified range were found to decrease at a constant level until a closure stress of 6000 psi (41400 kPa) where a marked reduction was observed. This downward trend continued until the maximum closure of 10000 psi (69000 kPa) where only 65% of the proppant was found to lie within the specified 20/40 range. At stresses below 3000 psi (20700 kPa) the production of fines of up to 3% was not considered to be a problem. Increasing the closure stress to 5000 psi (34500 kPa) more than doubled the amount of fines produced. At closure stresses of 6000 psi (41400 kPa) and above, fines production was found to be considerable and reached a maximum value of 30% at the maximum closure stress.

5.10.5 Comparison of Crush Test and Linear Flow Cell data

Recalling the linear flow cell results presented in the previous section, the average permeability of 20/40 Sintered Bauxite decreased to a value of 45% of its initial level as a result of applying 15000 psi (103500 kPa) closure stress. The dry crush tests indicated that 4.6% of the proppant was undersize at this maximum closure stress. Interprop, which had a higher permeability than Sintered Bauxite at low levels of closure stress, but a lower permeability at high stress, suffered a permeability reduction of around 75%. The percentage fines measured for Interprop at the maximum closure stress was 14.1%. It was therefore apparent that the reduction in permeability of Interprop with respect to Sintered Bauxite was attributed to the high amount of fines produced. The

variation in permeability and wetted surface area for the Interprop was also greater than for Sintered Bauxite, thus indicating that fines migration was more severe with Interprop. There did not appear to be a direct relationship between the onset of excessive proppant crushing and a marked reduction in permeability for the Interprop as the permeability reduced at a fairly constant rate. This was also true for Sintered Bauxite although crushing occurred to a much lesser degree. Accordingly, it may be possible that the degree of crushing which would have an adverse effect on permeability had not occurred and that crushing in excess of 14% would be required before a marked reduction in permeability would be observed.

A good correlation was found between the crush test data and the permeability data for the frac sand. At closure stresses of 5000 psi (34500 kPa) and above, the percentage fines produced increased steeply, while at similar values of closure stress, the permeability measured in the linear flow cell was found to decrease sharply. Proppant wetted surface area also increased dramatically at these closure stress levels, thus indicating a greater concentration of fines. The measured variation between the upstream and downstream permeability values was greater with the frac sand than for the other proppants tested. This was especially true at high levels of closure stress where about 30% of the proppant was measured to be undersize. This confirmed that fines migration was more of a problem with the frac sand.

5.10.6 Conclusions

In general, the crush tests conducted on 20/40 Sintered Bauxite confirmed its superiority in crush resistance when compared to the other proppants investigated.

It can be concluded that the extended dry proppant crush tests provide valuable information about the behaviour of the various proppants under stress as the test gives an indication of the closure stress that a proppant can withstand.

As the tests were performed at intervals of 1000 psi (6900 kPa) up to a maximum of 15000 psi (103500 kPa) closure stress at a rate of 1000 psi/minute, the time involved in providing the test data was considerable. Such an extended approach to proppant crush analysis may therefore be prohibitive if a large number of proppants are to be tested. However, testing such proppants at only one or two levels of closure stress would not provide comprehensive information.

A good correlation between the linear flow cell tests and dry crush resistance was found for 20/40 sand, while a less convincing relationship was found for 20/40 Sintered Bauxite and 20/40 Interprop. As stated, the most likely reason for this was that the the intermeadiate- and high-strength proppants did not crush to the extent of the frac sand.

5.11 APPLICATION OF DATA-BASE TO FORMATION SAMPLES

5.11.1 Introduction

This section details the application of the data-base of wetted surface areas to formation samples to arrive at an in-situ value for fracture conductivity and permeability which allows for proppant embedment. Knowing the fracture porosity as determined by the fracture porosimeter, the width of the fracture and the appropriate wetted surface area from the data-base, the in-situ fracture conductivity may be determined from the Kozeny-Carmen equation.

As stated previously, the fracture porosimeter is simply a triaxial cell which is used to measure the change in porosity of a bed of proppant sandwiched between two pieces of rock as a result of applying closure stress. When using a triaxial cell as a fracture porosimeter, the vertical in-situ stress is applied as the confining stress and the closure stress is applied to the ends of the core, as indicated in Figure 5.39.

It was initially proposed to refine Wendorff's technique by monitoring changes in specimen volume within the fracture porosimeter, thus allowing for proppant compaction in a lateral direction as well as in the axial direction measured by Wendorff. However, due to leaking seals in the servo-controlled pressure intensifier, it was not possible to obtain accurate readings and accordingly, compaction was measured only in the axial direction.

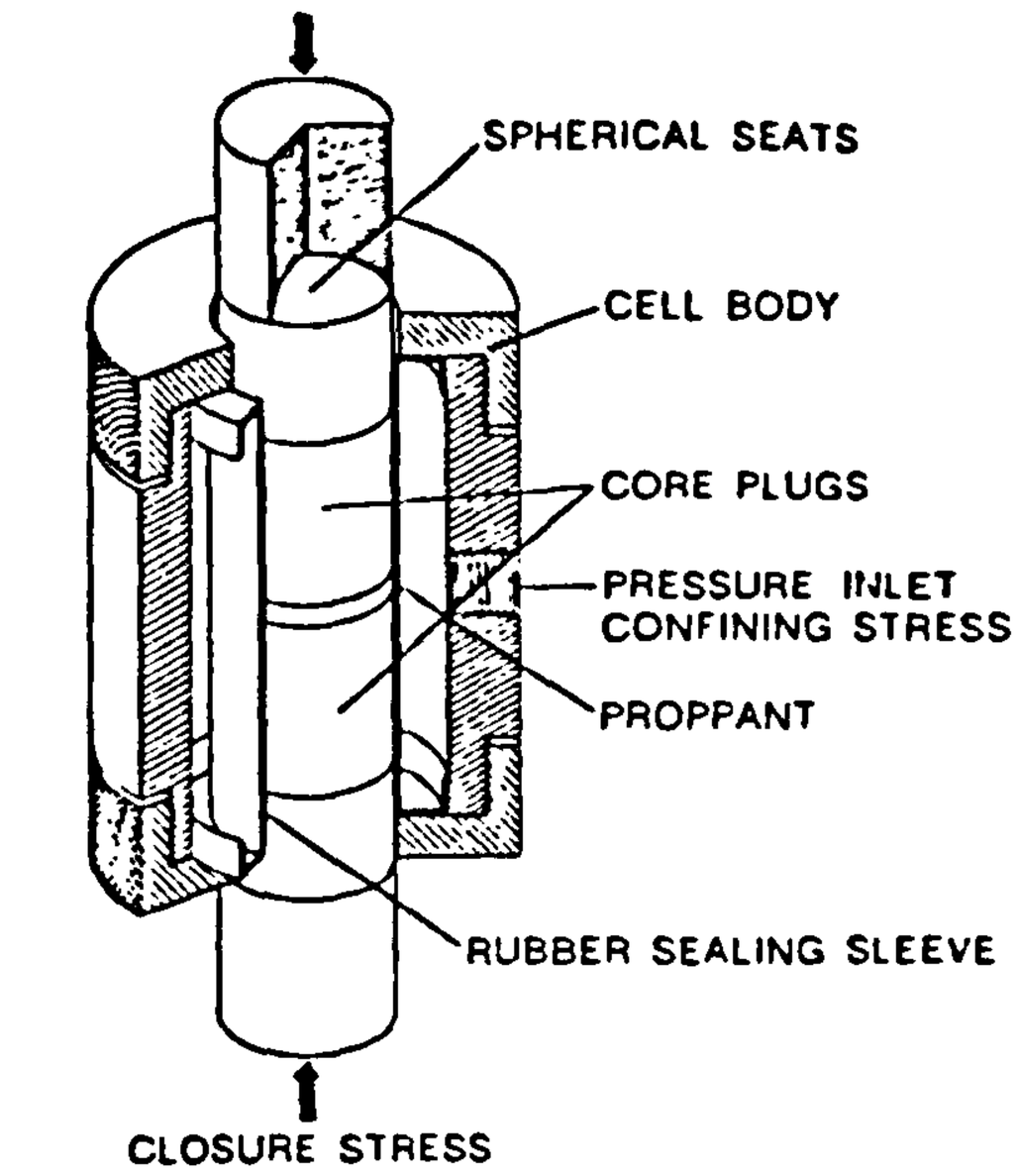

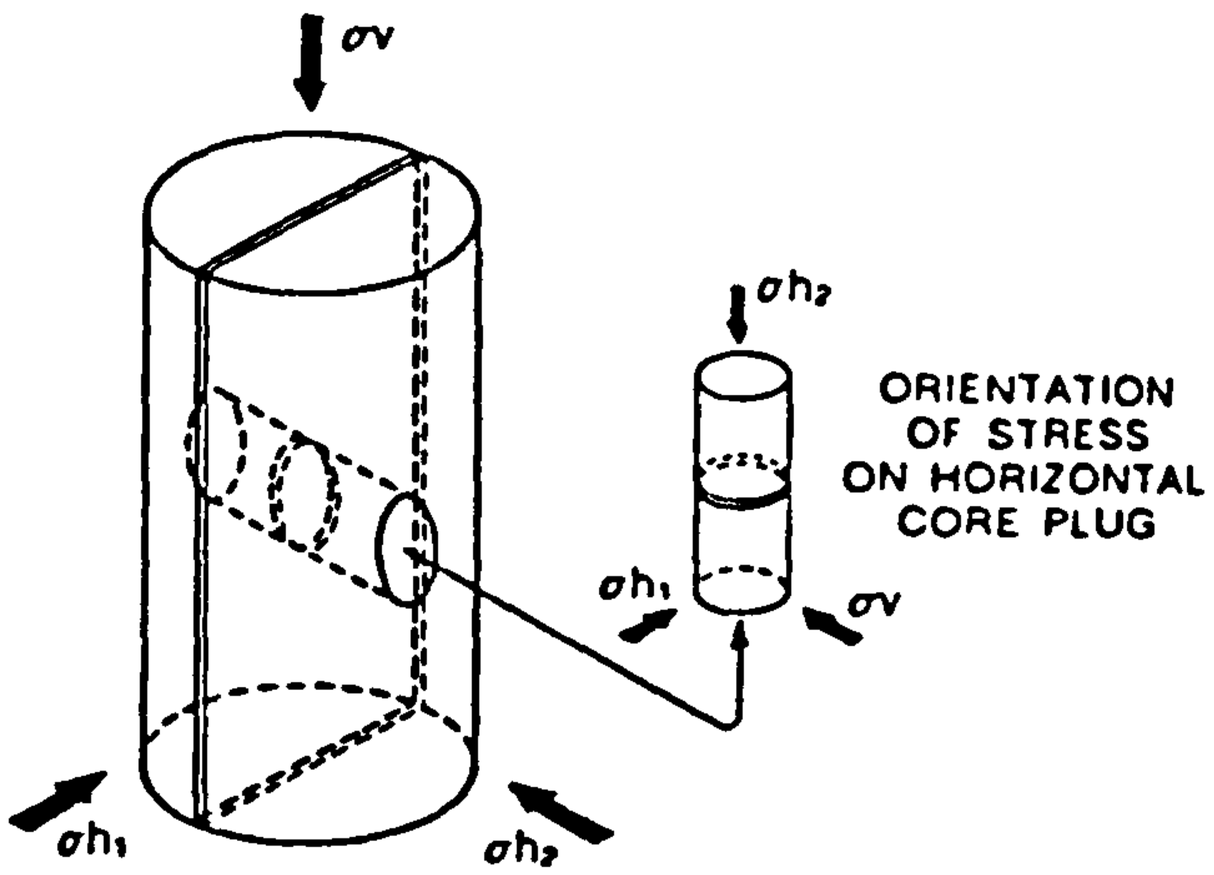

Figure 5.39 : The Fracture Porosimeter (Hoek Triaxial Cell) (after Wendorff [115])

5.11.2 Sample Preparation

Formation core samples from four offshore wells in the Beatrice field (Block 11/30a) were available for testing. The core halves should ideally come from the the same plug to avoid surface and modulus irregularities between samples. The 4 inch diameter reservoir core which was provided for testing, however, had been cut along its axis and core plugs had been taken by service companies. Accordingly, it was not always possible to obtain a core plug of sufficient length. As a result of this, it was sometimes necessary to 'match' core plugs taken from the same sample depth. In all tests conducted, one inch diameter plugs were used. When a core plug of sufficient length was obtained, prior to cutting the simulated fracture, the sample was marked along its axis with a vertical line to enable re-alignment. The cut face of the plugs were checked to ensure they were parallel to each other and perpendicular to the core axis. Due to the poor quality of some of the cores provided, however, it was not always possible to strictly adhere to the recommendations of the ISRM (Table 3.5, Section 3.3.2).

For each of the four wells from which formation samples were available, three core plugs were taken from four different depths. Thus a total of 48 core plugs were obtained and accordingly, 96 core halves were prepared. The core halves were marked to ensure that they could be matched with their respective partners and to allow identification.

5.11.3 Procedure for Measuring Formation Fracture Porosity

The test consisted of two parts, each using the same formation sample.

(1) The two core halves were aligned and placed end to end in the fracture porosimeter. After the insertion of the plattens, a low confining pressure was applied to hold the cores and plattens in place. The fracture porosimeter was then placed in a compression machine and an initial axial (closure) stress of 1000 psi (6900 kPa) applied in conjunction with the equivalent in confining pressure. The length of the plattens and core halves were then determined by averaging a set of three measurements taken with a digital micrometer. The change in fracture width was obtained by averaging the output from three LVDT position sensors.

The closure stress was then increased to 2000 psi (13800 kPa) at a rate of 1000 psi/minute, again increasing the confining pressure by a similar amount. The average LVDT reading was then recorded, thus allowing the change in sample length to be determined.

The closure stress and confining pressure were then increased in 2000 psi (13800 kPa) increments at the same rate as before and the average LVDT reading recorded. This procedure was repeated up to a maximum of 15000 psi (103500

kPa) for the high and intermediate strength proppants and 10000 psi (69000 kPa) for frac sand. Due to the limitations of the triaxial cell, which was rated to 10000 psi (69000 kPa), the maximum confining pressure was limited to this value.

After the closure stress and confining pressure were reduced to zero, the core halves were removed and inspected for damage. A plastic sleeve, comprising of a layer of paper sandwiched between two strips of tape, was wrapped round the core halves. The upper core was then removed and a prescribed weight of proppant was poured into the sleeve and levelled. The upper upper core was then replaced, taking care to align the faces correctly.

(2) The complete unit was then replaced in the fracture porosimeter and the above procedure and measurements were repeated. The fracture widths at various closure stresses were then calculated by subtracting the respective length of the plattens and core halves from the total length of plattens, core halves and proppant bed at the desired closure stress.

5.11.4 Data Analysis and Presentation of Results

5.11.4.1 Sample Description and Fracture Porosimeter Results

As in the case of the linear flow cell, the fracture porosimeter results were calculated using a spreadsheet program. The fracture

width at each closure stress level was obtained from equation (5.15), this allowed the calculation of propped fracture porosity by means of equation (5.11).

The results were displayed in a two-page format, as presented in Figures 5.40(a) and 5.40(b).

The first page featured a general description of the formation sample and detailed properties such as rock type, colour, texture and sorting. A small sub-section giving details of sample density, embedment pressure and Brinell hardness was also included on this page. The second page detailed the proppant porosity and fracture width as a function of closure stress in tabular form. A brief sub-section indicating proppant properties such as roundness, sphericity and grain density was included, as was the weight of proppant tested and the percentage recovery of proppant and crushed rock. A recovery in excess of 100% indicated that damage had been caused to the core faces. For ease of comparison, the spreadsheet has been designed to produce an output of the above parameters of three different proppants on a single page.

The sample description and formation sample results for each of the 16 formation samples (four from each well), were given the extension '.POR' to allow identification in the data-base of spreadsheet files. The 16 formation sample data were stored in files SAMPLE1.POR to SAMPLE16.POR respectively.

FORMATION SAMPLE DATA

Well Number : 11/30-2
Core Number : 10
Sample Depth : 6952 ft
Box Number : 129
Reference Number : 1 A,B,C

SAMPLE DESCRIPTION

Rock Type : SANDSTONE

Colour : Medium brown, light brown banding and stringers.

Texture : Upper fine grain size (0.2 mm dia.)
Sphericity : 0.7
Roundness : 0.7

Sorting : Very well sorted

Cement : Silica

Matrix : Clay

GENERAL DESCRIPTION

Upper fine grained sandstone, medium brown in colour with light brown banding and occasional stringers of clay material. The grains have moderate sphericity, are rounded and are very well sorted.

ROCK PROPERTIES

Sample Density : 2237.54 Kg/m^3 (139.66 lb/ft^3)

Embedment Pressure : ****

Brinell Hardness : 25.5

(3.19 mm Indenter)

Units :

Load (kg)
Indentation (mm)
BHN (Kg/mm^2)

Load	Indentation	BHN
0	.0000	**
5	.0197	25
10	.0400	25
15	.0583	26
20	.0773	26
25	.0973	26
30	.1173	26

Figure 5.40(a) : Fracture Porosimeter Data Sheet #1
Detailing Formation Sample Description

FRACTURE POROSIMETER RESULTS

Well Number : 11/30-2
Depth : 6952 ft

PROPPANT DATA : Ref. 1A

Type/Size : 20/40 Sintered Bauxite
Supplier : Norton

Gr. Density : 3.64 g/cc
Roundness : 0.80
Sphericity : 0.78

Sample Wt. : 5.0004 g
Recovery : 100.194 %

Closure Stress	Fracture Width	Proppant Porosity
1000	.1634	33.13
2000	.1620	32.58
4000	.1615	32.37
6000	.1614	32.29
8000	.1607	32.01
10000	.1605	31.94
12000	.1597	31.58
14000	.1585	31.07
15000	.1582	30.93

PROPPANT DATA : Ref. 1B

Type/size : 20/40 Sand
Supplier : Colorado Silica Sand Inc.

Gr. Density : 2.64 g/cc
Roundness : 0.70
Sphericity : 0.69

Sample Wt. : 5.0009 g
Recovery : 100 %

Closure Stress	Fracture Width	Proppant Porosity
1000	.2157	30.17
2000	.2147	29.84
4000	.2139	29.57
6000	.2127	29.18
8000	.2094	28.04
10000	.2058	26.80
12000	*****	*****
14000	*****	*****
15000	*****	*****

PROPPANT DATA : Ref. 1C

Type/size : 20/40 Interprop I
Supplier : Norton

Gr. Density : 3.12 g/cc
Roundness : 0.81
Sphericity : 0.82

Sample Wt. : 5.0002 g
Recovery : 100.090 %

Closure Stress	Fracture Width	Proppant Porosity
1000	.1776	28.22
2000	.1765	27.81
4000	.1765	27.81
6000	.1755	27.39
8000	.1747	27.04
10000	.1740	26.76
12000	.1730	26.33
14000	.1717	25.75
15000	.1708	25.39

TEST UNITS :
Closure Stress (psi)
Fracture Width (in)
Propped Fracture Porosity (%)

Figure 5.40(b) : Fracture Porosimeter Data Sheet #2 Detailing Proppant Porosity Results

5.11.4.2 Assessment of Embedment using the Fracture Porosimeter

The fracture width and porosity results determined from the fracture porosimeter were then inserted into the Kozeny-Carmen relationship, equation (5.8) in conjunction with the wetted surface area results obtained from the linear flow tests. This provided a fracture conductivity value for each of the three pressure port combinations which considered both proppant crushing and embedment. The fracture permeability was also calculated from equation (5.22). In the following discussion, 'fracture conductivity/permeability' refers to the value calculated as above, while 'flow cell conductivity/ permeability' refers to the value calculated from the linear flow cell results. Figure 5.40(c) shows a sample data sheet. The sheet gives details of the data-base reference to allow the various files to be cross-checked. To allow a comparison between the 'flow cell' and 'fracture' conductivity/permeability results, both sets of results have been reproduced. These data sheets and spreadsheet files were given the extension '.APP' to allow identification. More details may be found in Appendix 2.

5.11.5 Experimental results

The experimental results for the above tests may be found in Appendix 2. In the following analysis, the fracture conductivity results calculated over ports A-C for each formation sample have been averaged to arrive at a typical value for fracture conductivity. They are presented in tabular form in conjunction with the flow cell conductivity values (over ports A-C). The average

FRACTURE CONDUCTIVITY / PERMEABILITY RESULTS Ref : INTER-1.APP

FORMATION / PROPPANT DATA — DATA BASE REFERENCE

Proppant Type	:	20/40 Interprop I	INTER-A.FLO
Supplier	:	Norton	
Concentration	:	2 lbs/sq.ft.	
Well Number	:	11/30-2	SAMPLE1.POR
Depth	:	6952 ft	

FRACTURE CONDUCTIVITY RESULTS

Closure Stress (psi)	Flow Cell Conductivity A-B	B-C	A-C	Fracture Conductivity A-B	B-C	A-C
1000	6.534	6.371	6.468	1.506	1.468	1.491
2000	5.714	5.264	5.579	1.146	1.056	1.119
4000	5.106	4.685	4.882	1.150	1.055	1.099
6000	4.555	3.908	4.212	1.105	.948	1.021
8000	3.991	3.275	3.628	1.068	.876	.971
10000	3.073	2.438	2.720	.955	.757	.845
12000	2.629	2.034	2.207	.888	.687	.746
14000	1.969	1.486	1.689	.697	.526	.598
15000	1.659	1.182	1.391	.635	.452	.533

FRACTURE PERMEABILITY RESULTS

Closure Stress (psi)	Flow Cell Permeability A-B	B-C	A-C	Fracture Permeability A-B	B-C	A-C
1000	385.6	375.9	381.7	101.8	99.2	100.7
2000	337.4	310.8	329.4	77.9	71.8	76.1
4000	302.8	277.8	289.5	78.2	71.7	74.7
6000	275.0	235.9	254.2	75.5	64.8	69.8
8000	245.5	201.4	223.2	73.3	60.2	66.7
10000	193.4	153.4	171.2	65.8	52.2	58.3
12000	168.4	130.3	141.4	61.6	47.7	51.7
14000	128.0	96.6	109.8	48.7	36.8	41.8
15000	109.5	78.0	91.8	44.6	31.8	37.4

UNITS : Flow Cell / Fracture Conductivity (Darcy*ft)
===== Flow Cell / Fracture Permeability (Darcies)

Figure 5.40(c) : Combination of Fracture Porosimeter Data with Linear Flow Cell Data to arrive at an 'in-situ' value for Fracture Conductivity & Permeability

fracture conductivities for the various proppants were also plotted against closure stress.

5.11.5.1 Well 11/30-2

Table 5.8 shows the fracture conductivity results obtained from the four formation samples tested with each proppant type. The average fracture conductivities were plotted against closure stress and are shown in Figure 5.41.

From an examination of this figure, it was evident that 20/40 Interprop provided the the highest fracture conductivity up to closure stresses of 13000 psi (89700 kPa), thereafter the fracture conductivity of 20/40 Bauxite was superior. In all cases, the fracture conductivity was less than the measured flow cell conductivity, thus indicating that a degree of proppant embedment had occurred. This difference was greatest at low values of closure stress. With 20/40 Bauxite at 1000 psi (6900 kPa) closure stress, the conductivity was reduced by 52% as a result of considering proppant embedment, while at 15000 psi (103500 kPa), the conductivity was reduced by only 35%. With 20/40 Interprop, the conductivities at 1000 psi (6900 kPa) and 15000 psi (103500 kPa) were reduced by over 62% and 26% respectively. The reduction between the measured flow cell conductivity and the calculated fracture conductivity for sand was around 59% at 1000 psi (6900 kPa), while at 10000 psi (69000 kPa), this difference had reduced to 15%.

As detailed in Table 5.8, formation sample #3 provided the highest

	Closure Stress	Flow Cell	Sample #1	Sample #2	Sample #3	Sample #4	Average
SINTERED BAUXITE	1000	4.50	1.87	2.12	2.70	1.91	2.15
	2000	3.84	1.61	1.86	2.40	1.65	1.88
	4000	3.35	1.52	1.69	2.17	1.37	1.69
	6000	3.03	1.46	1.58	2.02	1.23	1.57
	8000	2.67	1.36	1.48	1.87	1.18	1.47
	10000	2.34	1.44	1.53	****	1.22	1.40
	12000	2.04	1.37	1.47	****	1.18	1.34
	14000	1.92	1.21	1.33	****	1.05	1.20
	15000	1.86	1.23	1.35	****	1.04	1.21
INTERPROP	1000	6.47	1.49	2.86	3.20	2.52	2.52
	2000	5.58	1.12	2.42	2.81	2.08	2.11
	4000	4.88	1.10	2.14	2.37	1.79	1.85
	6000	4.21	1.02	2.05	2.31	1.72	1.78
	8000	3.63	.97	2.00	2.26	1.66	1.72
	10000	2.72	.85	1.74	1.99	1.44	1.51
	12000	2.21	.75	1.56	1.82	****	1.37
	14000	1.69	.60	1.28	1.52	****	1.13
	15000	1.39	.53	1.15	1.37	****	1.02
SAND	1000	2.55	.79	1.22	1.72	.45	1.05
	2000	1.97	.63	.98	1.39	.37	.84
	4000	1.61	.59	.90	1.30	.35	.79
	6000	.85	.39	.58	.85	.24	.52
	8000	.37	.20	.30	.46	.13	.27
	10000	.20	.12	.18	.29	.08	.17

Units : Closure Stress (psi)
Frac Conductivity (D.ft)

Sample Depths
Well 11/30-2

Sample #1 : 6952 ft
Sample #2 : 6977 ft
Sample #3 : 6986 ft
Sample #4 : 7010 ft

***Table5.8** : Fracture Conductivity Results - Well 11/30-2*

Fracture Conductivity : Well 11/30-2

Average Results between 6952ft and 7010ft

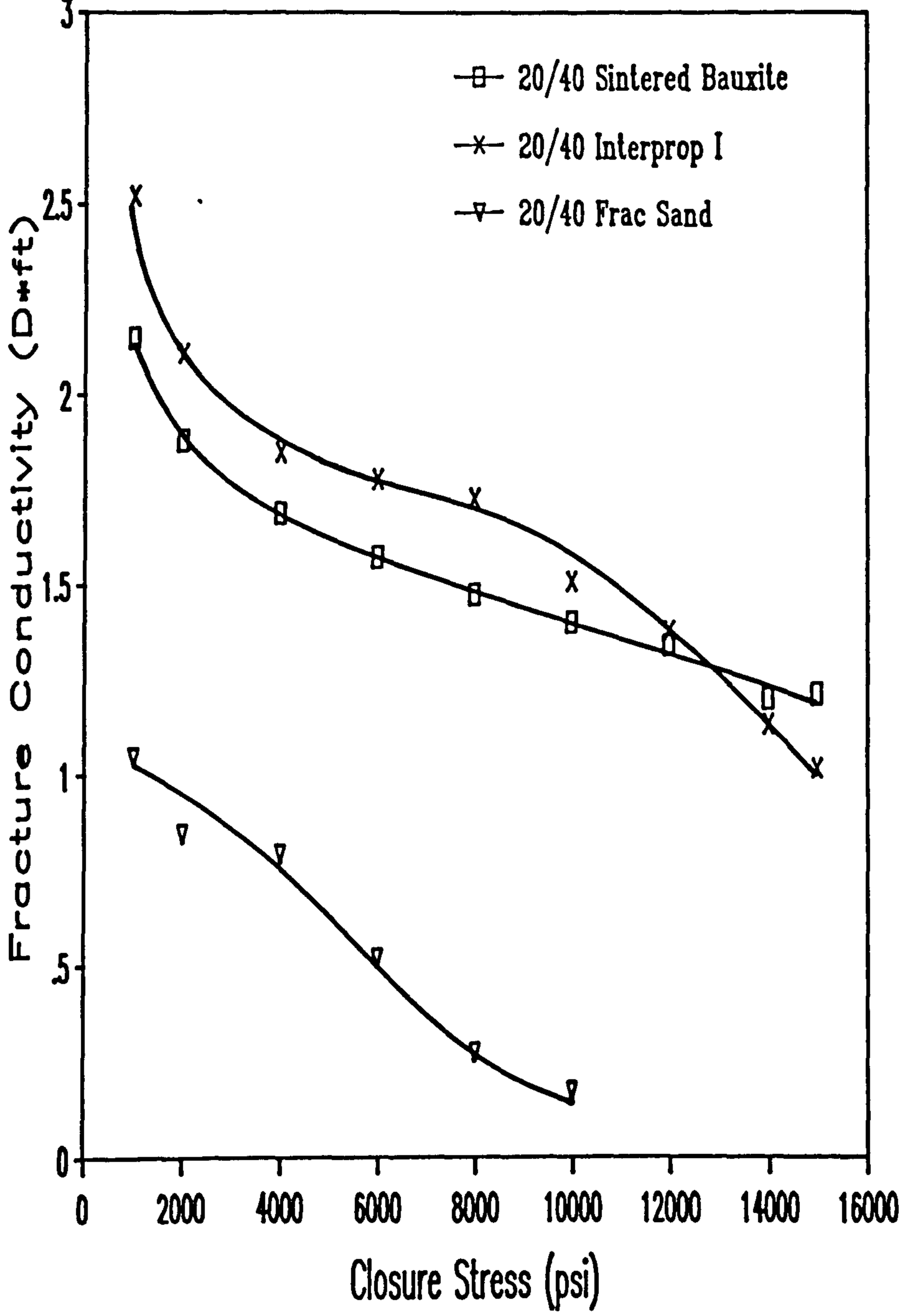

Figure 5.41 : Fracture Conductivity Results - Well 11/30-2

overall fracture conductivity for each of the three proppants tested. This formation sample had a relatively high Brinell hardness which was similar to that of sample #2. Formation samples #1 and #4 were found to have a lower Brinell hardness and accordingly their fracture conductivities were lower than that of the harder formation samples. This indicated that proppant embedment was less severe with samples displaying a higher Brinell hardness.

5.11.5.2 Well 11/30-5

The flow cell and fracture conductivity results for well 11/30-5 are given in Table 5.9, while the average fracture conductivity values for each proppant were plotted against closure stress and are shown in Figure 5.42.

Referring to this figure, it can be seen that 20/40 Sintered Bauxite provided the highest fracture conductivity over the range of closure stress. The fracture conductivities calculated from each sample were lower than the conductivity measured in the linear flow cell, thus indicating proppant embedment had occurred. At closure stresses of 1000 psi and 15000 psi (6900 kPa and 103500 kPa), the flow cell conductivity values of Sintered Bauxite were reduced by 42% and 6% respectively as a result of considering proppant embedment. At the same values of closure stress, the flow cell conductivity values of Interprop were reduced by around 60% and 33% respectively. The flow cell conductivities of frac sand at 1000 psi and 10000 psi (6900 and 69000 kPa) were found to have decreased by 62% and 30% respectively.

	Closure Stress	Flow Cell	Sample #5	Sample #6	Sample #7	Sample #8	Average
SINTERED BAUXITE	1000	4.50	3.56	3.08	1.67	2.16	2.62
	2000	3.84	3.15	2.81	1.48	1.99	2.36
	4000	3.35	2.94	2.64	1.34	1.73	2.16
	6000	3.03	2.76	2.53	1.27	1.58	2.04
	8000	2.67	2.58	2.39	1.19	1.44	1.90
	10000	2.34	2.71	2.53	1.24	1.48	1.99
	12000	2.04	2.31	2.45	1.75	1.37	1.97
	14000	1.92	2.37	2.30	1.07	1.22	1.74
	15000	1.86	2.40	2.34	1.07	1.20	1.75
INTERPROP	1000	6.47	2.81	3.50	2.26	1.75	2.58
	2000	5.58	2.43	3.05	1.87	1.63	2.25
	4000	4.88	2.17	2.74	1.62	1.24	1.94
	6000	4.21	2.09	2.70	1.56	1.15	1.87
	8000	3.63	2.03	2.66	1.49	1.09	1.82
	10000	2.72	1.80	2.38	1.28	.94	1.60
	12000	2.21	1.64	2.21	1.14	.83	1.45
	14000	1.69	1.32	1.82	.91	.65	1.18
	15000	1.39	1.19	1.65	.80	.57	1.05
SAND	1000	2.55	1.30	1.11	.88	.54	.96
	2000	1.97	1.05	.91	.72	.42	.78
	4000	1.61	1.00	.83	.65	.38	.72
	6000	.85	.64	.53	.40	.24	.45
	8000	.37	.31	.27	.20	.12	.23
	10000	.20	.19	.17	.12	.07	.14

Units : Closure Stress (psi)
Frac Conductivity (D.ft)

Sample Depths
Well 11/30-5

Sample #5 : 7270 ft
Sample #6 : 7275 ft
Sample #7 : 7308 ft
Sample #8 : 7318 ft

Table5.9 : Fracture Conductivity Results - Well 11/30-5

Fracture Conductivity : Well 11/30-5

Average Results between 7270ft and 7318ft

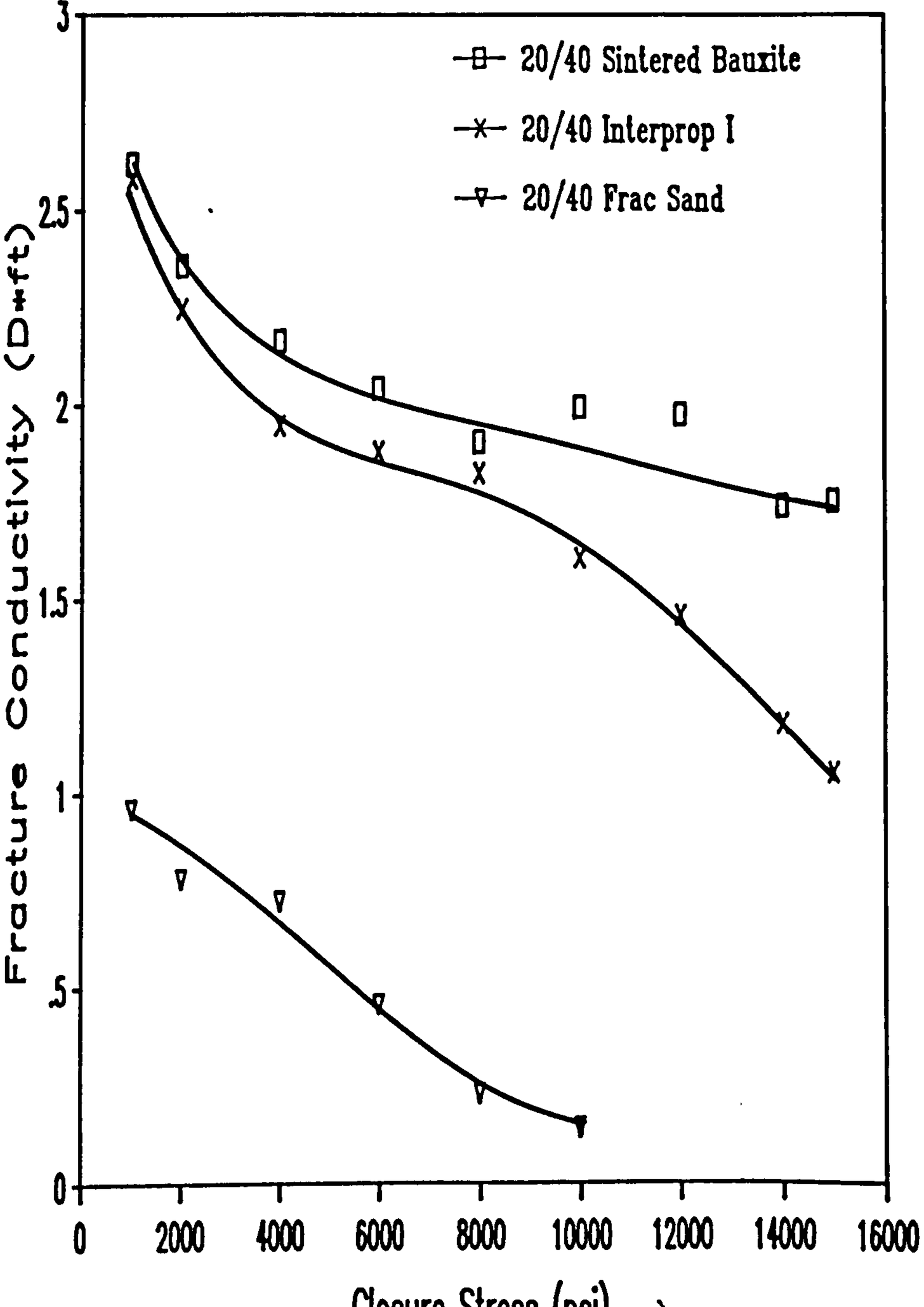

Figure 5.42 : Fracture Conductivity Results - Well 11/30-5

As shown in Table 5.9, formation samples #5 and #6 were found to yield the higher conductivity. These samples had a high Brinell hardness (42 and 47 kg/mm² respectively). Again this indicated that samples with the higher Brinell hardness were less susceptible to proppant embedment.

5.11.5.3 Well 11/30a-A4

The average fracture conductivity results for well 11/30a-A4 are presented in Figure 5.43 and in Table 5.10. The general trend of conductivity results for well 11/30a-A4 were similar to that of 11/30-2, with the exception that the calculated fracture conductivity values were marginally higher. In this well, no apparent relationship between Brinell hardness and conductivity reduction was evident.

As evident from the table, the flow cell conductivity values measured for 20/40 Sintered Bauxite at closure stresses of 1000 psi (6900 kPa) and 15000 psi (103500 kPa) were reduced by 45% and 24% respectively as a result of considering proppant embedment. For the same extremes of closure stress, the flow cell conductivity values of 20/40 Interprop reduced by 53% and 18% respectively. For the case of the frac sand, the measured flow cell conductivity was found to have been reduced by 60% at 1000 psi (6900 kPa) closure and by 25% at the maximum closure stress of 10000 psi (69000 kPa).

	Closure Stress	Flow Cell	Sample #9	Sample #10	Sample #11	Sample #12	Average
SINTERED BAUXITE	1000	4.50	2.08	2.03	2.65	3.14	2.47
	2000	3.84	1.90	1.80	2.29	2.70	2.17
	4000	3.35	1.80	1.60	2.04	2.38	1.95
	6000	3.03	1.69	1.49	1.84	2.19	1.80
	8000	2.67	1.62	1.37	1.66	1.99	1.66
	10000	2.34	1.71	1.41	1.73	2.05	1.72
	12000	2.04	1.67	1.33	1.58	1.80	1.60
	14000	1.92	1.52	1.19	1.38	1.55	1.41
	15000	1.86	1.55	1.17	1.35	1.52	1.40
INTERPROP	1000	6.47	2.50	4.03	2.86	2.65	3.01
	2000	5.58	2.13	3.65	2.34	2.11	2.56
	4000	4.88	1.83	3.17	1.98	1.01	2.00
	6000	4.21	1.71	3.00	1.87	1.68	2.06
	8000	3.63	1.63	2.92	1.76	1.59	1.97
	10000	2.72	1.39	2.55	1.49	****	1.81
	12000	2.21	1.27	2.32	1.28	****	1.62
	14000	1.69	.99	1.90	1.00	****	1.29
	15000	1.39	.86	1.68	.84	****	1.13
SAND	1000	2.55	.67	1.25	1.07	1.01	1.00
	2000	1.97	.55	1.01	.89	.80	.81
	4000	1.61	.51	.94	.79	.73	.74
	6000	.85	.32	.60	.50	.47	.47
	8000	.37	.17	.30	.26	.25	.24
	10000	.20	.10	.19	.16	.15	.15

Units : Closure Stress (psi)
Frac Conductivity (D.ft)

Sample Depths
Well 11/30-A4

Sample #9 : 6969 ft
Sample #10 : 6984 ft
Sample #11 : 7089 ft
Sample #12 : 7093 ft

Table5.10** : Fracture Conductivity Results - **Well 11/30-A4

Fracture Conductivity : Well 11/30a-A4

Average Results between 6969ft and 7095ft

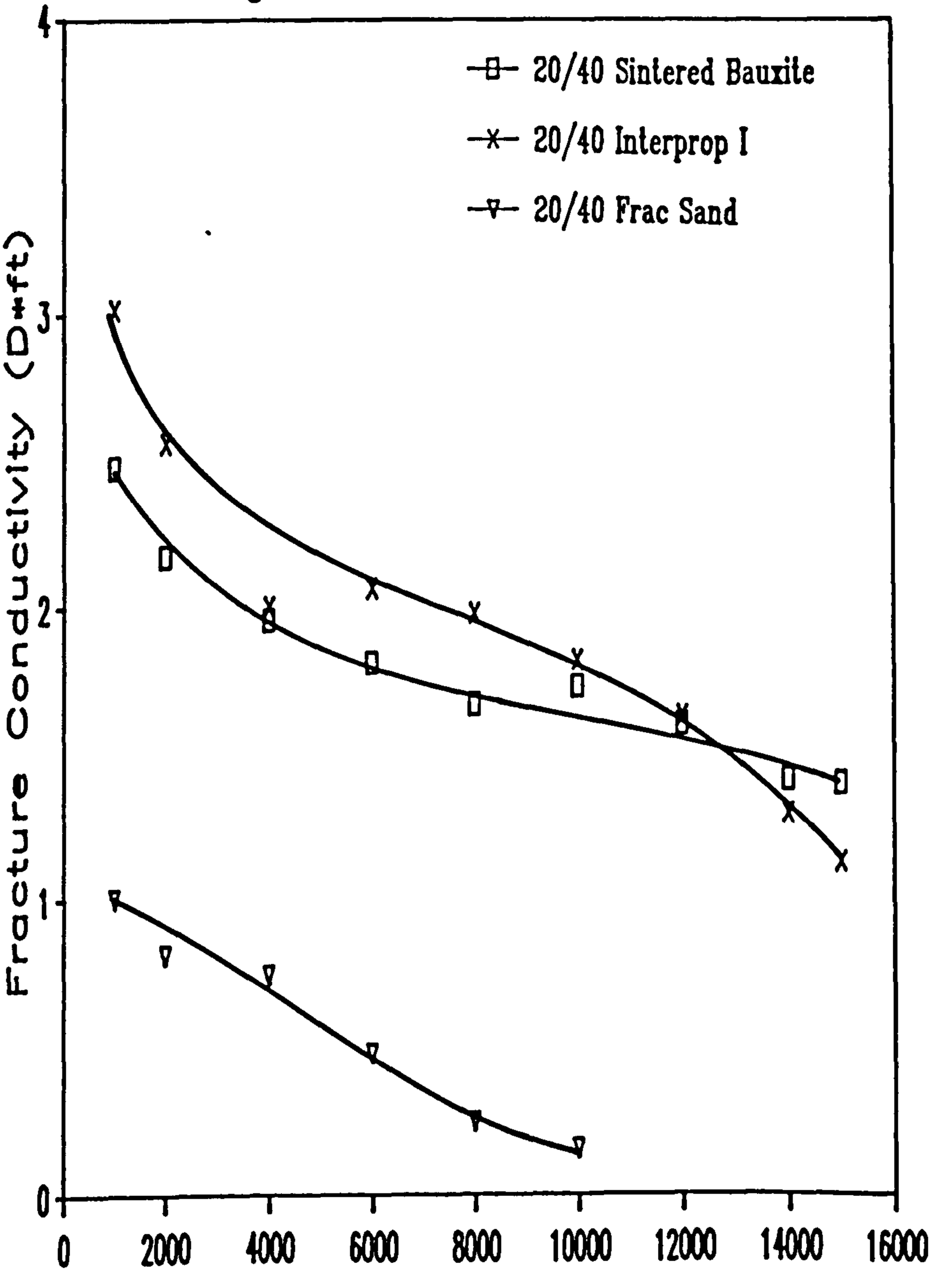

Figure 5.43 : Fracture Conductivity Results - Well 11/30-A4

5.11.5.4 Well 11/30a-A6

The fracture conductivity results for well 11/30a-A6 are given in Table 5.11, while the typical conductivity for each proppant is plotted against closure stress in Figure 5.44. From this figure, it can be seen that 20/40 Interprop curve provided a marginally higher conductivity than 20/40 Sintered Bauxite at closure stresses up to 11000 psi (75900 kPa), thereafter Bauxite provided the superior fracture conductivity. With this well, no apparent relationship between the Brinell hardness and conductivity reduction was evident.

There was a large variation in the conductivity results for the four samples tested. Sample #14 actually yielded a higher fracture conductivity than the flow cell conductivity. This was due to the fracture porosimeter measuring a higher proppant porosity than measured in the linear flow cell. It was therefore apparent that for this sample, the Sintered Bauxite proppant had not been properly levelled in the porosimeter.

As a result of integrating the fracture porosimeter data, the flow cell conductivity values for Sintered Bauxite at closure stresses of 1000 psi and 15000 psi (6900 and 103500 kPa) were reduced by 35% and 14% respectively, while the respective flow cell conductivities for Interprop reduced by 50% and 14%. With the frac sand, the flow cell conductivity measured at 1000 psi and 10000 psi (6900 and 69000 kPa) was reduced by 66% and 35% respectively.

	Closure Stress	Flow Cell	Sample #13	Sample #14	Sample #15	Sample #16	Average
SINTERED BAUXITE	1000	4.50	2.60	5.52	1.91	1.71	2.93
	2000	3.84	2.28	4.70	1.62	1.50	2.53
	4000	3.35	2.05	4.01	1.43	1.33	2.20
	6000	3.03	1.93	3.61	1.27	1.24	2.01
	8000	2.67	1.77	3.29	1.15	1.16	1.84
	10000	2.34	1.84	3.36	1.17	1.22	1.90
	12000	2.04	1.76	3.20	1.03	1.18	1.79
	14000	1.92	1.59	2.87	.88	1.09	1.61
	15000	1.86	1.57	2.87	.84	1.12	1.60
INTERPROP	1000	6.47	3.03	3.20	2.50	4.02	3.19
	2000	5.58	2.46	2.77	2.13	3.28	2.66
	4000	4.88	2.08	2.32	1.83	2.83	2.27
	6000	4.21	2.00	2.20	1.71	2.69	2.15
	8000	3.63	1.95	2.16	1.63	2.53	2.07
	10000	2.72	1.75	1.91	1.39	2.251	1.83
	12000	2.21	1.53	1.70	1.27	2.056	1.64
	14000	1.69	1.28	1.38	.99	1.734	1.35
	15000	1.39	1.14	1.26	.86	1.557	1.20
SAND	1000	2.55	.51	1.26	.48	1.17	.86
	2000	1.97	.41	1.00	.37	.93	.68
	4000	1.61	.37	.92	.32	.87	.62
	6000	.85	.24	.60	.21	.54	.40
	8000	.37	.12	.32	.09	.28	.20
	10000	.20	.07	.23	.05	.17	.13

Units : Closure Stress (psi)
Frac Conductivity (D.ft)

Sample Depths
Well 11/30-A6

Sample #13 : 6820 ft
Sample #14 : 6841 ft
Sample #15 : 6844 ft
Sample #16 : 6855 ft

***Table5.11** : Fracture Conductivity Results - Well 11/30-A6*

Fracture Conductivity : Well 11/30a-A6

Average Results between 6820ft and 6855ft

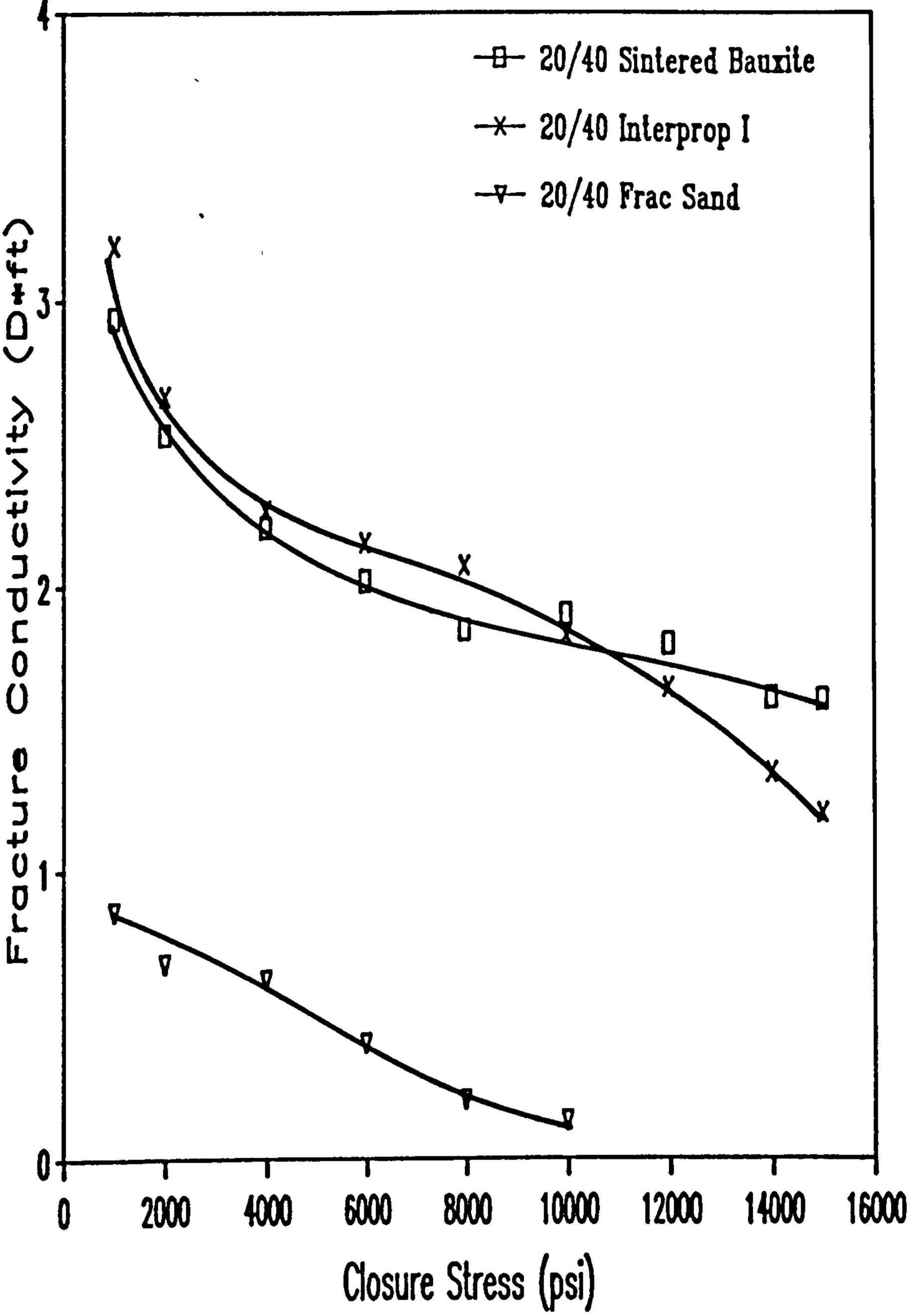

Figure 5.44 : Fracture Conductivity Results - Well 11/30-A6

5.11.5.5 Discussion of Results

From the above analysis, it was apparent that proppant embedment has a marked effect on fracture conductivity estimations.

Of the two stronger proppants tested, 20/40 Sintered Bauxite was found to show the least overall reduction in fracture conductivity with respect to the linear flow cell data at low closure stress, while at high levels of closure stress, it generally suffered the greatest conductivity reduction. For 20/40 sand, the smallest difference between flow cell conductivity and fracture conductivity was generally found to occur at high closure stress. This indicated that proppant embedment contributed more to the reduction in fracture conductivity for 20/40 Sintered Bauxite, while the conductivity reduction for frac sand was attributed to excessive crushing.

5.11.6 Correlation Between Brinell Hardness and Fracture Porosity

As stated above, the fracture porosimeter enables the porosity of a proppant pack sandwiched between two rock cores to be measured at various levels of closure stress. It therefore measures the combined extent of proppant crushing and embedment in the rock. Previous workers [35,103] have indicated that proppant embedment is a function of rock hardness and consequently, softer formations are more susceptible to proppant embedment. To investigate if any correlation existed between Brinell hardness and proppant porosity reduction, the fracture porosimeter test results were summarised and

compared with Brinell hardness values of each formation sample.

Table 5.12 shows the initial proppant porosity measured at 1000 psi (6900 kPa) together with the total reduction in porosity at maximum closure stress for the three proppants tested with each formation sample. The Brinell hardness number for each sample is also given to allow a comparison.

The relationship between initial proppant porosity of 20/40 Sintered Bauxite and Brinell hardness is presented in Figure 5.45(a). From an examination of this figure, it was evident that the harder samples displayed a higher proppant porosity. Figure 5.45(b) illustrates the total reduction in proppant porosity measured at 15000 psi (103500 kPa) as a function of Brinell hardness. Although some scatter of results was evident, it was apparent that the samples with the higher Brinell hardness yielded the lower reduction in proppant porosity.

Figure 5.46(a) shows the initial proppant porosity at 1000 psi (6900 kPa) for 20/40 Interprop plotted against Brinell hardness. It can be seen that the samples which had a higher Brinell hardness were generally found to have a higher initial porosity. This was in accordance with the bauxite test data. The total proppant reduction at 15000 psi (103500 kPa) closure stress was also plotted against Brinell hardness and is shown in Figure 5.46(b). In this case, a more definite relationship was evident with the harder samples displaying a lower reduction in proppant porosity.

Well Number		Porosity at 1000 psi (%) Bauxite	Sand	Interprop	Porosity Reduction (%) Bauxite	Sand	Interprop	BHN
11/30-2	(1)	33.13	30.17	28.22	2.20	3.37	2.83	25.50
	(2)	34.09	33.34	32.83	2.50	3.83	2.27	33.60
	(3)	35.91	35.91	33.65	****	3.18	1.85	33.20
	(4)	33.29	26.37	31.89	3.54	2.51	****	27.10
11/30-5	(5)	38.06	33.80	32.69	2.20	4.05	1.90	42.00
	(6)	36.93	32.80	34.32	1.25	3.58	1.15	47.70
	(7)	32.31	30.93	31.11	2.41	4.30	3.07	23.20
	(8)	34.24	27.53	29.30	3.50	4.22	3.53	17.90
11/30a-A4	(9)	33.93	29.01	31.84	1.37	3.61	3.34	36.90
	(10)	33.77	33.49	35.89	3.19	3.65	2.59	31.40
	(11)	35.76	32.40	32.83	4.20	3.83	4.44	28.10
	(12)	37.08	31.92	32.27	4.65	3.83	****	27.70
11/30a-A6	(13)	35.62	27.25	33.24	2.94	4.05	2.76	22.60
	(14)	41.57	33.57	33.66	4.28	3.37	2.47	24.10
	(15)	33.29	26.58	33.66	5.01	5.28	2.79	29.40
	(16)	32.47	32.99	35.37	2.25	4.21	2.64	30.40

Table 5.12 : *Initial Porosity and Porosity Reduction as Measured by the Fracture Porosimeter*

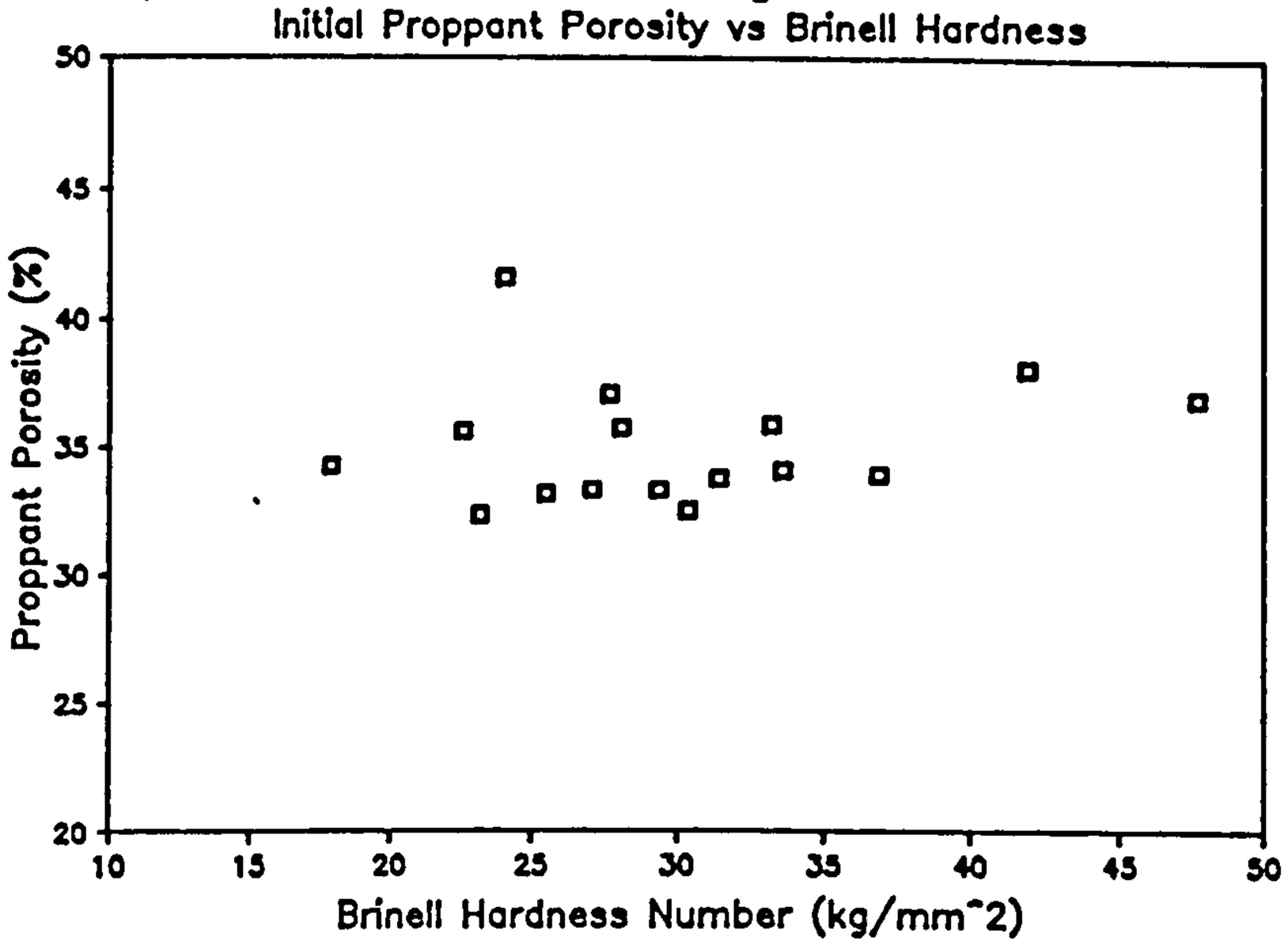

Figure 5.45(a)

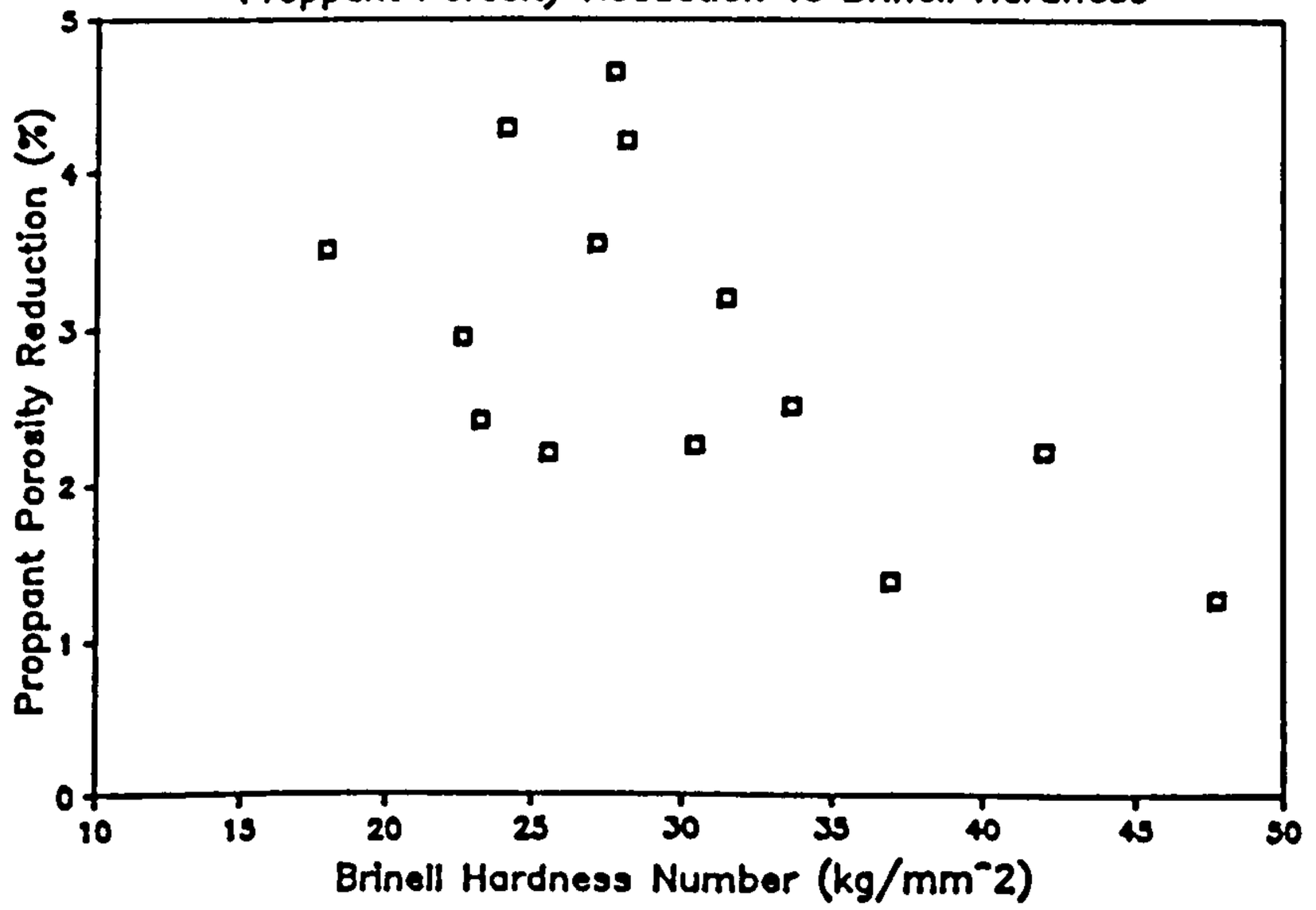

Figure 5.45(b)

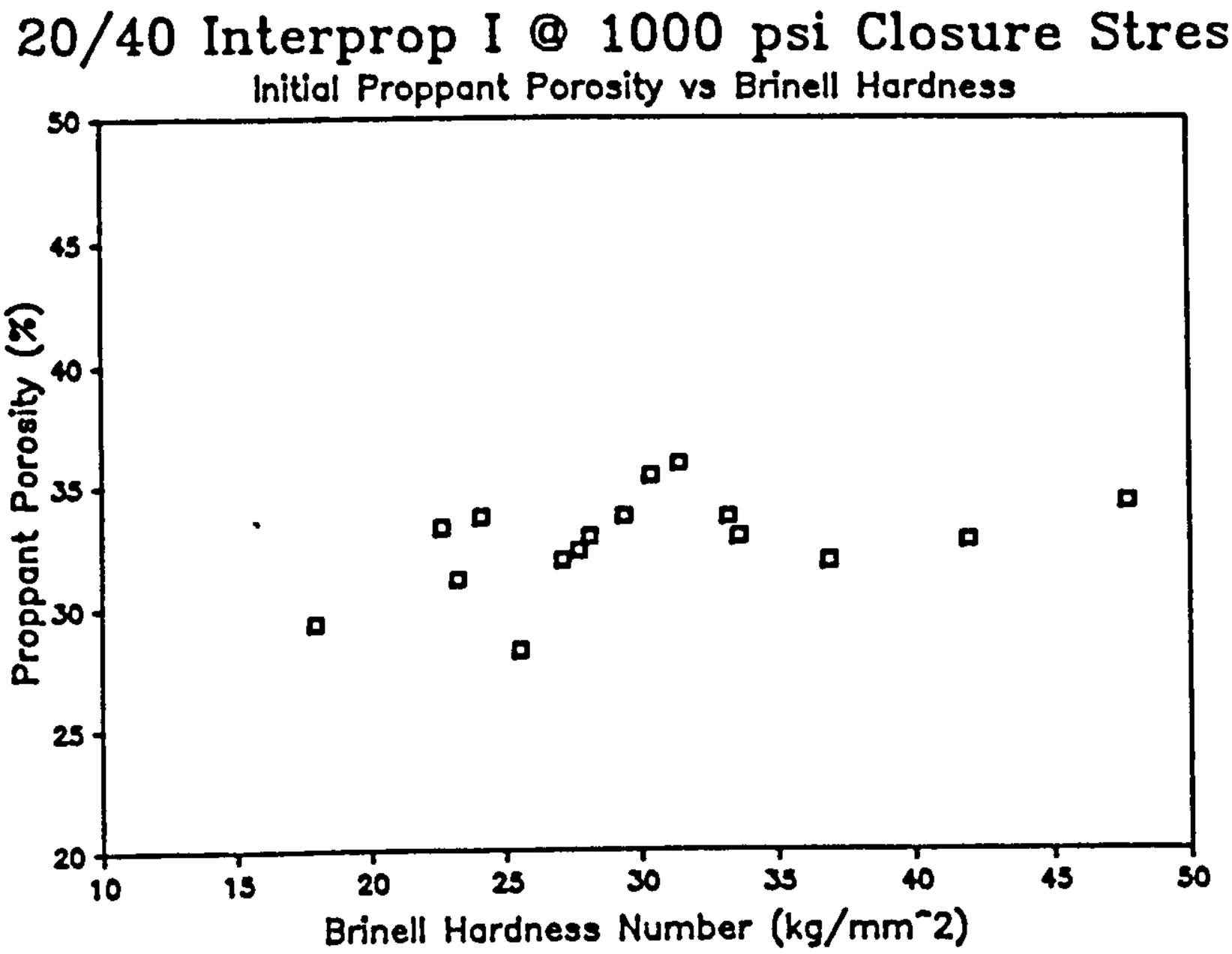

Figure 5.46(a)

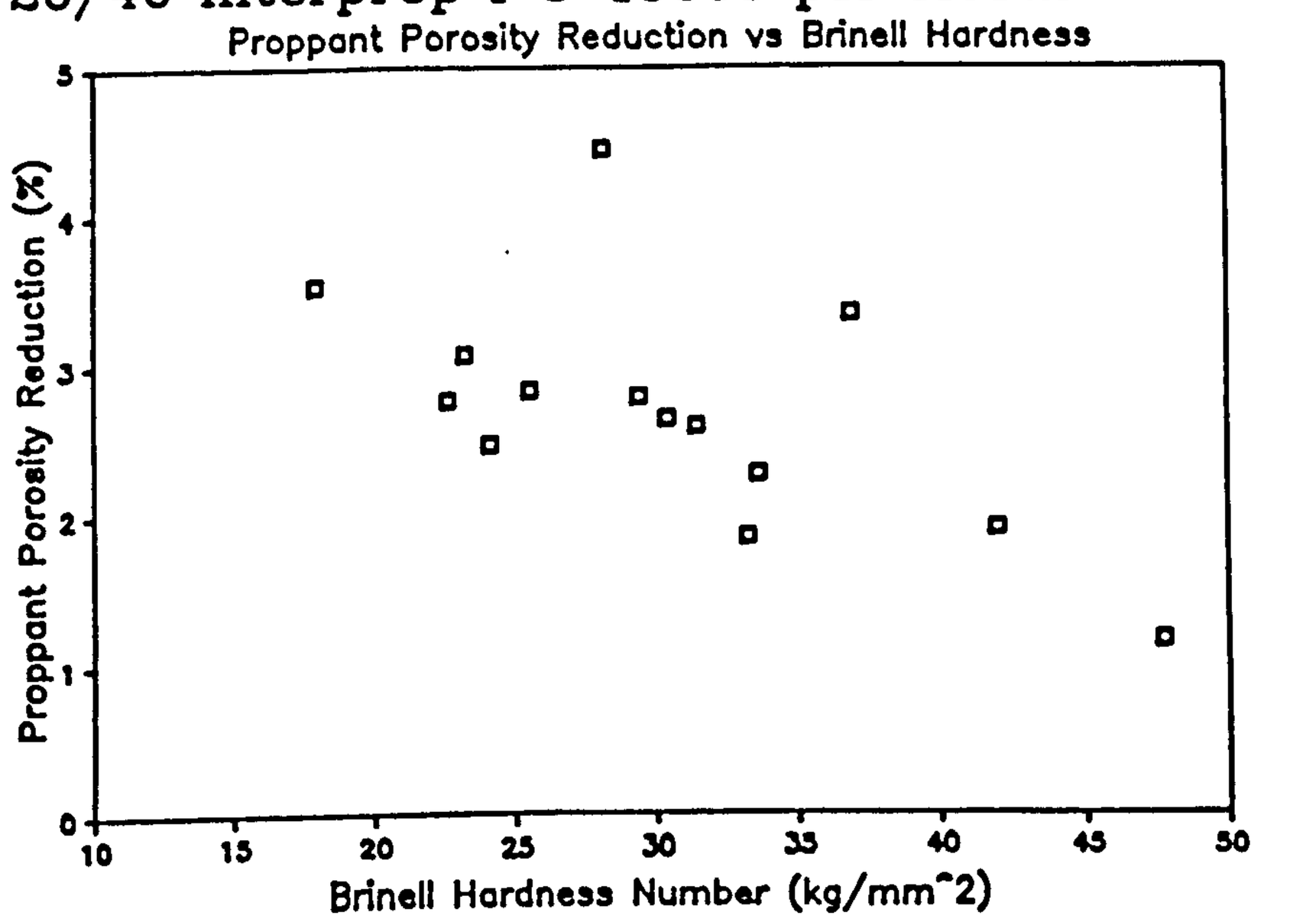

Figure 5.46(b)

Similar graphs were plotted for 20/40 frac sand and are shown in Figures 5.47(a) and 5.47(b) respectively. Referring to Figure 5.47(a), it can be seen that the harder formation samples generally had a higher initial proppant porosity. However, from an examination of Figure 5.47(b) it was apparent that sample hardness had little effect on proppant porosity reduction, although a general trend was present.

From the above analysis it can be claimed that a correlation was found to exist between proppant porosity reduction and Brinell hardness. With the three types of proppant tested, the general trend was that the higher the Brinell hardness of the rock sample, the lower the total reduction in proppant porosity.

It can therefore be concluded that the Brinell hardness of a rock may be used as an indication of the initial proppant porosity and the likely porosity reduction as a result of applied stress. In this analysis, no attempt has been made to determine the mathematical relationship between proppant porosity reduction and rock hardness as this would have required a larger number of tests. Such a mathematical relationship, however, may be developed as a result of on-going tests.

5.11.7 Discussion and Conclusions

It has been shown that the fracture conductivity/permeability estimates obtained with the fracture porosimeter were less than that measured with the linear flow cell, which assumed negligable

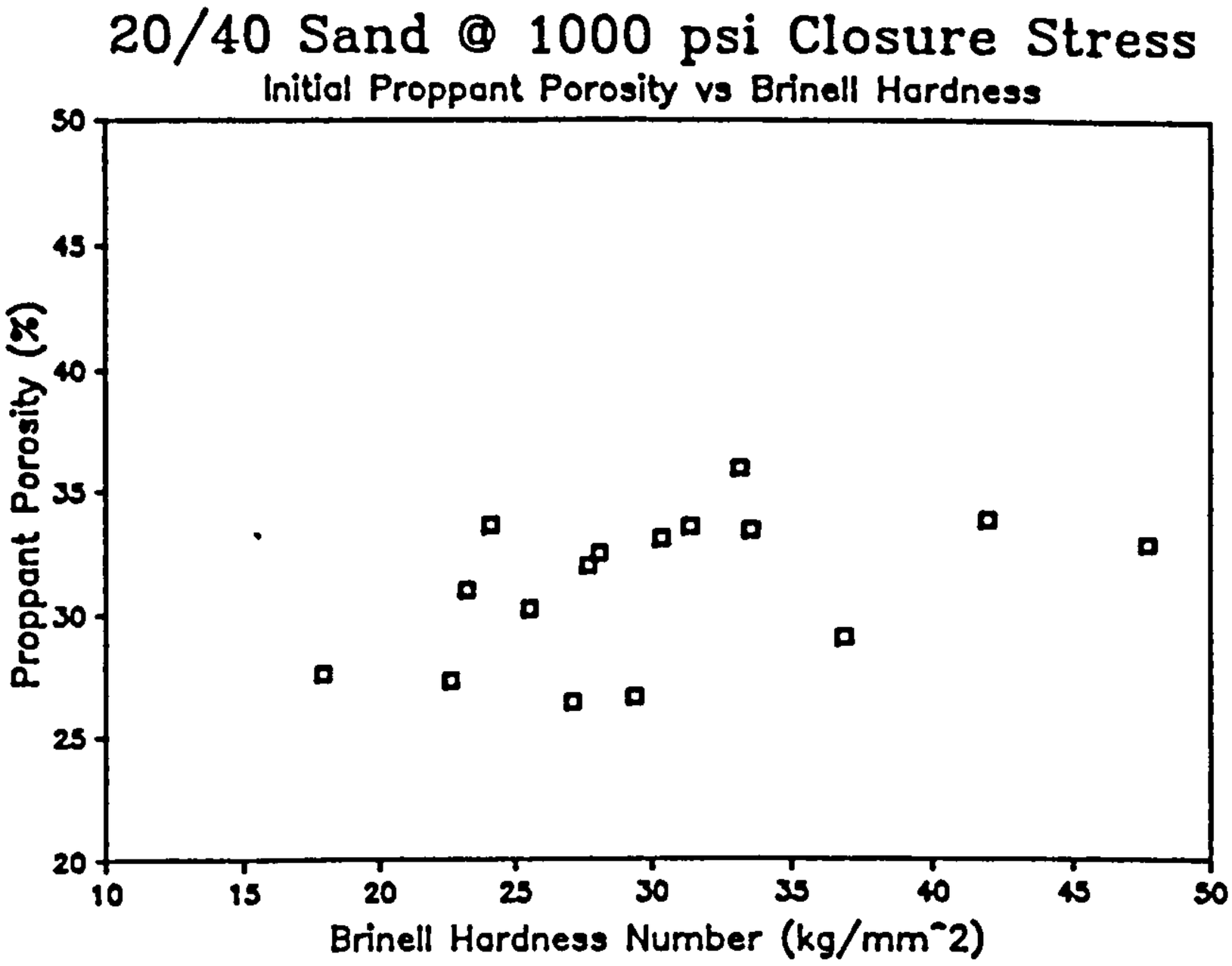

Figure 5.47(a)

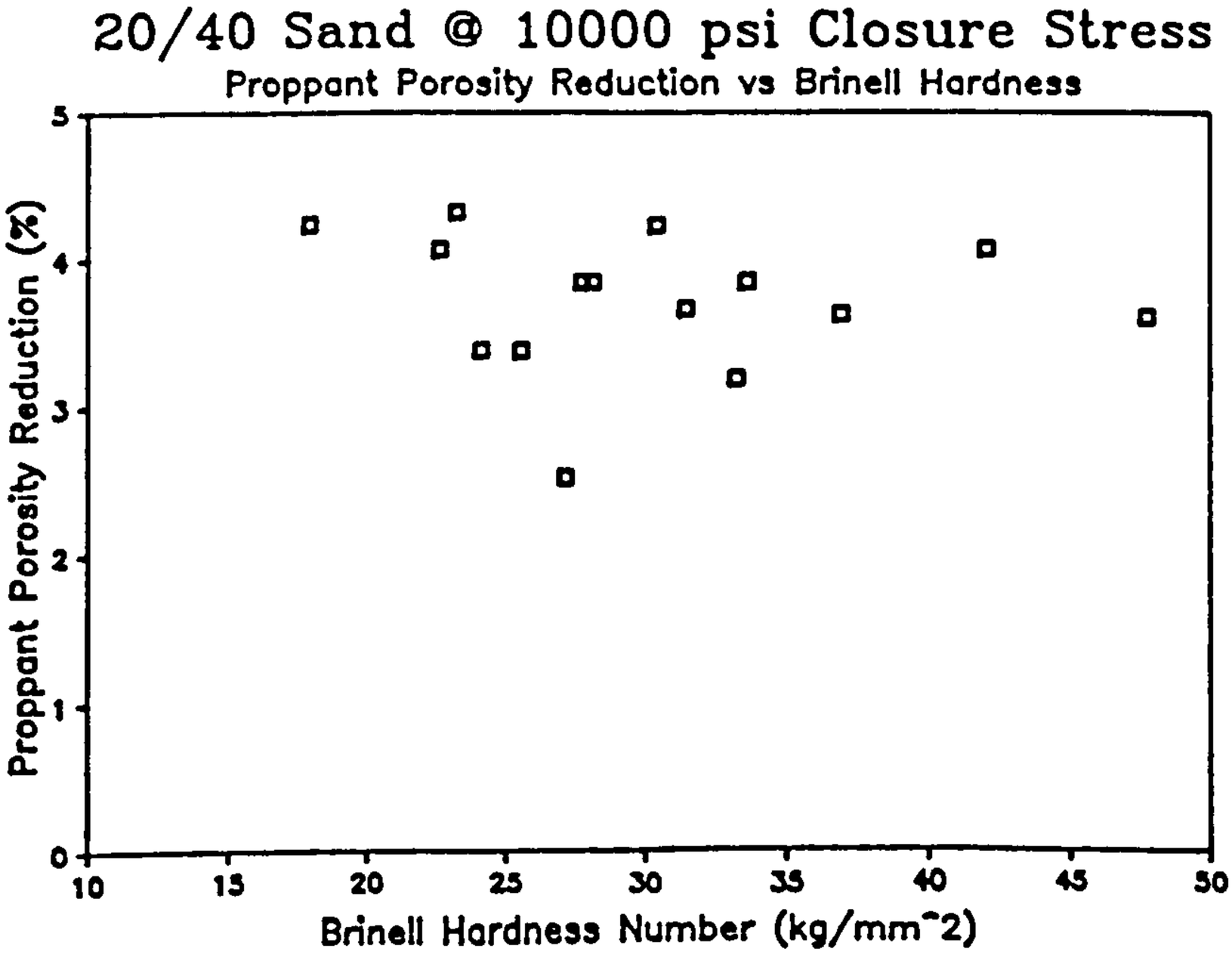

Figure 5.47(b)

embedment. It was also shown that this reduction was not constant over the range of closure stress, with the greatest conductivity reduction occurring at the lower valves of closure stress. In the fracture porosimeter tests, the total reduction in the porosity of the proppant pack under stress varied from 1.5% to about 5%, while in the linear flow cell, the proppant porosity reduction was typically between 5% and 10%. It should be stated, however, that the initial proppant porosity measured with the fracture porosimeter was always lower than measured in the linear flow cell for each proppant type. As the fracture porosimeter indirectly measured the embedment of the proppant in the formation sample, it was expected that the greatest porosity reduction as a result of applied stress would be obtained from this test. The most likely reason for this difference was considered to be the 1:1 confining pressure to closure stress ratio which was used throughout the fracture porosimeter tests (remembering that the closure stress was applied in the axial direction). This did not allow the proppant pack to expand in a lateral direction as was considered to have occurred with the linear flow tests, in which the stress was applied in the axial direction. As the proppant was confined only by the walls of the linear flow cell test chamber, the proppant could expand laterally, thus the porosity reduction would be greater. In the present design of linear flow cell, it is not possible to apply confining pressure to the proppant pack. Unpublished tests by the author have indicated that if a lower confining pressure to closure stress ratio is used for the fracture porosimeter, a greater reduction in proppant porosity is obtained. More extensive tests would be required to establish the stress ratio which would enable the proppant in the fracture

porosimeter to laterally expand by a similar amount as occurs in the linear flow cell, and thus provide more comparable results.

5.12 EFFECT OF A YIELD ZONE ON THE ESTIMATION OF CLOSURE STRESS AND THE CONSEQUENT REDUCTION IN FRACTURE CONDUCTIVITY

The effect of a yield zone on the estimation of closure stress is shown qualitively in Figure 5.48(a). It is evident that the maximum closure stress may be considerably greater than that predicted using existing methods where the closure stress is taken to equal the minimum horizontal principal stress. In this figure, the closure stress acting on the wall of a propped fracture is represented by the hoop stress, i.e. the stress that acts at 90° to the fracture face. Although this stress abutment (termed the 'maximum closure stress') is localised, it may act to form a 'bottleneck' and accordingly restrict the flow of fluid through the propped fracture when the well is produced, as postulated in Figure 5.48(b). In addition, if fines migration occurs to the extent suggested by the linear flow cell test results, the proppant fines may concentrate in this region and reduce the flow capacity further.

To illustrate the effect of a yield zone surrounding a wellbore on the estimation of closure stress and the consequent reduction in fracture conductivity, use was made of the conductivity data obtained for the four wells examined in the previous section. The closure stress was calculated by the traditional method (i.e. equal to the minimum horizontal principal stress) and the maximum closure stress was taken to be the abutment peak (i.e. the fracture

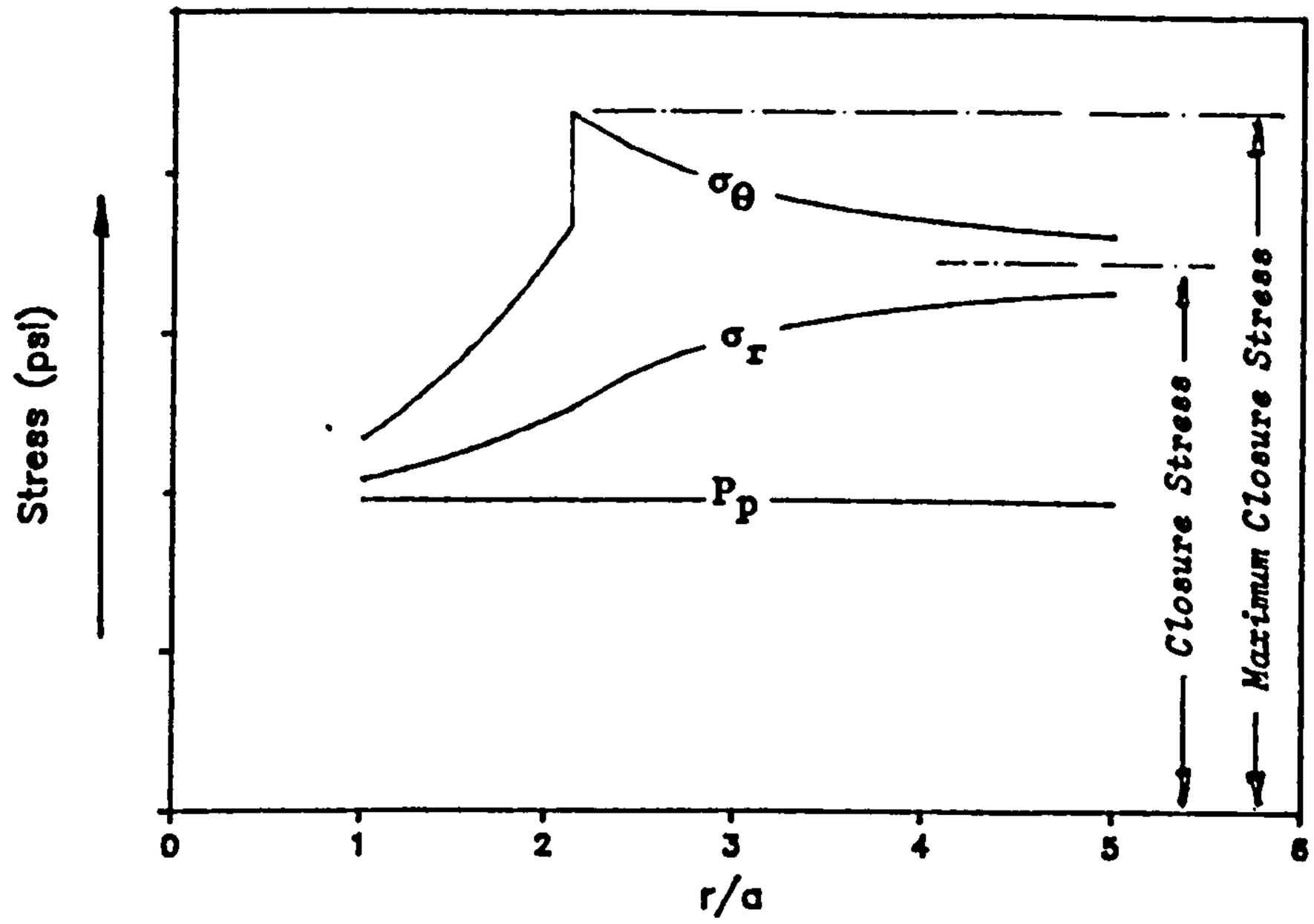

Figure 5.48(a) : Effect of a Yield Zone on the Estimation of Closure Stress

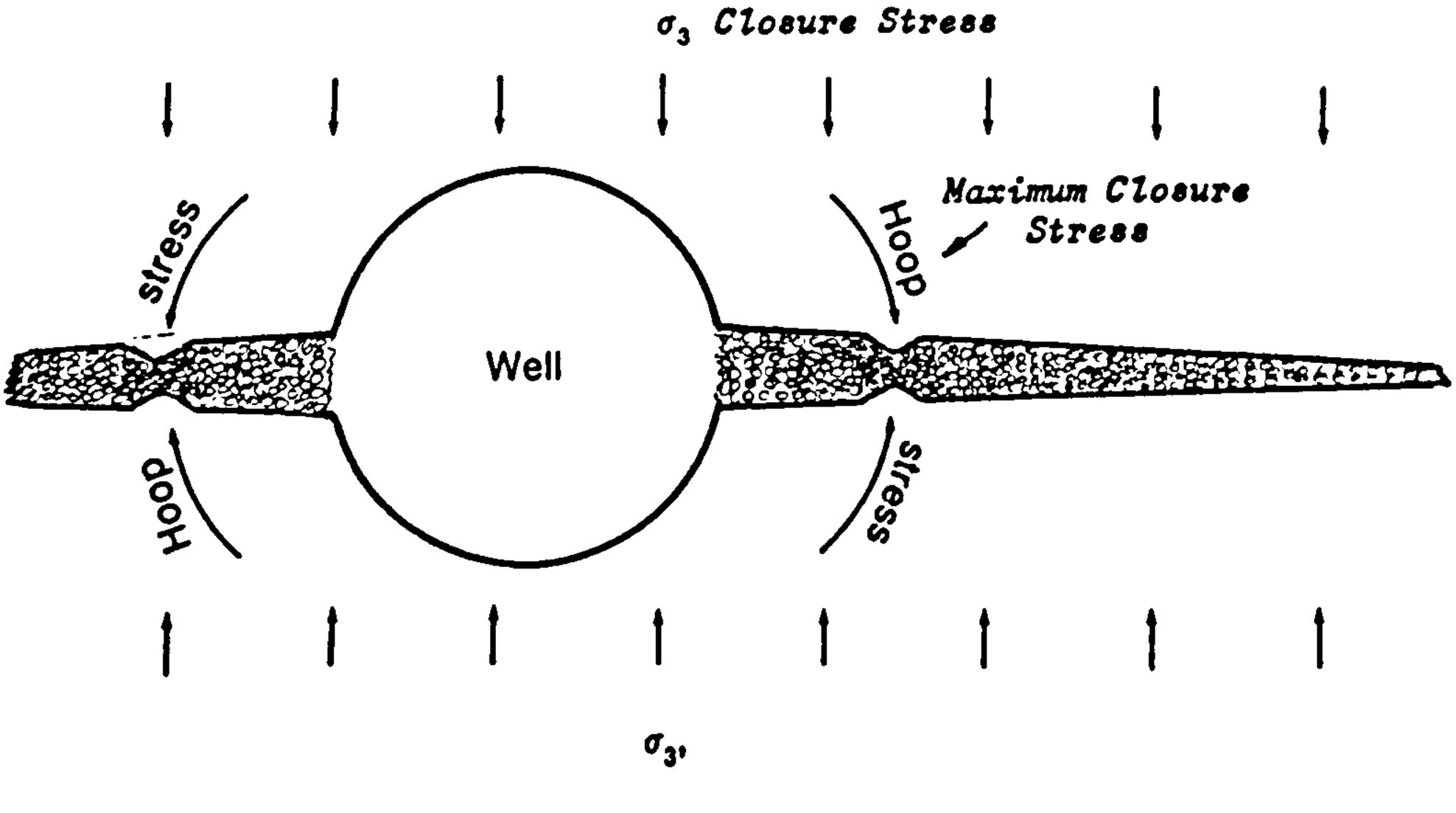

Figure 5.48(b) : Effect of Maximum Closure Stress on a Propped Fracture

initiation pressure using the yield zone concept), and was calculated from equation (4.34). In calculating the respective closure stress values, it was necessary to make several assumptions. The overburden pressure was assumed to be in the order of 1 psi/ft (22.6 kPa/m), the horizontal to vertical stress ratio was taken to be 0.75:1 and a pore pressure gradient of 0.465 psi/ft was assumed. The effect of water depth was not considered and the well was assumed to be vertical. As no information was available about the mechanical properties of the formation samples, it was assumed that the in-situ uniaxial compressive strength was 1500 psi (10000 kPa) and the triaxial stress factor was 3.

After calculating the upper and lower values of closure stress for each well, conductivity values for the various proppants were read off the respective fracture conductivity vs closure stress graphs (see Section 5.11.5, Figures 5.41 to 5.44). The reduction in fracture conductivity for each proppant as a result of the maximum closure stress was then calculated as a percentage. The results are given in Table 5.13.

From the table it can be seen that the maximum closure stress predicted using the yield zone concept was between 17% to 20% higher than the closure stress estimated from the minimum horizontal principal stress. The reduction in fracture conductivity due to the presence of a yield zone was between 3.8% and 8.6% for Sintered Bauxite. With Interprop, a slightly lower reduction in fracture conductivity of between 3% and 5.5% was calculated. With frac sand however, the fracture conductivity was reduced to between 26.5% and

Method (a) : Closure Stress Calculated from Minimum Horizontal Stress
Method (b) : Closure Stress Calculated from Yield Zone Approach

Well No	Proppant Type	Closure Stress (a)	Maximum Closure (b)	Fracture Conductivity from (a)	from (b)	% Conductivity Reduction
11/30-2	Bauxite Interprop Frac Sand	5200 psi	6500 psi	1.62 Dxft 1.82 Dxft 0.64 Dxft	1.54 Dxft 1.75 Dxft 0.46 Dxft	5.9% 3.0% 28.1%
11/30-5	Bauxite Interprop Frac Sand	5500 psi	6600 psi	2.07 Dxft 1.92 Dxft 0.53 Dxft	1.99 Dxft 1.85 Dxft 0.38 Dxft	3.8% 3.7% 26.5%
11/30a-A4	Bauxite Interprop Frac Sand	5200 psi	6500 psi	1.87 Dxft 2.17 Dxft 0.58 Dxft	1.71 Dxft 2.05 Dxft 0.41 Dxft	8.6% 5.5% 30.1%
11/30a-A6	Bauxite Interprop Frac Sand	5150 psi	6400 psi	2.05 Dxft 2.19 Dxft 0.48 Dxft	1.92 Dxft 2.07 Dxft 0.33 Dxft	6.2% 5.2% 31.0%

***Table 5.13** : The Effect of a Yield Zone on Closure Stress Estimations and the Resulting Reduction in Fracture Conductivity*

31.2% of the original value. The optimum proppant for use to withstand these elevated closure stresses would be 20/40 Interprop, as 20/40 frac sand would crush excessively and the additional expense of using 20/40 Sintered Bauxite could not be justified at this depth.

It can therefore be concluded that the fracture conductivity of weaker proppants, such as frac sand, may be considerably reduced if a yield zone is assumed to surround the well. In the examples shown, the fracture conductivity of frac sand was reduced by an average of 30%. If stronger rock and a higher stress ratio had been assumed, this reduction in fracture conductivity would have been greater.

To avoid a detremental reduction in conductivity as a result of the presence of a yield zone, the propping agent chosen must be able to withstand the localised maximum value of closure stress. Indeed, for shallow wells where frac sand is normally used as a propping agent, the maximum closure stress may be sufficient to induce excessive proppant crushing which will have the adverse effect of decreasing fracture conductivity and reduce the longterm effectiveness of the fracturing treatment. This may also explain why the fracture conductivities measured in the field are typically much lower than the laboratory data. It can therefore be concluded that the localised maximum closure stress produced by the presence of a yield zone should be considered when calculating the closure stress acting on a propped fracture. If no yield zone exists around the well, then the increased value will merely act as an added safety factor.

5.13 CONCLUSIONS

The objective of this chapter was to develop a laboratory technique which could be used on a routine basis to determine a realistic value for fracture conductivity at various levels of closure stress. A data-base outlining the properties of various commercially available proppants has been established and may be used to select the optimum proppant for a specific formation.

A preliminary investigation using a nitrogen permeameter and a triaxial cell to simulate downhole stress lead to the conclusion that the physical properties of the formation must be taken into consideration when selecting a proppant.

A test system comprising of a linear flow cell, oil permeameter (both manufactured specifically for this project), triaxial cell, servo-controlled testing machine and intensifier, sieves and electronic balances, and data-processing software has been assembled and appropriate experimental techniques established. As well as the tests planned at the outset of this project, additional tests have been devised to confirm the previously unreported effect of fines migration through the linear flow cell and to make the data-base more comprehensive.

The results obtained generally reflect the published properties of the various proppants, viz. the high-strength proppants provide the greater permeability/conductivity at higher levels of closure stress. It can be concluded that 20/40 frac sand should only be used

in wells where the closure stress will not exceed 4000 psi (27600 kPa), otherwise excessive loss of permeability will occur. It can also be concluded that although 20/40 Interprop can withstand elevated closure stress, 20/40 Sintered Bauxite should be used to provide superior permeability at closure stresses above 11000 psi (76000 kPa). As a result of performing additional tests, it can be concluded that proppant fines migrate downstream in the linear flow cell and the magnitude of which can be measured. In extreme cases, upstream permeabilities of up to four times the the downstream values have been measured. Although the literature is aware that fines migration exists, the author has not detected acknowledgement of this effect when quoting values obtained from the various ports of the linear flow cell.

As a result of conducting dry proppant crush tests, it can be concluded that the reduction in permeability of 20/40 Interprop with respect to 20/40 Sintered Bauxite at high closure stress was attributed to the the high amount of fines produced. The variation in permeability and wetted surface area data for Interprop was also greater than for Sintered Bauxite. However, there did not appear to be a direct relationship between the reduction in conductivity and excessive crushing for the higher strength proppants.

The technique has been applied to rock samples from four wells. From this application, it may be concluded that proppant embedment has a marked effect on fracture conductivity estimations. Of the two stronger proppants tested, 20/40 Sintered Bauxite was found to show the least overall reduction in fracture conductivity with respect to

the linear flow cell data at low closure stress, while at high levels of closure stress, it generally suffered the greatest conductivity reduction. For 20/40 sand, however, the smallest difference between flow cell conductivity and fracture conductivity was generally found to occur at high closure stress. Therefore, it can be concluded that proppant embedment contributed more to the reduction in fracture conductivity for 20/40 Sintered Bauxite, while the conductivity reduction for frac sand was attributed to excessive crushing. It can therefore be concluded that the adopted technique, which was originally proposed by Wendorff [115], provides a satisfactory method of allowing for proppant embedment by combining test data obtained from a linear flow cell with that obtained from embedment tests using a fracture porosimeter.

A tentative correlation between Brinell hardness and proppant porosity reduction as measured in the fracture porosimeter has been established. With the three proppant types tested, the general trend was that the higher the Brinell hardness of the rock sample, the lower the total reduction in proppant porosity. This relationship was more apparent with the intermediate- and high-strength proppants. It can therefore be concluded that the Brinell hardness of a rock may be used as an indication of the initial proppant porosity and the likely porosity reduction as a result of applied stress. However, an extensive laboratory testing programme would be required to define a mathematical relationship.

The direct effect of a yield zone on the closure stress acting on the face of a propped fracture has been investigated. It can be

concluded that the yield zone causes an increase in the closure stress estimations and accordingly reduces fracture conductivity. Of the three proppant types examined, the greatest percentage reduction in fracture conductivity occurred with 20/40 frac sand. Therefore, it can be concluded that, especially for shallow wells where sand is generally used as the propping agent, the maximum closure stress may be sufficient to induce excessive proppant crushing which will have the adverse effect of decreasing fracture conductivity and consequently reduce the longterm effectiveness of the fracturing treatment. As stated, this may also explain why fracture conductivity values measured in the field are typically much lower than the laboratory data. It can therefore be concluded that the localised maximum closure stress produced by the presence of a yield zone should be considered when calculating the closure stress acting on a propped fracture.

CHAPTER SIX

SUMMARY CONCLUSIONS AND RECOMMENDATIONS

6.1 SUMMARY CONCLUSIONS

The primary objective of this investigation was to examine and develop methods of predicting the stress distribution around both vertical and inclined boreholes under non-hydrostatic stress conditions to enable the prediction of borehole stability. The secondary objective was to apply the above analysis to provide more realistic estimates of the closure stress acting in the immediate vicinity of the hole in order to optimise proppant selection. This section summarises the manner in which these objectives were met and compiles the various conclusions which have been drawn from the preceding chapters.

The induced state of stress around inclined boreholes was initially investigated using the three-dimensional photoelastic technique of stress freezing. The results of the photoelastic analysis revealed several characteristics of the stress distribution around both vertical and inclined boreholes situated in a non-hydrostatic stress field.

For a vertical borehole, the tangential or hoop stress was found to be constant at all points around the periphery of the hole and had a value of twice the horizontal in-situ stress. This was in accordance with elastic theory and confirmed the accuracy of the technique. The effect of inclining the borehole was to decrease the hoop stress acting on the 'roof' of the hole and to increase the hoop stress acting at the 'side' of the borehole. This effect was more apparent with the higher angle holes. This lead to the conclusion that, under

normal in-situ stress conditions, the 'roof' of an inclined borehole is more likely to fail in tension while the 'side' of the hole is more likely to fail in compression.

Although the effect of mud weight was not considered in this initial analysis due to difficulties in applying wellbore pressure within the loading frame, the investigation proved beneficial as it experimentally demonstrated the varying state of stress around inclined boreholes and identified regions of potential instability. Such a physical modelling approach, however, could not be used to realistically predict the stability of a wellbore as the solutions did not consider the mechanical properties of the rock in the neighbourhood of the hole. Although the secondary principal stresses were separated by a microcomputer using a spreadsheet package, obtaining the photoelastic parameters from the model was a laborious process. In addition to this, a single photoelastic model could only provide information about a limited number of hole angles and in-situ stress conditions and it would have required a number of subsequent models to provide comprehensive data. It was therefore apparent that a more rigorous technique was required and it was consequently decided to extend the physical modelling approach to analytical methods. This allowed the inclusion of failure criteria and enabled an computer based investigation into the effect of rock strength, mud weight, hole angle and in-situ stress to be conducted.

Before conducting such a mathematical analysis, an extensive laboratory testing programme was performed to provide failure criteria. Rock mechanical properties were determined from core

samples of two North Sea wells. During this laboratory examination, the opportunity was taken to investigate the validity of the Brinell hardness test as applied to rock, and to establish if a relationship exists between Brinell hardness and the elastic moduli of the rock. As a result of this investigation, it was concluded that the Brinell hardness test was a quick and simple method of assessing the physical rock properties. In general, the test results appeared to corroborate the existence of a relationship between Brinell hardness and the elastic moduli of rock. A relationship between sample density and P-wave velocity was also reported, although this was less apparent. As for the other mechanical properties, no direct conclusions were drawn.

The repeatability and linearity of the initial results using the modified oedometer indicate that the instrument is capable of producing accurate rock hardness values. The attraction with the technique developed is that a prepared core sample can be tested using the apparatus, without suffering damage, prior to mechanical property testing. This has the advantage of increasing the likelihood of generating consistent and meaningful results. It can also be concluded that the modified NCB cone indenter, although not as accurate as the modified oedometer, is nevertheless of value as a Brinell tester as it is pocket-sized, easy to use and can accept small samples of rock. The instrument is therefore suitable for field use and as the test does not require prepared core samples, it is possible that it could be used for providing estimates of rock hardness from drill cuttings or other small fragments of rock.

Mohr-Coulomb and three-dimensional Griffiths failure relationships have been developed using the failure criteria obtained from the laboratory investigation. These relationships were then applied to existing analytical solutions in order to examine the possibility of maintaining the rock in the neighbourhood of the well in an elastic condition. These were in turn used to predict the mud weight required to prevent hole collapse for the two North Sea wells from which rock property data was available. The approach was also used to provide an indication of the maximum drawdown pressure before theoretical hole collapse. Of the two criteria applied, the 3D Griffith criterion appeared to predict critical mud weights which were too low. A modification to the 3D Griffith theory was proposed which involved decreasing the compressive strength by a factor to enable results of the same order of the Mohr-Coulomb theory to be obtained.

The analytical analysis confirmed that inclined boreholes have a reduced ability to withstand high mud weights before fracturing while they require increased mud weight to prevent hole collapse. It can also be concluded that for an inclined borehole in a normal stress regime, tensile and compressional failure will initiate at 90° to each other. This work illustrated that the minimum rotated tangential stress occurs at the 'roof' (and 'floor') of an inclined borehole. Thus it can be concluded that tensile failure will be initiated in this direction. After the stress concentration effects of the hole are passed, the fracture will, of course, propagate in a manner perpendicular to the direction of the least principal stress. As the maximum rotated tangential stress acts on the 'side' of the

hole, it may be concluded that hole collapse will be initiated in the direction of the least principal stress.

The yield zone hypothesis has been extended to cover non-hydrostatic stress conditions and the effect of pore pressure. This allowed an analysis of the stability of inclined boreholes surrounded by a zone of yielded rock and enabled the post-failure behaviour of the borehole to be examined. It can be concluded that the yield zone analysis predicted that a higher mud weight would be required to maintain stability than predicted by the elastic analysis. This was due to the fact that an 'in-situ' value of compressive strength was used for the yield zone analysis, while the laboratory values were used for the Mohr-Coulomb and three-dimensional Griffith approach. It can therefore be concluded that rock strength, but more especially the triaxial stress factor, plays a major role in deciding the stability or instability of an inclined borehole. The simple rule being, the higher the triaxial stress factor, the more stable the borehole. From the mud weight vs depth curves produced for various rock strengths, it can be concluded that, at great depth, it is the mechanical properties which dictate hole stability.

The development of a yield zone around an inclined hole has been illustrated. It has been established that the 'first stage' of yielding occurs at the 'side' of an inclined hole, i.e. in the direction of the minimum rotated horizontal stress. Thus, it can be concluded that although a small yield zone may exist at the 'side' of an inclined borehole, the rock at the 'roof' of the hole may be within its elastic limit, and therefore stable. It can also be

concluded that the shape of a yield zone around an inclined hole depends not only upon the hole inclination, but on the regional in-situ horizontal to vertical stress ratio. It has been shown that the lower stress ratio produces the more distorted yield zone radius, while higher stress ratios produce a more ellipical yield zone. It has also been postulated that the yield zone hypothesis can explain why some boreholes are not circular. The stress distribution in the yield and elastic zones as a function of radial distance have been illustrated for the case of non-hydrostatic conditions.

The effect of fluid flow has been examined by the application of simple Darcy flow equations and assuming steady state conditions in the yield zone with semi-steady state conditions applying beyond. It can be concluded that the effect of increasing the flow rate from an uncased well increases the width of the yield zone. It can also be concluded that casing and cementing the well has the effect of reducing the width of the yielded region. However, it should be noted that even if the yield zone reduces in width, the physical properties of the rock may not return to their original state. The effect of a reduced permeability in the yield zone has been examined. This analysis indicated that the width of the yield zone would increase in the direction of the minimum rotated horizontal stress, but decrease in the direction of the maximum rotated horizontal stress. The approach has also been applied to generate mud weight curves for specific wells. It was shown that fracture initiation pressures, assuming a non-penetrating fluid, calculated by the yield zone hypothesis predicted values which were lower than estimated using classical fracturing theory. Thus it can be

concluded that rock strength has an effect on fracture pressures, i.e. the softer rock fracturing at lower pressures.

To fulfil the secondary objective, which was to apply the above yield zone analysis to provide more realistic predictions of the closure stress acting in the immediate vicinity of the hole and to estimate resulting decrease in fracture conductivity required the facility to measure fracture conductivity/permeability in the laboratory.

A preliminary investigation using a nitrogen permeameter and a triaxial cell to simulate downhole stress lead to the conclusion that the physical properties of the formation must be taken into consideration when selecting a proppant.

A test system comprising of a linear flow cell, oil permeameter (both manufactured specifically for this project), triaxial cell, servo-controlled testing machine and intensifier, sieves and electronic balances, and data-processing software has been assembled and appropriate experimental techniques established. As well as the tests planned at the outset of this project, additional tests have been devised to confirm the previously unreported effect of fines migration through the linear flow cell and to make the data-base more comprehensive.

The results obtained generally reflect the published properties of the various proppants, viz. the high-strength proppants provide the greater permeability/conductivity at higher levels of closure

stress. As a result of performing additional tests, it can be concluded that proppant fines migrate downstream in the linear flow cell. In extreme cases, upstream permeabilities of up to four times the the downstream values have been measured. Although the literature is aware that fines migration exists, the author has not detected acknowledgement of this effect when quoting values obtained from the various ports of the linear flow cell.

As a result of conducting dry proppant crush tests, it can be concluded that the reduction in permeability of 20/40 Interprop with respect to 20/40 Sintered Bauxite at high closure stress was attributed to the the high amount of fines produced. The variation in permeability and wetted surface area data for Interprop was also greater than for Sintered Bauxite. However, there did not appear to be a direct relationship between the reduction in conductivity and excessive crushing for the higher strength proppants.

The technique has been applied to rock samples from four wells. From this application, it may be concluded that proppant embedment has a marked effect on fracture conductivity estimations. A modified Kozeny-Carmen equation was used to enable the combination of conductivity tests conducted on proppant in a linear flow cell, with embedment assumed to be negligible, and porosity tests performed on a proppant layer loaded triaxially between cores of host rocks, in which embedment occurs, to give estimated in-situ values for fracture conductivity. The technique allows the effect of proppant type, closure stress and host rock on fracture conductivity to be examined. From this analysis, it can be concluded that proppant

embedment contributed more to the reduction in fracture conductivity for 20/40 Sintered Bauxite, while the conductivity reduction for 20/40 frac sand was attributed to excessive crushing.

A tentative correlation between Brinell hardness and proppant porosity reduction as measured in the fracture porosimeter has been established. It can therefore be concluded that the Brinell hardness of a rock may be used as an indication of the initial proppant porosity and the likely porosity reduction as a result of applied stress. However, an extensive laboratory testing programme would be required to define a mathematical relationship.

Finally, the direct effect of a yield zone on the closure stress acting on the face of a propped fracture has been investigated. It can be concluded that a yield zone causes a localised increase in the closure stress and accordingly reduces the fracture conductivity. Of the proppant types examined, the greatest percentage reduction in fracture conductivity was found to occur with 20/40 frac sand, where the typical reducion was 30%. For shallow wells where frac sand is generally used as the propping agent, the maximum closure stress may be sufficient to induce excessive proppant crushing which will have the adverse effect of decreasing fracture conductivity. Therefore, it can be concluded that the localised maximum closure stress produced by the presence of a yield zone should be considered when calculating the closure stress acting on a propped fracture.

6.2 RECOMMENDATIONS FOR FUTURE RESEARCH

The rock testing programme illustrated the apparent shortcomings of determining the Poisson's ratio and Young's Modulus of a rock from a multi-failure triaxial test. The stress-strain curves produced were found to flatten as the applied axial stress was increased. This indicated that the rock was displaying plastic behaviour before the onset of failure. This leads to the recommendation that when generating test data for borehole stability analysis, Young's Modulus and Poisson's Ratio should be determined independently from the multi-failure triaxial test as it is desirable to obtain stress-strain data from the linear sections of the graph.

It is recommended that further research should be conducted towards establishing a retationship between Brinell hardness and the mechanical properties of rock. If such a relationship is derived, it may be possible to provide an indication of the strength of the rock surrounding a wellbore as it is being drilled by the testing of drill cuttings with a modified NCB cone indenter.

It is also recommended that a laboratory investigation should be performed to compare the permeability of a granular material which has been infiltrated by mud under pressure with that of the solid rock. If further research indicates that the yield zone is in fact a zone of reduced permeability, then this may have implications on the manner that the 'skin' or 'damaged region' surrounding a well is assessed

One possible area of error when applying the yield zone approach is in the estimation of the 'f' factor by which to reduce the laboratory value of uniaxial compressive strength to obtain a realistic in-situ value. Further investigation into the difference between the in-situ and laboratory strength is recommended.

In the examples given, the data points were often far apart and accordingly no direct conculsions could be made from the areas between the data points. To obtain a more detailed picture of the stability limits of a well, it is recommended that formation rock samples would be required to be taken at intervals of no more than 10 ft (3.05 m).

For the work presented in this thesis, the effect of mud on the mechanical properties was not considered. It is consequently proposed that research be conducted towards an analysis of the chemi-mechanical failure mechanism within the yield zone and to determine the deformation characteristics which would allow an estimation of the shape and size of the borehole.

The assumptions of plane strain may not be fully applicable in non-hydrostatic stress fields and although more complex, may warrent further analysis.

As regards the fracture conductivity/permeability testing, futher research is required to confirm a relationship between proppant embedment and Brinell hardness. It is also recommended that the proppant data-base be extended to examine the properties of a wider

variety of proppants. The conductivity/permeability data presented in this work were those of short-term tests performed at ambient temperatures. It is therefore recommended that a more rigorous examination of time dependency should be conducted and the equipment modified to enable the current tests to be performed at temperatures up to 250 °F.

A testing programme should be performed to investigate the effect of varying the closure stress (axial load) to confining pressure ratio on the reduction of proppant porosity as measured by the fracture porosimeter. It is also suggested that 1.5 inch diameter core samples should be tested in place of the one inch diameter plugs. This would provide a greater surface contact area with the rock-proppant system.

Permeability reduction due to gel residue and fluid loss additive could be investigated by modifying the linear flow cell to accommodate reservoir rock plattens and the transverse measurement of permeability. Alternatively, a re-configuration of the fracture porosimeter would allow these effects to be studied.

REFERENCES

REFERENCES

[1] Timoshenko, S. P. and Goodier, J. N, 'Theory of Elasticity', 2nd Edition, (1951), New York, McGraw-Hill.

[2] Terzaghi, K. Van., 'Theoretical Soil Mechanics', New York, Wiley

[3] Handin, J. Hager, R. V., Friedman, M. and Feather, J.N, 'Experimental Deformation of Sedimentary Rocks Under Confining Pressure : Pore Pressure Tests', (1963), Bull. Am. Ass. Petrol. Geol., 47, pp.717-55.

[4] Jaeger, J. C. and Cook, N. G. W., 'Fundamentals of Rock Mechanics', 2nd Edition, Chapman and Hall, London, (1976).

[5] Wilson, A. H., 'The Stability of Underground Workings in the Soft Rocks of the Coal Measures', PhD Thesis, Univ. of Nottingham, (1980).

[6] Hubbert, M. K. and Willis, D. G., 'Mechanics of Hydraulic Fracturing', Trans., AIME (1957) Vol. 210, pp.153-168.

[7] Whittaker, A., 'Theory and Evaluation of Formation Pressures', EXLOG Series of Petroleum Geology and Engineering Handbooks, Reidel Publishing Company, (1985).

[8] Bradley, W. B. 'An Analysis of Borehole Stability Problems

Near Salt Domes', Technical Progress Report BRC-EP 2-75-P, Shell Development Company.

[9] Fergison, A., Lecture Notes, (1984), Dept. of Min. Res. Eng., Univ. of Strathclyde.

[10] NSI Technologies Inc, 'Hydraulic Fracturing', 1st Edition, (January 1987)

[11] Teufel, L. W., 'In-Situ Stress Measurements in Inclined Holes in the North Sea: Application to Water flooding and Enhanced Oil Recovery', paper SPE 13986/1 presented at Offshore Europe 1985, Aberdeen.

[12] Fertl, W. H., 'Abnormal Formation Pressures', Elsevier Press, (1973).

[13] Obert, L. and Duvall, W. I., 'Rock Mechanics and the Design of Structures in Rock', John Wiley, London, (1967).

[14] Franklin, J. A., 'Triaxial Strength of Rock Materials',Rock Mech., Vol. 3, (1971), pp.86-98.

[15] Coulomb, C. A., (1773), Information extracted from Ref. [4].

[16] Mohr, O., (1900), Information extracted from Ref. [4].

[17] Griffith, A. A., 'Theory of Rupture', Proc. 1st Int. Congr.

App. Mech., Delft, (1924), pp.163-198.

[18] Coates, D. F., 'Rock Mechanics Principles', Monograph No. 874 (Revised 1967), Mines Branch Dept. of Energy, Mines and Resources, Canada.

[19] McLintock, F. A. and Walsh, J. B., 'Friction on Griffith Cracks in Rocks Under Pressure', Proc. 4th U.S. Congr. Appl. Mech., Am. Soc. Mech. Engrs., New York, (1963), pp.1015-1021.

[20] Murrell, S. A. F., 'A Criterion for Brittle Fracture of Rocks and Concrete Under Triaxial Stress and the Effect of Pore Pressure on the Criterion', Proc. 5th Rock Mech. Symposium, Univ. of Minnesota:- see Fairhurst, C., 'Rock Mechanics', Oxford, Pergamon, pp.563-77.

[21] Nadai, A, 'Theory of Flow and Fracture of Solids', McGraw-Hill, New York, Vol. 1, 1950, Vol. 2, (1963).

[22] Carr, P. A., 'Investigations of Deformation Processes Around Mine Excavations With Special Reference to Strata Chatacteristics', PhD Thesis, Univ. College, Cardiff, (1982).

[23] Westergaard, H. M, 'Plastic State of Stress around a Deep Well', J. Boston Soc. Civil Engrs, Vol. 27, pp.1-5.

[24] Biot, M. A., 'General Theory of Three-Dimensional Consolidation', J. Appl. Phys., (Feb. 1941), Vol. 12, pp.144-64.

[25] Pasley, P. R. and Cheatham, J. B., 'Rock Stresses Induced by Flow of Fluids into Boreholes', Soc. Pet. Eng. J., (March 1963), pp.85-94.

[26] Mahtab, M. A. and Goodman, R. E., 'Stresses Around Wellbores in Nonlinear Rock', Soc. Pet. Eng. J., (Sept. 1968), pp.304-312.

[27] Miles, A. J. and Topping, A. D., 'Stresses Around a Deep Well', Trans., AIME (1949), Vol. 179, pp.186-191.

[28] Galle, E, M. and Wilhoit, J. C., 'Stresses Around a Wellbore Due to Internal Pressure and Unequal Principal Geostatic Gradients', Soc. Pet. Eng. J., (June 1962), pp.145-155.

[29] Word, H. S. and Wilhoit, J. C, ' Photoelastic Analysis of the Stresses Around the Bottom of a Cylindrical Borehole Due to Overburden and Fluid Column Pressure', Proc. SESA, (1960), Vol. XVII, No.2

[30] Gnirk, P., 'The Mechanical Behaviour of Uncased Well bores Situated in Elastic/Plastic Media Under Hydrostatic Stress', Soc. Pet. Eng. J., (Feb. 1972), pp.49-59.

[31] Bradley, W. B., 'Failure of Inclined Boreholes', J. Energy Resources Tech., (Dec. 1979), pp.233-39, Trans., ASME, 101.

[32] Fairhurst, C., 'Methods of Determining In-Situ Rock Stresses at Great Depth', TRI-68, Missouri River Div., Corps of Engineer, (Feb. 1968).

[33] Bradley, W. B., 'Borehole Failure Near Salt Domes', Oil and Gas J., (April 1979), pp.125-136.

[34] Geertsma, J., 'Some Rock-Mechanical Aspects of Oil and Gas Well Completion', paper EUR 38 presented at the European Offshore Petroleum Conference and Exhibition, London, Oct. 24-27, (1978).

[35] Van der Vlis, A. C., 'Rock Classification by a Simple Hardness Test', Proc. 2nd Congr. Intl. Soc. for Rock Mechanics, Belgrade (1970), pp.1-8.

[36] Risnes, R., Bratli, R. K. and Horsrud, P., 'Sand Stresses Around a Wellbore', Soc. Pet. Eng. J., (Dec. 1982), pp. 883-94, Trans., AIME, 273.

[37] Bratli, R. K. and Rinses, R., 'Stability and Failure of Sand Arches', Soc. Pet Eng. J., (April 1981), pp. 236-248.

[38] Brandis, S. C. and Barton, N., 'Failure Modes of Deep Boreholes', 27th U.S. Symposium on Rock Mechanics, Alabama, (June 1986), pp.599-604.

[39] Infante, E. F. and Chenevert, M. E., 'Stability of Boreholes

Drilled Through Salt Formations Displaying Plastic Behaviour', SPE paper 15513, presented at the 61st Annual SPE Techvnical Conference and Exhibition, New Orleans, Oct. 5-6, (1986).

[40] Tixier, M. P. Loveless, G. W., and Anderson, R. A., 'Estimation of Formation Strength Based on the Mechanical Properties Log', (1973), SPE Reprint Series - Well Completions, No. 5a, Vol. II, pp. 103-113.

[41] Edwards, D., 'Mechanical Properties and its Applications', Schlumberger Technical Services Inc., Europe Unit, Interpretation Development, (Dec. 1985).

[42] Darley, H. C. H., 'A Laboratory Investigation of Borehole Stability', J. Pet. Tech., (July 1969), pp.883-892.

[43] Chenevert, M. E., 'Shale Control With Balanced Activity Oil Muds', J. Pet. Tech., (Oct. 1970), pp.1309-1316.

[44] Simpson, J., 'Drilling Fluids - Today and Tomorrow', J. Pet. Tech., (Nov. 1971), pp.1294-1298.

[45] Dempster, F. M., 'Borehole Instability in Relation to Clay Minerals - A Review', MSc thesis, (Aug. 1986), Univ. of Strathclyde.

[46] Fertl, W. H., 'Predicting Fracture Pressure Gradients for More Efficient Drilling', Engineering Essentials of Modern

Drilling, Energy Publications, Dallas, (1977), pp.76-79.

[47] Clark, J. B., 'A Hydraulic Process for Increasing the Productivity of Wells', Trans., AIME (1949), Vol. 186.

[48] Howard, G. C. and Fast, C. R., 'Hydraulic Fracturing', Monograph Series, SPE-AIME, Dallas, (1970).

[49] 'Well Stimulation', Shell Science and Technology, Issue No. 2, (Aug. 1984).

[50] Matthews, W .R. and Kelly, J., 'How to Predict Formation Pressure and Fracture Gradient', Oil and Gas J., (1968), 65(8), pp.92-106.

[51] Eaton, B. A., 'Fracture Gradient Prediction and its Application in Oilfield Operations', J. Pet. Tech., (Oct 1969), pp.1353-1360.

[52] Macpherson, L. A. and Berry, L. N., 'Prediction of Fracture Gradients from Log Derived Elastic Moduli', Log Analyst, (1972), 13(5), pp.12-29.

[53] Haimson, B. and Fairhurst, C., 'Initiation and Extension of Hydraulic Fractures in Rocks', Soc. Pet. Eng. J., (1967), pp.310-318.

[54] Medlin, W. L. and Masse, L., 'Laboratory Investigation of

Fracture Initiation Pressure and Orientation', Soc. Pet. Eng. J., Vol. 19, (1979), pp.129-144.

[55] Horsrud, P., Rinses, R. and Bratli, R. K., 'Fracture Initiation Pressures in Permeable Poorly Consolidated Sands', Int. J. Rock Mech. Min. Sci. and Geomech. Abstr., Vol. 19, (1982), pp.255-266.

[56] Daines, S. R., 'Prediction of Fracture Pressures for Wildcat Wells', j. Pet. Tech., (April 1982), pp.863-872

[57] Dowell Schlumberger, 'Proppant Selection Guide'.

[58] McLennan, J. D. and Roegiers, J. C., 'How Instanteaeous are Instantaneous Shut-In Pressures', paper SPE 11064, Annual Technical Conference and Exhibition, New Orleans, (Sept. 1982), pp.26-29.

[59] Coker, L. N. G. and Filon, E. G., 'A Treatise on Photoelasticity', 2nd Edition, 1957, Cambridge University Press, London.

[60] Frocht, M. M. and Guernsey, R., 'Studies in Three-Dimensional Photoelasticity - The Application of the Shear Difference to the General Space Problem', Proc. 1st U.S. Nat. Congr. of App. Mech., (Dec. 1952).

[61] Hendry, A. W., 'Photoelastic Analysis', Pergamon Press, (1974).

[62] Kuske, A. and Robertson, G., 'Photoelastic Stress Analysis', John Wiley and Sons Inc., New York, (1974).

[63] Frocht, M. M., 'Photoelsticity', Vol. 1, (1941), John Wiley and Sons Inc., New York.

[64] Sharples Bulletin No. 5, 'Isoclinics and Stress Trajectories'

[65] Sharples Bulletin No. 9, 'The Tardy Method of Compensation'

[66] Leven, M. M., 'Quantitative Three-Dimensional Photoelasticity', Proc. Soc. Exp. Stress Analysis, Vol. 2, (Sept. 1954), pp.157-171.

[67] Srinath, L. S. 'Photoelastic Compensators', Proc. Soc. Exp. Stress Anal., Annual Meeting, (Dec 1959).,

[68] Frocht, M. M. and Guernsey, R., 'Further Work on the General Three-Dimensional Photoelastic Problem', J. App. Mech., Vol. 22, (June 1955).

[69] Weller, R., 'A New Method for Photoelasticity in Three-Dimensions', J. App. Phys., Vol. 10, No. 4, (April 1939).

[70] Jessop, H. T., 'The Scattered Light Method of Exploration of Stresses in Two- and Three-Dimensional models', Brit. J. App. Phys., Vol. 2, (Sept. 1951).

[71] Srinath, L. S., 'Scattered Light in Photoelastic Analysis, Basic Equipments and Techniques', 4th Nat. Congr. of App. Mech., (1962).

[72] Davies, D. O. D., 'An Application of Photoelasticity as a Modelling Technique to Some Mining Situations', PhD Thesis (1976), Univ. of Strathclyde.

[73] Filon, E.G., Information extracted from ref [62]

[74] Drucker, D. C., 'Photoelatic Separation of Principal Stresses by Oblique Incidence', J. App. Mech., ASME, Vol. 10, No. 3, Sept. (1963), pp.A156-60.

[75] Frocht, M. M., 'Photoelsticity', Vol. 2, John Wiley and Sons Inc, New York, (1948).

[76] Frocht, M. M. and Sevin, E., 'Isopachic Patterns and Principlal Stresses in Bars With Deep Notches in Tension', Proc. Soc. Exp. Stress Anal., Annual Meeting, (Dec 1949).

[77] Jessop, H. T. and Harris, F. C., 'Photoelasticity, Principles and Methods', Cleaver-Hume Press, London, (1949).

[78] Karim, A. W., 'Photoelastic Investigations into the Interface Stress Distribution in Relation to Mine Pillar Design Using the Method of Stress Freezing', PhD Thesis, (1981), Univ. of

Strathclyde.

[79] Ciba-Geigy, Instruction Sheet No. C1, (Sept. 1974).

[80] Davies, D. O. D., Senior Lecturer, Dept. Min. Res. Eng., Univ. of Strathclyde:- Personal Communication.

[81] MFC Survival Ltd, Tonnypandy, Wales:- Personal Communication.

[82] Mohs, (1824), Information extracted from 'A Dictionary of Geology', Penguin Reference Books, (1976), pp.222.

[83] NCB Cone Indenter - MRDE Handbook, No. 5, (1977)

[84] Szlavin, J., 'Relationships Between Some Physical Properties of Rock Determined by Laboratory Tests', Int. J. Rock Mech. Min. Sci., (1975), Vol. 11, pp.57-66.

[85] Coates, D. F., 'Classification of Rocks for Rock Mechanics', Int. J. Rock Mech. Min. Sci., (1964), Vol. 1, pp.421.

[86] Brinell, 'Methods of Testing Steel', Inter Assoc. Test Mat. Proc., Vol. 2, (1901), pp.81.

[87] Huitt, J. L. and McGlothlin, B. B., 'The Propping of Fractures in Formations Suscepible to Propping-Sand Embedment', Drill. and Prod. Practice, (1958), pp.115-121.

[88] Hawkes, I. and Mellor, M., 'Uniaxial Testing on Rock Mechanics Laboratories', Eng. Geol. Vol 4, (1968), pp.A22-A26.

[89] I.S.R.M. 'Committee on Laboratory Testing: Suggested Methods of Determining the Uniaxial Compressive Strength of Rock Materials and Point Load Index', Document No. 1, pp.12.

[90] Joseph, K., 'The Effect of Stress ans Saturation on the Time Taken for Ultrasonic Waves to Travel Through Various Sandstones', MSc Thsis, (1986), Dept. Min. Res. Eng., Univ. of Strathclyde.

[91] Airey, E. M., 'A Study of Yield Zones Around Roadways', NCB Final Report on ECSC Research Project 6220 - AB/8/802, (1977)

[92] Panek, L. A., 'Calculation of the Average Ground Stress Components From Measurements of the Diameteral Deformation of a Drill Hole', Bureau of Mines Report of Investigations, No. 6732, U.S. Dept. of Interior, (1966), pp.22.

[93] Wilson, A. H., 'A Method of Estimating th Closure and Strength of Lining Required in Drivages Surrounded by a Yield Zone', Int. J. Rock Mech. Min. Sci., Vol. 17, (1980), pp.349-355.

[94] Whittaker, B. N., 'Stability Aspects of Major Coal Mining Tunnel Projects', in 'Design and Performance of Underground Excavations', ISRM/BGS, Cambridge, (1984), pp.461-470.

[95] Hobbs, D. W., 'The Behaviour of Broken Rock Under Triaxial Compression', Int. J. Rock Mech. Min. Sci., Vol. 7, (1970), pp.125-148.

[96] Duncan Fama, M. E., 'A New Constitutive Equation for a Coulomb Material', in 'Design and Performance of Underground Excavations', ISRM/BGS, Cambridge (1984), pp.139-147.

[97] Gough, D.I. and Bell, J. S., 'Stress Orientations from Oil-Well Fractures in Alberta and Texas', Can. J. Earth Sci., Vol. 18, (1981), pp.638-645.

[98] Somerville, J. M., Lecturer, Dept. Min. Res. Eng., Univ. of Strathclyde:- Personal Communication.

[99] Dake, L. P., 'Fundamentals of Reservoir Engineering', Developments in Petroleum Science, No. 8, Elsevier Scientific Publishing Company, (1978), pp148.

[100] Scheidegger, A. E., 'The Physics of Flow Through Porous Media', 3rd Edition, (1974), Univ. of Toronto Press.

[101] Kozeny, J., 'Uber Kapillare Leitung des Wassers in Broden', Sitzungsber, Akad. Wiss, Wien., Vol. 136, (1927), pp.127. (Information extracted from Bear, J., 'Dynamics of Fluid in Porous Media', Elsevier Publishing Co., 1972.)

[102] Carmen, P. C., 'Permeability of Saturated Sands, Soils and

Clays', J. Agri. Sci., Vol. 29, pp.262.

[103] Darin, S. R. and Huitt, J. L., 'Effect of a Partial Monolayer of Propping Agent on Fracture Flow Capacity', Trans., AIME (1960), Vol. 219, pp.31-37.

[104] Wyllie, M. R. J. and Gregory, A. R., 'Fluid Flow Through Unconsolidated Porous Aggregates', Ind. and Eng. Chem., (1955), Vol. XLVII, pp.1379.

[105] Steanson, R. E., Elbel, J. L. and Wendorff, C. L., 'How to Select a Propping Agent for Hydraulic Fracturing Treatments', Pet. Eng. Int., (July 1979).

[106] American Petroleum Institute, 'API RP56, Recommended Practices for Testing Sand Used in Hydraulic Fracturing Operations', First Edition, (1983).

[107] Western Petroleum Services, 'Proppants', 2nd Edition, (1984).

[108] Cooke, C. E., 'Conductivity of Fracture Proppants in Multiple Layers', J. Pet. Tech., (Sept. 1973), pp.1101-1107.

[109] Cooke, C. E., 'Effect of Fracturing Fluids on Fracture Conductivity', J. Pet. Tech., (Oct. 1975), pp.1273-1282.

[110] Cooke, C. E., 'Fracturing With a High Strength Proppant', J. Pet. Tech., (Oct. 1977), pp.1222-1226.

[111] Cutler, R. A., Enniss, D. O., Jones, A. H. and Carroll, H. B., 'Comparison of the Fracture Conductivity of Commercially Available and Experimental Proppants at Intermeadiate and High Closure Stresses', Soc. Pet. Eng. J., (April 1985).

[112] Brown, W. E. and Much, M. G., 'An Evaluation of Four Commonly Used Proppants', Norton-Alcoa Conference Summary, (Feb. 1986).

[113] Brown, W. E. and Much, M. G., 'Performance of Proppants Under Simulated Downhole Conditions - Stress Corrosion Effects', Norton-Alcoa Proppants, Dallas, (June 1986).

[114] McDaniel, B. W., 'Conductivity Testing of Proppants at High Temperatures and Stress', SPE paper 15067, presented at Society of Petroleum Engineers California Regional Meeting, Oakland, California, (April 1986).

[115] Wendorff, C. L., 'Fracture Porosimeter - A New Tool for Determining Fracture Conductivity under Downhole Stress', SPE paper 10963, presented at 57th Annual SPE Technical Conference and Exhibition, New Orleans, (Sept. 1982).

[116] Grant, L. E., 'Conductivity Measurements of Simulated Propped Fractures Using a Gas Permeameter', BSc Thesis, (1986), Dept. Min. Res. Eng., Univ. of Strathclyde.

[117] Edinburgh Petroleum Development Services, 'Nitrogen Gas

Permeameter Operation Manual'.

[118] Zambonini, M., 'Determination of Absolute Permeability Under Conditions of Triaxial Stress', MSc Thesis, (1983), Dept. Min. Res. Eng., Univ. of Strathclyde.

[119] Much, M. G., 'Proppant Evaluation Test Improved', Oil and Gas Report, Oil and Gas J., (April 1987), pp.33-36.

[120] Abdullah, A. A., 'An Investigation into the Effect of Confining Pressure and Temperature on Single-Phase and Two-Phase Flow Properties of Sandstone and Limestone Reservoir Rocks', PhD Thesis, (1978), Univ. of Strathclyde.

[121] Al-Fattal, H .M. A., 'An Investigation into the effect of Stress on Directional Rock Permeability', MSc Thesis, (1977), Dept. Min. Res. Eng., Univ. of Strathclyde.

[122] Shell International Petroleum Company Ltd., 'Technical Data on Shell Tellus Oils', (1967).

[123] Muskat, M., 'Physical Principles of Oil Production', (1949), McGraw-Hill.

[124] Hair, A. C., 'A Measuring System to Determine Absolute Permeability of Reservoir Rocks Under Triaxial Stress Conditions', BSc Thesis, (1985), Dept. Min. Res. Eng., Univ. of Strathclyde.

[125] Thomas, T. C. P. N., 'An Investigation into the Variation of Absolute Permeability of Sandstone Cores with Applied Stress', MSc Thesis, (1984), Dept. Min. Res. Eng., Univ. of Strathclyde.

[126] Smart, B. G. D. and MacGregor, K. W., 'Conductivity and Permeabity Tests on Two Colorado Silicsa Sand Proppants', (1987), Dept. Min. Res. Eng., Univ. of Strathclyde.

[127] Smart, B. G. D. and MacGregor, K. W., 'Measurement of Hydraulic Fracture Conductivity', Final Report to Britoil plc., (June 1987), Dept. Min. Res. Eng., Univ. of Strathclyde.

APPENDIX 1

PROPPANT DATA-BASE

PERMEABILITY AND WETTED SURFACE AREA RESULTS

FOR

20/40 SINTERED BAUXITE (Norton)

20/40 SAND (Colorado Silica Sand UK)

20/40 INTERPROP I (Norton)

API RP56 Roundness & Sphericity Test

Proppant Type : 20/40 Sintered Bauxite
Supplier : Norton

Test Centre : University of Strathclyde
Department of Mining & Petroleum Engineering

Sample Photograph

Grain	Roundness	Sphericity	Grain	Roundness	Sphericity
1	.8	.8	11	.8	.8
2	.8	.8	12	.8	.8
3	.9	.9	13	.8	.8
4	.8	.8	14	.9	.8
5	.8	.8	15	.8	.8
6	.7	.8	16	.8	.7
7	.7	.7	17	.9	.7
8	.7	.8	18	.8	.8
9	.9	.8	19	.7	.7
10	.7	.8	20	.8	.7

Average Roundness : .80 (API Minimum : 0.7)
Sphericity : .78 (API Minimum : 0.7)

LINEAR FLOW CELL TEST RESULTS

Proppant Type : 20/40 Sintered Bauxite
Supplier : Norton
Reference No : Baux20/40-1

TEST CONDITIONS

Test Cell Type : 10 sq.in. Linear Flow Cell (API Spec.)
Proppant Concentration : 2 lbs/sq.ft.
Proppant Grain Density : 3.640 g/cc
Test Fluid Type : Shell Tellus No. 10
Fracture Width @ 1000 psi : 4.470 mm (.1760 in)

DATA INPUT : Test Number 1 of 2

Closure Stress (psi)	Differential Pressure A-B	B-C	A-C	Volumetric Flow Rate A-B	B-C	A-C	Average Temp.	LVDT Value
1000	22.59	24.52	46.50	7.12	7.20	7.00	23.44	435
2000	23.78	25.12	46.00	6.05	6.25	6.00	23.60	408
4000	20.12	21.95	38.60	5.05	4.85	4.52	23.73	378
6000	23.95	25.85	45.12	5.25	5.05	4.96	23.83	358
8000	29.25	30.51	56.25	5.89	5.95	5.76	23.87	336
10000	33.12	36.52	64.02	6.09	5.88	5.75	23.95	319
12000	40.22	47.23	80.10	7.12	7.00	6.45	24.04	294
14000	43.12	48.52	97.02	7.45	7.12	7.51	24.21	280
15000	45.12	51.25	98.00	7.41	7.18	7.15	24.31	269

RESULTS OUTPUT : Test Number 1 of 2

Closure Stress (psi)	Wetted Surface Area A-B	B-C	A-C	Flow-Cell Permeability A-B	B-C	A-C	Frac. Width	Porosity (%)
1000	273.1	282.9	279.4	311.8	290.4	297.8	.1760	39.91
2000	290.1	293.4	286.5	252.7	247.1	259.1	.1736	39.10
4000	277.0	295.2	286.8	251.1	221.0	234.3	.1711	38.20
6000	288.1	305.2	287.7	219.8	195.8	220.4	.1698	37.71
8000	286.8	291.5	284.4	203.8	197.4	207.3	.1677	36.96
10000	279.1	298.2	282.4	188.7	165.2	184.3	.1647	35.80
12000	265.9	290.5	278.7	183.7	153.8	167.1	.1620	34.73
14000	274.0	297.4	289.5	177.0	150.4	158.6	.1625	34.94
15000	273.2	295.7	289.8	168.6	143.8	149.8	.1613	34.46

UNITS : Differential Pressure (mbar) Wetted Surface Area (in^2/in^3)
Volumetric Flow Rate (cc/min) Flow Cell Permeability (Darcy)
Fluid Temperature (Celcius) Fracture Width (in)

LINEAR FLOW CELL TEST RESULTS

Proppant Type : 20/40 Sintered Bauxite
Supplier : Norton
Reference No : Baux20/40-2

TEST CONDITIONS

Test Cell Type : 10 sq.in. Linear Flow Cell (API Spec.)
Proppant Concentration : 2 lbs/sq.ft.
Proppant Grain Density : 3.640 g/cc
Test Fluid Type : Shell Tellus No. 10
Fracture Width @ 1000 psi : 4.510 mm (.1776 in)

DATA INPUT : Test Number 2 of 2

Closure Stress (psi)	Differential Pressure A-B	B-C	A-C	Volumetric Flow-Rate A-B	B-C	A-C	Average Temp.	LVDT Value
1000	24.62	25.08	49.52	7.48	7.52	7.80	23.24	504
2000	26.25	27.25	54.25	7.51	7.40	7.30	23.40	480
4000	24.12	25.25	50.12	5.54	5.91	5.94	23.84	452
6000	24.25	28.25	54.25	5.50	5.92	5.78	24.23	430
8000	32.00	35.25	69.25	5.94	6.22	6.28	24.43	409
10000	33.20	35.58	68.59	5.48	5.50	5.41	24.46	378
12000	40.20	42.25	94.25	6.08	6.40	6.40	24.47	355
14000	44.10	47.58	98.58	6.68	6.20	6.16	24.64	332
15000	46.25	51.25	98.25	6.35	6.35	6.25	24.83	320

RESULTS OUTPUT : Test Number 2 of 2

Closure Stress (psi)	Wetted Surface Area A-B	B-C	A-C	Flow-Cell Permeability A-B	B-C	A-C	Frac. Width	Porosity (%)
1000	285.8	287.7	280.7	301.4	297.4	312.5	.1776	40.45
2000	284.6	292.1	293.4	284.1	269.7	267.2	.1757	39.82
4000	306.7	303.8	301.9	225.1	229.4	232.3	.1735	39.06
6000	300.6	312.7	310.1	219.6	202.9	206.3	.1718	38.46
8000	320.2	328.4	323.9	179.6	170.7	175.5	.1700	37.79
10000	298.0	307.9	304.8	164.7	154.2	157.4	.1646	35.76
12000	292.9	292.7	309.1	153.0	153.2	137.4	.1622	34.83
14000	286.2	308.6	315.1	152.7	131.4	126.0	.1612	34.42
15000	291.3	306.6	302.6	138.1	124.7	128.0	.1599	33.87

UNITS : Differential Pressure (mbar) Wetted Surface Area (in^2/in^3)
Volumetric Flow Rate (cc/min) Flow Cell Permeability (Darcy)
Fluid Temperature (Celcius) Fracture Width (in)

LINEAR FLOW CELL TEST RESULTS

Proppant Type : 20/40 Sintered Bauxite
Supplier : Norton
Reference No : Baux20/40-AVE

TEST CONDITIONS

Test Cell Type : 10 sq.in. Linear Flow Cell (API Spec.)
Proppant Concentration : 2 lbs/sq.ft.
Proppant Grain Density : 3.640 g/cc
Test Fluid Type : Shell Tellus No. 10
Fracture Width @ 1000 psi : 4.490 mm (.1768 in)

DATA INPUT : Average of 2 Tests

Closure Stress (psi)	Differential Pressure A-B	B-C	A-C	Volumetric Flow-Rate A-B	B-C	A-C	Average Temp.	LVDT Value
1000	23.61	24.80	48.01	7.30	7.36	7.40	23.34	470
2000	25.02	26.19	50.13	6.78	6.83	6.65	23.50	444
4000	22.12	23.60	44.36	5.30	5.38	5.23	23.79	415
6000	24.10	27.05	49.69	5.38	5.49	5.37	24.03	394
8000	30.63	32.88	62.75	5.92	6.09	6.02	24.15	373
10000	33.16	36.05	66.31	5.79	5.69	5.58	24.21	349
12000	40.21	44.74	87.18	6.60	6.70	6.43	24.26	325
14000	43.61	48.05	97.80	7.07	6.66	6.84	24.43	306
15000	45.69	51.25	98.13	6.88	6.77	6.70	24.57	295

RESULTS OUTPUT : Average of 2 Tests

Closure Stress (psi)	Wetted Surface Area A-B	B-C	A-C	Flow-Cell Permeability A-B	B-C	A-C	Frac. Width	Porosity (%)
1000	279.5	285.3	279.9	306.3	294.0	305.3	.1768	40.18
2000	286.7	292.4	289.8	269.2	258.8	263.5	.1747	39.46
4000	292.0	299.2	294.2	237.0	225.7	233.5	.1723	38.63
6000	294.3	308.7	298.9	219.7	199.7	212.9	.1708	38.09
8000	303.3	309.8	304.3	191.1	183.1	189.9	.1689	37.38
10000	288.2	303.0	293.4	176.5	159.7	170.3	.1647	35.78
12000	278.6	291.7	294.0	168.2	153.4	151.0	.1621	34.78
14000	279.9	302.6	301.3	164.7	140.9	142.1	.1619	34.68
15000	281.7	300.9	295.8	153.0	134.1	138.8	.1606	34.16

UNITS : Differential Pressure (mbar) Wetted Surface Area (in^2/in^3)
Volumetric Flow Rate (cc/min) Flow Cell Permeability (Darcy)
Fluid Temperature (Celcius) Fracture Width (in)

API RP56 Roundness & Sphericity Test
==========

Proppant Type : 20/40 Sand
Supplier : Colorado Silica Sand UK

Test Centre : University of Strathclyde
Department of Mining & Petroleum Engineering

Sample Photograph
==========

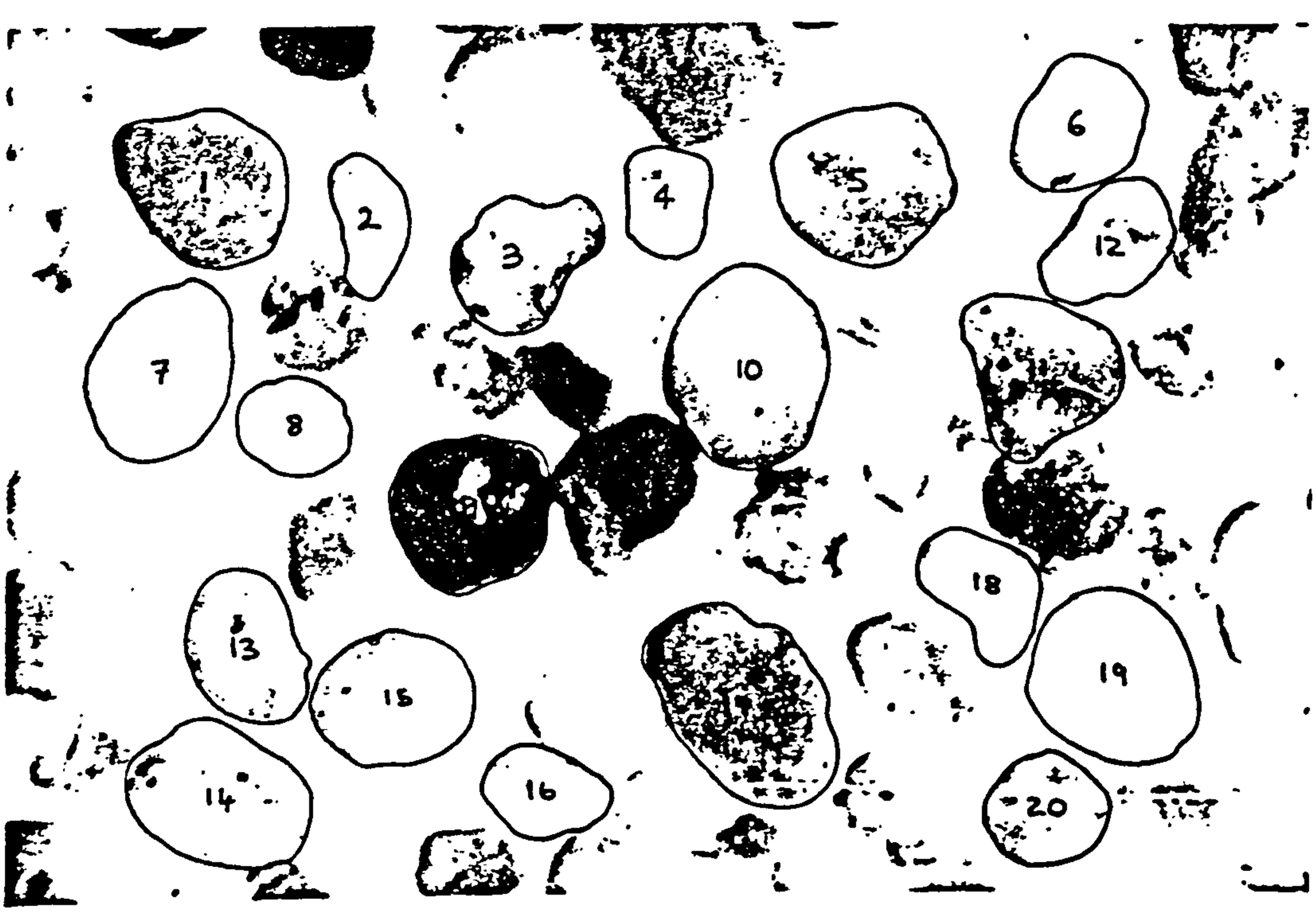

Grain	Roundness	Sphericity	Grain	Roundness	Sphericity
1	.7	.7	11	.7	.5
2	.7	.4	12	.7	.6
3	.6	.6	13	.7	.7
4	.7	.7	14	.7	.6
5	.7	.8	15	.7	.7
6	.7	.7	16	.7	.7
7	.7	.7	17	.7	.6
8	.8	.8	18	.6	.6
9	.7	.9	19	.7	.8
10	.8	.8	20	.7	.9

Average Roundness : .70 (API RP56 Minimum : 0.6)
Sphericity : .69 (API RP56 Minimum : 0.6)

LINEAR FLOW CELL TEST RESULTS

Proppant Type : 20/40 Sand (old sample)
Supplier : Colorado Silica Sand
Reference No : Co120/40-1

TEST CONDITIONS

Test Cell Type : 10 sq.in. Linear Flow Cell (API Spec.)
Proppant Concentration : 2 lbs/sq.ft.
Proppant Grain Density : 2.640 g/cc
Test Fluid Type : Shell Tellus No. 10
Fracture Width @ 1000 psi : 6.040 mm (.2378 in)

DATA INPUT : Test Number 1 of 2

Closure Stress (psi)	Differential Pressure A-B	B-C	A-C	Volumetric Flow Rate A-B	B-C	A-C	Average Temp.	LVDT Value
1000	50.20	46.98	81.56	6.85	6.08	5.30	25.98	504
2000	61.13	80.50	146.25	8.54	8.64	8.90	26.72	484
4000	75.02	117.55	187.20	9.48	10.00	9.70	26.70	451
6000	129.25	168.25	298.56	9.56	9.00	9.64	27.30	400
8000	98.88	138.98	218.50	3.76	3.48	3.58	27.85	345
10000	107.25	375.23	455.20	3.20	5.60	5.02	28.86	302
12000	*****	*****	*****	*****	*****	*****	*****	***
14000	*****	*****	*****	*****	*****	*****	*****	***
15000	*****	*****	*****	*****	*****	*****	*****	***

RESULTS OUTPUT : Test Number 1 of 2

Closure Stress (psi)	Wetted Surface Area A-B	B-C	A-C	Flow-Cell Permeability A-B	B-C	A-C	Frac. Width	Porosity (%)
1000	484.1	497.1	496.0	86.8	82.3	82.6	.2378	38.69
2000	478.4	545.8	512.5	85.9	66.0	74.8	.2366	38.38
4000	477.8	582.3	527.6	78.8	53.0	64.6	.2336	37.58
6000	564.4	663.7	604.0	46.0	33.3	40.2	.2270	35.78
8000	689.0	849.1	742.3	23.8	15.7	20.5	.2195	33.56
10000	680.0	961.5	790.9	18.4	9.2	13.6	.2121	31.24
12000	*****	*****	*****	*****	*****	*****	*****	*****
14000	*****	*****	*****	*****	*****	*****	*****	*****
15000	*****	*****	*****	*****	*****	*****	*****	*****

UNITS : Differential Pressure (mbar) Wetted Surface Area (in^2/in^3)
Volumetric Flow Rate (cc/min) Flow Cell Permeability (Darcy)
Fluid Temperature (Celcius) Fracture Width (in)

LINEAR FLOW CELL TEST RESULTS

Proppant Type : 20/40 Sand (old sample)
Supplier : Colorado Silica Sand
Reference No : Co120/40-2

TEST CONDITIONS

Test Cell Type : 10 sq.in. Linear Flow Cell (API Spec.)
Proppant Concentration : 2 lbs/sq.ft.
Proppant Grain Density : 2.640 g/cc
Test Fluid Type : Shell Tellus No. 10
Fracture Width @ 1000 psi : 6.150 mm (.2421 in)

DATA INPUT : Test Number 2 of 2

Closure Stress (psi)	Differential Pressure A-B	B-C	A-C	Volumetric Flow-Rate A-B	B-C	A-C	Average Temp.	LVDT Value
1000	32.90	28.88	60.07	8.88	8.36	9.04	26.01	723
2000	33.12	32.50	63.13	8.00	8.00	8.00	26.43	690
4000	66.93	65.38	126.23	10.92	10.92	10.76	26.14	627
6000	89.60	116.46	213.12	9.44	8.16	8.40	26.47	562
8000	53.46	175.31	146.20	2.50	1.64	2.11	27.06	498
10000	75.26	186.23	256.56	1.04	1.11	1.23	27.12	461
12000	*****	*****	*****	*****	*****	*****	*****	***
14000	*****	*****	*****	*****	*****	*****	*****	***
15000	*****	*****	*****	*****	*****	*****	*****	***

RESULTS OUTPUT : Test Number 2 of 2

Closure Stress (psi)	Wetted Surface Area A-B	B-C	A-C	Flow-Cell Permeability A-B	B-C	A-C	Frac. Width	Porosity (%)
1000	369.1	356.4	349.5	168.3	180.5	187.6	.2421	39.78
2000	374.0	370.5	365.1	149.4	152.2	156.8	.2388	38.94
4000	394.0	389.5	385.5	106.0	108.5	110.8	.2307	36.80
6000	418.7	513.5	484.1	70.0	46.6	52.4	.2218	34.26
8000	527.1	1,178.6	670.5	31.4	6.3	19.4	.2127	31.45
10000	835.3	1,271.9	1,002.8	9.5	4.1	6.6	.2063	29.32
12000	*****	*****	*****	*****	*****	*****	*****	*****
14000	*****	*****	*****	*****	*****	*****	*****	*****
15000	*****	*****	*****	*****	*****	*****	*****	*****

UNITS : Differential Pressure (mbar) Wetted Surface Area (in^2/in^3)
Volumetric Flow Rate (cc/min) Flow Cell Permeability (Darcy)
Fluid Temperature (Celcius) Fracture Width (in)

LINEAR FLOW CELL TEST RESULTS

Proppant Type : 20/40 Sand (old sample)
Supplier : Colorado Silica Sand
Reference No : Col20/40-AVE

TEST CONDITIONS

Test Cell Type : 10 sq.in. Linear Flow Cell (API Spec.)
Proppant Concentration : 2 lbs/sq.ft.
Proppant Grain Density : 2.640 g/cc
Test Fluid Type : Shell Tellus No. 10
Fracture Width @ 1000 psi : 6.095 mm (.2400 in)

DATA INPUT : Average of 2 Tests

Closure Stress (psi)	Differential Pressure A-B	B-C	A-C	Volumetric Flow-Rate A-B	B-C	A-C	Average Temp.	LVDT Value
1000	41.55	37.93	70.82	7.87	7.22	7.17	26.00	614
2000	47.13	56.50	104.69	8.27	8.32	8.45	26.58	587
4000	70.98	91.47	156.72	10.20	10.46	10.23	26.42	539
6000	109.43	142.36	255.84	9.50	8.58	9.02	26.89	481
8000	76.17	157.15	182.35	3.13	2.56	2.85	27.46	422
10000	91.26	280.73	355.88	2.12	3.36	3.13	27.99	382
12000	*****	*****	*****	*****	*****	*****	*****	***
14000	*****	*****	*****	*****	*****	*****	*****	***
15000	*****	*****	*****	*****	*****	*****	*****	***

RESULTS OUTPUT : Average of 2 Tests

Closure Stress (psi)	Wetted Surface Area A-B	B-C	A-C	Flow-Cell Permeability A-B	B-C	A-C	Frac. Width	Porosity (%)
1000	425.8	424.6	411.7	119.2	119.8	127.5	.2400	39.24
2000	432.8	472.5	451.3	108.2	90.8	99.5	.2377	38.66
4000	433.8	486.3	455.2	91.5	72.8	83.1	.2321	37.19
6000	490.7	588.9	544.4	55.8	38.7	45.3	.2244	35.03
8000	611.6	971.4	701.7	26.7	10.6	20.3	.2161	32.52
10000	705.9	984.3	811.9	15.2	7.8	11.5	.2092	30.30
12000	*****	*****	*****	*****	*****	*****	*****	*****
14000	*****	*****	*****	*****	*****	*****	*****	*****
15000	*****	*****	*****	*****	*****	*****	*****	*****

UNITS : Differential Pressure (mbar) Wetted Surface Area (in^2/in^3)
Volumetric Flow Rate (cc/min) Flow Cell Permeability (Darcy)
Fluid Temperature (Celcius) Fracture Width (in)

API RP56 Roundness & Sphericity Test

Proppant Type : 20/40 Interprop I
Supplier : Norton

Test Centre : University of Strathclyde
Department of Mining & Petroleum Engineering

Sample Photograph

Grain	Roundness	Sphericity	Grain	Roundness	Sphericity
1	.8	.8	11	.7	.8
2	.8	.9	12	.8	.8
3	.8	.8	13	.8	.9
4	.7	.7	14	.8	.8
5	.9	.9	15	.8	.7
6	.8	.8	16	.8	.8
7	.8	.9	17	.8	.9
8	.7	.7	18	.8	.7
9	.9	.9	19	.9	.9
10	.8	.8	20	.9	.8

Average Roundness : .81 (API Minimum : 0.7)
Sphericity : .82 (API Minimum : 0.7)

LINEAR FLOW CELL TEST RESULTS

Proppant Type : 20/40 Interprop I
Supplier : Norton
Reference No : INT20/40-1

TEST CONDITIONS

Test Cell Type : 10 sq.in. Linear Flow Cell (API Spec.)
Proppant Concentration : 2 lbs/sq.ft.
Proppant Grain Density : 3.120 g/cc
Test Fluid Type : Shell Tellus No. 10
Fracture Width @ 1000 psi : 5.140 mm (.2024 in)

DATA INPUT : Test Number 1 of 2

Closure Stress (psi)	Differential Pressure A-B	B-C	A-C	Volumetric Flow Rate A-B	B-C	A-C	Average Temp.	LVDT Value
1000	28.93	29.55	58.33	15.44	15.25	15.28	25.57	552
2000	28.80	30.32	58.91	13.90	14.05	14.10	25.57	537
4000	30.51	33.34	63.45	13.52	13.42	13.40	25.56	504
6000	33.18	38.60	71.14	12.52	12.70	12.68	25.56	466
8000	36.64	48.55	86.66	12.32	12.46	12.00	25.60	428
10000	48.53	64.92	114.23	11.96	11.62	11.62	25.61	385
12000	53.62	73.93	128.38	11.08	10.94	10.62	25.65	362
14000	76.58	110.54	187.20	11.24	11.22	10.65	25.74	339
15000	82.20	130.30	211.75	10.00	10.36	10.00	25.75	318

RESULTS OUTPUT : Test Number 1 of 2

Closure Stress (psi)	Wetted Surface Area A-B	B-C	A-C	Flow-Cell Permeability A-B	B-C	A-C	Frac. Width	Porosity (%)
1000	227.7	231.5	229.8	407.5	394.1	400.1	.2024	39.04
2000	241.7	246.7	242.7	367.6	353.0	364.6	.2029	39.19
4000	248.2	260.4	254.2	339.1	308.0	323.2	.2020	38.93
6000	248.5	266.2	255.7	294.7	256.9	278.4	.1980	37.69
8000	240.7	275.5	265.3	267.9	204.5	220.7	.1936	36.28
10000	248.6	291.7	273.6	202.1	146.8	166.8	.1881	34.40
12000	257.1	303.8	287.3	171.2	122.6	137.1	.1857	33.57
14000	289.8	348.5	329.1	122.5	84.7	94.9	.1835	32.78
15000	296.0	366.1	335.9	103.1	67.4	80.0	.1807	31.71

UNITS : Differential Pressure (mbar) Wetted Surface Area (in^2/in^3)
Volumetric Flow Rate (cc/min) Flow Cell Permeability (Darcy)
Fluid Temperature (Celcius) Fracture Width (in)

LINEAR FLOW CELL TEST RESULTS

Proppant Type : 20/40 Interprop I
Supplier : Norton
Reference No : INT20/40-2

TEST CONDITIONS

Test Cell Type : 10 sq.in. Linear Flow Cell (API Spec.)
Proppant Concentration : 2 lbs/sq.ft.
Proppant Grain Density : 3.120 g/cc
Test Fluid Type : Shell Tellus No. 10
Fracture Width @ 1000 psi : 5.190 mm (.2043 in)

DATA INPUT : Test Number 2 of 2

Closure Stress (psi)	Differential Pressure A-B	B-C	A-C	Volumetric Flow-Rate A-B	B-C	A-C	Average Temp.	LVDT Value
1000	26.15	26.70	53.25	12.01	12.08	12.24	24.90	684
2000	31.85	36.51	68.42	12.64	12.89	13.10	25.05	662
4000	36.05	40.15	76.74	12.64	13.08	12.94	25.25	628
6000	36.64	53.95	100.50	12.10	15.30	15.30	25.46	596
8000	49.78	57.80	100.05	14.40	14.52	14.24	25.45	566
10000	35.53	37.36	70.60	8.20	7.84	8.00	25.72	536
12000	45.23	50.20	114.25	9.28	8.84	10.36	25.82	502
14000	58.56	67.81	120.23	9.72	9.66	9.80	25.94	471
15000	63.89	78.95	138.52	9.16	9.18	9.25	26.05	452

RESULTS OUTPUT : Test Number 2 of 2

Closure Stress (psi)	Wetted Surface Area A-B	B-C	A-C	Flow-Cell Permeability A-B	B-C	A-C	Frac. Width	Porosity (%)
1000	250.1	252.0	250.0	360.2	354.8	360.5	.2043	39.62
2000	266.8	282.8	271.6	309.7	275.5	298.8	.2037	39.42
4000	280.0	290.5	285.5	272.0	252.7	261.6	.2026	39.12
6000	273.7	295.3	285.0	257.1	220.8	237.1	.1996	38.20
8000	275.1	295.2	277.3	228.8	198.7	225.2	.1966	37.25
10000	289.1	303.2	291.7	183.1	166.5	179.8	.1932	36.15
12000	280.1	302.3	297.9	165.5	142.1	146.3	.1890	34.73
14000	287.5	310.3	290.1	135.6	116.4	133.2	.1855	33.49
15000	291.5	323.7	302.1	118.0	95.7	110.0	.1830	32.57

UNITS : Differential Pressure (mbar) Wetted Surface Area (in^2/in^3)
Volumetric Flow Rate (cc/min) Flow Cell Permeability (Darcy)
Fluid Temperature (Celcius) Fracture Width (in)

LINEAR FLOW CELL TEST RESULTS

Proppant Type : 20/40 Interprop I
Supplier : Norton
Reference No : INT20/40-AVE

TEST CONDITIONS

Test Cell Type : 10 sq in Linear Flow Cell (API Spec.)
Proppant Concentration : 2 lbs/sq ft
Proppant Grain Density : 3.120 g/cc
Test Fluid Type : Shell Tellus No. 10
Fracture Width @ 1000 psi : 5.165 mm (.2033 in)

DATA INPUT : Average of 2 Tests

Closure Stress (psi)	Differential Pressure A-B	B-C	A-C	Volumetric Flow-Rate A-B	B-C	A-C	Average Temp.	LVDT Value
1000	27.54	28.13	55.79	13.73	13.67	13.76	25.24	618
2000	30.33	33.42	63.67	13.27	13.47	13.60	25.31	600
4000	33.28	36.75	70.10	13.08	13.25	13.17	25.41	566
6000	34.91	46.28	85.82	12.31	14.00	13.99	25.51	531
8000	43.21	53.18	93.36	13.36	13.49	13.12	25.53	497
10000	42.03	51.14	92.42	10.08	9.73	9.81	25.67	461
12000	49.43	62.07	121.32	10.18	9.89	10.49	25.74	432
14000	67.57	89.18	153.72	10.48	10.44	10.23	25.84	405
15000	73.05	104.63	175.14	9.58	9.77	9.63	25.90	385

RESULTS OUTPUT : Average of 2 Tests

Closure Stress (psi)	Wetted Surface Area A-B	B-C	A-C	Flow-Cell Permeability A-B	B-C	A-C	Frac. Width	Porosity (%)
1000	237.9	240.9	239.1	385.6	375.9	381.7	.2033	39.33
2000	254.0	264.6	257.0	337.4	310.8	329.4	.2033	39.31
4000	264.0	275.6	270.0	302.8	277.8	289.5	.2023	39.03
6000	261.0	281.7	271.4	275.0	235.9	254.2	.1988	37.94
8000	258.5	285.4	271.2	245.5	201.4	223.2	.1951	36.77
10000	267.6	300.5	284.4	193.4	153.4	171.2	.1906	35.29
12000	268.4	305.2	292.9	168.4	130.3	141.4	.1874	34.16
14000	289.6	333.4	312.7	128.0	96.6	109.8	.1845	33.13
15000	294.9	349.4	322.1	109.5	78.0	91.8	.1818	32.14

UNITS : Differential Pressure (mbar) Wetted Surface Area (in^2/in^3)
Volumetric Flow Rate (cc/min) Flow Cell Permeability (Darcy)
Fluid Temperature (Celcius) Fracture Width (in)

LINEAR FLOW CELL TEST RESULTS

Proppant Type : 20/40 Silica Sand
Supplier : Colorado Silica Sand UK
Reference No : Sil20/40-1

TEST CONDITIONS

Test Cell Type : 10 sq in Linear Flow Cell (API Spec.)
Proppant Concentration : 2 lbs/sq ft
Proppant Grain Density : 2.640 g/cc
Test Fluid Type : Shell Tellus No. 10
Fracture Width @ 1000 psi : 6.050 mm (.2382 in)

DATA INPUT

Closure Stress (psi)	Differential Pressure A-B	B-C	A-C	Volumetric Flow Rate A-B	B-C	A-C	Average Temp.	LVDT Value
1000	25.20	22.85	44.32	9.12	8.76	8.40	25.60	603
2000	23.25	24.30	43.23	7.70	6.68	7.00	25.69	563
4000	42.12	51.50	78.40	11.44	9.90	7.88	25.99	505
6000	45.13	128.25	165.00	7.68	8.40	6.84	26.18	447
8000	27.25	112.00	120.00	3.32	2.56	3.80	26.45	391
10000	9.00	225.00	233.00	.36	1.20	1.16	26.85	341
12000	*****	*****	*****	*****	*****	*****	*****	***
14000	*****	*****	*****	*****	*****	*****	*****	***
15000	*****	*****	*****	*****	*****	*****	*****	***

RESULTS OUTPUT

Closure Stress (psi)	Wetted Surface Area A-B	B-C	A-C	Flow-Cell Permeability A-B	B-C	A-C	Frac. Width	Porosity (%)
1000	296.2	287.7	289.4	234.4	248.3	245.5	.2382	38.79
2000	287.7	315.8	291.0	217.6	180.6	212.8	.2345	37.82
4000	281.5	334.6	327.2	181.3	128.3	134.2	.2294	36.45
6000	307.2	495.2	440.1	116.4	44.8	56.7	.2220	34.34
8000	309.0	713.3	428.5	85.2	16.0	44.3	.2146	32.07
10000	440.8	1,207.1	883.5	28.6	3.8	7.1	.2079	29.87
12000	*****	*****	*****	*****	*****	*****	*****	*****
14000	*****	*****	*****	*****	*****	*****	*****	*****
15000	*****	*****	*****	*****	*****	*****	*****	*****

UNITS : Differential Pressure (mbar) Wetted Surface Area (in^2/in^3)
Volumetric Flow Rate (cc/min) Flow Cell Permeability (Darcy)
Fluid Temperature (Celcius) Fracture Width (in)

APPENDIX 2

FORMATION SAMPLE DATA AND APPLICATION OF DATA-BASE

TO

Well 11/30-2

Well 11/30-5

Well 11/30a-A4

Well 11/30a-A6

FORMATION SAMPLE DATA

Well Number : 11/30-2
Core Number : 10
Sample Depth : 6952 ft
Box Number : 129
Reference Number : 1 A,B,C

SAMPLE DESCRIPTION

Rock Type : SANDSTONE

Colour : Medium brown, light brown banding and stringers.

Texture : Upper fine grain size (0.2 mm dia.)
Sphericity : 0.7
Roundness : 0.7

Sorting : Very well sorted

Cement : Silica

Matrix : Clay

GENERAL DESCRIPTION

Upper fine grained sandstone, medium brown in colour with light brown banding and occasional stringers of clay material. The grains have moderate sphericity, are rounded and are very well sorted.

ROCK PROPERTIES

Sample Density : 2237.54 Kg/m^3 (139.66 lb/ft^3)

Embedment Pressure : ****

Brinell Hardness : 25.5

(3.19 mm Indenter)

Units :

Load (kg)
Indentation (mm)
BHN (Kg/mm^2)

Load	Indentation	BHN
0	.0000	**
5	.0197	25
10	.0400	25
15	.0583	26
20	.0773	26
25	.0973	26
30	.1173	26

FRACTURE POROSIMETER RESULTS

Well Number : 11/30-2
Depth : 6952 ft

PROPPANT DATA : Ref. 1A

Type/Size : 20/40 Sintered Bauxite
Supplier : Norton

Gr. Density : 3.64 g/cc
Roundness : 0.80
Sphericity : 0.78

Sample Wt. : 5.0004 g
Recovery : 100.194 %

Closure Stress	Fracture Width	Proppant Porosity
1000	.1634	33.13
2000	.1620	32.58
4000	.1615	32.37
6000	.1614	32.29
8000	.1607	32.01
10000	.1605	31.94
12000	.1597	31.58
14000	.1585	31.07
15000	.1582	30.93

PROPPANT DATA : Ref. 1B

Type/size : 20/40 Sand
Supplier : Colorado Silica Sand Inc.

Gr. Density : 2.64 g/cc
Roundness : 0.70
Sphericity : 0.69

Sample Wt. : 5.0009 g
Recovery : 100 %

Closure Stress	Fracture Width	Proppant Porosity
1000	.2157	30.17
2000	.2147	29.84
4000	.2139	29.57
6000	.2127	29.18
8000	.2094	28.04
10000	.2058	26.80
12000	*****	*****
14000	*****	*****
15000	*****	*****

PROPPANT DATA : Ref. 1C

Type/size : 20/40 Interprop I
Supplier : Norton

Gr. Density : 3.12 g/cc
Roundness : 0.81
Sphericity : 0.82

Sample Wt. : 5.0002 g
Recovery : 100.090 %

Closure Stress	Fracture Width	Proppant Porosity
1000	.1776	28.22
2000	.1765	27.81
4000	.1765	27.81
6000	.1755	27.39
8000	.1747	27.04
10000	.1740	26.76
12000	.1730	26.33
14000	.1717	25.75
15000	.1708	25.39

TEST UNITS :
Closure Stress (psi)
Fracture Width (in)
Propped Fracture Porosity (%)

FRACTURE CONDUCTIVITY / PERMEABILITY RESULTS Ref : BAUX-1.APP

FORMATION / PROPPANT DATA			DATA BASE REFERENCE
Proppant Type	:	20/40 Sintered Bauxite	BAUX-A.FLO
Supplier	:	Norton	
Concentration	:	2 lbs/sq.ft.	
Well Number	:	11/30-2	SAMPLE1.POR
Depth	:	6952 ft	

FRACTURE CONDUCTIVITY RESULTS

Closure Stress (psi)	Flow Cell Conductivity A-B	B-C	A-C	Fracture Conductivity A-B	B-C	A-C
1000	4.512	4.330	4.498	1.871	1.796	1.865
2000	3.918	3.768	3.835	1.649	1.586	1.614
4000	3.404	3.241	3.353	1.545	1.471	1.522
6000	3.127	2.843	3.031	1.505	1.369	1.459
8000	2.690	2.577	2.672	1.364	1.307	1.355
10000	2.422	2.191	2.336	1.495	1.353	1.443
12000	2.272	2.073	2.040	1.522	1.389	1.367
14000	2.221	1.900	1.916	1.405	1.202	1.212
15000	2.048	1.795	1.857	1.360	1.192	1.233

FRACTURE PERMEABILITY RESULTS

Closure Stress (psi)	Flow Cell Permeability A-B	B-C	A-C	Fracture Permeability A-B	B-C	A-C
1000	306.3	294.0	305.3	137.4	131.9	137.0
2000	269.2	258.8	263.5	122.2	117.5	119.6
4000	237.0	225.7	233.5	114.8	109.3	113.1
6000	219.7	199.7	212.9	111.9	101.8	108.5
8000	191.1	183.1	189.9	101.8	97.6	101.2
10000	176.5	159.7	170.3	111.8	101.1	107.9
12000	168.2	153.4	151.0	114.4	104.4	102.7
14000	164.7	140.9	142.1	106.4	91.0	91.8
15000	153.0	134.1	138.8	103.2	90.4	93.5

UNITS : Flow Cell / Fracture Conductivity (Darcy*ft)
===== Flow Cell / Fracture Permeability (Darcies)

FRACTURE CONDUCTIVITY / PERMEABILITY RESULTS Ref : COLOR-1.APP

FORMATION / PROPPANT DATA

DATA BASE REFERENCE

Proppant Type	:	20/40 Sand (old)	COLOR-A.FLO
Supplier	:	Colorado Silica Sand	
Concentration	:	2 lbs/sq.ft.	
Well Number	:	10/30-2	SAMPLE1.POR
Depth	:	6952 ft	

FRACTURE CONDUCTIVITY RESULTS

Closure Stress (psi)	Flow Cell Conductivity A-B	B-C	A-C	Fracture Conductivity A-B	B-C	A-C
1000	2.383	2.396	2.549	.737	.741	.789
2000	2.143	1.799	1.972	.681	.571	.626
4000	1.769	1.408	1.607	.652	.519	.592
6000	1.044	.725	.848	.481	.334	.391
8000	.480	.190	.365	.262	.104	.199
10000	.264	.136	.200	.163	.084	.123
12000	*****	*****	*****	*****	*****	*****
14000	*****	*****	*****	*****	*****	*****
15000	*****	*****	*****	*****	*****	*****

FRACTURE PERMEABILITY RESULTS

Closure Stress (psi)	Flow Cell Permeability A-B	B-C	A-C	Fracture Permeability A-B	B-C	A-C
1000	119.2	119.8	127.5	41.0	41.2	43.9
2000	108.2	90.8	99.5	38.0	31.9	35.0
4000	91.5	72.8	83.1	36.6	29.1	33.2
6000	55.8	38.7	45.3	27.2	18.9	22.1
8000	26.7	10.6	20.3	15.0	6.0	11.4
10000	15.2	7.8	11.5	9.5	4.9	7.2
12000	*****	*****	*****	*****	*****	*****
14000	*****	*****	*****	*****	*****	*****
15000	*****	*****	*****	*****	*****	*****

UNITS : Flow Cell / Fracture Conductivity (Darcy*ft)
***** Flow Cell / Fracture Permeability (Darcies)

FRACTURE CONDUCTIVITY / PERMEABILITY RESULTS Ref : INTER-1.APP

FORMATION / PROPPANT DATA DATA BASE REFERENCE

Proppant Type	:	20/40 Interprop I	INTER-A.FLO
Supplier	:	Norton	
Concentration	:	2 lbs/sq.ft.	
Well Number	:	11/30-2	SAMPLE1.POR
Depth	:	6952 ft	

FRACTURE CONDUCTIVITY RESULTS

Closure Stress (psi)	Flow Cell Conductivity A-B	B-C	A-C	Fracture Conductivity A-B	B-C	A-C
1000	6.534	6.371	6.468	1.506	1.468	1.491
2000	5.714	5.264	5.579	1.146	1.056	1.119
4000	5.106	4.685	4.882	1.150	1.055	1.099
6000	4.555	3.908	4.212	1.105	.948	1.021
8000	3.991	3.275	3.628	1.068	.876	.971
10000	3.073	2.438	2.720	.955	.757	.845
12000	2.629	2.034	2.207	.888	.687	.746
14000	1.969	1.486	1.689	.697	.526	.598
15000	1.659	1.182	1.391	.635	.452	.533

FRACTURE PERMEABILITY RESULTS

Closure Stress (psi)	Flow Cell Permeability A-B	B-C	A-C	Fracture Permeability A-B	B-C	A-C
1000	385.6	375.9	381.7	101.8	99.2	100.7
2000	337.4	310.8	329.4	77.9	71.8	76.1
4000	302.8	277.8	289.5	78.2	71.7	74.7
6000	275.0	235.9	254.2	75.5	64.8	69.8
8000	245.5	201.4	223.2	73.3	60.2	66.7
10000	193.4	153.4	171.2	65.8	52.2	58.3
12000	168.4	130.3	141.4	61.6	47.7	51.7
14000	128.0	96.6	109.8	48.7	36.8	41.8
15000	109.5	78.0	91.8	44.6	31.8	37.4

UNITS : Flow Cell / Fracture Conductivity (Darcy*ft)
===== Flow Cell / Fracture Permeability (Darcies)

FORMATION SAMPLE DATA

Well Number : 11/30-2
Core Number : 10
Sample Depth : 6977 ft
Box Number : 134
Reference Number : 2 A,B,C

SAMPLE DESCRIPTION

Rock Type : SANDSTONE

Colour : Dark brown with occasional fine, black stringers.

Texture : Lower fine grain size (0.15 mm dia.)
Sphericity : 0.9
Roundness : 0.9

Sorting : Very well sorted

Cement : Silica

Matrix : Clay

GENERAL DESCRIPTION

Lower fine grained sandstone, dark brown in colour and displaying occasional stringers of clay material. The grains have high sphericity, are well rounded and are very well sorted.

ROCK PROPERTIES

Sample Density : 2244.0 Kg/m^3 (140.06 lb/ft^3)

Embedment Pressure : ****

Brinell Hardness : 33.6

(3.19 mm Indenter)

Units :

Load (kg)
Indentation (mm)
BHN (Kg/mm^2)

Load	Indentation	BHN
0	.0000	**
5	.0153	33
10	.0307	33
15	.0443	34
20	.0580	34
25	.0727	34
30	.0887	34

FRACTURE POROSIMETER RESULTS

Well Number : 11/30-2
Depth : 6977 ft

PROPPANT DATA : Ref. 2A

Type/Size : 20/40 Sintered Bauxite
Supplier : Norton

Gr. Density : 3.64 g/cc
Roundness : 0.80
Sphericity : 0.78

Sample Wt. : 5.0001 g
Recovery : 100.188 %

Closure Stress	Fracture Width	Proppant Porosity
1000	.1657	34.09
2000	.1646	33.62
4000	.1634	33.14
6000	.1627	32.86
8000	.1622	32.65
10000	.1615	32.37
12000	.1609	32.09
14000	.1600	31.73
15000	.1597	31.59

PROPPANT DATA : Ref. 2B

Type/size : 20/40 Sand
Supplier : Colorado Silica Sand Inc.

Gr. Density : 2.64 g/cc
Roundness : 0.70
Sphericity : 0.69

Sample Wt. : 5.0003 g
Recovery : 100.012 %

Closure Stress	Fracture Width	Proppant Porosity
1000	.2260	33.34
2000	.2250	33.04
4000	.2233	32.54
6000	.2214	31.98
8000	.2179	30.87
10000	.2137	29.51
12000	*****	*****
14000	*****	*****
15000	*****	*****

PROPPANT DATA : Ref. 2C

Type/size : 20/40 Interprop I
Supplier : Norton

Gr. Density : 3.12 g/cc
Roundness : 0.81
Sphericity : 0.82

Sample Wt. : 5.0002 g
Recovery : 100.090 %

Closure Stress	Fracture Width	Proppant Porosity
1000	.1898	32.83
2000	.1893	32.65
4000	.1888	32.47
6000	.1881	32.23
8000	.1876	32.05
10000	.1867	31.74
12000	.1857	31.37
14000	.1844	30.87
15000	.1835	30.56

TEST UNITS :
Closure Stress (psi)
Fracture Width (in)
Propped Fracture Porosity (%)

FRACTURE CONDUCTIVITY / PERMEABILITY RESULTS Ref : BAUX-2.APP

FORMATION / PROPPANT DATA | DATA BASE REFERENCE

Proppant Type	:	20/40 Sintered Bauxite	BAUX-A.FLO
Supplier	:	Norton	
Concentration	:	2 lbs/sq.ft.	
Well Number	:	11/30-2	SAMPLE2.POR
Depth	:	6977 ft	

FRACTURE CONDUCTIVITY RESULTS

Closure Stress (psi)	Flow Cell Conductivity A-B	B-C	A-C	Fracture Conductivity A-B	B-C	A-C
1000	4.512	4.330	4.498	2.128	2.042	2.121
2000	3.918	3.768	3.835	1.899	1.827	1.859
4000	3.404	3.241	3.353	1.716	1.635	1.691
6000	3.127	2.843	3.031	1.626	1.479	1.576
8000	2.690	2.577	2.672	1.488	1.426	1.479
10000	2.422	2.191	2.336	1.586	1.435	1.530
12000	2.272	2.073	2.040	1.634	1.490	1.467
14000	2.221	1.900	1.916	1.540	1.317	1.328
15000	2.048	1.795	1.857	1.491	1.307	1.352

FRACTURE PERMEABILITY RESULTS

Closure Stress (psi)	Flow Cell Permeability A-B	B-C	A-C	Fracture Permeability A-B	B-C	A-C
1000	306.3	294.0	305.3	154.1	147.9	153.6
2000	269.2	258.8	263.5	138.5	133.2	135.6
4000	237.0	225.7	233.5	126.1	120.0	124.2
6000	219.7	199.7	212.9	120.0	109.1	116.3
8000	191.1	183.1	189.9	110.1	105.5	109.4
10000	176.5	159.7	170.3	117.9	106.6	113.7
12000	168.2	153.4	151.0	121.8	111.2	109.4
14000	164.7	140.9	142.1	115.5	98.8	99.6
15000	153.0	134.1	138.8	112.0	98.2	101.6

UNITS : Flow Cell / Fracture Conductivity (Darcy*ft)
===== Flow Cell / Fracture Permeability (Darcies)

FRACTURE CONDUCTIVITY / PERMEABILITY RESULTS Ref : COLOR-2.APP

FORMATION / PROPPANT DATA			DATA BASE REFERENCE
Proppant Type	:	20/40 Sand (old)	COLOR-A.FLO
Supplier	:	Colorado Silica Sand	
Concentration	:	2 lbs/sq.ft.	
Well Number	:	10/30-2	SAMPLE2.POR
Depth	:	6977 ft	

FRACTURE CONDUCTIVITY RESULTS

Closure Stress (psi)	Flow Cell Conductivity A-B	B-C	A-C	Fracture Conductivity A-B	B-C	A-C
1000	2.383	2.396	2.549	1.144	1.150	1.223
2000	2.143	1.799	1.972	1.063	.892	.978
4000	1.769	1.408	1.607	.988	.786	.898
6000	1.044	.725	.848	.715	.496	.581
8000	.480	.190	.365	.394	.156	.300
10000	.264	.136	.200	.244	.125	.184
12000	*****	*****	*****	*****	*****	*****
14000	*****	*****	*****	*****	*****	*****
15000	*****	*****	*****	*****	*****	*****

FRACTURE PERMEABILITY RESULTS

Closure Stress (psi)	Flow Cell Permeability A-B	B-C	A-C	Fracture Permeability A-B	B-C	A-C
1000	119.2	119.8	127.5	60.7	61.1	65.0
2000	108.2	90.8	99.5	56.7	47.6	52.1
4000	91.5	72.8	83.1	53.1	42.3	48.2
6000	55.8	38.7	45.3	38.8	26.9	31.5
8000	26.7	10.6	20.3	21.7	8.6	16.5
10000	15.2	7.8	11.5	13.7	7.0	10.4
12000	*****	*****	*****	*****	*****	*****
14000	*****	*****	*****	*****	*****	*****
15000	*****	*****	*****	*****	*****	*****

UNITS : Flow Cell / Fracture Conductivity (Darcy*ft)
***** Flow Cell / Fracture Permeability (Darcies)

FORMATION SAMPLE DATA
=====================

Well Number : 11/30-2
Core Number : 10
Sample Depth : 6986 ft
Box Number : 136
Reference Number : 3 A,B,C

SAMPLE DESCRIPTION
==================

Rock Type : SANDSTONE, Shaley sandstone

Colour : Dark grey, dark grey/black speckles.

Texture : Lower fine grain size (0.15 mm dia.)
Sphericity : 0.9
Roundness : 0.9

Sorting : Very well sorted.

Cement : Silica

Matrix : Clay

GENERAL DESCRIPTION
===================

Lower fine grained shaley sandstone, dark grey in colour and displaying extensive shale/clay speckles. The grains posess a high sphericity, are well rounded and are very well sorted.

ROCK PROPERTIES
===============

Sample Density : 2245.37 Kg/m^3 (140.15 lb/ft^3)

Embedment Pressure : ****

Brinell Hardness : 33.2

(3.19 mm Indenter) Units :
=======

Load (kg)
Indentation (mm)
BHN (Kg/mm^2)

Load	Indentation	BHN
0	.0000	**
5	.0160	31
10	.0317	32
15	.0453	33
20	.0593	34
25	.0720	35
30	.0847	35

FRACTURE CONDUCTIVITY / PERMEABILITY RESULTS Ref : INTER-2.APP

FORMATION / PROPPANT DATA DATA BASE REFERENCE

Proppant Type	:	20/40 Interprop I	INTER-A.FLO
Supplier	:	Norton	
Concentration	:	2 lbs/sq.ft.	
Well Number	:	11/30-2	SAMPLE2.POR
Depth	:	6977 ft	

FRACTURE CONDUCTIVITY RESULTS

Closure Stress (psi)	Flow Cell Conductivity A-B	B-C	A-C	Fracture Conductivity A-B	B-C	A-C
1000	6.534	6.371	6.468	2.894	2.821	2.864
2000	5.714	5.264	5.579	2.477	2.282	2.419
4000	5.106	4.685	4.882	2.237	2.052	2.138
6000	4.555	3.908	4.212	2.215	1.900	2.048
8000	3.991	3.275	3.628	2.201	1.806	2.001
10000	3.073	2.438	2.720	1.968	1.561	1.742
12000	2.629	2.034	2.207	1.858	1.438	1.560
14000	1.969	1.486	1.689	1.489	1.124	1.277
15000	1.659	1.182	1.391	1.367	.973	1.145

FRACTURE PERMEABILITY RESULTS

Closure Stress (psi)	Flow Cell Permeability A-B	B-C	A-C	Fracture Permeability A-B	B-C	A-C
1000	385.6	375.9	381.7	183.0	178.4	181.1
2000	337.4	310.8	329.4	157.0	144.7	153.3
4000	302.8	277.8	289.5	142.2	130.4	135.9
6000	275.0	235.9	254.2	141.3	121.2	130.6
8000	245.5	201.4	223.2	140.8	115.5	128.0
10000	193.4	153.4	171.2	126.5	100.3	112.0
12000	168.4	130.3	141.4	120.1	92.9	100.8
14000	128.0	96.6	109.8	96.9	73.1	83.1
15000	109.5	78.0	91.8	89.9	64.0	75.3

UNITS : Flow Cell / Fracture Conductivity (Darcy*ft)
===== Flow Cell / Fracture Permeability (Darcies)

FRACTURE POROSIMETER RESULTS

Well Number : 11/30-2
Depth : 6986 ft

PROPPANT DATA : Ref. 3A

Type/Size : 20/40 Sintered Bauxite
Supplier : Norton

Gr. Density : 3.64 g/cc
Roundness : 0.80
Sphericity : 0.78

Sample Wt. : 5.0002 g
Recovery : 0 %

Closure Stress	Fracture Width	Proppant Porosity
1000	.1705	35.91
2000	.1695	35.53
4000	.1681	35.02
6000	.1673	34.69
8000	.1666	34.42
10000	*****	*****
12000	*****	Sample
14000	*****	Failed
15000	*****	*****

PROPPANT DATA : Ref. 3B

Type/size : 20/40 Sand
Supplier : Colorado Silica Sand Inc.

Gr. Density : 2.64 g/cc
Roundness : 0.70
Sphericity : 0.69

Sample Wt. : 5.0006 g
Recovery : 99.8880 %

Closure Stress	Fracture Width	Proppant Porosity
1000	.2350	35.91
2000	.2342	35.68
4000	.2329	35.30
6000	.2310	34.79
8000	.2281	33.97
10000	.2239	32.73
12000	*****	*****
14000	*****	*****
15000	*****	*****

PROPPANT DATA : Ref. 3C

Type/size : 20/40 Interprop I
Supplier : Norton

Gr. Density : 3.12 g/cc
Roundness : 0.81
Sphericity : 0.82

Sample Wt. : 5.0008 g
Recovery : 100.092 %

Closure Stress	Fracture Width	Proppant Porosity
1000	.1921	33.65
2000	.1918	33.53
4000	.1911	33.30
6000	.1906	33.12
8000	.1901	32.95
10000	.1894	32.71
12000	.1888	32.47
14000	.1878	32.11
15000	.1869	31.80

TEST UNITS : Closure Stress (psi)
Fracture Width (in)
Propped Fracture Porosity (%)

FRACTURE CONDUCTIVITY / PERMEABILITY RESULTS Ref : BAUX-3.APP

FORMATION / PROPPANT DATA DATA BASE REFERENCE

Proppant Type : 20/40 Sintered Bauxite BAUX-A.FLO
Supplier : Norton
Concentration : 2 lbs/sq.ft.

Well Number : 11/30-2 SAMPLE3.POR
Depth : 6986 ft

FRACTURE CONDUCTIVITY RESULTS

Closure Stress (psi)	Flow Cell Conductivity A-B	B-C	A-C	Fracture Conductivity A-B	B-C	A-C
1000	4.512	4.330	4.498	2.707	2.597	2.698
2000	3.918	3.768	3.835	2.447	2.354	2.396
4000	3.404	3.241	3.353	2.206	2.101	2.173
6000	3.127	2.843	3.031	2.080	1.891	2.015
8000	2.690	2.577	2.672	1.889	1.810	1.877
10000	2.422	2.191	2.336	.000	.000	.000
12000	2.272	2.073	2.040	.000	.000	.000
14000	2.221	1.900	1.916	.000	.000	.000
15000	2.048	1.795	1.857	.000	.000	.000

FRACTURE PERMEABILITY RESULTS

Closure Stress (psi)	Flow Cell Permeability A-B	B-C	A-C	Fracture Permeability A-B	B-C	A-C
1000	306.3	294.0	305.3	190.5	182.8	189.9
2000	269.2	258.8	263.5	173.3	166.6	169.6
4000	237.0	225.7	233.5	157.5	150.0	155.1
6000	219.7	199.7	212.9	149.2	135.6	144.6
8000	191.1	183.1	189.9	136.1	130.4	135.2
10000	176.5	159.7	170.3	.0	.0	.0
12000	168.2	153.4	151.0	.0	.0	.0
14000	164.7	140.9	142.1	.0	.0	.0
15000	153.0	134.1	138.8	.0	.0	.0

UNITS : Flow Cell / Fracture Conductivity (Darcy*ft)
===== Flow Cell / Fracture Permeability (Darcies)

FRACTURE CONDUCTIVITY / PERMEABILITY RESULTS Ref : COLOR-3.APP

FORMATION / PROPPANT DATA DATA BASE REFERENCE

Proppant Type	:	20/40 Sand (old)	COLOR-A.FLO
Supplier	:	Colorado Silica Sand	
Concentration	:	2 lbs/sq.ft.	
Well Number	:	10/30-2	SAMPLE3.POR
Depth	:	6986 ft	

FRACTURE CONDUCTIVITY RESULTS

Closure Stress (psi)	Flow Cell Conductivity A-B	B-C	A-C	Fracture Conductivity A-B	B-C	A-C
1000	2.383	2.396	2.549	1.608	1.617	1.720
2000	2.143	1.799	1.972	1.510	1.267	1.389
4000	1.769	1.408	1.607	1.430	1.138	1.299
6000	1.044	.725	.848	1.045	.726	.849
8000	.480	.190	.365	.603	.239	.458
10000	.264	.136	.200	.383	.197	.289
12000	*****	*****	*****	*****	*****	*****
14000	*****	*****	*****	*****	*****	*****
15000	*****	*****	*****	*****	*****	*****

FRACTURE PERMEABILITY RESULTS

Closure Stress (psi)	Flow Cell Permeability A-B	B-C	A-C	Fracture Permeability A-B	B-C	A-C
1000	119.2	119.8	127.5	82.1	82.5	87.8
2000	108.2	90.8	99.5	77.4	64.9	71.2
4000	91.5	72.8	83.1	73.7	58.6	66.9
6000	55.8	38.7	45.3	54.3	37.7	44.1
8000	26.7	10.6	20.3	31.7	12.6	24.1
10000	15.2	7.8	11.5	20.5	10.6	15.5
12000	*****	*****	*****	*****	*****	*****
14000	*****	*****	*****	*****	*****	*****
15000	*****	*****	*****	*****	*****	*****

UNITS : Flow Cell / Fracture Conductivity (Darcy*ft)
===== Flow Cell / Fracture Permeability (Darcies)

FRACTURE CONDUCTIVITY / PERMEABILITY RESULTS Ref : INTER-3.APP

FORMATION / PROPPANT DATA DATA BASE REFERENCE

Proppant Type	:	20/40 Interprop I	INTER-A.FLO
Supplier	:	Norton	
Concentration	:	2 lbs/sq.ft.	
Well Number	:	11/30-2	SAMPLE3.POR
Depth	:	6986 ft	

FRACTURE CONDUCTIVITY RESULTS

Closure Stress (psi)	Flow Cell Conductivity A-B	B-C	A-C	Fracture Conductivity A-B	B-C	A-C
1000	6.534	6.371	6.468	3.232	3.151	3.199
2000	5.714	5.264	5.579	2.882	2.655	2.814
4000	5.106	4.685	4.882	2.473	2.269	2.365
6000	4.555	3.908	4.212	2.500	2.145	2.312
8000	3.991	3.275	3.628	2.489	2.042	2.263
10000	3.073	2.438	2.720	2.248	1.784	1.990
12000	2.629	2.034	2.207	2.164	1.674	1.817
14000	1.969	1.486	1.689	1.769	1.335	1.517
15000	1.659	1.182	1.391	1.635	1.164	1.370

FRACTURE PERMEABILITY RESULTS

Closure Stress (psi)	Flow Cell Permeability A-B	B-C	A-C	Fracture Permeability A-B	B-C	A-C
1000	385.6	375.9	381.7	201.9	196.8	199.9
2000	337.4	310.8	329.4	174.6	160.8	170.5
4000	302.8	277.8	289.5	155.3	142.5	148.5
6000	275.0	235.9	254.2	157.4	135.1	145.6
8000	245.5	201.4	223.2	157.1	128.9	142.8
10000	193.4	153.4	171.2	142.5	113.0	126.1
12000	168.4	130.3	141.4	137.5	106.4	115.5
14000	128.0	96.6	109.8	113.0	85.3	97.0
15000	109.5	78.0	91.8	105.0	74.7	88.0

UNITS : Flow Cell / Fracture Conductivity (Darcy*ft)
===== Flow Cell / Fracture Permeability (Darcies)

FORMATION SAMPLE DATA

Well Number : 11/30-2
Core Number : 10
Sample Depth : 7010 ft
Box Number : 141
Reference Number : 4 A,B,C

SAMPLE DESCRIPTION

Rock Type : SANDSTONE, Shaley sandstone.

Colour : Medium grey, extensive black stringers.

Texture : Upper very fine grain size (0.1 mm dia.)
Sphericity : 0.9
Roundness : 0.9

Sorting : Very well sorted.

Cement : Silica

Matrix : Clay

GENERAL DESCRIPTION

Upper very fine grained shaley sandstone, medium grey in colour and displaying extensive stringers of clay material. The grains are of high sphericity, are well rounded and are very well sorted.

ROCK PROPERTIES

Sample Density : 2281.27 Kg/m^3 (142.39 lb/ft^3)

Embedment Pressure : ****

Brinell Hardness : 27.1

(3.19 mm Indenter)

Units :

Load (kg)
Indentation (mm)
BHN (Kg/mm^2)

Load	Indentation	BHN
0	.0000	**
5	.0183	27
10	.0387	26
15	.0560	27
20	.0740	27
25	.0893	28
30	.1060	28

FRACTURE POROSIMETER RESULTS

Well Number : 11/30-2
Depth : 7010 ft

PROPPANT DATA : Ref. 4A

Type/Size : 20/40 Sintered Bauxite
Supplier : Norton

Gr. Density : 3.64 g/cc
Roundness : 0.80
Sphericity : 0.78

Sample Wt. : 5.0005 g
Recovery : 100.164 %

Closure Stress	Fracture Width	Proppant Porosity
1000	.1638	33.29
2000	.1624	32.74
4000	.1606	31.96
6000	.1596	31.53
8000	.1584	31.02
10000	.1577	30.73
12000	.1572	30.51
14000	.1562	30.06
15000	.1555	29.75

PROPPANT DATA : Ref. 4B

Type/size : 20/40 Sand
Supplier : Colorado Silica Sand Inc.

Gr. Density : 2.64 g/cc
Roundness : 0.70
Sphericity : 0.69

Sample Wt. : 5.004 g
Recovery : 99.8901 %

Closure Stress	Fracture Width	Proppant Porosity
1000	.2047	26.37
2000	.2046	26.31
4000	.2041	26.12
6000	.2035	25.94
8000	.2012	25.07
10000	.1980	23.86
12000	*****	*****
14000	*****	*****
15000	*****	*****

PROPPANT DATA : Ref. 4C

Type/size : 20/40 Interprop I
Supplier : Norton

Gr. Density : 3.12 g/cc
Roundness : 0.81
Sphericity : 0.82

Sample Wt. : 5.007 g
Recovery : 99.9101 %

Closure Stress	Fracture Width	Proppant Porosity
1000	.1874	31.89
2000	.1864	31.53
4000	.1856	31.21
6000	.1849	30.96
8000	.1842	30.71
10000	.1834	30.39
12000	*****	*****
14000	*****	Sample
15000	*****	Failed

TEST UNITS :
Closure Stress (psi)
Fracture Width (in)
Propped Fracture Porosity (%)

FRACTURE CONDUCTIVITY / PERMEABILITY RESULTS Ref : BAUX-4.APP

FORMATION / PROPPANT DATA

			DATA BASE REFERENCE
Proppant Type	:	20/40 Sintered Bauxite	BAUX-A.FLO
Supplier	:	Norton	
Concentration	:	2 lbs/sq.ft.	
Well Number	:	11/30-2	SAMPLE4.POR
Depth	:	7010 ft	

FRACTURE CONDUCTIVITY RESULTS

Closure Stress (psi)	Flow Cell Conductivity A-B	B-C	A-C	Fracture Conductivity A-B	B-C	A-C
1000	4.512	4.330	4.498	1.912	1.835	1.906
2000	3.918	3.768	3.835	1.686	1.621	1.650
4000	3.404	3.241	3.353	1.385	1.319	1.365
6000	3.127	2.843	3.031	1.272	1.156	1.232
8000	2.690	2.577	2.672	1.188	1.139	1.181
10000	2.422	2.191	2.336	1.263	1.143	1.219
12000	2.272	2.073	2.040	1.310	1.195	1.176
14000	2.221	1.900	1.916	1.218	1.042	1.051
15000	2.048	1.795	1.857	1.150	1.008	1.043

FRACTURE PERMEABILITY RESULTS

Closure Stress (psi)	Flow Cell Permeability A-B	B-C	A-C	Fracture Permeability A-B	B-C	A-C
1000	306.3	294.0	305.3	140.1	134.4	139.6
2000	269.2	258.8	263.5	124.6	119.8	121.9
4000	237.0	225.7	233.5	103.5	98.6	102.0
6000	219.7	199.7	212.9	95.6	86.9	92.7
8000	191.1	183.1	189.9	90.0	86.3	89.4
10000	176.5	159.7	170.3	96.1	87.0	92.7
12000	168.2	153.4	151.0	100.0	91.2	89.8
14000	164.7	140.9	142.1	93.6	80.0	80.7
15000	153.0	134.1	138.8	88.7	77.8	80.5

UNITS : Flow Cell / Fracture Conductivity (Darcy*ft)
===== Flow Cell / Fracture Permeability (Darcies)

FRACTURE CONDUCTIVITY / PERMEABILITY RESULTS Ref : COLOR-4.APP

FORMATION / PROPPANT DATA

DATA BASE REFERENCE

Proppant Type	:	20/40 Sand (old)	COLOR-A.FLO
Supplier	:	Colorado Silica Sand	
Concentration	:	2 lbs/sq.ft.	
Well Number	:	10/30-2	SAMPLE4.POR
Depth	:	7010 ft	

FRACTURE CONDUCTIVITY RESULTS

Closure Stress (psi)	Flow Cell Conductivity A-B	B-C	A-C	Fracture Conductivity A-B	B-C	A-C
1000	2.383	2.396	2.549	.420	.422	.449
2000	2.143	1.799	1.972	.403	.338	.371
4000	1.769	1.408	1.607	.389	.310	.354
6000	1.044	.725	.848	.296	.205	.240
8000	.480	.190	.365	.166	.066	.126
10000	.264	.136	.200	.102	.053	.077
12000	*****	*****	*****	*****	*****	*****
14000	*****	*****	*****	*****	*****	*****
15000	*****	*****	*****	*****	*****	*****

FRACTURE PERMEABILITY RESULTS

Closure Stress (psi)	Flow Cell Permeability A-B	B-C	A-C	Fracture Permeability A-B	B-C	A-C
1000	119.2	119.8	127.5	24.6	24.8	26.3
2000	108.2	90.8	99.5	23.6	19.8	21.7
4000	91.5	72.8	83.1	22.9	18.2	20.8
6000	55.8	38.7	45.3	17.4	12.1	14.2
8000	26.7	10.6	20.3	9.9	3.9	7.5
10000	15.2	7.8	11.5	6.2	3.2	4.7
12000	*****	*****	*****	*****	*****	*****
14000	*****	*****	*****	*****	*****	*****
15000	*****	*****	*****	*****	*****	*****

UNITS : Flow Cell / Fracture Conductivity (Darcy*ft)
===== Flow Cell / Fracture Permeability (Darcies)

FRACTURE CONDUCTIVITY / PERMEABILITY RESULTS Ref : INTER-4.APP

FORMATION / PROPPANT DATA

DATA BASE REFERENCE

Proppant Type	:	20/40 Interprop I	INTER-A.FLO
Supplier	:	Norton	
Concentration	:	2 lbs/sq.ft.	
Well Number	:	11/30-2	SAMPLE4.POR
Depth	:	7010 ft	

FRACTURE CONDUCTIVITY RESULTS

Closure Stress (psi)	Flow Cell Conductivity A-B	B-C	A-C	Fracture Conductivity A-B	B-C	A-C
1000	6.534	6.371	6.468	2.547	2.483	2.521
2000	5.714	5.264	5.579	2.125	1.958	2.075
4000	5.106	4.685	4.882	1.882	1.726	1.799
6000	4.555	3.908	4.212	1.859	1.595	1.719
8000	3.991	3.275	3.628	1.829	1.500	1.662
10000	3.073	2.438	2.720	1.632	1.294	1.444
12000	2.629	2.034	2.207	*****	*****	*****
14000	1.969	1.486	1.689	*** Sample Failed ***		
15000	1.659	1.182	1.391	*****	*****	*****

FRACTURE PERMEABILITY RESULTS

Closure Stress (psi)	Flow Cell Permeability A-B	B-C	A-C	Fracture Permeability A-B	B-C	A-C
1000	385.6	375.9	381.7	163.1	159.0	161.4
2000	337.4	310.8	329.4	136.8	126.0	133.6
4000	302.8	277.8	289.5	121.7	111.6	116.3
6000	275.0	235.9	254.2	120.7	103.5	111.6
8000	245.5	201.4	223.2	119.1	97.7	108.3
10000	193.4	153.4	171.2	106.8	84.7	94.5
12000	168.4	130.3	141.4	*****	*****	*****
14000	128.0	96.6	109.8	*** Sample Failed ***		
15000	109.5	78.0	91.8	*****	*****	*****

UNITS : Flow Cell / Fracture Conductivity (Darcy*ft)
===== Flow Cell / Fracture Permeability (Darcies)

FORMATION SAMPLE DATA

Well Number : 11/30-5
Core Number : 5
Sample Depth : 7270 ft
Box Number : 9
Reference Number : 5 A,B,C

SAMPLE DESCRIPTION

Rock Type : SANDSTONE

Colour : White/light grey with irregular brown spots and streaks.

Texture : Medium grain size (0.4 mm dia.)
Sphericity : 0.9
Roundness : 0.7

Sorting : Well sorted.

Cement : Silica

Matrix : Clay

GENERAL DESCRIPTION

Medium grained, light coloured sandstone with irregular brown spots and streaks. The sandstone has grains of high sphericity which are rounded and well sorted.

ROCK PROPERTIES

Sample Density : 2367.42 Kg/m^3 (147.77 lb/ft^3)

Embedment Pressure : ****

Brinell Hardness : 42.0

(3.19 mm Indenter)

Units :

Load (kg)
Indentation (mm)
BHN (Kg/mm^2)

Load	Indentation	BHN
0	.0000	**
5	.0123	40
10	.0233	43
15	.0343	44
20	.0447	45
25	.0603	41
30	.0760	39

FRACTURE POROSIMETER RESULTS

Well Number : 11/30-5
Depth : 7270 ft

PROPPANT DATA : Ref. 5A

Type/Size : 20/40 Sintered Bauxite
Supplier : Norton

Gr. Density : 3.64 g/cc
Roundness : 0.80
Sphericity : 0.78

Sample Wt. : 5.0003 g
Recovery : 100.414 %

Closure Stress	Fracture Width	Proppant Porosity
1000	.1764	38.06
2000	.1752	37.64
4000	.1744	37.34
6000	.1737	37.10
8000	.1730	36.85
10000	.1725	36.67
12000	.1718	36.42
14000	.1708	36.04
15000	.1703	35.86

PROPPANT DATA : Ref. 5B

Type/size : 20/40 Sand
Supplier : Colorado Silica Sand Inc.

Gr. Density : 2.64 g/cc
Roundness : 0.70
Sphericity : 0.69

Sample Wt. : 5.0004 g
Recovery : 99.4720 %

Closure Stress	Fracture Width	Proppant Porosity
1000	.2276	33.80
2000	.2267	33.56
4000	.2260	33.36
6000	.2239	32.71
8000	.2188	31.16
10000	.2144	29.75
12000	*****	*****
14000	*****	*****
15000	*****	*****

PROPPANT DATA : Ref. 5C

Type/size : 20/40 Interprop I
Supplier : Norton

Gr. Density : 3.12 g/cc
Roundness : 0.81
Sphericity : 0.82

Sample Wt. : 5.0003 g
Recovery : 100.662 %

Closure Stress	Fracture Width	Proppant Porosity
1000	.1894	32.69
2000	.1894	32.69
4000	.1890	32.57
6000	.1885	32.39
8000	.1879	32.15
10000	.1874	31.97
12000	.1867	31.72
14000	.1850	31.10
15000	.1842	30.79

TEST UNITS :
Closure Stress (psi)
Fracture Width (in)
Propped Fracture Porosity (%)

FRACTURE CONDUCTIVITY / PERMEABILITY RESULTS Ref : BAUX-5.APP

FORMATION / PROPPANT DATA DATA BASE REFERENCE

Proppant Type	:	20/40 Sintered Bauxite	BAUX-A.FLO
Supplier	:	Norton	
Concentration	:	2 lbs/sq.ft.	
Well Number	:	11/30-5	SAMPLE5.POR
Depth	:	7270 ft	

FRACTURE CONDUCTIVITY RESULTS

Closure Stress (psi)	Flow Cell Conductivity A-B	B-C	A-C	Fracture Conductivity A-B	B-C	A-C
1000	4.512	4.330	4.498	3.570	3.425	3.558
2000	3.918	3.768	3.835	3.215	3.091	3.147
4000	3.404	3.241	3.353	2.984	2.841	2.939
6000	3.127	2.843	3.031	2.847	2.589	2.760
8000	2.690	2.577	2.672	2.596	2.488	2.579
10000	2.422	2.191	2.336	2.809	2.541	2.710
12000	2.272	2.073	2.040	2.909	2.654	2.612
14000	2.221	1.900	1.916	2.744	2.348	2.367
15000	2.048	1.795	1.857	2.646	2.319	2.399

FRACTURE PERMEABILITY RESULTS

Closure Stress (psi)	Flow Cell Permeability A-B	B-C	A-C	Fracture Permeability A-B	B-C	A-C
1000	306.3	294.0	305.3	242.8	233.0	242.0
2000	269.2	258.8	263.5	220.2	211.7	215.5
4000	237.0	225.7	233.5	205.3	195.5	202.2
6000	219.7	199.7	212.9	196.7	178.8	190.6
8000	191.1	183.1	189.9	180.1	172.5	178.9
10000	176.5	159.7	170.3	195.4	176.8	188.5
12000	168.2	153.4	151.0	203.2	185.4	182.5
14000	164.7	140.9	142.1	192.8	164.9	166.3
15000	153.0	134.1	138.8	186.4	163.4	169.0

UNITS : Flow Cell / Fracture Conductivity (Darcy*ft)
===== Flow Cell / Fracture Permeability (Darcies)

FRACTURE CONDUCTIVITY / PERMEABILITY RESULTS Ref : COLOR-5.APP

FORMATION / PROPPANT DATA DATA BASE REFERENCE

Proppant Type : 20/40 Sand (old) COLOR-A.FLO
Supplier : Colorado Silica Sand
Concentration : 2 lbs/sq.ft.

Well Number : 10/30-5 SAMPLE5.POR
Depth : 7270 ft

FRACTURE CONDUCTIVITY RESULTS

Closure Stress (psi)	Flow Cell Conductivity A-B	B-C	A-C	Fracture Conductivity A-B	B-C	A-C
1000	2.383	2.396	2.549	1.217	1.224	1.302
2000	2.143	1.799	1.972	1.140	.957	1.049
4000	1.769	1.408	1.607	1.104	.879	1.003
6000	1.044	.725	.848	.791	.549	.642
8000	.480	.190	.365	.411	.163	.312
10000	.264	.136	.200	.252	.130	.191
12000	*****	*****	*****	*****	*****	*****
14000	*****	*****	*****	*****	*****	*****
15000	*****	*****	*****	*****	*****	*****

FRACTURE PERMEABILITY RESULTS

Closure Stress (psi)	Flow Cell Permeability A-B	B-C	A-C	Fracture Permeability A-B	B-C	A-C
1000	119.2	119.8	127.5	64.2	64.5	68.6
2000	108.2	90.8	99.5	60.3	50.6	55.5
4000	91.5	72.8	83.1	58.6	46.7	53.3
6000	55.8	38.7	45.3	42.4	29.4	34.4
8000	26.7	10.6	20.3	22.5	8.9	17.1
10000	15.2	7.8	11.5	14.1	7.3	10.7
12000	*****	*****	*****	*****	*****	*****
14000	*****	*****	*****	*****	*****	*****
15000	*****	*****	*****	*****	*****	*****

UNITS : Flow Cell / Fracture Conductivity (Darcy*ft)
===== Flow Cell / Fracture Permeability (Darcies)

FRACTURE CONDUCTIVITY / PERMEABILITY RESULTS Ref : INTER-5.APP

FORMATION / PROPPANT DATA

			DATA BASE REFERENCE
Proppant Type	:	20/40 Interprop I	INTER-A.FLO
Supplier	:	Norton	
Concentration	:	2 lbs/sq.ft.	
Well Number	:	11/30-5	SAMPLE5.POR
Depth	:	7270 ft	

FRACTURE CONDUCTIVITY RESULTS

Closure Stress (psi)	Flow Cell Conductivity A-B	B-C	A-C	Fracture Conductivity A-B	B-C	A-C
1000	6.534	6.371	6.468	2.839	2.768	2.810
2000	5.714	5.264	5.579	2.491	2.294	2.432
4000	5.106	4.685	4.882	2.266	2.079	2.167
6000	4.555	3.908	4.212	2.263	1.942	2.093
8000	3.991	3.275	3.628	2.232	1.831	2.029
10000	3.073	2.438	2.720	2.032	1.612	1.799
12000	2.629	2.034	2.207	1.951	1.510	1.638
14000	1.969	1.486	1.689	1.537	1.160	1.319
15000	1.659	1.182	1.391	1.420	1.011	1.190

FRACTURE PERMEABILITY RESULTS

Closure Stress (psi)	Flow Cell Permeability A-B	B-C	A-C	Fracture Permeability A-B	B-C	A-C
1000	385.6	375.9	381.7	179.9	175.4	178.0
2000	337.4	310.8	329.4	157.8	145.4	154.1
4000	302.8	277.8	289.5	143.9	132.0	137.6
6000	275.0	235.9	254.2	144.1	123.6	133.2
8000	245.5	201.4	223.2	142.5	117.0	129.6
10000	193.4	153.4	171.2	130.1	103.2	115.2
12000	168.4	130.3	141.4	125.4	97.0	105.3
14000	128.0	96.6	109.8	99.7	75.3	85.5
15000	109.5	78.0	91.8	92.5	65.9	77.5

UNITS : Flow Cell / Fracture Conductivity (Darcy*ft)
===== Flow Cell / Fracture Permeability (Darcies)

FORMATION SAMPLE DATA

Well Number : 11/30-5
Core Number : 5
Sample Depth : 7275 ft
Box Number : 10
Reference Number : 6 A,B,C

SAMPLE DESCRIPTION

Rock Type : SANDSTONE

Colour : Medium grey, occasional black/dark spots.

Texture : Lower coarse grain size (0.55 mm dia.)
Sphericity : 0.7
Roundness : 0.7

Sorting : Well sorted

Cement : Silica

Matrix : Clay

GENERAL DESCRIPTION

Lower coarse grained sandstone, medium grey in colour and displaying occasional spots of clay material. The grains have moderate sphericity, are rounded and are well sorted.

ROCK PROPERTIES

Sample Density : 2382.39 Kg/m^3 (148.70 lb/ft^3)

Embedment Pressure : ****

Brinell Hardness : 47.7

(3.19 mm Indenter) Units :

Load (kg)
Indentation (mm)
BHN (Kg/mm^2)

Load	Indentation	BHN
0	.0000	**
5	.0113	44
10	.0230	43
15	.0323	46
20	.0410	49
25	.0490	51
30	.0567	53

FRACTURE POROSIMETER RESULTS

Well Number : 11/30-5
Depth : 7275 ft

PROPPANT DATA : Ref. 6A

Type/Size : 20/40 Sintered Bauxite
Supplier : Norton

Gr. Density : 3.64 g/cc
Roundness : 0.80
Sphericity : 0.78

Sample Wt. : 5.0003 g
Recovery : 100.354 %

Closure Stress	Fracture Width	Proppant Porosity
1000	.1732	36.93
2000	.1727	36.75
4000	.1721	36.50
6000	.1719	36.44
8000	.1714	36.25
10000	.1710	36.13
12000	.1705	35.94
14000	.1702	35.81
15000	.1699	35.68

PROPPANT DATA : Ref. 6B

Type/size : 20/40 Sand
Supplier : Colorado Silica Sand Inc.

Gr. Density : 2.64 g/cc
Roundness : 0.70
Sphericity : 0.69

Sample Wt. : 5.0003 g
Recovery : 99.7740 %

Closure Stress	Fracture Width	Proppant Porosity
1000	.2236	32.64
2000	.2228	32.38
4000	.2214	31.97
6000	.2194	31.35
8000	.2159	30.22
10000	.2123	29.06
12000	*****	*****
14000	*****	*****
15000	*****	*****

PROPPANT DATA : Ref. 6C

Type/size : 20/40 Interprop I
Supplier : Norton

Gr. Density : 3.12 g/cc
Roundness : 0.81
Sphericity : 0.82

Sample Wt. : 5.0008 g
Recovery : 100.058 %

Closure Stress	Fracture Width	Proppant Porosity
1000	.1941	34.32
2000	.1943	34.38
4000	.1941	34.32
6000	.1939	34.27
8000	.1936	34.15
10000	.1933	34.04
12000	.1929	33.92
14000	.1916	33.46
15000	.1907	33.17

TEST UNITS :
Closure Stress (psi)
Fracture Width (in)
Propped Fracture Porosity (%)

FRACTURE CONDUCTIVITY / PERMEABILITY RESULTS Ref : BAUX-6.APP

FORMATION / PROPPANT DATA			DATA BASE REFERENCE
Proppant Type	:	20/40 Sintered Bauxite	BAUX-A.FLO
Supplier	:	Norton	
Concentration	:	2 lbs/sq.ft.	
Well Number	:	11/30-5	SAMPLE6.POR
Depth	:	7275 ft	

FRACTURE CONDUCTIVITY RESULTS

Closure Stress (psi)	Flow Cell Conductivity A-B	B-C	A-C	Fracture Conductivity A-B	B-C	A-C
1000	4.512	4.330	4.498	3.088	2.963	3.078
2000	3.918	3.768	3.835	2.867	2.757	2.807
4000	3.404	3.241	3.353	2.678	2.550	2.638
6000	3.127	2.843	3.031	2.615	2.377	2.534
8000	2.690	2.577	2.672	2.403	2.302	2.387
10000	2.422	2.191	2.336	2.618	2.369	2.526
12000	2.272	2.073	2.040	2.733	2.493	2.454
14000	2.221	1.900	1.916	2.663	2.278	2.298
15000	2.048	1.795	1.857	2.585	2.266	2.344

FRACTURE PERMEABILITY RESULTS

Closure Stress (psi)	Flow Cell Permeability A-B	B-C	A-C	Fracture Permeability A-B	B-C	A-C
1000	306.3	294.0	305.3	214.0	205.3	213.3
2000	269.2	258.8	263.5	199.2	191.6	195.0
4000	237.0	225.7	233.5	186.7	177.8	183.9
6000	219.7	199.7	212.9	182.5	166.0	176.9
8000	191.1	183.1	189.9	168.2	161.2	167.1
10000	176.5	159.7	170.3	183.7	166.2	177.3
12000	168.2	153.4	151.0	192.3	175.5	172.7
14000	164.7	140.9	142.1	187.8	160.6	162.0
15000	153.0	134.1	138.8	182.6	160.1	165.6

UNITS : Flow Cell / Fracture Conductivity (Darcy*ft)
===== Flow Cell / Fracture Permeability (Darcies)

FRACTURE CONDUCTIVITY / PERMEABILITY RESULTS Ref : COLOR-6.APP

FORMATION / PROPPANT DATA DATA BASE REFERENCE

Proppant Type	:	20/40 Sand (old)	COLOR-A.FLO
Supplier	:	Colorado Silica Sand	
Concentration	:	2 lbs/sq.ft.	
Well Number	:	10/30-5	SAMPLE6.POR
Depth	:	7275 ft	

FRACTURE CONDUCTIVITY RESULTS

Closure Stress (psi)	Flow Cell Conductivity A-B	B-C	A-C	Fracture Conductivity A-B	B-C	A-C
1000	2.383	2.396	2.549	1.040	1.046	1.112
2000	2.143	1.799	1.972	.994	.834	.914
4000	1.769	1.408	1.607	.914	.727	.830
6000	1.044	.725	.848	.655	.455	.532
8000	.480	.190	.365	.360	.143	.273
10000	.264	.136	.200	.229	.118	.173
12000	*****	*****	*****	*****	*****	*****
14000	*****	*****	*****	*****	*****	*****
15000	*****	*****	*****	*****	*****	*****

FRACTURE PERMEABILITY RESULTS

Closure Stress (psi)	Flow Cell Permeability A-B	B-C	A-C	Fracture Permeability A-B	B-C	A-C
1000	119.2	119.8	127.5	55.8	56.1	59.7
2000	108.2	90.8	99.5	52.3	43.9	48.1
4000	91.5	72.8	83.1	49.5	39.4	45.0
6000	55.8	38.7	45.3	35.8	24.9	29.1
8000	26.7	10.6	20.3	20.0	7.9	15.2
10000	15.2	7.8	11.5	12.9	6.6	9.8
12000	*****	*****	*****	*****	*****	*****
14000	*****	*****	*****	*****	*****	*****
15000	*****	*****	*****	*****	*****	*****

UNITS : Flow Cell / Fracture Conductivity (Darcy*ft)
===== Flow Cell / Fracture Permeability (Darcies)

FRACTURE CONDUCTIVITY / PERMEABILITY RESULTS

Ref : INTER-6.APP

FORMATION / PROPPANT DATA			DATA BASE REFERENCE
Proppant Type	:	20/40 Interprop I	INTER-A.FLO
Supplier	:	Norton	
Concentration	:	2 lbs/sq.ft.	
Well Number	:	11/30-5	SAMPLE6.POR
Depth	:	7275 ft	

FRACTURE CONDUCTIVITY RESULTS

Closure Stress (psi)	Flow Cell Conductivity A-B	B-C	A-C	Fracture Conductivity A-B	B-C	A-C
1000	6.534	6.371	6.468	3.536	3.447	3.500
2000	5.714	5.264	5.579	3.127	2.881	3.053
4000	5.106	4.685	4.882	2.870	2.633	2.744
6000	4.555	3.908	4.212	2.917	2.503	2.697
8000	3.991	3.275	3.628	2.926	2.401	2.660
10000	3.073	2.438	2.720	2.691	2.135	2.383
12000	2.629	2.034	2.207	2.632	2.036	2.210
14000	1.969	1.486	1.689	2.126	1.605	1.823
15000	1.659	1.182	1.391	1.972	1.404	1.652

FRACTURE PERMEABILITY RESULTS

Closure Stress (psi)	Flow Cell Permeability A-B	B-C	A-C	Fracture Permeability A-B	B-C	A-C
1000	385.6	375.9	381.7	218.6	213.1	216.4
2000	337.4	310.8	329.4	193.1	177.9	188.6
4000	302.8	277.8	289.5	177.5	162.8	169.7
6000	275.0	235.9	254.2	180.6	154.9	166.9
8000	245.5	201.4	223.2	181.4	148.8	164.9
10000	193.4	153.4	171.2	167.1	132.6	147.9
12000	168.4	130.3	141.4	163.7	126.7	137.5
14000	128.0	96.6	109.8	133.1	100.5	114.2
15000	109.5	78.0	91.8	124.1	88.3	104.0

UNITS : Flow Cell / Fracture Conductivity (Darcy*ft)
Flow Cell / Fracture Permeability (Darcies)

FORMATION SAMPLE DATA

Well Number : 11/30-5
Core Number : 5
Sample Depth : 7308 ft
Box Number : 17
Reference Number : 7 A,B,C

SAMPLE DESCRIPTION

Rock Type : SANDSTONE

Colour : Medium brown with white quartz streaks.

Texture : Medium grain size (0.4 mm)
Sphericity : 0.8
Roundness : 0.8

Sorting : Very well sorted

Cement : Silica

Matrix : Clay

GENERAL DESCRIPTION

Medium grained sandstone, brown in coulour with streaks of white quartz. The grains possess a moderate to high sphericity, are rounded and very well sorted.

ROCK PROPERTIES

Sample Density : 2204.23 Kg/m^3 (137.58 lb/ft^3)

Embedment Pressure : ****

Brinell Hardness : 23.2

(3.19 mm Indenter) Units :

Load (kg)
Indentation (mm)
BHN (Kg/mm^2)

Load	Indentation	BHN
0	.0000	**
5	.0220	23
10	.0447	22
15	.0667	22
20	.0873	23
25	.1033	24
30	.1200	25

FRACTURE POROSIMETER RESULTS

Well Number : 11/30-5
Depth : 7308 ft

PROPPANT DATA : Ref. 7A

Type/Size : 20/40 Sintered Bauxite
Supplier : Norton

Gr. Density : 3.64 g/cc
Roundness : 0.80
Sphericity : 0.78

Sample Wt. : 5.0005 g
Recovery : 100.270 %

Closure Stress	Fracture Width	Proppant Porosity
1000	.1614	32.31
2000	.1606	31.96
4000	.1594	31.46
6000	.1591	31.31
8000	.1586	31.09
10000	.1581	30.87
12000	.1572	30.50
14000	.1567	30.28
15000	.1559	29.90

PROPPANT DATA : Ref. 7B

Type/size : 20/40 Sand
Supplier : Colorado Silica Sand Inc.

Gr. Density : 2.64 g/cc
Roundness : 0.70
Sphericity : 0.69

Sample Wt. : 5.0009 g
Recovery : 99.0662 %

Closure Stress	Fracture Width	Proppant Porosity
1000	.2181	30.93
2000	.2176	30.77
4000	.2159	30.23
6000	.2132	29.35
8000	.2094	28.04
10000	.2053	26.63
12000	*****	*****
14000	*****	*****
15000	*****	*****

PROPPANT DATA : Ref. 7C

Type/size : 20/40 Interprop I
Supplier : Norton

Gr. Density : 3.12 g/cc
Roundness : 0.81
Sphericity : 0.82

Sample Wt. : 5.0005 g
Recovery : 100.080 %

Closure Stress	Fracture Width	Proppant Porosity
1000	.1850	31.11
2000	.1842	30.80
4000	.1834	30.48
6000	.1829	30.29
8000	.1820	29.97
10000	.1810	29.58
12000	.1800	29.18
14000	.1783	28.51
15000	.1771	28.04

TEST UNITS :
Closure Stress (psi)
Fracture Width (in)
Propped Fracture Porosity (%)

FRACTURE CONDUCTIVITY / PERMEABILITY RESULTS

Ref : BAUX-7.APP

FORMATION / PROPPANT DATA

			DATA BASE REFERENCE
Proppant Type	:	20/40 Sintered Bauxite	BAUX-A.FLO
Supplier	:	Norton	
Concentration	:	2 lbs/sq.ft.	
Well Number	:	11/30-5	SAMPLE7.POR
Depth	:	7308 ft	

FRACTURE CONDUCTIVITY RESULTS

Closure Stress (psi)	Flow Cell Conductivity A-B	B-C	A-C	Fracture Conductivity A-B	B-C	A-C
1000	4.512	4.330	4.498	1.673	1.606	1.668
2000	3.918	3.768	3.835	1.515	1.457	1.483
4000	3.404	3.241	3.353	1.363	1.298	1.343
6000	3.127	2.843	3.031	1.314	1.195	1.274
8000	2.690	2.577	2.672	1.200	1.150	1.192
10000	2.422	2.191	2.336	1.289	1.166	1.244
12000	2.272	2.073	2.040	1.308	1.194	1.175
14000	2.221	1.900	1.916	1.257	1.075	1.084
15000	2.048	1.795	1.857	1.175	1.030	1.066

FRACTURE PERMEABILITY RESULTS

Closure Stress (psi)	Flow Cell Permeability A-B	B-C	A-C	Fracture Permeability A-B	B-C	A-C
1000	306.3	294.0	305.3	124.4	119.4	124.0
2000	269.2	258.8	263.5	113.2	108.9	110.8
4000	237.0	225.7	233.5	102.6	97.7	101.1
6000	219.7	199.7	212.9	99.1	90.1	96.1
8000	191.1	183.1	189.9	90.8	87.0	90.2
10000	176.5	159.7	170.3	97.8	88.5	94.4
12000	168.2	153.4	151.0	99.9	91.1	89.7
14000	164.7	140.9	142.1	96.2	82.3	83.0
15000	153.0	134.1	138.8	90.5	79.3	82.0

UNITS : Flow Cell / Fracture Conductivity (Darcy*ft)
Flow Cell / Fracture Permeability (Darcies)

FRACTURE CONDUCTIVITY / PERMEABILITY RESULTS Ref : COLOR-7.APP

FORMATION / PROPPANT DATA DATA BASE REFERENCE

Proppant Type	:	20/40 Sand (old)	COLOR-A.FLO
Supplier	:	Colorado Silica Sand	
Concentration	:	2 lbs/sq.ft.	
Well Number	:	10/30-5	SAMPLE7.POR
Depth	:	7308 ft	

FRACTURE CONDUCTIVITY RESULTS

Closure Stress (psi)	Flow Cell Conductivity A-B	B-C	A-C	Fracture Conductivity A-B	B-C	A-C
1000	2.383	2.396	2.549	.821	.825	.878
2000	2.143	1.799	1.972	.777	.652	.715
4000	1.769	1.408	1.607	.716	.570	.651
6000	1.044	.725	.848	.493	.343	.401
8000	.480	.190	.365	.262	.104	.199
10000	.264	.136	.200	.159	.082	.120
12000	*****	*****	*****	*****	*****	*****
14000	*****	*****	*****	*****	*****	*****
15000	*****	*****	*****	*****	*****	*****

FRACTURE PERMEABILITY RESULTS

Closure Stress (psi)	Flow Cell Permeability A-B	B-C	A-C	Fracture Permeability A-B	B-C	A-C
1000	119.2	119.8	127.5	45.2	45.4	48.3
2000	108.2	90.8	99.5	42.8	35.9	39.4
4000	91.5	72.8	83.1	39.8	31.7	36.2
6000	55.8	38.7	45.3	27.8	19.3	22.6
8000	26.7	10.6	20.3	15.0	6.0	11.4
10000	15.2	7.8	11.5	9.3	4.8	7.0
12000	*****	*****	*****	*****	*****	*****
14000	*****	*****	*****	*****	*****	*****
15000	*****	*****	*****	*****	*****	*****

UNITS : Flow Cell / Fracture Conductivity (Darcy*ft)
----- Flow Cell / Fracture Permeability (Darcies)

FRACTURE CONDUCTIVITY / PERMEABILITY RESULTS Ref : INTER-7.APP

FORMATION / PROPPANT DATA

			DATA BASE REFERENCE
Proppant Type	:	20/40 Interprop I	INTER-A.FLO
Supplier	:	Norton	
Concentration	:	2 lbs/sq.ft.	
Well Number	:	11/30-5	SAMPLE7.POR
Depth	:	7308 ft	

FRACTURE CONDUCTIVITY RESULTS

Closure Stress (psi)	Flow Cell Conductivity A-B	B-C	A-C	Fracture Conductivity A-B	B-C	A-C
1000	6.534	6.371	6.468	2.282	2.225	2.258
2000	5.714	5.264	5.579	1.917	1.766	1.871
4000	5.106	4.685	4.882	1.696	1.556	1.621
6000	4.555	3.908	4.212	1.689	1.449	1.562
8000	3.991	3.275	3.628	1.644	1.349	1.494
10000	3.073	2.438	2.720	1.451	1.151	1.284
12000	2.629	2.034	2.207	1.361	1.053	1.143
14000	1.969	1.486	1.689	1.060	.800	.909
15000	1.659	1.182	1.391	.954	.679	.800

FRACTURE PERMEABILITY RESULTS

Closure Stress (psi)	Flow Cell Permeability A-B	B-C	A-C	Fracture Permeability A-B	B-C	A-C
1000	385.6	375.9	381.7	148.0	144.3	146.5
2000	337.4	310.8	329.4	124.9	115.0	121.9
4000	302.8	277.8	289.5	111.0	101.8	106.1
6000	275.0	235.9	254.2	110.8	95.1	102.5
8000	245.5	201.4	223.2	108.4	88.9	98.5
10000	193.4	153.4	171.2	96.2	76.3	85.2
12000	168.4	130.3	141.4	90.8	70.2	76.2
14000	128.0	96.6	109.8	71.4	53.9	61.2
15000	109.5	78.0	91.8	64.6	46.0	54.2

UNITS : Flow Cell / Fracture Conductivity (Darcy*ft)
----- Flow Cell / Fracture Permeability (Darcies)

FORMATION SAMPLE DATA

Well Number : 11/30-5
Core Number : 5
Sample Depth : 7318 ft
Box Number : 19
Reference Number : 8 A,B,C

SAMPLE DESCRIPTION

Rock Type : SANDSTONE

Colour : Light brown/grey, occasional fine banding of brown/white.

Texture : Lower medium grain size (0.3 mm dia.)
Sphericity : 0.7
Roundness : 0.7

Sorting : Well sorted

Cement : Silica

Matrix : Clay

GENERAL DESCRIPTION

Lower medium grained, light brown/grey coloured sandstone displaying occasional banding of clay material and quartz. The grains have a moderate sphericity, are rounded and are well sorted.

ROCK PROPERTIES

Sample Density : 2140.79 Kg/m^3 (133.62 lb/ft^3)

Embedment Pressure : ****

Brinell Hardness : 17.9

(3.19 mm Indenter)

Units :

Load (kg)
Indentation (mm)
BHN (Kg/mm^2)

Load	Indentation	BHN
0	.0000	**
5	.0233	21
10	.0523	19
15	.0857	17
20	.1213	16
25	.1473	17
30	.1830	16

FRACTURE POROSIMETER RESULTS

Well Number : 11/30-5
Depth : 7318 ft

PROPPANT DATA : Ref. 8A

Type/Size : 20/40 Sintered Bauxite
Supplier : Norton

Gr. Density : 3.64 g/cc
Roundness : 0.80
Sphericity : 0.78

Sample Wt. : 5.0001 g
Recovery : 100.348 %

Closure Stress	Fracture Width	Proppant Porosity
1000	.1661	34.24
2000	.1658	34.11
4000	.1638	33.30
6000	.1628	32.89
8000	.1618	32.47
10000	.1609	32.11
12000	.1597	31.61
14000	.1586	31.10
15000	.1577	30.74

PROPPANT DATA : Ref. 8B

Type/size : 20/40 Sand
Supplier : Colorado Silica Sand Inc.

Gr. Density : 2.64 g/cc
Roundness : 0.70
Sphericity : 0.69

Sample Wt. : 5.0007 g
Recovery : 99.7760 %

Closure Stress	Fracture Width	Proppant Porosity
1000	.2079	27.53
2000	.2069	27.18
4000	.2054	26.64
6000	.2035	25.97
8000	.2005	24.85
10000	.1964	23.31
12000	*****	*****
14000	*****	*****
15000	*****	*****

PROPPANT DATA : Ref. 8C

Type/size : 20/40 Interprop I
Supplier : Norton

Gr. Density : 3.12 g/cc
Roundness : 0.81
Sphericity : 0.82

Sample Wt. : 5.0009 g
Recovery : 100.254 %

Closure Stress	Fracture Width	Proppant Porosity
1000	.1803	29.30
2000	.1805	29.37
4000	.1786	28.64
6000	.1775	28.16
8000	.1766	27.82
10000	.1758	27.48
12000	.1746	26.99
14000	.1729	26.28
15000	.1717	25.77

TEST UNITS :
Closure Stress (psi)
Fracture Width (in)
Propped Fracture Porosity (%)

FRACTURE CONDUCTIVITY / PERMEABILITY RESULTS Ref : BAUX-8.APP

FORMATION / PROPPANT DATA DATA BASE REFERENCE

Proppant Type	:	20/40 Sintered Bauxite	BAUX-A.FLO
Supplier	:	Norton	
Concentration	:	2 lbs/sq.ft.	
Well Number	:	11/30-5	SAMPLE8.POR
Depth	:	7318 ft	

FRACTURE CONDUCTIVITY RESULTS

Closure Stress (psi)	Flow Cell Conductivity A-B	B-C	A-C	Fracture Conductivity A-B	B-C	A-C
1000	4.512	4.330	4.498	2.171	2.084	2.164
2000	3.918	3.768	3.835	2.028	1.950	1.985
4000	3.404	3.241	3.353	1.754	1.670	1.728
6000	3.127	2.843	3.031	1.629	1.481	1.579
8000	2.690	2.577	2.672	1.453	1.392	1.443
10000	2.422	2.191	2.336	1.531	1.385	1.477
12000	2.272	2.073	2.040	1.528	1.394	1.372
14000	2.221	1.900	1.916	1.411	1.207	1.217
15000	2.048	1.795	1.857	1.323	1.160	1.200

FRACTURE PERMEABILITY RESULTS

Closure Stress (psi)	Flow Cell Permeability A-B	B-C	A-C	Fracture Permeability A-B	B-C	A-C
1000	306.3	294.0	305.3	156.9	150.5	156.4
2000	269.2	258.8	263.5	146.8	141.1	143.7
4000	237.0	225.7	233.5	128.5	122.4	126.6
6000	219.7	199.7	212.9	120.1	109.2	116.4
8000	191.1	183.1	189.9	107.7	103.2	107.0
10000	176.5	159.7	170.3	114.2	103.3	110.1
12000	168.2	153.4	151.0	114.8	104.8	103.1
14000	164.7	140.9	142.1	106.8	91.3	92.1
15000	153.0	134.1	138.8	100.7	88.3	91.3

UNITS : Flow Cell / Fracture Conductivity (Darcy*ft)
----- Flow Cell / Fracture Permeability (Darcies)

FRACTURE CONDUCTIVITY / PERMEABILITY RESULTS Ref : COLOR-8.APP

FORMATION / PROPPANT DATA — DATA BASE REFERENCE

Proppant Type	:	20/40 Sand (old)	COLOR-A.FLO
Supplier	:	Colorado Silica Sand	
Concentration	:	2 lbs/sq.ft.	
Well Number	:	10/30-5	SAMPLE8.POR
Depth	:	7318 ft	

FRACTURE CONDUCTIVITY RESULTS

Closure Stress (psi)	Flow Cell Conductivity A-B	B-C	A-C	Fracture Conductivity A-B	B-C	A-C
1000	2.383	2.396	2.549	.501	.504	.536
2000	2.143	1.799	1.972	.460	.386	.423
4000	1.769	1.408	1.607	.422	.336	.383
6000	1.044	.725	.848	.297	.206	.241
8000	.480	.190	.365	.160	.064	.122
10000	.264	.136	.200	.093	.048	.071
12000	*****	*****	*****	*****	*****	*****
14000	*****	*****	*****	*****	*****	*****
15000	*****	*****	*****	*****	*****	*****

FRACTURE PERMEABILITY RESULTS

Closure Stress (psi)	Flow Cell Permeability A-B	B-C	A-C	Fracture Permeability A-B	B-C	A-C
1000	119.2	119.8	127.5	28.9	29.1	30.9
2000	108.2	90.8	99.5	26.7	22.4	24.5
4000	91.5	72.8	83.1	24.6	19.6	22.4
6000	55.8	38.7	45.3	17.5	12.2	14.2
8000	26.7	10.6	20.3	9.6	3.8	7.3
10000	15.2	7.8	11.5	5.7	2.9	4.3
12000	*****	*****	*****	*****	*****	*****
14000	*****	*****	*****	*****	*****	*****
15000	*****	*****	*****	*****	*****	*****

UNITS : Flow Cell / Fracture Conductivity (Darcy*ft)
----- Flow Cell / Fracture Permeability (Darcies)

FRACTURE CONDUCTIVITY / PERMEABILITY RESULTS Ref : INTER-8.APP

FORMATION / PROPPANT DATA

			DATA BASE REFERENCE
Proppant Type	:	20/40 Interprop I	INTER-A.FLO
Supplier	:	Norton	
Concentration	:	2 lbs/sq.ft.	
Well Number	:	11/30-5	SAMPLE8.POR
Depth	:	7318 ft	

FRACTURE CONDUCTIVITY RESULTS

Closure Stress (psi)	Flow Cell Conductivity A-B	B-C	A-C	Fracture Conductivity A-B	B-C	A-C
1000	6.534	6.371	6.468	1.764	1.720	1.746
2000	5.714	5.264	5.579	1.563	1.440	1.526
4000	5.106	4.685	4.882	1.300	1.193	1.243
6000	4.555	3.908	4.212	1.240	1.064	1.147
8000	3.991	3.275	3.628	1.201	.985	1.092
10000	3.073	2.438	2.720	1.065	.845	.943
12000	2.629	2.034	2.207	.983	.761	.826
14000	1.969	1.486	1.689	.757	.572	.650
15000	1.659	1.182	1.391	.675	.480	.565

FRACTURE PERMEABILITY RESULTS

Closure Stress (psi)	Flow Cell Permeability A-B	B-C	A-C	Fracture Permeability A-B	B-C	A-C
1000	385.6	375.9	381.7	117.4	114.5	116.2
2000	337.4	310.8	329.4	103.9	95.7	101.5
4000	302.8	277.8	289.5	87.4	80.2	83.5
6000	275.0	235.9	254.2	83.9	71.9	77.5
8000	245.5	201.4	223.2	81.6	67.0	74.2
10000	193.4	153.4	171.2	72.7	57.7	64.4
12000	168.4	130.3	141.4	67.6	52.3	56.7
14000	128.0	96.6	109.8	52.6	39.7	45.1
15000	109.5	78.0	91.8	47.2	33.6	39.5

UNITS : Flow Cell / Fracture Conductivity (Darcy*ft)
===== Flow Cell / Fracture Permeability (Darcies)

FORMATION SAMPLE DATA

Well Number : 11/30a-A4
Core Number : 8
Sample Depth : 6969 ft
Box Number : 71
Reference Number : 9 A,B,C

SAMPLE DESCRIPTION

Rock Type : SANDSTONE, Shaley Sandstone

Colour : Dark brown/grey with black bands and white speckles.

Texture : Lower medium grain size (0.3 mm dia.)
Sphericity : 0.9
Roundness : 0.9

Sorting : Very well sorted

Cement : Silica

Matrix : Clay

GENERAL DESCRIPTION

Lower medium grained shaley sandstone, dark brown/grey in colour with bands of clay material. The sample has well sorted grains which are rounded and are of high sphericity.

ROCK PROPERTIES

Sample Density : 2195 Kg/m^3 (137.05 lb/ft^3)

Embedment Pressure : ****

Brinell Hardness : 36.9
(3.19 mm Indenter)

Units :

Load (kg)
Indentation (mm)
BHN (Kg/mm^2)

Load	Indentation	BHN
0	.0000	**
5	.0133	37
10	.0287	35
15	.0420	36
20	.0543	37
25	.0653	38
30	.0780	38

FRACTURE POROSIMETER RESULTS

Well Number : 11/30a-A4
Depth : 6969 ft

PROPPANT DATA : Ref. 9A

Type/Size : 20/40 Sintered Bauxite
Supplier : Norton

Gr. Density : 3.64 g/cc
Roundness : 0.80
Sphericity : 0.78

Sample Wt. : 5.0001 g
Recovery : 100.504 %

Closure Stress	Fracture Width	Proppant Porosity
1000	.1654	33.93
2000	.1650	33.80
4000	.1645	33.59
6000	.1640	33.39
8000	.1638	33.32
10000	.1635	33.18
12000	.1632	33.05
14000	.1623	32.70
15000	.1620	32.56

PROPPANT DATA : Ref. 9B

Type/size : 20/40 Sand
Supplier : Colorado Silica Sand Inc.

Gr. Density : 2.64 g/cc
Roundness : 0.70
Sphericity : 0.69

Sample Wt. : 5.0007 g
Recovery : 100.102 %

Closure Stress	Fracture Width	Proppant Porosity
1000	.2122	29.01
2000	.2120	28.95
4000	.2109	28.56
6000	.2088	27.86
8000	.2058	26.80
10000	.2019	25.40
12000	*****	*****
14000	*****	*****
15000	*****	*****

PROPPANT DATA : Ref. 9C

Type/size : 20/40 Interprop I
Supplier : Norton

Gr. Density : 3.12 g/cc
Roundness : 0.81
Sphericity : 0.82

Sample Wt. : 5.0003 g
Recovery : 100.816 %

Closure Stress	Fracture Width	Proppant Porosity
1000	.1870	31.84
2000	.1867	31.72
4000	.1857	31.35
6000	.1845	30.91
8000	.1836	30.59
10000	.1825	30.15
12000	.1818	29.89
14000	.1798	29.10
15000	.1783	28.50

TEST UNITS :
Closure Stress (psi)
Fracture Width (in)
Propped Fracture Porosity (%)

FRACTURE CONDUCTIVITY / PERMEABILITY RESULTS Ref : BAUX-9.APP

FORMATION / PROPPANT DATA DATA BASE REFERENCE

Proppant Type	:	20/40 Sintered Bauxite	BAUX-A.FLO
Supplier	:	Norton	
Concentration	:	2 lbs/sq.ft.	
Well Number	:	11/30a-A4	SAMPLE9.POR
Depth	:	6969 ft	

FRACTURE CONDUCTIVITY RESULTS

Closure Stress (psi)	Flow Cell Conductivity A-B	B-C	A-C	Fracture Conductivity A-B	B-C	A-C
1000	4.512	4.330	4.498	2.084	2.000	2.077
2000	3.918	3.768	3.835	1.945	1.871	1.904
4000	3.404	3.241	3.353	1.824	1.737	1.797
6000	3.127	2.843	3.031	1.748	1.589	1.694
8000	2.690	2.577	2.672	1.630	1.562	1.619
10000	2.422	2.191	2.336	1.772	1.603	1.709
12000	2.272	2.073	2.040	1.862	1.699	1.673
14000	2.221	1.900	1.916	1.759	1.505	1.518
15000	2.048	1.795	1.857	1.704	1.494	1.545

FRACTURE PERMEABILITY RESULTS

Closure Stress (psi)	Flow Cell Permeability A-B	B-C	A-C	Fracture Permeability A-B	B-C	A-C
1000	306.3	294.0	305.3	151.2	145.1	150.7
2000	269.2	258.8	263.5	141.5	136.0	138.5
4000	237.0	225.7	233.5	133.0	126.7	131.1
6000	219.7	199.7	212.9	127.9	116.3	123.9
8000	191.1	183.1	189.9	119.4	114.4	118.6
10000	176.5	159.7	170.3	130.0	117.6	125.4
12000	168.2	153.4	151.0	136.9	124.9	123.0
14000	164.7	140.9	142.1	130.1	111.3	112.2
15000	153.0	134.1	138.8	126.2	110.6	114.5

UNITS : Flow Cell / Fracture Conductivity (Darcy*ft)
===== Flow Cell / Fracture Permeability (Darcies)

FRACTURE CONDUCTIVITY / PERMEABILITY RESULTS Ref : COLOR-9.APP

FORMATION / PROPPANT DATA

			DATA BASE REFERENCE
Proppant Type	:	20/40 Sand (old)	COLOR-A.FLO
Supplier	:	Colorado Silica Sand	
Concentration	:	2 lbs/sq.ft.	
Well Number	:	11/30a-A4	SAMPLE9.POR
Depth	:	6969 ft	

FRACTURE CONDUCTIVITY RESULTS

Closure Stress (psi)	Flow Cell Conductivity A-B	B-C	A-C	Fracture Conductivity A-B	B-C	A-C
1000	2.383	2.396	2.549	.624	.627	.667
2000	2.143	1.799	1.972	.598	.502	.550
4000	1.769	1.408	1.607	.563	.448	.511
6000	1.044	.725	.848	.396	.275	.322
8000	.480	.190	.365	.217	.086	.165
10000	.264	.136	.200	.131	.068	.099
12000	*****	*****	*****	*****	*****	*****
14000	*****	*****	*****	*****	*****	*****
15000	*****	*****	*****	*****	*****	*****

FRACTURE PERMEABILITY RESULTS

Closure Stress (psi)	Flow Cell Permeability A-B	B-C	A-C	Fracture Permeability A-B	B-C	A-C
1000	119.2	119.8	127.5	35.3	35.5	37.7
2000	108.2	90.8	99.5	33.9	28.4	31.2
4000	91.5	72.8	83.1	32.0	25.5	29.1
6000	55.8	38.7	45.3	22.8	15.8	18.5
8000	26.7	10.6	20.3	12.7	5.0	9.6
10000	15.2	7.8	11.5	7.8	4.0	5.9
12000	*****	*****	*****	*****	*****	*****
14000	*****	*****	*****	*****	*****	*****
15000	*****	*****	*****	*****	*****	*****

UNITS : Flow Cell / Fracture Conductivity (Darcy*ft)
----- Flow Cell / Fracture Permeability (Darcies)

FRACTURE CONDUCTIVITY / PERMEABILITY RESULTS Ref : INTER-9.APP

FORMATION / PROPPANT DATA DATA BASE REFERENCE

Proppant Type : 20/40 Interprop I INTER-A.FLO
Supplier : Norton
Concentration : 2 lbs/sq.ft.

Well Number : 11/30a-A4 SAMPLE9.POR
Depth : 6969 ft

FRACTURE CONDUCTIVITY RESULTS

Closure Stress (psi)	Flow Cell Conductivity A-B	B-C	A-C	Fracture Conductivity A-B	B-C	A-C
1000	6.534	6.371	6.468	2.526	2.463	2.500
2000	5.714	5.264	5.579	2.180	2.008	2.128
4000	5.106	4.685	4.882	1.916	1.758	1.832
6000	4.555	3.908	4.212	1.844	1.582	1.705
8000	3.991	3.275	3.628	1.795	1.473	1.632
10000	3.073	2.438	2.720	1.574	1.249	1.394
12000	2.629	2.034	2.207	1.508	1.167	1.266
14000	1.969	1.486	1.689	1.156	.872	.991
15000	1.659	1.182	1.391	1.022	.727	.856

FRACTURE PERMEABILITY RESULTS

Closure Stress (psi)	Flow Cell Permeability A-B	B-C	A-C	Fracture Permeability A-B	B-C	A-C
1000	385.6	375.9	381.7	162.1	158.0	160.4
2000	337.4	310.8	329.4	140.1	129.1	136.8
4000	302.8	277.8	289.5	123.8	113.6	118.4
6000	275.0	235.9	254.2	119.9	102.9	110.9
8000	245.5	201.4	223.2	117.3	96.3	106.7
10000	193.4	153.4	171.2	103.5	82.1	91.6
12000	168.4	130.3	141.4	99.5	77.0	83.6
14000	128.0	96.6	109.8	77.1	58.2	66.2
15000	109.5	78.0	91.8	68.8	49.0	57.6

UNITS : Flow Cell / Fracture Conductivity (Darcy*ft)
----- Flow Cell / Fracture Permeability (Darcies)

FORMATION SAMPLE DATA

Well Number : 11/30a-A4
Core Number : 8
Sample Depth : 6984 ft
Box Number : 74
Reference Number : 10 A,B,C

SAMPLE DESCRIPTION

Rock Type : SANDSTONE

Colour : Light brown/grey with black bands.

Texture : Upper fine grain size (0.2 mm dia.)
Sphericity : 0.9
Roundness : 0.9

Sorting : Very well sorted

Cement : Silica

Matrix : Clay

GENERAL DESCRIPTION

Fine grained, light brown coloured sandstone with streaks and bands of clay material. The sandstone is very well sorted, and has grains of high sphericity and are well rounded.

ROCK PROPERTIES

Sample Density : 2277.3 Kg/m^3 (142.14 lb/ft^3)

Embedment Pressure : ****

Brinell Hardness : 31.4

(3.19 mm Indenter) Units :

Load (kg)
Indentation (mm)
BHN (Kg/mm^2)

Load	Indentation	BHN
0	.0000	**
5	.0160	31
10	.0333	30
15	.0483	31
20	.0627	32
25	.0773	32
30	.0923	32

FRACTURE POROSIMETER RESULTS

Well Number : 11/30a-A4
Depth : 6984 ft

PROPPANT DATA : Ref. 10A

Type/Size : 20/40 Sintered Bauxite
Supplier : Norton

Gr. Density : 3.64 g/cc
Roundness : 0.80
Sphericity : 0.78

Sample Wt. : 5.0003 g
Recovery : 100.324 %

Closure Stress	Fracture Width	Proppant Porosity
1000	.1650	33.77
2000	.1640	33.36
4000	.1624	32.74
6000	.1618	32.46
8000	.1609	32.11
10000	.1601	31.75
12000	.1592	31.39
14000	.1582	30.95
15000	.1574	30.58

PROPPANT DATA : Ref. 10B

Type/size : 20/40 Sand
Supplier : Colorado Silica Sand Inc.

Gr. Density : 2.64 g/cc
Roundness : 0.70
Sphericity : 0.69

Sample Wt. : 5.0004 g
Recovery : 99.5620 %

Closure Stress	Fracture Width	Proppant Porosity
1000	.2265	33.49
2000	.2257	33.24
4000	.2243	32.84
6000	.2223	32.23
8000	.2183	30.98
10000	.2147	29.84
12000	*****	*****
14000	*****	*****
15000	*****	*****

PROPPANT DATA : Ref. 10C

Type/size : 20/40 Interprop I
Supplier : Norton

Gr. Density : 3.12 g/cc
Roundness : 0.81
Sphericity : 0.82

Sample Wt. : 5.0002 g
Recovery : 100.148 %

Closure Stress	Fracture Width	Proppant Porosity
1000	.1988	35.89
2000	.1983	35.73
4000	.1973	35.40
6000	.1963	35.07
8000	.1956	34.84
10000	.1948	34.56
12000	.1939	34.28
14000	.1924	33.76
15000	.1911	33.30

TEST UNITS :
Closure Stress (psi)
Fracture Width (in)
Propped Fracture Porosity (%)

FRACTURE CONDUCTIVITY / PERMEABILITY RESULTS Ref : BAUX-10.APP

FORMATION / PROPPANT DATA DATA BASE REFERENCE

Proppant Type : 20/40 Sintered Bauxite BAUX-A.FLO
Supplier : Norton
Concentration : 2 lbs/sq.ft.

Well Number : 11/30a-A4 SAMPLE10.POR
Depth : 6984 ft

FRACTURE CONDUCTIVITY RESULTS

Closure Stress (psi)	Flow Cell Conductivity A-B	B-C	A-C	Fracture Conductivity A-B	B-C	A-C
1000	4.512	4.330	4.498	2.040	1.958	2.033
2000	3.918	3.768	3.835	1.834	1.764	1.796
4000	3.404	3.241	3.353	1.625	1.548	1.601
6000	3.127	2.843	3.031	1.541	1.401	1.493
8000	2.690	2.577	2.672	1.382	1.324	1.373
10000	2.422	2.191	2.336	1.457	1.318	1.406
12000	2.272	2.073	2.040	1.482	1.352	1.331
14000	2.221	1.900	1.916	1.381	1.182	1.192
15000	2.048	1.795	1.857	1.294	1.135	1.174

FRACTURE PERMEABILITY RESULTS

Closure Stress (psi)	Flow Cell Permeability A-B	B-C	A-C	Fracture Permeability A-B	B-C	A-C
1000	306.3	294.0	305.3	148.4	142.4	147.9
2000	269.2	258.8	263.5	134.2	129.1	131.4
4000	237.0	225.7	233.5	120.1	114.4	118.3
6000	219.7	199.7	212.9	114.3	103.9	110.7
8000	191.1	183.1	189.9	103.1	98.8	102.4
10000	176.5	159.7	170.3	109.2	98.8	105.4
12000	168.2	153.4	151.0	111.7	101.9	100.3
14000	164.7	140.9	142.1	104.8	89.6	90.4
15000	153.0	134.1	138.8	98.7	86.5	89.5

UNITS : Flow Cell / Fracture Conductivity (Darcy*ft)
===== Flow Cell / Fracture Permeability (Darcies)

FRACTURE CONDUCTIVITY / PERMEABILITY RESULTS

Ref : COLOR-10.APP

FORMATION / PROPPANT DATA

			DATA BASE REFERENCE
Proppant Type	:	20/40 Sand (old)	COLOR-A.FLO
Supplier	:	Colorado Silica Sand	
Concentration	:	2 lbs/sq.ft.	
Well Number	:	10/30a-A4	SAMPLE10.POR
Depth	:	6984 ft	

FRACTURE CONDUCTIVITY RESULTS

Closure Stress (psi)	Flow Cell Conductivity A-B	B-C	A-C	Fracture Conductivity A-B	B-C	A-C
1000	2.383	2.396	2.549	1.167	1.174	1.248
2000	2.143	1.799	1.972	1.092	.916	1.005
4000	1.769	1.408	1.607	1.029	.819	.935
6000	1.044	.725	.848	.740	.514	.601
8000	.480	.190	.365	.401	.159	.304
10000	.264	.136	.200	.256	.132	.193
12000	*****	*****	*****	*****	*****	*****
14000	*****	*****	*****	*****	*****	*****
15000	*****	*****	*****	*****	*****	*****

FRACTURE PERMEABILITY RESULTS

Closure Stress (psi)	Flow Cell Permeability A-B	B-C	A-C	Fracture Permeability A-B	B-C	A-C
1000	119.2	119.8	127.5	61.8	62.2	66.1
2000	108.2	90.8	99.5	58.1	48.7	53.4
4000	91.5	72.8	83.1	55.1	43.8	50.0
6000	55.8	38.7	45.3	40.0	27.7	32.5
8000	26.7	10.6	20.3	22.0	8.7	16.7
10000	15.2	7.8	11.5	14.3	7.4	10.8
12000	*****	*****	*****	*****	*****	*****
14000	*****	*****	*****	*****	*****	*****
15000	*****	*****	*****	*****	*****	*****

UNITS : Flow Cell / Fracture Conductivity (Darcy*ft)
----- Flow Cell / Fracture Permeability (Darcies)

FRACTURE CONDUCTIVITY / PERMEABILITY RESULTS Ref : INTER-10.APP

FORMATION / PROPPANT DATA			DATA BASE REFERENCE
Proppant Type	:	20/40 Interprop I	INTER-A.FLO
Supplier	:	Norton	
Concentration	:	2 lbs/sq.ft.	
Well Number	:	11/30a-A4	SAMPLE10.POR
Depth	:	6984 ft	

FRACTURE CONDUCTIVITY RESULTS

Closure Stress (psi)	Flow Cell Conductivity A-B	B-C	A-C	Fracture Conductivity A-B	B-C	A-C
1000	6.534	6.371	6.468	4.347	4.238	4.303
2000	5.714	5.264	5.579	3.735	3.440	3.646
4000	5.106	4.685	4.882	3.310	3.037	3.165
6000	4.555	3.908	4.212	3.244	2.783	2.999
8000	3.991	3.275	3.628	3.206	2.631	2.915
10000	3.073	2.438	2.720	2.884	2.288	2.553
12000	2.629	2.034	2.207	2.761	2.136	2.318
14000	1.969	1.486	1.689	2.213	1.670	1.898
15000	1.659	1.182	1.391	2.007	1.429	1.682

FRACTURE PERMEABILITY RESULTS

Closure Stress (psi)	Flow Cell Permeability A-B	B-C	A-C	Fracture Permeability A-B	B-C	A-C
1000	385.6	375.9	381.7	262.4	255.8	259.7
2000	337.4	310.8	329.4	226.0	208.2	220.6
4000	302.8	277.8	289.5	201.3	184.7	192.5
6000	275.0	235.9	254.2	198.3	170.1	183.3
8000	245.5	201.4	223.2	196.7	161.4	178.8
10000	193.4	153.4	171.2	177.7	140.9	157.3
12000	168.4	130.3	141.4	170.9	132.2	143.5
14000	128.0	96.6	109.8	138.0	104.2	118.4
15000	109.5	78.0	91.8	126.0	89.7	105.6

UNITS : Flow Cell / Fracture Conductivity (Darcy*ft)
----- Flow Cell / Fracture Permeability (Darcies)

FORMATION SAMPLE DATA

Well Number : 11/30a-A4
Core Number : 10
Sample Depth : 7089 ft
Box Number : 93
Reference Number : 11 A,B,C

SAMPLE DESCRIPTION

Rock Type : SANDSTONE

Colour : Medium brown/grey with thin black streaks.

Texture : Upper very fine grain size (0.1 mm dia.)
Sphericity : 0.9
Roundness : 0.7

Sorting : Well sorted

Cement : Silica

Matrix : Clay

GENERAL DESCRIPTION

Medium brown/grey coloured sandstone displaying fine black streaks of shale/clay material. The sandstone is well sorted, has upper very fine sized grains of high sphericity and are rounded.

ROCK PROPERTIES

Sample Density : 2223.15 Kg/m^3 (138.76 lb/ft^3)

Embedment Pressure : ****

Brinell Hardness : 28.1

(3.19 mm Indenter) Units :

Load (kg)
Indentation (mm)
BHN (Kg/mm^2)

Load	Indentation	BHN
0	.0000	**
5	.0173	29
10	.0357	28
15	.0527	28
20	.0707	28
25	.0903	28
30	.1093	27

FRACTURE POROSIMETER RESULTS

Well Number : 11/30a-A4
Depth : 7089 ft

PROPPANT DATA : Ref. 11A

Type/Size : 20/40 Sintered Bauxite
Supplier : Norton

Gr. Density : 3.64 g/cc
Roundness : 0.80
Sphericity : 0.78

Sample Wt. : 5.0006 g
Recovery : 100.018 %

Closure Stress	Fracture Width	Proppant Porosity
1000	.1701	35.76
2000	.1686	35.18
4000	.1669	34.53
6000	.1655	34.00
8000	.1644	33.52
10000	.1637	33.25
12000	.1622	32.63
14000	.1607	31.99
15000	.1596	31.56

PROPPANT DATA : Ref. 11B

Type/size : 20/40 Sand
Supplier : Colorado Silica Sand Inc.

Gr. Density : 2.645 g/cc
Roundness : 0.70
Sphericity : 0.69

Sample Wt. : 5.0006 g
Recovery : 100.006 %

Closure Stress	Fracture Width	Proppant Porosity
1000	.2224	32.40
2000	.2213	32.04
4000	.2197	31.58
6000	.2177	30.94
8000	.2144	29.86
10000	.2105	28.57
12000	*****	*****
14000	*****	*****
15000	*****	*****

PROPPANT DATA : Ref. 11C

Type/size : 20/40 Interprop I
Supplier : Norton

Gr. Density : 3.12 g/cc
Roundness : 0.81
Sphericity : 0.82

Sample Wt. : 5.0001 g
Recovery : 100.236 %

Closure Stress	Fracture Width	Proppant Porosity
1000	.1898	32.83
2000	.1886	32.42
4000	.1872	31.93
6000	.1862	31.56
8000	.1851	31.12
10000	.1837	30.62
12000	.1820	29.98
14000	.1798	29.13
15000	.1780	28.39

TEST UNITS : Closure Stress (psi)
Fracture Width (in)
Propped Fracture Porosity (%)

FRACTURE CONDUCTIVITY / PERMEABILITY RESULTS Ref : BAUX-11.APP

FORMATION / PROPPANT DATA DATA BASE REFERENCE

Proppant Type	:	20/40 Sintered Bauxite	BAUX-A.FLO
Supplier	:	Norton	
Concentration	:	2 lbs/sq.ft.	
Well Number	:	11/30a-A4	SAMPLE11.POR
Depth	:	7089 ft	

FRACTURE CONDUCTIVITY RESULTS

Closure Stress (psi)	Flow Cell Conductivity A-B	B-C	A-C	Fracture Conductivity A-B	B-C	A-C
1000	4.512	4.330	4.498	2.654	2.547	2.646
2000	3.918	3.768	3.835	2.338	2.248	2.288
4000	3.404	3.241	3.353	2.068	1.970	2.037
6000	3.127	2.843	3.031	1.897	1.724	1.838
8000	2.690	2.577	2.672	1.675	1.605	1.664
10000	2.422	2.191	2.336	1.789	1.618	1.726
12000	2.272	2.073	2.040	1.759	1.605	1.580
14000	2.221	1.900	1.916	1.597	1.366	1.378
15000	2.048	1.795	1.857	1.484	1.301	1.346

FRACTURE PERMEABILITY RESULTS

Closure Stress (psi)	Flow Cell Permeability A-B	B-C	A-C	Fracture Permeability A-B	B-C	A-C
1000	306.3	294.0	305.3	187.2	179.7	186.6
2000	269.2	258.8	263.5	166.4	160.0	162.9
4000	237.0	225.7	233.5	148.7	141.6	146.5
6000	219.7	199.7	212.9	137.5	125.0	133.3
8000	191.1	183.1	189.9	122.3	117.2	121.5
10000	176.5	159.7	170.3	131.1	118.6	126.5
12000	168.2	153.4	151.0	130.2	118.7	116.9
14000	164.7	140.9	142.1	119.2	102.0	102.9
15000	153.0	134.1	138.8	111.6	97.8	101.2

UNITS : Flow Cell / Fracture Conductivity (Darcy*ft)
===== Flow Cell / Fracture Permeability (Darcies)

FRACTURE CONDUCTIVITY / PERMEABILITY RESULTS Ref : COLOR-11.APP

FORMATION / PROPPANT DATA			DATA BASE REFERENCE
Proppant Type	:	20/40 Sand (old)	COLOR-A.FLO
Supplier	:	Colorado Silica Sand	
Concentration	:	2 lbs/sq.ft.	
Well Number	:	11/30a-A4	SAMPLE11.POR
Depth	:	7089 ft	

FRACTURE CONDUCTIVITY RESULTS

Closure Stress (psi)	Flow Cell Conductivity A-B	B-C	A-C	Fracture Conductivity A-B	B-C	A-C
1000	2.383	2.396	2.549	1.004	1.010	1.074
2000	2.143	1.799	1.972	.967	.812	.890
4000	1.769	1.408	1.607	.864	.687	.785
6000	1.044	.725	.848	.618	.429	.502
8000	.480	.190	.365	.341	.135	.259
10000	.264	.136	.200	.212	.109	.161
12000	*****	*****	*****	*****	*****	*****
14000	*****	*****	*****	*****	*****	*****
15000	*****	*****	*****	*****	*****	*****

FRACTURE PERMEABILITY RESULTS

Closure Stress (psi)	Flow Cell Permeability A-B	B-C	A-C	Fracture Permeability A-B	B-C	A-C
1000	119.2	119.8	127.5	54.2	54.5	58.0
2000	108.2	90.8	99.5	52.5	44.0	48.2
4000	91.5	72.8	83.1	47.2	37.5	42.9
6000	55.8	38.7	45.3	34.1	23.6	27.7
8000	26.7	10.6	20.3	19.1	7.6	14.5
10000	15.2	7.8	11.5	12.1	6.2	9.2
12000	*****	*****	*****	*****	*****	*****
14000	*****	*****	*****	*****	*****	*****
15000	*****	*****	*****	*****	*****	*****

UNITS : Flow Cell / Fracture Conductivity (Darcy*ft)
===== Flow Cell / Fracture Permeability (Darcies)

FRACTURE CONDUCTIVITY / PERMEABILITY RESULTS Ref : INTER-11.APP

FORMATION / PROPPANT DATA

			DATA BASE REFERENCE
Proppant Type	:	20/40 Interprop I	INTER-A.FLO
Supplier	:	Norton	
Concentration	:	2 lbs/sq.ft.	
Well Number	:	11/30a-A4	SAMPLE11.POR
Depth	:	7089 ft	

FRACTURE CONDUCTIVITY RESULTS

Closure Stress (psi)	Flow Cell Conductivity A-B	B-C	A-C	Fracture Conductivity A-B	B-C	A-C
1000	6.534	6.371	6.468	2.894	2.821	2.864
2000	5.714	5.264	5.579	2.400	2.211	2.343
4000	5.106	4.685	4.882	2.076	1.904	1.984
6000	4.555	3.908	4.212	2.018	1.732	1.866
8000	3.991	3.275	3.628	1.935	1.588	1.759
10000	3.073	2.438	2.720	1.683	1.335	1.490
12000	2.629	2.034	2.207	1.527	1.182	1.282
14000	1.969	1.486	1.689	1.160	.876	.995
15000	1.659	1.182	1.391	1.005	.716	.842

FRACTURE PERMEABILITY RESULTS

Closure Stress (psi)	Flow Cell Permeability A-B	B-C	A-C	Fracture Permeability A-B	B-C	A-C
1000	385.6	375.9	381.7	183.0	178.4	181.1
2000	337.4	310.8	329.4	152.7	140.7	149.1
4000	302.8	277.8	289.5	133.0	122.1	127.2
6000	275.0	235.9	254.2	130.1	111.6	120.3
8000	245.5	201.4	223.2	125.4	102.9	114.0
10000	193.4	153.4	171.2	109.9	87.2	97.3
12000	168.4	130.3	141.4	100.7	77.9	84.5
14000	128.0	96.6	109.8	77.4	58.5	66.4
15000	109.5	78.0	91.8	67.8	48.2	56.8

UNITS : Flow Cell / Fracture Conductivity (Darcy*ft)
===== Flow Cell / Fracture Permeability (Darcies)

FORMATION SAMPLE DATA

Well Number : 11/30a-A4
Core Number : 10
Sample Depth : 7093 ft
Box Number : 94
Reference Number : 12 A,B,C

SAMPLE DESCRIPTION

Rock Type : SANDSTONE, Shaley Sandstone

Colour : Medium/dark grey with black banding/streaks.

Texture : Lower fine grain size (0.15 mm dia.)
Sphericity : 0.9
Roundness : 0.9

Sorting : Very well sorted

Cement : Silica

Matrix : Clay

GENERAL DESCRIPTION

Medium/dark grey coloured shaley sandstone displaying bands of clay/shale material. The sample posesses lower fine sized grains which are of high sphericity, well rounded are very well sorted.

ROCK PROPERTIES

Sample Density : 2345.71 Kg/m^3 (146.41 lb/ft^3)

Embedment Pressure : ****

Brinell Hardness : 27.7

(3.19 mm Indenter)

Units :

Load (kg)
Indentation (mm)
BHN (Kg/mm^2)

Load	Indentation	BHN
0	.0000	**
5	.0170	29
10	.0367	27
15	.0560	27
20	.0740	27
25	.0900	28
30	.1067	28

FRACTURE POROSIMETER RESULTS

Well Number : 11/30a-A4
Depth : 7093 ft

PROPPANT DATA : Ref. 12A

Type/Size : 20/40 Sintered Bauxite
Supplier : Norton

Gr. Density : 3.64 g/cc
Roundness : 0.80
Sphericity : 0.78

Sample Wt. : 5.0002 g
Recovery : 100.198 %

Closure Stress	Fracture Width	Proppant Porosity
1000	.1736	37.08
2000	.1719	36.46
4000	.1699	35.71
6000	.1689	35.32
8000	.1677	34.87
10000	.1669	34.54
12000	.1650	33.80
14000	.1627	32.85
15000	.1617	32.43

PROPPANT DATA : Ref. 12B

Type/size : 20/40 Sand
Supplier : Colorado Silica Sand Inc.

Gr. Density : 2.64 g/cc
Roundness : 0.70
Sphericity : 0.69

Sample Wt. : 5.0003 g
Recovery : 99.5120 %

Closure Stress	Fracture Width	Proppant Porosity
1000	.2213	31.92
2000	.2201	31.55
4000	.2184	31.03
6000	.2167	30.49
8000	.2139	29.56
10000	.2095	28.09
12000	*****	*****
14000	*****	*****
15000	*****	*****

PROPPANT DATA : Ref. 12C

Type/size : 20/40 Interprop I
Supplier : Norton

Gr. Density : 3.12 g/cc
Roundness : 0.81
Sphericity : 0.82

Sample Wt. : 5.0001 g
Recovery : 100.028 %

Closure Stress	Fracture Width	Proppant Porosity
1000	.1882	32.27
2000	.1865	31.66
4000	.1853	31.23
6000	.1842	30.79
8000	.1831	30.41
10000	*****	*****
12000	*****	Sample
14000	*****	Failed
15000	*****	*****

TEST UNITS : Closure Stress (psi)
Fracture Width (in)
Propped Fracture Porosity (%)

FRACTURE CONDUCTIVITY / PERMEABILITY RESULTS Ref : BAUX-12.APP

FORMATION / PROPPANT DATA			DATA BASE REFERENCE
Proppant Type	:	20/40 Sintered Bauxite	BAUX-A.FLO
Supplier	:	Norton	
Concentration	:	2 lbs/sq.ft.	
Well Number	:	11/30a-A4	SAMPLE12.POR
Depth	:	7095 ft	

FRACTURE CONDUCTIVITY RESULTS

Closure Stress (psi)	Flow Cell Conductivity A-B	B-C	A-C	Fracture Conductivity A-B	B-C	A-C
1000	4.512	4.330	4.498	3.148	3.021	3.138
2000	3.918	3.768	3.835	2.761	2.655	2.703
4000	3.404	3.241	3.353	2.415	2.300	2.379
6000	3.127	2.843	3.031	2.259	2.054	2.190
8000	2.690	2.577	2.672	2.005	1.921	1.991
10000	2.422	2.191	2.336	2.126	1.923	2.051
12000	2.272	2.073	2.040	2.060	1.879	1.850
14000	2.221	1.900	1.916	1.796	1.536	1.549
15000	2.048	1.795	1.857	1.674	1.467	1.518

FRACTURE PERMEABILITY RESULTS

Closure Stress (psi)	Flow Cell Permeability A-B	B-C	A-C	Fracture Permeability A-B	B-C	A-C
1000	306.3	294.0	305.3	217.6	208.8	216.9
2000	269.2	258.8	263.5	192.7	185.4	188.7
4000	237.0	225.7	233.5	170.6	162.4	168.0
6000	219.7	199.7	212.9	160.5	145.9	155.6
8000	191.1	183.1	189.9	143.4	137.4	142.5
10000	176.5	159.7	170.3	152.8	138.3	147.4
12000	168.2	153.4	151.0	149.8	136.7	134.5
14000	164.7	140.9	142.1	132.4	113.3	114.3
15000	153.0	134.1	138.8	124.2	108.9	112.7

UNITS : Flow Cell / Fracture Conductivity (Darcy*ft)
===== Flow Cell / Fracture Permeability (Darcies)

FRACTURE CONDUCTIVITY / PERMEABILITY RESULTS

Ref : COLOR-12.APP

FORMATION / PROPPANT DATA			DATA BASE REFERENCE
Proppant Type	:	20/40 Sand (old)	COLOR-A.FLO
Supplier	:	Colorado Silica Sand	
Concentration	:	2 lbs/sq.ft.	
Well Number	:	11/30a-A4	SAMPLE12.POR
Depth	:	7093 ft	

FRACTURE CONDUCTIVITY RESULTS

Closure Stress (psi)	Flow Cell Conductivity A-B	B-C	A-C	Fracture Conductivity A-B	B-C	A-C
1000	2.383	2.396	2.549	.942	.947	1.008
2000	2.143	1.799	1.972	.866	.727	.797
4000	1.769	1.408	1.607	.802	.638	.728
6000	1.044	.725	.848	.581	.403	.472
8000	.480	.190	.365	.327	.130	.249
10000	.264	.136	.200	.198	.102	.150
12000	*****	*****	*****	*****	*****	*****
14000	*****	*****	*****	*****	*****	*****
15000	*****	*****	*****	*****	*****	*****

FRACTURE PERMEABILITY RESULTS

Closure Stress (psi)	Flow Cell Permeability A-B	B-C	A-C	Fracture Permeability A-B	B-C	A-C
1000	119.2	119.8	127.5	51.1	51.4	54.7
2000	108.2	90.8	99.5	47.2	39.6	43.4
4000	91.5	72.8	83.1	44.1	35.1	40.0
6000	55.8	38.7	45.3	32.2	22.3	26.1
8000	26.7	10.6	20.3	18.4	7.3	14.0
10000	15.2	7.8	11.5	11.4	5.8	8.6
12000	*****	*****	*****	*****	*****	*****
14000	*****	*****	*****	*****	*****	*****
15000	*****	*****	*****	*****	*****	*****

UNITS : Flow Cell / Fracture Conductivity (Darcy*ft)
===== Flow Cell / Fracture Permeability (Darcies)

FRACTURE CONDUCTIVITY / PERMEABILITY RESULTS Ref : INTER-12.APP

FORMATION / PROPPANT DATA | DATA BASE REFERENCE

Proppant Type	:	20/40 Interprop I	INTER-A.FLO
Supplier	:	Norton	
Concentration	:	2 lbs/sq.ft.	
Well Number	:	11/30a-A4	SAMPLE12.POR
Depth	:	7093 ft	

FRACTURE CONDUCTIVITY RESULTS

Closure Stress (psi)	Flow Cell Conductivity A-B	B-C	A-C	Fracture Conductivity A-B	B-C	A-C
1000	6.534	6.371	6.468	2.680	2.613	2.653
2000	5.714	5.264	5.579	2.161	1.991	2.110
4000	5.106	4.685	4.882	1.883	1.728	1.801
6000	4.555	3.908	4.212	1.813	1.555	1.676
8000	3.991	3.275	3.628	1.750	1.436	1.591
10000	3.073	2.438	2.720	*****	*****	*****
12000	2.629	2.034	2.207	*****	*****	*****
14000	1.969	1.486	1.689	*** Sample Failed ***		
15000	1.659	1.182	1.391	*****	*****	*****

FRACTURE PERMEABILITY RESULTS

Closure Stress (psi)	Flow Cell Permeability A-B	B-C	A-C	Fracture Permeability A-B	B-C	A-C
1000	385.6	375.9	381.7	170.9	166.6	169.1
2000	337.4	310.8	329.4	139.1	128.1	135.8
4000	302.8	277.8	289.5	122.0	111.9	116.6
6000	275.0	235.9	254.2	118.1	101.3	109.2
8000	245.5	201.4	223.2	114.7	94.1	104.2
10000	193.4	153.4	171.2	*****	*****	*****
12000	168.4	130.3	141.4	*****	*****	*****
14000	128.0	96.6	109.8	*** Sample Failed ***		
15000	109.5	78.0	91.8	*****	*****	*****

UNITS : Flow Cell / Fracture Conductivity (Darcy*ft)
===== Flow Cell / Fracture Permeability (Darcies)

FORMATION SAMPLE DATA

Well Number : 11/30a-A6
Core Number : 12
Sample Depth : 6820 ft
Box Number : 22
Reference Number : 13 A,B,C

SAMPLE DESCRIPTION

Rock Type : SANDSTONE

Colour : Light brown with white spots and streaks.

Texture : Upper medium grain size (0.4 mm dia.)
Sphericity : 0.7
Roundness : 0.5

Sorting : Poorly sorted

Cement : Silica

Matrix : Clay

GENERAL DESCRIPTION

Light brown coloured sandstone, upper medium grain size with large quartz grains. The sample is poorly sorted, the grains having moderate sphericity and are in general, sub-rounded.

ROCK PROPERTIES

Sample Density : 2261.78 Kg/m^3 (141.17 lb/ft^3)

Embedment Pressure : ****

Brinell Hardness : 22.6

(3.19 mm Indenter)

Units :

Load (kg)
Indentation (mm)
BHN (Kg/mm^2)

Load	Indentation	BHN
0	.0000	**
5	.0237	21
10	.0457	22
15	.0643	23
20	.0857	23
25	.1080	23
30	.1287	23

FRACTURE POROSIMETER RESULTS

Well Number : 11/30a-A6
Depth : 6820 ft

PROPPANT DATA : Ref. 13A

Type/Size : 20/40 Sintered Bauxite
Supplier : Norton

Gr. Density : 3.64 g/cc
Roundness : 0.80
Sphericity : 0.78

Sample Wt. : 5.0001 g
Recovery : 100.432 %

Closure Stress	Fracture Width	Proppant Porosity
1000	.1697	35.62
2000	.1685	35.17
4000	.1670	34.58
6000	.1665	34.38
8000	.1655	33.98
10000	.1648	33.71
12000	.1641	33.44
14000	.1631	33.03
15000	.1623	32.68

PROPPANT DATA : Ref. 13B

Type/size : 20/40 Sand
Supplier : Colorado Silica Sand Inc.

Gr. Density : 2.64 g/cc
Roundness : 0.70
Sphericity : 0.69

Sample Wt. : 5.0009 g
Recovery : 99.6821 %

Closure Stress	Fracture Width	Proppant Porosity
1000	.2071	27.25
2000	.2062	26.95
4000	.2047	26.41
6000	.2034	25.93
8000	.2004	24.81
10000	.1962	23.20
12000	*****	*****
14000	*****	*****
15000	*****	*****

PROPPANT DATA : Ref. 13C

Type/size : 20/40 Interprop I
Supplier : Norton

Gr. Density : 3.12 g/cc
Roundness : 0.81
Sphericity : 0.82

Sample Wt. : 5.0009 g
Recovery : 100.276 %

Closure Stress	Fracture Width	Proppant Porosity
1000	.1909	33.24
2000	.1894	32.71
4000	.1883	32.28
6000	.1876	32.04
8000	.1871	31.86
10000	.1867	31.74
12000	.1854	31.24
14000	.1844	30.86
15000	.1834	30.48

TEST UNITS :
Closure Stress (psi)
Fracture Width (in)
Propped Fracture Porosity (%)

FRACTURE CONDUCTIVITY / PERMEABILITY RESULTS Ref : BAUX-13.APP

FORMATION / PROPPANT DATA DATA BASE REFERENCE

Proppant Type	:	20/40 Sintered Bauxite	BAUX-A.FLO
Supplier	:	Norton	
Concentration	:	2 lbs/sq.ft.	
Well Number	:	11/30a-A6	SAMPLE13.POR
Depth	:	6820 ft	

FRACTURE CONDUCTIVITY RESULTS

Closure Stress (psi)	Flow Cell Conductivity A-B	B-C	A-C	Fracture Conductivity A-B	B-C	A-C
1000	4.512	4.330	4.498	2.606	2.500	2.597
2000	3.918	3.768	3.835	2.334	2.244	2.284
4000	3.404	3.241	3.353	2.082	1.982	2.051
6000	3.127	2.843	3.031	1.996	1.814	1.934
8000	2.690	2.577	2.672	1.782	1.707	1.770
10000	2.422	2.191	2.336	1.903	1.721	1.836
12000	2.272	2.073	2.040	1.963	1.791	1.763
14000	2.221	1.900	1.916	1.840	1.574	1.587
15000	2.048	1.795	1.857	1.732	1.518	1.571

FRACTURE PERMEABILITY RESULTS

Closure Stress (psi)	Flow Cell Permeability A-B	B-C	A-C	Fracture Permeability A-B	B-C	A-C
1000	306.3	294.0	305.3	184.2	176.8	183.7
2000	269.2	258.8	263.5	166.2	159.8	162.7
4000	237.0	225.7	233.5	149.6	142.5	147.3
6000	219.7	199.7	212.9	143.8	130.8	139.4
8000	191.1	183.1	189.9	129.2	123.8	128.3
10000	176.5	159.7	170.3	138.5	125.3	133.7
12000	168.2	153.4	151.0	143.5	130.9	128.9
14000	164.7	140.9	142.1	135.4	115.8	116.8
15000	153.0	134.1	138.8	128.1	112.3	116.1

UNITS : Flow Cell / Fracture Conductivity (Darcy*ft)
===== Flow Cell / Fracture Permeability (Darcies)

FRACTURE CONDUCTIVITY / PERMEABILITY RESULTS Ref : COLOR-13.APP

FORMATION / PROPPANT DATA

			DATA BASE REFERENCE
Proppant Type	:	20/40 Sand (old)	COLOR-A.FLO
Supplier	:	Colorado Silica Sand	
Concentration	:	2 lbs/sq.ft.	
Well Number	:	11/30a-A6	SAMPLE13.POR
Depth	:	6820 ft	

FRACTURE CONDUCTIVITY RESULTS

Closure Stress (psi)	Flow Cell Conductivity A-B	B-C	A-C	Fracture Conductivity A-B	B-C	A-C
1000	2.383	2.396	2.549	.480	.483	.514
2000	2.143	1.799	1.972	.444	.373	.409
4000	1.769	1.408	1.607	.407	.324	.370
6000	1.044	.725	.848	.295	.205	.240
8000	.480	.190	.365	.159	.063	.121
10000	.264	.136	.200	.092	.047	.069
12000	*****	*****	*****	*****	*****	*****
14000	*****	*****	*****	*****	*****	*****
15000	*****	*****	*****	*****	*****	*****

FRACTURE PERMEABILITY RESULTS

Closure Stress (psi)	Flow Cell Permeability A-B	B-C	A-C	Fracture Permeability A-B	B-C	A-C
1000	119.2	119.8	127.5	27.8	28.0	29.8
2000	108.2	90.8	99.5	25.8	21.7	23.8
4000	91.5	72.8	83.1	23.9	19.0	21.7
6000	55.8	38.7	45.3	17.4	12.1	14.2
8000	26.7	10.6	20.3	9.5	3.8	7.2
10000	15.2	7.8	11.5	5.6	2.9	4.2
12000	*****	*****	*****	*****	*****	*****
14000	*****	*****	*****	*****	*****	*****
15000	*****	*****	*****	*****	*****	*****

UNITS : Flow Cell / Fracture Conductivity (Darcy*ft)
===== Flow Cell / Fracture Permeability (Darcies)

FRACTURE CONDUCTIVITY / PERMEABILITY RESULTS Ref : INTER-13.APP

FORMATION / PROPPANT DATA

			DATA BASE REFERENCE
Proppant Type	:	20/40 Interprop I	INTER-A.FLO
Supplier	:	Norton	
Concentration	:	2 lbs/sq.ft.	
Well Number	:	11/30a-A6	SAMPLE13.POR
Depth	:	6820 ft	

FRACTURE CONDUCTIVITY RESULTS

Closure Stress (psi)	Flow Cell Conductivity A-B	B-C	A-C	Fracture Conductivity A-B	B-C	A-C
1000	6.534	6.371	6.468	3.058	2.981	3.027
2000	5.714	5.264	5.579	2.516	2.318	2.457
4000	5.106	4.685	4.882	2.179	2.000	2.084
6000	4.555	3.908	4.212	2.158	1.851	1.995
8000	3.991	3.275	3.628	2.145	1.760	1.950
10000	3.073	2.438	2.720	1.972	1.564	1.746
12000	2.629	2.034	2.207	1.825	1.412	1.533
14000	1.969	1.486	1.689	1.487	1.122	1.275
15000	1.659	1.182	1.391	1.360	.968	1.139

FRACTURE PERMEABILITY RESULTS

Closure Stress (psi)	Flow Cell Permeability A-B	B-C	A-C	Fracture Permeability A-B	B-C	A-C
1000	385.6	375.9	381.7	192.2	187.4	190.3
2000	337.4	310.8	329.4	158.2	145.7	154.4
4000	302.8	277.8	289.5	138.9	127.4	132.8
6000	275.0	235.9	254.2	138.0	118.4	127.6
8000	245.5	201.4	223.2	137.5	112.9	125.0
10000	193.4	153.4	171.2	126.5	100.3	112.0
12000	168.4	130.3	141.4	118.1	91.4	99.2
14000	128.0	96.6	109.8	96.7	73.0	83.0
15000	109.5	78.0	91.8	89.0	63.3	74.6

UNITS : Flow Cell / Fracture Conductivity (Darcy*ft)
===== Flow Cell / Fracture Permeability (Darcies)

FORMATION SAMPLE DATA

Well Number : 11/30a-A6
Core Number : 13
Sample Depth : 6841 ft
Box Number : 8
Reference Number : 14 A,B,C

SAMPLE DESCRIPTION

Rock Type : SANDSTONE

Colour : Light brown with thin, black streaks.

Texture : Upper fine grain size (0.2 mm dia.)
Sphericity : 0.9
Roundness : 0.9

Sorting : Very well sorted

Cement : Silica

Matrix : Clay

GENERAL DESCRIPTION

Light brown sandstone with stringers of clay material. The sample displays upper fine sized grains which are of high sphericity, are well rounded and are very well sorted.

ROCK PROPERTIES

Sample Density : 2185 Kg/m^3 (136.44 lb/ft^3)

Embedment Pressure : ****

Brinell Hardness : 24.1

(3.19 mm Indenter)

Units :

Load (kg)
Indentation (mm)
BHN (Kg/mm^2)

Load	Indentation	BHN
0	.0000	**
5	.0187	27
10	.0423	24
15	.0633	24
20	.0853	23
25	.1067	23
30	.1247	24

FRACTURE POROSIMETER RESULTS

Well Number : 11/30a-A6
Depth : 6841 ft

PROPPANT DATA : Ref. 14A

Type/Size : 20/40 Sintered Bauxite
Supplier : Norton

Gr. Density : 3.64 g/cc
Roundness : 0.80
Sphericity : 0.78

Sample Wt. : 5.0007 g
Recovery : 100.322 %

Closure Stress	Fracture Width	Proppant Porosity
1000	.1870	41.57
2000	.1847	40.83
4000	.1815	39.79
6000	.1626	32.81
8000	.1784	38.76
10000	.1772	38.36
12000	.1762	38.00
14000	.1749	37.53
15000	.1742	37.29

PROPPANT DATA : Ref. 14B

Type/size : 20/40 Sand
Supplier : Colorado Silica Sand Inc.

Gr. Density : 2.64 g/cc
Roundness : 0.70
Sphericity : 0.69

Sample Wt. : 5.0006 g
Recovery : 99.9920 %

Closure Stress	Fracture Width	Proppant Porosity
1000	.2268	33.57
2000	.2256	33.22
4000	.2239	32.72
6000	.2224	32.26
8000	.2197	31.43
10000	.2158	30.20
12000	*****	*****
14000	*****	*****
15000	*****	*****

PROPPANT DATA : Ref. 14C

Type/size : 20/40 Interprop I
Supplier : Norton

Gr. Density : 3.12 g/cc
Roundness : 0.81
Sphericity : 0.82

Sample Wt. : 5.0003 g
Recovery : 100.196 %

Closure Stress	Fracture Width	Proppant Porosity
1000	.1921	33.66
2000	.1921	33.66
4000	.1904	33.07
6000	.1896	32.77
8000	.1891	32.60
10000	.1886	32.41
12000	.1874	31.99
14000	.1859	31.44
15000	.1852	31.19

TEST UNITS :
Closure Stress (psi)
Fracture Width (in)
Propped Fracture Porosity (%)

FRACTURE CONDUCTIVITY / PERMEABILITY RESULTS Ref : BAUX-14.APP

FORMATION / PROPPANT DATA

			DATA BASE REFERENCE
Proppant Type	:	20/40 Sintered Bauxite	BAUX-A.FLO
Supplier	:	Norton	
Concentration	:	2 lbs/sq.ft.	
Well Number	:	11/30a-A6	SAMPLE14.POR
Depth	:	6841 ft	

FRACTURE CONDUCTIVITY RESULTS

Closure Stress	Flow Cell Conductivity			Fracture Conductivity		
(psi)	A-B	B-C	A-C	A-B	B-C	A-C
1000	4.512	4.330	4.498	5.541	5.317	5.523
2000	3.918	3.768	3.835	4.805	4.620	4.704
4000	3.404	3.241	3.353	4.069	3.875	4.008
6000	3.127	2.843	3.031	3.725	3.387	3.610
8000	2.690	2.577	2.672	3.313	3.174	3.291
10000	2.422	2.191	2.336	3.486	3.154	3.364
12000	2.272	2.073	2.040	3.564	3.252	3.201
14000	2.221	1.900	1.916	3.326	2.846	2.870
15000	2.048	1.795	1.857	3.183	2.790	2.887

FRACTURE PERMEABILITY RESULTS

Closure Stress	Flow Cell Permeability			Fracture Permeability		
(psi)	A-B	B-C	A-C	A-B	B-C	A-C
1000	306.3	294.0	305.3	355.5	341.2	354.4
2000	269.2	258.8	263.5	312.2	300.2	305.6
4000	237.0	225.7	233.5	269.0	256.2	265.0
6000	219.7	199.7	212.9	248.3	225.8	240.7
8000	191.1	183.1	189.9	222.8	213.5	221.4
10000	176.5	159.7	170.3	236.1	213.6	227.8
12000	168.2	153.4	151.0	242.7	221.4	218.0
14000	164.7	140.9	142.1	228.2	195.2	196.9
15000	153.0	134.1	138.8	219.3	192.2	198.9

UNITS : Flow Cell / Fracture Conductivity (Darcy*ft)
===== Flow Cell / Fracture Permeability (Darcies)

FRACTURE CONDUCTIVITY / PERMEABILITY RESULTS Ref : COLOR-14.APP

FORMATION / PROPPANT DATA

			DATA BASE REFERENCE
Proppant Type	:	20/40 Sand (old)	COLOR-A.FLO
Supplier	:	Colorado Silica Sand	
Concentration	:	2 lbs/sq.ft.	
Well Number	:	11/30a-A6	SAMPLE14.POR
Depth	:	6841 ft	

FRACTURE CONDUCTIVITY RESULTS

Closure Stress (psi)	Flow Cell Conductivity A-B	B-C	A-C	Fracture Conductivity A-B	B-C	A-C
1000	2.383	2.396	2.549	1.180	1.186	1.262
2000	2.143	1.799	1.972	1.089	.914	1.002
4000	1.769	1.408	1.607	1.013	.806	.920
6000	1.044	.725	.848	.743	.516	.604
8000	.480	.190	.365	.427	.169	.324
10000	.264	.136	.200	.306	.157	.231
12000	*****	*****	*****	*****	*****	*****
14000	*****	*****	*****	*****	*****	*****
15000	*****	*****	*****	*****	*****	*****

FRACTURE PERMEABILITY RESULTS

Closure Stress (psi)	Flow Cell Permeability A-B	B-C	A-C	Fracture Permeability A-B	B-C	A-C
1000	119.2	119.8	127.5	62.4	62.8	66.8
2000	108.2	90.8	99.5	57.9	48.6	53.3
4000	91.5	72.8	83.1	54.3	43.2	49.3
6000	55.8	38.7	45.3	40.1	27.9	32.6
8000	26.7	10.6	20.3	23.3	9.2	17.7
10000	15.2	7.8	11.5	17.0	8.7	12.8
12000	*****	*****	*****	*****	*****	*****
14000	*****	*****	*****	*****	*****	*****
15000	*****	*****	*****	*****	*****	*****

UNITS : Flow Cell / Fracture Conductivity (Darcy*ft)
===== Flow Cell / Fracture Permeability (Darcies)

FRACTURE CONDUCTIVITY / PERMEABILITY RESULTS Ref : INTER-14.APP

FORMATION / PROPPANT DATA DATA BASE REFERENCE

Proppant Type	:	20/40 Interprop I	INTER-A.FLO
Supplier	:	Norton	
Concentration	:	2 lbs/sq.ft.	
Well Number	:	11/30a-A6	SAMPLE14.POR
Depth	:	6841 ft	

FRACTURE CONDUCTIVITY RESULTS

Closure Stress (psi)	Flow Cell Conductivity A-B	B-C	A-C	Fracture Conductivity A-B	B-C	A-C
1000	6.534	6.371	6.468	3.236	3.155	3.203
2000	5.714	5.264	5.579	2.839	2.615	2.772
4000	5.106	4.685	4.882	2.426	2.226	2.319
6000	4.555	3.908	4.212	2.384	2.046	2.204
8000	3.991	3.275	3.628	2.373	1.947	2.157
10000	3.073	2.438	2.720	2.159	1.712	1.911
12000	2.629	2.034	2.207	2.025	1.567	1.700
14000	1.969	1.486	1.689	1.612	1.217	1.383
15000	1.659	1.182	1.391	1.502	1.069	1.258

FRACTURE PERMEABILITY RESULTS

Closure Stress (psi)	Flow Cell Permeability A-B	B-C	A-C	Fracture Permeability A-B	B-C	A-C
1000	385.6	375.9	381.7	202.2	197.1	200.1
2000	337.4	310.8	329.4	177.3	163.4	173.1
4000	302.8	277.8	289.5	152.9	140.3	146.2
6000	275.0	235.9	254.2	150.9	129.5	139.5
8000	245.5	201.4	223.2	150.6	123.6	136.9
10000	193.4	153.4	171.2	137.3	109.0	121.6
12000	168.4	130.3	141.4	129.7	100.3	108.9
14000	128.0	96.6	109.8	104.0	78.5	89.2
15000	109.5	78.0	91.8	97.3	69.3	81.5

UNITS : Flow Cell / Fracture Conductivity (Darcy*ft)
----- Flow Cell / Fracture Permeability (Darcies)

FORMATION SAMPLE DATA

Well Number : 11/30a-A6
Core Number : 13
Sample Depth : 6844 ft
Box Number : 9
Reference Number : 15 A,B,C

SAMPLE DESCRIPTION

Rock Type : SANDSTONE

Colour : Light brown/grey with very fine black stringers.

Texture : Upper fine grain size (0.2 mm dia.)
Sphericity : 0.9
Roundness : 0.9

Sorting : Very well sorted

Cement : Silica

Matrix : Clay

GENERAL DESCRIPTION

Light brown/grey coloured sandstone with very fine, irregular black stringers of clay/shale material. The sandstone is very well sorted, has upper fine sized grains of high sphericity and are well rounded.

ROCK PROPERTIES

Sample Density : 2200.33 Kg/m^3 (138.59 lb/ft^3)

Embedment Pressure : ****

Brinell Hardness : 29.4

(3.19 mm Indenter)

Units :

Load (kg)
Indentation (mm)
BHN (Kg/mm^2)

Load	Indentation	BHN
0	.0000	**
5	.0177	28
10	.0347	29
15	.0510	29
20	.0670	30
25	.0833	30
30	.0980	31

FRACTURE POROSIMETER RESULTS

Well Number : 11/30a-A6
Depth : 6844 ft

PROPPANT DATA : Ref. 15A

Type/Size : 20/40 Sintered Bauxite
Supplier : Norton

Gr. Density : 3.64 g/cc
Roundness : 0.80
Sphericity : 0.78

Sample Wt. : 5.0006 g
Recovery : 100.278 %

Closure Stress	Fracture Width	Proppant Porosity
1000	.1638	33.29
2000	.1621	32.60
4000	.1604	31.89
6000	.1591	31.31
8000	.1579	30.80
10000	.1570	30.43
12000	.1552	29.60
14000	.1535	28.83
15000	.1523	28.28

PROPPANT DATA : Ref. 15B

Type/size : 20/40 Sand
Supplier : Colorado Silica Sand Inc.

Gr. Density : 2.64 g/cc
Roundness : 0.70
Sphericity : 0.69

Sample Wt. : 5.0009 g
Recovery : 99.1622 %

Closure Stress	Fracture Width	Proppant Porosity
1000	.2059	26.83
2000	.2042	26.23
4000	.2022	25.49
6000	.2009	25.00
8000	.1963	23.26
10000	.1921	21.58
12000	*****	*****
14000	*****	*****
15000	*****	*****

PROPPANT DATA : Ref. 15C

Type/size : 20/40 Interprop I
Supplier : Norton

Gr. Density : 3.12 g/cc
Roundness : 0.81
Sphericity : 0.82

Sample Wt. : 5.0001 g
Recovery : 100.200 %

Closure Stress	Fracture Width	Proppant Porosity
1000	.1917	33.52
2000	.1902	33.00
4000	.1889	32.52
6000	.1884	32.34
8000	.1877	32.09
10000	.1872	31.91
12000	.1862	31.54
14000	.1850	31.11
15000	.1840	30.73

TEST UNITS :
Closure Stress (psi)
Fracture Width (in)
Propped Fracture Porosity (%)

FRACTURE CONDUCTIVITY / PERMEABILITY RESULTS Ref : BAUX-15.APP

FORMATION / PROPPANT DATA			DATA BASE REFERENCE
Proppant Type	:	20/40 Sintered Bauxite	BAUX-A.FLO
Supplier	:	Norton	
Concentration	:	2 lbs/sq.ft.	
Well Number	:	11/30a-A6	SAMPLE15.POR
Depth	:	6844 ft	

FRACTURE CONDUCTIVITY RESULTS

Closure Stress (psi)	Flow Cell Conductivity A-B	B-C	A-C	Fracture Conductivity A-B	B-C	A-C
1000	4.512	4.330	4.498	1.912	1.835	1.906
2000	3.918	3.768	3.835	1.654	1.591	1.619
4000	3.404	3.241	3.353	1.447	1.378	1.425
6000	3.127	2.843	3.031	1.314	1.195	1.274
8000	2.690	2.577	2.672	1.152	1.104	1.145
10000	2.422	2.191	2.336	1.211	1.095	1.168
12000	2.272	2.073	2.040	1.151	1.050	1.033
14000	2.221	1.900	1.916	1.020	.872	.880
15000	2.048	1.795	1.857	.928	.814	.842

FRACTURE PERMEABILITY RESULTS

Closure Stress (psi)	Flow Cell Permeability A-B	B-C	A-C	Fracture Permeability A-B	B-C	A-C
1000	306.3	294.0	305.3	140.1	134.4	139.6
2000	269.2	258.8	263.5	122.5	117.8	119.9
4000	237.0	225.7	233.5	108.2	103.1	106.6
6000	219.7	199.7	212.9	99.1	90.1	96.1
8000	191.1	183.1	189.9	87.6	83.9	87.0
10000	176.5	159.7	170.3	92.5	83.7	89.3
12000	168.2	153.4	151.0	89.0	81.2	79.9
14000	164.7	140.9	142.1	79.7	68.2	68.8
15000	153.0	134.1	138.8	73.1	64.1	66.3

UNITS : Flow Cell / Fracture Conductivity (Darcy*ft)
===== Flow Cell / Fracture Permeability (Darcies)

FRACTURE CONDUCTIVITY / PERMEABILITY RESULTS Ref : COLOR-15.APP

FORMATION / PROPPANT DATA | DATA BASE REFERENCE

Proppant Type	:	20/40 Sand (old)	COLOR-A.FLO
Supplier	:	Colorado Silica Sand	
Concentration	:	2 lbs/sq.ft.	
Well Number	:	11/30a-A6	SAMPLE15.POR
Depth	:	6844 ft	

FRACTURE CONDUCTIVITY RESULTS

Closure Stress (psi)	Flow Cell Conductivity A-B	B-C	A-C	Fracture Conductivity A-B	B-C	A-C
1000	2.383	2.396	2.549	.451	.453	.482
2000	2.143	1.799	1.972	.398	.334	.366
4000	1.769	1.408	1.607	.353	.281	.320
6000	1.044	.725	.848	.255	.177	.207
8000	.480	.190	.365	.123	.049	.094
10000	.264	.136	.200	.069	.036	.052
12000	*****	*****	*****	*****	*****	*****
14000	*****	*****	*****	*****	*****	*****
15000	*****	*****	*****	*****	*****	*****

FRACTURE PERMEABILITY RESULTS

Closure Stress (psi)	Flow Cell Permeability A-B	B-C	A-C	Fracture Permeability A-B	B-C	A-C
1000	119.2	119.8	127.5	26.3	26.4	28.1
2000	108.2	90.8	99.5	23.4	19.6	21.5
4000	91.5	72.8	83.1	20.9	16.6	19.0
6000	55.8	38.7	45.3	15.2	10.6	12.4
8000	26.7	10.6	20.3	7.5	3.0	5.7
10000	15.2	7.8	11.5	4.3	2.2	3.3
12000	*****	*****	*****	*****	*****	*****
14000	*****	*****	*****	*****	*****	*****
15000	*****	*****	*****	*****	*****	*****

UNITS : Flow Cell / Fracture Conductivity (Darcy*ft)
===== Flow Cell / Fracture Permeability (Darcies)

FRACTURE CONDUCTIVITY / PERMEABILITY RESULTS Ref : INTER-15.APP

FORMATION / PROPPANT DATA

			DATA BASE REFERENCE
Proppant Type	:	20/40 Interprop I	INTER-A.FLO
Supplier	:	Norton	
Concentration	:	2 lbs/sq.ft.	
Well Number	:	11/30a-A6	SAMPLE15.POR
Depth	:	6844 ft	

FRACTURE CONDUCTIVITY RESULTS

Closure Stress	Flow Cell Conductivity			Fracture Conductivity		
(psi)	A-B	B-C	A-C	A-B	B-C	A-C
1000	6.534	6.371	6.468	2.526	2.463	2.500
2000	5.714	5.264	5.579	2.180	2.008	2.128
4000	5.106	4.685	4.882	1.916	1.758	1.832
6000	4.555	3.908	4.212	1.844	1.582	1.705
8000	3.991	3.275	3.628	1.795	1.473	1.632
10000	3.073	2.438	2.720	1.574	1.249	1.394
12000	2.629	2.034	2.207	1.508	1.167	1.266
14000	1.969	1.486	1.689	1.156	.872	.991
15000	1.659	1.182	1.391	1.022	.727	.856

FRACTURE PERMEABILITY RESULTS

Closure Stress	Flow Cell Permeability			Fracture Permeability		
(psi)	A-B	B-C	A-C	A-B	B-C	A-C
1000	385.6	375.9	381.7	162.1	158.0	160.4
2000	337.4	310.8	329.4	140.1	129.1	136.8
4000	302.8	277.8	289.5	123.8	113.6	118.4
6000	275.0	235.9	254.2	119.9	102.9	110.9
8000	245.5	201.4	223.2	117.3	96.3	106.7
10000	193.4	153.4	171.2	103.5	82.1	91.6
12000	168.4	130.3	141.4	99.5	77.0	83.6
14000	128.0	96.6	109.8	77.1	58.2	66.2
15000	109.5	78.0	91.8	68.8	49.0	57.6

UNITS : Flow Cell / Fracture Conductivity (Darcy*ft)
===== Flow Cell / Fracture Permeability (Darcies)

FORMATION SAMPLE DATA

Well Number : 11/30a-A6
Core Number : 14
Sample Depth : 6855 ft
Box Number : 3
Reference Number : 16 A,B,C

SAMPLE DESCRIPTION

Rock Type : SANDSTONE

Colour : Medium brown with black and light grey specks.

Texture : Lower medium grain size (0.3 mm dia.)
Sphericity : 0.7
Roundness : 0.7

Sorting : Well sorted

Cement : Silica

Matrix : Clay

GENERAL DESCRIPTION

Medium brown coloured sandstone with black and light grey specles. The sandstone displays a lower medium grain size, which are of moderate sphericity and roundness, and are well sorted.

ROCK PROPERTIES

Sample Density : 2211.46 Kg/m^3 (138.03 lb/ft^3)

Embedment Pressure : ****

Brinell Hardness : 30.4

(3.19 mm Indenter) Units :

Load (kg)
Indentation (mm)
BHN (Kg/mm^2)

Load	Indentation	BHN
0	.0000	**
5	.0147	34
10	.0473	21
15	.0463	32
20	.0633	32
25	.0787	32
30	.0947	32

FRACTURE POROSIMETER RESULTS

Well Number : 11/30a-A6
Depth : 6855 ft

PROPPANT DATA : Ref. 16A

Type/Size : 20/40 Sintered Bauxite
Supplier : Norton

Gr. Density : 3.64 g/cc
Roundness : 0.80
Sphericity : 0.78

Sample Wt. : 5.001 g
Recovery : 100.274 %

Closure Stress	Fracture Width	Proppant Porosity
1000	.1618	32.47
2000	.1608	32.05
4000	.1593	31.40
6000	.1586	31.11
8000	.1581	30.89
10000	.1578	30.74
12000	.1573	30.52
14000	.1568	30.30
15000	.1566	30.22

PROPPANT DATA : Ref. 16B

Type/size : 20/40 Sand
Supplier : Colorado Silica Sand Inc.

Gr. Density : 2.64 g/cc
Roundness : 0.70
Sphericity : 0.69

Sample Wt. : 5.0002 g
Recovery : 98.9140 %

Closure Stress	Fracture Width	Proppant Porosity
1000	.2248	32.99
2000	.2236	32.64
4000	.2224	32.28
6000	.2199	31.51
8000	.2161	30.28
10000	.2115	28.78
12000	*****	*****
14000	*****	*****
15000	*****	*****

PROPPANT DATA : Ref. 16C

Type/size : 20/40 Interprop I
Supplier : Norton

Gr. Density : 3.12 g/cc
Roundness : 0.81
Sphericity : 0.82

Sample Wt. : 5.0008 g
Recovery : 100.034 %

Closure Stress	Fracture Width	Proppant Porosity
1000	.1972	35.37
2000	.1959	34.93
4000	.1947	34.54
6000	.1939	34.25
8000	.1925	33.79
10000	.1920	33.62
12000	.1914	33.38
14000	.1905	33.09
15000	.1895	32.73

TEST UNITS :
Closure Stress (psi)
Fracture Width (in)
Propped Fracture Porosity (%)

FRACTURE CONDUCTIVITY / PERMEABILITY RESULTS Ref : BAUX-16.APP

FORMATION / PROPPANT DATA			DATA BASE REFERENCE
Proppant Type	:	20/40 Sintered Bauxite	BAUX-A.FLO
Supplier	:	Norton	
Concentration	:	2 lbs/sq.ft.	
Well Number	:	11/30a-A6	SAMPLE16.POR
Depth	:	6855 ft	

FRACTURE CONDUCTIVITY RESULTS

Closure Stress (psi)	Flow Cell Conductivity A-B	B-C	A-C	Fracture Conductivity A-B	B-C	A-C
1000	4.512	4.330	4.498	1.710	1.641	1.705
2000	3.918	3.768	3.835	1.534	1.475	1.502
4000	3.404	3.241	3.353	1.352	1.288	1.332
6000	3.127	2.843	3.031	1.278	1.162	1.239
8000	2.690	2.577	2.672	1.167	1.118	1.159
10000	2.422	2.191	2.336	1.266	1.145	1.221
12000	2.272	2.073	2.040	1.313	1.198	1.179
14000	2.221	1.900	1.916	1.261	1.078	1.088
15000	2.048	1.795	1.857	1.230	1.078	1.115

FRACTURE PERMEABILITY RESULTS

Closure Stress (psi)	Flow Cell Permeability A-B	B-C	A-C	Fracture Permeability A-B	B-C	A-C
1000	306.3	294.0	305.3	126.8	121.7	126.4
2000	269.2	258.8	263.5	114.5	110.1	112.1
4000	237.0	225.7	233.5	101.9	97.0	100.3
6000	219.7	199.7	212.9	96.7	87.9	93.7
8000	191.1	183.1	189.9	88.6	84.9	88.0
10000	176.5	159.7	170.3	96.2	87.1	92.8
12000	168.2	153.4	151.0	100.1	91.4	89.9
14000	164.7	140.9	142.1	96.5	82.5	83.2
15000	153.0	134.1	138.8	94.3	82.6	85.5

UNITS : Flow Cell / Fracture Conductivity (Darcy*ft)
===== Flow Cell / Fracture Permeability (Darcies)

FRACTURE CONDUCTIVITY / PERMEABILITY RESULTS Ref : COLOR-16.APP

FORMATION / PROPPANT DATA

DATA BASE REFERENCE

Proppant Type	:	20/40 Sand (old)	COLOR-A.FLO
Supplier	:	Colorado Silica Sand	
Concentration	:	2 lbs/sq.ft.	
Well Number	:	11/30a-A6	SAMPLE16.POR
Depth	:	6855 ft	

FRACTURE CONDUCTIVITY RESULTS

Closure Stress (psi)	Flow Cell Conductivity A-B	B-C	A-C	Fracture Conductivity A-B	B-C	A-C
1000	2.383	2.396	2.549	1.091	1.097	1.167
2000	2.143	1.799	1.972	1.006	.844	.926
4000	1.769	1.408	1.607	.953	.759	.866
6000	1.044	.725	.848	.670	.465	.544
8000	.480	.190	.365	.363	.144	.276
10000	.264	.136	.200	.219	.113	.166
12000	*****	*****	*****	*****	*****	*****
14000	*****	*****	*****	*****	*****	*****
15000	*****	*****	*****	*****	*****	*****

FRACTURE PERMEABILITY RESULTS

Closure Stress (psi)	Flow Cell Permeability A-B	B-C	A-C	Fracture Permeability A-B	B-C	A-C
1000	119.2	119.8	127.5	58.2	58.5	62.3
2000	108.2	90.8	99.5	54.0	45.3	49.7
4000	91.5	72.8	83.1	51.4	40.9	46.7
6000	55.8	38.7	45.3	36.6	25.4	29.7
8000	26.7	10.6	20.3	20.2	8.0	15.3
10000	15.2	7.8	11.5	12.4	6.4	9.4
12000	*****	*****	*****	*****	*****	*****
14000	*****	*****	*****	*****	*****	*****
15000	*****	*****	*****	*****	*****	*****

UNITS : Flow Cell / Fracture Conductivity (Darcy*ft)
===== Flow Cell / Fracture Permeability (Darcies)

FRACTURE CONDUCTIVITY / PERMEABILITY RESULTS Ref : INTER-16.APP

FORMATION / PROPPANT DATA | DATA BASE REFERENCE

Proppant Type	:	20/40 Interprop I	INTER-A.FLO
Supplier	:	Norton	
Concentration	:	2 lbs/sq.ft.	
Well Number	:	11/30a-A6	SAMPLE16.POR
Depth	:	6855 ft	

FRACTURE CONDUCTIVITY RESULTS

Closure Stress (psi)	Flow Cell Conductivity A-B	B-C	A-C	Fracture Conductivity A-B	B-C	A-C
1000	6.534	6.371	6.468	4.061	3.959	4.020
2000	5.714	5.264	5.579	3.363	3.098	3.283
4000	5.106	4.685	4.882	2.955	2.711	2.825
6000	4.555	3.908	4.212	2.911	2.497	2.691
8000	3.991	3.275	3.628	2.788	2.287	2.534
10000	3.073	2.438	2.720	2.543	2.018	2.251
12000	2.629	2.034	2.207	2.449	1.895	2.056
14000	1.969	1.486	1.689	2.022	1.526	1.734
15000	1.659	1.182	1.391	1.858	1.323	1.557

FRACTURE PERMEABILITY RESULTS

Closure Stress (psi)	Flow Cell Permeability A-B	B-C	A-C	Fracture Permeability A-B	B-C	A-C
1000	385.6	375.9	381.7	247.1	240.9	244.6
2000	337.4	310.8	329.4	206.0	189.8	201.1
4000	302.8	277.8	289.5	182.1	167.1	174.1
6000	275.0	235.9	254.2	180.1	154.5	166.5
8000	245.5	201.4	223.2	173.8	142.6	158.0
10000	193.4	153.4	171.2	158.9	126.1	140.7
12000	168.4	130.3	141.4	153.5	118.8	128.9
14000	128.0	96.6	109.8	127.4	96.1	109.2
15000	109.5	78.0	91.8	117.6	83.8	98.6

UNITS : Flow Cell / Fracture Conductivity (Darcy*ft)
===== Flow Cell / Fracture Permeability (Darcies)